Second International Symposium on Magnetic Suspension Technology

Edited by
Nelson J. Groom and Colin P. Britcher

Second International Symposium on Magnetic Suspension Technology

Edited by
Nelson J. Groom
Langley Research Center • Hampton, Virginia

Colin P. Britcher
Old Dominion University • Norfolk, Virginia

May 1994

INTRODUCTION

The 2nd International Symposium on Magnetic Suspension Technology was held at the Westin Hotel in Seattle, Washington on August 11–13, 1993. The symposium was sponsored by the Spacecraft Controls Branch of the Langley Research Center in coordination with the Office of Advanced Concepts and Technology (OACT) at NASA Headquarters. The symposium was chaired by the following people:

Nelson J. Groom, Chairman
NASA
Langley Research Center
Hampton, VA 23681-0001

Dr. Colin P. Britcher, Technical Program Chairman
Dept. of Aerospace Engineering
Old Dominion University
Norfolk, VA 23529-0247

Virginia B. Marks, Administrative Chairman
NASA
Langley Research Center
Hampton, VA 23681-0001

An international steering committee assisted in selecting and reviewing submitted abstracts and in structuring the symposium sessions. The steering committee consisted of the following people:

Dr. Karl Boden
KFA–IGV
PF–1913
W–5170 Julich
GERMANY

Dr. James Downer
SatCon Technology Corporation
161 First Street
Cambridge, MA 02142–1207
USA

Dr. Michael J. Goodyer
Department of Aeronautics and Astronautics
University of Southampton
Southampton, SO9 5NH
ENGLAND

Dr. Robert A. Kilgore
CES Hampton
P.O. Box 4006
Hampton, VA 23664–0006
USA

Dr. Alexander V. Kuzin
Microprocessor Systems, Electronics and Electrical Engineering
Moscow Aviation–Technological Institute
Petrovka, 27
103737, Moscow, K–31
RUSSIA

Dr. Chin E. Lin
Institute of Aeronautics and Astronautics
National Cheng Kung University
Tainan, Taiwan
REPUBLIC OF CHINA

Dr. Hideo Sawada
Aircraft Aerodynamics Division
National Aerospace Laboratory
7–44–1 Jindaiji–higashi–machi
Chofu
Tokyo 182
JAPAN

Dr. Roland Siegwart
Mecos Traxler AG
Gutstrasse 38
CH–8400 Winterthur
SWITZERLAND

Dr. David L. Trumper
Department of Electrical Engineering
Massachusetts Institute of Technology
Cambridge, MA 02139
USA

The goal of the symposium was to examine the state of technology of all areas of magnetic suspension and to review related recent developments in sensors and control approaches, superconducting magnet technology, and design/implementation practices. The symposium included 18 technical sessions in which a total of 44 papers were presented. The technical sessions covered the areas of bearings, bearing modeling, controls, vibration isolation, micromachines, superconductivity, wind tunnel magnetic suspension systems, magnetically levitated trains (MagLev), rotating machinery and energy storage, and applications. A list of attendees is presented in the Appendix.

The first symposium in this series was held at NASA Langley Research Center, Hampton, Virginia in August 1991. The proceedings of this symposium are available as NASA Conference Publication 3152, Parts 1 and 2.

CONTENTS

PART 1

SESSION 1—Magnetic Bearings
Chairman: Nelson J. Groom, NASA Langley Research Center

SESSION 2—Applications
Chairman: Willard W. Anderson, NASA Langley Research Center

SESSION 3—Maglev
Chairman: Claude R. Keckler, NASA Langley Research Center

SESSION 4—Superconductivity
Chairman: Nelson J. Groom, NASA Langley Research Center

SESSION 5a—Bearings
Chairman: Karl Boden, KFA-IGV

SESSION 5b—Maglev
Chairman: Michael J. Goodyer, University of Southampton

SESSION 6a—Controls
Chairman: Roland Siegwart, MECOS Traxler

SESSION 6b—MSBS
Chairman: Colin P. Britcher, Old Dominion University

SESSION 7a—Bearing Modeling
Chairman: Hideo Sawada, National Aerospace Laboratory

SESSION 7b—Controls
Chairman: Claude R. Keckler, NASA Langley Research Center

PART 2*

SESSION 8—Applications
Chairman: Nelson J. Groom, NASA Langley Research Center

---

*Part 2 is presented under separate cover.

PART 1

Session 1 – Magnetic Bearings

Chairman: Nelson J. Groom
NASA Langley Research Center

AEROSPACE APPLICATIONS OF MAGNETIC BEARINGS

James Downer, James Goldie, Vijay Gondhalekar, and Richard Hockney
SatCon Technology Corporation
Cambridge, Massachusetts

ABSTRACT

Magnetic bearings have traditionally been considered for use in aerospace applications only where performance advantages have been the primary, if not only, consideration. Conventional wisdom has been that magnetic bearings have certain performance advantages which must be traded off against increased weight, volume, electric power consumption, and system complexity. These perceptions have hampered the use of magnetic bearings in many aerospace applications because weight, volume, and power are almost always primary considerations.

This paper will review progress on several active aerospace magnetic bearing programs at SatCon Technology Corporation. The magnetic bearing programs at SatCon cover a broad spectrum of applications including:

(1) a magnetically-suspended spacecraft integrated power and attitude control system (IPACS)
(2) a magnetically-suspended momentum wheel
(3) magnetic bearings for the gas generator rotor of a turboshaft engine
(4) a vibration-attenuating magnetic bearing system for an airborne telescope
(5) magnetic bearings for the compressor of a space-rated heat pump system

The emphasis of these programs is to develop magnetic bearing technologies to the point where magnetic bearings can be truly useful, reliable, and well tested components for the aerospace community.

- SatCon has three current programs involving magnetic bearings, two in fabrication/testing stage, one in final design.

- Usual disadvantages:

    More expensive hardware

    Complicated controller

    Backup bearings

- Usual advantages of magnetic bearings:

    Vibration control

    No lubrication

    High speed

    No wear
        Extended life
        Less heat

THE FREON COMPRESSOR (PHASE II, SDIO)

- Rationale: Heat pump/thermal management system shown to be more efficient in reducing mass and radiation area.

- Goal: Develop with Mainstream Engineering, integrated freon heat pump capable of 5 year lifetime.

- Sensors, actuators, and auxiliary bearings integrated in a small package with a high-speed induction motor.

- Design Specifications:

Operating speed:	24 krpm
Rotor mass:	≈ 5 kg
Overall mass:	15 kg
Required motor output:	7 hp
Rotor 1st flexible mode	> 500 Hz

Environmental conditions:

Temperature Range:	230 K - 400 K

Magnetic bearing loads up to 2 g's + Compressor
Axial load
Components must operate in Freon 113

- **Schematic of system:**

AUXILIARY BEARINGS   PHASE CHANGE CHAMBER

LIP SEALS

MOTOR

RADIAL MAGNETIC BEARINGS

AXIAL MAGNETIC BEARING

HOUSINGS AND IMPELLERS
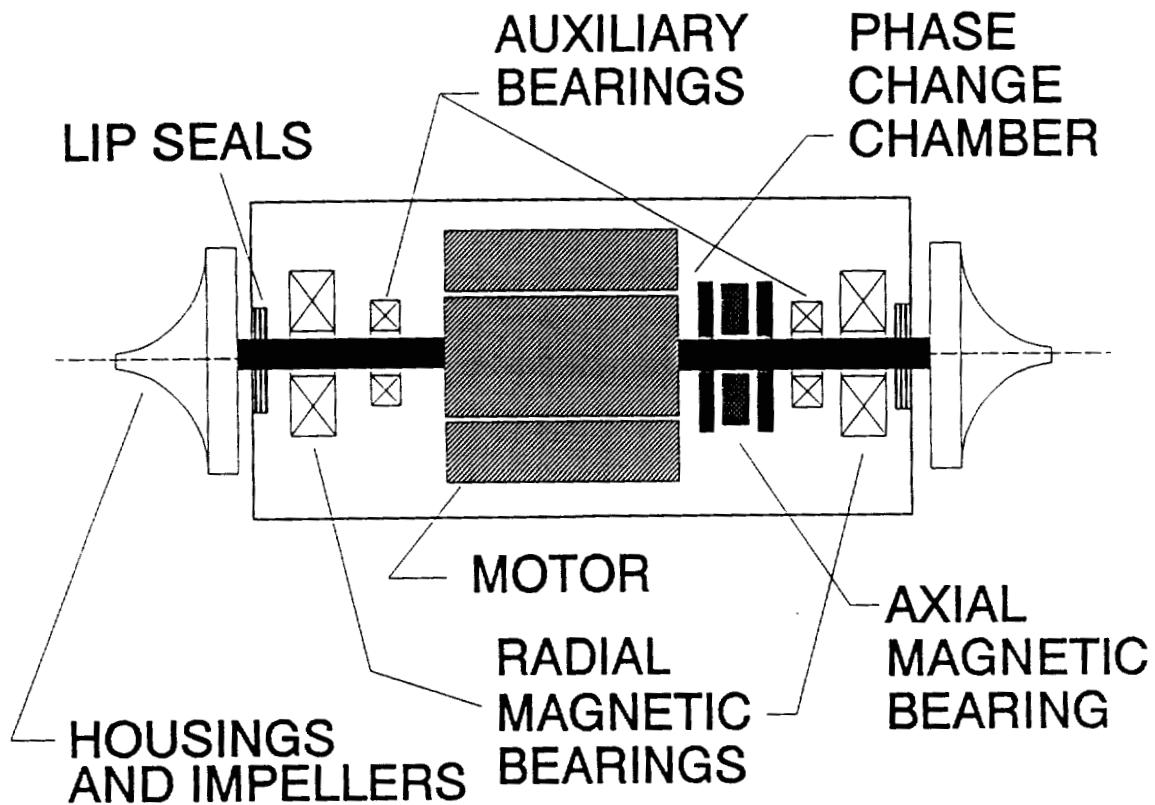
Freon Compressor Schematic

- Two radial bearings and one axial bearing.

- Bearing geometry dictated by flexural consideration.

BEARING ACTUATOR

Radial

- Real time force control requirements: 2 g of shaft acceleration for both the radial and thrust systems and capability of the thrust bearing to compensate the thrust load from the compressor (450 N)

- Separated bias and control coils: reduces power amplifier number to four and single bias supply.
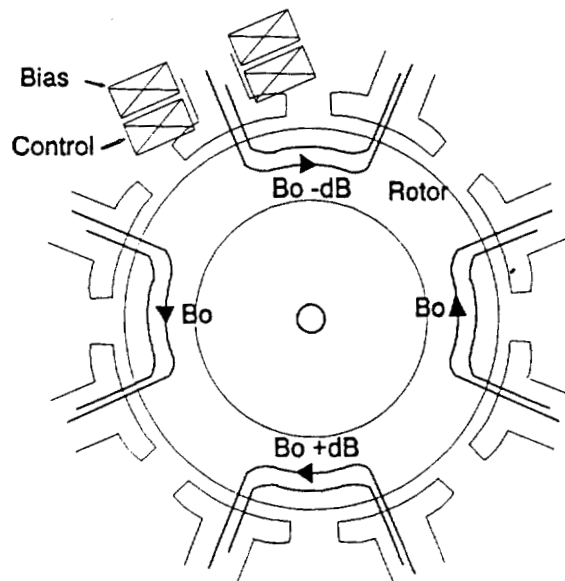
Magnetic configuration of eight pole radial bearing showing flux paths and coil arrangement.

Copper end turns

Laminated Rotor

Insulation

Laminated Rotor
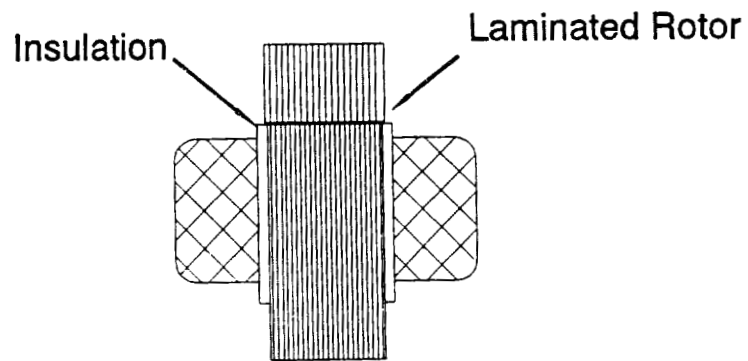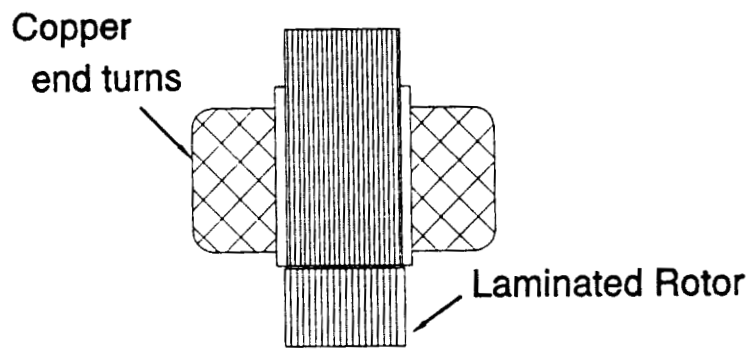
Radial actuator side view to scale.

Thrust

- Require 450 N bi-directional with ±2g superimposed

- Startup requirement mandates ramping capability under closed loop control.

- Geometry: dual rotor/single geometry (fewer components and less V-A capability but greater mass)

- P-M Magnetic Bias.

- Un-laminated. Core losses acceptable.

Control Flux   Bias Flux

S   N   N   S

Control Coils   Rotors

Permanent Magnets   Pole Pieces
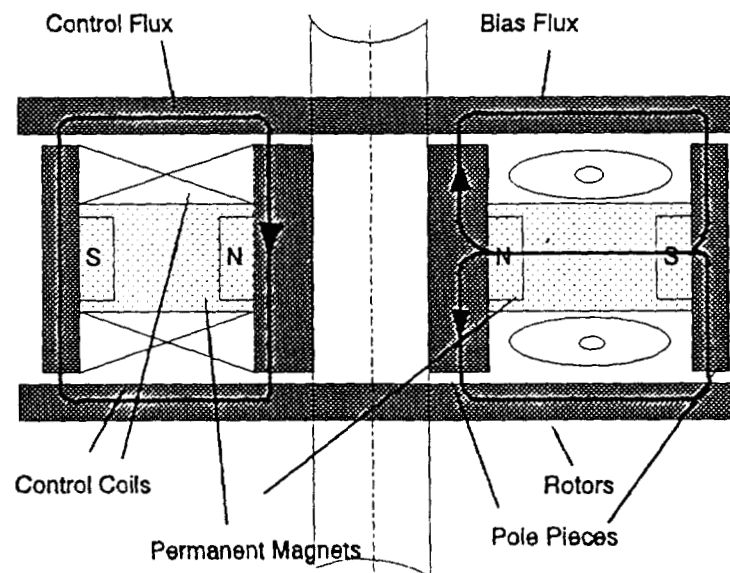
Permanent magnet biased geometry for thrust actuator with flux paths indicated.

Freon Thrust Bearing Phase change — all solid

rho = 5 x 10^-7 ohm-cm

rho = 1 x 10^-7 ohm-cm

Freon Thrust Bearing Current Compliance — all solid

rho = 5 x 10^-7 ohm -cm

rho = 1 x 10^-7 ohm-cm
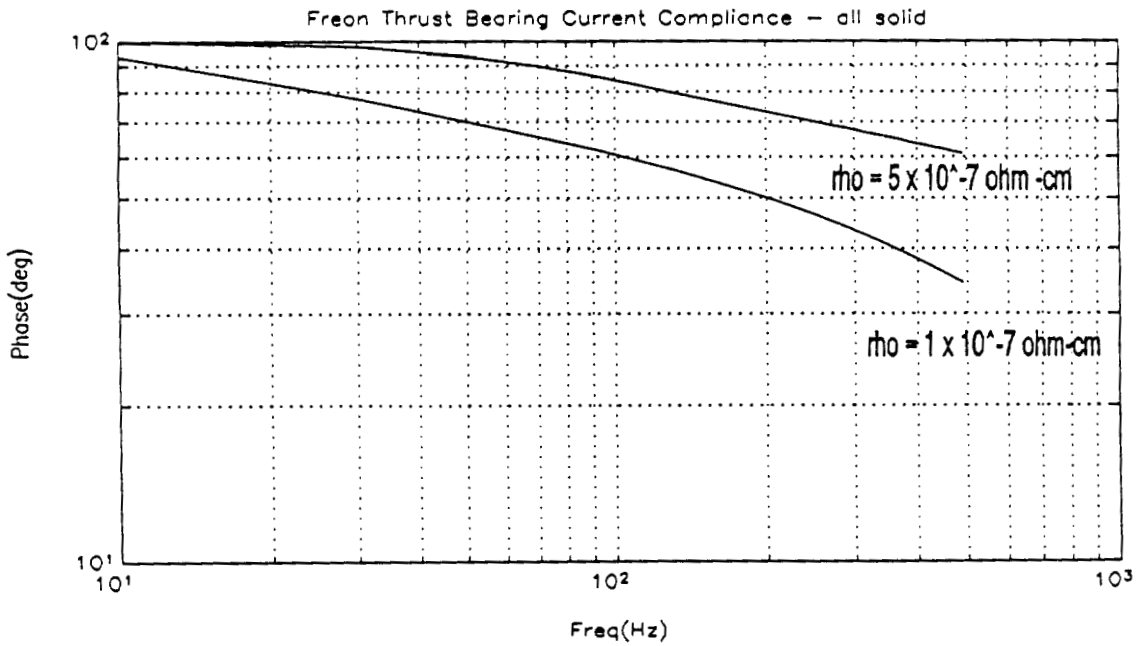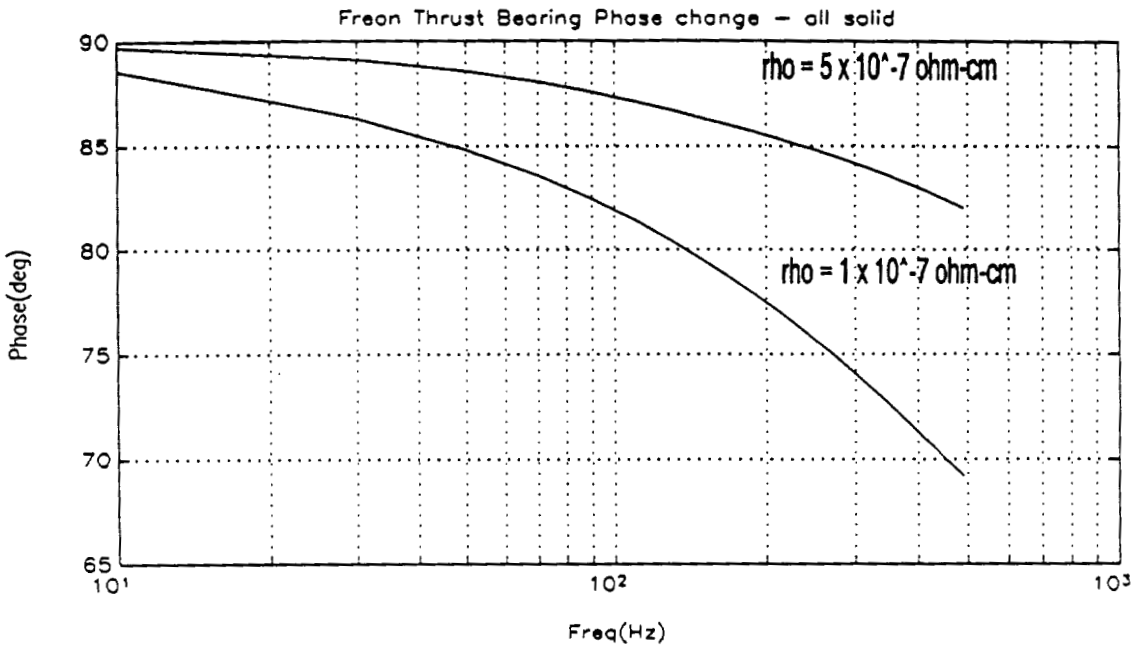
**Phase and compliance as a function of frequency for axial actuator.
The two curves are for different core resistivities.**

- Precision journals on center shaft as targets for the radial inductive sensors.

- Unit is designed to run in zero-g; it must be tested with the shaft oriented both vertically and horizontally.

- Auxiliary Bearings:

  - Momentary support during failures and startup.

  - Two sets of duplex angular contact bearings integrated into the end housings and pre-loaded.

  - Unlubricated, since incompatible with Freon 113
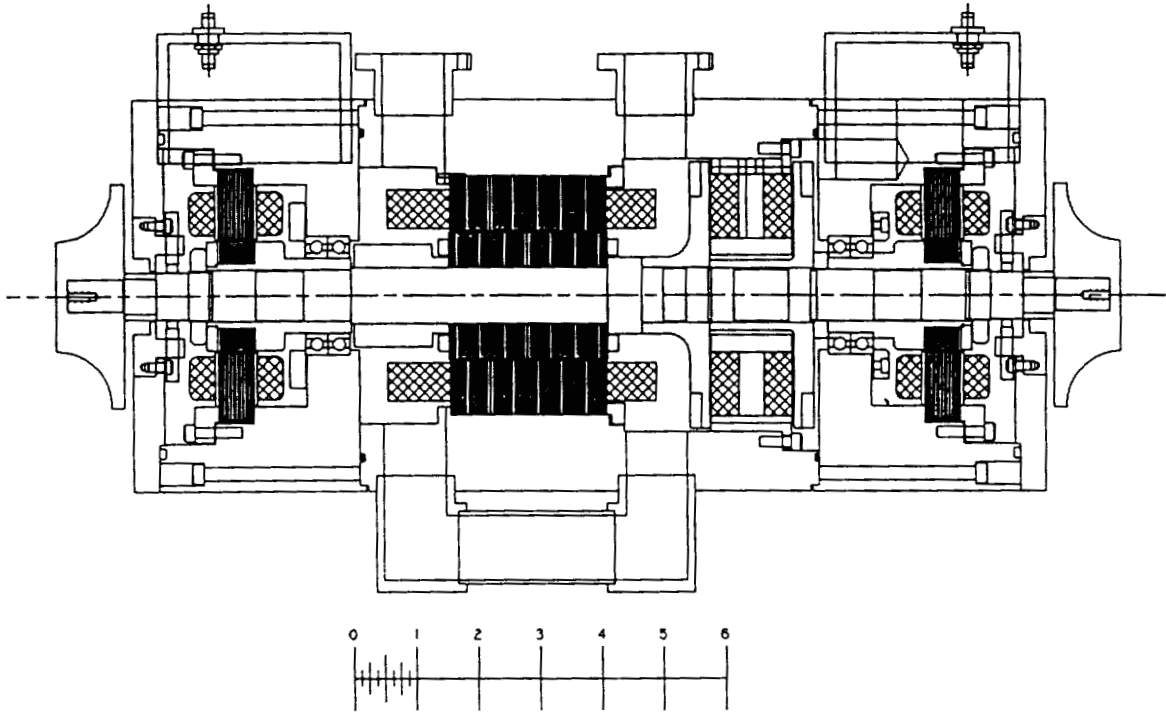
Complete compressor showing positions of magnetic bearing actuators.

Status

- Thrust loop has been closed.

- One directional radial loop shakedown underway, non-zero bias from complementary actuators complicates testing.

- Compressor impellers not yet designed.

MOMENTUM WHEEL (SBIR PHASE II, NASA, GODDARD)

- Rationale: Vibrations of momentum wheel bearings in spacecraft degrade instrument and pointing performance.

- Standard Approaches: Design structure to separate modal from vibrational frequencies, minimize residual mass imbalance, passive isolators.

- Alternately: Use magnetic bearings to eliminate vibrations and mass imbalance by use of bearings with programmable compliance.

- Goals: Design and fabricate magnetically suspended momentum wheel and test for operation in 1g ground experiment.

SPECIFICATIONS

Base line TELDIX DR-68 momentum wheel

Momentum	68 Nms (92.2 ft-lb) at 6000 rpm
Speed range	3500 - 6600 rpm
Inertia	0.1082 kgm^2
Run Up time	19 min (1140 sec)
T_{min} (designed)	0.06 Nm
T_{min} (measured)	0.092 Nm

Critical design criteria for SatCon Momentum Wheel

Nominal op. speed	6000 rpm
Nominal Stored Momentum	68 Nms at 6000 rpm
Motor Peak Torque	0.1 Nm
Maximum bus power available	120 W
Torque for precessing wheel	0.57 Nm

DESIGN ISSUES AND QUALITATIVE GUIDELINES

- **Must operate in 1 g**

- **Spins about inertial axis**

- **Concentrate mass at periphery to maximize inertial**

- **Touchdown bearings fabricated with conventional technology**

- **Magnetics with overcapacity in terms of forcing and torquing**

- **Actuators to utilize large lever arms for precessional torque**

- **Sensor gaps measured at pole faces (collocated).**

Thrust Axis

Radial Magnetic Bearings

Wheel Rim
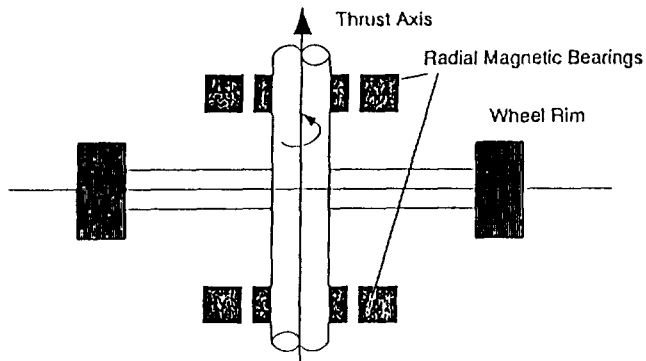
Active Radial Control.   Passive Thrust Control

OPTION A

Thrust Axis

Wheel Rim
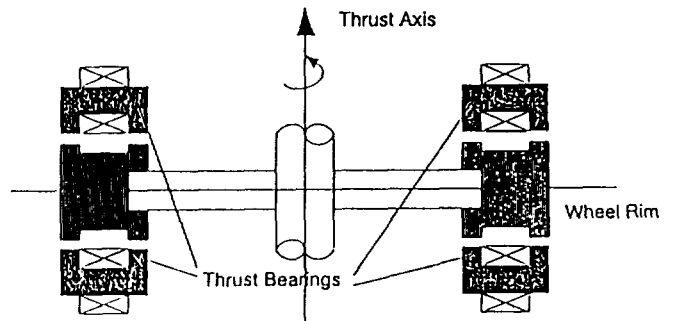
Thrust Bearings

Active Thrust Control.   Passive Radial Control

OPTION B

Radial Bearings

Thrust Axis

Thrust Bearings

OPTION C

Thrust Axis

Radial Magnetic Bearings

Thrust Bearings
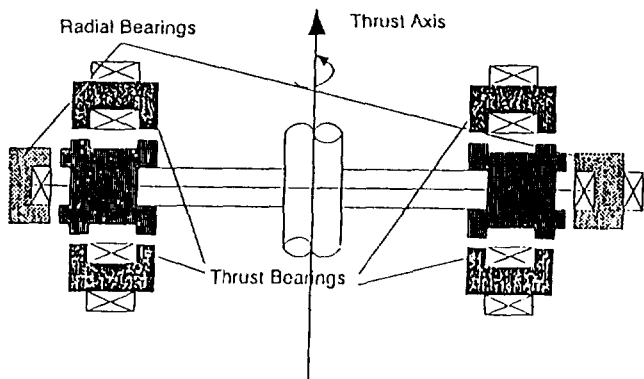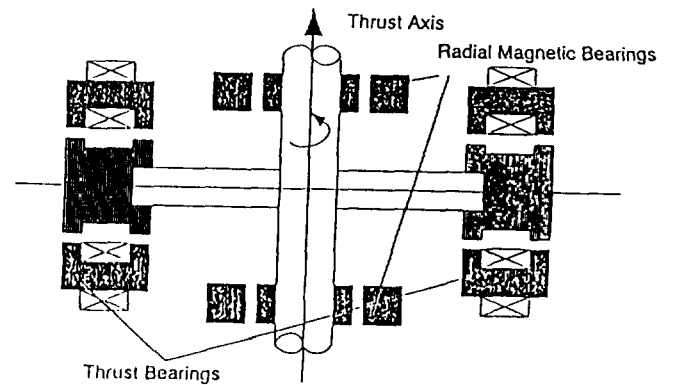
OPTION D

Alternate Magnetic Bearing Actuator Configurations in Momentum Wheel.

ACTUATOR GEOMETRY

- Four bearings at periphery for torques (τ_x, τ_y, and forces F_z)

- Radial bearing at hub (F_x, F_y)

- Non-laminated.

- Drive motor at center of hub

MECHANICAL DESIGN

- Rotor

- Housing structure

- Inertial rings

- Bearing actuators

- Motor drive
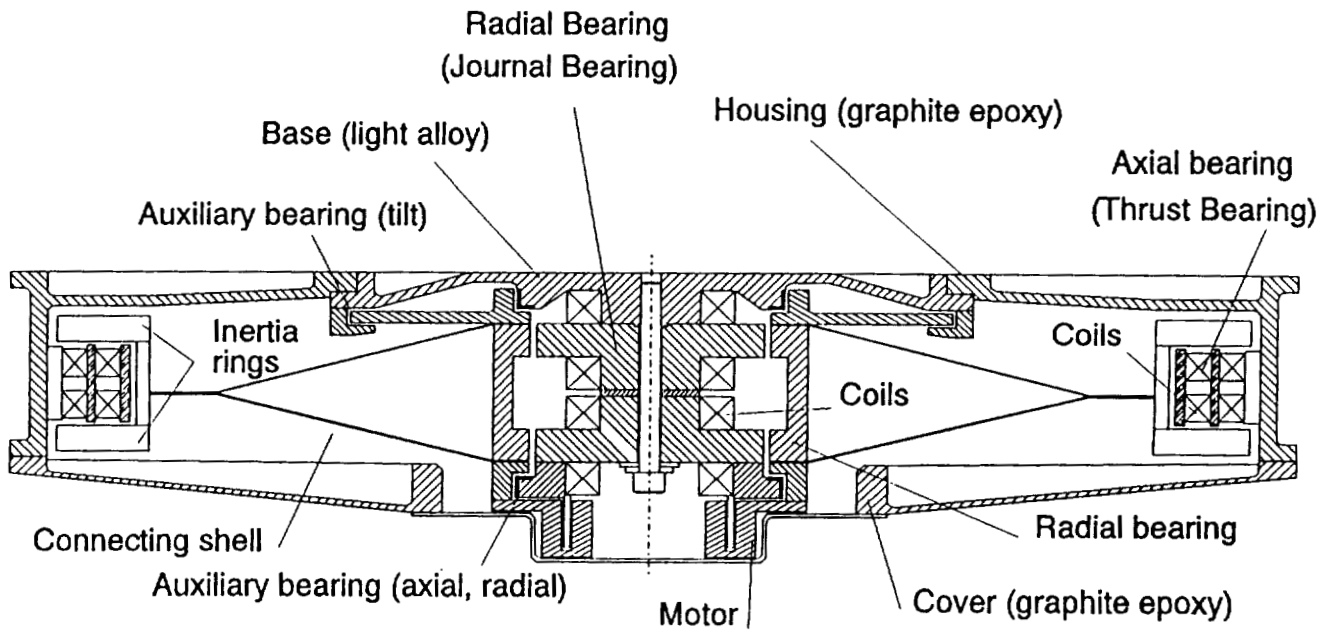
Thrust and radial bearing placement in the low noise momentum wheel design

- **Touchdown surfaces:**
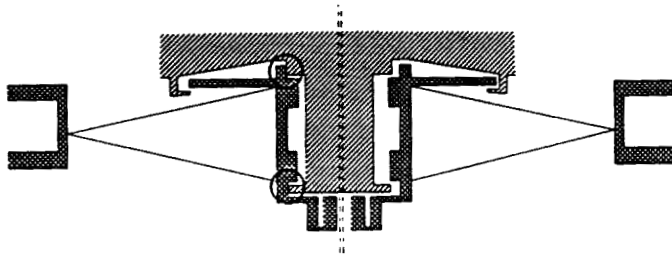
Radial Touchdown
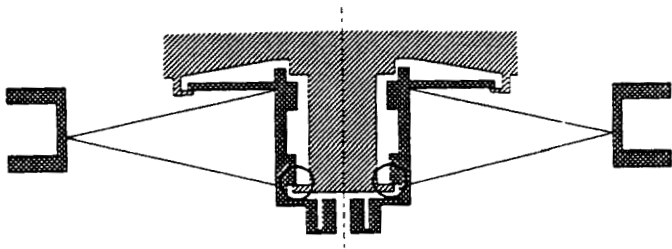
Axial Touchdown
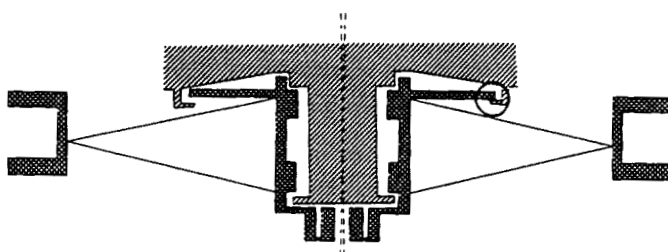
Tilt Touchdown

Auxiliary Bearing Operation
- Use 'Vespel' (DuPont) - dimensional stability, low friction, high
  PV limit.

- **Stress loading at 6000 RPM:**

.018 mm

.042 mm

.03 mm

.026 mm

Deformed and undeformed shapes are overimposed.
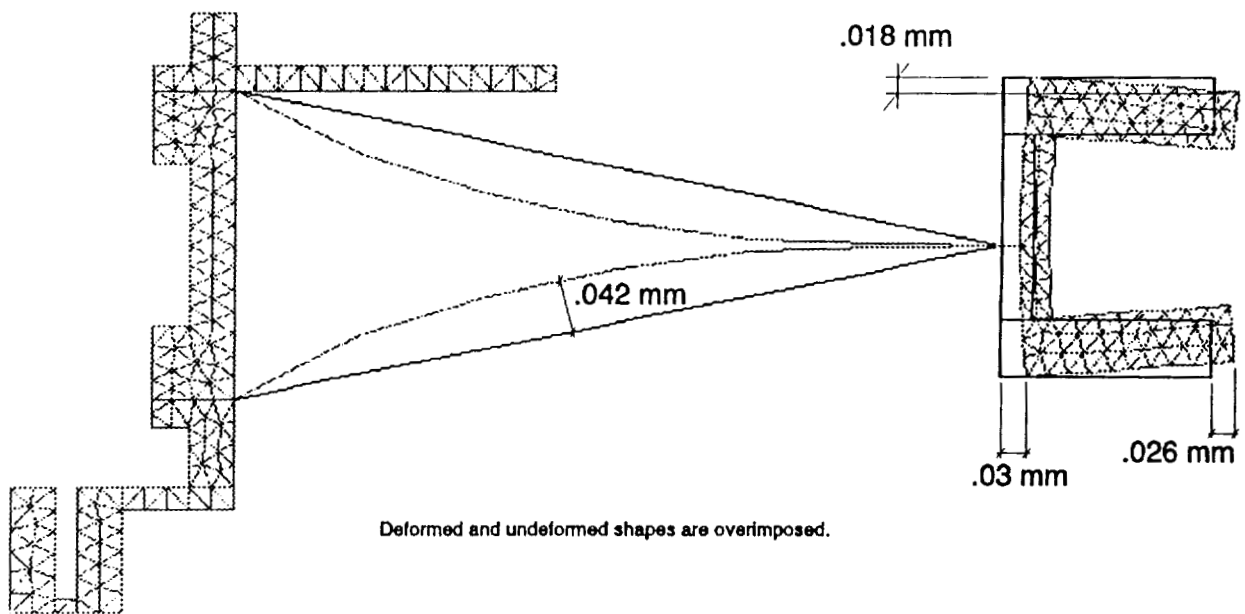
Deformation of the Rotor Under Centrifugal Loading
- **Thrust Sensors Operate in Pairs to Reject Common Mode Signals**

MAGNETICS DESIGN

- **Axial Bearing: 80 N, maximum, 0.6 N-m**

Pole Pieces

Coils

Permanent
Magnet

Momentum Wheel
Backiron

N S
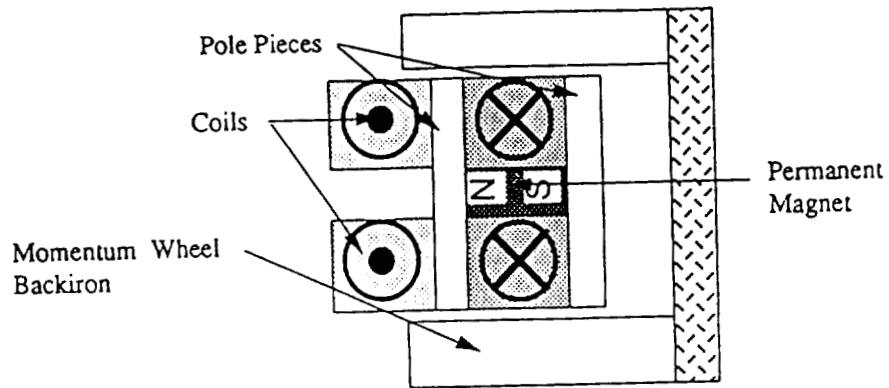
Thrust Actuator Configuration
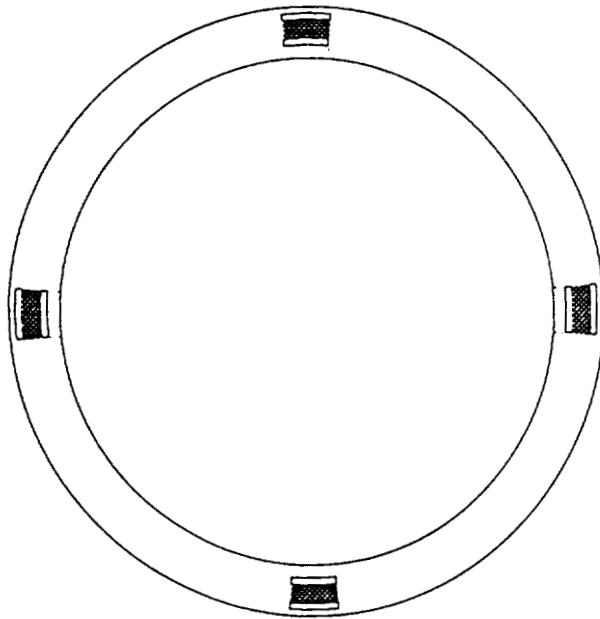
Thrust Actuator Location

- **Radial Bearing Actuator: 80 N max, Bias at .26 T, 400 A-T/coil, Tandem Sets of Four Poles**

Rotating Part

Stationary Pole Face

N

N

S

S

X

Sensor A

Sensor B

Coils
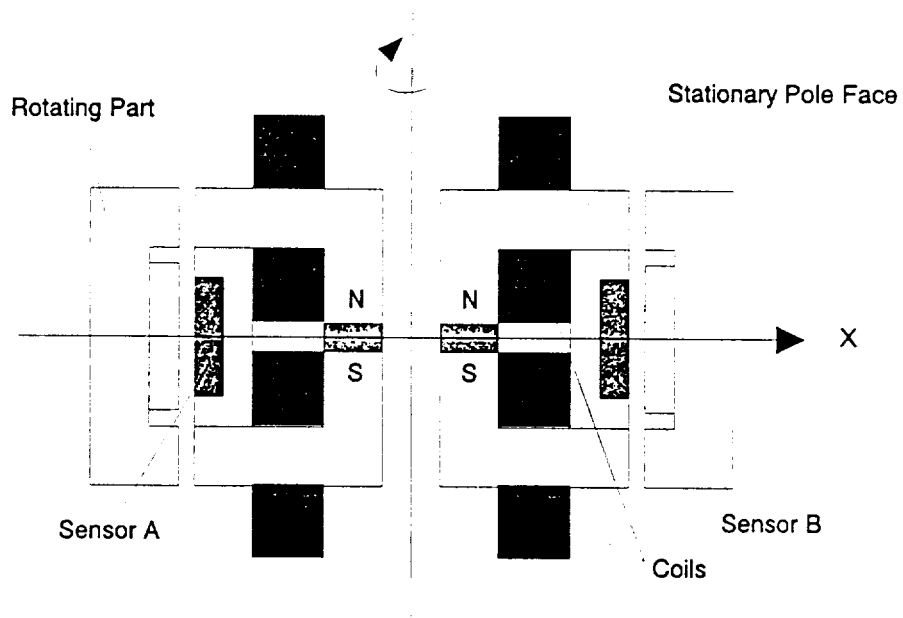
Radial bearing gap measurement with 2 sensor heads

- **Torque Motor: Lorentz Force, 0.1 N/m, 3-phase, Ironless Armature, 4-pole**
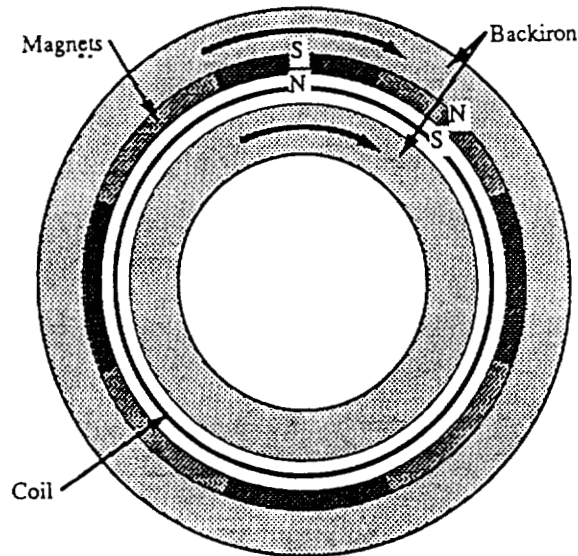
Torque Motor Configuration

CONTROLLER IMPLEMENTATION

- **Designed to compensate for mass unbalance (rotation around mass center vs. geometric center)**

- **Elimination of synchronous disturbances**

CONCLUSIONS

	TELDIX DR-68 Momentum Wheel	SatCon Low Vibration Momentum Wheel
Total Mass	8 Kg	8.3 Kg
Dimensions	350 mm Diameter 120 mm Height	384 mm Diameter 88 mm Height
Steady State Power	< 26.5 Watts	< 10 Watts in 1g < 5 Watts in 0g
Maximum Wheel Precession Rate	-	0.03 rad/sec in 1g 0.08 rad/sec in 0g (min required 7.6×10^{-3})
Torque Vibration at GOES spacecraft mass center	Forces at 6000rpm with 0.75 gm cm residual static imbalance F = 4.7 N Measured at 6000rpm Tx = 7.46 Nm Ty = 6.83 Nm Tz = 7.46 Nm	Forces at 6600 rpm assuming 0.75 gm cm static imbalance F = 0.27 N Simulated including measurement error Tx=Ty=Tz < 0.7 Nm

MAGNETICALLY-SUSPENDED SPACECRAFT INTEGRATED POWER AND ATTITUDE CONTROL SYSTEM (SBIR PHASE II, NASA, MARSHALL).

- Rationale:

  Spacecraft utilizing solar power generation use batteries as energy storage elements.

  Flywheel Storage: Potentially longer operational life-time, lower maintenance requirements, higher energy densities, and peak power capability.

- Goal:

  Integration of all current technology advances into working model.

  Design, build, and evaluate system capable of 2 kW-hr at 40 W-hr/kg and 2 kW and charge/discharge efficiency greater than 85% all in 1 g.

Schematic of Fabricated Device:

- **Actual Geometry:**

combined radial/thrust bearing

auxiliary bearing

motor generator

Sav<u>C</u>on

LAYOUT -
IPACS

1036400

25
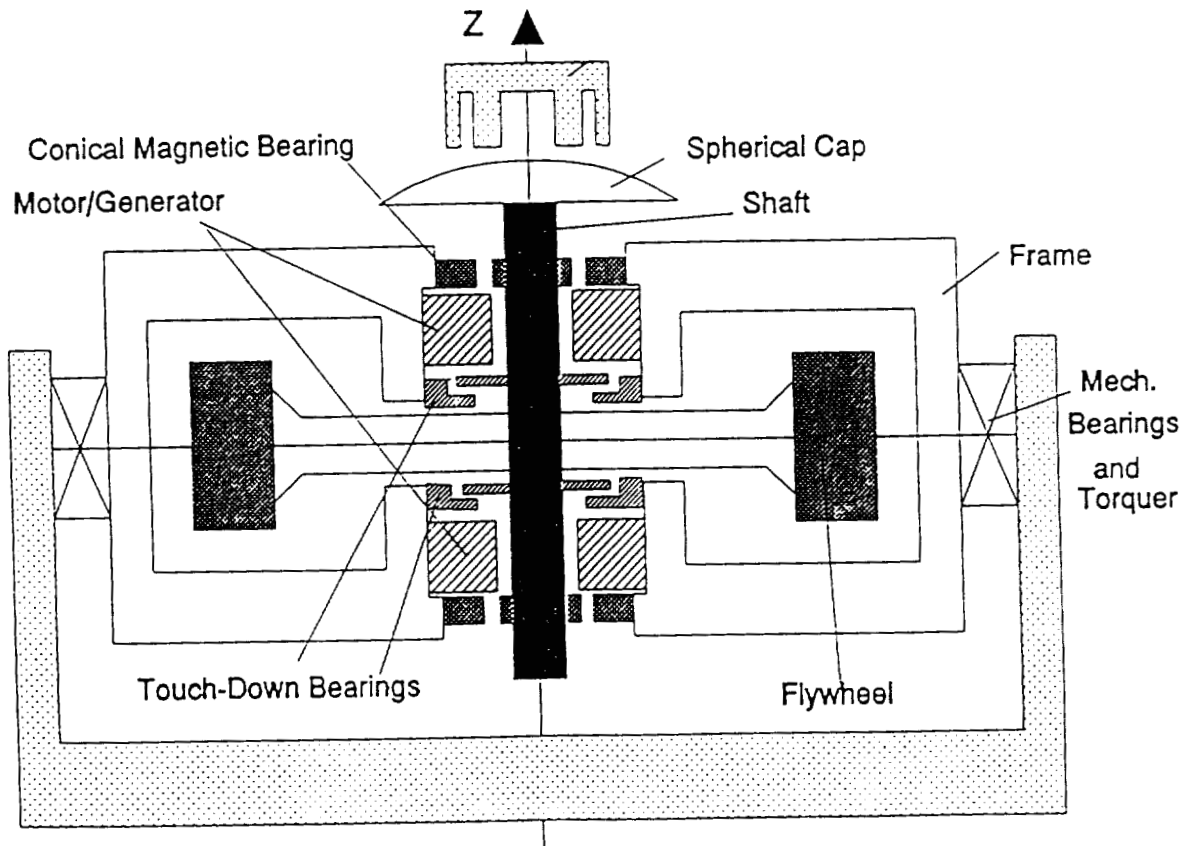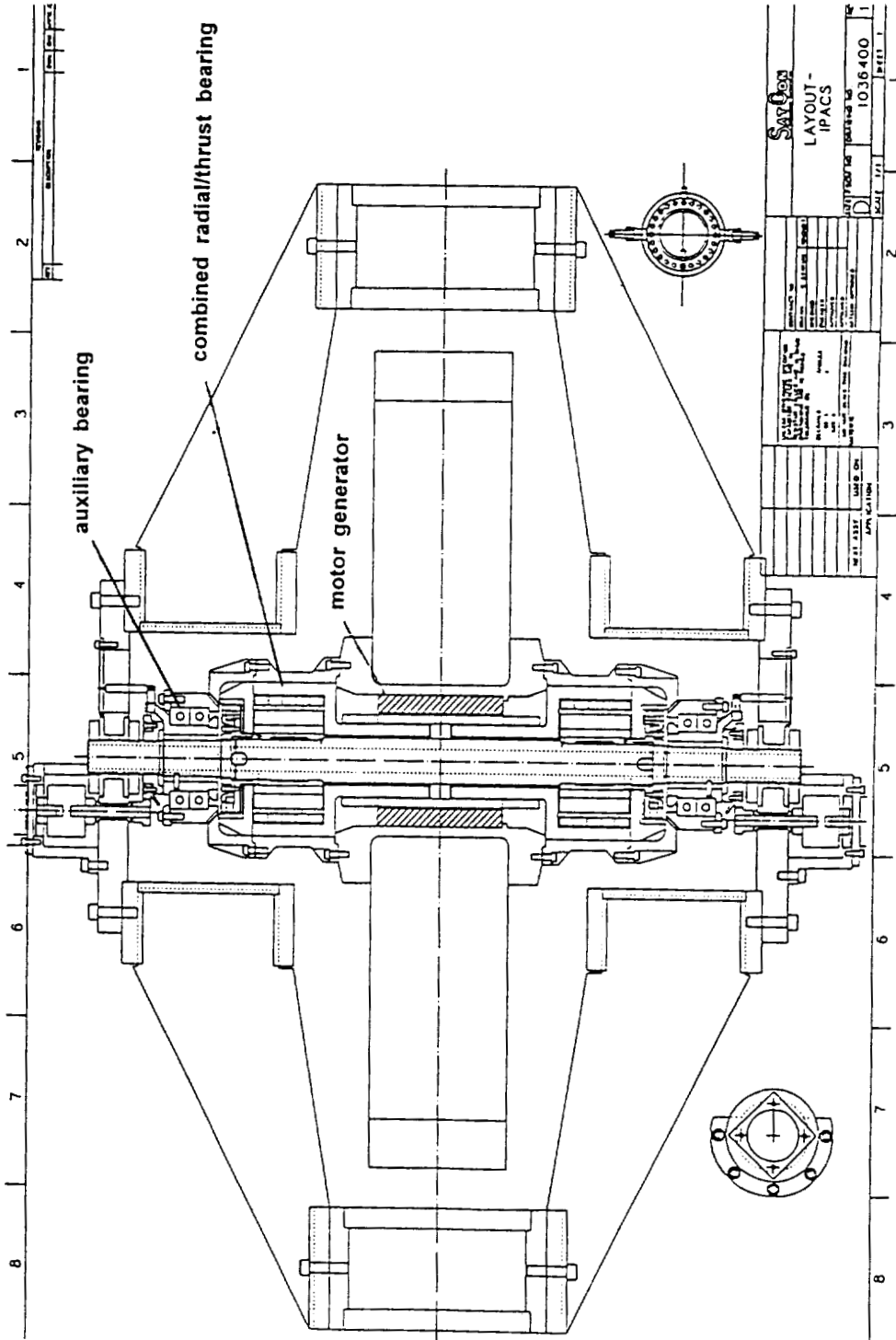
- Status:

  - Assembly complete

  - Ready for testing

  - Instrumentation in progress

Nonlinear Control of Magnetic Bearings

A. K. Pradeep*   R. Gurumoorthy[†]

June 16, 1993

Abstract: *In this paper we present a variety of nonlinear controllers for the magnetic bearing that ensure both stability and robustness. We utilize techniques of discontinuous control to design novel control laws for the magnetic bearing. We present in particular sliding mode controllers, time optimal controllers, winding algorithm based controllers, nested switching controllers, fractional controllers and synchronous switching controllers for the magnetic bearing. We show existence of solutions to systems governed by discontinuous control laws, and prove stability and robustness of the chosen control laws in a rigorous setting. We design sliding mode observers for the magnetic bearing, and prove the convergence of the state estimates to their true values. We present simulation results of the performance of the magnetic bearing subject to the aforementioned control laws, and conclude with comments on design.*

1 Introduction

Magnetic bearings require high precision control systems to ensure adequate stability, stiffness and robustness. Magnetic bearing controllers are typically linear controllers that perform pole placement through state feedback. Nonlinear control techniques on the other hand provide surprisingly simple, yet stable and robust controllers. It is our contention that nonlinearities can be introduced and exploited in a controlled manner to provide significant performance enhancements without increasing the complexity of control. To this end we present the following control techniques and controllers for the magnetic bearing.

- Sliding mode control of magnetic bearings.
- Minimum time control of magnetic bearings.
- Winding algorithm based control of magnetic bearings.
- Nested switching control of magnetic bearings.
- Synchronous control of magnetic bearings.
- Fractional control of magnetic bearings.
- Sliding mode observers for magnetic bearings.

Each of the aforementioned control methodologies utilizes discontinuous control of the magnetic bearing. We show rigorously the existence of solutions to these highly nonlinear systems and prove the stability and convergence of the magnetic bearing system subject to each of these control laws.

The organization of this paper is as follows. In the first section we present the basics of the theory of differential equations with discontinuous righthand sides. The second section presents the dynamical equations of the magnetic bearing. The third section presents the theory, proof and simulation of a sliding mode controller of a magnetic bearing. In the fourth section we present the theory, proof and simulation of a minimum time controller of a magnetic bearing. Section V of this paper presents winding algorithm based control of the magnetic bearing. The sixth section presents the theory, proof and simulation of a nested switching controller of a magnetic bearing and is followed by the synchronous controller in the eighth section. The ninth section of this paper presents a fractional controller and a conjecture pertaining to the stability of the fractional controller. We conclude this paper with a presentation of sliding mode observers in the tenth section. The appendix lists facts and definitions from real analysis useful towards understanding the mathematics presented in this paper.

*Control Systems Laboratory, Corporate Research and Development, General Electric Company. Schenectady NY 12065

[†]Electonics Systems Laboratory, Corporate Research and Development, General Electric Company. Schenectady NY 12065

2 Differential Equations with Discontinuous Righthand Sides

As a prelude we compare and classify ordinary differential equations based on the nature of their right hand sides. Consider a differential equation of the following form.

$$\dot{x} = f(x, t) \tag{1}$$
$$x(0) = x_0 \tag{2}$$
$$x \in \Re^n \ t \in \Re_+ \tag{3}$$
$$f(x, t) : \Re^n \times \Re_+ \to \Re^n \tag{4}$$
$$\tag{5}$$

The smoothness assumptions on $f(x, t)$ determine the kind of differential system referred to by (1).
The three major kinds of differential systems are

1. **Cauchy Differential Systems:** In the domain D of the (x, t) space,

   - $f(x, t) : \Re^n \times \Re_+ \to \Re^n$ is continuous in x.
   - $f(x, t) : \Re^n \times \Re_+ \to \Re^n$ is continuous in t.

2. **Caratheodory Differential Systems:** In the domain D of the (x, t) space,

   - $f(x, t) : \Re^n \times \Re_+ \to \Re^n$ is continuous in x.
   - $f(x, t) : \Re^n \times \Re_+ \to \Re^n$ is discontinuous in t on sets of zero measure.

3. **Filippov Differential Systems:** In the domain D of the (x, t) space,

   - $f(x, t) : \Re^n \times \Re_+ \to \Re^n$ is discontinuous in x and t on sets of zero measure.

The nature of the righthand sides indicates the kinds of solutions (strong or weak) that exist for the differential system. From a control systems engineering standpoint, the use of discontinuous controls necessitates the need for a careful stability analysis owing to the nature of the solutions that exist for such systems.

2.1 Filippov Differential Systems

In this section we will develop solution concepts and conditions for existence of solutions to differential equations with discontinuous right hand sides. Such equations represent physical systems governed by switching behaviours.

Instead of describing solutions for differential equations with discontinuous right hand sides, we will consider differential inclusions which include the said discontinuity as a special case. We will then describe generalized solution concepts for these differential inclusions, and will present conditions for existense of generalized solutions to differential inclusions.

We consider Filippov Differential Systems of the following form.

$$\dot{x} = f(x, t) \tag{6}$$
$$x(t = 0) = x_0 \tag{7}$$
$$x \in \Re^n \ t \in \Re_+ \tag{8}$$
$$f(x, t) : \Re^n \times \Re_+ \to \Re^n \tag{9}$$
$$\tag{10}$$

where in the domain D of the (x, t) space,

- $f(x, t) : \Re^n \times \Re_+ \to \Re^n$ is discontinuous in $x \in D$ on sets of zero measure.
- $f(x, t) : \Re^n \times \Re_+ \to \Re^n$ is discontinuous in $t \in D$ on sets of zero measure.
- $f(x, t) : \Re^n \times \Re_+ \to \Re^n$ is measurable in $t \in D$ for each $x \in D$.
- $\|f(x, t)\| \leq K_f(t) \ \forall \ (x, t) \in D$ where $K_f(t) : \Re_+ \to \Re$ is summable.

The aforementioned conditions on the function $f(x, t) \Re^n \times \Re_+ \to \Re^n$ are also called Filippov conditions.

We will now consider a differential inclusion that adequately describes the discontinuous system. Though the function $f(x, t) : \Re^n \times \Re_+ \to \Re^n$ of equation (6) is undefined on sets of zero measure, we choose instead to represent the function $f(x, t) : \Re^n \times \Re_+ \to \Re^n$ by a set valued map on such sets of zero measure. That is to say, if for instance the function is undefined at a point $(x^*, t^*) \in \Re^n \times \Re_+$, we formally define the function to be set valued at the point (x^*, t^*). Indeed, depending on the set-value attributed to the function at the point (x^*, t^*), we may show the existence of certain generalized solutions to the system (6). To construct the inclusion intelligently, we need some knowledge about the behaviour of the function $f(x, t) : \Re^n \times \Re_+ \to \Re^n$, in a neighbourhood of the point of

discontinuity. To justify the use of the inclusion, we must show that given any arbitrary $\epsilon \in \Re_+$, there exists a small enough $\delta \in \Re_+$ neighbourhood of the point of discontinuity, such that, the trajectories of the differential equation in this δ neighbourhood are ϵ close to the solutions of the differential inclusion. Furthermore, as the size of the set containing the point of discontinuity shrinks to zero, that is $\delta \to 0$, the solutions of the differential equation tend to the solution of the differential inclusion. That is to say, that the trajectories of the differential equation weakly converge to the solution of the differential inclusion. We will say more about this later.

Indeed, given a discontinuous differential system of the form (6), henceforth we will replace it (whenever possible) with a *differential inclusion* of the following form.

$$\dot{x} \quad \in \quad \mathcal{F}(x,t) \tag{11}$$

$$x(t=0) \quad = \quad x_0 \tag{12}$$

$$x \in \Re^n \ t \in \Re_+ \tag{13}$$

$$\mathcal{F}(x,t) : \Re^n \times \Re_+ \to S \in \Re^n \tag{14}$$

$$\tag{15}$$

where S is a set in $\Re^n$ and in the domain D of the (x,t) space,

- the set valued map $\mathcal{F}(x,t) : \Re^n \times \Re_+ \to S \in \Re^n$ is *upper semi-continuous*.
- The $Range[\mathcal{F}(x,t)] \in \Re^n$ is *compact and convex*.

Comment 2.1 The definition of the inclusion $\mathcal{F}(x,t)$ is such that it is single-valued in the domain of continuity of the function $f(x,t)$; indeed it is equal to $f(x,t)$ in the domains of continuity, but is set valued in the domains of discontinuity of $f(x,t)$.

Comment 2.2 It is important to note the properties of the set $S \in \Re^n$ which will be used for the existence of solutions.

We now formally define the solution of a Filippov differential system.

Filippov Solution Concept: *An absolutely continuous vector function $s(t) : \Re_+ \to \Re^n$ is defined to be a Filippov solution of the Filippov differential system (11) if for almost all $t \in D$,*

$$\frac{ds}{dt}\Big|_{t=t^*} \in \mathcal{F}(s(t^*), t^*) \tag{16}$$

where

$$\mathcal{F}(s(t^*), t^*) \quad = \quad f(s(t^*), t^*) \text{ in the domains of continuity} \tag{17}$$

$$\mathcal{F}(s(t^*), t^*) \quad = \quad \bigcap_{\delta>0} \bigcap_{\mu N=0} convex\text{-}hull(B(x,\delta) - N, t) \tag{18}$$

and $\bigcap_{\mu N=0}$ denotes the intersection over all sets N of Lebesgue measure zero where the function $f(x,t)$ is either undefined or discontinuous.

Comment 2.3 In the domains of continuity of $f(x,t) : \Re_+^n \to \Re^n$, the inclusion $\mathcal{F}(x,t)$ is the same as the function and therefore the set operation $\in$ in equation (158) must be replaced with the strict equality $=$

The utility of the Filippov solution concept is that it is indeed the limit of solutions to (6) averaged over neighbourhoods of diminishing size. The key point to be understood is that the Filippov trajectories of the discontinuous system remain close to the true trajectories.

As is evidenced in the proofs of the Cauchy and Caratheodory systems, the method of constructing solutions to differential equations begins by constructing sequences of approximating solutions, and then ensuring that the approximations converge in some sense.

We now state the theorem that guarantees the local existence of Filippov solutions.

Theorem 2.1 *Local Existence Of Filippov Solutions To Filippov Differential Systems*

Given *(G1) A Filippov differential system of the form (11).*

If *(I1) The domain D where $f(x,t)$ is specified for almost all t*
$(x,t) \in \Re^n \times \Re_+ : ||x - x_0|| \le K_x$ and $t \le K_t$

(I2) $f(x,t) : \Re^n \times \Re_+ \to \Re^n$ is measurable in $t \in \Re_+$ for all $x \in \Re^n$

(I3) $||f(x,t)|| \le K_f(t) \ \forall \ (x,t) \in D$ where $K_f(t) : \Re_+ \to \Re$ is summable. Furthermore there exists $K_f \in \Re_+$ such that $K_f > |K_f(t)| \ \forall \ t \in D$

(I4) The differential inclusion in (11), $\mathcal{F}(x,t) : \Re^n \times \Re_+ \to S \in \Re^n$, where S is a set in $\Re^n$ and in the domain D of the (x,t) space satisfies the following two assumptions.

* *the set valued map $\mathcal{F}(x,t) : \Re^n \times \Re_+ \to S \in \Re^n$ is upper semi-continuous.*

* *the set $S \in \Re^n$ is compact and convex.*

Then *(T1) The differential system (11) has at least one Filippov solution $s(t) : \Re_+ \to \Re^n$ for $t \le min(K_t, \frac{K_x}{K_f})$ satisfying the initial condition $s(0) = x_0$.*

3 Dynamic Equations of the Magnetic Bearing

The dynamic equations of the magnetic bearing [RG93] may be written as follows.

$$\begin{bmatrix} \dot{x}_1 \\ \dot{x}_2 \end{bmatrix} = \begin{bmatrix} 0_{4\times4} & I_{4\times4} \\ 0_{4\times4} & A[\omega] \end{bmatrix} \begin{bmatrix} x_1 \\ x_2 \end{bmatrix} + \begin{bmatrix} 0 \\ B \end{bmatrix} u \tag{19}$$

$$y = \begin{bmatrix} I_{4\times4} & 0_{4\times4} \end{bmatrix} \begin{bmatrix} x_1^i \\ x_2^i \end{bmatrix} \tag{20}$$

where,

$$x_1^i \in \Re^4 = \begin{bmatrix} x_1^1 \\ x_1^2 \\ x_1^3 \\ x_1^4 \end{bmatrix} \tag{21}$$

$$x_2^i \in \Re^4 = \begin{bmatrix} x_2^1 \\ x_2^2 \\ x_2^3 \\ x_2^4 \end{bmatrix} \tag{22}$$

$$u \in \Re^4 = \begin{bmatrix} u^1 \\ u^2 \\ u^3 \\ u^4 \end{bmatrix} \tag{23}$$

$$y \in \Re^4 = \begin{bmatrix} y^1 \\ y^2 \\ y^3 \\ y^4 \end{bmatrix} \tag{24}$$

$$A : \Re^+ \to \Re^{4\times4} = \begin{bmatrix} 0 & 0 & 0 & 0 \\ 0 & 0 & 0 & 0 \\ 0 & 0 & 0 & -a\omega \\ 0 & 0 & a\omega & 0 \end{bmatrix} \tag{25}$$

$$I \in \Re^{4\times4} = \begin{bmatrix} 1 & 0 & 0 & 0 \\ 0 & 1 & 0 & 0 \\ 0 & 0 & 1 & 0 \\ 0 & 0 & 0 & 1 \end{bmatrix} \tag{26}$$

$$B \in \Re^{4\times4} = \begin{bmatrix} \frac{1}{m} & \frac{1}{m} & 0 & 0 \\ 0 & 0 & \frac{1}{m} & \frac{1}{m} \\ 0 & 0 & -l_1 & l_2 \\ l_1 & -l_2 & 0 & 0 \end{bmatrix} \tag{27}$$

$$\tag{28}$$

The state variables $x_1 \in \Re^4$ are the generalized positions and rotational angles while the state variables $x_2 \in \Re^4$ are the generalized linear and angular velocities.

Now choose a control law of the following form.

$$u = B^{-1}[-A[\omega]x_2 + v] \tag{29}$$

$$v = \begin{bmatrix} v^1 \\ v^2 \\ v^3 \\ v^4 \end{bmatrix} \tag{30}$$

where the control inputs $v \in \Re^4$ will be specified later. Substituting control law (29) in the dynamical equations (19) - (20), we arrive at the decoupled form of the state equations written as follows.

$$\dot{x}_1^i = x_2^i \tag{31}$$

$$\dot{x}_2^i = v^i \quad i = 1, 2, \ldots, 4 \tag{32}$$

4 Sliding Mode Control of the Magnetic Bearing

In this section, we specialize the theory of discontinuous systems to a special class of systems of the following form.

$$\dot{x} \;=\; f_+(x) \text{ for } [x : s(x) > 0] \tag{33}$$

$$\;=\; f_-(x) \text{ for } [x : s(x) < 0] \tag{34}$$

where $x \in \Re^n$, and $f(x) : \Re^n \to \Re^n$ and $s(x) : \Re^n \to \Re$. Note that $S = \{x : s(x) = 0\}$ is a manifold of dimension $n - 1$. This manifold S is called the *sliding manifold* or *sliding surface*. The dynamics of the system on this manifold S is called the *sliding dynamics* or *sliding modes* of the system. The design of the manifold S is such that it is globally attractive, and trajectories commencing from arbitrary initial conditions reach S in finite time. Furthermore, the dynamics on S achieves the control objective.

Local existence of solutions is verified by modelling the system represented by equations (33) - (34) by the appropriate differential inclusions and verifying whether the inclusion satisfies the hypotheses of the theorem concerning local existence of Filippov solutions.

Uniqueness, in the sense of the Filippov solution is shown if either $\frac{\partial s(x)}{\partial x} f_+(x) < 0$ or $\frac{\partial s(x)}{\partial x} f_-(x) > 0$. This is shown in [SS83], [Fil88], [Fil61]. The physical interpretation of these conditions is simply that the trajectories of the system are always directed towards S, thus rendering it attractive.

Example 4.1

$$\dot{x} \;=\; -ksgn[x] \tag{35}$$

$$sgn[x] \;=\; 1 \text{ if } x > 0 \tag{36}$$

$$sgn[x] \;=\; -1 \text{ if } x < 0 \tag{37}$$

Modelling the system (35) by a simple differential inclusion, we rewrite (35) as

$$\dot{x} \in \mathcal{F}(x) \tag{38}$$

where

$$\mathcal{F}(x) \;=\; sgn[x] \text{ if } x \neq 0 \tag{39}$$

$$\mathcal{F}(x) \;\in\; [-1,1] \text{ if } x = 0 \tag{40}$$

The inclusion in (38) is closed, bounded, convex and uppersemicontinuous and therefore by the theorem on existence of Filippov solutions, Filippov solutions exist for this system.

The sliding modes of a system, defined to be the Filippov solutions to the system on the manifold S, are calculated by performing Filippov averaging, which is a convex combination of dynamics on either side of the manifold S. Indeed, by dynamics on either side of the manifold S, we merely refer to $f_+(x)$ and $f_-(x)$. The simple extension of the notion of sliding manifolds to non-autonomous systems is shown in [SS83].

While the theory of existense of solutions has been developed for general nonlinear systems with discontinuous controls, the methodology to design sliding mode controls to achieve stabilization or tracking is well understood only for a restricted class of systems [SRS91]. In the following sections, we will present the theory for Linear Time Invariant Systems - SISO and MIMO.

4.1   Sliding Mode Design For LTI Systems

Consider linear time invariant systems represented by the following equations

$$\dot{\bar{x}} = A\bar{x} + Bu \tag{41}$$

where $\bar{x} \in \Re^n$, $A \in \Re^{n \times n}$, $B \in \Re^{m \times n}$ and the controls $u \in \Re^m$. We will now prescribe the sliding mode controller design procedure in a sequence of steps.

Step 1.

Check to see if the system is completely controllable. If the system is not completely controllable, a sliding mode controller cannot be designed.

Step 2.

If the system is completely controllable, find a linear transformation of the state that recasts the system in the controllable canonical form. That is find a transformation

$$x = T\bar{x} \quad T \in \Re^{n \times n} \tag{42}$$

such that the state equations are of the form

$$\begin{bmatrix} \dot{x}_1 \\ \vdots \\ \dot{x}_n \end{bmatrix} = \begin{bmatrix} 0 & 1\cdots & & 0 \\ \vdots & \ddots & \ddots & \vdots \\ 0 & 0 & 0 & 1 \\ b_1 & b_2 & \cdots & b_n \end{bmatrix} + \begin{bmatrix} 0 \\ \vdots \\ 0 \\ 1 \end{bmatrix} u \tag{43}$$

Step 3.

We define $S(x) : \Re^n \to \Re$ as

$$S(x) = a_1 x_1 + a_2 x_2 + \cdots + a_{n-1} x_{n-1} + x_n \tag{44}$$

where the coefficients a_i $i = 1, 2, \ldots, n - 1$ of (44) are such that the polynomial $S(x)$ is a Hurwitz polynomial. Furthermore, note that $S = 0$ is an $n - 1$ dimensional manifold, called the sliding surface.

Indeed now choose the control input u to be

$$u(t) = -b_1 x_1 - b_2 x_2 \cdots - b_n x_n - v_1(t) \tag{45}$$

$$v(t) = -a_1 x_2 - a_2 x_3 - \cdots - a_{n-1} x_n - k sgn[S(x)] \tag{46}$$

Choice of control u enables us to rewrite the system in the form

$$\dot{x}_1 = x_2 \tag{47}$$

$$\dot{x}_2 = x_3 \tag{48}$$

$$\dot{x}_{n-1} = -a_1 x_1 - a_2 x_2 - \cdots - a_{n-1} x_{n-1} + S(x) \tag{49}$$

$$\dot{S}(x) = -k sgn[s(x)] \tag{50}$$

It is easy to show that Filippov solutions exist, and that $S(x) = 0$ is reached in finite time from arbitrary initial conditions. Furthermore on the $n - 1$ dimensional manifold $S = 0$, the reduced order dynamics is exponentially stable. Consequently global exponential stability of the system is shown.

The choice of discontinuous input induces chatter in the system. To reduce the chatter, we utilize various regularizations and smoothings of the discontinuous sgn function. The common smoothing technique is the use of the saturation function, which is presented in [SS83].

We now present a choice of *continuous control input* that enables us to reach the sliding surface $S = 0$ in finite time. Indeed, consider the control given by

$$u(t) = -b_1 x_1 - b_2 x_2 \cdots - b_n x_n - v_1(t) \tag{51}$$

$$v(t) = -a_1 x_2 - a_2 x_3 - \cdots - a_{n-1} x_n - k |S(x)|^{\frac{1}{m}} sgn[S(x)] \tag{52}$$

$$m > 1 \tag{53}$$

Such a choice of control u enables us to recast the system equations in the form

$$\dot{x}_1 = x_2 \tag{54}$$

$$\dot{x}_2 = x_3 \tag{55}$$

$$\dot{x}_{n-1} = -a_1 x_1 - a_2 x_2 - \cdots - a_{n-1} x_{n-1} + S(x) \tag{56}$$

$$\dot{S}(x) = -k |S(x)|^{\frac{1}{m}} sgn[s(x)] \tag{57}$$

It is easy to show that Filippov solutions exist, and that the $n - 1$ dimensional manifold $S(x) = 0$ is reached in finite time. Furthermore on the $n - 1$ dimensional manifold given by $S = 0$, we see that the reduced order dynamics is exponentially stable. Consequently global exponential stability of the system is shown. This control law u is interesting in that it is continuous, but not differentiable.

Comment 4.1 The disturbance rejection properties of the discontinuous control law are significantly better than that of the continuous control law. This indeed is the design tradeoff involved in designing continuous control laws.

Comment 4.2 The extension of the sliding mode control techniques to controllable MIMO systems that are decouplable is trivial. Once the system equations are transformed into decoupled systems, each of which is in the controllable canonical form, we apply the design method outlined earlier to design sliding surfaces for the decoupled system. Note however that sliding occurs not at the individual surfaces, but at the intersection of all these surfaces.

Theorem 4.1 *Sliding mode control of a magnetic bearing system.*

Given *(G1) A magnetic bearing system of the form (31) - (32).*

If *(I1) The controls v^i $i = 1, 2, \ldots, 4$ are chosen as*

$$v^i_{sliding} = -a^i_1 x^i_2 - k * sgn[a^i_1 x^i_1 + x^i_2] \tag{58}$$

Then *(T1) Filippov solutions exist for the system (31) - (32) subject to the control law (58).*

(T2) The trajectories of the system (31) - (32) subject to the control law (58) reach the origin in finite time.

Figure 1: Sliding Mode Control of a Single Axis of a Magnetic Bearing

Proof: ♠ ▷ To show the existence of generalized Filippov solutions we first note that the dynamical system represented by equations (31) - (32) subject to the control law (58) can be modelled by the following inclusion.

$$\dot{x}_1^i = -a_1^i x_1^i + S \tag{59}$$

$$\dot{S} \in \mathcal{F}^i(x) \tag{60}$$

where the inclusions $\mathcal{F}^i(x) : \Re \to [-k, k]$ are specified as

$$\mathcal{F}^i(x) = -k * sgn[a_1^i x_1^i + x_2^i] \text{ if } ||x||_2 > 0 \tag{61}$$

$$\in [-k, k] \text{ else} \tag{62}$$

$$i = 1, 2, \ldots, 4 \tag{63}$$

The inclusions $\mathcal{F}^i(x)$ $i = 1, 2, \ldots, 4$ are

- closed, bounded, convex and uppersemicontinuous.

Invoking the theorem on the existence of generalized Filippov solutions, we conclude that Filippov solutions exist for the system (31) - (32) subject to the control law (58).

Stability and robustness of the magnetic bearing follow from the earlier discussions. ◁ ♠

The phase portrait of trajectories subject to the sliding mode control is given below.

5 Minimum Time Control of the Magnetic Bearing

It is many times desirable in a magnetic bearing to choose a control law to perform regulation in minimum time. Such minimum time regulation ensures good response to impulsive perturbation forces. To achieve regulation in minimum time, we formulate the optimal control problem as specified in [AEB75].

Consider the minimum time optimal control problem with the functional to be minimized, given by

$$J = \int_0^{t_f} dt \tag{64}$$

Theorem 5.1 *Minimum time control of a magnetic bearing system.*

Given *(G1) A magnetic bearing system of the form (31) - (32).*

(G2) A functional to be extremized of the form (64).

If *(I1) The controls v^i $i = 1, 2, \ldots, 4$ are chosen as*

$$v_{optimal}^i = \begin{cases} -sgn[x_1^i + \frac{x_2^i |x_2^i|}{2}] & \text{if } |x_1^i + \frac{x_2^i |x_2^i|}{2}| > 0 \\ -sgn[x_2^i] & \text{if } |x_1^i + \frac{x_2^i |x_2^i|}{2}| = 0 \end{cases} \tag{65}$$

33

Then *(T1) The trajectories of the system (31) - (32) subject to the control law (65) reach the origin in minimum time.*

Proof: ♠ ▷ Using standard methods of optimal control [AEB75], we write down the Hamiltonian function $H(x, u, \lambda, t)$ as

$$H(x, u, \lambda, t) = 1 + \lambda_1 x_2^i + \lambda_2 v^i \tag{66}$$

Inspection of equation (66) reveals that the control v^i that minimizes the Hamiltonian is given by

$$v^i = -sgn[\lambda_2]v_{max}^i \tag{67}$$

where v_{max}^i is the maximum permissible value of control. Without loss of generality, we will assume that $v_{max}^i = 1$. where λ_1 and λ_2 are the co-state variables. The co-state equations are given by

$$\dot{\lambda}_1 = 0 \tag{68}$$

$$\dot{\lambda}_2 = -\lambda_1 \tag{69}$$

Integrating the co-state equations yields

$$\lambda_2(t) = -\lambda_1(0)t - \lambda_2(0) \tag{70}$$

Therefore the optimal control is given as

$$v^i = sgn[-\lambda_1(0)t - \lambda_2(0)] \tag{71}$$

The control can assume only two values $+1$ or -1. When $v^i = +1$, we integrate the state equations to obtain

$$x_2^i(t) = t + x_2^i(0) \tag{72}$$

$$x_1^i(t) = \frac{t^2}{2} + x_2^i(0)t + x_1^i(0) \tag{73}$$

$$\text{Eliminating } t \text{ we obtain} \tag{74}$$

$$x_1^i = \frac{[x_2^i]^2}{2} + x_1^i(0) - \frac{[x_2^i]^2(0)}{2} \tag{75}$$

Similarly, when $v^i = -1$, integrating the state equations we obtain

$$x_2^i(t) = -t + x_2^i(0) \tag{76}$$

$$x_1^i(t) = -\frac{t^2}{2} + x_2^i(0)t + x_1^i(0) \tag{77}$$

$$\text{Eliminating } t \text{ we obtain} \tag{78}$$

$$x_1^i = -\frac{[x_2^i]^2}{2} + x_1^i(0) - \frac{[x_2^i]^2(0)}{2} \tag{79}$$

These curves describe a family of parabolas, whose switching curve may be written as

$$S(x, t) = x_1^i + \frac{x_2^i|x_2^i|}{2} \tag{80}$$

In terms of the switching curve, the control $v_{optimal}^i$ may be written as

$$v_{optimal}^i = \begin{cases} -sgn[x_1^i + \frac{x_2^i|x_2^i|}{2}] & \text{if } |x_1^i + \frac{x_2^i|x_2^i|}{2}| > 0 \\ -sgn[x_2^i] & \text{if } |x_1^i + \frac{x_2^i|x_2^i|}{2}| = 0 \end{cases} \tag{81}$$

◁♠

The phase portrait of trajectories subject to the optimal control $v_{optimal}^i$ is given below. Note the trajectories converging to the switching curve, which is nonlinear (while the switching curve in conventional sliding mode systems is linear). The chosen control gains are

$$k_1 = 1 \tag{82}$$

$$k_2 = 2 \tag{83}$$

34
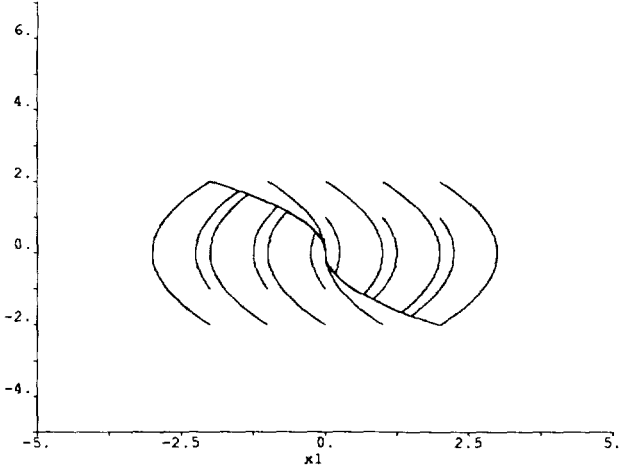
Figure 2: Minimum Time Control of a Single Axis of a Magnetic Bearing

6 Winding Algorithm Based Control of the Magnetic Bearing

The winding algorithm was introduced by [Kor68], [Pra92] and makes use of continuous switching between the surfaces $x_1^i = 0$ and $x_2^i = 0$ to reach the origin. The interesting feature of this control technique is that the control has two switches. One switch is used to change the direction, and the other is used to change the magnitude. By repeatedly switching between the surfaces $x_1^i = 0$ and $x_2^i = 0$, we wind closer to the origin.

Theorem 6.1 *Magnetic bearing control utilizing the winding algorithm.*

Given *(G1)* *A magnetic bearing system of the form (31) - (32).*

If *(I1)* *The controls v^i $i = 1, 2, \ldots, 4$ are chosen as*

$$v_{winding}^i = -k_1 sgn[x_1^i] - k_2 sgn[x_2^i] \quad k_1 > k_2 > 0 \tag{84}$$

Then *(T1)* *Filippov solutions exist for the system (31) - (32) subject to the control law (84).*

(T2) *The trajectories of the system (31) - (32) subject to the control law (84) wind to the origin in finite time.*

Proof: ◆ ▷ To show the existence of generalized Filippov solutions we first note that the dynamical system represented by equations (31) - (32) subject to the control law (84) can be modelled by the following inclusion.

$$\dot{x}_1^i = x_2^i \tag{85}$$

$$\dot{x}_2^i \in \mathcal{F}^i(x) \tag{86}$$

where the inclusions $\mathcal{F}^i(x) : \Re \rightarrow [-(k_1 + k_2), (k_1 + k_2)]$ are specified as

$$\mathcal{F}^i(x) = -k_1 sgn[x_1^i] - k_2 sgn[x_2^i] \text{ if } ||x||_2 > 0 \tag{87}$$

$$\in [-(k_1 + k_2), (k_1 + k_2)] \text{ else} \tag{88}$$

$$i = 1, 2, \ldots, 4 \tag{89}$$

The inclusions $\mathcal{F}^i(x)$ $i = 1, 2, \ldots, 4$ are

- closed, bounded, convex and uppersemicontinuous.

Invoking the theorem on the existence of generalized Filippov solutions, we conclude that Filippov solutions exist for the system (31) - (32) subject to the control law (84).

Let us first prove the stability and finite time stabilization of the algorithm. To show stability, we use the extended Lyapunov theorem, [AKP91] proofs for which may be found in [AC84]. The theorem is primarily used to conclude *weak-stability* of differential inclusions by investigating generalized gradients of non-differentiable Lyapunov functions. A brief statement of the theorem would be as follows.

Given a differential inclusion $\dot{x} \in F(x, t)$ and a nondifferentiable Lyapunov function $V(x)$. If for every element v in the generalized gradient of V, there exists at least one element $f \in F(x, t)$, such that $L_F V \leq 0$, then the zero-solution is weakly asymptotically stable. Indeed, weak asymptotic stability is the best we could hope for when dealing with set-valued differential inclusions.

35

Now consider the system (31) - (32) subject to the controls $u_{winding}$. The system equations are

$$\dot{x}_1 = x_2^i \tag{90}$$

$$\dot{x}_2 = -k_1 sgn[x_1^i] - k_2 sgn[x_2^i] \tag{91}$$

Consider a candidate Lyapunov function

$$V = |x_1^i| + \frac{x_2^i}{2k_1} \tag{92}$$

The derivative for $x_1^i, x_2^i \neq 0$ is given by

$$\dot{V} = -\frac{k_2 x_2^2}{k_1} \tag{93}$$

$$\leq 0 \tag{94}$$

Therefore $x_2^i \rightarrow 0$, and the reduced dynamics is such that $x_1^i \rightarrow 0$. However, when $x_1^i = 0$, it is clear that we have to investigate the properties of the generalized gradient of V. However, it is obvious that when $x_1^i = 0$, for every element v of the generalized gradient of V, (which in this case happens to be any real number in (-1,1)) there exists an element of the inclusion $F(x,t)$ (indeed, choose $f = v$) such that the generalized gradient of V along the flow of the inclusion $F(x,t)$ is negative definite. The conditions of the generalized Lyapunov theorem are satisfied, and hence the result.

Finite time is shown by considering the state equations of the planar dynamical system in the various quadrants. Indeed, if the portrait of the system were to be drawn with x_1^i along the x axis and x_2^i along the y axis, we would note the following.

$$x_1^i = \pm\frac{[x_2^i]^2}{k_1 + k_2} \text{ in the first and third quadrants} \tag{95}$$

$$x_2^i = \mp\frac{[x_2^i]^2}{k_1 - k_2} \text{ in the second and fourth quadrants} \tag{96}$$

Every instance the trajectory moves from the first quadrant through the fourth quadrant to hit the y axis, we see a contraction occurring in the magnitude of x_2^i in the following manner.

$$[x_2^i]^2(t_1) = \frac{k_1 - k_2}{k_1 + k_2}[x_2^i]^2(0) \tag{97}$$

From the third quadrant through the second to strike the y axis again, we see the following contraction.

$$[x_2^i]^2(t_2) = \frac{k_1 - k_2}{k_1 + k_2}[x_2^i]^2(t_1) \tag{98}$$

The state trajectory therefore winds to the origin. ◁♠

The phase portrait of the planar dynamical system subject to the winding algorithm is illustrated below. Note the very interesting way in which the state trajectories wind to the origin. The values of chosen control gains are

$$k_1 = 2 \tag{99}$$

$$k_2 = 1 \tag{100}$$

7 Nested Switching Control of the Magnetic Bearing

Nested switching controls work well for planar dynamical systems [Pra92]. The basic approach is to permit chatter about the dual sliding surfaces $x_1^i = 0$ and $x_2^i = 0$. It is to be noted that chatter for multiple sliding surfaces is the equivalent of limit-cycle like behaviour. Consequently, by utilizing multiple sliding surfaces, and nondifferentiable controls, we are willing to tolerate limit-cycle like behaviour at the origin. Indeed, the problems associated with eliminating chatter in one-dimensional systems naturally extend to the higher order systems also. The use of saturation functions to perform nested switching is an extension of the idea of using saturation functions in one-dimensional systems, to many dimensions.

Theorem 7.1 *Magnetic bearing control utilizing the winding algorithm.*

Given *(G1) A magnetic bearing system of the form (31) - (32).*

If *(I1) The controls v^i $i = 1, 2, \ldots, 4$ are chosen as*

$$v_{nested}^i = -k_2 sgn[x_2^i - k_1 sgn[x_1^i]] \tag{101}$$

36
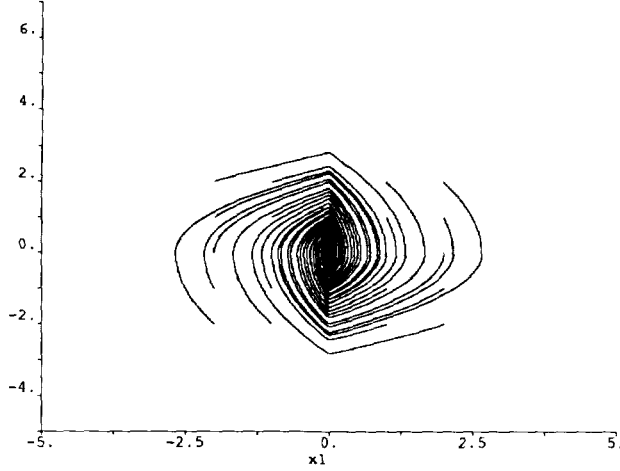
Figure 3: Winding Algorithm Based Control of a Single Axis of a Magnetic Bearing

Then *(T1)* *Filippov solutions exist for the system (31) - (32) subject to the control law (101).*

(T2) *The trajectories of the system (31) - (32) subject to the control law (101) reach the origin in finite time.*
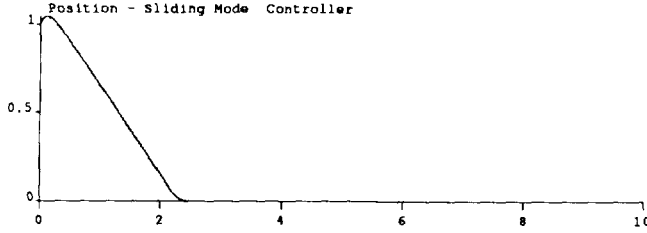
Proof: ♠ ▷

To show the existence of generalized Filippov solutions we first note that the dynamical system represented by equations (31) - (32) subject to the control law (101) can be modelled by the following inclusion.

$$\dot{x}_1^i = x_2^i \tag{102}$$

$$\dot{x}_2^i \in \mathcal{F}^i(x) \tag{103}$$

where the inclusions $\mathcal{F}^i(x) : \Re \to [-(k_1 + k_2), (k_1 + k_2)]$ are specified as

$$\mathcal{F}^i(x) = -k_2 sgn[x_2^i - k_1 sgn[x_1^i]] \text{ if } ||x||_2 > 0 \tag{104}$$

$$\in [-k_2, k_2] \text{ else} \tag{105}$$

$$i = 1, 2, \ldots, 4 \tag{106}$$

The inclusions $\mathcal{F}^i(x)$ $i = 1, 2, \ldots, 4$ are

- closed, bounded, convex and uppersemicontinuous.

Invoking the theorem on the existence of generalized Filippov solutions, we conclude that Filippov solutions exist for the system (31) - (32) subject to the control law (84).

Consider the system (31)-(32) subject to the nested switching control law given by

$$\dot{x}_1 = x_2^i \tag{107}$$

$$\dot{x}_2 = -k_2 sgn[x_2^i + k_1 sgn[x_1^i]] \tag{108}$$

Now consider the following nondifferentiable Lyapunov function

$$V = \frac{[x_2^i + k_1 sgn[x_1^i]]^2}{2} \tag{109}$$

$$\dot{V} = [x_2^i + k_1 sgn[x_1^i]][\dot{x}_2 + 0] \text{if } |x_1^i| > 0 \tag{110}$$

$$= -k_2 |x_2^i + k_1 sgn[x_1^i]| \tag{111}$$

$$\leq 0 \tag{112}$$

Therefore $x_2^i \to -k_1 sgn[x_1^i]$. Indeed, it is easy to see that this happens in finite time. As in finite time $x_2^i = -k_1 sgn[x_1^i]$; now consider the Lyapunov function

$$V_1 = \frac{[x_1^i]^2}{2} \tag{113}$$
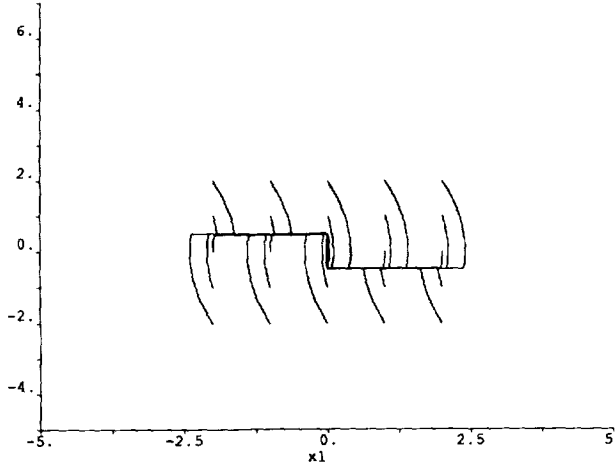
Figure 4: Nested Switching Control of a Single Axis of a Magnetic Bearing

$$\dot{V}_1 \;=\; x_1^i x_2^i \tag{114}$$

$$=\; x_1^i[-k_1 sgn[x_1^i]] \text{ in finite time} \tag{115}$$

$$\leq\; k_1|x_1^i| \tag{116}$$

$$\leq\; 0 \tag{117}$$

It is clear that $x_1^i \to 0$ in finite time. However, when $x_1^i = 0$, $x_2^i \in [-k_1, k_1]$, and is not equal to 0. This is where chatter commences, and the system limit cycles between the surfaces $x_1^i = 0$ and $x_2^i = k_1 sgn[x_1^i]$. Such limit cycling behaviour is present as the gain k_1 is not slowly reduced as $x_1^i \to 0$. Indeed if the multiplicand of $sgn[x_1^i]$ was to decrease in magnitude and finally equal 0 when $x_1^i = 0$, we can expect x_2^i to also be equal to 0 without chatter. This indeed is the principle behind using saturation functions as opposed to sgn functions in nested control. We will now show an extension of this method, without using saturation functions.

We now try to eliminate the problem of limit cycling between switching surfaces that was mentioned earlier. We do this using the switching control law mentioned earlier which is of the form.

$$u_{switching} = -k_2 sgn[x_2^i + k_1|x_1^i|^{\frac{1}{m}} sgn[x_1^i]] \tag{118}$$

Denote $S = x_2^i + k_1|x_1^i|^{\frac{1}{m}} sgn[x_1^i]$. Note that S is not differentiable at $x_1^i = 0$. However, almost everywhere, the derivative of S may be written as

$$\dot{S} = -k_2 sgn[S] + k_1 \frac{x_2^i}{|x_1^i|^{1-\frac{1}{m}}} \tag{119}$$

By choosing a large value of k_2, we hope to swamp the term $k_1 \frac{x_2^i}{|x_1^i|^{1-\frac{1}{m}}}$. Indeed, only in cases when this is possible, it is possible to conclude that

$$x_2^i = -k_1|x_1^i|^{\frac{1}{m}} sgn[x_1^i] \tag{120}$$

And the conclusions of the previous section follow, without the limit cycle behaviour.

The phase portrait shown below illustrates the properties of the control law. The values of chosen gains are

$$k_1 \;=\; 0.5 \tag{121}$$

$$k_2 \;=\; 5 \tag{122}$$

$$m \;=\; 2 \tag{123}$$

For the same values of control gains, it is possible to choose a higher order fractional index, and the resulting phase portrait is shown below.

38
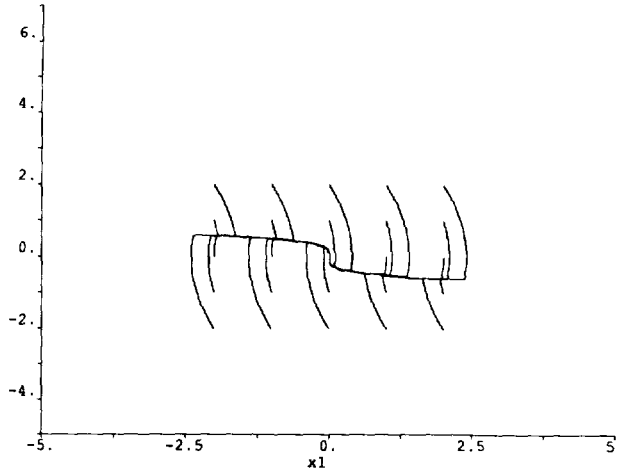
Figure 5: Nested Higher Order Switching Control of a Single Axis of Magnetic Bearing

8 Synchronous Sliding Control of the Magnetic Bearing

In this section, we present an interesting property of a modified vector sliding mode control law [AKP92a], [AKP92b], [AKP 5], and its possible application. The property of this modified vector sliding mode control law is such that it achieves simultaneous regulation for a group of n scalar systems with n inputs [SMSar], [SMS93], [SMS 7].This control technique has interesting implications for the magnetic bearing. Using this control technique it is possible to regulate the states of the multivarious magnetic bearings to the origin synchronously thus eliminating the possibility of inducing overshoot torques. The control law has the interesting property that it is a closed loop control law which can be prescribed without *explicit* reference to the initial conditions of the system. The law is interesting in that it introduces coupling between decoupled systems to achieve the synchronization objective. We present the basic theory of synchronous sliding control, and later specialize it to the case of the magnetic bearing.

8.1 Synchronous Sliding

Consider a group of n scalar decoupled systems of the form

$$\begin{bmatrix} \dot{x}_1 \\ \vdots \\ \dot{x}_n \end{bmatrix} = \begin{bmatrix} u_1 \\ \vdots \\ u_n \end{bmatrix} \tag{124}$$

$$\begin{bmatrix} x_1(0) \\ \vdots \\ x_n(0) \end{bmatrix} = \begin{bmatrix} x_{10} \\ \vdots \\ x_{n0} \end{bmatrix} \tag{125}$$

where the states $x_i \in \Re$, the controls $u_i \in \Re$ $i = 1, 2, \ldots, n$ the initial conditions $x_{i0} \in \Re$ $i = 1, 2, \ldots, n$. With minor abuse of notation, we create a new state vector $x \in \Re^n$, where $x = \begin{bmatrix} x_1 & \cdots & x_n \end{bmatrix}^T$

The control objective is to regulate the states from non-zero initial conditions to the origin, in finite time. That is, that there exist instants of time $t_i^* < \infty \in \Re_+$ $i = 1, 2, \ldots, n$ such that the following is true.

$$x_i(t) = 0 \ \forall \ t \geq t_i^* \ i = 1, 2, \ldots, n \tag{126}$$

We choose n sliding mode control laws of the following form to ensure achievement of the control objective.

$$u_i = -k_i \frac{x_i}{|x_i|} \quad \text{if } |x_i| \neq 0 \quad i = 1, 2, \ldots, n \tag{127}$$

where $k_i \in \Re_+$

Comment 8.1 We note here that the controls u_i $i = 1, 2, \ldots$ are decoupled, in that u_i is a function only of x_i. Also note that the time taken by each state x_i $i = 1, 2, \ldots, n$ to reach the origin is a function of its initial value $x_i(0)$ $i = 1, 2, \ldots, n$ and the control gains k_i $i = 1, 2, \ldots, n$.

39

Comment 8.2 Also note in equation (127) we did not specify the control law at $|x_i| = 0$ $i = 1, 2, \ldots, n$. Indeed, $u_i = -k_i sgn[x_i]$ $|x_i| \neq 0$. We do not specify the control at $|x_i| = 0$. As the control is not specified only on sets of zero measure, it does not affect the existence of Filippov solutions shown by modelling the system by a differential inclusion.

We now present some interesting properties of a modified sliding mode control law that deliberately introduces coupling between the decoupled systems. We present proof of existence of solutions, proof of stability, and proof of synchronous finite time convergence for the modified sliding mode control law. In order to do so, we formalize the notion of *synchronous finite time convergence*.

Definition 8.1 *A set of $n \in Z_+$ variables $x_i(t) : \Re_+ \to \Re$ $i = 1, 2, \ldots, n$ are said to reach the origin synchronously commencing from nonzero initial conditions $x_i(0) \neq 0$ $i = 1, 2, \ldots, n$ if there exists an instant of time $t^* < \infty \in \Re_+$ such that the following is true.*

$$x_i(t) \neq 0 \; \forall t < t^* \tag{128}$$

$$x_i(t) = 0 \; \forall t \geq t^* \tag{129}$$

$$i = 1, 2, \ldots, n \tag{130}$$

That is to say, that the states with nonzero initial conditions (an assumption we make without loss of generality) are regulated to 0 at the *same* instant of time t^*. There are many practical applications where such *synchronous* regulation is important. A typical application is a multifingered robot hand that grips an object. It is important to ensure that the fingers touch the object *synchronously* and thus cause force closure without imparting motion to the object. We will say more about this later.

It is possible to ensure synchronous motion using a simple sliding mode feedback where the control gains are chosen with explicit dependence on initial conditions. Indeed, given the initial conditions exactly, we choose a decoupled control law that uses the values of initial conditions to derive control gains that guarantee synchronous reaching of the origin. For the sake of completeness we state the control law as follows.

Theorem 8.1 *Synchronous regulation with explicit dependence on initial conditions.*

Given *(G1)* A nonlinear system of the form (124) - (125).

(G2) A control law of the form (127)

If *(I1)* k_i $i = 1, 2, \ldots, n$ are chosen such that

$$\frac{|x_i(0)|}{k_i} = \frac{|x_j(0)|}{k_j} \; i = 1, 2, \ldots, n \; j = 1, 2, \ldots, n \tag{131}$$

Then *(T1)* Filippov solutions exist for the system (124) - (125) subject to the control law (127).

(T2) The surfaces $x_i = 0$ $i = 1, 2, \ldots n$ are reached synchronously at a time $t^* = \frac{x_1(0)}{k_1}$.

Proof: ♠ ▷ The proof is quite straightforward and utilizes standard facts from sliding mode control theory.

The existence of Filippov solutions is shown using the fact that the modelling differential inclusions $\mathcal{F}_i(x) : \Re \to [-1, 1]$ are closed, bounded, convex and uppersemicontinuous. Note that $\mathcal{F}_i(x) : \Re \to [-1, 1]$ are defined as follows

$$\mathcal{F}_i(x) = -k_i \frac{x_i}{|x_i|} \text{ if } |x_i| \neq 0 \tag{132}$$

$$\in [-1, 1] \text{ if } |x_i| = 0 \tag{133}$$

Stability is shown using the candidate Lyapunov function $V(x) : \Re^n \to \Re_+$ given by $V(x) = \sum_{i=1}^n \frac{x_i^2}{2}$ whose derivative along the flow of (124) - (125) is given by $\dot{V} = -\sum_{i=1}^n |x_i|$. Indeed $\dot{V}$ is negative definite proving global exponential stability of the origin.

Finally, the time taken to reach the origin is given by $t_i^* = \frac{|x_i(0)|}{k_i}$ $i = 1, 2, \ldots, n$. Now using the assumption that $\frac{|x_i(0)|}{k_i} = \frac{|x_j(0)|}{k_j}$ $i = 1, 2, \ldots, n$ $j = 1, 2, \ldots, n$, we see that $t_1^* = t_2^* \ldots = t_n^* = t^*$.

This completes the proof of the theorem. ◁ ♠

Comment 8.3 The control law is inelegant to implement as it explicitly depends on the initial conditions. It would be desirable to develop a state feedback control law that would achieve the same objective, but one whose control gains do not explicitly depend on initial conditions.

We now propose a state feedback control law that would ensure synchronous regulation.

Theorem 8.2 *Synchronous regulation with state feedback.*

Given *(G1)* A nonlinear system of the form (124) - (125).

If *(I1)* *The controls* u_i *$i = 1, 2, \ldots, n$ in equations (124) - (125) are chosen to be*

$$u_i = -k^\star \frac{x_i}{||x||_2} \quad \text{if} \quad ||x||_2 > 0 \quad i = 1, 2, \ldots, n \tag{134}$$

$$||x||_2 = [\sum_{i=1}^{n} x_i^2]^{\frac{1}{2}} \tag{135}$$

$$\tag{136}$$

where $k^\star \in \Re_+$

Then *(T1) Filippov solutions exist for the system (124) - (125) subject to the control law (134).*

(T2) The surfaces $x_i = 0$ *$i = 1, 2, \ldots n$ are reached synchronously at a time* $t^\star = \frac{||x(0)||_2}{k^\star}$ *where* $||x(0)||_2$ *is the 2-norm of the vector of initial conditions, given by* $||x(0)||_2 = [\sum_{i=1}^{n} x_i^2(0)]^{\frac{1}{2}}$

Proof: ♠ ▷ We prove the theorem in three steps. First we show existence of generalized Filippov solutions to the system (124) - (125) subject to the control law (134). We then show attractivity of the origin when subject to the control law using a simple Lyapunov argument. Finally we show the achievement of synchronous regulation, by explicitly computing the times taken to reach the origin. We first make the following comments.

Comment 8.4 It is interesting to compare the control laws given by equations (127) and (134). While the control specified by (127) decouples the system entirely, the control specified by (134) introduces a coupling between the through the 2-norm of the state vector $||x||_2$. *Furthermore, note that the control gains* $k^\star$ *remain the same for all* u_i *$i = 1, 2, \ldots, n$.*

Comment 8.5 The discontinuous control law (134) is not defined at the origin, the same way the function $sgn[(\cdot)]$: $\Re \rightarrow [-1, 1]$ *is not defined when* $(\cdot) = 0$. *But also note that the control law specified by (134) is bounded by* $k^\star$. *Indeed, as* $\frac{x_i}{||x||_2} \leq 1$ *$i = 1, 2, \ldots, n$,* $u_i \leq k^\star$ *$i = 1, 2, \ldots, n$.*

Step 1: Existence Of Filippov Solutions

To show the existence of generalized Filippov solutions we model the system (124) - (125) subject to the control law (134) by the following differential inclusion.

$$\begin{bmatrix} \dot{x}_1 \\ \vdots \\ \dot{x}_n \end{bmatrix} \in \begin{bmatrix} \mathcal{F}_1(x) \\ \vdots \\ \mathcal{F}_n(x) \end{bmatrix} \tag{137}$$

where the inclusions $\mathcal{F}_i(x) : \Re \rightarrow [-k^\star, k^\star]$ are specified as

$$\mathcal{F}_i(x) = -k^\star \frac{x_i}{||x||_2} \quad \text{if} \quad ||x||_2 > 0 \tag{138}$$

$$\in [-k^\star, k^\star] \text{ if } ||x||_2 = 0 \tag{139}$$

$$i = 1, 2, \ldots, n \tag{140}$$

The inclusions $\mathcal{F}_i(x)$ $i = 1, 2, \ldots, n$ are

- closed, bounded, convex and uppersemicontinuous.

Invoking the theorem on the existence of generalized Filippov solutions, we conclude that Filippov solutions exist for the system (124) - (125) subject to the control law (134).

Step 2: Attractivity Of The Origin

Consider a candidate Lyapunov function $V(x) : \Re^n \rightarrow \Re_+$ given by

$$V = \frac{x^T x}{2} \tag{141}$$

Differentiating V along the flow of (124) - (125) subject to the control law (134), we find

$$\dot{V} = \begin{bmatrix} x_1 & \ldots & x_n \end{bmatrix} \begin{bmatrix} -k^\star \frac{x_1}{||x||_2} \\ \vdots \\ -k^\star \frac{x_n}{||x||_2} \end{bmatrix} \tag{142}$$

$$= -k^\star \frac{||x||_2^2}{||x||_2} \tag{143}$$

$$= -k^\star ||x||_2 \quad \text{if} \quad ||x||_2 \neq 0 \tag{144}$$

$$\leq 0 \tag{145}$$

41

Negative definiteness of $\dot{V}$ confirms the global exponential stability of the origin.

Step 3: Synchronous Reaching

From system (124) - (125) subject to the control law (134) the following is true for any i, j

$$\dot{x}_i = -k^\star \frac{x_i}{||x||_2} \tag{146}$$

$$\dot{x}_j = -k^\star \frac{x_j}{||x||_2} \tag{147}$$

$$\frac{dx_i}{dx_j} = \frac{x_i}{x_j} \tag{148}$$

$$\forall \, i, j \leq n \quad i \neq j \; ||x||_2 \neq 0 \tag{149}$$

Solving (148), we obtain explicit expressions for constraints on state trajectories as

$$x_i(t) = \frac{x_i(0)}{x_j(0)} x_j(t) \forall \, i, j \leq n \quad i \neq j \; ||x||_2 \neq 0 \tag{150}$$

Using (150) in (146), we recast (146) in the form

$$\dot{x}_i = -k^\star \frac{x_i}{||x||_2} \tag{151}$$

$$= -k^\star \frac{x_i}{[\sum_{k=1}^n x_k^2]^{\frac{1}{2}}} \tag{152}$$

$$= -k^\star \frac{x_i}{[x_i^2 + \sum_{k=1, \, k \neq i}^n x_k^2]^{\frac{1}{2}}} \tag{153}$$

$$= -k^\star \frac{x_i}{[x_i^2 + \sum_{k=1, \, k \neq i}^n \frac{x_k^2(0)}{x_i^2(0)} x_i^2]^{\frac{1}{2}}} \tag{154}$$

$$= -k^\star \frac{x_i}{x_i[1 + \sum_{k=1, \, k \neq i}^n \frac{x_k^2(0)}{x_i^2(0)}]^{\frac{1}{2}}} \tag{155}$$

$$= -k^\star \frac{x_i(0)}{[x_i^2(0) + \sum_{k=1, \, k \neq i}^n x_k^2(0)]^{\frac{1}{2}}} \tag{156}$$

$$\dot{x}_i = -k^\star \frac{x_i(0)}{||x(0)||_2} \quad i = 1, 2, \ldots, n \tag{157}$$

The righthandside of (157) is a real constant, and therefore the solution of (157) is given by

$$x_i(t) = -k^\star \frac{x_i(0)}{||x(0)||_2} t + x_i(0) \quad i = 1, 2, \ldots, n \tag{158}$$

From (158), we obtain the time $t^\star$ taken by $x_i(t)$ $i = 1, 2, \ldots, n$ to reach the origin, starting from arbitrary nonzero initial conditions by setting the righthand side of (158) to 0.

$$0 = -k^\star \frac{x_i(0)}{||x(0)||_2} t^\star + x_i(0) \tag{159}$$

$$t^\star = \frac{||x(0)||_2}{k^\star} \quad i = 1, 2, \ldots, n \tag{160}$$

Synchronous convergence of state trajectories commencing from nonzero initial conditions is thus shown. This concludes the proof of the theorem. ◁♠

8.2 Design Of Tracking Control Laws

The control laws that we have developed are discontinuous. As a prelude to presenting tracking control laws that involve discontinuities, let us analyze a simple linear pole-placement control law from another perspective. Consider a system represented as a chain of integrators of the form,

$$\dot{x}_1 = x_2 \tag{161}$$

$$\vdots \quad \vdots \quad \vdots \tag{162}$$

$$\dot{x}_{n-1} = x_n \tag{163}$$

$$\dot{x}_n = u \tag{164}$$

where the state vector $x \in \Re^n$ and the control input $u \in \Re$. Given a desired smooth trajectory $x_{1d}(t) : \Re_+ \rightarrow \Re$ to be tracked by the state x_1 we present a tracking control law that uses successive derivative of desired trajectories. We define recursively, a set of desired trajectories for the states as

$$x_{id}(t) = \frac{dx_{i-1,d}(t)}{dt} - k_{i-1}[x_i(t) - x_{i,d}(t)] \quad i = 2, 3, \ldots, n \tag{165}$$

While we are *given* a desired trajectory to be tracked by the state $x_1(t)$, we define desired trajectories for the remaining states the tracking of which automatically ensures the original tracking objective for $x_1(t)$. Indeed, the intuition behind such a definition of desired trajectories becomes clear when we look at $x_{2d}(t)$.

$$x_{2d}(t) = \frac{dx_{1d}(t)}{dt} - k_1[x_1(t) - x_{1d}(t)] \tag{166}$$

From (166) it is clear that when the surface $x_2 = x_{2d}$ the resulting dynamics for $x_1(t)$ is given as

$$\dot{x}_1(t) = x_2(t) \tag{167}$$

$$= x_{2d}(t) \tag{168}$$

$$= \frac{dx_{1d}(t)}{dt} - k_1[x_1(t) - x_{1d}(t)] \tag{169}$$

The dynamics of the system is such as to ensure that $x_1(t) \rightarrow x_{1d}(t)$ exponentially. However, if the surface $x_2 - x_{2d} = 0$ can only be reached exponentially, then the dynamics of $\dot{x}_1$ is perturbed by an exponentially decaying signal, and therefore invoking the result on the exponentially stable systems perturbed by exponentially decaying perturbations, we conclude exponential convergence of $x_1(t)$ to $x_{1,d}(t)$. We now show the relationship between control laws developed using the recursively defined desired trajectories and the standard pole-placement control law.

Theorem 8.3 *Connection between pole-placement and recursive trajectory definition.*

Given *(G1) A nonlinear system of the form (161) - (164).*

(G2) Given a set of desired trajectories of the form (165)

If *(I1) The controls u in equation (164) are chosen to be*

$$u = \frac{dx_{nd}(t)}{dt} - k_n[x_n(t) - x_{nd}(t)] \tag{170}$$

where $x_{i,d}(t) : \Re^n \times \Re_+ \rightarrow \Re$ $i = 2, 3, \ldots, n$ is specified by (165) and $k_n \in \Re_+$.

Then *(T1) The control law specified by (170) is a stable pole-placement control with the n eigenvalues each being equal to $-k_i$ $i = 1, 2, \ldots, n$*

Proof: ♠ ▷ The proof is obvious by writing the dynamics for $\dot{x}_1$ and $\dot{x}_2$. Indeed,

$$\dot{x}_1 = x_2 \tag{171}$$

$$\dot{x}_2 = \frac{dx_{2d}(t)}{dt} - k_2[x_2(t) - x_{2d}(t)] \tag{172}$$

Using the definition of $x_{2d}(t)$ provided by (165), we rewrite (172) as

$$\dot{x}_1 = x_2 \tag{173}$$

$$\dot{x}_2 = \frac{d[\frac{dx_{1d}(t)}{dt} - k_1[x_1(t) - x_{1d}(t)]]}{dt} \tag{174}$$

$$-k_2[x_2(t) - [\frac{dx_{1d}(t)}{dt} - k_1[x_1(t) - x_{1d}(t)]]] \tag{175}$$

Which may be rewritten as

$$\dot{x}_1 = x_2 \tag{176}$$

$$\dot{x}_2 = \frac{d^2 x_{1d}(t)}{dt^2} + [k_1 + k_2]\frac{dx_{1d}(t)}{dt} + [k_1 k_2]x_{1d}(t) \tag{177}$$

$$-[k_1 + k_2]x_2(t) - [k_1 k_2]x_1(t) \tag{178}$$

That is to say

$$\begin{bmatrix} \dot{x}_1 \\ \dot{x}_2 \end{bmatrix} = \begin{bmatrix} 0 \\ \frac{d^2 x_{1d}(t)}{dt^2} + [k_1 + k_2]\frac{dx_{1d}(t)}{dt} + [k_1 k_2]x_{1d}(t) \end{bmatrix} \tag{179}$$

$$- \begin{bmatrix} 0 & 1 \\ -[k_1 k_2] & -[k_1 + k_2] \end{bmatrix} \begin{bmatrix} x_1 \\ x_2 \end{bmatrix} \tag{180}$$

The placement of poles through recursive trajectory definition is trivially obvious by inspection of equation (180). This concludes the proof of the theorem. ◁ ♠

Comment 8.6 It is to be noted that this tracking control law is valid for any specification of desired trajectories that are smooth, the tracking of which guarantees achievement of the control objective. That is, we are free to specify any smooth set of trajectories $x_{id}(t)$ $i = 2, 3, \ldots, n$, the only constraint being $x_i(t) = x_{id}(t)$ $i = 2, 3, \ldots, n$ $\Rightarrow$ $x_{i-1}(t) \rightarrow x_{i-1,d}(t)$. Indeed, the linear pole-placement control law is just a special case of control laws that achieve this tracking objective.

Comment 8.7 We now ask if it is possible to relax the smoothness assumption on the desired trajectories $x_{id}(t)$. Indeed, the first relaxation would be to consider desired trajectories that are differentiable almost everywhere, except possibly on sets of zero measure. The Nested and Switching control laws presented in the previous chapter are examples of such discontinuous control laws, the discontinuities existing on sets of zero measure. The proofs of such control laws are much harder in general, though the regularization of such control laws that involve saturation functions have been used in the recent literature. We have been inspired by the attempts of [Tee92] in developing control laws that use Filippov averaging instead of regularization. That is to say, that we are prepared to tolerate chatter and limit cycling by using discontinuous control laws. The drawback however is that we can show finite time synchronous stabilization only on the average, whereas a regularized control law, by eliminating the discontinuity would permit smooth stabilization, though exponentially, without the chatter.

Comment 8.8 Our interest in relaxing the smoothness assumption on the desired trajectories merely enables us to utilize the discontinuous, synchronous control law for a practical mechanical system.

We will first present the control law for a group of $n \in Z_+$ mechanical systems, and then apply it to a well known example of the magnetic bearing. Many mechanical systems are represented by Newtons force and torque balance equations that assume the form

$$\dot{x}_1^i = x_2^i \tag{181}$$

$$\dot{x}_2^i = v^i \tag{182}$$

where $x^i \in \Re^2$ is the state of the ith mechanical system where $i \leq n \in Z_+$, and $v^i(x, t) : \Re^2 \times \Re_+ \rightarrow \Re$ is the input force. Typically, x_1^i represents the generalized position coordinate of the mechanical system, and x_2^i represents the generalized velocity coordinate. These equations, though simple in form, serve to illustrate the application of the theory, and also represent a large class of useful physical systems. Given desired trajectories $x_{1d}^i(t) : \Re_+ \rightarrow \Re$ to be tracked by the states $x_1^i(t)$, we attempt to find control laws u^i that ensure synchronous tracking for the states $x_1^i(t)$.

We now state the theorem that ensures synchronous tracking for the systems of the form (181)-(182).

Theorem 8.4 *Synchronous tracking for a class of mechanical systems.*

Given *(G1)* *n mechanical systems, each of the form (181) - (182).*

(G2) Given a set of desired trajectories of the form $x_{1d}^i(t) : \Re_+ \rightarrow \Re$ $i = 1, 2, \ldots, n$

If *(I1) The controls $u^i(x, t)$ $i = 1, 2, \ldots, n$ in equation (182) are chosen to be*

$$v^i = \frac{dx_{2d}^i}{dt} - k_2^\star \frac{x_2^i - x_{2d}^i}{[\sum_{j=1}^n [x_2^j - x_{2d}^j]^2]^{\frac{1}{2}}} \tag{183}$$

$$x_{2d}^i = \frac{dx_{1d}^i}{dt} - k_1^\star \frac{x_1^i - x_{1d}^i}{[\sum_{j=1}^n [x_1^j - x_{1d}^j]^2]^{\frac{1}{2}}} \tag{184}$$

where $k_1, k_2 \in \Re_+$.

Then *(T1) Filippov solutions exist for system (181) - (182) subject to control (183).*

(T2) States $x_1^i(t)$ track their respective trajectories $x_{1d}^i(t)$ synchronously.

Proof: ♠ ▷ The proof is simple once we realize the validity of the system equations (181) - (182) subject to the control law (183) for arbitrarily small neighborhoods of the origin. Indeed, the control law is undefined only on a set of zero measure. As this set of zero measure is indeed the set we desire to make invariant, and the control law directs system trajectories to this set, and hence maintains invariance, the conclusions of the theorem naturally follow. The theorem can also be proved invoking the results of the nested and switching control laws mentioned in the previous section. ◁♠

8.3 Application to the Magnetic Bearing

In this subsection we apply the proposed tracking control law to magnetic bearings.

The dynamics of magnetic bearings are given by the following equations.

$$\dot{x}_1^i = x_2^i \tag{185}$$

$$\dot{x}_2^i = v^i \tag{186}$$

$$i = 1, 2, \ldots, 4 \tag{187}$$

Given desired trajectories $x_{1d}^i(t)$ $i = 1, 2, \ldots, 4$ to be tracked by the respective state variables $x_1^i(t)$ $i = 1, 2, \ldots, 4$, We now define the following set of vectors.

$$e_j^i(t) = x_j^i(t) - x_{jd}^i(t) \quad i = 1, 2, \ldots, 4 \quad j = 1, 2 \tag{188}$$

$$e_1(t) = \begin{bmatrix} e_1^1(t) & \cdots & e_1^4(t) \end{bmatrix}^T \tag{189}$$

$$e_2(t) = \begin{bmatrix} e_2^1(t) & \cdots & e_2^4(t) \end{bmatrix}^T \tag{190}$$

where

$$x_{2d}^i(t) = \frac{dx_{1d}^i(t)}{dt} - k_1^\star \frac{x_1^i(t) - x_{1d}^i(t)}{\|e_1(t)\|} \quad \text{if } \|e_1(t)\|_2 \neq 0 \tag{191}$$

$$= \frac{dx_{1d}^i(t)}{dt} \quad \text{if } \|e_1(t)\|_2 = 0 \tag{192}$$

Now note that $x_{2d}^i(t)$, is not strictly differentiable at the origin, but has a derivative that exists almost everywhere. Indeed define the generalized derivative as

$$\dot{x}_{2d}^i(t) = \frac{dx_{2d}^i(t)}{dt} - \frac{k_1^\star N_1^i(t)}{\|e_1(t)\|^{\frac{3}{2}}} \quad \text{if } \|e_1(t)\|_2 \neq 0 \tag{193}$$

$$= \frac{dx_{2d}^i(t)}{dt} \quad \text{if } \|e_1(t)\|_2 = 0 \tag{194}$$

where

$$N_1^i(t) = \sum e_1^j(t)[e_1^j(t)\dot{e}_1^i(t) - \dot{e}_1^j(t)e_1^i(t)] \quad j = 1, 2, 3, 4 \quad j \neq i \tag{195}$$

$$\dot{e}_1^i(t) = x_2^i(t) - \dot{x}_{id}^i(t) \quad i = 1, 2, \ldots, 4 \tag{196}$$

We now choose v^i $i = 1, 2, \ldots, 4$ in the following manner.

$$v^i(t) = \dot{x}_{2d}^i(t) - k_2^\star \frac{x_2^i(t) - x_{2d}^i(t)}{\|e_2(t)\|} \quad \text{if } \|e_2(t)\|_2 \neq 0 \tag{197}$$

$$= \frac{dx_{1d}^i(t)}{dt} \quad \text{if } \|e_2(t)\|_2 = 0 \tag{198}$$

Claim 8.1 *Synchronous Tracking for a Magnetic Bearing.*

Given *(G1)* *Mechanical systems, each of the form (187).*

    (G2) *Given a set of desired trajectories of the form $x_1^i d(t) : \Re_+ \rightarrow \Re$ $i = 1, 2, \ldots, n$*

If *(I1)* *The controls $v^i(x, t)$ $i = 1, 2, \ldots, n$ in equation (187) are specified by (197). where $k_1, k_2 \in \Re_+$.*

Then *(T1)* *Filippov solutions exist for system (187) - subject to control (197).*

    (T2) *States $x_1^i(t)$ track their respective trajectories $x_{1d}^i(t)$ synchronously.*

Proof: ♠ ▷ The proof of the claim is by invoking the theorem proved earlier for the more general case of a group of mechanical systems.

Indeed, it is easily seen that the application of control (197) would cause the states $x_2^i(t)$ $i = 1, 2, \ldots, 4$ to reach their desired values in finite time, and the desired trajectories are so chosen that the reduced dynamics ensures finite time tracking for $x_{1d}^i(t)$. ◁ ♠

Results of simulation are shown for the following conditions. The chosen desired trajectories were as follows. $x_{1d}^1(t) = \sin t$, $x_{1d}^2(t) = 5$, $x_{1d}^3(t) = -2$, $x_{1d}^4(t) = 5$. The initial conditions were as follows $x_1^1(0) = 1$, $x_1^2(0) = 7$, $x_1^3(0) = -1$, $x_1^4(0) = 2$, $x_2^1(0) = 0$, $x_2^2(0) = 0$, $x_2^3(0) = 0$, $x_2^4(0) = 0$.

Simulation results are in excellent agreement with the predicted behaviour. Indeed, note that the trajectory errors vanish identically at the same instant of time. This indeed was the motivation for considering the synchronous tracking control law.
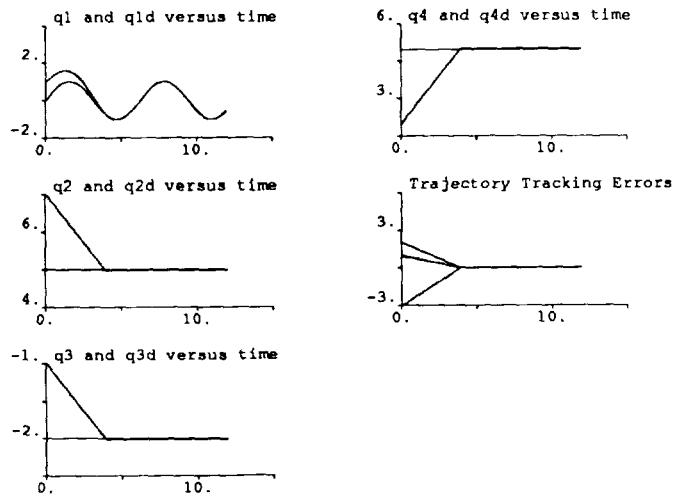
Figure 6: Synchronous Control of a Magnetic Bearing

9 Fractional Control of the Magnetic Bearing

9.1 Introduction

In this section, we will present an interesting variable structure control law for a vector dynamical system, that is a bounded control law, but whose convergence rate is faster than a comparable linear control law, and whose robustness properties are much better than comparable linear control laws [Pra92]. We will clarify what we mean by *comparable linear control laws* in the following subsections. We use the term fractional control law to indicate that this is a particular form of variable structure control law where the powers of indices are positive fractions.

We will present qualitative arguments for the conjecture, and will provide simulation results that are in agreement with the conjecture. However the proof of this conjecture has been quite elusive, and we have been unable to present anything more tangible than this conjecture. We leave the proof of this control method as an open problem to the reader.

9.2 Finite Time With Continuous Control - Scalar Systems

Consider a scalar dynamical system of the form

$$\dot{x} = u \tag{199}$$

where $x \in \Re$ and the control $u \in \Re$. Given the control objective of regulating the state of the system (199) to the origin commencing from arbitrary initial conditions in finite time, we choose u in the following manner.

$$u = -k|x|^{\frac{1}{r}} sgn[x] \tag{200}$$

where $k \in \Re_+$ and $r > 1$.

Comment 9.1 The choice of u is novel since the control is obviously continuous, but not differentiable at the origin. Also note that the control law involves raising the power of $|x|$ to a fraction, and hence the term fractional control.

We now make the following claim regarding existence of trajectories, stability and convergence for the system (199).

Claim 9.1 *Existence of solutions, stability and convergence for fractional control of scalar systems.*

Given

(G1) System dynamics of the form (199)

If

(I1) The control u is specified as in (200)

Then

(T1) Cauchy solutions exist for (199) subject to (200).

46

(T2) $x = 0$ *is stable.*

(T3) Indeed $x \to 0$ in finite time t^*, given by $t^* = \frac{|x(0)|^{1-\frac{1}{k}}}{k[1-\frac{1}{k}]}$

Proof: ♠ ▷ Existence of Cauchy solutions is easily seen by the fact that the righthand side of the differential system is continuous.

Considering the candidate Lyapunov function $V(x) : \Re \to \Re_+$ given by

$$V = \frac{x^2}{2} \tag{201}$$

Indeed $\dot{V} = -k|x|^{1+\frac{1}{r}} \le 0$. Attractivity of the origin is therefore confirmed.

To show finite time convergence we solve the equation

$$\dot{x} = -k|x|^{\frac{1}{r}} sgn[x] \tag{202}$$

to obtain that $t^* = \frac{|x(0)|^{1-\frac{1}{k}}}{k[1-\frac{1}{k}]}$. The proof of the claim is complete. ◁ ♠

We now make a comparison between three kinds of control laws that regulate the state of the system (199) to the origin.

$$u_{linear} = -kx \tag{203}$$

$$u_{sliding} = -\frac{k}{|x|}x \quad \text{if } |x| > 0 \tag{204}$$

$$u_{fractional} = -\frac{k}{|x|^{1-\frac{1}{r}}}x \quad \text{if } |x| > 0 \tag{205}$$

Comparison of control efforts reveals something interesting. For all $|x| > 1$, the linear controller has the maximum gain, closely followed by the fractional controller, and the sliding mode controller has the smallest gain. However the situation is reversed when $|x| < 1$. .

Similarly, the times taken to reach the origin from initial conditions $x(0) \ne 0$ are

$$t_{linear} = \infty \tag{206}$$

$$t_{sliding} = \frac{|x(0)|}{k} \tag{207}$$

$$t_{fractional} = \frac{|x(0)|^{1-\frac{1}{k}}}{k[1 - \frac{1}{k}]} \tag{208}$$

We now formulate an alternative control law that combines the best of both the linear and the fractional control law to give

$$u^* = -kx \quad \text{if } |x| > 1 \tag{209}$$

$$= -\frac{k}{|x|^p}x \quad \text{if } 0 < |x| \le 1 \tag{210}$$

$$p > 1 \tag{211}$$

Note that we do not bother to define the control law at the origin.

There is yet another viewpoint as to why this control law does better than a linear control law when $|x| < 1$. The linear control law has an eigenvalue $-k$, and but u^* has an eigenvalue $\frac{-k}{|x|^{\frac{1}{p}}}$ (we use the term eigenvalue very loosely here, since strictly speaking even the term eigenvalues does not make sense in a nonlinear context) that is increasing to ∞ as $|x| \to 0$. Though both control laws are bounded, qualitatively, the fractional control law converges much faster to the origin as seen in the following scalar example.

Example 9.1 *Fractional Control - Scalar Case*
Consider the simple scalar example given by the equations

$$\dot{x} = u \tag{212}$$

Choose

$$u_{linear} = -kx \tag{213}$$

$$u^* = -kx \quad \text{if } |x| > 1 \tag{214}$$

$$= -\frac{k}{|x|^p}x \quad \text{if } 0 < |x| \le 1 \tag{215}$$

$$k = 2 \tag{216}$$

$$p = 2 \tag{217}$$

It is clear from the simulation plots that the modified fractional control law outperforms the linear control law.

Now consider a linear system in the controllable canonical form, given by the following equations.

$$\dot{x}_1 = x_2 \tag{218}$$

$$\vdots \quad \vdots \quad \vdots \tag{219}$$

$$\dot{x}_n = u \tag{220}$$

where $x \in \Re^n$, $u \in \Re$.

Now choose the control u to be of the following form

$$u = -k_1 x_1 - k_2 x_2 - \cdots - k_n x_n \quad \text{if } ||x||_2 > 1 \tag{221}$$

$$= -\frac{k_1}{||x||_2^{\frac{n}{r}}} x_1 - \frac{k_2}{||x||_2^{\frac{n-1}{r}}} x_2 - \cdots - \frac{k_n}{||x||_2^{\frac{1}{r}}} x_2 \quad \text{if } 0 < ||x||_2 < 1 \tag{222}$$

where

$$||x||_2 = \sum_{i=1}^{n} x_i^2 \tag{223}$$

$$r > n \tag{224}$$

$$s^n + k_n s^{n-1} + \cdots + k_1 \text{ is a stable Hurwitz polynomial} \tag{225}$$

We now formulate the following conjecture.

Conjecture 9.1 *Existence of solutions, stability and convergence for fractional control of controllable linear systems.*
Given

(G1) System dynamics of the form (218) - (220)

If

(I1) The control u is specified as in (221) - (225)

Then

(T1) Filippov solutions exist for systems (218) - (220) subject to control (221) - (225)

(T2) $x = 0$ is globally stable

(T3) Indeed $x \to 0$ faster than a comparable linear control law of the form $u_{linear} = -k_1 x_1 - k_2 x_2 - \cdots - k_n x_n$

Qualitative Proof:
First we note that within the unit ball ($||x||_2 < 1$), the control effort is bounded by

$$|u| \le \sum_{i=1}^{n} k_i \tag{226}$$

So the control does not blow up at any instant of time. We have used the notion that in the nonlinear setting, within the unit ball, we have each eigenvalue λ_i $i = 1, 2, \ldots, n$ of this system being replaced by $\frac{-\lambda_i}{||x||_2^{\frac{1}{r}}}$ where $r > n$.

Consequently, from the way the λ_i $i = 1, 2, \ldots, n$ combine to form the k_i of the control law, the form of the control law is intuitively obvious.

We find by simulation that the robustness, and rate of convergence of the proposed nonlinear law are much superior to a linear control law. The proof of this conjecture, however, has eluded us.

Example 9.2 *Fractional Control for Magnetic Bearing*
We present simulation results for a system of the form

$$\dot{x}_1^i = x_2^i \tag{227}$$

$$\dot{x}_2^i = v^i \tag{228}$$

where

$$v^i = -k_1 x_1^i - k_2 x_2^i \quad if \ ||x||_2 > 1 \tag{229}$$

$$= -\frac{k_1}{||x||_2^{\frac{4}{9}}} x_1^i - \frac{k_2}{||x||_2^{\frac{2}{3}}} x_2^i \quad if \ 0 < ||x||_2 < 1 \tag{230}$$

$$k_1 = 6 \tag{231}$$

$$k_2 = 11 \tag{232}$$

The results show the faster convergence of the state subject to fractional control.
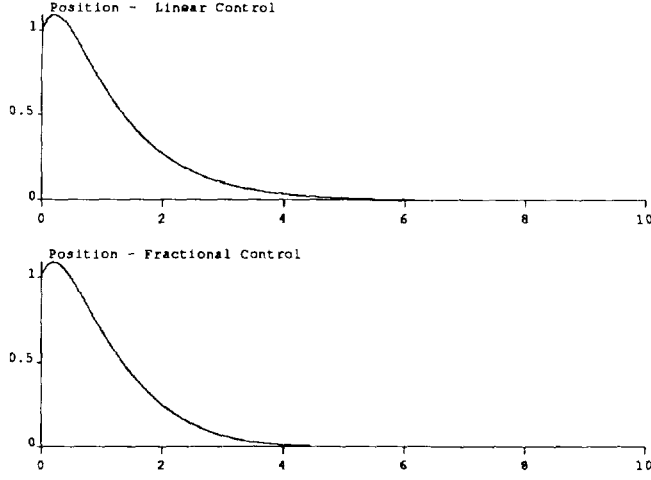
Figure 7: Fractional Control of a Single Axis of a Magnetic Bearing

10 Sliding Mode Observers for the Magnetic Bearing

10.1 Introduction

We first present the basic theory of sliding mode observers for mechanical systems, and prove the existence of generalized Filippov solutions and stability. We then show the convergence of the observer state errors to zero. We then present the problem with existing theory, and present bounds on variables that would prevent observer failure. Finally we remark on the utilization of the computed bounds as a design rule to help design such sliding mode observers.

The problem of designing observers using sliding mode theory was first introduced and studied by [Mis88]. Here the observation problem is treated as a special case of a state regulation problem. Sliding surfaces are designed based on the error dynamics, and reaching a sliding surface is equivalent to the error in the estimate of the measured state decaying to zero. In sliding mode control, the surface $S = 0$ is reached in finite time, and on that surface the states decay exponentially. Similarly, in sliding mode observer theory, the error in the estimate of the measured state decays in finite time. All other state errors decay exponentially.

Consider a simple mechanical system of the form

$$\dot{x}_1 = x_2 \tag{233}$$
$$\dot{x}_2 = u \tag{234}$$

where $x \in \Re^2$ and $u \in \Re$. Now consider an observer of the following form.

$$\dot{\hat{x}}_1 = \hat{x}_2 + k_1 sgn[\tilde{x}_1] \tag{235}$$
$$\dot{\hat{x}}_2 = k_2 sgn[\tilde{x}_2] \tag{236}$$
$$\tilde{x} = x - \hat{x} \tag{237}$$

Such an observer structure equation leads to error dynamics of the form

$$\dot{\tilde{x}}_1 = \tilde{x}_2 - k_1 sgn(\tilde{x}_1) \tag{238}$$
$$\dot{\tilde{x}}_2 = -k_2 sgn[\tilde{x}_1] \tag{239}$$

Theorem 10.1 *Convergence of the state estimation errors:*

Given

(G1) Error dynamics of the form (238)- (239)

  If

(I1) $|\tilde{x}_2| < k_1$

Then

(T1) Generalized Filippov Solutions exist for the system (238)- (239)

(T2) The one-dimensional manifold $\tilde{x}_1 = 0$ is attractive

(T3) The averaged dynamics of $\tilde{x}_2$ about the surface $\tilde{x}_1 = 0$ decays exponentially.

Proof: ♠ ▷ Existence of Filippov solutions is due to the fact that the governing differential inclusions are closed, bounded, convex and uppersemicontinuous.

We will prove the theorem using simple Lyapunov analysis. Consider the candidate Lyapunov function,

$$V = \frac{\tilde{x}_1^2}{2} \tag{240}$$

Differentiating V along the flow of the system(238), we get,

$$\dot{V} = \tilde{x}_1[\tilde{x}_2 + k_1 sgn[\tilde{x}_1]] \tag{241}$$

$$< -||\tilde{x}_1||[k_1 - \tilde{x}_2 sgn[\tilde{x}_1]] \tag{242}$$

Thus as long $\tilde{x}_2 < k_1$, $\dot{V} < 0$, indeed the surface $\tilde{x} = 0$ is attractive.

Comment 10.1 The Theorem asserts the existence of a tubular neighbourhood around the $\tilde{x}_2 = 0$ axis where the trajectories converge to the manifold given by $\tilde{x}_1 = 0$. It is to be noted that $\tilde{x}_2$ must not be greater than k_1 until the trajectories converge to $\tilde{x}_1 = 0$. Some additional conditions are necessary to prevent such an occurrence.

The dynamics of the system when constrained to evolve on the surface $\tilde{x}_1 = 0$, can be derived using the Fillipov solution concept. Thus, taking a convex combination of the dynamics on either side of the sliding surface, we get,

$$\dot{\tilde{x}}_1 = \gamma[\tilde{x}_2 + k_1] + (1 - \gamma)[\tilde{x}_2 - k_1] \tag{243}$$

$$\dot{\tilde{x}}_2 = \gamma k_2 + (1 - \gamma)(-k_2] \tag{244}$$

From the above equations, we eliminate γ, and from the invariance of the sliding surface, we get,

$$\dot{\tilde{x}}_1 = 0 \tag{245}$$

$$\dot{\tilde{x}}_2 = -\frac{k_2}{k_1}\tilde{x}_2 \tag{246}$$

Exponential decay of $\tilde{x}_2$ is clear from the above equation. The proof of the theorem is complete. ◁ ♠

We will now utilize this design technique to design sliding mode observers for the magnetic bearing. Consider the magnetic bearing system represented by the following equations.

$$\dot{x}_1^1 = x_2^1 \tag{247}$$

$$\dot{x}_2^1 = u^1 \tag{248}$$

$$\dot{x}_1^2 = x_2^2 \tag{249}$$

$$\dot{x}_2^2 = u^2 \tag{250}$$

$$\dot{x}_1^3 = x_2^3 \tag{251}$$

$$\dot{x}_2^3 = -a * \omega * x_2^4 + u^3 \tag{252}$$

$$\dot{x}_1^4 = x_2^4 \tag{253}$$

$$\dot{x}_2^4 = a * \omega * x_2^4 + u^1 \tag{254}$$

We design a sliding mode observer for this system of the following form,

$$\dot{\hat{x}}_1^1 = \hat{x}_2^1 + k_1 sgn[\tilde{x}_1^1] \tag{255}$$

$$\dot{\hat{x}}_2^1 = u^1 + k_2 sgn[\tilde{x}_1^1] \tag{256}$$

$$\dot{\hat{x}}_1^2 = \hat{x}_2^2 + k_1 sgn[\tilde{x}_1^2] \tag{257}$$

$$\dot{\hat{x}}_2^2 = u^2 + k_2 sgn[\tilde{x}_1^2] \tag{258}$$

$$\dot{\hat{x}}_1^3 = \hat{x}_2^3 + k_1 sgn[\tilde{x}_1^3] \tag{259}$$

$$\dot{\hat{x}}_2^3 = -a * \omega * \hat{x}_2^4 + u^3 + k_2 sgn[\tilde{x}_1^3] \tag{260}$$

$$\dot{\hat{x}}_1^4 = \hat{x}_2^4 + k_1 sgn[\tilde{x}_1^4] \tag{261}$$

$$\dot{\hat{x}}_2^4 = a * \omega * \hat{x}_2^3 + u^4 + k_2 sgn[\tilde{x}_1^4] \tag{262}$$

where $\tilde{x}_j^i = x_j^i - \hat{x}_j^i$ $i = 1, 2, \dots, 4$ $j = 1, 2$, and $k_1, k_2 > 0$.

50

We write the observer error equations as follows.

$$\dot{\tilde{x}}_1^1 = \tilde{x}_2^1 - k_1 sgn[\tilde{x}_1^1] \tag{263}$$

$$\dot{\tilde{x}}_2^1 = -k_2 sgn[\tilde{x}_1^1] \tag{264}$$

$$\dot{\tilde{x}}_1^2 = \tilde{x}_2^2 - k_1 sgn[\tilde{x}_1^2] \tag{265}$$

$$\dot{\tilde{x}}_2^2 = -k_2 sgn[\tilde{x}_1^2] \tag{266}$$

$$\dot{\tilde{x}}_1^3 = \tilde{x}_2^3 - k_1 sgn[\tilde{x}_1^3] \tag{267}$$

$$\dot{\tilde{x}}_2^3 = -a * \omega * \tilde{x}_2^4 - k_2 sgn[\tilde{x}_1^3] \tag{268}$$

$$\dot{\tilde{x}}_1^4 = \tilde{x}_2^4 - k_1 sgn[\tilde{x}_1^4] \tag{269}$$

$$\dot{\tilde{x}}_2^4 = a * \omega * \tilde{x}_2^3 - k_2 sgn[\tilde{x}_1^4] \tag{270}$$

We now state the result concerning the stability and convergence of the observer states to their true values.

Theorem 10.2 *Convergence of the state estimation errors:*

Given

(G1) Error dynamics of the form (263)- (270)

If

(I1) $|\tilde{x}_2^i| < k_1$

Then

(T1) Generalized Filippov Solutions exist for the system (238)- (239).

(T2) The one-dimensional manifold $\tilde{x}_1^i = 0$ is attractive.

(T3) The averaged dynamics of $\tilde{x}_2^i$ about the surface $\tilde{x}_1^i = 0$ decays exponentially.

Proof: ♠ ▷ Stability of the error dynamics is easily shown utilizing the following Lyapunov function.

$$V = \sum_{i=1}^{4} k_2 |\tilde{x}_1^i| + \frac{[\tilde{x}_2^i]^2}{2} \tag{271}$$

$$\dot{V} = -k_1 k_2 \sum_{i=1}^{4} [sgn[\tilde{x}_1^i]]^2 \tag{272}$$

$$\leq 0 \tag{273}$$

Furthermore, $\dot{V} = 0 \rightarrow sgn[\tilde{x}_1^i] = 0$. Invoking the invariance principle of LaSalle, it is seen that the largest invariant set containing the set $\tilde{x}_1^i = 0$ $i = 1.2 \dots, 4$ is the set $\tilde{x}_2^i = 0, i = 1, 2, \dots, 4$. Stability, and hence convergence to the origin is therefore assured.

We show convergence of the states $\tilde{x}_1^i, i = 1, 2, \dots, 4$ to the origin in finite time as follows. As the system is asymptotically stable, there exists an instant of time t^* such that for all $t > t^{star}$, $||\tilde{x}||_2 < k_1$, $\rightarrow |\tilde{x}_2^i| < k_1$. Invoking the theorem on the finite time convergence of the sliding mode observer, the observer states converge in finite time. ◁ ♠

11 Closure

We have shown a variety of nonlinear controllers for the magnetic bearing that are simple and robust to build and are guaranteed to be stable. We believe that the design of controllers utilizing principles of nonlinear analysis provides new richness, insight and excitement in the design of high precision magnetic bearings.

References

[AB90]   Charalambos D. Aliprantis and Owen Burkinshaw. *Principles Of Real Analysis*. Academic Press Inc., 1990.

[AC84]   Jean-Pierre Aubin and Arrigo Cellina. *Differential Inclusions - Set-Valued Maps and Viability Theory*. Springer-Verlag, 1984.

[AEB75]   Y. C.Ho A. E. Bryson. *Applied Optimal Control*. Hemisphere Publishing Corporation, 1975.

[AKP91]   R. Gurumoorthy A. K. Pradeep. On concluding stability for Lyapunov analysis of max-functions. *Proceedings of VARSCON 91, Variable Structure Control of Power Conversion Systems, Reno Nevada*, June 1991.

[AKP92a]   S. M. Shahruz A. K. Pradeep. A control law that achieves simultaneous tracking for a group of systems in finite time. *International Journal of Control*, 56:1419–1428, 1992.

[AKP92b]   S. M. Shahruz A. K. Pradeep. A control law that achieves simultaneous tracking for a group of systems in finite time. *Proceedings of the 1992 American Control Conference*, pages 3134–3135, June 1992.

[AKP 5]   S. M. Shahruz A. K. Pradeep. Design of control laws that achieve simultaneous tracking for a group of systems in finite time. *ESRC Technical Report - UC Berkeley*, pages 3134–3135, ESRC 91-5.

[Bar76]   Robert G. Bartle. *The Elements Of Real Analysis*. John Wiley & Sons., 1976.

[Fil61]   A. F. Filippov. Application of theory of differential equations with discontinuous righthand sides to nonlinear problems. *Proceedings Of The 1st IFAC Congress*, 1:923–927, 1961.

[Fil88]   A. F. Filippov. *Differential Equations with Discontinuous Righthand Sides*. Kluwer Academic Publishers, 1988.

[KF70]   A. N. Kolmogorov and S. V. Fomin. *Introductory Real Analysis*. Dover Publications Inc, 1970.

[Kor68]   Korivin. Planar dynamical systems. *J. Math. Mech*, 8:47–60, 1968.

[Mis88]   A. Misawa. *Observation of Nonlinear Dynamical Systems*. PhD thesis, Massachussetts Institute of Technology, 1988.

[Pra92]   A. K. Pradeep. *Sliding Mode Control of Perturbed Nonlinear Systems*. PhD thesis, University of California, Berkeley, 1992.

[RG93]   A. K. Pradeep R. Gurumoorthy. Modelling and control of a rotor supported by magnetic bearings. *Proceedings of the Second International Symposium on Magnetic Suspension Technology, Seattle WA*, August 1993.

[Rud64]   Walter Rudin. *Principles Of Mathematical Analysis*. McGraw-Hill Book Company, 1964.

[SMS93]   A. K. Pradeep S. M. Shahruz. A high precision synchronizing control system for biaxial positioning tables. *Proceedings of the 1993 American Control Conference*, pages 2239–2240, June 1993.

[SMS 7]   A. K. Pradeep S. M. Shahruz. A high precision synchronizing control system for biaxial positioning tables. *ESRC Technical Report - UC Berkeley*, March 1992, ESRC 92-7.

[SMSar]   A. K. Pradeep S. M. Shahruz. A high precision synchronizing control system for biaxial positioning tables. *ASME Journal of Dynamic Systems, Measurement, and Control*, December 1993 (to appear).

[SRS91]   B. Sheng S. R. Sanders, R. Gurumoorthy. Analysis technique for practical implementation of variable structure control systems. *Proceedings of VARSCON 91, Variable Structure Control of Power Conversion Systems, Reno Nevada*, June 1991.

[SS83]   J. J. Slotine and S. S. Sastry. Tracking control of nonlinear systems using sliding surfaces with applications to robot manipulators. *International Journal Of Control*, 38. No.2:465–492, 1983.

[Tee92]   A. Teel. Global stabilization and restricted tracking for multiple integrators with bounded controls. *Systems and Control Letters*, 18, 1992.

[YCBDB82]   C. D. Morette Y. C. Bruhat and M. Dillard-Bleick. *Analysis, Manifolds And Physics*. Elsevier Science Publishers, 1982.

12 Appendix - Mathematical Foundations of Discontinuous Control

In this section we present basic definitions, facts, and examples about measures of sets and functions, integrability, absolute continuity, convexity, and differential inclusions. For further details about the definitions to follow, refer to [KF70], [AB90], [YCBDB82], [Rud64], [Bar76], [AC84]. We will use the following concepts to develop solutions of differential equations with discontinuous right hand sides.

12.1 Measure of Sets

We commence by formalizing the notion of an interval.

Definition 12.1 *Let $\Re^p$ denote p dimensional Euclidean space. By an* **interval** *in $\Re^p$, we refer to the set of points $x = [x_1^1, \ldots, x_p]^T$ such that*

$$\exists a_i \leq x_i \leq b_i \quad (i = 1, \ldots, p) \tag{274}$$

52

The possibility that $a_i = b_i$ is not ruled out, and the empty set is also included as a possible candidate for the intervals. An interval can be understood to refer to a p dimensional cube in $\Re^p$.

Definition 12.2 *If A is the union of a finite number of intervals, then A is said to be an* **elementary set.**

Definition 12.3 *If I is an interval in* $\Re^p$, *the* **measure** μ *of the interval I is defined to be*

$$\mu : \Re^p \to \Re = \times_{i=1}^{p}(b_i - a_i) \tag{275}$$

The measure of a set is in some rough sense the volume of the geometric object formed by that set. Indeed, the measure of a $k \leq n - 1$ dimensional object in n dimensional space is 0. Therefore, the measure of a point in $\Re^2$ is 0, and the measure of a plane in $\Re^3$ is also 0. The kinds of control we work with will vanish on an $n - 1$ dimensional subspace of n dimensional space. Therefore they vanish on a subspace of 0 measure.

Definition 12.4 *If the set A is the union of a finite number of pairwise disjoint intervals, (i.e) $A = \bigcup_{j=1}^{n} I_j$, where $I_j \bigcap I_k = \emptyset \; \forall \; j \neq k$, then the* **measure** μ *of the set A is*

$$\mu(A) = \sum_{j=1}^{n} \mu(I_j) \tag{276}$$

Fact 12.4.1 Open sets are measurable.

Fact 12.4.2 The union of a sequence of measurable sets is also measurable.

Fact 12.4.3 The complement of a measurable set is also measurable.

Fact 12.4.4 A set consisting of one point is measurable. Its measure is 0.

Fact 12.4.5 A denumerable set (a union of a sequence of countably many one-point sets) is measurable. Its measure is 0.

Fact 12.4.6 Every subset of a set of measure 0 is measurable. Its measure is 0.

Example 12.1 *Measure of Set of Undefined Control*
Consider the control $u(t) : \Re_+ \to \Re$ given by

$$u(t) = -sgn[x] \tag{277}$$

where $x \in \Re$. Note that the function $sgn[x] : \Re - \{0\} \to [-1, 1]$ is not defined at 0. Using fact (12.4.4), we assert that the control is not defined on a set of zero measure.

Definition 12.5 *By* **almost everywhere,** *we mean everywhere excepting possibly on a set of measure 0.*

Simply, by saying a relation holds true almost everywhere, we assert that the set of points where the relation fails to hold, has measure zero.

Example 12.2 *Behaviour of Functions*
Consider functions $f : X \to \Re$, $g : X \to \Re$, $f_n : X \to \Re \; n = 1, 2, \ldots$. The following are the instances of almost everywhere relations between the functions.

1. $f = g$ almost everywhere, if $\mu\{x \in X : f(x) \neq g(x)\} = 0$.

2. $f \geq g$ almost everywhere, if $\mu\{x \in X : f(x) < g(x)\} = 0$.

3. $f_n \to f$ almost everywhere, if $\mu\{x \in X : f_n(x) \neq f(x)\} = 0$.

4. $f_n \uparrow f$ almost everywhere, if $f_n \leq f_{n+1}$ almost everywhere for all n and $f_n \to f$ almost everywhere.

5. $f_n \downarrow f$ almost everywhere, if $f_{n+1} \leq f_n$ almost everywhere for all n and $f_n \to f$ almost everywhere.

Example 12.3 *Controls Defined Almost Everywhere*
Consider the control $u(t) : \Re_+ \to \Re$ given by

$$u(t) = -sgn[x] \tag{278}$$

where $x \in \Re$ Note that the control $u(t)$ is defined almost everywhere.

12.2 Measurable Functions

In the definitions to follow, we will consider real valued functions that map a measurable space X with measure μ to the extended real line $\Re$.

Definition 12.6 *A function $f : X \to \Re$ is measurable if the set $S = \{x \in X : |f(x)| < a\}$ is measurable for all $a > 0 \in \Re$.*

Measurability of a function is a property of the function, based on the measurability of a certain set in its domain.

Example 12.4 *Measurable Functions*
All continuous functions $f : \Re^n \to \Re$ are measurable. Proof is by showing that by definition, S is open, and hence measurable.

The following are some facts based on operations between measurable functions.

Fact 12.6.7 Given $f : X \to \Re$, if f is measurable, then $\forall k \in \Re$, kf is measurable.

Fact 12.6.8 Given $f : X \to \Re$, and $g : X \to \Re$, if f and g are measurable, then $f + g$, $f - g$, and fg are measurable.

Fact 12.6.9 Given $p : X \to \Re$, and $f : X \to \Re$, if f is measurable, and if $f(x) = p(x)$ almost everywhere, then p is also measurable.

We now present a fact concerning the properties of the limit function, based on the properties of the convergent functions.

Fact 12.6.10 Given a sequence of functions $f_i : X \to \Re$ $i = 1, 2, \ldots$ convergent almost everywhere to the function $f : X \to \Re$, if each $f_i, i = 1, 2, \ldots$ is measurable then the function f is also measurable.

12.3 Integrable Functions

The key idea of the integral developed by Lesbegue is as follows. In Riemann integration, if $f : [a, b] \in \Re \to \Re$, then to form the Riemann integral we divide the domain of f, $[a, b]$ into many subintervals and group together neighboring points in the domain of the function f. On the other hand, the Lesbegue integral is formed by grouping together points of the domain where the function f takes neighboring values in the *range !* Indeed, the key idea is to partition the range of a function rather than the domain. It is immediately obvious that such a technique allows us to consider functions that have multiple points of discontinuity, or may not even be defined at some points.

The functions in this section map a measurable space X with measure μ into the extended real line $\Re$.

Definition 12.7 *Let $f : X \to \Re$ be a measurable function. Furthermore, let f take no more than countably many distinct values $y_1, y_2, \ldots, y_n, \ldots$ in its range. Then, the Lesbegue integral of the function f over the set A, denoted by $\int_A f(x)d\mu$, is given by*

$$\int_A f(x)d\mu = \sum_j y_j \mu(A_j) \tag{279}$$

where

$$A_j = \{x : x \in A, f(x) = y_j\} \tag{280}$$

if the series (280) is convergent. If the Lesbegue integral of the function f exists, then we say the function is integrable, or summable with respect to the measure μ on the set A.

Example 12.5 *Integrable Functions*
Consider the constant function $f(x) = 1$. Let us evaluate the Lesbegue integral of the function. Indeed,

$$\int_A f(x)d\mu = \int_A 1 d\mu \tag{281}$$
$$= \mu(A) \tag{282}$$

As the Lesbegue integral exists, the function is said to be integrable.

Fact 12.7.11 Given a measurable function $f : X \to \Re$, if there exists a sequence $f_n : X \to \Re$ of integrable functions converging uniformly to f on the set A, then the function f is said to be integrable.

54

Fact 12.7.12 Given $f : X \to \Re$, $g : X \to \Re$, if $g > 0$, and g is integrable on a set A, and $|f(x)| \leq g(x)$ almost everywhere on A, then f is also integrable on A, and

$$\left| \int_A f(x)d\mu \right| \leq \int_A \phi(x)d\mu \tag{283}$$

Fact 12.7.13 Given $f : X \to \Re$, if f is bounded and measurable on a set A, then f is integrable on A.

Fact 12.7.14 Given $f : X \to \Re$, if f is integrable on a set A, then f is integrable on every measurable subset of A.

Fact 12.7.15 Given $f_n : X \to \Re$ $i = 1, 2, \ldots$, a sequence of functions converging to a limit $f : X \to \Re$ almost everywhere on a set A, if there exists a function $g : X \to \Re$ integrable on the set A, and $|f(x)| \leq g(x)$, $\forall x$ almost everywhere in A, then f is integrable on A, and

$$\lim_{n \to \infty} \int_A f_n(x)d\mu = \int_A f(x)d\mu \tag{284}$$

Fact 12.7.16 Given $f_n : X \to \Re$, a sequence of functions converging to a limit $f : X \to \Re$ almost everywhere on a set A, if $\exists k \in \Re$ such that $|f(x)| \leq k$, $\forall x$ almost everywhere in A $n = 1, 2, \ldots$, then f is integrable on A, and

$$\lim_{n \to \infty} \int_A f_n(x)d\mu = \int_A f(x)d\mu \tag{285}$$

12.4 Absolute Continuity

Definition 12.8 *The function $f : X \to \Re$ is said to be absolutely continuous on the interval $[a, b] \in \Re$ if for any $\epsilon > 0$, there exists $\delta > 0$ such that for finitely many disjoint open intervals $(a_i, b_i) \subset [a, b]$*

$$\sum_{i=1}^{n} |b_i - a_i| < \delta \Rightarrow \sum_{i}^{n} |f(b_i) - f(a_i)| < \epsilon \tag{286}$$

That is, the function is of bounded variation. It is to be noted, however, that functions of bounded variation need not necessarily be absolutely continuous.

Fact 12.8.17 An absolutely continuous function $f : X \to \Re$ is necessarily continuous.

Note however, that the converse is not true. We will now present an example to illustrate that the converse is not true.

Example 12.6 *Continuity and Absolute Continuity*
Consider the function $f : [0, 1] \to \Re$ defined as follows

$$f(0) = 0 \tag{287}$$

$$f(x) = x^2 \cos \frac{1}{x^2} \quad 0 < x \leq 1 \tag{288}$$

The function f is differentiable at each $x \in [0, 1]$, but is not of bounded variation. This is trivially shown by considering a partitioning as follows.

$$P_n = \{0, \sqrt{\frac{2}{2n\pi}}, \sqrt{\frac{2}{(2n-1)\pi}}, \ldots, \sqrt{\frac{2}{3\pi}}, \sqrt{\frac{2}{2\pi}}, 1\} \tag{289}$$

$$\text{Variation of } f = \cos 1 + \frac{2}{\pi} \sum_{j=1}^{n} \frac{1}{j} \tag{290}$$

$$= \infty \tag{291}$$

The function is not of bounded variation, and hence is not absolutely continuous. We have thus shown an example of a continuous function that is not absolutely continuous.

Fact 12.8.18 If $f : X \to \Re$, then if f is differentiable, the f is absolutely continuous.

Fact 12.8.19 Any function that satisfies the Lipschitz condition is absolutely continuous.

The importance of absolute continuity is that for Lesbegue integration, the fundamental theorem of calculus holds precisely only for absolutely continuous functions.

12.5 Convexity

Definition 12.9 *A set $M \in \Re^n$ is said to be* **convex** *if it contains the joining of any two points in the set.*

Example 12.7 *Set of Bounded Functions*

Consider $C_{[a,b]}$, the space of all continuous real valued functions $f : [a,b] \in \Re \to \Re$, and let M be the subset of $C_{[a,b]}$ defined as follows

$$M = \{f \in C_{[a,b]} : |f(x)| \le 1\} \tag{292}$$

Then, the set M is convex. This is easily evidenced by considering the join of two functions $f(x), g(x) \in M$. For any $\alpha, \beta > 0$ such that $\alpha + \beta = 1$, we have

$$|\alpha f(x) + \beta g(x)| \le |\alpha + \beta| \tag{293}$$
$$\le 1 \tag{294}$$
$$\in M \tag{295}$$

The join of two elements of M belongs to M, and convexity is shown.

Fact 12.9.20 *If a set M is convex, so is its interior.*

Fact 12.9.21 *The intersection of a finite number of convex sets is also convex. That is,*

$$\bigcap_{i=1}^{n} M_i \ \text{is convex} \tag{296}$$

where each M_i is convex.

Definition 12.10 *The minimal convex set containing a convex set M is called the* **convex hull** *of M.*

12.6 Set Valued Maps

Definition 12.11 *A function $f(x) : \Re^n \to \Re$ is said to be* **upper semi-continuous** *at a point $x^\star \in \Re^n$ if*

$$f(x^\star) = \limsup_{x \to x^\star} f(x) \tag{297}$$

Example 12.8 *Upper-Semicontinuous sgn Function*

Consider the function $sgn[x] : \Re \to [-1, 1]$ defined as follows

$$sgn[x] = 1 \quad x \ge 0 \tag{298}$$
$$= -1 \quad x < 0 \tag{299}$$

It is obvious that at $x = 0$, the function is upper-semicontinuous.

Definition 12.12 *Having defined some properties of real-valued functions, we now move on to discussing some important properties of set-valued functions. Given two sets X and Y, we define a map $F : X \to Y$ to be* **set-valued**, *if $F : X \to Y$ associates to any $x \in X$, a subset $F(x) \in Y$.*

Definition 12.13 *The* **domain** *of a set valued map $F : X \to Y$ is defined to be $Domain(F) = \{x \in X : F(x) \ne 0\}$ and the* **range** *$Range(F)$ of a set valued map $F : X \to Y$ is defined to be $\bigcup_{x \in X} F(x)$.*

Definition 12.14 *The domain $Domain(F)$ of a set valued map $F : X \to Y$ is defined to be* **strict** *if $Domain(F) = X$, and is defined to be* **proper** *if $Domain(F) \ne 0$.*

Definition 12.15 *A set-valued map $F : X \to Y$ is defined to be* **compact** *if its range $Range(F)$ is a compact subset of Y.*

Definition 12.16 *A set valued map $F : X \to Y$ is* **upper semicontinuous** *at $x^\star \in X$, if for any open set S_Y containing $F(x^\star)$ there exists a neighbourhood S_X of $x^\star$ such that $F(S_X) \subset S_Y$.*

In this section we present basic results for the local existence of solutions of differential equations with discontinuous righthand sides. We define a sliding mode, and present conditions for the existence of a sliding mode. We then present briefly the development of the sliding mode control law, and the various regularizations of it.

We will now state without proof the following two important results from analysis that we will need.

Arzela-Ascoli Theorem:

Let K be a compact subset of R^p and let F be a collection of functions which are continuous on K and have values in R^q. The following properties are equivalent.

1. *The family F is uniformly bounded and equicontinuous on K.*

2. *Every sequence from F has a subsequence which is uniformly convergent on K.*

The theorem allows us to define a sequence of approximate solutions of a differential equation, and guarantees convergence of the approximate solutions to a limit function of the sequence is equicontinuous and uniformly bounded.

Filippov Convergence Lemma:

Given a differential inclusion of the form $\dot{x} = \mathcal{F}(x, t)$. If the inclusion $\mathcal{F}(x, t)$ is closed, bounded, convex, and uppersemicontinuous, the limit of any uniformly convergent sequence of approximate solutions of the differential inclusion is also a solution of this inclusion, in the domain of convergence.

That the limit function satisfies the differential inclusion is the main reason for invoking the lemma.

Session 2 – Applications

Chairman: Willard W. Anderson
NASA Langley Research Center

HIGH PERFORMANCE DATA ACQUISITION, IDENTIFICATION, AND MONITORING FOR ACTIVE MAGNETIC BEARINGS

Raoul Herzog
International Center for Magnetic Bearings
ETH Zurich, Switzerland

Roland Siegwart
MECOS Traxler AG
8400 Winterthur, Switzerland

SUMMARY

Future Active Magnetic Bearing systems (AMB) must feature easier on–site tuning, higher stiffness and damping, better robustness with respect to undesirable vibrations in housing and foundation, and enhanced monitoring and identification abilities. To get closer to these goals we developed a fast parallel link from the digitally controlled AMB to Matlab[1], which is used on a host computer for data processing, identification and controller layout. This enables the magnetic bearing to take its frequency responses without using any additional measurement equipment. These measurements can be used for AMB identification.

INTRODUCTION

Active Magnetic Bearing systems have already shown their feasibility in various applications [1]. Thanks to the progresses in AMB control [3],[6], the number of demanding AMB applications is growing fast. For that reason, there is a strong need for tools and facilities which enable rapid and cost effective prototyping.

A MATLAB INTERFACE FOR DIGITALLY CONTROLLED AMBs

We implemented digital AMB control on a fast TMS320C25 digital signal processor board (DSP) which enables stand–alone operation of the final AMB application. For installation and optimization purposes a fast parallel link to a host PC can be plugged onto the signal processor board. For the putting into operation of new AMB prototypes and for on–site tuning we developed a powerful Matlab–based environment on the host PC. This enables us to use all of Matlab's built–in facilities: numerics, signal processing, graphics, as well as the extensibility offered by available toolboxes on control, robust control and system identification.

---

[1] Matlab is a trademark of The MathWorks Inc. and has become an industrial standard software package for numerical computations.

The *low level* interface layer between Matlab and the AMB application basically consists of two commands for data reading from and writing to specified memory addresses of the signal processor board. This low level interfacing is implemented using Matlab's MEX facility of calling compiled and dynamically linked C subroutines.

With the *mid-level* interface layer between Matlab and the AMB controller board specific memory addresses no longer have to be kept in mind. Variables on the AMB controller board can be accessed by *name*, see figure 1, through a hidden cross reference table. This cross reference table not only manages the bookkeeping of memory addresses and variable names, but also enables the use of vector and matrix objects with *variable* size. This is particularly important for loading or changing controller state space matrices.

The *high level* Matlab interface layer incorporates tools for taking time history measurements of AMB controller variables, see figure 1. Frequency response measurements can be effectuated by a sine wave sweep. The sine wave is generated in the AMB signal processor program. It is completely configurable; i.e. frequency, amplitude, and excitation variables are controlled through the interactive Matlab user interface. We extended this measurement procedure for the multivariable case (MIMO). This is particularly useful for measuring radial couplings between different bearing planes. Finally, the high level Matlab interface automatically performs the controller parameter scalings needed for the fixed-point DSP board. Although floating point DSP boards have gained influence in the last few years they are still relatively expensive for industrial applications. Automatic controller parameter scaling eliminates some of the disadvantages caused by fixed point processing.

```
ts = 1000;
tmsvar('tsamp', ts);      % Writing to an AMB controller variable.
ts = tmsvar('tsamp');     % Reading back an AMB controller variable.
Ac = [0 1; 0 0];
tmsvar('a_cntr', Ac);     % Writing a matrix valued variable.
xt = scope('x');          % Time history of an AMB controller variable.
plot(xt);
```

Figure 1: Matlab access of AMB controller variables.

IDENTIFICATION OF MAGNETIC BEARING SYSTEMS

The aim of AMB identification consists in deriving a mathematical model of a magnetic bearing system by carrying out a (finite) number of input/output experiments. Frequency domain input/-output experiments (sine wave excitation with spectral analysis of the responses) are perfectly suitable for filtering out noise and non-linear phenomena.

A) Identification using much a-priori knowledge

The frequency domain measurements can be used to determine the numerator and denominator coefficients of the AMB plant using least square methods. In the case of voltage controlled magnetic bearings the plant transfer function can be accurately described by a third order system with no (finite) transmission zeros:

$$G(s) = \frac{1}{a_3 s^3 + a_2 s^2 + a_1 s + a_0}$$

Figure 2 shows the least square identification of a voltage controlled magnetic bearing (VCMB).
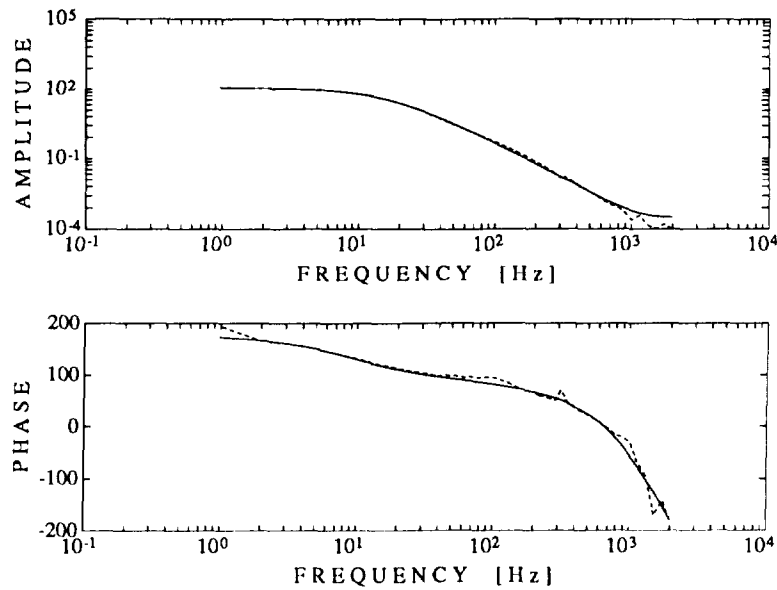
Figure 2: Solid: identification result, Dashed: measured frequency response of a VCMB.

The measured transfer function in figure 2 which relates displacement to input voltage was taken on a magnetically levitated tube spindle. In some cases it is useful to determine the bearing dynamics as a separate block. Since the modelling of the rotor is very accurately known in most cases, the parameter associated with the bearing dynamics can be identified using the overall frequency response measurements and the known rotor dynamics; see figure 3. This approach takes maximum use of available a-priori knowledge.

B) "Robust Identification Methods" using little a-priori knowledge

It is desirable that an identification algorithm be "stable" under small measurement noise or small perturbations of the data. For example, Lagrange interpolation (fitting a polynomial of minimal degree through the data) is known not to have this property. Figure 4 shows this bad behaviour of Lagrange interpolation. The noisy measurement data (marked with o) causes large oscillations of the identification output (solid curve). Although the identification error evaluated at the measurement points remains small, the deviation between the original transfer function (dashed) and the identification output (solid) is important. Robust identification seeks to prevent this salient bad behavior.
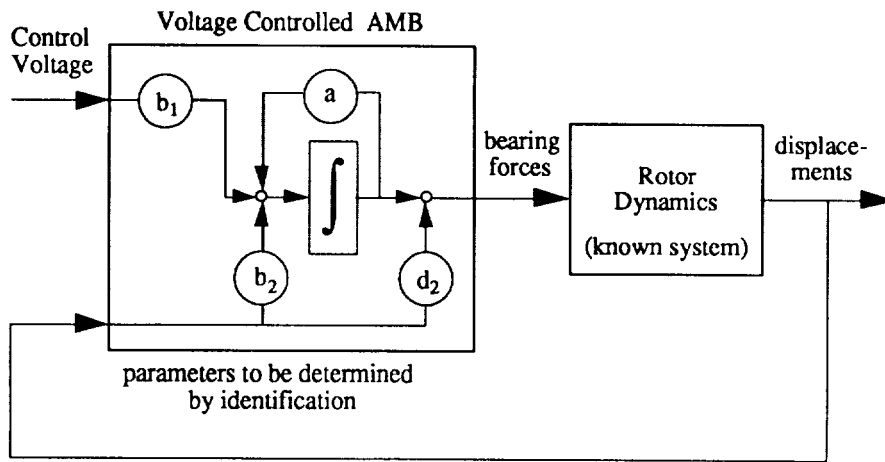
Figure 3: Identification of a voltage controlled magnetic bearing plant.
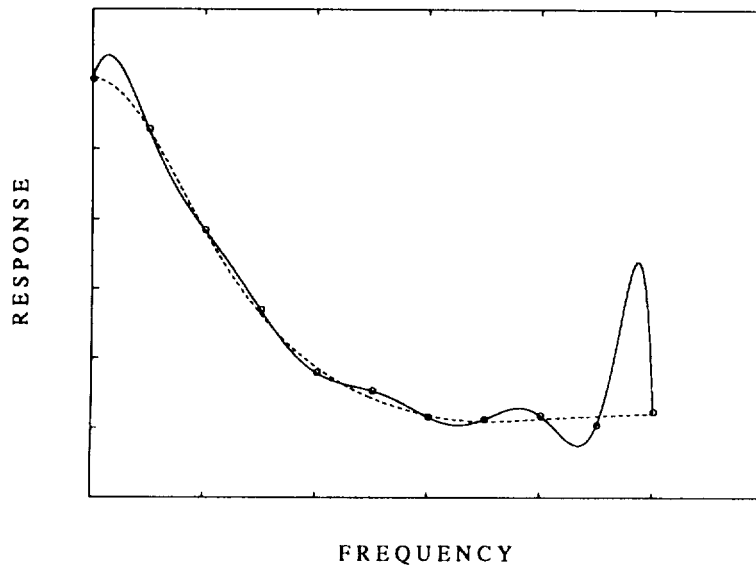
Figure 4: Robust identification seeks to prevent large sensitivities w.r.t. noisy data.
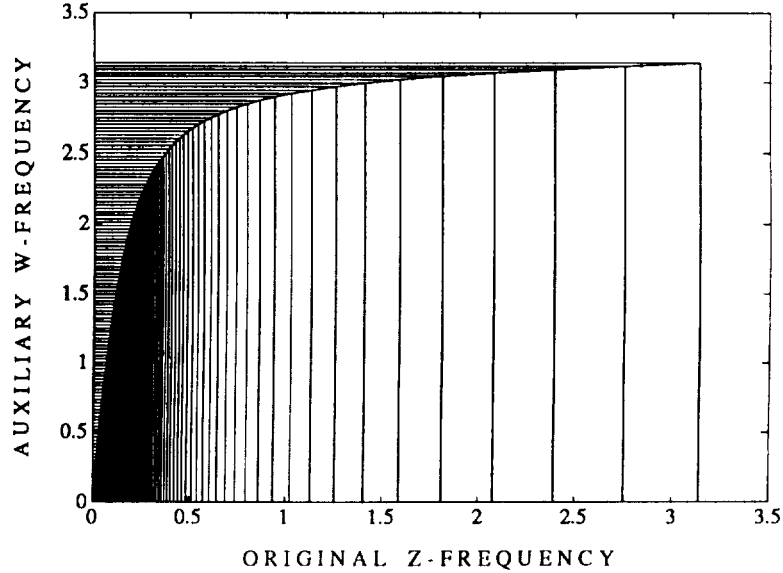
Figure 5: Bilinear frequency stretching.

The mathematical framework of "robust identification" and various identification algorithms were proposed recently in literature [4], [5], [7]. Most of these algorithms consist of two steps. In the first step, the frequency points are transformed to an impulse response function $\sum_{-N}^{+N} h_k z^k$ using inverse FFT and windowing functions. In the second step, the anti-causal part of the impulse response is approximated by a stable function using Nehari extension. Both steps can be easily implemented in Matlab since they rely only on standard matrix computations. The following section reports some of our experience with this identification approach.

When using methods [4], [5], [7] to identify a voltage controlled magnetic bearing of a tube spindle, we realized the following three points:

- Usually, the sampling rate is quite fast, compared to the open–loop system dynamics. For identification in the z-plane a very high number N of terms in the impulse response function $\sum_{-N}^{+N} h_k z^k$ is needed for accurate results. We lessened this problem by applying a bilinear transform which maps the unit disc $\{|z| < 1\}$ onto a unit disc $\{|w| < 1\}$ in a new w-plane. An equally spaced w frequency grid $w_k = e^{i\varphi_k}$ corresponds to an irregularly spaced z frequency grid, which in turn is closely spaced at low frequencies and more loosely at high frequencies; see figure 5. This bilinear transform allows us to diminish the number N of terms in the series $\sum_{-N}^{+N} \tilde{h}_k w^k$. After carrying out the identification in the w plane, the result is transformed back to the z-plane.

- The fast roll–off rate of transfer functions from voltage controlled magnetic bearings (60 dB/decade) causes an important *relative* identification error at high frequencies. Generally, an identification procedure achieving small *relative* error would be desirable. We used frequency weightings to incorporate this requirement.

- The methods proposed in [5], [6] are only applicable to stable systems. Since magnetic bearings

are unstable plants one could identify closed–loop functions, e.g. the sensitivity function $S(s) = (1 - P(s) \cdot C(s))^{-1}$, and determine plant $P(s)$ using the known controller $C(s)$. This approach [8] ends up with a pole–zero cancellation which is a numerically delicate operation. Therefore, we preferred to identify the unstable plant and to replace the Nehari step in [5], [6] by a model reduction [2] of the two–sided impulse response $\sum_{-N}^{+N} \tilde{h}_k w^k$.

These three realizations allowed us a successful first step in "robust identification" of magnetic bearing systems. The detailed identification results will be published soon in a separate paper. Further investigations are required in order to determine for which cases which identification procedure, and which a–priori knowledge yields the "best" result.

SUMMARY

A Matlab-based environment for AMB prototyping and on–site tuning was developed. This environment includes tools for frequency response measurements and AMB identification. These tools proved extremely valuable for increasing the efficiency and reducing the costs of AMB prototyping and on–site tuning.

REFERENCES

1. Allaire P.E. (ed.): Proc. of the 3rd Int. Symp. on Magnetic Bearings, Technomic Publishing Co., Virginia, 1992.

2. Balas G.J., Doyle J.C., Glover K., Packard A. and R. Smith: μ–analysis and synth. toolbox, Matlab User's guide, 1991.

3. Fujita M., Matsumura F., and T. Namerikawa: μ–Analysis and Synth. of a Flex. Beam Mag. Suspension System, Proc. of the 3rd Int. Symp. on Mag. Bearings, Virginia, 1992.

4. Gu G. and P. Khargonekar: A Class of Algorithms for Identification in $\mathcal{H}_\infty$, Automatica, Vol. 28, No. 2, pp. 299–312,1992.

5. Helmicki A.J., Jacobson C.A. and C.N. Nett: Control Oriented System Identification, A Worst–Case Deterministic Approach in $\mathcal{H}_\infty$ IEEE Trans. AC, Vol. 36, No. 10, Oct. 1991.

6. Herzog R. and H. Bleuler: On achievable $\mathcal{H}_\infty$ disturbance attenuation in AMB Control, Proc. of the 3rd Int. Symp. on Mag. Bearings, Virginia, 1992.

7. Mäkilä P.M. and J.R. Partington: Robust Identification of Strongly Stabilizable Systems, IEEE Trans. AC Vol. 37, No. 11, pp. 1709–1716, Nov. 1992.

Session 3 – Maglev

Chairman: Claude R. Keckler
NASA Langley Research Center

System Concept Definition of the Grumman Superconducting Electromagnetic Suspension (EMS) Maglev Design

M. Proise

Grumman Corporation, Bethpage, New York

SUMMARY

Grumman, under contract to the Army Corps of Engineers, completed a System Concept Definition (SCD) study to design a high-speed 134 m/s (300 m.p.h.) magnetically levitated (Maglev) transportation system. The primary development goals were to design a Maglev that is safe, reliable, environmentally acceptable, and low-cost. The cost issue was a predominant one, since previous studies [1] have shown that an economically viable Maglev system (one that is attractive to investors for future modes of passenger and/or freight transportation) requires a cost that is about $12.4M/km ($20 Million per mile).

The design (Fig. 1) is based on the electromagnetic suspension (EMS) system using superconducting iron-core magnets mounted along both sides of the vehicle. The EMS system has several advantages compared to the electrodynamic suspension (EDS) Maglev systems such as low stray magnetic fields in the passenger cabin and the surrounding areas, uniform load distribution along the full length of the vehicle, and small pole pitch for smoother propulsion and ride comfort. It is also levitated at all speeds and incorporates a wrap-around design for safer operation. The Grumman design has all the advantages of an EMS system identified above, while eliminating (or significantly improving) drawbacks associated with normal magnet powered EMS systems. Improvements include larger gap clearance, lighter weight, lower number of control servos, and higher off line switching speeds. The design also incorporates vehicle tilt (±9°) for higher coordinated turn and turn out speed capability.

INTRODUCTION

The Grumman Corporation assembled a team of six corporations and one university that were exceptionally qualified to perform the identified SCD study. The Grumman team members and associated responsibilities were:

- *Grumman Corporation* - system analysis and vehicle design
- *Parsons Brinckerhoff* - guideway structure design
- *Intermagnetics General Corp. (IGC)* - superconducting magnet design
- *PSM Technologies* - linear synchronous motor (LSM) propulsion system design
- *Honeywell* - communication, command, and control (C^3) design
- *Battelle* - safety and environmental impact analysis
- *NYSIS* - high temperature superconductor (HTSC) and magnetic shielding analysis.

The "Baseline Configuration" is 100 passengers with 5 across seating. The seats have a 0.96 meter spacing.
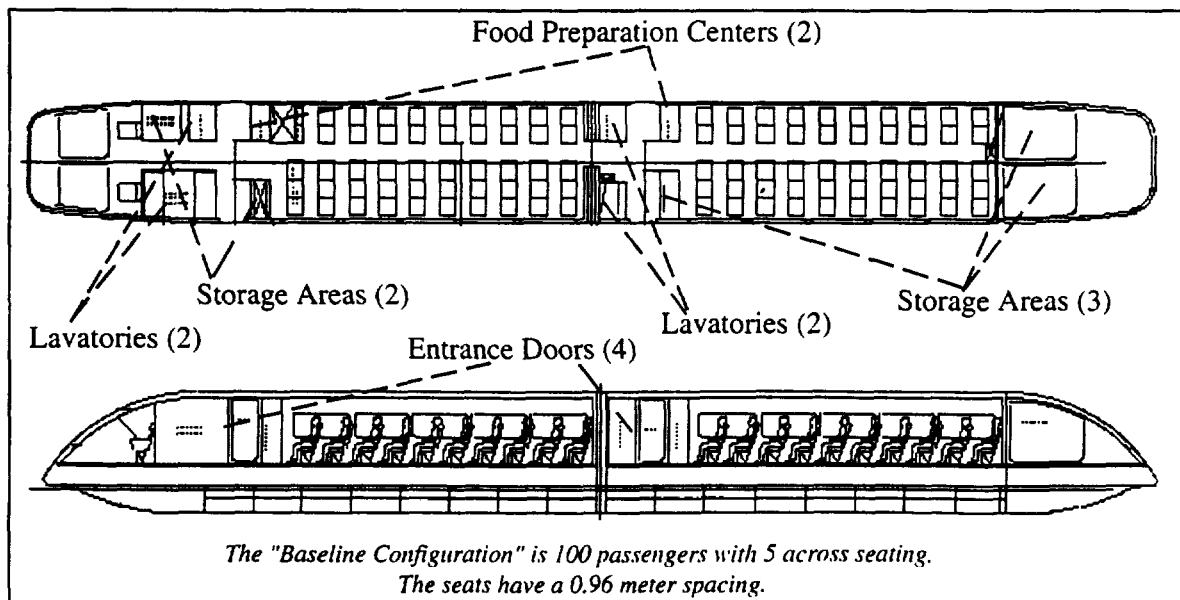
Fig. 1 . Grumman baseline Maglev vehicle configuration

As a result of the team's efforts, a unique high-speed Maglev system concept (Fig. 1), was identified. If implemented, this design would meet all the goals specified in the abstract and would satisfy U.S. transportation needs well into the 21st century. The design is based on the electromagnetic suspension (EMS or Attractive) system concept using superconducting (SC) iron core magnets mounted along both sides of the vehicle.

The Grumman team selected an EMS design instead of an electrodynamic suspension (EDS or Repulsive) design because of the following significant advantages that the EMS offers over the EDS system:

- Low magnetic fields in the cabin and surrounding areas (this eliminates or minimizes the need for magnetic shielding and non-metallic rebar in concrete guideways)
- Uniform load distribution along the full length of vehicle (minimizing guideway loads and vibrations in the cabin and contributes to the elinination of a secondary suspension system)

- Small pole pitch (results in smoother propulsion)
- Magnetically levitated at all speeds (needs no supplemental wheel support)
- Wrap-around configuration (safer operation).

EMS systems exist. However, the German Transrapid TR-07 and the Japanese High Speed Surface Transportation (HSST) systems, which use copper wire iron cored magnets instead of SC coils, have a number of basic disadvantages:

- Small gap clearance (1 cm (0.4 in.)), which results in tighter guideway tolerance requirements
- Heavier weight with limited or no tilt capability to perform coordinated turns and maximize average route speed
- Limited off-line switch speed capability (56 m/s maximum)
- Large number of magnets and control servos (≈100 total).

The Grumman team design has retained all of the advantages of an EMS system. At the same time it has succeeded in eliminating, or significantly improving, every aspect of the identified EMS disadvantages. A brief description of our baseline system and how it has accomplished this goal follows.

LEVITATION, GUIDANCE & PROPULSION SYSTEM DESIGN

Fig. 2 shows a cross section of the vehicle with the iron core magnets and guideway rail identified in black. The laminated iron core magnets and iron rail are oriented in an inverted "V" configuration with the attractive forces between the magnets and rail acting through the vehicle's center of gravity (cg). Vertical control forces are generated by sensing the gap clearance on the left and right side of the vehicle and adjusting the currents in the control coils to maintain a relatively large 4 cm (1.6 in.) gap between the iron rail and the magnet face. Lateral control is achieved by differential measurements of the gap clearance between the left and right sides of the vehicle magnets. The corresponding magnet control coil currents are differentially driven for lateral guidance control. There are 48 magnets, 24 on each side of a 100 passenger vehicle. In this manner control of the vehicle relative to the rail can be achieved in the vertical, lateral, pitch, and yaw directions. Vehicle speed and roll attitude control are discussed below.
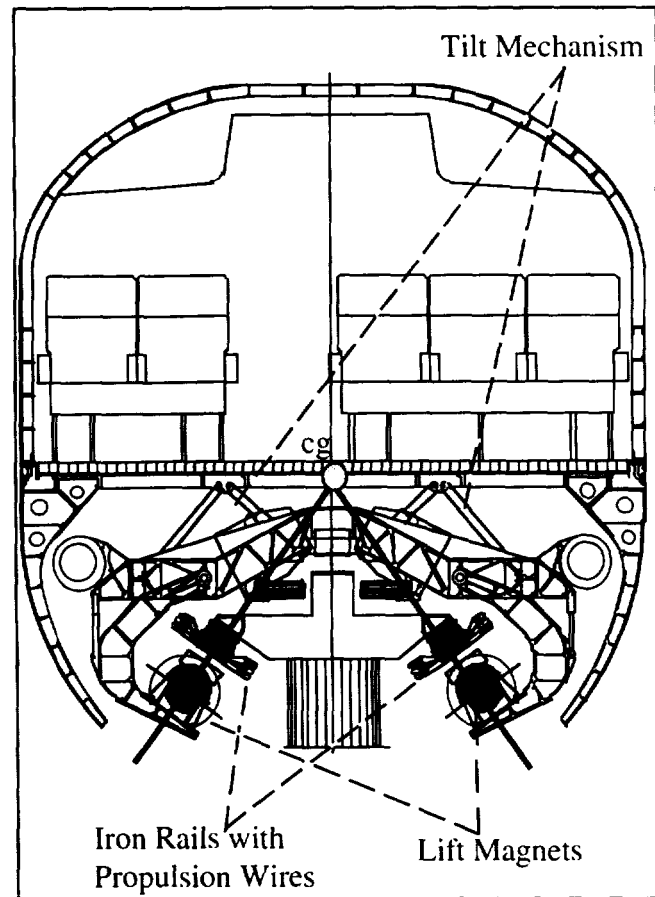
Fig. 2. Cross section of vehicle showing lift magnets, iron rail, guideway and tilt mechanism.
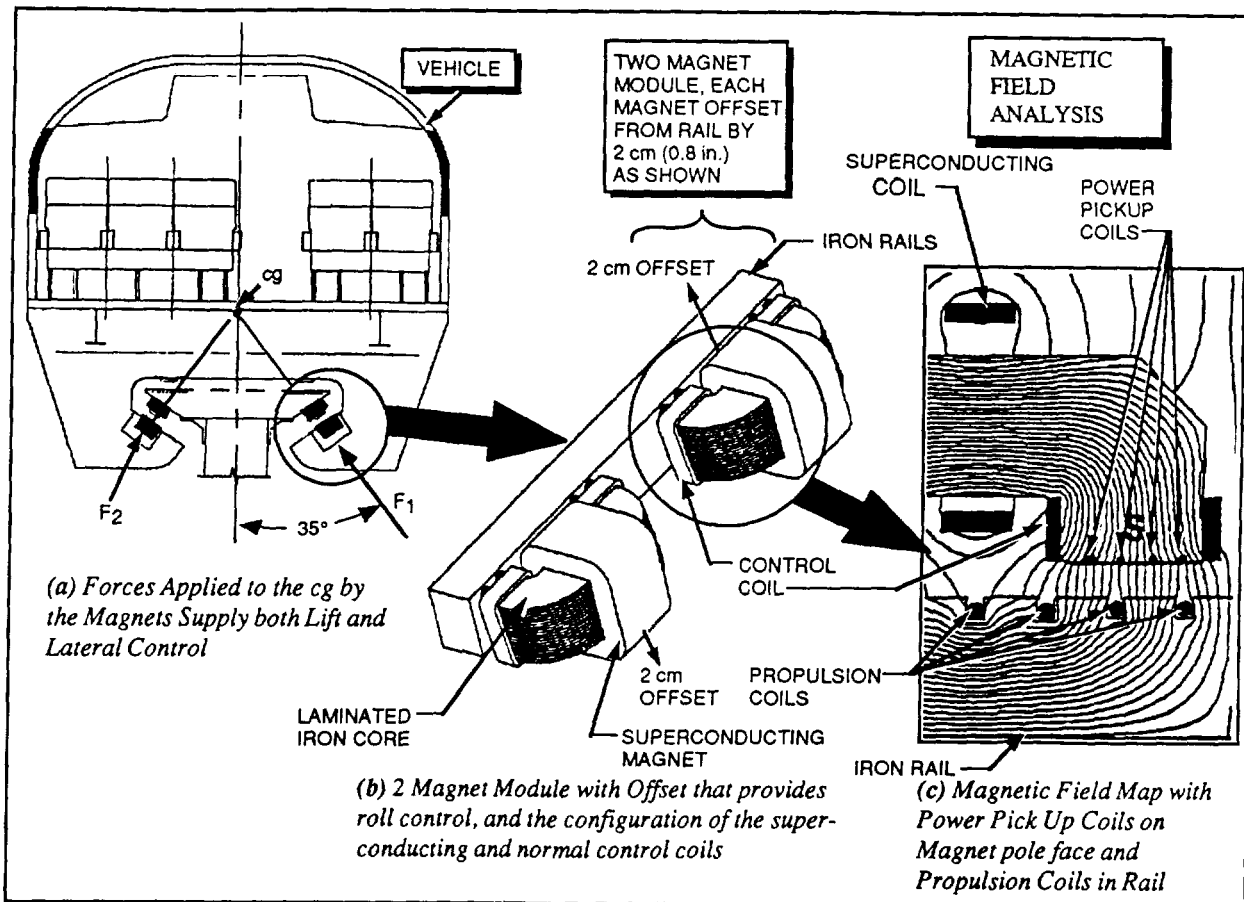
Fig. 3. Configuration of magnets and the control, propulsion and power pick-up coils

Two magnets combined as shown in Fig. 3 make up a "magnet module." Each magnet in a magnet module is a "C" shaped, laminated iron core with a SC coil wrapped around the center body of the magnet, and two copper control coils wrapped around each leg. Vehicle roll control is achieved by offsetting the magnets by 2 cm (0.8 in.) in a module to the left and right side of a 20 cm (8 in.) wide rail. Control is achieved by sensing the vehicle's roll position relative to the rail and differentially driving the offset control coils to correct for roll errors. The total number of independent control loops required for a complete 100 passenger vehicle control is 26 (1 for each of the 24 modules and 2 for roll control).

The iron rail shown in Fig. 3 (b) also is laminated and contains slots for the installation of a set of 3-phased alternating current (ac) Linear Synchronous Motor (LSM) propulsion coils. The coils are powered with a variable-frequency variable-amplitude current that is synchronized to the vehicle's speed. Speed variations are achieved by increasing or decreasing the frequency of the ac current.

Comprehensive two and three dimensional magnetic analyses [2] have been performed to assure that the magnetic design will simultaneously meet all levitation, guidance and propulsion control requirements identified above, and do it without magnetically saturating the iron core. An example of this analysis is shown in Fig. 3 (c).

Power pickup coils are located on each magnet pole face designed to operate at all speed, including standing still, using a unique inductive approach described in [3].

Low magnetic fields in the passenger compartment and surrounding areas represent an important aspect of this design. Fig. 4 identifies constant flux densities in the cabin and station platform that can be expected for the baseline design. Flux density levels above the seat are less than 1 gauss, which is very close to the earth's 0.5 gauss field level. On the platform, magnetic levels, when the vehicle is in the station, do not exceed 5 gauss, which is considered acceptable in hospitals using magnetic resonant imaging (MRI) equipment. The data in Fig. 4 is based on a three-dimensional magnetic analysis program and assumes no shielding. With a modest amount of shielding, these levels could be further reduced should future studies (now under way) indicate a need for lower values. Similarly, ac magnetic fields are anticipated to be within acceptable levels.

Another important aspect of the magnet design is the use of SC wire in place of copper coils used in existing EMS systems. This allows us to operate with a large 4 cm (1.6 in.) gap clearance without paying the heavy weight penalty required if copper coils were used for the same purpose.

The use of an iron core with the SC coil provides an added advantage. The magnetic flux is primarily concentrated in the iron core, not the SC coils as is the case of an EDS system. This reduces the flux density and loads in the SC wire to very low values (<0.35 Tesla and 17. 5 kPa, respectively). In addition we have implemented a patented constant current loop controller [4] on the SC coil that diminishes rapid current variations on the coil, minimizes the potential of SC coil quenching and allows for the use of state-of-the-art SC wire.

The use of iron-cored SC magnets with their associated low flux density and load levels identified above affords an added advantage of our design over EDS concepts. High temperature SC technology has progressed to the point that the field levels these magnets require are achievable with existing High temperature SC wire. It is now reasonable to consider the application of this new emerging technology to this concept. Although we are not baselining the use of high temperature SC for this application (except for its use as lead-in wire to the low temperature SC coil), we are pursuing a development program at this time to manufacture samples of high temperature SC coils of sufficient length and with adequate current carrying density to satisfy our requirements.

Magnetic Fields in Cabin are Less Than 1 Gauss (Twice the Earths Magnetic Field) and on the Passenger Platform are less than 5 Gauss

Fig. 4. Magnetic fields in cabin and surrounding area

In summary, the use of SC iron-core magnets resulted in significant advantages for this concept:

- Large gap size - 4 cm (1.6 in.)
- Low magnetic fields in SC coil - <0.35 T

- Low fields in passenger cabin - <1.0 gauss dc
- Low load forces in SC coil- 17.5 kP a

VEHICLE DESIGN

A number of important system trade studies were performed to arrive at the baseline vehicle configuration shown in Fig. 1. An example is given in Fig. 5 which identifies how the total system cost,

Assumptions:
- 492 km (300 mile) trip
- 134 mps (300 m.p.h.) speed
- 16 hr/day operation
- Cap. Recov. Fac. = 0.103 (6% 15 yrs.)
- $.05 per kilo volt ampere power cost
- 5 seats across
- 12.7 m long module
- 50 seats per module
- 30 m spans
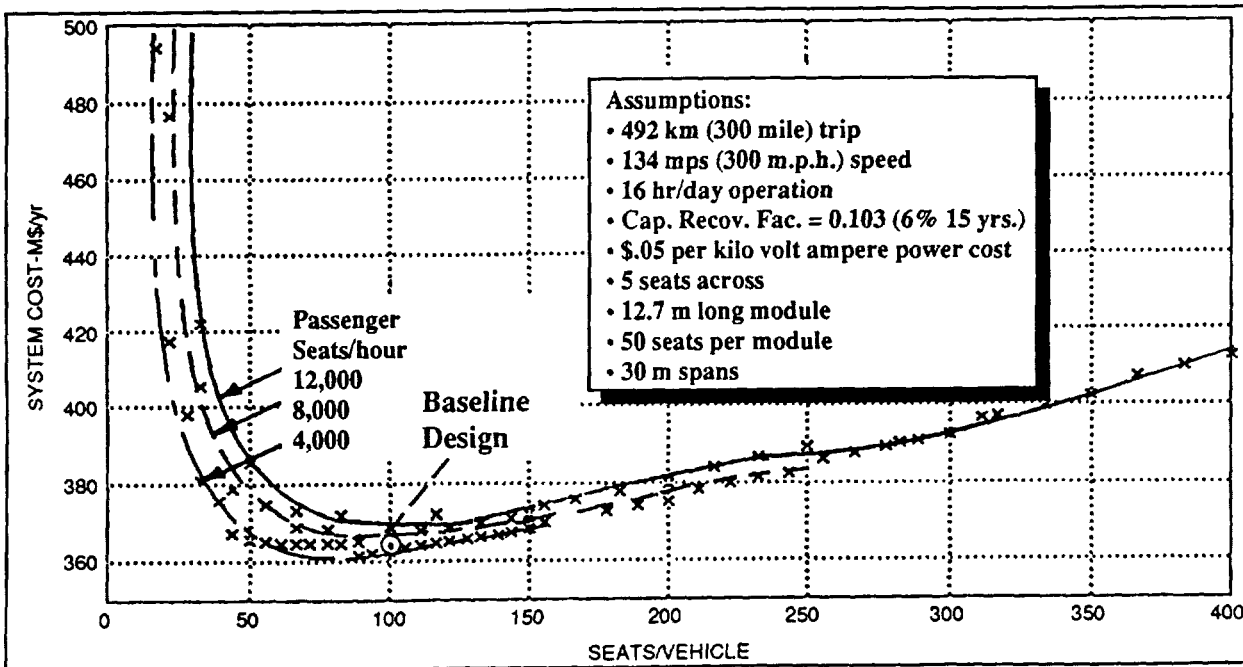
Fig. 5. System cost trade study

72

which includes the guideway, vehicles, levitation, propulsion, and operating cost, is affected by the number of passenger seats in the vehicle and the number of passengers per hour utilizing the system. Note that minimum cost results are between 50 and 150 seats per vehicle. We have chosen 100 passenger seats per vehicle for our baseline configuration.

The 100 passenger baseline system shown in Fig. 1 lends itself to other single and multi-vehicle (train) configurations that can be developed based on two basic building block modules. The main module consists of a 12.7 m (41.7 ft) long section, which seats 50 passengers with 2 entrance doors (one on each side of the vehicle), 2 lavatories (one designed to accommodate handicapped passengers), multiple overhead and closet storage facilities and a galley area. The forward and aft sections of the vehicle utilize the second module, which consists of a 4.9 m (16 ft) long section that is externally identical, but internally different, depending on its forward or rear location on the vehicle. We have adopted one-way

Fig. 6. Distribution of costs across the four major components of the Maglev system

vehicle operation to minimize the impact of weight for reverse facing seat mechanisms and cost duplicating all the electrical controls and displays on both sides of the vehicle. We also chose to include business-type aircraft seats with an ample 0.96 m (38 in.) spacing between seats to assure a comfortable seating arrangement for all passengers. Additional detailed vehicle characteristics are given in [5].

Comprehensive two and three-dimensional Navier Stokes computational aerodynamic analyses [6] were also performed on the baseline design to estimate drag and other disturbances acting on the vehicle. Vehicle speeds up to 134 m/s (300 m.p.h.) with 22.3 m/s (50 m.p.h.) crosswinds where investigated.

GUIDEWAY DESIGN

The guideway is an important aspect of our system design because it represents the largest percentage of the total system cost. Fig. 6 shows how system cost distributes between the four major components, i.e., guideway (64.4%); electrical and communication (14.8%); vehicles (13.3%); and the ancillary facilities such as stations, buildings and vehicle parking (7.46%). Details of our system costing procedures are given in [7].

A number of different guideway designs were investigated. Four are shown in Fig. 7 and are identified in terms of increasing cost.

In each case our design mandated that a center platform exist along the full length of the guideway to provide a safe exit for the passengers, in case of an emergency such as a fire or smoke in the cabin.

Analysis of the four guideway configurations identified in Fig. 7 showed that the "spine girder" guideway design is not only lowest in cost, but also is relatively insensitive to span length [8]. This has important implications when the guideway must be installed in areas such as the U.S. Interstate Highway system, which will require wide ranges in span length depending on local road conditions. In summary, based on this and other considerations, the "spline girder" configuration shown in Fig. 8 was chosen as our baseline for the following reasons:

- Lowest cost dual- guideway ($7.99M/km, for spread footing including iron rail cost)
- Smaller footprint
- Can be more closely designed to suit span variations

- Visually less intrusive with single column
- Creates less shadow
- Esthetically pleasant.

Detailed descriptions of the baseline guideway and associated cost estimates are given in [9] and [8] respectively. The total system cost, which includes guideway, electrical and communication, vehicles, station buildings etc. was estimated at $12.4M/km ($20M/mile) [7].

A 5 degree-of-freedom analysis of the interactive effects of the vehicle traveling over a flexible guideway was undertaken [10]. Guideway irregularities resulting from random step changes, camber variations, span misalignment and rail roughness where included in the simulation. Also included where linearized versions of the vehicle levitation and lateral control loops. The results indicated that passenger comfort levels could be maintained without the need for a secondary suspension system.
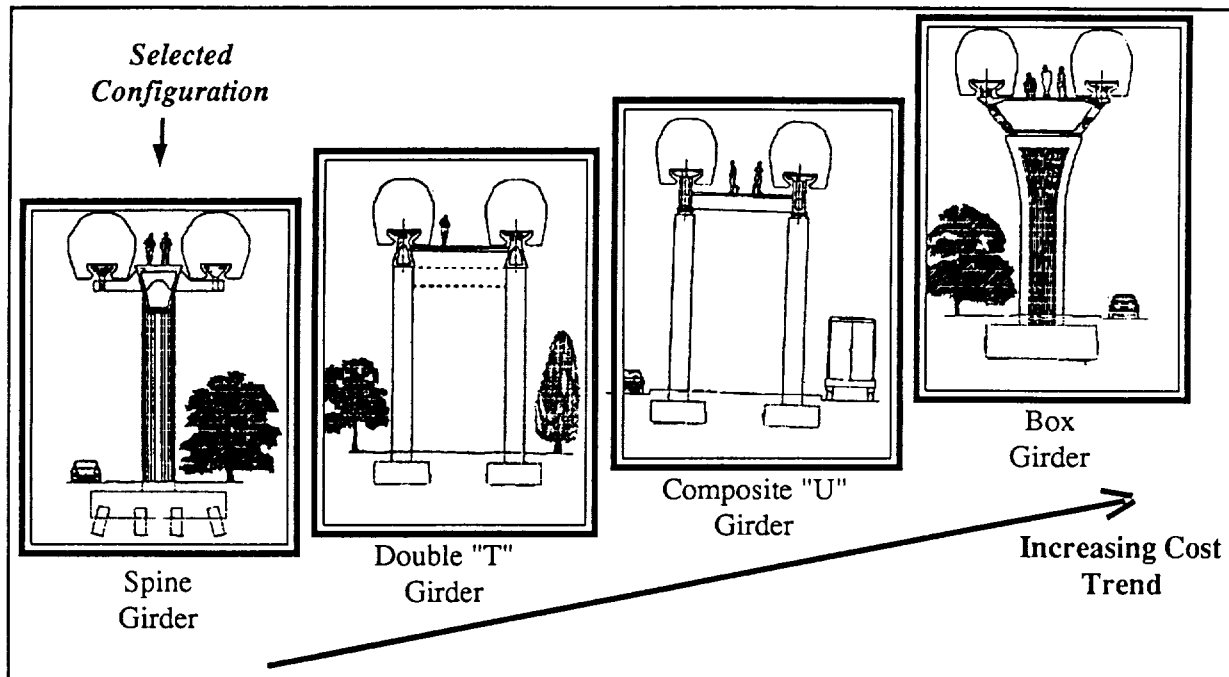
Fig. 7. Alternate guideway structures considered

HIGH SPEED OFF-LINE SWITCHING

Another important aspect of our design is the capability of providing high-speed off-line switching. Unlike the German Transrapid design, which moves one 150 m (492 ft) section of the track laterally 3.61 m (12 ft), we move two sections laterally 3.0 m (10.0 ft) with one actuator motion. The track switching concept is shown in Fig. 9. It identifies the two sections of the track that are moved to accomplish this function. The lower figure shows the through traffic condition for the track switch. The upper figure identifies how the 60 m long switch, A, is flexed to a curved section, while the right hand 60 m long switch, B, is pivoted about the fixed switch points. This combined motion of the two sections (120 m total length) provides a turnout speed of 65 m/s (143 m.p.h.). A 182 m switch length will allow off-line switching at 100 m/s (220 m.p.h.). Transrapid turnout is limited to 56 m/s (123 m.p.h.) with a section length of 150 m.

VEHICLE CABIN TILT DESIGN

Unlike any of the other existing high-speed Maglev designs, such as, the Transrapid TR07 or the Japanese MLU002, we are providing the capability of tilting the vehicle passenger compartment by ±9 degrees relative to the guideway. In this manner, the
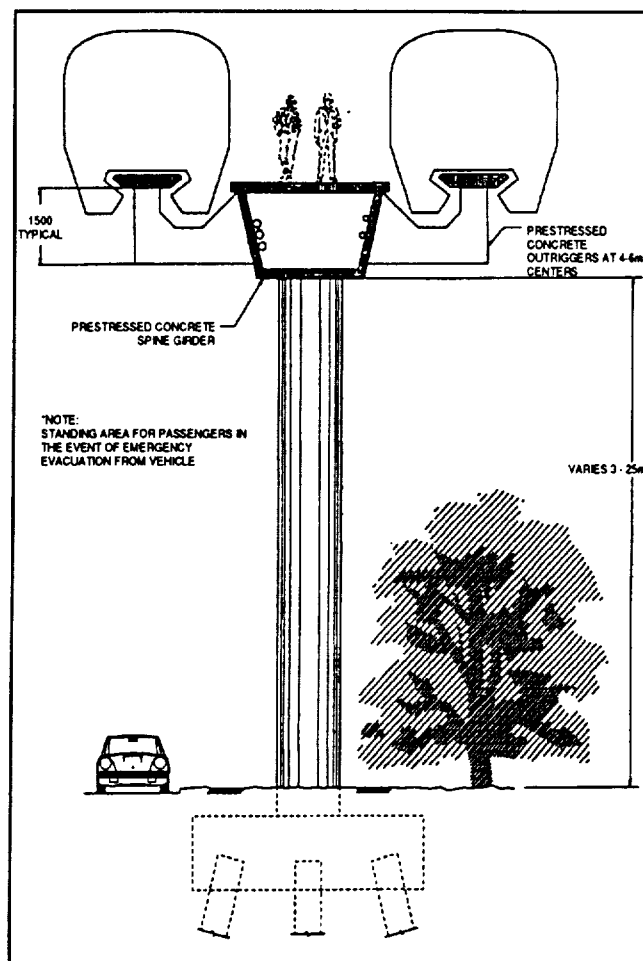
Fig. 8. Baseline spine girder configuration

74

The switching approach selected allows high speed turn out up to 100 m/s (220 mph)
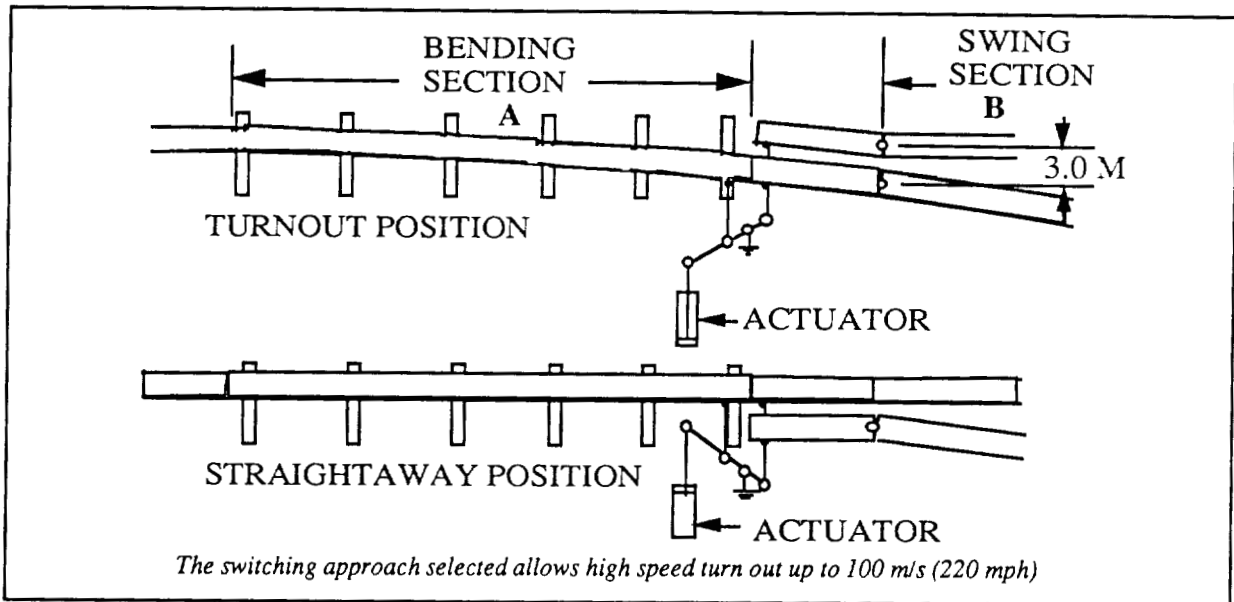
Fig. 9. Off-line switching concept

design, as shown in Fig. 10, will allow for coordinated turns up to ±24 degrees banking (±15 degrees in the guideway and ±9 degrees in the vehicle). This capability will assure that all coordinated turns can be performed at the appropriate tilt angle independent of the speed with which the vehicle is traversing the turn, as well as allowing for high-speed off-line switching.

ECONOMIC ANALYSIS

An economic forecast analysis for a Maglev system was performed as a function of two primary cost drivers: total cost of the major Maglev elements identified in Fig 6, and the passengers per hour utilizing the system. The results of this analysis are presented in Fig. 11 with the as-
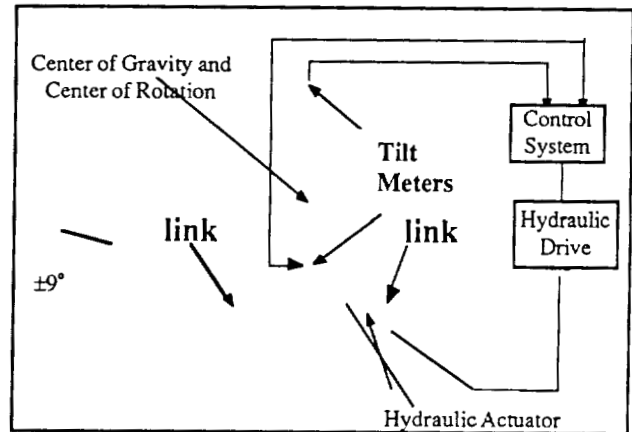
Fig. 10. Tilting mechanism and control system
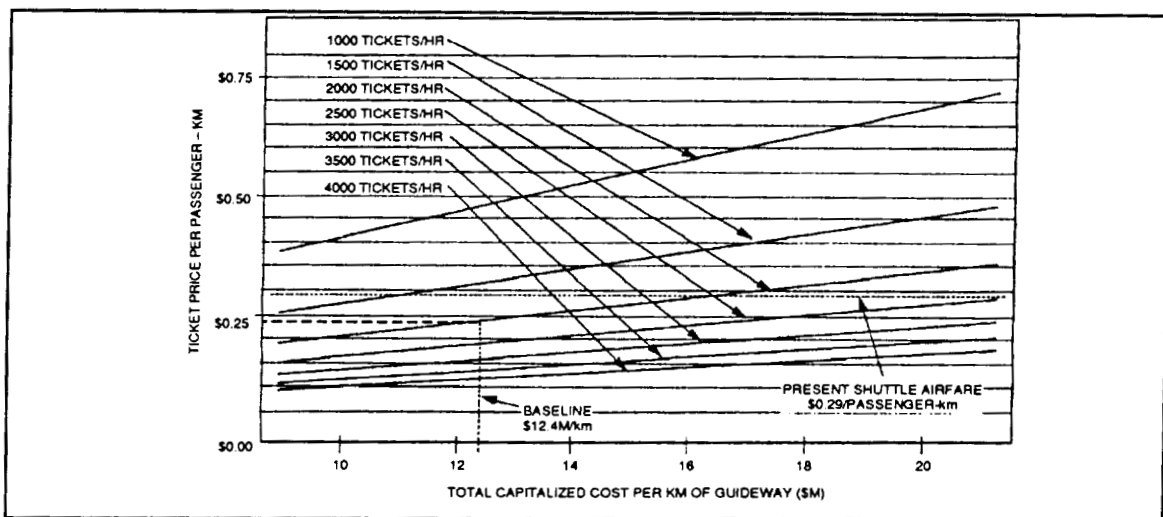
Fig. 11. Economic analysis

sumptions listed below:

- 493 km (300 mile) corridor
- Development and demonstration cost of the Maglev system is not included
- Federal, state and local governments supply right-of-way at no cost
- Ridership is based on 260 days/year, 16 hours/day, 60% capacity

- 20% pre-tax margin on ticket price based on 5 year build, 15 year operation
- Future interest (8%) & inflation rate (5.4%)

If we assume a 2,000 passenger per hour usage (typical of high volume routes like Boston/New York/Washington DC) with the previously identified $12.4M/km ($20M/mile) for the baseline system cost the ticket price that would have to be levied is $0.23/km ($0.38/mile); this would still provide a 20% profit margin on the ticket cost for the system operator. Also shown on the figure is the $0.29/km ($0.47/mile) present charge for the New York/Washington, DC/Boston corridor. The results indicate that a Maglev system of the type being recommended in this paper can pay for itself during its first 15 years of operation. The implication is that after 15 years, when the capital investments have been fully paid, the proceeds from the high volume traveled routes could be used to support the building and operation of Maglev routes that are located in less densely populated areas. This means that system route miles can double every fifteen years, implying that by the mid twentieth century there could be over 4000 miles of maglev lines in the U.S.

CONCLUSION

It is our opinion that the Grumman Team superconducting EMS Maglev concept as described in this paper will provide an effective low cost U. S. Maglev transportation system that can meet all of the goals identified in the abstract and at the same time minimize the negative issues previously discussed. We believe that the Grumman team has performed sufficient analyses in the areas of guideway design, levitation, propulsion and guidance, vehicle structural design, aerodynamics, controllability, dynamic interaction, environmental, safety, and reliability to warrant this optimism.

REFERENCES

[1] R. Gran, "Benefits of Magnetically Levitated High Speed Transportation for the United States," SAE Future Transportation Conference, San Diego, CA, August, 1990, Paper No. 901475

[2] S. Kalsi, R. Herbermann, C. Falkowski, M. Hennessy, A. Bourdillon, "Levitation Magnet Design Optimization for Grumman Maglev Concept,"presented at the Maglev 93 Conference, Argonne National Laboratory, May 19-21, 1993, Paper No. PS2-7

[3] S. Kalsi, "On-Vehicle Power Generation at all Speeds for Electromagnetic Maglev Concept," presented at the Maglev 93 Conference, Argonne National Laboratory, May 19-21, 1993, Paper No. PS5-12

[4] R. Herbermann, "Self Nulling Hybrid Maglev Suspension System,"presented at the Maglev 93 Conference, Argonne National Laboratory, May 19-21, 1993, Paper No. PS1-7

[5] P. Shaw, "Overview of Maglev Vehicle Structural Design Philosophy, Material Selection and Manufacturing Approach," presented at the Maglev 93 Conference, Argonne National Laboratory, May 19-21, 1993, Paper No. PS4-9

[6] R. Ende, M. Siclari, G. Carpenter, "Aerodynamic Analysis of Grumman Maglev Vehicle," presented at the Maglev 93 Conference, Argonne National Laboratory, May 19-21, 1993, Paper No. PS5-9

[7] L. Deutsch, "Maglev Cost and Performance Parameters," presented at the Maglev 93 Conference Argonne National Laboratory, May 19-21, 1993, Paper No. OS5-1

[8] B. Bohlke, D. Burg, "Parametric Design and Cost Analysis for EMS Maglev Guideway," presented at the Maglev 93 Conference, Argonne National Laboratory, May 19-21, 1993, Paper No. PS3-2

[9] J. Allen, M. Ghali, "Innovative Spine Girder Guideway Design for Superconducting EMS Maev System," presented at the Maglev 93 Conference, Argonne National Laboratory, May 19-21, 1993, Paper No. PS3-1

[10] R. Gran, M. Proise, "Five Degree of Freedom Analysis of the Grumman Superconducting Electromagnetic Maglev Vehicle Control/Guideway Interaction," presented at the Maglev 93 Conference, Argonne National Laboratory, May 19-21, 1993, Paper No. PS4-6

Transrapid – The First High-Speed Maglev Train System Certified "Ready for Application": Development Status and Prospects for Deployment

Reinhard F. -Luerken
Thyssen Henschel America, Inc.

Contents

1. History: Milestones of Development

Starting point of the Transrapid development more than two decades ago was the idea to create a

- contact-free
- cost effective
- energy efficient
- environmentally sound and
- comfortable

system for high-speed ground transportation which is superior to competing modes. (→ chart: Transrapid Development Chronology)

In the development history of the Transrapid maglev system a great number of highlights are worth mentioning, among others

- the demonstration of the first long-stator-propelled vehicle (HMB 2) in 1976

- the first public maglev service by the TR05 vehicle during the IVA in Hamburg 1979

- the first full-size maglev vehicle TR06 to go into testing and demonstration in 1984

- several world records for manned maglev vehicles (most recently 450 km/h [280 mph] clocked by the TR07 vehicle).

On the other hand it must not be forgotten how difficult, time consuming and costly it was to overcome all the problems that arose during all stages of the development. Several times the program was endangered for lack of funds and political support. All the more the personal commitment, engagement and sacrifice of the people involved in the program has to be appreciated. Nobody should ever underestimate the difficulties and risks related to the development process of a completely new transportation system!

2. Technology

2.1 Function

The Transrapid maglev system basicly features electronicly controlled attractive electromagnetic forces to provide

- vertical and horizontal support functions

- and (by interaction with an electric synchronous long-stator motor in the
  guideway) both propulsion and regenerative braking
  (→ chart: Vehicle/Guideway Components)

The levitation system consists of electromagnets (and related control systems) integrated in the vehicle structure in a way that they attract the vehicle to the guideway from below by interacting with ferromagnetic reaction rails attached to the underside of the guideway.

The guidance system holds the vehicle laterally on the track also by means of a second sort of electromagnets. These magnets and the related control systems are integrated on both sides in the vehicle structure so that they attract towards the lateral flanges attached to the guideway structure.

Both levitation and guidance magnets are fed from the on-board power system and controlled by means of electronic choppers so that a gap of 8 - 10 mm (approx. 3/8") is safely maintained ["safe hovering"].

The propulsion system consists of a linear motor featuring the long-stator component with two three-phase windings with laminated iron core in the guideway and the levitation magnets of the vehicle providing an excitation field so that the vehicle travels synchronously with the AC wave of variable fredquency fed into the long-stator winding.

2.2 Benefits

Due to its technical features, Transrapid maglev technology is superior to other transportation systems, particularly in terms of

- safety and ride comfort
- acceleration and travel speed
- grade capability and alignment flexibility
- cost effectiveness and operational versatility

(→ chart: Performance Capability)

It is interesting to see that despite the current success of advanced wheel-on-rail projects there is more and more initiative worldwide to make maglev technology available for the future replacement of conventional railroads.

In order to justify Transrapid consideration for public service, the German Government requested an unbiased evaluation whether or not the maglev technology is ready for application. This evaluation focused on the following questions:

- Is the development and testing status of the system sufficiently advanced to consider the technology for concrete application cases and project planning procedures?

- Are there any inherent safety risks in the entire system or in any of the subsystems?

- As far as specific solutions have not yet been demonstrated, will these solutions be available by the time of application?

- Is there sufficient certainty in the calculation of specific investment costs at the time of assessment?

A special task force under leadership of the German Federal Railways conducted thorough investigations of the comprehensive documentation and additional experiments on the test facility, altogether more than two years of intensive

study work. The team ended up with fully positive answers to the above questions: Transrapid maglev technology is technically ready for application as a public transportation system!

2.3 Performance Highlights

During an extended test period early in June 1993, the opportunity was taken to demonstrate again the performance capabilities of the Transrapid technology.

The outstanding result of these demonstrations was a new world record for manned maglev vehicles at 450 kph (280 mph). This peak velocity was reached several times, first on June 10, 1993.

The numerous endurance runs during the same testing period may be even more significant to prove the system's suitability for commercial high speed long distance operation; the longest non-stop run was 1,674 km (1,040 miles) at top speeds up to 380 kph (236 mph).

Perhaps even more impressive and meaningful than these performance highlights as such is the way they were obtained. Without any particular preparation of the vehicle or the propulsion system, the record speed could be reached repeatedly. And no limits of the technology were recognizable. The only reason why the test crew could not head for higher speeds is because the alignment of the test track does not allow it to go faster [it was originally designed for 400 kph (249 mph)].

Due to the contact-free levitation, guidance and propulsion/braking coming with the maglev technology, high-speed operation is not related to any mechanical wear. On the contrary, rail-bound trains are facing a substantial increase in wear of their mechanical components such as the wheel and rail profiles, motors and gears, brakes, overhead power catenary and pantographs. Typically, the excessive wear and tear resulting from fast railway operation and the associated dramatic increase in operation and maintenance costs are the controlling factors that limit the design speed for wheel-on-rail projects.

3. Application

Considering

- the overall acknowledged benefits of the German Transrapid maglev technology,
- its brilliant performance highlights, and
- its development status reached so far which is topped by the certification for public service in the country of origin,

there is no doubt that the time has come for commercial deployment.

3.1 Germany: The Berlin - Hamburg Project

The Federal Master Transportation Plan for Germany, currently under parliamentary discussion, features numerous projects to upgrade the infrastructure urgently needed for the fostering of the economic development of the country after unification in 1990. One of the most important projects in the plan is the high-speed passenger transportation link between Berlin and Hamburg. This project has been dedicated to maglev technology provided all conditions can be met.

An overview of the key features of this project is given in the Project Data Berlin-Hamburg chart. (→ chart: Project Data Berlin-Hamburg Maglev Link)

Up to now, intercity transportation in Germany is an issue of Federal responsibility and thus entirely publicly funded. For the first time ever, the Berlin-Hamburg maglev project is intended to be established as a public-private partnership featuring a substantial private contribution in the funding. Thyssen as the development leader of the technology was invited to come up with a feasible financing scheme to meet the governmental requirements. Together with our industrial partners of the Magnetschnellbahn Berlin-Hamburg GmbH (Siemens, Daimler Benz/AEG) and leading German banks (Deutsche Bank, Kreditanstalt für Wiederaufbau) Thyssen submitted a conceptual proposal on this matter earlier this year. Currently the proposal is being reviewed and modified to meet the imposed conditions. The whole task is particularly difficult as major portions of the rail-related legislation to be referred to are presently in a process of being restructured towards part privatization of the German railways system.

However, we anticipate getting the political go-ahead for the Berlin-Hamburg project after the final approval of the financing concept which is due by the end of this year. (→ chart: Financing Scheme Berlin-Hamburg Maglev Link)

3.2 USA: The American MagLine Group

After decades of unlimited growth of both automobile and aircraft traffic in the U.S., it has become obvious that high-speed ground transportaion is a must to further provide adequate transportation quality. Otherwise, the ever increasing mobility demand would face more and more unacceptable conditions in terms of gridlock and pollution.

Maglev technology in fact has been identified as the most promising approach to cope with this situation. As a consequence, the National Maglev Initiative (NMI) has been started to develop a system capable of meeting the requirements. However, serious evaluation of the NMI intentions has to admit that it is at least questionable whether these efforts can ever fulfill the high expectations, particularly in terms of

- safe and reliable performance,
- commercially viable operation, and
- availability for public service within less than a decade.

In May 1993, the American MagLine Group (AMG) was founded by four U.S. companies:

- Booz, Allen & Hamilton, Inc., a Delaware corporation particularly experienced in transportation systems engineering;

- General Atomics, a California corporation with broad expertise in the design of sophisticated power supply and conditioning systems;

- Hughes Aircraft Company, a Delaware corporation with great experience in systems engineering and command and control systems, and

- Thyssen Henschel America, Inc., a wholly-owned California subsidiary of Thyssen Industrie AG from Germany, which holds the lead in the development of the Transrapid maglev technology to date. (→ chart: AMG Cover Chart)

The objectives of the AMG target the development of a high-speed ground transportation infrastructure, which creates real and enduring economic and social benefits to the U.S. (→ chart: Our Objectives)

The intent is to make maglev available for application in the U.S. by Americanization of existing designs.

Based on a transfer of the original design and manufacturing know-how, "Americanization" means (→ chart: Americanization of Transrapid)

- to create subsystems based on U.S. state of the art: operation control, communications, propulsion, power distribution, etc.

- to establish the American subcontractor/supplier infrastructure and American manufacturing base

- to develop the data needed to facilitate DOT certification of the system.

Taking advantage of the expertise of the AMG partners, a preliminary assignment of work has been agreed on. (→ chart: AMG Partners and Work Assignment)

The AMG program plan allows use of the readily developed Transrapid technology to quickly implement a maglev project and to create a large number of jobs. (→ chart: AMG Program Plan)

Thus, the technology can be made available very soon, allowing a fast start on a commercial U.S. project (→ chart: System Upgrade and Conversion)

The time factor is particularly interesting with regard to the jobs resulting from such a project. The example of a LAX - Palmdale connection based on Transrapid technology shows how soon construction can start, as preparatory work does not significantly exceed the amount involved in conventional train projects. (→ chart: Maglev Project Example)

There are plenty of both potential U.S. and overseas candidate projects for maglev application as offered by AMG, including California, Florida, Pennsylvania and the DOT High-Speed Corridors as well as in the Pacific rim. (→ chart: Potential Transrapid-based Projects)

The effect of job creation in AMG's maglev system program is particularly impressive compared to alternative approaches. (→ chart: Job Creation in Maglev System Program)

Considering the current decrease of the defense sector, conversion to civilian technologies is most time-critical to avoid serious damage to the economy. Assuming the overall volume of jobs generated by a maglev project is independent of the specific technology, it is most important to come up with a concept providing occupation in the field of high tech development and manufacture the sooner the better. Under this criterion the AMG approach is obviously superior to other alternatives as it takes advantage of the Transrapid state of development reached so far.

4. Summary

The Transrapid maglev technology is at the threshold of commercial deployment and technologically all prerequisites for the successful operation of the system in public service are given.

In post unification Germany the domestic maglev technology is envisioned to be applied in the Berlin-Hamburg project. At present, a public-private funding concept is being prepared and the lengthy planning process is about to be initiated.

In the USA the AMG has presented a program to Americanize the technology and to make it available for commercial use in the U.S. in the very near future.
(→ chart: AMG Program Summary)

The paramount features of this program

- generate economic development
- provide a basis for transportation technology development
- create opportunities for U.S. industry
- improve the U.S. transportation infrastructure and
- improve the environment and traveler safety.

Maglev is ready for the U.S.; is the U.S. ready for maglev?

TRANSRAPID DEVELOPMENT CHRONOLOGY

1976 - FIRST LONG STATOR VEHICLE (HMB2) DEMONSTRATED

1977 - EMS SYSTEM SELECTED OVER EDS SYSTEM

1979 - TR05 DEMONSTRATED AT HAMBURG EXPOSITION

1980-87 - CONSTRUCTION OF THE EMSLAND TEST TRACK

1984 - FULL SYSTEM DEMONSTRATED BY TR06 ON EMSLAND TEST TRACK

1988 - TR07 BEGINS FULL PERFORMANCE & RELIABILITY TESTING

1991 - TRANSRAPID SELECTED BY FLORIDA FOR ORLANDO PROJECT

1992 - TRANSRAPID TECHNOLOGY APPROVED FOR PUBLIC USE BY THE GERMAN GOVERNMENT

1993 - HAMBURG TO BERLIN LINE USING TRANSRAPID TECHNOLOGY INCLUDED IN GERMAN MASTER TRANSPORTATION PLAN

1993 - FORMATION OF THE AMERICAN MAGLINE GROUP TO BUILD TRANSRAPID BASED HIGH SPEED GROUND TRANSPORTATION SYSTEMS IN THE U.S.

TRANSRAPID TECHNOLOGY REPRESENTS TWO DECADES OF CONTINUOUS COMMITMENT TO REVOLUTIONIZING HIGH SPEED GROUND TRANSPORTATION

Vehicle/Guideway components

TRANSRAPID SYSTEM PERFORMANCE CAPABILITY

OPERATING SPEED	300 MPH
GRADE CAPABILITY	10%, REDUCES NEED FOR TUNNELS AND BRIDGES
SAFETY	WRAPS AROUND GUIDEWAY, CANNOT DERAIL
ELECTRO-MAGNETIC EMISSIONS	WELL BELOW EXISTING STANDARDS (U.S. REPORT DOT/FRA/ORD-92/09)
MAINTENANCE	LOW DUE TO CONTACTLESS OPERATION AND NO ROTATING MACHINERY
ALIGNMENT	EASILY ELEVATED, TIGHT RADII, HIGH GRADE CAPABILITY, SMALL FOOT PRINT - OFFERS FLEXIBILITY IN URBAN & ROUGH TERRAIN ALIGNMENTS
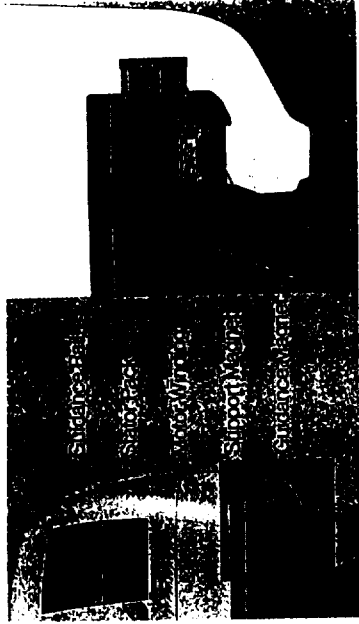
Project Data Berlin - Hamburg Maglev Link

Distance Berlin - Hamburg	283 km	(176 mi)
Design Speed	400 km/h	(250 mph)
Trip Time	approx. 55 min.	
Service Concept	96 roundtrips per day, 10 min. service interval (peak)	
Ridership Volume	14.7 million pax per year	
Investment Cost		
- fixed facilities	6.6 bill.DM	= 23.3 mill.DM/km (23.3 mill.$ per mi)**
- vehicles (trains, cars e.a.)	0.6 bill.DM	
TOTAL	7.2 bill.DM	= 25.4 mill.DM/km (25.4 mill.$ per mi)**
Operating Costs*	0.05 DM/pass.km (0.05 $ per pass.mi)**	
Construction Time	1994 - 2002	
(provided the availability of r-o-w and building permits)		

*) Standard basis of all Fed. Master Transportation Plan Projects: 1989 DM

**) Conversion: 1 DM per km = 1 $ per mile

1 mile = 1.609 km
1 $ = 1.61 DM (June 1993)

C-2.

THE AMERICAN MAGLINE GROUP

OUR VISION IS THE CREATION OF A NEW AMERICAN INDUSTRY THAT WILL REVOLUTIONIZE THE GROUND TRANSPORTATION INFRASTRUCTURE IN THE UNITED STATES AND THE WORLD BASED ON MAGLEV TECHNOLOGY

BOOZ ALLEN & HAMILTON INC

THYSSEN HENSCHEL AMERICA, INC.

HUGHES

GENERAL ATOMICS

Structural Reform Model

| Government |
| Guideway Corporation |
| Operation Corporation |
| Interested Industry |
| General Contractor |
| Construction/ Supplier Companies |
| Bank Consortium |

Corp. Contract
Corp. Contract
Use Contract (Guideway)
Credit Contract
Contract for Risk Capital
General Contractor Contract
Work/Service Contract

Transrapid Berlin - Hamburg — **Financing**

OUR INTENT IS TO AMERICANIZE THE TRANSRAPID SYSTEM

- TRANSFER THE BASIC DESIGN AND MANUFACTURING KNOW-HOW

- CREATE SUBSYSTEMS BASED ON U.S. STATE OF THE ART: OPERATION CONTROL, COMMUNICATIONS, PROPULSION, POWER DISTRIBUTION

- ESTABLISH THE AMERICAN SUBCONTRACTOR/SUPPLIER INFRASTRUCTURE AND AMERICAN MANUFACTURING BASE(S)

- DEVELOP THE DATA NEEDED TO FACILITATE DOT CERTIFICATION OF THE SYSTEM

OUR OBJECTIVES

- CREATION OF TENS OF THOUSANDS OF HIGH SKILL, HIGH WAGE U.S. JOBS THAT WILL BE LONG LASTING

- MINIMIZING THE DEVELOPMENT TIME AND COST BY LEVERAGING THE $3 BILLION GERMAN TRANSRAPID INVESTMENT

- INCORPORATING ADVANCED U.S. TECHNOLOGIES INTO THE SYSTEM TO MAINTAIN THE MARKET LEAD OF THE U.S. PRODUCT

- CREATION OF TECHNOLOGY AND BUSINESS SPIN OFFS THAT WILL ENHANCE AMERICAN COMPETITIVENESS

- EXPORTING PRODUCTS WORLDWIDE

DEVELOPMENT OF A HIGH SPEED GROUND TRANSPORTATION INFRASTRUCTURE WHICH CREATES REAL AND ENDURING ECONOMIC AND SOCIAL BENEFITS TO THE U.S.

AMERICAN MAGLINE GROUP PROGRAM PLAN

- OBJECTIVES - DEVELOP A NEW U.S. MANUFACTURING BASE AND A NEW U.S. HIGH SPEED GROUND TRANSPORTATION SYSTEM

- ENABLING TECHNOLOGY ACTIVITIES FOR THE PROGRAM
  - TRANSFER IN DETAIL THE TRANSRAPID TECHNOLOGY TO U.S. FIRMS
  - AMERICANIZE THE SYSTEM, ADAPTING IT TO U.S. REQUIREMENTS & INCORPORATING STATE OF THE ART U.S. TECHNOLOGIES
  - PLANNING FOR THE U.S. MANUFACTURING INFRASTRUCTURE
  - INITIAL PLANNING OF PROJECTS INCLUDING PERMITTING REQUIREMENTS

- IMPLEMENTATION OF A MAGLEV SYSTEM PROJECT
  - PROJECT DETAILED DESIGN
  - ESTABLISH MANUFACTURING BASE
  - SYSTEMATIC BUILDING OF THE HIGH SPEED GROUND TRANSPORTATION NETWORK

USE OF THE TRANSRAPID TECHNOLOGY ALLOWS US TO QUICKLY IMPLEMENT A PROJECT & CREATE A LARGE NUMBER OF JOBS

MAGLEV PROJECT EXAMPLE (LAX-PALMDALE)

CHARACTERISTICS - 71 MILE LONG, DOUBLE TRACK
13 STATIONS
BASIC CAPACITY 6000 PPHPD

FINAL PROPOSALS DUE
INITIATE CONTRACT
PRELIMINARY DESIGN
NEGOTIATIONS
FINAL DESIGN
CONSTRUCTION
START-UP TESTING

TOTAL PROJECT*
RELATED JOBS
(MAN-YEARS/YEAR)
IN THOUSANDS

*INCLUDES 140% INDIRECT JOBS
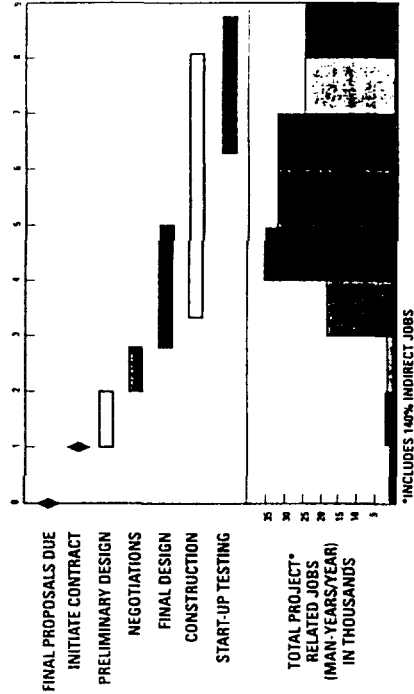
AMERICAN MAGLINE GROUP
Building on Transrapid Technology

THYSSEN HENSCHEL AMERICA Los Angeles, CA — VEHICLES, GUIDEWAY
BOOZ-ALLEN & HAMILTON Los Angeles, CA — TRANSPORTATION SYSTEM ENGINEERING
HUGHES AIRCRAFT CO Los Angeles, CA — CONTROL AND COMMUNICATIONS
GENERAL ATOMICS San Diego, CA — PROPULSION SYSTEM
PROJECT SUPPORT Site Specific — CIVIL WORKS
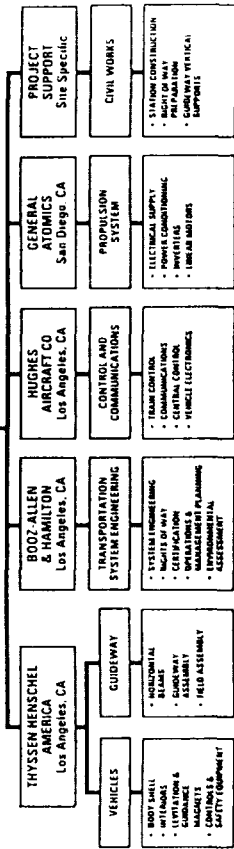
TRANSRAPID, THE ONLY PROVEN & CERTIFIED MAGLEV SYSTEM, PROVIDES QUIET, SAFE, ENVIRONMENTALLY FRIENDLY & COMFORTABLE 300 MPH GROUND TRANSPORTATION
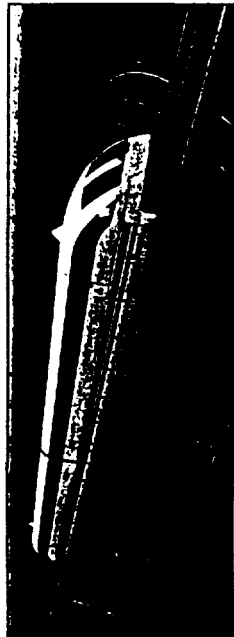
"WE WILL BRING THIS SYSTEM TO THE U.S. TO BE BUILT BY U.S. COMPANIES USING U.S. ENGINEERS"

SYSTEM UPGRADE AND CONVERSION ACTIVITIES

ACTIVITY	DESCRIPTION	MONTHS
SYSTEM COMMAND AND CONTROL DESIGN	DEVELOPMENT OF THE BASIC ARCHITECTURE OF THE COMMUNICATIONS AND CONTROL SYSTEM FOR A REVENUE SERVICE NETWORK INVOLVING MULTIPLE VEHICLES, MULTIPLE LINES AND O&M FACILITIES	
PROPULSION POWER SYSTEM	DESIGN AND MODULAR PROTOTYPING OF THE PROPULSION POWER SYSTEM INVERTERS AND ITS CONTROL UNIT. APPROACH WILL BE BASED ON CURRENT STATE-OF-THE-ART U.S. SWITCHING DEVICES.	
MANUFACTURING PLANNING	DEVELOP INFRASTRUCTURE INCLUDING INITIAL QUALIFICATION OF U.S. VENDORS & SUPPLIER FOR THE SYSTEM. PRELIMINARY MANUFACTURING PROCESS DESIGN AND SITING STUDIES. INCLUDES VEHICLE & GUIDEWAY DESIGN CONVERSION & UPGRADE	
PERMITTING AND CERTIFICATION	GENERATE TECHNICAL INFORMATION REQUIRED TO OBTAIN FRA CERTIFICATION OF THE SYSTEM. GENERATE DATABASE OF INFORMATION REQUIRED FOR ENVIRONMENTAL AND OTHER PERMITS WHICH WILL BE REQUIRED FOR A PROJECT	
PROJECT PLANNING	DETAILED PLANNING BY THE GROUP OF A SPECIFIC PROJECT DONE IN CONCERT WITH THE SPONSOR OF THE PROJECT	

THESE ACTIVITIES AND THE TECHNOLOGY TRANSFER WILL ALLOW A FAST START ON A U.S. PROJECT

JOB CREATION IN MAGLEV SYSTEM PROGRAM

AMG PROGRAM PLAN IS THE OPPORTUNITY FOR
U.S. TO BE IN THE FOREFRONT OF MAGLEV SYSTEMS

POTENTIAL TRANSRAPID BASED PROJECTS

SPECIFIC PROJECTS BEING STUDIED INCLUDE:

ORLANDO AIRPORT DEMONSTRATION

BERLIN - HAMBURG

PITTSBURGH DEMONSTRATION

LAX - PALMDALE

POTENTIAL MARKETS INCLUDE:

CALIFORNIA SPINE PROJECT

THE OTHER FOUR FRA DESIGNATED CORRIDORS

CHINA AND OTHER ASIAN MARKETS

THE U.S. & EXPORT MARKETS FOR MAGLEV
SYSTEMS ARE VERY LARGE

AMERICAN MAGLINE GROUP PROGRAM SUMMARY

- IMPROVE THE U.S. TRANSPORTATION INFRASTRUCTURE
  - RELIEVES AIRPORT AND HIGHWAY CONGESTION
  - SUPPORTS INTERMODALISM
  - REDUCES LOST PRODUCTIVITY DUE TO TRAVEL TIME

- IMPROVE THE ENVIRONMENT AND TRAVELER SAFETY
  - SAFER THAN AUTO, STEEL WHEEL RAIL OR AIR TRAVEL
  - REDUCES SINGLE OCCUPANT AUTO TRAVEL
  - REDUCES FUEL CONSUMPTION PER TRIP
  - LOWER EMISSIONS FROM REMOTE SINGLE POINT POWER SOURCE
  - LOWER ENVIRONMENTAL IMPACT FROM ALIGNMENT (ELEVATABLE)
  - QUIETER OPERATION

MAGLEV SYSTEM WILL IMPROVE QUALITY
OF LIFE: FAST, SAFE, AFFORDABLE, GREEN

AMERICAN MAGLINE GROUP PROGRAM SUMMARY

- GENERATE ECONOMIC DEVELOPMENT
  - CREATE IMMEDIATE AND LASTING JOBS
  - CREATE A U.S. MANUFACTURING BASE FOR HSGT
  - HELP THE TRADE BALANCE BY ELIMINATING IMPORTS
  - HELP THE TRADE BALANCE BY CREATING EXPORTS

- PROVIDE A BASIS FOR TRANSPORTATION TECHNOLOGY DEVELOPMENT
  - TRANSRAPID IS AN OPERATING BASIS FOR TECHNOLOGY IMPROVEMENTS
  - CONDUCT FURTHER DEVELOPMENT WORK ON THE TRANSRAPID SYSTEM
  - INCORPORATE TECHNOLOGIES AS THEY MATURE (E.G. SUPERCONDUCTORS)

- CREATE OPPORTUNITIES FOR U.S. INDUSTRY
  - SUPPLIER BASE FOR SYSTEM WILL BE FROM ALL OVER THE U.S.
  - HALF OF ANY PROJECT WILL BE BY LOCAL INDUSTRY

LOW O&M, FUEL AND ENVIRONMENTAL COSTS PLUS HIGH SPEED,
PRODUCE REAL WEALTH FOR THE U.S.

CONTROL OF MAGLEV VEHICLES WITH AERODYNAMIC AND GUIDEWAY DISTURBANCES[†]

Karl Flueckiger, Steve Mark, and Ruth Caswell
The Charles Stark Draper Laboratory, Inc.
Cambridge, MA

Duncan McCallum
Harvard University
Cambridge, MA

SUMMARY

A modeling, analysis, and control design methodology is presented for maglev vehicle ride quality performance improvement as measured by the Pepler Index. Ride quality enhancement is considered through active control of secondary suspension elements and active aerodynamic surfaces mounted on the train.

To analyze and quantify the benefits of active control, the authors have developed a five degree-of-freedom lumped parameter model suitable for describing a large class of maglev vehicles, including both channel and box-beam guideway configurations. Elements of this modeling capability have been recently employed in studies sponsored by the U.S. Department of Transportation (DOT).

A perturbation analysis about an operating point, defined by vehicle and average crosswind velocities, yields a suitable linearized state space model for multivariable control system analysis and synthesis. Neglecting passenger compartment noise, the ride quality as quantified by the Pepler Index is readily computed from the system states. A statistical analysis is performed by modeling the crosswind disturbances and guideway variations as filtered white noise, whereby the Pepler Index is established in closed form through the solution to a matrix Lyapunov equation. Data is presented which indicates the anticipated ride quality achieved through various closed-loop control arrangements.

1. INTRODUCTION

A maglev vehicle's suspension system is required to maintain the primary suspension air gap while minimizing passenger compartment vibrations in the presence of guideway irregularities and aerodynamic disturbances. It must meet these requirements while: (1) minimizing the size of the required air gap so that more efficient lift magnets can be employed; (2) minimizing the

---

stroke length of the secondary suspension so that vehicle frontal area and drag are as small as possible; (3) minimizing the size, weight, and required power of active suspension elements. Unfortunately, these design goals conflict with the desire to increase the allowable guideway roughness (to reduce guideway cost) and maximize crosswind disturbance rejection. Active control offers great potential to improve suspension performance. Constructing a maglev transportation system, or even a short test section, is a very expensive venture. Therefore, it is cost effective to develop analytic tools that can predict trade-offs between the various conflicting system requirements and performance metrics. This allows design alternatives to be examined before building either an actual system or scale model. Unfortunately, the scaling properties associated with magnetic systems preclude construction of accurate maglev vehicle scale models.

In this paper we describe a modeling, analysis, and control design methodology specifically for ride quality improvement as measured by the Pepler Index. We consider a generic EDS type maglev vehicle having a null flux primary suspension and bogies. This is a variation of the vehicle proposed by the Bechtel consortium's System Concept Definition (SCD) study [1]. The model incorporates front and rear bogies, each having roll but no pitch or yaw dynamics. The guideway disturbance is modeled in three directions (vertical, lateral, and roll) as linear systems driven by white noise. A crosswind disturbance, which acts against the side of the vehicle, is also modeled in this fashion. We consider control authority produced by an active secondary suspension consisting of actively controlled elements (hydraulic or electro-mechanical actuators) that exert forces between the vehicle and its suspension bogies. We also analyze the potential benefits of actively controlled aerodynamic surfaces implemented in conjunction with the conventional secondary suspension. The aerodynamic control surfaces considered here are winglets that exert forces directly on the vehicle body, which, due to high vehicle operating speeds, can produce reasonably large forces when modestly sized. Aerodynamic control surfaces have the advantage of exerting forces directly on the vehicle without exerting reaction forces on the bogies.

Wormley and Young developed a heave and pitch model of a vehicle subjected to simultaneous guideway and external (such as wind) disturbances [2]. A methodology for optimizing the passive suspension performance in the presence of these simultaneous disturbances was derived and the results evaluated. Guenther and Leonides developed a multiple degree-of-freedom model for a maglev vehicle that includes front and rear bogies, with a time-delayed guideway disturbance to the rear bogie [3]. A control system was developed based on the solution to the stochastic optimal control problem. Gottzein, Lange, and Franzes developed a secondary suspension model with an active control system for a Transrapid type EMS vehicle [4]. A Linear Quadratic Gaussian (LQG) controller was developed for the vertical direction.

The research presented here is a natural extension of the works cited above to provide an integrated five degree-of-freedom model that includes guideway irregularities and aerodynamic effects. The remainder of this paper is organized as follows: §2 contains an overview of the model employed in our analysis; §3 hosts a discussion of the control system analysis and design methodology employed by the authors to obtain results given in §4; §5 concludes with summary remarks about and consequences of our findings.

2. ANALYSIS MODEL OVERVIEW

Key elements of the analytic model developed for ride quality analysis and control system synthesis are presented within this section. Assumptions imbued in the modeling process are

stated explicitly. However, for the sake of brevity, a rigorous treatment of vehicle dynamics is not developed here. The interested reader is referred to [1],[5], and [6] for more lengthy discussions.

A depiction of the maglev system under discussion is given in Fig. 1, which shows the vehicle body suspended on two bogies. The bogies contain superconducting magnets required for the primary suspension which suspends the bogies relative to the guideway. The secondary suspension is composed of passive spring and damper elements as well as active components that exert forces between the bogies and the vehicle body. We assume that the primary and secondary suspension elements exert forces in the vertical and lateral directions, as well as roll torques. Additional control authority is provided by six active aerosurfaces mounted on the train.
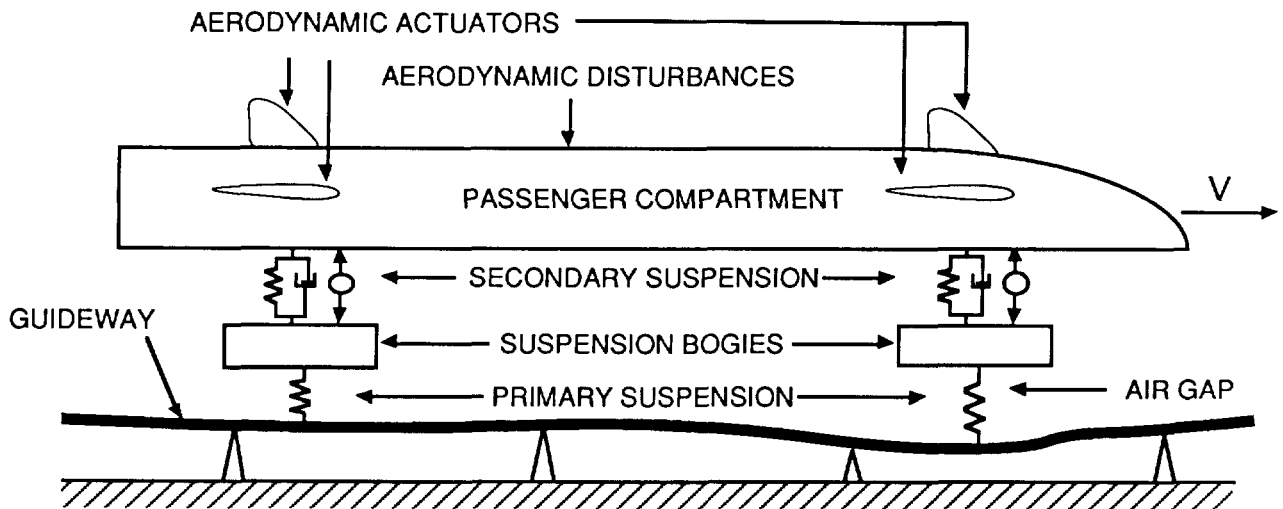
Figure 1. Maglev Vehicle Concept.

Disturbances to the system are guideway irregularities and aerodynamic forces due to crosswinds. The guideway is assumed to be perfectly rigid, but with an irregular surface that can be described by three sets of independent statistics: one each for vertical, lateral, and roll disturbances. For analysis purposes, we assume a worst case scenario where crosswind disturbances act in the lateral direction.

We assume that the vehicle forward velocity, V, is constant and that there is no coupling between the magnetic propulsion and levitation systems. The vehicle body and bogies are permitted to move in the vertical and lateral directions, and also to roll. The vehicle body has the additional freedom to yaw and pitch. Variations about the vehicle's forward velocity are not included in the model. The allowable directions of motion are sketched in Figures 2 and 3, where the variable y represents the lateral direction, z vertical, ϕ roll, θ pitch, and ψ yaw. The lack of bogie yaw and pitch dynamics is not seen to be a major analytic deficiency. Due to the large moment arm about the vehicle body's center of gravity (CG), the torque on the vehicle body caused by bogie yawing is expected to be small compared to that due to lateral displacement of the bogie. A similar argument applies to the omission of bogie pitch dynamics. In conjunction with this restriction, there is no finite magnet length filtering of the guideway disturbances, as might be the case for an actual vehicle.

The following additional assumptions are made: the vehicle body's and bogies' CGs are in the geometric center of the respective bodies, both laterally and longitudinally; the vehicle body and bogies are completely rigid; the passengers and their baggage are fixed to the vehicle body; both bogies have identical dimensions, mass properties, and primary suspension stiffnesses; and small angle approximations are valid throughout the linear suspension model when relating linear to angular displacements.

The maglev vehicle's physical parameter values in our analyses are similar to a box-beam guideway design developed by the Bechtel consortium for the U.S. Department of Transportation [1]. Representative gross physical properties are summarized in Table 1. The remainder of this section consists of a brief synopsis of the suspension force models followed by a discussion of the active aerodynamic surfaces considered. The section is concluded with descriptions of the guideway and crosswind disturbance models utilized.

A. Suspension Forces

To obtain a suitable linear system description, we model the maglev vehicle in a lumped mass fashion. All suspension elements are modeled as massless generalized springs. For example, the suspension force, F, due to the displacement between the front bogie and the guideway is determined by the relationship below:

$$F = Kr + D\dot{r} \qquad (1)$$

where K is the spring stiffness matrix, D is the damping, and r is the equilibrium displacement vector. The spring constants for the primary suspension system are dependent upon forward velocity; representative values as a function of train speed are given in Table 2. Damping for this type of magnetic suspension is believed to be very low [7] and therefore is assumed zero for modeling purposes. Passive secondary suspension spring constants and damping ratios are selected to improve ride quality while simultaneously preventing touchdown and limiting the active secondary suspension stroke. The optimization procedure is discussed in §3.
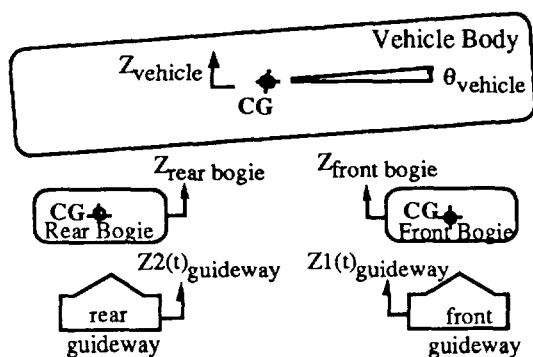
Figure 2. Degrees of Freedom: Side View
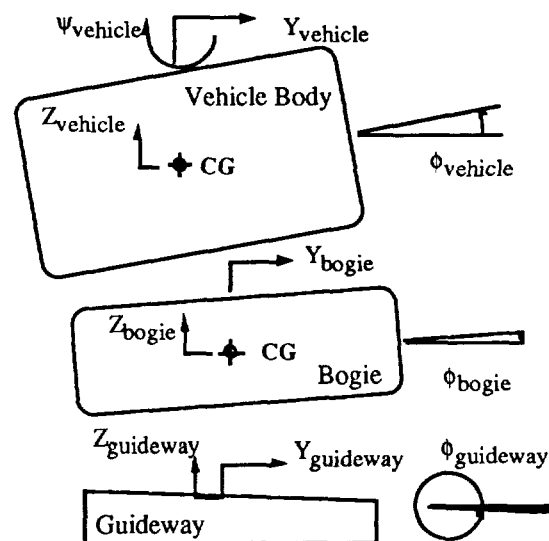
Figure 3. Degrees of Freedom: Front View.

| Table 1 | | Table 2 | |
Representative Physical Dimensions / Primary Suspension Stiffness

Table 1
Representative Physical Dimensions

Parameter	Value
Vehicle Height	4.9m
Vehicle Length	36.1m
Vehicle Width	3.7m
Total Mass	64400kg
Passenger Compartment Mass	40830kg
Distance Between Bogies	18.7m
Bogie Height	0.75m
Bogie Width	1.5m
Top Winglet CP to Train CG (vertical)	2.3m
Side Winglet CP to Train CG (horizontal)	2.4m

Table 2
Primary Suspension Stiffness

Vehicle Speed	Lateral Stiffness	Vertical Stiffness
50.0 m/s	-1.09e7 N/m	-3.23e7 N/m
134.0 m/s	-1.35e7 N/m	-3.97e7 N/m
150.0 m/s	-1.36e7 N/m	-4.01e7 N/m

It is assumed that all suspension forces act in equal and opposite directions across the gap between the elements under consideration. For simplicity, we model these forces as being applied to fixed points relative to the guideway's, bogies', and passenger compartment's centers of gravity.

B. Aerodynamic Actuation

Six active aerodynamic surfaces, as shown in Figure 1, are available to the control system for improving ride quality. We assume that these actuators operate in "free-stream" and are modeled as winglets with one degree-of-freedom. Four winglets are mounted on the sides of the train and produce vertical forces at the surfaces' centers of pressure (CP): two in front on opposite sides, and two in back on opposite sides. Two winglets are mounted on the top of the train (in "rudder-like" arrangements) to provide lateral forces.

The lift force for a flap in free-stream is given by:

$$F_L = \frac{1}{2}\rho|V_{air}|^2 AC_L(\alpha) \qquad (2)$$

where ρ is air density, A is area, V_{air} is the velocity of the air mass relative to the winglet, and α represents angle of attack. We consider only the lift component of the flap forces. The induced drag of the flaps is calculated to determine the drawbacks of aerodynamic control in [5], but its effect on ride quality is not considered here. Since induced drag acts parallel to the velocity vector, drag forces lie in a direction not included in our model. The lift coefficient is obtained from conventional aerodynamic theory [8] and is nearly linear for small angles of attack. A linear equation for $C_L(\alpha)$ results: $C_L(\alpha) = C_L\alpha$, where $C_L = 0.0264/°$. We assume that V_{air} in (2) is equal to the train's velocity and ignore the effects of crosswind and vehicle rotation. Also, we use a small angle approximation for α to model the lift force as perpendicular to the undeflected winglet surface.

In theory, a very large aerodynamic force can be obtained for relatively low aero-actuator torque. Since the flaps rotate about their centers of pressure, the aerodynamic torques across

flap rotation joints are small when compared to the forces generated by the flaps. However, the actual force required in a hydraulic system that drives a winglet can still be large, due to physical constraints and practical considerations. The dynamics of the closed-loop system may dictate a high actuator bandwidth resulting in large actuator power requirements.

C. System Disturbances

Guideway irregularities are captured by the stochastic model:

$$\Phi_{guideway}(\omega) = \frac{A_r V}{\omega^2} \tag{3}$$

where $\Phi_{guideway}$ is the guideway Power Spectral Density (PSD), A_r is the Roughness Parameter, and V is the train's forward velocity. A roughness parameter corresponding to welded steel rail (gage 4-6) is used to define the guideway PSD, which is subsequently used to form a linear system driven by white noise to describe the guideway position variations. While a typical guideway will not be made of steel and its irregularities as seen by the train will be dominated instead by the misalignment of guideway coils, its roughness parameters are expected to fall in the range of those of welded steel rail. Roughness parameters are given in Table 3.

We assume further that the guideway disturbances act upon the front and rear of the train at the bogie locations. Since the guideway is assumed rigid, the disturbance affecting the rear bogie is identical to that acting on the front bogie, but delayed in time. Therefore, we model the rear guideway dynamics by the time delayed front guideway position variation. Clearly, the time delay is inversely proportional to vehicle forward velocity: $T_{delay} = L/V$, where L is the distance between bogies. Since a time delay cannot be described by an exact finite dimensional continuous time state space representation, a Pade approximation is incorporated into the control system analysis and synthesis model:

$$e^{-sT} \approx \frac{2 + T_{delay}s + \frac{1}{2!}(-T_{delay}s)^2 + \frac{1}{3!}(-T_{delay}s)^3 + ...}{2 + T_{delay}s + \frac{1}{2!}(T_{delay}s)^2 + \frac{1}{3!}(T_{delay}s)^3 + ...} \tag{4}$$

The crosswind description consists of the sum of two terms: a constant, steady-state mean value and a time variant random process. The mean crosswind velocity is equal to half of the peak crosswind velocity, assuming a maximum three sigma variation from the mean. In our analysis we assume 26.8m/s (60mph) crosswind peak. The PSD of the time varying crosswind component is given by:

$$\Phi_{wind}(\omega) = \frac{2\sigma_w^2 v}{\omega^2 + v^2} \tag{5}$$

where the break frequency, v, is 1.0 rad/sec, and the RMS wind velocity, σ_w, is 4.8 m/s (10mph). Φ_{wind} is implemented by a linear system driven by white noise. We assume that the crosswind is perpendicular to the guideway. This maximizes vehicle sideslip, effectively softening the lateral suspension stiffness and thereby degrading system performance.

Table 3
Guideway Roughness Parameters

Parameter	Value
A_r (vertical)	1.2e-6 rad^2-m/s
A_r (lateral)	1.2e-6 rad^2-m/s
A_r (roll)	5.7e-7 rad^4/m-s

3. ANALYSIS

Analysis of the system model begins with choosing the passive secondary suspension's stiffness and damping parameters. The function of the secondary suspension system is to improve ride quality while simultaneously preventing vehicle contact (touchdown) on the guideway. The active secondary suspension stroke must also be kept within practical limits. Typically, the passive suspension parameters cannot be selected to optimize all of these criteria simultaneously, and hence, the parameters are determined through trade-off analyses. Once the suspension elements have been defined, a force balance condition is exploited to determine nominal operating equilibrium values for the vehicle's center of pressure and sideslip angle (given forward and average crosswind velocities). Finally, the linear perturbation model is assembled and a candidate control law synthesized. The resulting closed-loop system is analyzed in a statistical framework. The remainder of this section presents further details of these procedures.

A. Secondary Suspension Parameter Optimization

The primary suspension design involves an inherent conflict between ride quality and guideway tracking. A stiff primary suspension provides improved guideway tracking at the expense of significant guideway and wind disturbance transmission to the passenger compartment. Additionally, a stiff magnetic suspension generally exhibits efficient power consumption. Power considerations, rather than ride quality factors, generally dictate primary suspension design. With the primary suspension parameters assumed given, the secondary suspension parameters are chosen to address the trade-off between the system performance measures of interest, with the overall goal of achieving the best ride quality.

System performance can be evaluated through the root mean squared (RMS) values of relevant quantities in our model. RMS velocity and acceleration levels can be used to compute the Pepler index. The primary air gap and secondary suspension stroke requirements can also be estimated from the RMS variations of these variables, which provides a method of specifying the primary and secondary suspension stroke limits through stochastic control techniques. The motivation behind this treatment stems from the guideway and wind disturbances being characterized by linear systems driven by white noise, whereby it is natural to determine the system outputs for analysis in a similar form.

Details of the trade-off studies used for characterizing the passive secondary suspension system are beyond the scope of this paper, but can be found in [1],[5], and [6]. The design parameter values are listed in Table 4.

Table 4
Passive Secondary Suspension Parameters

Vertical Natural Frequency	0.8 Hz
Vertical Damping Ratio	0.10
Lateral Natural Frequency	1.5 Hz
Lateral Damping Ratio	0.5
Roll Stiffness	0.0 N-m/rad
Roll Damping	2.0e6 N-m-s/rad

B. Operating Point Force Balance

To obtain a linear state space perturbation analysis model, we need to determine the vehicle steady-state sideslip angle, β, and the location of the center of pressure (CP) relative to the CG. This is performed through a force balance analysis, where forces and moments arising from the constant component of crosswind velocity are canceled by the primary and passive suspension systems (Equation (1)). Crosswind forces on the train are modeled as a side force acting at the CP perpendicular to forward velocity. The aerodynamic side force is given by:

$$\left[F_y\right]_{aero} = \frac{1}{2}\rho\left|V_{air}\right|^2 A_t C_y(\beta) \tag{6}$$

where A_t is the train's cross-sectional area and $C_y(\beta)$ is the coefficient of side force. The air-relative train velocity, V_{air}, is the vector sum of the train's earth-relative and crosswind velocities. The aerodynamic coefficient, $C_y(\beta)$, is non-linearly dependent on the sideslip angle and is described by a third order polynomial fit to data generated in [5].

Thus, given forward vehicle velocity and steady-state crosswind speed, the aerodynamic forces on the vehicle are computed as a function of β and CP location via (6). A set of nonlinear equations is solved numerically to determine β and CP by balancing $[F_y]_{aero}$ against the nonaerodynamic forces contained in the model, where all time-varying zero mean disturbances and actuator displacements are nulled. For the data presented in §4, the vehicle and mean wind velocities are 150m/s (336mph) and 13.4m/s (30mph) respectively. The resulting steady-state sideslip, β, is 0.092rad (5.27°), which corresponds to a 0.0026rad (0.149°) vehicle yaw angle, ψ.

C. Covariance Analysis

To construct our linear perturbation model, we further assume that the passenger compartment and bogie angular rotation rates are small, and we neglect nonlinear coupling terms due to Coriolis accelerations and gyroscopic effects. The resulting linear equations of motion are placed in state space form, $\dot{x} = Ax + Bu + Fw$, where: the system state, x, contains train and bogie positions and velocities, and guideway positions (constrained to appropriate degrees of freedom); the system actuator input vector, u, contains active secondary suspension force and aerosurface deflection commands; and the disturbance input vector, w, is (Gaussian) unit intensity white noise.

A measure of ride quality commonly used for maglev vehicles is the Pepler ride quality criteria [9], P.I., which is given by:

$$P.I. = 1.0 + 0.5\sigma_{\dot{\phi}} + 17\sigma_{\ddot{z}} + 17\sigma_{\ddot{y}} + 0.1(dB(N) - 65) \tag{7}$$

where $\sigma_{\dot{\phi}}$ is the passenger RMS roll rate, $\sigma_{\ddot{z}}$ is the passenger RMS vertical acceleration, $\sigma_{\ddot{y}}$ is the passenger RMS lateral acceleration, and dB(N) is the passenger compartment noise level (decibels). Values of the Peplar Index varying from 1 (very comfortable) to 7 (very uncomfortable) provide an indication of perceived ride quality.

In our analysis, we ignore the compartment noise level. Hence, P.I. is a scalar sum of system statistics, which can be denoted $z = Cx + Du$ (ignoring the constant term, 1.0). By defining our analysis variables in this manner, we proceed to design a controller using Linear Quadratic Regulator (LQR) theory, which synthesizes a state feedback control law of form: $u = -Gx$. The gain matrix, G, is selected to minimize a quadratic cost functional that includes weighted terms containing performance variables of interest and control energy required. The cost functional, J, provides an optimal trade-off between actuator effort and closed-loop system performance:

$$J = \lim_{T \to \infty} E\left\{ \int_0^T \left(z(t)^T Q z(t) + u(t)^T R u(t) \right) dt \right\} \tag{8}$$

The matrices Q and R are used to vary the relative importance of the system outputs and control effort respectively (E denotes the expectation operator). The gain matrix G minimizing this cost functional is given by:

$$G = R^{-1}\left[D^T Q C + B^T K \right] \tag{9}$$

where K is the solution to an algebraic Riccati equation [10]:

$$KA + A^T K + C^T Q C - [KB + C^T Q D]R^{-1}[B^T K + D^T Q C] = 0 \tag{10}$$

We calculate the closed-loop system steady-state state covariances analytically. If A_{cl} is the closed-loop system matrix ($A_{cl} \equiv A - BG$), then the state covariance matrix steady-state solution, Σ_{xx}, is the solution to the Lyapunov equation [11]:

$$A_{cl}\Sigma_{xx} + \Sigma_{xx} A_{cl}{}^T + FF^T = 0 \tag{11}$$

A system output for analysis, denoted y, is defined as a linear combination of system states: $y = C_{out}x$. The output covariance matrix, Σ_{yy}, is given by:

$$\Sigma_{yy} = C_{out} \Sigma_{xx} C_{out}{}^T \tag{12}$$

The RMS of the output vector, y, is directly computed through the terms along the diagonal of Σ_{yy}. This analysis methodology permits us to compute analytically the statistics of important system properties, such as the Pepler Index, bogie displacements, and actuator commands, without having to resort to Monte Carlo schemes.

4. RESULTS

Results obtained using the analysis model described in §2 are presented here. Control algorithms are developed and the resulting closed-loop systems analyzed as per §3. We select the weighting matrices, Q and R in (8), to provide good ride quality while maintaining, if possible, the strict suspension gap requirements defined in [1]. Tables 5 through 8 present data indicating basic system performance for four candidate control strategies: (1) no active control (open-loop); (2) active secondary suspension control only; (3) active aerosurfaces only, and (4) active secondary suspension and aerosurfaces (hybrid control). The tables present results associated with guideway disturbances alone, crosswind disturbances alone, and the combination of both sets of disturbances. RMS accelerations are evaluated for passengers seated over the front bogie, at the center of the passenger compartment, and over the rear bogie. These RMS values, along with the RMS roll rate, permit ride quality to be evaluated in terms of the Pepler Index at these three locations.

We assume a forward vehicle velocity of 150m/s (336mph) and a peak crosswind (three-sigma) velocity of 26.8m/s (60mph). The nominal air gaps are 5 cm in the lateral direction and 10 cm in the vertical direction. We desire a five-sigma air gap variation requirement in response to disturbances. This requirement is most difficult to meet at the front of the vehicle, where the steady-sate air gap deviation is 0.85 cm in the lateral and 0.72 cm in vertical direction. For the secondary suspension strokes, the maximum allowable values are 19 cm in the lateral and 10 cm in the vertical direction, and in this case the requirement is relaxed to three-sigma variations. Again, the front of the vehicle has the largest steady-state deviation, 3.19 cm in the lateral direction and 2.43 cm in the vertical direction. Both the air gap variations and secondary suspension strokes are determined at the outside edge of the front and rear bogies.

A. Passive Secondary Suspension

Passive secondary suspension optimization was described in §2. The performance given by the passive system is given in Tables 5 through 8, and is taken as the baseline against which the actively controlled systems are compared. The ride quality, as measured by the Pepler index, is uncomfortable at the front and is tending toward somewhat uncomfortable at the center and rear of the vehicle. The acceleration, air gap, and secondary suspension stroke variations in the lateral direction are all largest at the front of the vehicle due to the location of the center of aerodynamic pressure ahead of the center of gravity. The requirement on the lateral air gap variations is not achievable for any secondary suspension design, and therefore indicates that a basic change in the primary suspension system is necessary. However, for the purposes of this paper, the lateral air gap variations will be minimized as much as possible. Also, although not unreasonable, the 26.8m/s (60mph) peak crosswind velocity assumed for this study is rather high; crosswinds of this level may not be present in all scenarios. However, since the crosswind force is approximately proportional to the product of vehicle velocity and crosswind velocity, a speed restriction during high wind conditions will ameliorate the detrimental effects of crosswinds.

B. Active Secondary Suspension

In this paper, active secondary suspension refers to a configuration where active hydraulic actuators are employed between the vehicle body and the bogies. The active and passive suspension elements are assumed collocated. Note that the RMS acceleration levels for this

system have been reduced when compared to the passive system in both the vertical and lateral directions. Since the passive system has vertical air gap variations which are below the system requirement, the optimal control design methodology was used to achieve smaller vertical accelerations at the expense of larger air gap variations, as discussed in §3. However, in the lateral direction, the passive design exhibited air gap variations which were larger than allowable and so this trade-off could not be utilized. In addition, the authors decided that the control design should not attempt to reduce the lateral air gap variations (relative to those achievable by passive suspension); we do not endorse an EDS vehicle design that depends on the active control system to maintain adequate air gap clearance. A failure of the control system could result in vehicle contact with the guideway.

An important accomplishment of the active secondary suspension is the reduction of the vehicle roll rate by approximately a factor of 10. This is especially significant since roll has been judged to be an especially uncomfortable motion by passengers: half of the roll rate RMS adds directly to the Pepler index. The Pepler index has been reduced by 2.0-2.5 at all three locations along the vehicle. This results in a ride quality which is considered better than average and towards comfortable at the center and rear.

A fundamental disadvantage of the active hydraulic actuators is that any force exerted against the vehicle body to cancel a disturbance will have an equal and opposite reaction force acting against the bogies. Thus there is a direct trade-off between air gap variations, secondary suspension strokes, and vehicle accelerations.

C. Active Aerodynamic Surfaces

The use of active aerodynamic control surfaces results in vertical accelerations which are smaller at all three locations along the vehicle and lateral accelerations which are lower at the center and rear but slightly higher at the front of the vehicle . The ride quality (as measured by the Pepler index) is the same at the front but slightly lower at the center and rear of the vehicle when compared to the active secondary suspension design. It is important to note that this ride quality improvement is obtained without any appreciable increase in the air gap variations, in contrast to the active hydraulic actuator suspension. Compared to the passive system, the secondary suspension strokes are larger, especially in the vertical direction, but remain within acceptable values. The roll rate is slightly less than that of the system with hydraulic actuators.

The primary advantage of the active aerodynamic surfaces is that they exert forces against the vehicle body with respect to an earth fixed (inertial) frame. Therefore, the effects of guideway disturbances on the vehicle body can be minimized without directly affecting the air gap variations. This is equivalent to holding the vehicle body stationary while the bogies bounce beneath it. Of course, this results in larger secondary suspension stroke variations, as illustrated by the data presented. The crosswind forces cannot be canceled directly even though, like the aerodynamic control surfaces, they act directly on the vehicle body. Two primary reasons for this arise because the crosswind disturbance is neither: (1) known beforehand, as the rear guideway disturbances are, nor (2) directly measurable. Another reason stems from non-collocation of crosswind forces and aerodynamic actuators.

The maximum RMS angle of attack of the aerodynamic surfaces was assumed to be 9°, based on the predicted deflection at which the aerodynamic surface stalls. This value was used for all of the aerodynamic surfaces. More control authority for the lateral fin at the front of the vehicle would have provided a greater potential for ride quality improvement. However, the size of the aerodynamic actuators at all locations was limited to practical values.

D. Active Hybrid Suspension

The hybrid active suspension, which incorporates hydraulic actuators between the vehicle body and bogies as well as aerodynamic actuators mounted to the vehicle body, achieves slightly lower lateral accelerations at the front and center of the vehicle when compared to the other active suspension configurations. The acceleration reduction in the lateral direction at the rear, and in the vertical direction at the front, center, and rear is more significant. The roll rate is controlled as well as for the system with active aerodynamic surfaces, and the Pepler index values are considerably lower than either of the other two active systems. According to the Pepler index, the ride quality at the front of the vehicle, despite the high lateral accelerations, is better than average , while at the center of the vehicle it is comfortable. The best ride quality is achieved at the rear of the vehicle.

The air gap variations in both directions are less than those of the passive suspension, while the vertical secondary suspension strokes are higher, but within specifications. The lateral secondary suspension strokes are lower than those of the passive suspension, Since additional resistance to crosswind disturbances can be gained both by making the vehicle's apparent mass larger and effectively making the entire vehicle's yaw and lateral stiffness larger, the secondary suspension stroke variation is reduced.

Note that for the inclusion of guideway disturbances only, all three active control designs resulted in better ride quality at the rear of the vehicle than at the front. This is due to the preview of the rear guideway disturbances from the moment the front bogie experiences them.

Table 5.
Pepler Ride Comfort Index Values
V = 150 m/s (336mph); RMS Wind = 4.8 m/s (10 mph)

	Passive Secondary	Active Hydraulic Secondary	Active Aero-Surfaces	Active Aero & Hydraulic Secondary
Front				
Guideway	3.62	2.05	1.91	1.63
Crosswinds	4.99	3.12	3.23	2.86
Combined	5.97	3.46	3.45	2.96
Center				
Guideway	3.32	1.81	1.60	1.32
Crosswinds	3.61	2.07	1.98	1.88
Combined	4.57	2.38	2.16	1.93
Rear				
Guideway	3.69	1.96	1.70	1.22
Crosswinds	3.52	1.88	1.77	1.48
Combined	4.74	2.33	2.05	1.53

Table 6.
RMS Vehicle Accelerations and Roll Rate
V = 150 m/s (336mph); RMS Wind = 4.8 m/s (10 mph)

	Passive Secondary	Active Hydraulic Secondary	Active Aero-Surfaces	Active Aero & Hydraulic Secondary
Front Y Train Accels Guideway Crosswinds Combined	5.32 g/100 14.26 g/100 15.22 g/100	4.09 g/100 11.09 g/100 11.82 g/100	4.08 g/100 12.00 g/100 12.68 g/100	3.23 g/100 9.81 g/100 10.33 g/100
Center Y Train Accels Guideway Crosswinds Combined	3.89 g/100 6.19 g/100 7.31 g/100	2.94 g/100 4.94 g/100 5.75 g/100	2.51 g/100 4.63 g/100 5.27 g/100	1.42 g/100 4.05 g/100 4.29 g/100
Rear Y Train Accels Guideway Crosswinds Combined	5.91 g/100 5.62 g/100 8.16 g/100	3.65 g/100 3.84 g/100 5.29 g/100	2.93 g/100 3.38 g/100 4.48 g/100	0.81 g/100 1.73 g/100 1.91 g/100
Front Z Train Accels Guideway Crosswinds Combined	6.38 g/100 3.62 g/100 7.34 g/100	1.76 g/100 0.71 g/100 1.90 g/100	1.04 g/100 0.62 g/100 1.21 g/100	0.33 g/100 0.61 g/100 0.69 g/100
Center Z Train Accels Guideway Crosswinds Combined	6.01 g/100 3.62 g/100 7.02 g/100	1.50 g/100 0.71 g/100 1.66 g/100	0.83 g/100 0.62 g/100 1.03 g/100	0.30 g/100 0.61 g/100 0.67 g/100
Rear Z Train Accels Guideway Crosswinds Combined	6.19 g/100 3.62 g/100 7.17 g/100	1.67 g/100 0.71 g/100 1.81 g/100	0.99 g/100 0.62 g/100 1.17 g/100	0.27 g/100 0.61 g/100 0.67 g/100
Roll Rate Guideway Crosswinds Combined	1.27 °/s 1.89 °/s 2.28 °/s	0.11 °/s 0.22 °/s 0.25 °/s	0.07 °/s 0.17 °/s 0.19 °/s	0.06 °/s 0.17 °/s 0.18 °/s

Table 7.
RMS Air Gap Variations
V = 150 m/s (336mph); RMS Wind = 4.8 m/s (10 mph)

	Passive Secondary	Active Hydraulic Secondary	Active Aero-Surfaces	Active Aero & Hydraulic Secondary
Front Y Guideway	0.333 cm	0.424 cm	0.289 cm	0.292 cm
Crosswinds	1.242 cm	1.153 cm	1.254 cm	1.178 cm
Combined	1.286 cm	1.228 cm	1.287 cm	1.214 cm
Rear Y Guideway	0.266 cm	0.450 cm	0.269 cm	0.269 cm
Crosswinds	0.355 cm	0.329 cm	0.369 cm	0.307 cm
Combined	0.443 cm	0.557 cm	0.457 cm	0.409 cm
Front Z Guideway	0.732 cm	1.346 cm	0.753 cm	0.484 cm
Crosswinds	0.941 cm	0.652 cm	0.714 cm	0.767 cm
Combined	1.192 cm	1.495 cm	1.038 cm	0.907 cm
Rear Z Guideway	0.720 cm	1.400 cm	0.756 cm	0.600 cm
Crosswinds	0.094 cm	0.230 cm	0.265 cm	0.216 cm
Combined	0.726 cm	1.419 cm	0.801 cm	0.637 cm

Table 8.
RMS Secondary Suspension Strokes
V = 150 m/s (336mph); RMS Wind = 4.8 m/s (10 mph)

	Passive Secondary	Active Hydraulic Secondary	Active Aero-Surfaces	Active Aero & Hydraulic Secondary
Front Y Guideway	0.380 cm	0.642 cm	0.369 cm	0.338 cm
Crosswinds	4.389 cm	5.518 cm	4.473 cm	2.481 cm
Combined	4.406 cm	5.555 cm	4.488 cm	2.504 cm
Rear Y Guideway	0.426 cm	1.029 cm	0.414 cm	0.590 cm
Crosswinds	1.132 cm	4.185 cm	1.308 cm	0.133 cm
Combined	1.209 cm	4.310 cm	1.372 cm	0.605 cm
Front Z Guideway	1.298 cm	3.362 cm	2.475 cm	2.972 cm
Crosswinds	1.126 cm	1.768 cm	1.321 cm	1.522 cm
Combined	1.718 cm	3.799 cm	2.805 cm	3.339 cm
Rear Z Guideway	1.111 cm	3.284 cm	2.427 cm	2.643 cm
Crosswinds	1.598 cm	1.531 cm	0.996 cm	1.088 cm
Combined	1.946 cm	3.623 cm	2.624 cm	2.858 cm

106

5. CONCLUDING REMARKS

To analyze and quantify the benefits of active control, the authors have developed a five degree-of-freedom lumped parameter modeling capability suitable for a broad class of maglev vehicle and guideway configurations. Perturbation analyses about an operating point defined by train and average cross-wind velocities yield linearized state-space descriptions of the maglev system for multivariable control system analysis and synthesis. Results presented in §4 indicate that the use of active aerodynamic control surfaces, in coordination with the active secondary suspension system, provides significant improvement to the passenger ride quality while ameliorating primary suspension gap requirements. Similar results by the authors ([1], [5], and [6]) for alternative system configurations support this conclusion.

Our analysis and design methodology permits us to alter physical properties, actuation (and potentially, sensing) elements, and disturbance inputs contained within the linear model description. This can be exploited to ascertain optimal system design parameters through parametric trade-off analyses. (We appreciate that specific performance predictions generated by linear analyses should ultimately be verified through high fidelity nonlinear simulation.) A natural extension to our work includes appending additional modeling capabilities, *e.g.*: curved and rolling guideways, vehicle bending modes, actuator and sensor dynamics and noise, and, of course, more sophisticated control techniques.

REFERENCES

[1] *Maglev System Concept Definition*, contract DTFR 53-92-C-00003, prepared by Bechtel/Draper/MIT/Hughes/General Motors for U.S. DOT: FRA.

[2] Wormley, D.N., Young, J.W., "Optimization of Linear Vehicle Suspensions Subjected to Simultaneous Guideway and External Force Disturbances," Journal of Dynamic Systems, Measurement, and Control: Transactions of the ASME, Paper No. 73-Aut-H, March 16,1973.

[3] Guenther, Christian R., Leonides, Cornelius T., "Synthesis of a High-Speed Tracked Vehicle Suspension System - Part I: Problem Statement, Suspension Structure, and Decomposition," IEEE Transactions on Automatic Control, vol. AC-22, No. 2, April 1977.

[4] Gottzein, E.; Lange, B., Ossenberg-Franzes, F., "Control System Concept for a Passenger Carrying Maglev Vehicle," High Speed Ground Transportation Journal, Vol 9, No. 1, 1975, pp 435-447.

[5] Barrows, T., McCallum, D, Mark, S, and Castellino, R. C, *Aerodynamic Forces on Maglev Vehicles*, contract DOT/FRA/NMI-92/21, prepared by C.S. Draper Lab. for U.S Department of Transportation: Federal Railroad Administration.

[6] Mark, Steve, *Modeling and Control of Maglev Vehicles*. Masters Thesis, MIT Department of Mechanical Engineering, 1993.

[7] Thornton, Richard D., "Magnetic Levitation and Propulsion, 1975," IEEE Transactions on Magnetics, Vol. Mag-11, No. 4, July 1975.

[8] Borst. H.V.; Hoerner, S.F., "Fluid-Dynamic Lift," published by Mrs Liselotte Hoerner, Bricktown, NJ, 1975.

[9] Dunlap and Associates, Inc., *Development of Techniques and Data for Evaluating Ride Quality Volume II: Ride Quality Research*, Report No. DOT-TSC-RSPD-77-1, II for U.S. Dept. of Transportation, February, 1978.

[10] Kwakernaak, H., and Sivan, R., *Linear Optimal Control Systems*. New York: Wiley-Interscience, 1972.

[11] Jazwinski, A., *Stochastic Processes and Filtering Theory*. New York: Academic Press, Inc., 1970.

Session 4 – Superconductivity

Chairman: Nelson J. Groom
NASA Langley Research Center

High Temperature Superconductors for Magnetic Suspension Applications

C. K. McMichael, R. S. Cooley, Q. Y. Chen, K. B. Ma, M. A. Lamb, R. L. Meng,
C. W. Chu and W. K. Chu
Texas Center for Superconductivity at the University of Houston (TcSUH)

SUMMARY

High temperature superconductors (HTS) hold the promise for applications in magnetic levitation bearing, vibration damping and torque coupling. Traditional magnetic suspension systems require active feedback and vibration controls, in which power consumption and low frequency vibration are among the major engineering concerns. HTS materials have been demonstrated to be an enabling approach towards such problems due to their flux trapping properties. In our laboratory at TCSUH, we have been conducting a series of experiments to explore various mechanical applications using HTS. We have constructed a 30 lb. model flywheel levitated by a hybrid superconducting magnetic bearing (HSMB). We are also developing a levitated and vibration-damped platform for high precision instrumentation. These applications would be ideal for space usages where ambient temperature is adequate for HTS to operate properly under greatly reduced cryogenic requirements. We will give a general overview of these potential applications and discuss the operating principles of the HTS devices we have developed.

INTRODUCTION

Many applications can be enhanced by reducing mechanical drag as well as structural vibration, utilizing magnetic levitation. Systems using active suspension such as electrical feedback controls or complex pneumatic gas bearing systems lack efficiency. However, the benefits of levitation have greatly increased the durability and life of such devices. Passive magnetic levitation has existed for many years at low temperature (liquid He), but not until recently has it been shown to be economically feasible to implement these laboratory devices into practical systems [1-5]. The introduction of high temperature superconductors (HTS) such as $YBa_2Cu_3O_{7-d}$ (YBCO) has opened up a new opportunity for the passive levitation approach which was not thought possible before. Now a simple permanent magnet can physically levitate a mass with 60 psi pressure in all six degrees of freedom at 77K. Being a type II superconductor, YBCO exhibits the unique properties of flux pinning and flux creep effects which can be used to damp unwanted mechanical vibrations. Many simple structures such as levitated platforms and high-load bearings have started to be developed using the hybrid magnet-superconductor concepts.

Although HTS materials technology has progressed significantly, even higher levitation or suspension and stiffnesses will be needed to incorporate these superconducting bearings into a wider range of applications. High load levitation can be achieved in a passive bearing system composed of strong permanent magnets, except for the inherent instability as stated in Earnshaw's theorem [6]. Such instability can be overcome by the presence of a field-trapped HTS. The HTS pins the flux lines and hence resists any change of interior magnetic inductions. In this report we will present the hybrid superconducting magnetic bearing (HSMB) design which circumvented the unstable magnet/magnet interactions by using a high quality melt textured YBCO superconductor [7]. The HSMB design allows for the greater stiffness values and maintains a much higher static load capacity than the traditional simple zero-field cooled magnet/superconductor bearing based on the Meissner effect. Small units of a prototype flywheel energy storage system and a vibration-damping platform using the hybrid design have been constructed in our laboratory. A brief comparison of material properties with the performance of the hybrid bearings will be given.

112

The prototype flywheel (Figure 1) with a diameter of 11.9 in. and 30 lb. in weight was constructed of aircraft aluminum alloy. At the axis of the flywheel are two embedded permanent
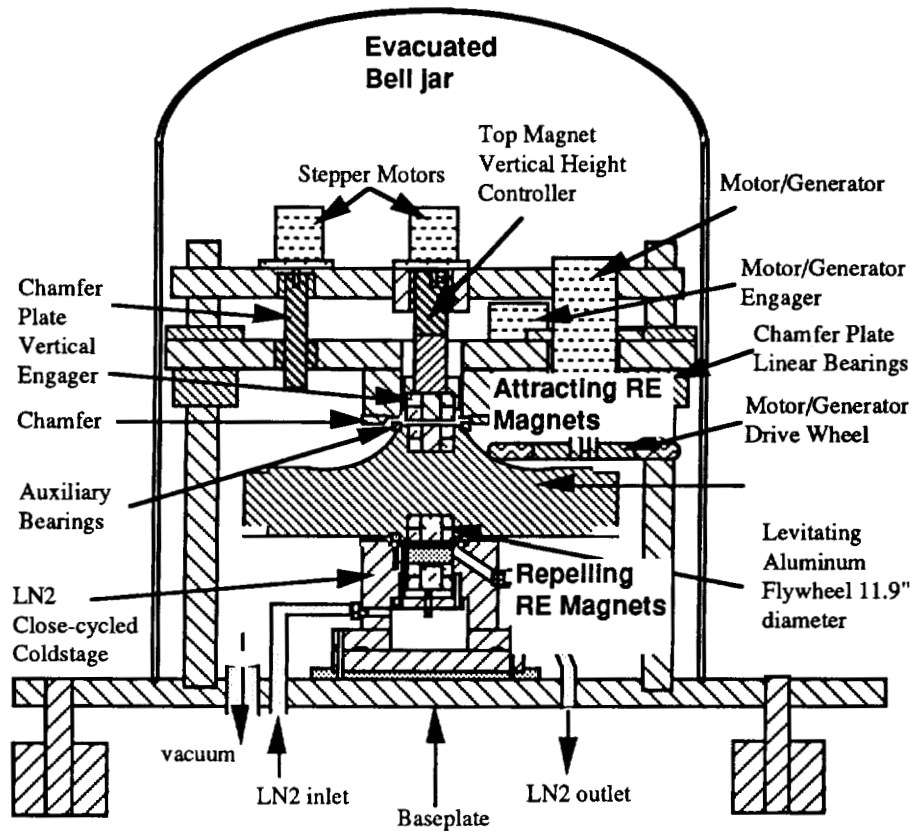
Figure 1: Line drawing of the flywheel being levitated by RE magnets and stabilized by HTS.

magnets that serve as the main magnetic bearings. The magnet on the top was used to lift most of the weight of the flywheel and at the same time assist in radial stability. The bottom magnet (double dipole) acted as a stabilizer against the magnet/magnet radial and axial instability. The double dipole consists of a ring magnet surrounding an equal surface area dipole magnet but of opposite axial magnetization in the center of the ring. A static and dynamic force measurement system [8] incorporating an elastic beam with strain gauges was attached to the double dipole permanent magnet used in the flywheel. The double dipole permanent magnets were made of NdBFe rare earth magnet material having dimensions of 1.9 cm long and 3.81 cm diameter and a surface field of 0.495 T. This cantilever beam was fixed to a motorized X-Y stage controlled by a computer. The bending of the

beam was sensed by strain gauges from which output voltages corresponding to the strain in the bent beam were monitored. A calibration was then done to correlate the strain gauge voltage with the
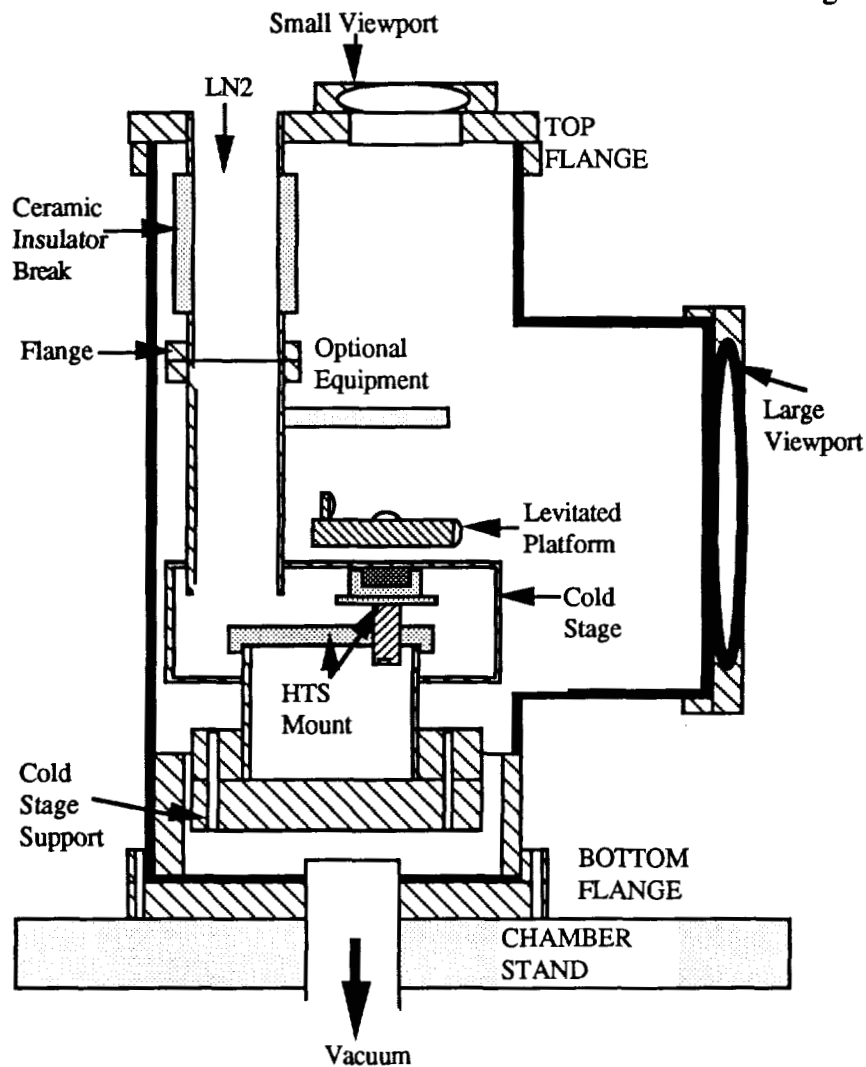
Figure 2: Line drawing of the levitated vibration-damped platform inside high vacuum chamber.

forces which produced the beam bending. With the same setup, a mirror was fixed to the end of the beam directing a laser to a position-sensitive optical detector. The signal from the optical detector was put through a spectrum analyzer to measure the damping qualities of the HTS. A stationary cold stage held fixed on an optical table was used to cool the HTS immersed in liquid nitrogen (T=77 K). The HTS material used in the measurements has dimensions of 8.89 mm thickness and 38.26 mm diameter. All measurements were conducted under field cooled conditions (FC), which implies a trapped field. Force and stiffness data were taken for both radial and axial directions on the thrust bearing configuration.

A vibration-damping platform (Figure 2) was made of an array of permanent magnets field cooled over an HTS disk inside a vacuum chamber. Spherical mirrors, a laser and a two dimensional displacement sensor were used to obtain non-contact vibration characteristics of the levitated stage. In the center of the stage is a magnet which lifts the extra weight while the HTS stabilizes and damps out the vibration.

RESULTS

Figure 3 is a plot of radial force hysteresis for small to large displacements when the YBCO
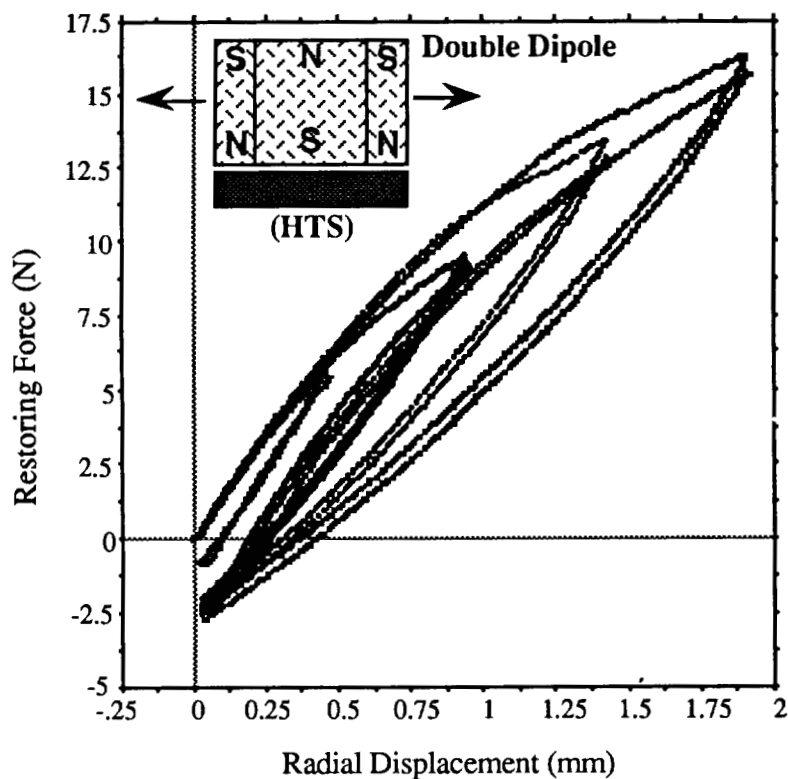
Figure 3: Radial force hysteresis over changing amplitudes. Note the larger area for larger displacements is attributed to flux motion (flux depinning) in the superconductor.

disk is in the FC state. In the FC case the radial magnetic stiffness was observed to be slightly amplitude dependent. However, the hysteresis area would increase as a function of changing amplitude because of the flux motion inside the superconductor. This flux motion exhibits an

energy loss which in turn acts as a damper when low frequency vibration occurs. In table 1, the radial magnetic stiffnesses are compared between the single dipole and the double dipole under these same

Sample	Double Dipole Rad. N/mm	Single Dipole Rad. N/mm	Double Dipole Axl. N/mm	Single Dipole Axl. N/mm
YSM88top	7.6452	3.4441	15.9338	13.2320
YSM88bottom	8.5235	3.2300	20.5569	16.3550
YSM57	6.4125	2.1153	16.9015	11.5855

Table 1: Magnetic stiffnesses of different HTS samples compared to single and double dipoles.

conditions. Also shown in table 1 is a comparison of the effects of superconducting grain size on stiffness when the HTS is measured on both faces of a bulk YBCO sample. The superconductor measured was produced by a seeded and melt-textured process that produced samples having a grain size of approximately 1.32 in.^{2} through the length. In figure 4, the vibration characteristics for the double dipole configuration are shown in comparison with the free beam vibration.
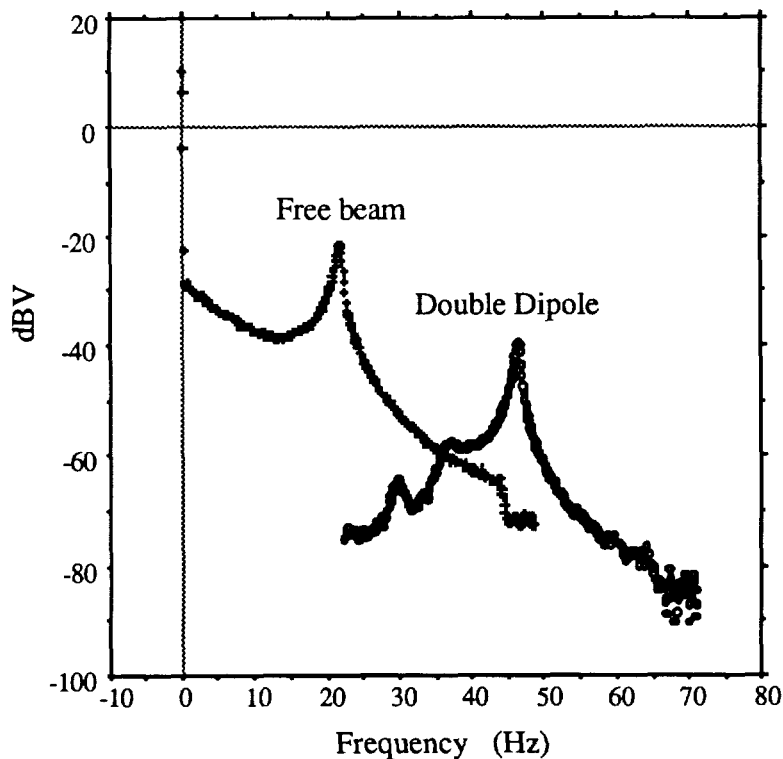
Figure 4: Vibration spectrum of a double dipole field cooled over a HTS compared to nonsuperconducting state.
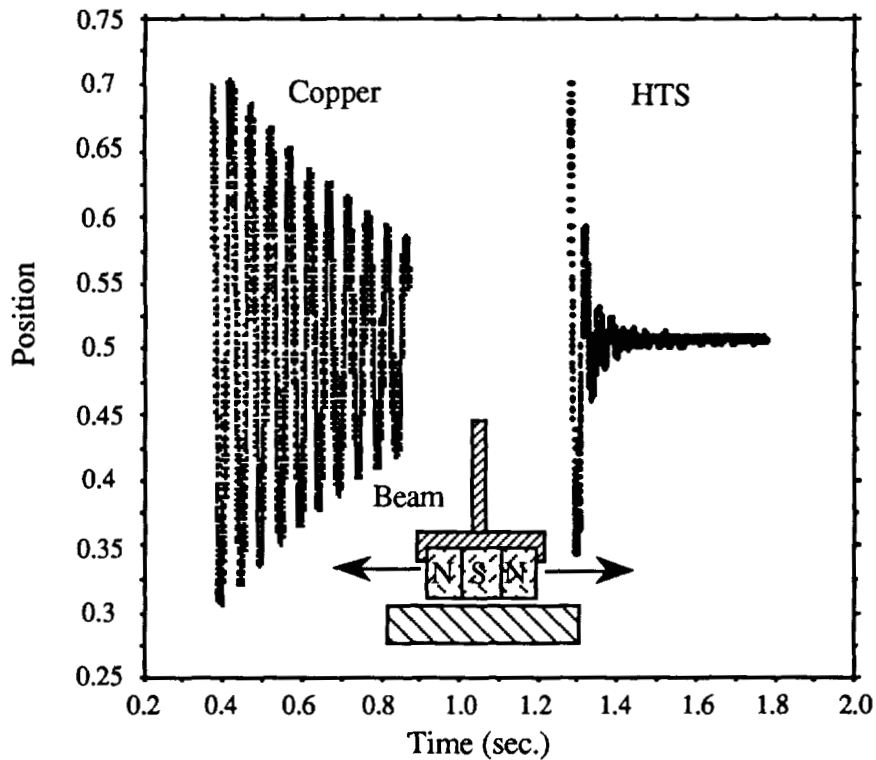
Figure 5: Vibration damping comparison between copper and HTS; the HTS damped the same impulse amplitude in 0.15 sec. compared to > 5.0 sec for the copper.

Figure 5 demonstrates the difference between copper and HTS damping by a multipole array of magnets attached to a vibrating beam. Using the frictionless behavior of magnets and HTS, it is possible to construct a totally decoupled system instead of a spring damper demonstrated here in this system.

CONCLUSION

It is apparent that the HSMB allows the ability and improvement in superconducting bearings. The HSMB design appears to be a good candidate for the flywheel energy storage device. Furthermore, the double dipole demonstrated higher stiffnesses in both the axial and radial directions above that of the conventional single dipole over HTS, due to its increased magnetic field gradient. The superconductor also has proven to be a good damper against unwanted low frequency vibration.

REFERENCES

1. Ki-Bui Ma, Jai-Rui Liu, Chase McMichael, Robert Bruce, David Mims, and Wei-Kan Chu J., Appl. Phys. 70, 3961 (1991)

2. C. K. McMichael, K. B. Ma, M. W. Lin, M. A. Lamb, R. L. Meng, Y. Y. Xue, P. H. Hor, and W. K. Chu, Appl. Phys. Lett. 59, 2442 (1991)

3. C. K. McMichael, K. B. Ma, M. W. Lin, M. A. Lamb, 1. Chow, R. L. Meng, P. H. Hor, and W. K. Chu, Appl. Phys. Lett. 60, 1893 (1992)

4. B. R. Weinberger, L. Lynds, and J. R. Hull, Supercond. Sci. Technol. 3, 381 (1990).

5. C. K. McMichael, K. B. Ma, M. A. Lamb, M. W. Lin, R. L. Meng, P. H. Hor, and W. K. Chu, Proc. of the Int. Symp. on Mag. Suspension Technol., NASA Langley Research Center, Aug. 19, 1991.

6. S. Earnshaw, "On the Nature of the Molecular Forces Which Regulate the Constitution of the Luminferous Ether," Trans. Camb. Phil. Soc. 7, pp. 97-112, (1842)

7. R. L. Meng, C. Kinalidis, Y. Y. Sun, L. Gao, Y. K. Tao, P. H. Hor and C. W. Chu, Nature 345, 326 (1990)

8. F. C. Moon and P. Z. Chang, Appl. Phys. Lett. 56, 397 (1990).

MEASUREMENT AND CHARACTERIZATION OF FORCE DYNAMICS IN HIGH T_c SUPERCONDUCTORS

Toshiro Higuchi
Kanagawa Academy of Science and Technology
Kawasaki, Japan
The University of Tokyo
Tokyo, Japan

Allan J. Kelley
The University of Tokyo
Tokyo, Japan

Yukio Tsutsui
Yaskawa Electric Corporation
Kitakyushu, Japan

ABSTRACT

Magnetic bearing implementations using more exotic superconducting phenomena have been proliferating in recent years because they have important advantages over conventional implementations. For example, the stable suspension of an object in 6 degrees-of-freedom by superconducting means can be achieved without a control system and with the use of only a single superconductor. It follows that the construction becomes much simpler with decreased need for position sensors and stabilizers. However, it is recognized that the design of superconducting systems can be difficult because important characteristics relating to the 6 degree-of-freedom dynamics of an object suspended magnetically are not readily available and the underlying principles of superconducting phenomena are not yet completely understood. To eliminate some of the guesswork in the design process, this paper proposes a system which can resolve the mechanical properties of suspension by superconductivity and provide position and orientation dependent data about the system's damping, stiffness, and frequency response characteristics. This system employs an actively-controlled magnetically-suspended fine-motion device that can also be used as a 6 degree-of-freedom force sensor. By attaching the force sensor to a permanent magnet that is being levitated above a superconducting magnet, mechanical characteristics of the superconductor levitation can be extracted. Such information would prove useful for checking the validity of theoretical models and may even give insights into superconducting phenomena.

INTRODUCTION

Since the discovery of high-temperature superconductors, research in the field has been flourishing. In addition to numerous studies into the physics of the superconducting phenomena, a wide variety of applications research are energetically being pursued with the aim of using high T_c superconductors in magnetic bearing, levitation, and suspension systems.[1-5] It is widely known that when the non-uniform magnetic field of a permanent magnet interacts with a superconductor, stable levitation of the magnet over or under the superconductor can be achieved via the Meissner effect and strong flux pinning forces. Friction-free magnetic bearing or levitation devices using this phenomenon possess the important characteristic that neither a complicated control system nor power source is needed.

To design an actual levitation device using superconductors, the restoration and damping forces acting on the levitated magnetic element need to be precisely understood; and as a result, many fundamental aspects of these issues have been addressed by various research groups.[3,5,6] To date, however, no complete physical model of forces in high T_c superconductors has been developed. Consequently, the design of applications such as magnetic bearings is still a trial-and-error process to some degree. Some of the important parameters needed for design are the magnitudes of vertical, lateral, and rotational forces along with their associated stiffness and damping characteristics. Static levitation pressure is an important force measure because it dictates the maximum load that the levitation system can bear and also levitation displacement under loaded conditions. Lateral and rotational forces govern the stability of the levitation. On the other hand, magnetic stiffnesses are important because they determine the system's natural resonant frequencies and are measures of the restorative forces acting on the levitated magnet when it is displaced by a transient disturbance. Damping, the dynamic characteristic which acts to suppress vibrational motion of the permanent magnet, is important because it contributes to levitational stability.

Several measurement techniques have been developed to obtain these quantitative characteristics experimentally. Some of the devices which have reportedly been used to measure static forces are a torsion balance,[7] a single pan balance,[3,8-11] and an elastic beam equipped with strain gauges.[2,5,10,12] Dynamic response measurements have been made using gaussmeter probes with an oscillating table as a disturbance source[3] and also by using the above strain gauge beam in combination with an optical tracking system.[5,8]

However, all these methods suffer from the drawback that they limit measurement to only one degree-of-freedom at a single time. Also, even after allowing for reconfiguration between measurements, these methods can only be used to characterize forces in the three (x, y, z) translational degrees-of-freedom. Certainly, for many applications, knowledge of force characteristics in the remaining three (θ, ϕ, ψ) rotational degrees-of-freedom is important. Additionally, it may be valuable to be able to characterize any dynamic cross-coupling dependencies between motion in one degree-of-freedom and a resultant force in another. Such information should prove useful to not only the engineering design process but also for the validation of future theoretical superconductor models.

It follows that a new high T_c superconductor force measurement system using an actively-controlled magnetically-levitated fine-motion mechanism is proposed in this paper. The mechanism would have the combined function of multiple degree-of-freedom force and position sensing

120

of a permanent magnet levitating above a superconductor. When used in actively-controlled force measurement mode, the sensing device could be used to perform automated static force measurements of the superconductor's spatially dependent, intrinsically hysteretic forces and torques. Additionally, when used in position control mode, the sensing device could be used to perform automated characterization of force dynamics in the superconductor.

Essentially, it is proposed that the actively-compensated magnetic servo levitation device can be used as a tool to characterize the passive compensation of the superconductor–magnet interaction. When the superconductor is not in its superconducting state (i.e. no force interaction with the magnet), the transient response of the magnetic suspension system can be determined. Then, by measuring the change in the entire system's transient response when the superconductor is switched to its superconducting state, it should be possible to quantify the superconductor's contribution to the system's force dynamics.

MEASUREMENT PRINCIPLE

Six Degree-of-Freedom Measurement Device Using Magnetic Servo Levitation

The type of device being proposed for use in a superconductor force measurement system is a 6 degree-of-freedom (DOF) actively-controlled magnetic servo levitation mechanism that can function as a precision force/position controllable actuator. The mechanism's levitated component, or flotor, is a free-moving rigid body that can be position-sensed and controlled in as many as 6 DOF. Because the motion of the flotor is free from troublesome friction and backlash, control can be achieved using PD digital control without difficulty. Some examples of relevant devices which fall into this category are the "magic" wrist developed at IBM[13] and the magnetically supported intelligent hands developed at Tokyo University.[14,15] Typical force and position sensing resolutions on the order of 1 mN and 1 μm can be expected from these devices.

Despite possessing flexibility in physical design, as represented by the unique constructions of each of these examples, these devices have some common features. In general, actuation is provided by either the attractive forces of strategically placed electromagnets[14-16] or the Lorentz forces of voice coil motors.[13-16] Flotor position-sensing is generally done by non-contact means such as gap sensors or position sensitive detectors.[16] For the purpose of using this type of device to measure superconductor forces, a construction which has sensing near the flotor's end-point (i.e. the permanent magnet levitating over the superconductor) would be best. Reference 16 gives an extensive discussion of related design issues so they will not be discussed further here.

Important to this discussion, however, is the understanding of the mechanism's dynamics and control. To do this, we will refer to a conceptual schematic view of a magnetic servo levitation device shown in Figure 1. The actual structure of the device shown here is not important since any of the previously mentioned example devices could be employed. Yet, it is significant to note the relationship between the permanent magnet attached to the magnetic servo levitation device's end-point and the bulk high T_c superconductor arranged below. Due to the limited motion range of magnetic servo levitation, the device would be mounted on a stage that would provide gross movement capability as needed. Figure 2 is

a photograph of the setup which we have begun to use in our experiments. Inside the dark plastic case and above the superconductor vessel is the "intelligent hand", developed at Tokyo University, being used as a force sensor.[14]
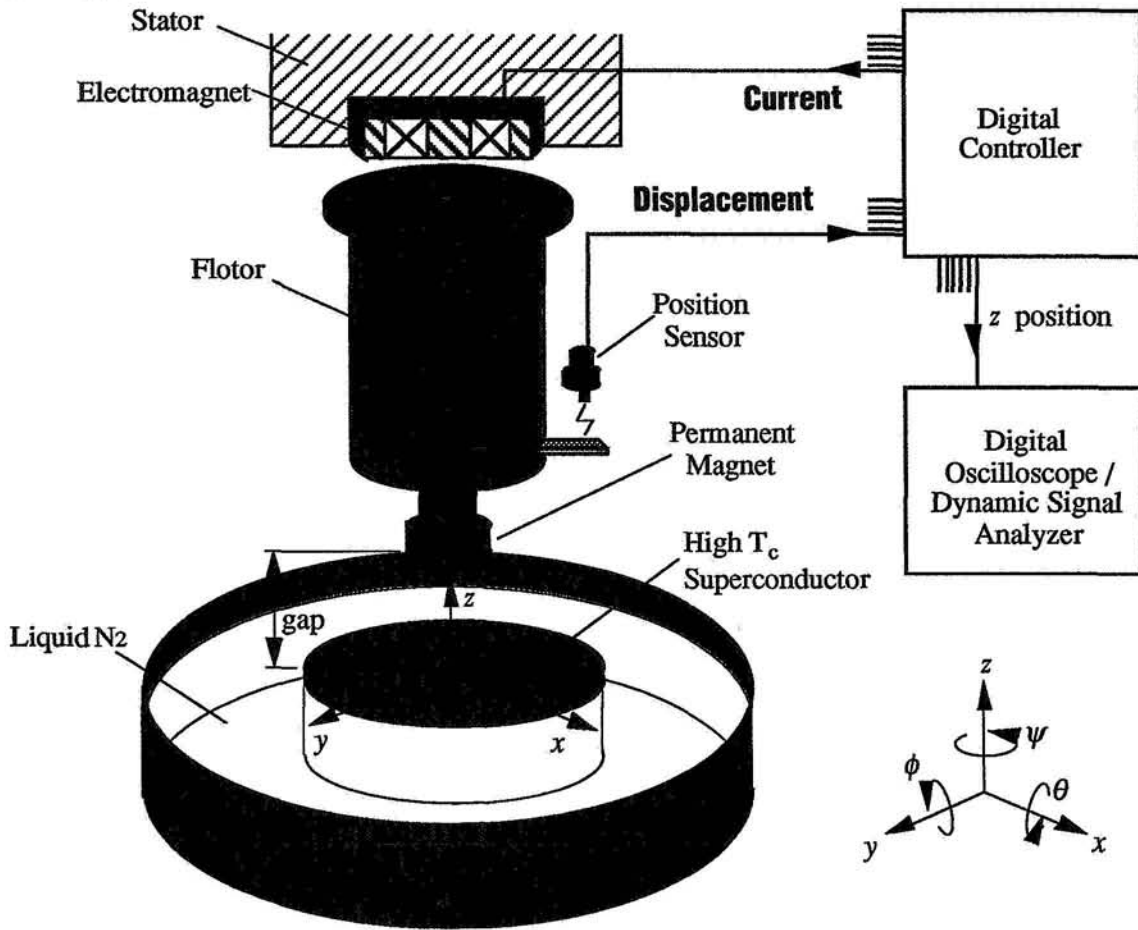
Figure 1. Schematic of magnetic servo levitation measuring system.
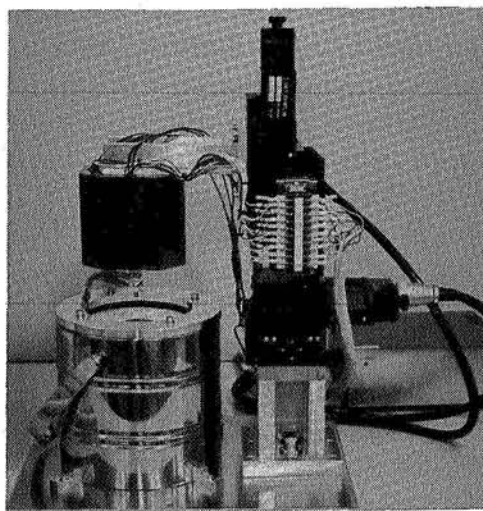
Figure 2. Photograph of measurement system using "magnetically supported intelligent hand".

Static Force Measurement

Although the flotor has forces acting on it in 6 DOF, only those acting in the translational z direction will be considered for simplicity. As shown, the forces acting against the flotor's levitation are gravity, Mg, and an external force, $f_{sc}(t)$, due to the superconductor–magnet interaction. Oppositely, the levitation forces provided by the actuators are a constant gravitational offset force, f_o, and a digitally controlled force, $f(t)$, which acts to isolate the flotor from any external disturbances and maintain the desired reference position, $z_d(t)$. It follows that the flotor's equation of motion can be written as

$$M\frac{\partial^2 z(t)}{\partial t^2} = f_o + f(t) - Mg - f_{sc}(t)$$

(1)

Because $f_o = Mg$, equation (1) can be reduced to

$$M\frac{\partial^2 z(t)}{\partial t^2} = f(t) - f_{sc}(t)$$

(2).

This can be viewed as a general equation of motion that can be applied to all remaining DOF since gravitational force considerations are no longer necessary. Because the controlled force, $f(t)$, is known and $f(t) - f_{sc}(t) = 0$ in the static case, the magnetic levitation device can be used to measure the external force of the superconductor, $f_{sc}(t)$.

Dynamic Force Measurement

To consider the dynamics of the system, equation (2) can be expressed by its Laplace transform as

$$s^2 MZ(s) = F(s) - F_{sc}(s) = F_T(s)$$

(3)

Momentarily ignoring the presence of any external superconductor force, a block diagram for a possible digital controller for the magnetic levitation system is shown in Figure 3. $D(z)$ is a discrete time compensator of the digital controller, $G_p(s)$ is the transfer function of the plant, and $H(s)$ is the transfer function of the feedback channel. Included are the A/D and D/A converters which interface the digital controller to the physical system. If we assume that a simple unity-feedback digital PD control is implemented, then $H(s) = 1$ and the compensator's transfer function can be written as the z-transform

$$D(z) = d_z + \frac{k_z(z - 1)}{Tz}$$

(4)

where T is the A/D converter sampling period and d_z and k_z are the desired damping and spring constants chosen by the operator and entered into the computer which supervises the digital control system.
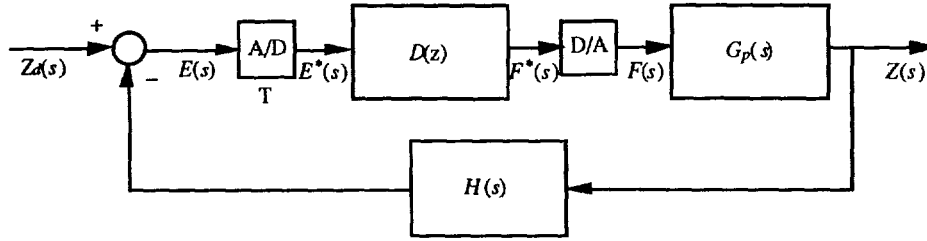
Figure 3. Block diagram of digital controller for magnetic servo levitation.

In practice, because magnetic levitation devices normally employ only position sensors, the velocity signal which is needed for PD control must be either calculated by numerical differentiation of the position signal or estimated by an adaptive control scheme.[15,16] To ensure accurate velocity calculation it is important to keep the sampling period, T, at a minimal value. Regardless of the actual implementation details of the digitally controlled magnetic levitation system, it is our goal to relate its actual measurable response with a purely analog model. One reason for doing this is that a simple transfer function for the sampling process in Figure 3 does not exist and the analysis is complicated.[17] Therefore, we will assume that the experimental determined transient response of the system can be modelled within a limited frequency range by the analog system whose block diagram is shown in Figure 4.
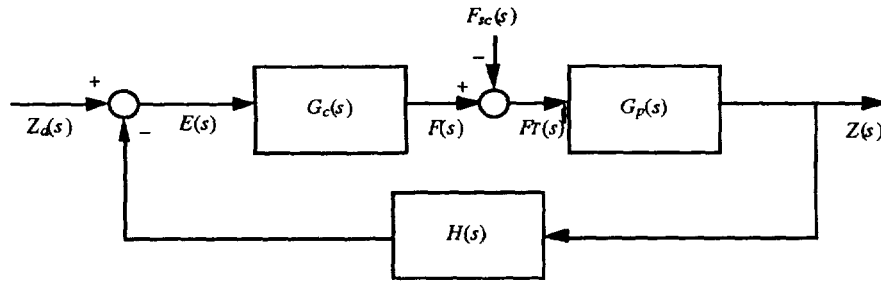
Figure 4. Block diagram of analog model of magnetic servo levitation system.

Again, assuming initially that $f_{sc}(t) = 0$ and unity feedback is employed, the transfer function for the system in Figure 4 can be written as

$$T(s) = \frac{Z(s)}{Z_d(s)} = \frac{G_c(s)G_p(s)}{1 + G_c(s)G_p(s)} \tag{5}$$

where the plant transfer function, $G_p(s)$, can be found from equation (3) and expressed as

$$G_p(s) = \frac{Z(s)}{F_T(s)} = \frac{1}{Ms^2} \tag{6}$$

For simple characterization of the magnetic levitation device's dynamics, we model the compensator, $G_c(s)$, with linear mechanical elements of damping and elastance to give a second-order system. The transfer function for this compensator is then given by

$$G_c(s) = d_o s + k_o \tag{7}$$

where d_o is the damping coefficient and k_o is the spring constant. The system's transfer function then reduces to the expression

$$T(s) = \frac{d_o s + k_o}{M s^2 + d_o s + k_o}$$ (8).

To experimentally quantify the effective damping coefficient and spring constant of the magnetic levitation device, a dynamic signal analyzer can be used to measure the frequency response and then automatically calculate the poles and zeros of equation (8). Alternatively, this information can also be revealed by observing the transient response of the position signal with an oscilloscope. Although, both impulse and step responses of the system can reveal the same information, in this discussion only the impulse response will be dealt with. Practically, an input which approximates an impulse can be provided by rapidly increasing and decreasing the flotor's desired servo position, z_d, via the computer supervising the digital control system.
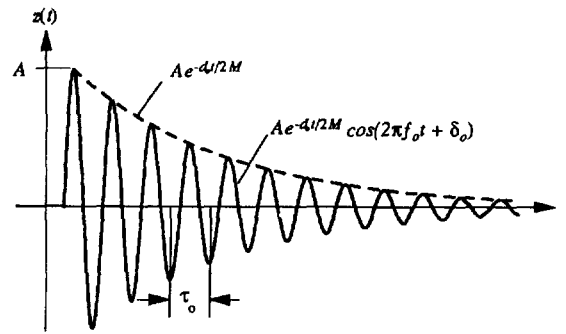
Figure 5. Impulse response for second-order system model of magnetic servo levitation.

Figure 5 shows a typical second-order response to an impulse input. The position signal in this figure exhibits damped oscillation, resembling a cosine curve with decaying amplitude, as the flotor settles toward the desired reference position. It follows that from the envelope of the curve, which decays exponentially with time, the damping coefficient, d_o, can be calculated. By measuring the quasiperiod of the signal, τ_o, which is defined as the time between successive maxima or minima, the quasicircular frequency of the oscillation, f_o, can be calculated using the relation [18]

$$f_o = \frac{1}{\tau_o}$$ (9).

It is then possible to calculate the spring constant of the system by [18]

$$k_o = 4\pi^2 M f_o^2 + \frac{d_o^2}{4M}$$ (10).

The second term in equation (10) cannot be neglected, as is often done, unless damping is very weak.

Next, we consider the case for which the superconductor's interaction with the permanent magnet contributes an external force on the flotor and permanent magnet combination. We choose to model the effect of the superconductor levitational force, $F_{sc}(s)$, with a second-order mechanical system that includes damping and elastance. The transfer function of this position compensation by the superconductor is defined by

$$G_{sc}(s) = \frac{Z(s)}{F_{sc}(s)} = d_{sc}s + k_{sc} \qquad (11).$$

Figure 6, a now modified block diagram of the magnetic servo levitation system, shows the stablizing negative-feedback force loop that acts the flotor by the superconductor in response to a change in position.
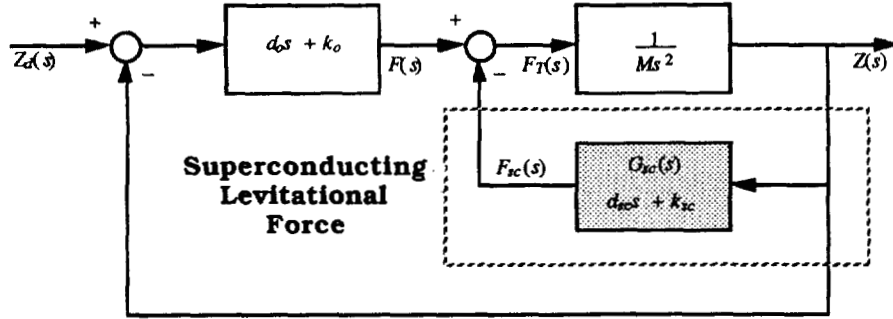
Figure 6. Block diagram of magnetic servo levitation system
model including superconductor forces.

The transfer function for the entire system now takes the form

$$T(s) = \frac{Z(s)}{Z_d(s)} = \frac{G_c(s)G_p(s)}{1 + [G_c(s) + G_{sc}(s)]G_p(s)} \qquad (12)$$

which can be reduced further to

$$T(s) = \frac{d_o s + k_o}{Ms^2 + (d_o + d_{sc})s + (k_o + k_{sc})} = \frac{d_o s + k_o}{Ms^2 + ds + k} \qquad (13).$$

By comparing equations (8) and (13) we can see the effect of adding the superconductor to the system is just a simple increase in total system damping and elastance. The entire system's damping is the simple sum of the independent damping coefficients respectively associated with the magnetic levitation portion of the system and the superconductor portion of the system. With a similar relationship for the system's elastance we have

$$d = d_o + d_{sc} \quad \text{and} \quad k = k_o + k_{sc} \qquad (14)\ (15).$$

Thus, we can calculate the damping coefficient and spring constant of the superconductor–magnet interaction if the transient response of the entire system is measured. A typical impulse response of this system would take the form shown in Figure 7. Because of increased damping and elastance due to the superconductor, this oscillatory signal's decay rate and the quasifrequency are both greater than those for the magnetic levitation device alone as shown in Figure 5. By employing the method described before to extract the damping coefficient, d , and spring constant, k , the relationships in equations (14) and (15) can be used to calculate d_{sc} and k_{sc}.

126
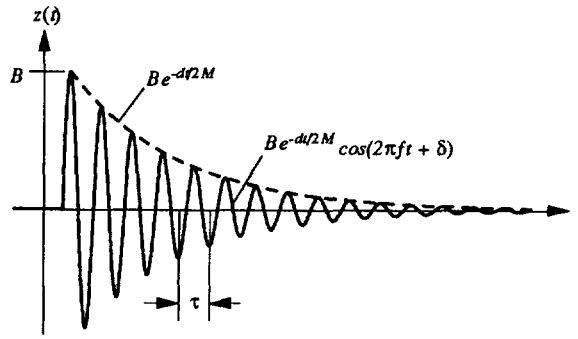
Figure 7. Impulse response for second-order system model of magnetic servo levitation including superconductor forces.

COMPLETE 6 DOF CHARACTERIZATION OF SUPERCONDUCTOR FORCES

Static Force Measurements

The static superconductor forces acting on a permanent magnet directly determine some very important performance quantifiers for any suspension application they may be used in. For example, in a magnetic bearing application, the levitation pressure governs the maximum vertical load that can be applied to the bearing. Similarly, lateral forces govern the maximum horizontal load that the bearing can stably support. Rotational forces, in turn, dictate how the bearing may perform if torsional loading conditions cause the permanent magnet to twist away from an equilibrium orientation . In all cases, these static forces also determine the loaded bearing's displacement from an unloaded equilibrium position.

The hysteretic nature of the static forces in superconductors is well known.[3,5,6,12,19] For example, if the height of the magnet over the superconductor is cycled at *very low* frequency the levitation force exhibits hysteresis which depends on whether the magnet is approaching or retreating from the superconductor. Thus, not only are the force magnitudes functions of position and orientation of the permanent magnet over the superconductor, but also the directions the magnet has been moved to arrive at that position and orientation. Whether the force is actually repulsive or attractive not only depends on position and orientation but also on superconductor composition[5] and whether cooling of the superconductor was done in zero magnetic-field cooled (ZFC) or field cooled (FC) conditions.[3,4]

In any case, we would like to express the 6 DOF static forces and torques acting on the magnet in vector form so that they are in a convenient form to be used in modelling or simulations of a suspension application using superconductors. We can write

$$f_{sc}(t) = f_{sc}(\mathbf{r}(t),\mathbf{sign}(\dot{\mathbf{r}})) = \begin{bmatrix} f_x \\ f_y \\ f_z \\ \tau_\theta \\ \tau_\phi \\ \tau_\psi \end{bmatrix} \qquad (16)$$

127

where the variable $r_{(t)}$ is a 6 DOF position and orientation vector and the variable $sign_{(\dot{r})}$ is a vector indicating on which branches of the hysteresis curves for each DOF the static force and torque measurements have been made. These vectors are defined as

$$r(t) = \begin{bmatrix} x \\ y \\ z \\ \theta \\ \phi \\ \psi \end{bmatrix} \quad \text{and} \quad \mathbf{sign}(\dot{r}) = \begin{bmatrix} sign(\dot{x}) \\ sign(\dot{y}) \\ sign(\dot{z}) \\ sign(\dot{\theta}) \\ sign(\dot{\phi}) \\ sign(\dot{\psi}) \end{bmatrix} \tag{17} (18).$$

where the elements, $sign(\dot{n})$, can take one of two values: + or –, indicating whether the position/orientation value n is steadily being changed in positive or negative steps along its respective hysteresis curve. It should be noted that to consider the force measurements to be truly static, the magnet should have no velocity during measurement. However, it has been reported that an extremely low constant velocity on the order of 100 μm/s or less can be tolerated.[5]

Considering that each element in the vector f_{sc} is effectively a function of 12 variables due to hysteresis in all 6 DOF, the number of measurements that are required for its identification over reasonable magnet motion ranges can be large. However, this measurement process could be automated by a computer system host to the force measuring magnetic levitation device that would systematically measure forces on all hysteresis branches for many combinations of positions and orientations. This process, not requiring human intervention, would be exceedingly hard to duplicate, if not impossible, using current force measurement technology.

One frequently used method to get an approximation of magnetic stiffness in superconductors is to use static force measurements. As one traces a major hysteresis loop, a small deviation from the loop can be made by momentarily reversing the direction of motion and a minor hysteresis loop can be traced out before returning to the major loop. By averaging the slope of these minor loops, a magnetic stiffness measurement can be made.[3,5,8] However, it has been reported that the values obtained this way may not actually reflect the true magnetic stiffness because they are dependent on the displacement size used.[5] Thus, it would be prudent to also determine stiffness by a dynamic method which can also yield important damping information at the same time. This will be covered in the next section.

Dynamic Force Measurements

The goal of measuring the dynamic characteristics of superconductors is to quantify the two important parameters of damping and elastance. With this data, it is then possible to design a magnetic suspension application using the superconductor–magnet interaction phenomenon with complete understanding of the transient response which can be expected when the system is assembled and operating. Therefore, it is important to identify damping coefficients and spring constants that describe the dynamic behaviour of the superconductor–magnet combination. These characteristics can then be summarized for 6 DOF in the following respective matrix forms:

128

$$\mathbf{d_{sc}} = \mathbf{d_{sc}(r,sign(\dot{r}))} = \begin{bmatrix} d_{xx} & d_{xy} & d_{xz} & d_{x\theta} & d_{x\phi} & d_{x\psi} \\ d_{yx} & d_{yy} & \cdot & \cdot & \cdot & \cdot \\ d_{zx} & \cdot & d_{zz} & \cdot & \cdot & \cdot \\ d_{\theta x} & \cdot & \cdot & d_{\theta\theta} & \cdot & \cdot \\ d_{\phi x} & \cdot & \cdot & \cdot & d_{\phi\phi} & \cdot \\ d_{\psi x} & \cdot & \cdot & \cdot & \cdot & d_{\psi\psi} \end{bmatrix}$$

(19)

and

$$\mathbf{k_{sc}} = \mathbf{k_{sc}(r,sign(\dot{r}))} = \begin{bmatrix} k_{xx} & k_{xy} & k_{xz} & k_{x\theta} & k_{x\phi} & k_{x\psi} \\ k_{yx} & k_{yy} & \cdot & \cdot & \cdot & \cdot \\ k_{zx} & \cdot & k_{zz} & \cdot & \cdot & \cdot \\ k_{\theta x} & \cdot & \cdot & k_{\theta\theta} & \cdot & \cdot \\ k_{\phi x} & \cdot & \cdot & \cdot & k_{\phi\phi} & \cdot \\ k_{\psi x} & \cdot & \cdot & \cdot & \cdot & k_{\psi\psi} \end{bmatrix}$$

(20)

The individual elements of the damping coefficient matrix, $\mathbf{d_{sc}}$, can be defined by

$$d_{ab} = d_{ab}(\mathbf{r},sign(\dot{r})) = -\frac{\Delta f_a}{\dot{b}} \qquad \text{for } a,b = x,y,z$$

(21)

and

$$d_{ab} = d_{ab}(\mathbf{r},sign(\dot{r})) = -\frac{\Delta \tau_a}{\dot{b}} \qquad \text{for } a,b = \theta,\phi,\psi$$

(22)

which show that damping is the oscillation reducing force that occurs in the direction a when the magnet has velocity in direction b. The individual elements of the spring constant matrix, $\mathbf{k_{sc}}$, can be defined by

$$k_{ab} = k_{ab}(\mathbf{r},sign(\dot{r})) \approx -\frac{\Delta f_a}{\Delta b} \qquad \text{for } a,b = x,y,z$$

(23)

and

$$k_{ab} = k_{ab}(\mathbf{r},sign(\dot{r})) \approx -\frac{\Delta \tau_a}{\Delta b} \qquad \text{for } a,b = \theta,\phi,\psi$$

(24)

which show that elastance is the restorative force exerted in direction a on the magnet when it is displaced by a *small* amount in direction b from some equilibrium position. Like static forces and torques, the dynamic characterisitics of damping and stiffness for the superconductor are functions of magnet position and orientation and also functions of which branches of the familiar hysteresis loops the superconductor–magnet interaction is operating on. Thus, it follows that each element of the damping coefficient and spring constant matrices is a function of 12 variables.

The impulse (or step) response analysis techniques discussed previously could also be automated by a computer system hosting the actively controlled magnetic levitation system. The damping coefficient and spring constant matrices could be systematically identfied by making measurements on all branches of the force–position hysteresis loops for many combinations of positions and orientations.

To our knowledge, none of the existing methods that have been reported in literature are capable of

identifying the full damping and elastance matrices. In fact, these one DOF implementations even require reconfiguration to measure only the diagonal elements of d_{xx}, d_{yy}, d_{zz}, k_{xx}, k_{yy}, and k_{zz}.[3,5,8]

The advantage of expressing damping and elastance properties in matrix form is that an equation of motion can then be written for the magnet–superconductor interaction (without a magnetically levitated measuring device attached) in the form

$$\mathbf{M}\frac{\partial^2 \mathbf{r}(t)}{\partial t^2} - \mathbf{d}_{sc}\frac{\partial \mathbf{r}(t)}{\partial t} - \mathbf{k}_{sc}(\mathbf{r}(t) - \mathbf{r}(0)) = 0 \tag{25}$$

where $\mathbf{r}(0)$ is the initial equilibrium position and orientation and $\mathbf{M}$ is the inertial matrix of the magnet which can be expressed as

$$\mathbf{M} = \begin{bmatrix} M & & & & & \\ & M & & & & \\ & & M & & & \\ & & & J_\theta & & \\ & & & & J_\phi & \\ & & & & & J_\psi \end{bmatrix} \tag{26}$$

Equation (25) fully describes the dynamic behaviour of the superconductor–magnet levitation sub-system. It follows that the sub-system has specific mechanical properties that can be simulated by computer and can be utilized as a single module in a larger application. It is important to remember however, that $\mathbf{d}_{sc}$ and $\mathbf{k}_{sc}$ are not constant, but instead functions of $\mathbf{r}(t)$ and $\mathrm{sign}(\dot{\mathbf{r}})$ as defined before.

SUMMARY

It has been proposed that an actively-controlled 6 DOF magnetic servo levitation device can be employed to characterize the force interaction between permanent magnets and superconductors. When this device is used in force measurement mode, it would be possible to measure static superconductor forces and torques in all 6 DOF and summarize them in matrix form. By monitoring the change in the transient or frequency response of the magnetic servo levitation system when superconductor forces are applied, the dynamics superconductor–magnet interaction, in the form of damping and elastance characteristics, can be quantified and summarized in matrix form.

Then, given the static force matrix, $f_{sc}(t)$, and the damping and elastance matrices, $\mathbf{d}_{sc}$ and $\mathbf{k}_{sc}$, an engineer designing superconductor levitation application can treat the superconductor–magnet combination as a well-defined "mechanical" element with known response characteristics. A complicated system can be designed with several of these elements and the total system's response can be calculated using principles of superposition and unification of coordinate systems. This should take much of the guesswork out of designing a superconductor magnetic levitation system and allow computer simulation to be used instead of trial-and-error prototype construction. Additionally, extensive knowledge of static and dynamic force characteristics may help to verify or create theoretical models concerning the physical principles of superconducting phenomena.

REFERENCES

1. Takahata, R.; Ueyama, H.; and Yotsuya, T.: Load Carrying Capacity of Superconducting Magnetic Bearings. *Electromagnetic Forces and Applications.* Elsevier Science Publishers B.V., 1992.

2. Takahata, Ryoichi; and Yotsuya, Tsutom: Rotational Decay Torques of Superconducting Magnetic Bearing. *IEEE Transactions on Magnetics*, vol. 27, no. 2, March 1991, pp. 2423-2426.

3. Weinberger, B.R.; Lynds, L.; and Hull, J.R.: Magnetic Bearings Using High-Temperature Superconductors: Some Practical Considerations. *Superconductor Science Technology*, vol. 3, 1990, pp. 381-388.

4. McMichael, C.K.; Ma, K.B.; Lamb, M.A.; Lin, M.W.; Chow, L.; Meng, R.L.; Hor, P.H.; and Chu, W.K.: Practical Adaption in Bulk Superconducting Magnetic Bearing Applications. *Applied Physics Letters*, vol. 60, no. 15, April 13, 1992, pp. 1893-1895.

5. Chang, Pei-Zen: Mechanics of Superconducting Magnetic Bearings. Ph.D. Dissertation, Cornell University, January, 1991.

6. Torng, Terry; and Chen, Q.Y.: Magnetic Forces for Type II Superconductors in a Levitation Field. *Journal of Applied Physics*, vol 73, no. 3, February 1, 1993, pp. 1198-1204.

7. Weeks, David E.: A Torsion Balance to Measure Hysteretic Levitation Forces in High Tc Superconductors. *Review of Scientific Instruments*, vol. 61, no. 1, January, 1990, pp. 197-200.

8. Weinberger, B.R.; Lynds L.; Van Valzah, J.; Eaton, H.E.; Hull, J.R.; Mulcahy, T.M.; and Basinger, S.A.: Characterization of Composite High Temperature Superconductors for Magnetic Bearing Applications. *IEEE Transactions on Magnetics*, vol. 27, no. 2, March 1991, pp. 2415-2422.

9. Ouseph, P.J.: Effect of an External Force on Levitation of a Magnet Over a Superconductor. *Applied Physics A*, vol. 50, 1990, pp. 361-364.

10. Unsworth, Joseph; Du, Jia; Crosby, Bryan J.; and Macfarlane, John C.: Magnetic Levitation Force Measurement on High Tc Superconducting Ceramic/Polymer Composites. *IEEE Transactions on Magnetics*, vol. 29, no. 1, January 1993, pp. 108-112.

11. Riise, A.B.; Johansen, T.H.; Bratsberg, H.; and Yang, Z.J.: Logarithmic Relaxation in the Levitation Force in a Magnet–High Tc Superconductor System. *Applied Physics Letters*, vol. 60., no. 18, May 4, 1992, pp. 2294-2296.

12. Moon, F.C.; Yanoviak, M.M.; and Ware, R.: Hysteretic Levitation Forces in Superconducting Ceramics. *Applied Physics Letters*, vol. 52, no. 18, May 2, 1988.

13. Hollis, R.L.; A.P. Allan; and Salcudean, S.; and : A Six Degree-of-Freedom Magnetically Levitated Variable Compliance Fine Motion Wrist. *Preprint of the 4th ISRR*, 1987, pp. 241-249.

14. Fujiwara, Shigeki; and Higuchi, Toshiro: Miniaturized and Lightened 6-Axis Controlled Magnetically Levitated Intelligent Hand, Dai 9 Nippon Robotto Gakkai Gakujutu Kouenkai, November 27-29, 1991, pp. 403-404.

15. Tsuda, Masahiro: Magnetic Servo Levitation and Its Applications. Ph.D. Dissertation, University of Tokyo.

16. Tsuda, Masahiro; and Higuchi, Toshiro: Design and Control of Magnetic Servo Levitation. *Report of the Insitute of Industrial Science, The University of Tokyo*, vol. 37, no. 2, serial no. 236, March, 1992.

17. Phillips, Charles L.; and Harbor, Royce D.: *Feedback Control Systems*. Prentice-Hall, Inc., 1988.

18. Boyce, William, E.; and DiPrima, Richard C.: *Elementary Differential Equations and Boundary Value Problems*. John Wiley & Sons, Inc., 1986.

19. Ishigaki, H.; Itoh, M.; Hida, A.; Endo, H.; Oya, T.; Ohyama, T.; and Minemoto, T.: Measurement of Repulsive Force of High T_c Materials due to Meissner Effect and its Two Dimensional Distribution. *IEEE Transactions on Magnetics*, vol. 27, no. 2, March 1991, pp. 2427-2430.

Session 5a – Bearings

Chairman: Karl Boden
KFA-IGV

MATERIALS FOR EFFICIENT HIGH-FLUX MAGNETIC BEARING ACTUATORS

M.E. Williams and D.L. Trumper

Dept. of Electrical Engineering
Univ. of N. Carolina at Charlotte
Charlotte, NC 28223

SUMMARY

Magnetic bearings have demonstrated the capability for achieving positioning accuracies at the nanometer level in precision motion control stages. This makes possible the positioning of a wafer in six degrees of freedom with the precision necessary for photolithography. To control the position of an object at the nanometer level, a model of the magnetic bearing actuator force-current-airgap relationship must be accurately obtained. Additionally, to reduce thermal effects the design of the actuator should be optimized to achieve maximum power efficiency and flux density. Optimization of the actuator is accomplished by proper pole face sizing and utilizing a magnetic core material which can be magnetized to the highest flux density with low magnetic loss properties. This paper describes the construction of a magnetic bearing calibration fixture designed for experimental measurement of the actuator force characteristics. The results of a material study that review the force properties of nickel-steel, silicon-steel, and cobalt-vanadium-iron, as they apply to magnetic bearing applications are also presented.

INTRODUCTION

Primarily, magnetic bearings are capable of applying forces and torques to a suspended object without rigidly constraining any of its degrees of freedom. The resolution of magnetic bearings is limited by sensors and control electronics, and not by the finish of a bearing surface. For these reasons, magnetic bearings appear to be ideal for performing wafer positioning in photolithography.

A theoretical model for the actuator force-current-airgap relationship can be derived from classical magnetic circuit theory. However, this is accurate only at very small airgaps and low flux densities. As the gap and the coil current increase, the actuator core saturates and the theoretical model is no longer effective. To obtain an accurate model, the actuator can be characterized for its force-current-airgap relationship. This characterization data can be linearized in real time and implemented in a digital control algorithm. A calibration fixture has been constructed to record the actuator force-current-airgap relationship throughout the useful range. Measurement data can then be stored as a three dimensional look-up table and linearized in real time to provide accurate control of the magnetic bearing over a wide range of airgaps.

An important consideration in the design of the magnetic actuators is the core material. Using the calibration fixture, various core materials can be evaluated for hysteresis, permeability, and saturation. Based on the results, the material that best fits the application criteria can be selected.

The actuators designed for a photolithography stage require the lowest possible hysteresis for all airgaps and sufficient force without excessive power requirements. Four identical test actuators were constructed with laminations cut from 49% nickel-steel, 80% nickel-steel, grain oriented silicon-steel, and Co-V-Fe. The characteristics of the test materials were determined and recorded as the airgap was varied from 80 to 650 μm.

This paper will briefly describe the magnetic levitation stage and the calibration fixture used to characterize the actuators. The method for optimizing the lamination pole face area will be presented. Finally an analysis of the core material properties and their effects on the performance of the actuators will be presented.

MAGNETIC BEARING PHOTOLITHOGRAPHY X-Y STAGE

The authors have previously reported on the design of a magnetic bearing stage for precision motion control[1,2,3]. The function of a stage for photolithographic systems is to align in six degrees of freedom a die site on a silicon wafer with the image plane of the lithographic lens. Although a previously reported magnetic bearing stage demonstrated proof-of-concept it did not possess the necessary range of motion to be directly applicable to photolithography systems.

An improved advanced stage that has the necessary range of motion and level of precision suitable for photolithography has been designed and is currently under construction. This next generation stage will provide 200 mm travel in the X-Y plane of the wafer allowing exposure over any portion of that area. For fine focusing the stage will provide 300 μm of travel normal to the wafer surface and milliradian rotations around three axes. One of the design objectives is to have the acceleration necessary to step and settle 20 mm in under 200 msec. At the die site the stage position must be maintained with a standard deviation better than 10 nm during the 300 msec exposure time. Magnetic bearings appear to be ideal for this application since the small rotational and focus motions can be provided without the need for additional fine stage mechanics. The design requirements have been fulfilled by a stage design that utilizes variable reluctance magnetic bearings to constrain five degrees of freedom, and a permanent magnet linear motor to position the stage 200 mm in the sixth degree of freedom (X). A conventional mechanical linear slide will be used to provide the necessary 200 mm of travel in the Y direction. This design increases power efficiency and yields better performance by capitalizing on the typical operation of a photolithography X-Y stage. Typical operation of a stage is to step in the X direction 10 - 20 times along a row of die sites, before a single step is made in the Y direction to the next row of die sites. Since the stage operation is dominated by X positioning, this mechanical-magnetic bearing stage design results in a simple magnetic bearing structure while simultaneously increasing the stage precision and throughput.

The advanced magnetic bearing stage will use three variable reluctance actuators each rotated by 90° contained in a common housing with four of these located at each corner of a 250 mm square platen. This configuration results in a total of twelve actuators as shown in Figure 1. The stage actuators are designed to have a nominal bearing airgap of 300 μm with displacements of $\pm$150 μm from the nominal. The actuators act on long laminated targets contained in the machine base and provide control in five degrees of freedom. To reduce the power dissipated, permanent magnets will be used to provide a DC lift to fully support the mass of the platen, enabling the actuators to be energized only for focusing control.
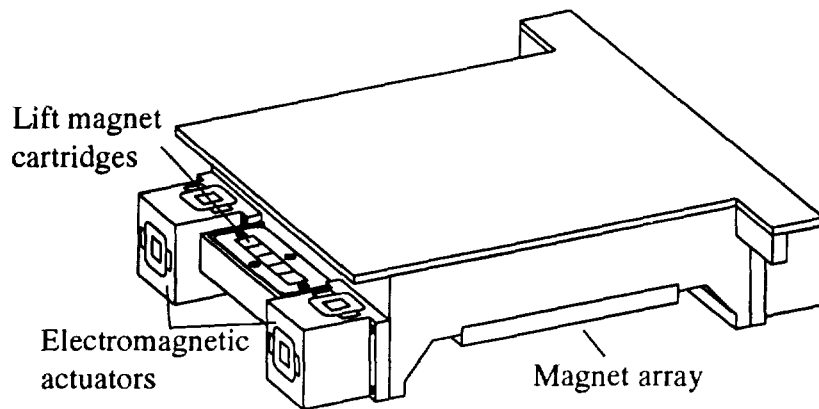
Figure 1: Advanced stage magnetic bearing suspended platen

To provide the long range X travel, a unique permanent magnet Lorentz type linear motor has been designed. The motor consists of a permanent magnet Halbach [4,5] array attached to the underside of the platen and a planar, ironless, six phase stator fixed in the machine frame. The magnet array uses four magnet blocks per period, with the magnetization axis rotating by 90° in each successive block. This array arrangement results in the fundamental field strength on one side of the array being increased by 1.4 over a conventional array and thus doubling the power efficiency of the motor. Figure 2 shows the finite element solution for a section of the magnet array. The arrows indicate the direction of magnetization. The motor design allows for a large area thermal path and the low motor height is compatible with the stage geometry.
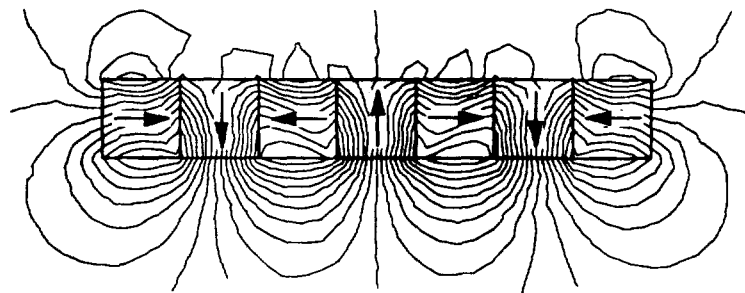
Figure 2: Single sided Halbach magnet array

The magnetic bearing as well as the linear motor will be controlled by a digital signal processor implemented on a VME bus chassis. Position feedback will be accomplished by capacitance gauging in the five actuator degrees of freedom to provide the controller with a true reading of the bearing airgap. Given the airgap and the desired force, the controller can linearize the bearing model and provide the required current. Laser interferometry will provide position feedback in the long travel X axis.

Further optimization is achieved through minimizing the platen mass without significantly sacrificing stiffness. The reduced mass will increase stage acceleration for a given input power. Having briefly covered the stage design the focus of the remainder of the paper is on the optimization and material selection for the variable reluctance actuators and the calibration fixture developed for this purpose.

ACTUATOR CALIBRATION FIXTURE

A test fixture has been developed to characterize the force of magnetic bearing actuators as a function of coil current and the target airgap. This fixture consists of a lightweight target platen constructed from composite materials mounted on to the fixture body through an extremely stiff silicon carbide gothic arch ball-and-groove coupling. This combination of high coupling stiffness and low platen mass results in a test fixture resonant frequency of 1.8 kHz, enabling the characterization of actuators at frequencies up to 1kHz. The calibration fixture was developed with the following design objectives:

- Measure the actuator force at airgaps ranging from 10 to 1000 μm.

- Achieve a peak force capability on the order of hundreds of newtons.

- Permit the adjustment of the target separation gap.

- Separation of the force and metrology loop to accurately measure the target airgap.

- Allow the testing of a variety of actuator sizes interchangeably.

The following section describes the mechanical design of the fixture and how the objectives were achieved. The actuator test procedure is described followed by the results of force testing the various magnetic actuator materials.

Calibration Fixture

The magnetic bearing calibration fixture consists of an aluminum fixture body and platform, three adjustable support columns with ball-and-groove kinematic couplings, three capacitance probes, and a target platen as shown in Figure 3. The electromagnet consists of E-shaped stacked laminations with a single coil surrounding the central leg and housed within a mounting cartridge. The cartridge is mounted inside the test fixture body so that its pole face is exposed upward toward the target platen. A laminated target made from the same material as the E-core is attached to the underside of the target platen. Located at 120 degree intervals around the perimeter of the fixture body are the three support columns, each consisting of a kinematic ball/groove coupling mounted on top of a piezoelectric load cell. The columns are supported by a shaft clamped to the fixture body and can be locked in position once located. The hemisphere mounted to the top of each load cell makes two points of contact in each of three grooves, thus the three couplings provide exactly six constraints on the six platen degrees of freedom. If properly designed this type of kinematic coupling, commonly referred to as a Maxwell mount, exhibits sub-micron positional repeatability. The micrometer head pushes against the end of the support shaft and is used to adjust the height of the platen above the electromagnet. The load cells measure the attractive force between the electromagnet and the target platen. Three capacitance probes mounted at the top perimeter of the fixture body are used to sense the distance between the electromagnet and three datum pads on the target platen. The coil is driven by a linear power amplifier capable of driving the electromagnets into saturation.
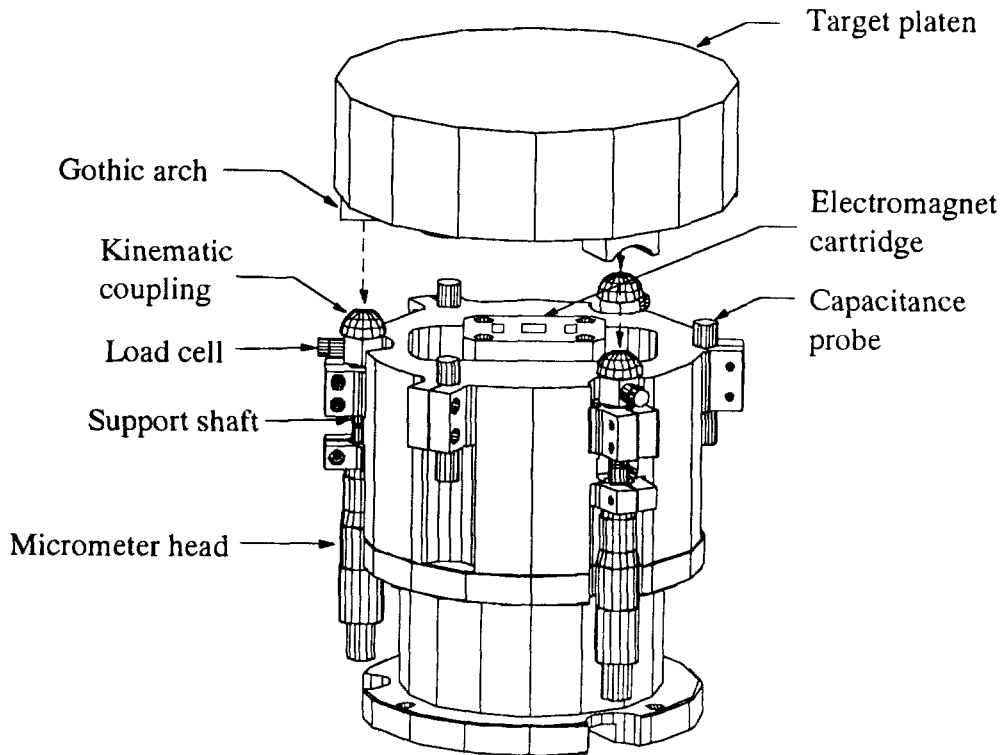
Figure 3: Magnetic bearing calibration fixture.

Actuator Calibration Procedure

Characterization data provides a 3-D matrix of force versus current, parametric on airgap format. In a real time control algorithm the coil current is interpolated from this data from the target airgap and the desired actuator force. The actuator force versus current curves are recorded for airgaps ranging from 50 - 650 μm in 50 μm increments. Data collection is performed on a 386 based PC and a block diagram of the complete calibration facility is shown in Figure 4.
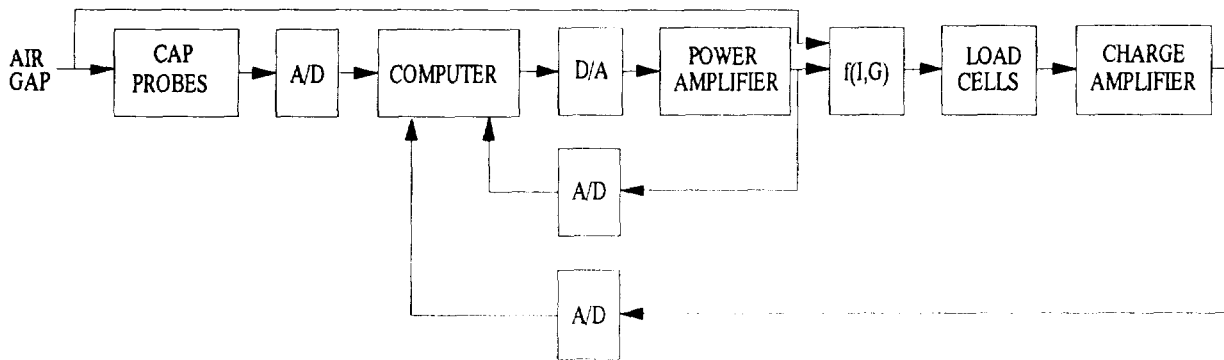
Figure 4: Magnetic bearing calibration procedure block diagram.

The airgap is manually set using the micrometer heads to position the platen. The airgap is determined from the capacitance gauges and fed back to the computer through analog to digital converters. When the desired airgap is set an automated data collection procedure is initiated.

The computer provides a signal to the power amplifier through the digital to analog converter that ramps the coil current up to a maximum of 1.5 amps and then returns to zero at the same rate. This triangular current input to the electromagnet results in a force at the target platen which transmits through the load cells and is monitored by the computer through an analog to digital converter. The airgap, force, and current are recorded in a data file after which the airgap is readjusted and the procedure repeated.

TEST ACTUATOR CONSTRUCTION AND SIZING

Selection of the core material is an important consideration in the design of high precision magnetic bearing actuators. A good material will possess low magnetic loss and coercive force but also be capable of high flux densities for low coil currents. General information about a material can be obtained from the B-H curve, but specific material performance for a given geometry of an electromagnetic actuator needs to be evaluated experimentally.

The four core materials considered were 49% nickel/steel alloy, 84% nickel/steel alloy, Co-V-Fe, and silicon steel. With the exception of the Co-V-Fe material the EI lamination pairs were obtained commercially . The Co-V-Fe EI laminations were custom laser cut and heat treated locally.

Four nominally identical actuators were fabricated using 0.014" laminations cut from these four materials. The most efficient configuration for the actuator is a lamination in the shape of an E with a single coil surrounding the central leg of the core. A single central coil is the shortest average coil length that will fill the core window. The shortest possible coil length is desirable in order to minimize resistance for a given number of amp-turns. A 240 turn coil wound with 22 awg magnet wire was used. Although a cut-core can be magnetized to higher flux densities, for our application laminations were the most economical means of obtaining a limited volume of material. Unlike a cut-core, while traversing through the back of the E lamination, the flux will be perpendicular to the direction of magnetization which has poor magnetic properties. Co-V-Fe has no preferred grain orientation and therefore E laminations will have the same magnetic properties as the more efficient cut-core [6].

The actuator target consisted of a laminated stack of I cores of the same material as the actuator and was tested as a pair. The surface of the target and the pole face of the actuator were both surface ground to ensure a reasonably flat and therefore consistent airgap.

In addition to the core material, the lamination size can be optimized for power. The dimensions of the core lamination can optimize force by sizing the pole face area in relation to the core length and height. Thus, for an optimum square pole face area the maximum force can be obtained for a given power level. The overall length and height of the core lamination are selected to place the operating point at nominal standoff in the middle, or most nearly linear region of the B-H curve of the core material.

The actuator force can be expressed in terms of the pole width and core window area. From magnetic circuit theory we define the relation for actuator force as

$$F = \frac{\mu_o A_p N^2 i^2}{4g^2} \tag{1}$$
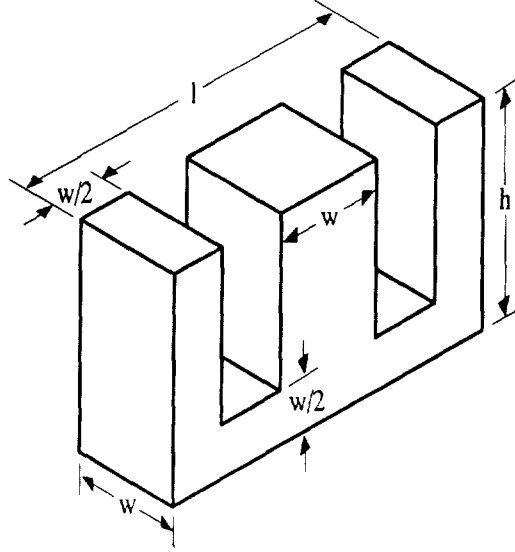
Figure 5: Electromagnet core sizing.

Since actuator power, $P = i^2 R$ we obtain the force-power relation

$$F = \frac{\mu_o A_p N^2 P}{4g^2 R} \tag{2}$$

where A_p is the pole face area, N is the number of coil turns, and g is the actuator airgap. Assuming a square pole face, and realizing that the number of coil turns is equal to the area of the core window multiplied by a packing factor constant, we can reduce N to the window area in terms of the pole face width and lamination length and height. The packing factor is a scaling term and can therefore be eliminated.

$$N = A_w = 2w^2 - (4h + l)w + 2hl \tag{3}$$

If the average coil turn diameter is located in the middle of the core window, the average turn length will then be approximately equal to $2l$. Realizing that the coil resistance is the product of the average turn length, the number of turns, and a resistance constant per unit length, we can eliminate the scaling constants and express the coil resistance as

$$R = lA_w \tag{4}$$

Substituting equation (3) and equation (4) into equation (2), and eliminating all scaling constants including constant power, we establish a unit force function expressed in terms of the lamination dimensions. Since we are concerned with maximizing the function and not with the magnitude of the force and power, we can eliminate the terms that have no dependance on the lamination dimensions.

$$F_u = 2w^4 - (4h + l)w^3 + 2hlw^2 \tag{5}$$

Solving

$$\frac{\partial F_u}{\partial w} = w(8w^2 - 3(4h + l)w + 4hl) = 0 \tag{6}$$

will result in a pole face width, w, that will provide the maximum force for a given lamination length and height. Any system of units for length can be used. The commercially obtained EI pair used was selected based on this analysis and is reasonably close to the optimum pole face size. For the optimized E core the total stage power dissipation for a lateral acceleration of one half the force of gravity is calculated to be approximately 1.5 watts. This type of stage acceleration requires six actuators to be energized: two will provide accelerating force and the remaining four will offset any torques that result from moments about the center of gravity.

CORE MATERIAL FORCE RESULTS

The test actuators were characterized for airgaps ranging from 80 - 650 μm and the resulting curves are shown in Figures 6 to 9. In magnetic bearings which convert electrical power into mechanical power, high flux density materials offer the advantage of reduced volume and lighter weight. This is especially important in our magnetic levitation stage where the actuators are contained on the suspended platen. For precision control of a suspended platen, it is also essential that the material have low magnetic losses to reduce hysteresis. A material with higher losses and coercive force will introduce errors into the actuator real-time linearized model.

The Co-V-Fe material demonstrated extremely high flux concentrations, but exhibited higher electromagnetic losses and coercive force than are acceptable for our application. The losses exhibited are contrary to the material B-H curve and are probably attributed to the heat treatment which was performed locally. This material was tested both with and without heat treatment. The flux density of the material without heat treatment is approximately 10% of the properly annealed flux density. The Co-V-Fe material is considerably more expensive than other materials, but is a good value if one considers the flux per unit weight. Grain oriented silicon-steel exhibits the best value in flux per unit cost. This material is capable of high flux densities, but has more magnetic losses than are desirable. The nickel-steel alloys both have very low magnetic losses, but the permeability of 80% nickel-steel is reduced significantly and the material cannot produce the necessary force. The best combination of low magnetic losses and high force for our precision magnetic bearing is the 49% nickel steel alloy. The expected operating region of the actuators will be with airgaps between 150 - 450 μm and an excitation current of less than 1 amp. In this region the losses are negligible and the force-current-airgap relationship is very nearly linear.

CONCLUSIONS

This paper has introduced a precision motion control magnetically levitated stage and some aspects of the stage optimal design have been presented. The magnetic bearing calibration test fixture used to experimentally measure the force-current-airgap relationship was presented including its construction and test procedure. The force-current-airgap relationship for various magnetic materials was experimentally measured and a core material was selected based on the analysis.
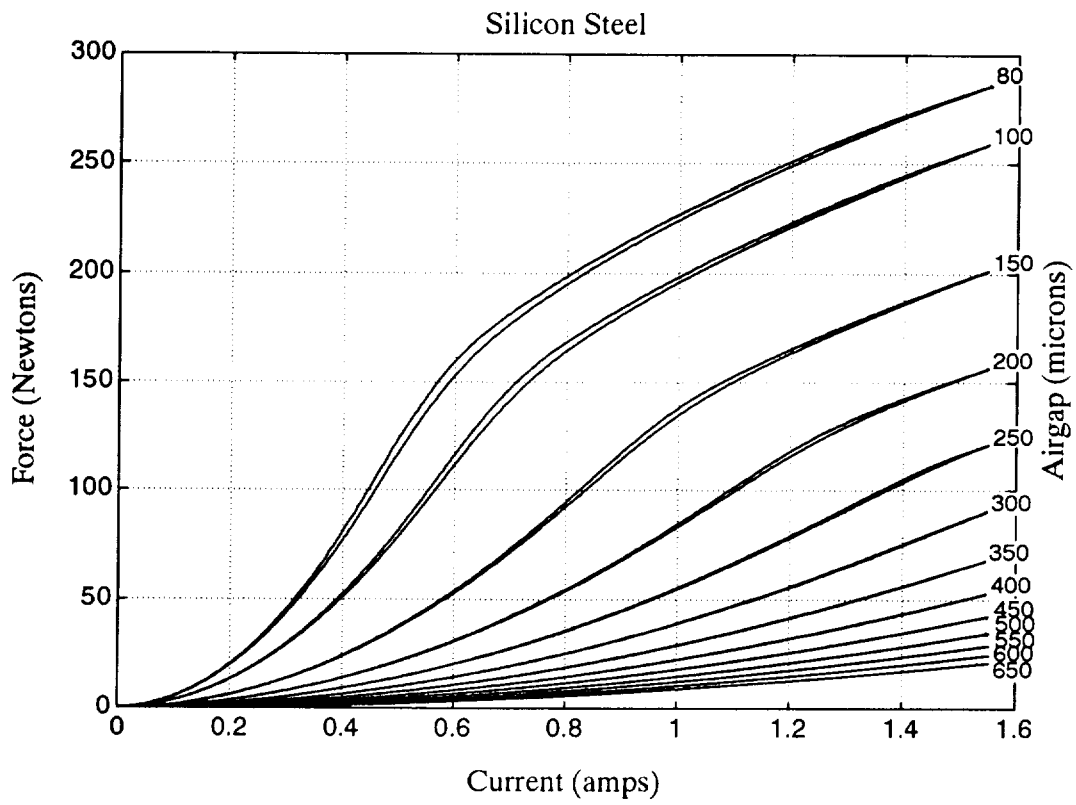
Figure 6: Silicon-steel force curves.
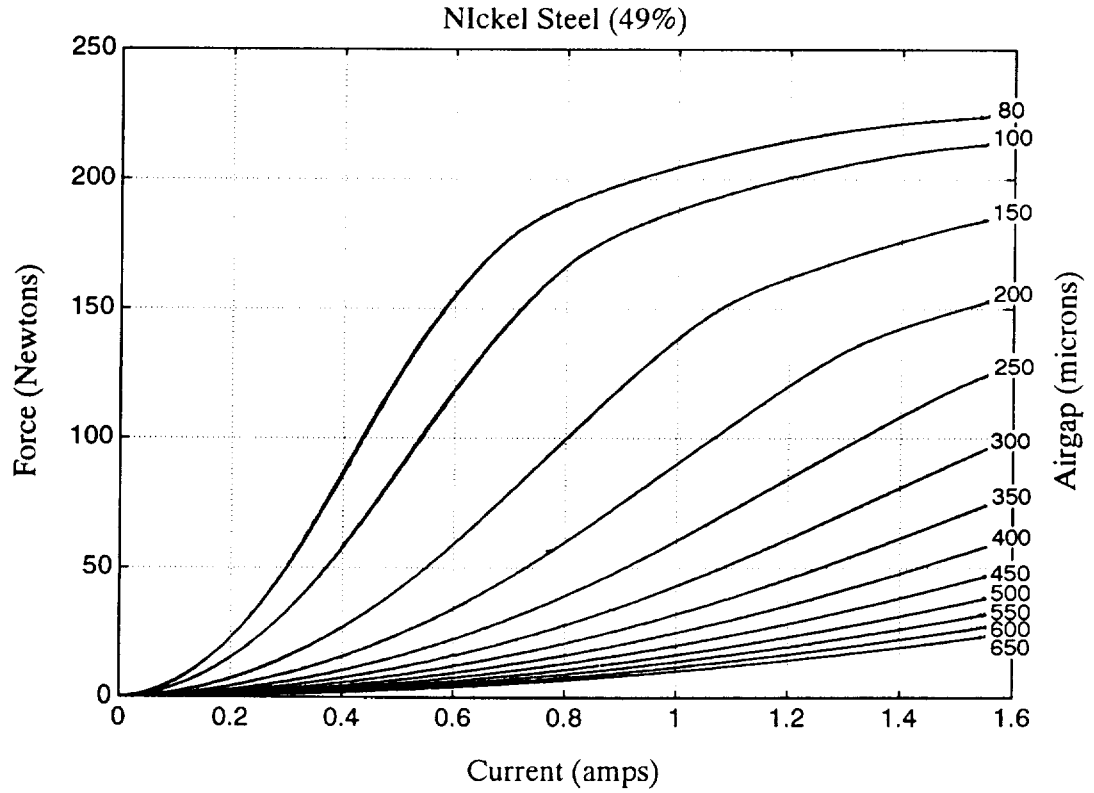
Figure 7: 49% Nickel-steel force curves.
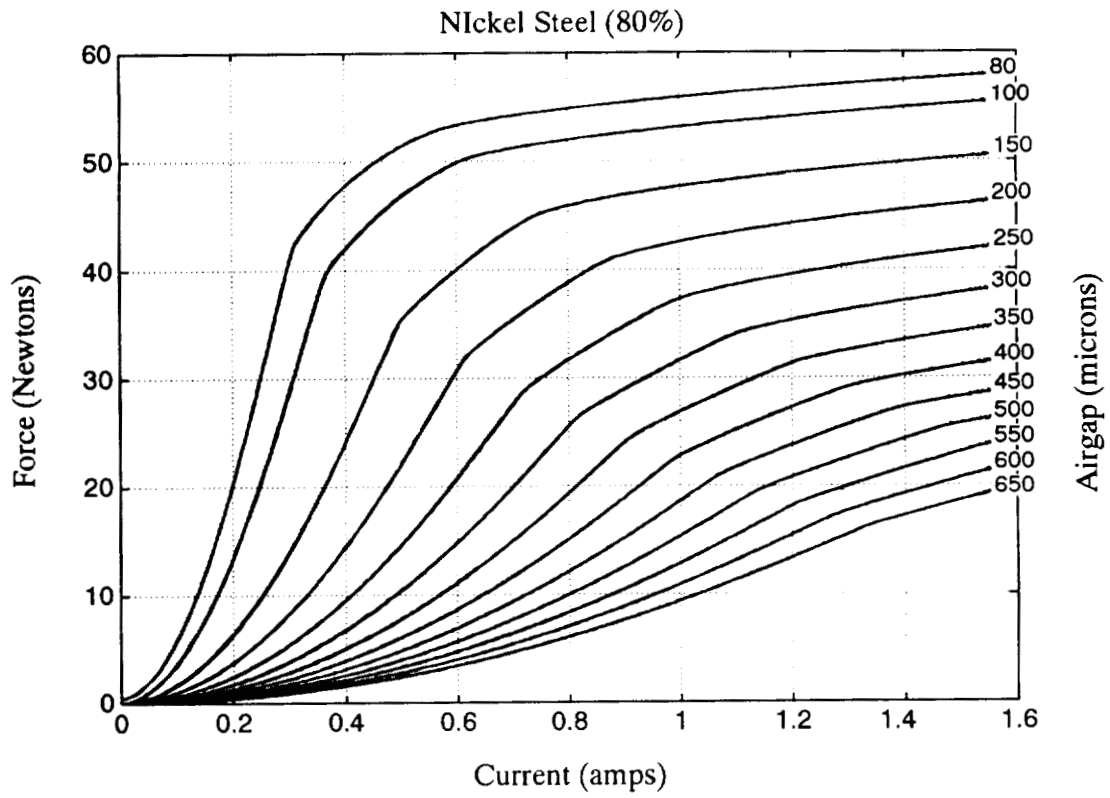
Figure 8: 80% Nickel-steel force curves.
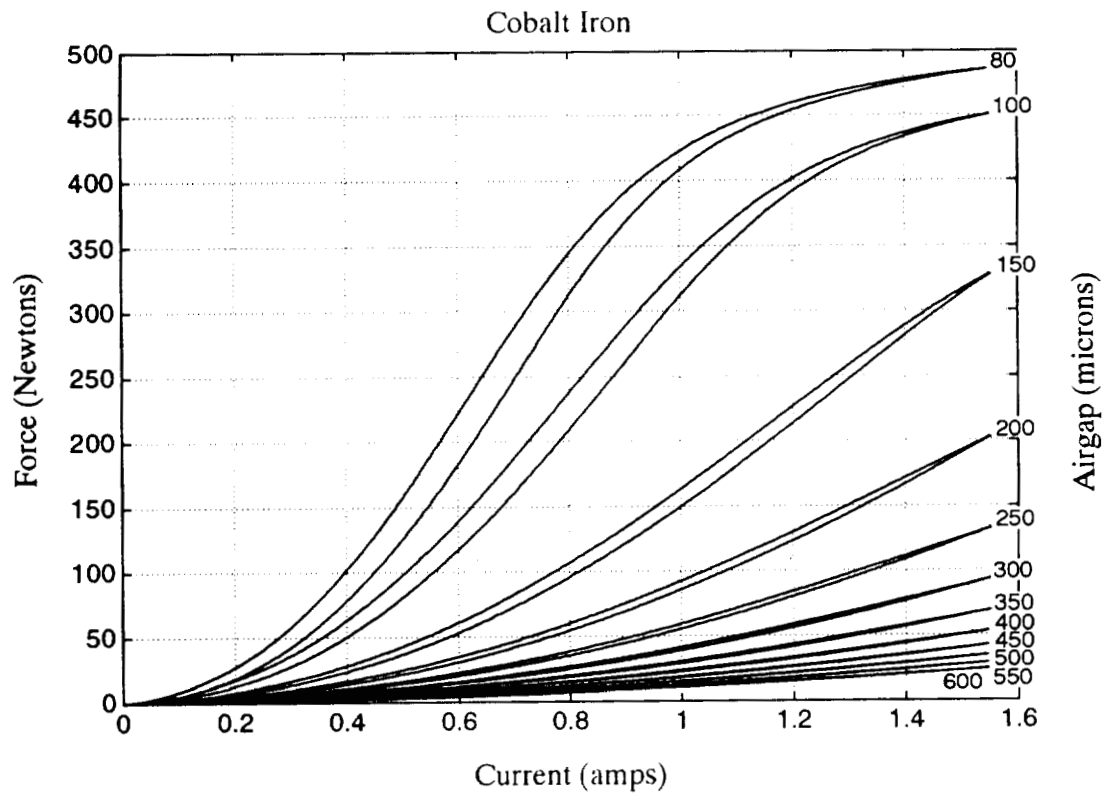
Figure 9: Co-V-Fe force curves.

144

References

[1] Trumper, D.L., "Magnetic Suspension Techniques for Precision Motion Control," Ph.D. Thesis, Dept. of Elec. Eng. and Comp. Sci., M.I.T., Camb., Mass., Sept., 1990.

[2] Trumper, D.L., and Slocum, A. H., "Five-Degree-of-Freedom Control of an Ultra-Precision Magnetically-Suspended Linear Bearing," NASA Workshop on Aerospace Applications of Magnetic Suspension Technology, NASA Langley Research Center, Hampton, VA, Sept. 25-27, 1990.

[3] Trumper, D.L., and Queen, M.A., "Precision Magnetic Suspension Linear Bearing," NASA International Symposium on Magnetic Suspension Technology, Aug. 19-23, 1991.

[4] Halbach, K., "Design of Permanent Multipole Magnets with Oriented Rare Earth Cobalt Material," Nuclear Instruments and Methods, 169, 1980, pp. 1-10, North-Holland Publishing Co.

[5] Halbach, K., "Physical and Optical Properties of Rare Earth Cobalt Magnets," Nuclear Instruments and Methods, 187, 1981, pp. 109-117, North-Holland Publishing Co.

[6] Finke, G., "Materials for High Flux Devices," Magnetic Metals Company, Camden, New Jersey.

DESIGN, CONSTRUCTION AND TESTING OF A FIVE
ACTIVE AXES MAGNETIC BEARING SYSTEM

Cristiana Delprete, Giancarlo Genta
Dipartimento di Meccanica, Politecnico di Torino
Torino, Italy

Stefano Carabelli
Dipartimento di Automatica e Informatica, Politecnico di Torino
Torino, Italy

SUMMARY

A high speed electric spindle based on active electromagnetic suspension technology has been designed, built and tested. The main goal of the research work was the construction of a highly modular unit which can be used both for teaching and research purposes. The design of the electromechanical components and of the control unit is described in detail, together with the characterization tests performed on the various subsystems. A description of the preliminary tests on the unit, conducted at speeds not in excess of the first deformation critical speed of the rotor, concludes the work.

INTRODUCTION

After having gained experience in the design and construction of passive magnetic bearing systems [1], [2], [3], at the Department of Mechanics of Politecnico di Torino, the design and construction of a five-active axes magnetic suspension was undertaken. The prototype chosen was an electric spindle which could be operated in a wide range of speeds and operating conditions. Together with the aim of gaining a direct experience in the field, the goal was to build a prototype which could be used both for teaching and research purposes.

The following design requirements were stated: modularity of both the mechanical and the electronic layout; low weight for enhancing transportability; easy access to the various parts for introducing instrumentation and for maintenance; possibility of visual check of the various parts during operation; possibility of changing the configuration of the mechanical parts by shifting axially the subsystems and substituting the shaft; conformity with IEC 348 electrical safety standard; control unit with separate boards for each controlled axis; possibility of substituting each mechanical or electronic component and to use external digital or analogic controllers for any one of the axes.

The present prototype has no aim of representing the optimum solution for any particular type of machine with magnetic suspension, neither for the electromechanical parts nor for the control architecture. The driving idea of the project is that of obtaining a flexible research tool for basic research in the field of magnetic bearings and their control systems, for testing new ideas and control strategies and finally for the development of practical design of components. The effects of different control architectures on the rigid-body or flexible-body dynamics of the system (SISO *PID*, Lead-Lag...) can be studied and different digital controllers (SISO and MIMO) can be compared. With some modifications the system can simulate the effects of the various controllers on machines with complex configuration such as gas turbines or turbomolecular pumps.

The device is also intended for teaching purposes, mainly to demonstrate the principles of active magnetic suspension to mechanical and electronic engineering students and to show them the effects of the various control parameters on the stability and the dynamic behaviour in general. By changing the values of the control parameters acting on the knobs of the control panel it is possible to demonstrate the effects of changes of the gains and time constants of the compensator on the dynamic behaviour of the rotor.

At present the research work is aimed to implementing various configurations of the compensator with the aim of controlling the first deformation mode of the rotor to operate at speeds higher than the corresponding critical speed; investigating modal control and automatic balancing strategies; developing and testing actuators biased by permanent magnets to reduce the power consumption, which is at any rate very low; and developing and testing digital controllers.

Wherever possible particular care was devoted to choose design alternatives leading to low-cost components, or, at least, components which could be produced at low cost if the unit had to be produced in a small quantity. Configurations which are standard in other types of electromechanical devices (e.g. electric motors) were used all where possible. As a result the cost of the whole research was very reasonable and the prototype can be produced in small quantities as a didactic and research rig at a very competitive cost.

The research and design work started with a survey of the literature existing on the subject. Since it is impossible to report a comprehensive bibliography here, a small number of papers are cited [4] - [10].

GENERAL LAYOUT

As already stated a modular design was chosen; the electro-mechanical subsystem consists of a shaft and five stator units which are bolted together, namely
- two radial bearing units which include the radial sensors and the emergency ball bearings;
- one axial bearing unit;`
- one asynchronous a.c. electric motor unit;
- a base which includes the axial sensor and carries all electrical connectors and signal conditioners of the sensors.

The power unit is a solid-state frequency converter which can feed the electric motor with a 3-phase alternating voltage with controllable frequency in the 30-1000 Hz range. The maximum voltage at 1000 Hz is 90 V. The maximum power rating of the converter is 2 kW.

The controller unit contains the five independent controller boards, each one containing its power amplifier. Both the controller and the power unit are fed directly from the two-phase, 50 Hz, 220 V mains.

A picture of the system is shown in Figure 1.

COMPONENT DESIGN

Axial actuator

The axial bearing is made by two electromagnets housed in a light-alloy (Al SG91 UNI 7369/3) cast support. The magnetic circuit (C40 steel UNI 7845) is made in two parts, each one carrying an electromagnet; it closes through a disc (39NiCrMo3 steel UNI 7845 hardened and tempered) shrunk-fit on the shaft on which the electromagnetic axial force is exerted (Figure 2). The steel disc is the largest part of the rotor and is the most stressed by centrifugal loading; for this reason a steel which is more suitable for highly stressed applications than for magnetic circuits has been used. The stress field in the disc has been computed using a standard procedure for rotating discs; the maximum speed of the rotor has then been stated at a value of 35000 rpm, at which the maximum equivalent stress (Von Mises criterion) is 163 MN/m^2.
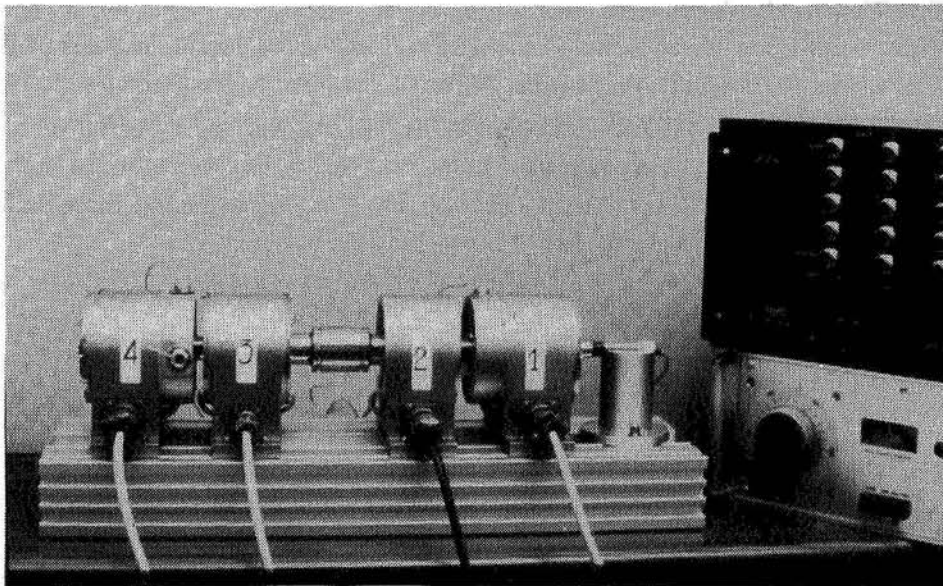
Figure 1. Picture of the complete system.
1: Radial actuator,
2: electric motor,
3: axial actuator,
4: Radial actuator.

Coil

Coil holder

Disc

Pole piece
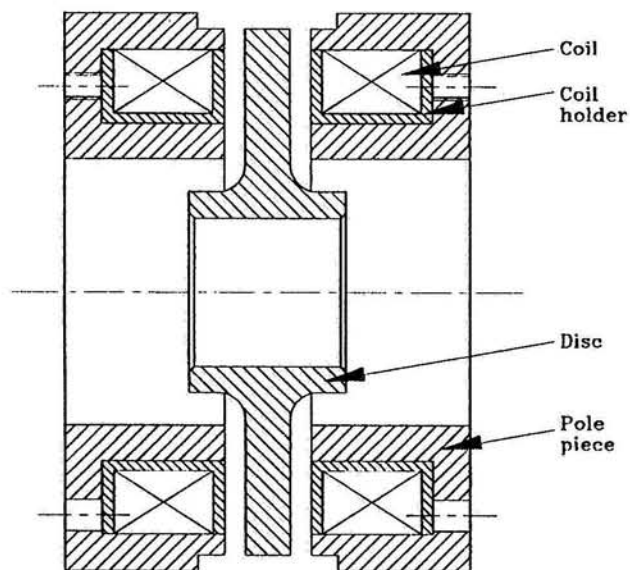
Figure 2. Magnetic circuit of the axial bearing (the air gap is not to scale).

The magnetic force was computed using a very simple model in which the material is assumed to have a linear magnetic behaviour (with μ_{Fe} = 1.6 10^{-3} H/m, equal to that of cast steel), no stray flux is accounted for, the reluctance of the iron parts is neglected if compared with that of the air gap and the flux is assumed to be constant on each area perpendicular to it. This model is adequate only for working conditions in which the magnetic circuit is far from saturation and the air gap is not too small and yields a value of the magnetic forces which is higher than the actual one.

By neglecting the reluctance of the pole pieces, the axial force, the resistance and inductance of the electromagnets are computed

$$F_{ax} = \frac{B_t^2 S_t}{2\mu_0} + \frac{B_{Fe}^2 S_{Fe}}{2\mu_{Fe}} \approx \mu_0 \frac{N^2 i^2}{4t^2} S_t \quad , \qquad R = \rho N \frac{l_{sm}}{S_f} \quad , \qquad L \approx \mu_0 \frac{N^2 S_t}{2t} \quad . \tag{1}$$

where B_t, B_{Fe}, μ_0, μ_{Fe}, S_t, S_{Fe}, N, i, l_{sm}, S_f and ρ are respectively the magnetic flux densities in the air gap and the pole pieces, the magnetic permeabilities of vacuum and the material, the cross sectional areas of the air gap and the magnetic circuit (assumed as constant), the number of turns, the current, the mean length of each turn, the cross section of the wire and the resistivity of copper. The nominal air gap is t = 0.75 mm.

For the coil 8 layers of 15 turns each (N = 120) of wire with a diameter of 1.3 mm was used. The current density at 10 A is J = 6.8 A/mm^2, within the allowable limits for copper. A maximum axial force of 243 N at 5 A with the nominal air gap of 0.75 mm is so computed.

Radial actuators

The two identical radial actuators are very similar to asynchronous squirrel cage a.c. motors, the differences mainly being in the different winding pattern and in the lack of the squirrel cage (copper conductors) in the laminations of the rotor (Figure 3). The actuators are housed in casings which are essentially equal to those of the axial bearing, being obtained from the same casting with some different machining. The rotoric and statoric magnetic circuits are obtained from 100 laminations of thin soft iron sheet (loss factor = 1.1 W/kg, μ_{Fe} = 5.7 10^{-3} H/m). 50 laminations are obtained from insulated sheets (thickness 0.43 mm) and 50 from noninsulated sheets (0.37 mm). The laminated structure is aimed to reduce losses due to eddy currents, as usual.

The magnetic circuit of the stator has eight slots and hence standard motor laminations cannot be used. As the number of layers is too low to justify the construction of a punch, they were obtained at a fairly low cost by chemical milling. The electromagnets are wound in such a way to obtain 4 horseshoe independent electromagnets at 90 degrees phasing.

The width of the pole pieces is l = 12 mm, giving way to an active surface S_t = 444 mm^2. The shape of the slots has been designed in such a way to avoid strong flux concentrations which could lead to saturated zones at high values of the current. A total of 110 turns of double wire of 0.9 mm diameter were wound. At a peak value of the current of 8 A, corresponding to 115% of the value which would cause the magnetic saturation of the soft iron pole pieces, the current density (J = 6.4 A/mm^2) is still acceptable.
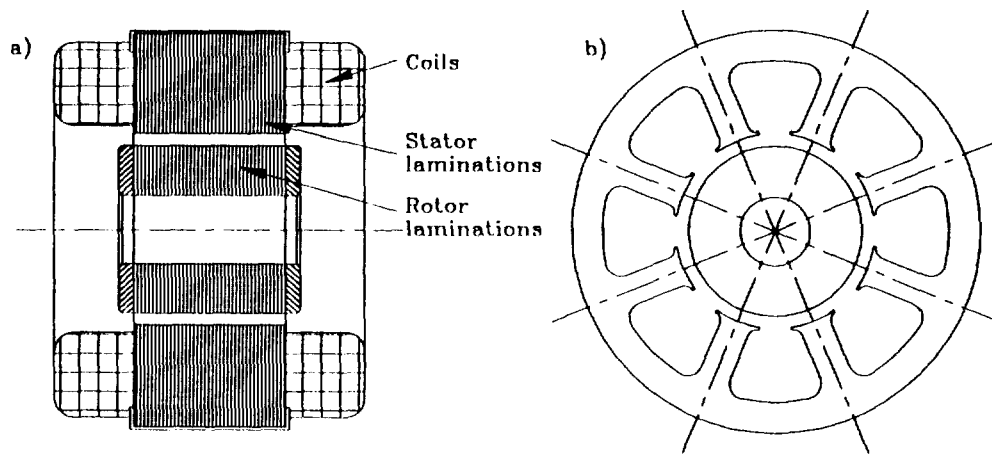
Figure 3. Radial bearing. a) Cross section of the magnetic circuit; b) shape of the rotor and stator laminations (the air gap is not to scale).

A first mathematical model which is essentially the same as that of the axial bearing was used for the initial evaluation of the force capability of the actuator. An added assumption in this case is that the curvature of the outer part of the pole pieces has negligible effects. The force exerted on the rotor by each pair of poles (i.e., by each one of the four horseshoe electromagnets) is

$$F_{rad} \approx \mu_0 \frac{N^2 i^2}{4 t^2} S_t \cos\left(\frac{\pi}{8}\right) , \tag{2}$$

where the nominal air gap is $t = 0.5$ mm. The resistance and the inductance of the electromagnets can be computed by the second and third equation (1). A maximum radial force of 160 N at 5 A with the nominal air gap of 0.5 mm is so computed.

This mathematical model does not allow us to study the effects of changes in the detailed design of the pole pieces, particularly where the fillets are concerned, and the possibility of the occurrence of local saturation of the material. A FEM simulation of the magnetic circuit was then undertaken with the aims of validating the simpler model and to gain a greater insight on the actual working of the actuator. The magnetostatic two-dimensional FEM model, built using ANSYS 4.4A code running on a Vax-Station 2000, includes 3198 4-node plane elements with a single degree of freedom per node (potential vector of the magnetic field), for a total of 2545 degrees of freedom. It takes into account the actual geometry of the cross section of the magnetic circuit and the magnetization curve of the soft-iron, including saturation. Being a plane model, it cannot take into account the end effects, which are at any rate assumed to be small and can be evaluated only at the cost of a very much more complex three-dimensional FEM model. An experimental validation was planned for this issue.

The model yields the value of the magnetic interaction force and the distribution of the magnetic field intensity H and the magnetic flux density B allowing us to verify the assumptions of uncoupling between the 4 electromagnets and to identify potential local saturation problems. The latter result is very useful to the end of optimizing the geometry of the magnetic circuit and particularly the fillet between the prismatic part of the poles and the pole shoes.
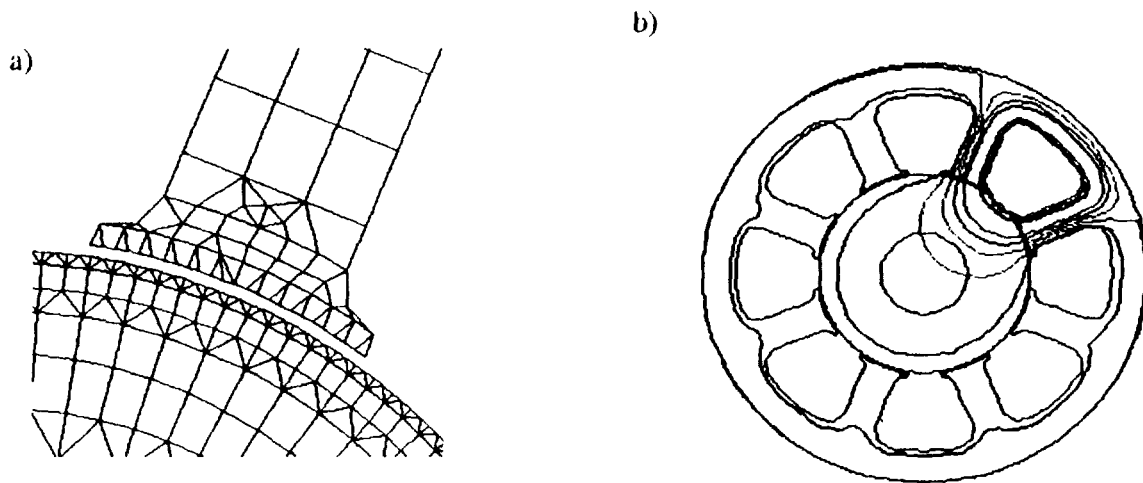
Figure 4. FEM model of the radial bearing. a) Particular of the mesh at the extremity of one pole piece. The elements simulating the air gap are not shown. b) Pattern of the magnetic field intensity H at $i = 5$ A and $t = 0.5$ mm.

Three numerical simulations were run: the first two with the rotor in the nominal position (air gap $t = 0.5$ mm) and values of the current of $i = 1$ A (within limits of linearity of the magnetic behaviour of the material) and $i = 5$ A, well into the saturation range of the material. For the highest value of the current, a further computation has been run with a larger value of the air gap, $t = 0.6$ mm, i.e. with the rotor in an off-centre position.

A particular of the FEM mesh is shown in Figure 4a. The pattern of the magnetic field intensity H obtained for the case of the higher current and rotor in the nominal position is shown in Figure 4b. The uncoupling between the electromagnets is clear, as the magnetic field is mainly confined in the zone adjacent to the working electromagnet. At this value of the current the magnetic circuit is partially saturated ($B = 1.4 - 1.5$ T). Enlargements of Figure 4b show that the distribution of the magnetic field in the pole shoes is not uniform and that saturation occurs mainly in the zone of the fillets. The value of the magnetic force is then lower in the case of the FEM than in that of the simpler model which neglects this effect (143 N against 160 N at 5 A with the nominal air gap of 0.50 mm).

Another interesting result is the fact that the magnetic field penetrates in the rotor deeper than the thickness of the soft iron laminations and interests the 39NiCrMo3 steel core. This effect can give way to eddy currents, with possible energy losses and heating of the shaft. The low value of the field in the core of the shaft leads to the suggestion that these effects are not strong and no modifications aimed at having a thinner shaft were planned at this stage.

The radial sensors are located in the same housing of the actuators. Initially Selet B18/5 OC inductive sensors were used but after the first tests it was clear that their performance was not adequate, particularly where the cutoff frequency is concerned; they were then substituted by Bently Nevada 3106 mod. 20886-01 inductive sensors. These last sensors cannot be exactly collocated with the actuators and in the present application the distance between the axes of the two elements is 52 mm; this can have an effect on the dynamic behaviour of the system and this issue was later studied in detail.

Also the emergency ball bearings are located in the same housings. A pair of deep groove Barden 104SST5CXO ball bearings were used, leaving a radial and axial clearance equal to half of the nominal air gap of the bearings (0.25 and 0.375 mm in radial and axial direction respectively).

The electric motor is a squirrel cage asynchronous motor. Its construction is similar to that of the radial bearings, with the difference being the squirrel cage in the rotor and the number of the slots (24) in the stator. The pattern of the windings is standard.

The shaft has been obtained from a single forging of 39NiCrMo3 steel UNI 7845, heat treated to a hardness of 43 HR_C at the surface (42 HR_C at the core). Its design incorporates a central zone on which a pulley or a flywheel can be fitted to experiment on the device. The rotors of the actuators and of the electric motor are directly shrink-fitted on the shaft. The measured inertial properties of the rotor assembly are mass 5.310 kg; moment of inertia about the rotation axis $1.8089 \ 10^{-3}$ kg m^2 and transversal moment of inertia $1.1500 \ 10^{-1}$ kg m^2.

The electromechanical parts are directly bolted on a light alloy base (anodized extruded bar of Al-MgSi0,5 UNI 3569-66). This solution allows a very simple interchangeability of the parts and the possibility of modifying the configuration of the device. The Selet B18/5 OC inductive axial sensor is directly bolted on it.

Control system, controller and power amplifier

A set of 5 equal SISO linear control systems has been designed, each one controlling a couple of electromagnets. No design difference in the controllers of the axial bearings or of the "vertical" or "horizontal" channels of the radial bearings has been introduced; however, as the control parameters can be adjusted by control handles on the front panel of the controller, the various controllers can have different settings.

The force-current characteristic of the electromagnets (equations 1 and 2 can be written in the synthetic form $F = K(i/t)^2$) is intrinsically nonlinear and must be linearized. Here the usual practice of superimposing a bias current to the control current is followed [11], even if provisions for attempting different strategies are included in the device and will be tested later.

Constant K can be either computed using equations (1) or (2), computed from results of finite element simulation, or measured experimentally. This approach does not include the saturation of the pole pieces, but this is not considered as a strong inconvenience, as linearization of the behaviour of the system is important only for values of the current which are low enough to prevent that phenomenon to occur. As shown in [4], [5], [11], the linearized expression of the force supplied by the pair of electromagnets connected to a single controller at varying control current i_c (i_o is the bias current) and displacement u from the nominal position is

$$F_{rad_{lin}} = -4K \frac{i_o}{c^2} i_c + 4K \frac{i_o^2}{c^3} u \tag{3}$$

where c is the clearance, which is assumed as constant as the linearization is performed about the centred position. The second term at the right hand side is linked with the unstable behaviour of the uncontrolled magnetic bearing.

A value of the bias current $i_0 = 0.45$ A was chosen as it allows to counteract the weight of the rotor in the "vertical" channels and insures a wide enough linear range without leading to a high power consumption (0.1 W per pair of electromagnets in the horizontal direction).

The problem of controlling the five axes of the rotor (a multivariable problem) has been reduced to the independent control of each axis by means of separate and identical controllers (a multiple monovariable problem). This approach is justified by the relative uncoupling of the machine (almost complete in the case of axial versus radial axes) and by the additional intrinsic uncoupling effect of feedback control. The independent axes solution is particularly advantageous in relation with the physical implementation of the control with analog active filters: the control of the five axis is then implemented by five identical boards carrying external potentiometers to adjust the single axis control parameters.

In order to design the control two simplified models of the rotor have been devised:

- 2 mode multivariable models obtained either by reducing the model on the actuator nodes (assuming collocated sensors) or by modal reduction; these models can describe rigid body modes only;
- single axis, i.e. monovariable, models obtained by structural analogy with a rigid body (Figure 5a) and with a flexible body (Figure 5b).

The first type of model has been used to assess stiffness and damping in terms of gains of a state space feedback control law obtained with standard pole-placement technique. The considered states being position and velocity, the control gains may be thought as a proportional and a derivative action directly on the position signal. For example, requiring the following pole shifting from unstable to stable and reasonably damped rigid modes

$$
\begin{Bmatrix} -60.517 \\ +60.517 \\ -88.389 \\ +88.389 \end{Bmatrix} \rightarrow \begin{Bmatrix} -30 + j300 \\ -30 - j300 \\ -45 + j380 \\ -45 - j380 \end{Bmatrix} ,
$$

(expressed in 1/s), the following gain position and velocity gain matrices are obtained

$$
[K_r] = \begin{bmatrix} 3.757 & 1.218 \\ 1.332 & 2.935 \end{bmatrix} \quad , \quad [K_v] = \begin{bmatrix} 2.237 10^{-3} & 7.346 10^{-4} \\ 7.957 10^{-4} & 1.796 10^{-3} \end{bmatrix} .
$$

The second type of model has been developed to take into account the flexural behavior of the rotor as "seen" by every position sensor and consequently fed back to the independent single axis controller. In this sense the damping action of the derivative term must be extended in order to cope with the flexural behavior even for sub-critical working velocities. The control loop of each axis is sketched in Figure 6.
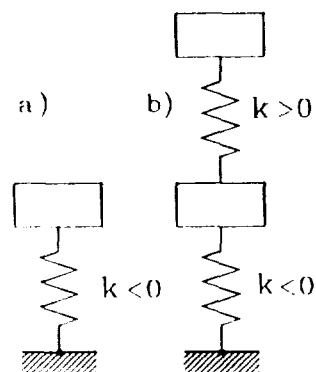
Figure 5. Single axis rigid body (a) and flexible body (b) model.
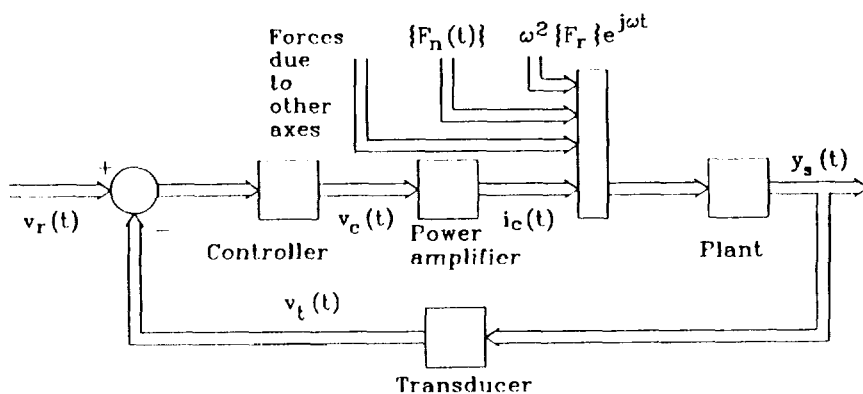
Figure 6. Single axis control loop.

154

Signal $r(t)$ is the position reference used to center the shaft with respect to the coil poles and emergency ball bearings. Since it remains unchanged during spindle operation the control problem is a pure regulation problem: to maintain the position in face of stationary and unbalance forces $\{F_n\}$ and $\omega^2\{F_r\}e^{j\omega t}$. Actually the controller has already been predisposed for a general two degrees of freedom control scheme with separate paths for sensor output and reference signals.

The basic structure of each axis' independent controller is the parallel of proportional, integrative and derivative command actions, that is a *PID* controller

$$v_c(t) = K_c\left(e(t) + \frac{1}{T_i s}\int_0^t e(\tau)d\tau + T_d\frac{d}{dt}v_s(t)\right) \quad , \tag{4}$$

where $v_c(t)$ is the controller output signal, $e(t) = v_r(t) - v_s(t)$ the error feedback signal, K_c the controller gain, T_i the integrative or reset time constant and T_d the derivative or prediction time constant. Including the causal pole in the derivative term on the error signal, the Laplace domain *PID* transfer function is

$$PID(s) = K_c\left(1 + \frac{1}{T_i s} + \frac{T_d s}{\tau_d s + 1}\right) \approx K_c\frac{1}{T_i}\frac{T_i s + 1}{s}\frac{T_d s + 1}{\tau_d s + 1} = PI(s)D(s) \quad . \tag{5}$$

The approximated expression holds if $T_i \gg T_d \gg \tau_d$ and can be interpreted as the series of a *PI* and phase lead filter.

The specifications assumed to design the controller may be summarized as follows:

- static stiffness greater than $0.5\ 10^6$ N/m;
- settling time to reach 90% of exact reference position, less than 5 s;
- reasonable damping in the frequency range covering rigid and flexural modes;
- attenuation of command action due to sensor high frequency disturbances.

The controller parameters obtained are then assumed as central value for the controller to be implemented circuitally: gain, $K_c = 3.0$, range $0.5 \div 5.5$; integrative time, $T_i = 5.0$ s, range $3.0 \div \infty$; and prediction time, $T_d = 6.3\ 10^{-4}$ s, range $1.0 \div 11.5\ 10^{-4}$. The causal pole has been placed in $\tau_d = 50\ 10^{-6}$ s. In order to improve compliance to the last piece of specification an additional filter may be added to the sensor output.

The electromagnet coils constitute a high inductance and low resistance load to the transconductance amplifier that conveys the levitation power to the shaft in accord with the controller output signal. The dissimilarity between the high voltage needed to change coil current and the low voltage needed to maintain it may result in an extremely low overall circuit efficiency with consequent dissipation problems. In order to increase the efficiency, the power section of the transconductance amplifier has been implemented with two Darlington pairs (TIP41C-BUV20) in parallel, one supplied with a low voltage to contribute the constant equilibrium and superposition currents acting on the resistive part of the load, and the other with a high voltage to output the high operating voltage needed to overpower the coil back-electromotive force.

The above described power section with roughly unit signal gain is then inserted in a high gain current feedback loop made by a high voltage operational amplifier (LM343) and an amplified shunt resistor, forcing unitary feedback. An adjustable overload limit circuit has also been added on the feedback path. A gain of 330k/10k moves the power amplifier cutoff frequency up to 812 Hz with almost unitary overall gain (1.023).

EXPERIMENTAL TESTING OF THE ELECTROMECHANICAL COMPONENTS

Axial bearing

The experimental testing on the axial bearing was based on the measurement of the magnetic interaction force between the stator and the rotor for different values of the current and different positions of the rotor. The inductance and the resistance of the electromagnets were also measured.

The force measurements were performed by fixing the housing of the bearing on a table which can be displaced along the axial and two radial directions by means of micrometric slides. The rotor disc was fixed on a shaft connected to a load cell. Only one electromagnet was powered and consequently only the attractive force in one direction was measured. The instrumentation used allowed us to obtain an accuracy of 0.01 mm for displacements (dial gauge), 0.03 N for forces (load cell - multimeter), 0.01 A for currents (stabilized current supply) and 0.1 mΩ for resistances (digital multimeter). The variation ranges of the values of the test parameters in the different tests were 0.75-1.5 mm (step 0.25 mm) for the air gap t and 0-7 A (step 0.5 A) for the current i. Each test was performed by repeating the measuring cycle 3 times for a total of 360 force measurements.

The force-current curves at constant air gap and the force-distance curves at constant current are reported in Figure 7. The experimental points are plotted together with least-squares fit. The exponents of the least square curves differ from the values 2 and -2 predicted by equation (1) and some difference between the curves obtained with increasing current (air gap) and those obtained with decreasing current (air gap) is evident. There is no doubt that the hysteresis effect is linked with the use of steel for the magnetic circuit instead of soft iron, while the displacement of the curves from the theoretical ones is due to saturation (force-current relationship) and to the finite value of the permeability of iron (force-distance relationship). A comparison between numerical and experimental results is shown in Table I and Table II.
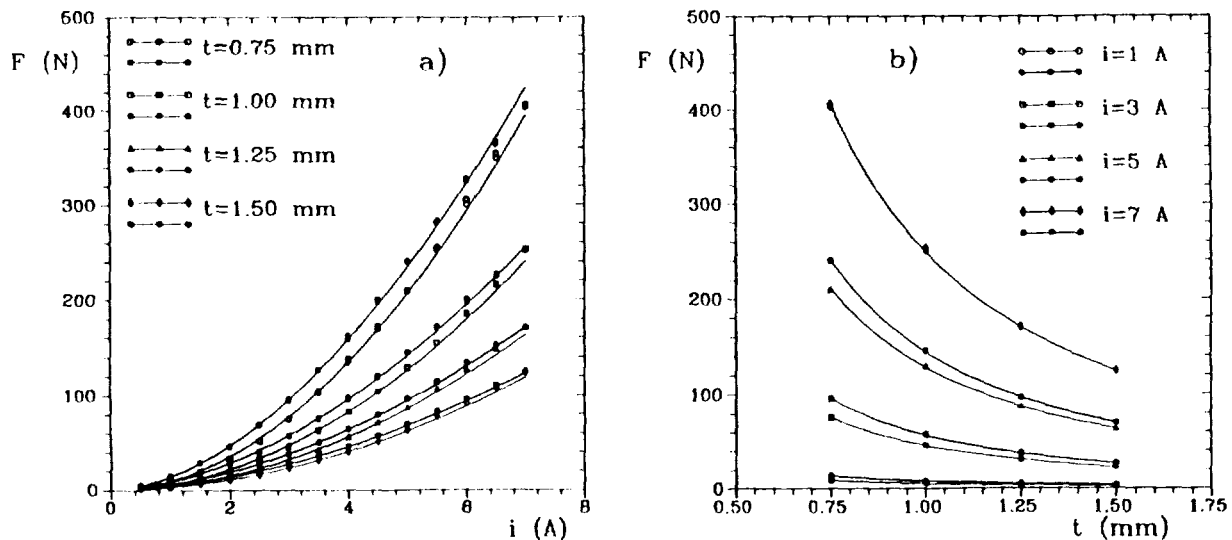
Figure 7. Results of the force tests for the axial bearing. a) Force versus current at constant distance. Experimental points and interpolating expression $F = ai^b$ with $b = 1.90$ for increasing current and $b = 1.75$ for decreasing current. b) Force versus air gap at constant current. Experimental points and interpolating expression $F = at^b$ with $b = -1.71$ for increasing air gap and $b = -1.79$ for decreasing air gap.

Table I. Measured and Computed Electrical Characteristics of the Axial Bearing

R [Ω]			L [mH]		
Computed	Exp. coil 1	Exp. coil 2	Computed	Exp. coil 1	Exp. coil 2
0.395	0.433	0.431	13.96	14.12	14.04

Table II. Measured and Computed Values of the Force of the Axial Bearing for Two Values of the Current and Nominal Air Gap t = 0.75 mm. (*) Eq. (2); (**) As Equation (2), but Without Neglecting the Reluctance of the Pole Pieces

	i = 1.00 A		i = 5.00 A	
	F [N]	error	F [N]	error
Experimental	8.8	---	210.1	---
Computed (*)	9.7	10.2 %	243.3	15.8 %
Computed (**)	8.9	1.1 %	223.6	6.4 %

Radial bearings

Two different pairs of radial actuators were built and tested, the difference being mainly in the number of conductors. Only the results obtained on the second prototype, whose performance proved to be better than that of the first one, are here reported.

The test rig and instrumentation used are the same seen for the axial bearing, and are the same for the test procedures. The variation ranges of the values of the test parameters in the different tests were 0.3-0.8 mm (step 0.1 mm) for the air gap t, 0-4 A (step 0.25 A) and 4-8 A (step 0.5 A) for the current i. Each test was performed by repeating the measuring cycle 3 times for a total of 612 force measurements.

The force-current curves at constant air gap and the force-distance curves at constant current are reported in Figure 8. Only tests conducted with currents up to 4 A are reported. The experimental points are plotted together with least-squares curves. In this case only negligible hysteresis effects have been found, owing to the use of soft iron for the pole pieces; no distinction between the curves obtained with increasing current (air gap) and those obtained with decreasing current (air gap) has been made. The exponent of the least square force versus current curve is very close to 2, as predicted by equation (2): in the present current range no noticeable saturation takes place. On the contrary the exponent of the least square force versus air gap curve is far from the value -2 predicted by the simplified model. A comparison between numerical and experimental results is shown in Table III and Table IV.

Curves similar to those of Figure 8a but also for higher values of the current are plotted in Figure 9. Some saturation at high current and low air gap is clearly present and a 4-th degree polynomial has been used for the least-square fit. The curves for the smallest air gap have been limited to 4 A to avoid overloading of the load cell.

157
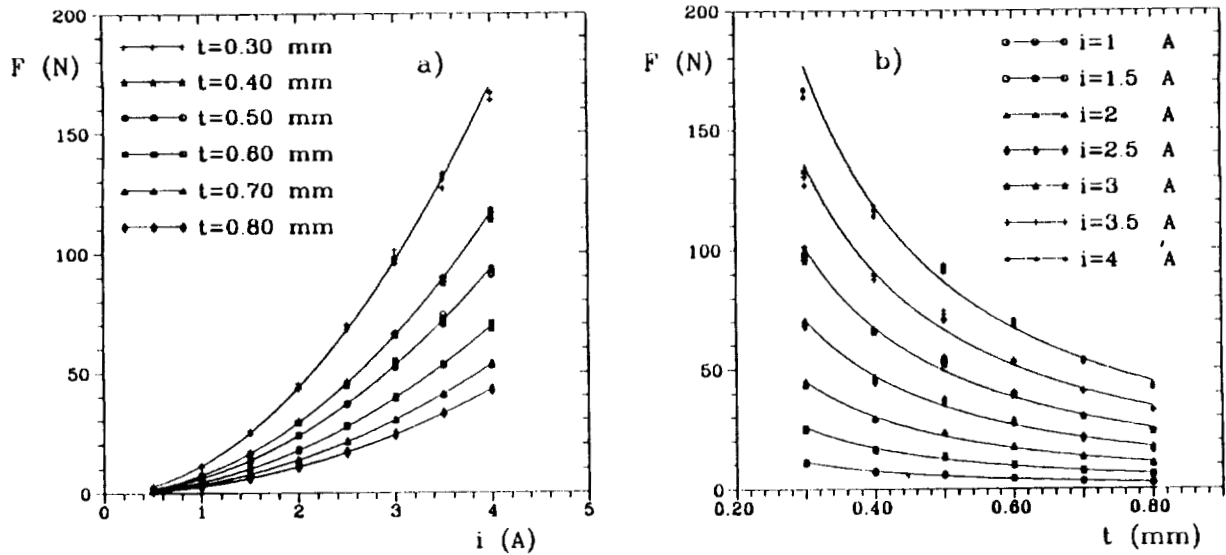
Figure 8. Results of the force tests for the radial bearing. a) Force versus current at constant distance. Experimental points and interpolating expression $F = ai^b$ with $b = 1.99$. b) Force versus air gap at constant current. Experimental points and interpolating expression $F = at^b$ with $b = -1.41$.
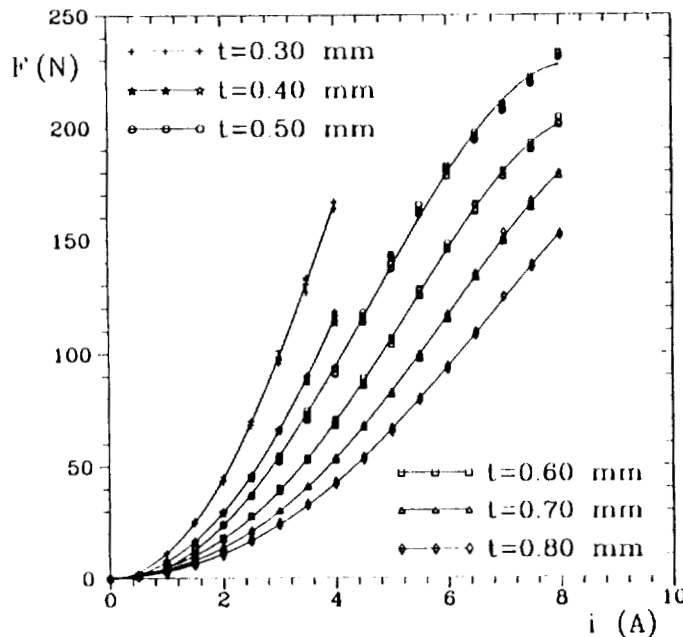
Figure 9. As Figure 8a, but for higher values of the current. Fourth degree polynomial least-square fit.

Further experimental tests were conducted to verify the linearization strategy mentioned above. The tests were conducted by superimposing a fixed bias current i_o to the control current i_c in a pair of opposite electromagnets and measuring the force with the rotor in the nominal (centred) position. The variation ranges of the values of the test parameters in the different tests were 1-2.5 A (step 0.5 A) for the bias current i_o, $0 - i_o$ A (step 0.25 A) and i_o-8 A (step 0.5 A) for the control current i_c. Each test was performed by repeating the measuring cycle 3 times for a total of 432 force measurements. The results are shown in Figure 10a.

Table III. Measured and Computed Electrical Characteristics of the Radial Bearings

R [Ω]			L [mH]		
Computed	Exp. rad. 1	Exp. rad. 2	Computed	Exp. rad. 1	Exp. rad. 2
0.205	0.225	0.224	6.75	6.53	6.49

Table IV. Measured and Computed Values of the Force of the Radial Bearings for Two Values of the Current and Two Values of the Air Gap

	t = 0.50 mm				t = 0.60 mm	
	i = 1.00 A		i = 5.00 A		i = 5.00 A	
	F [N]	error	F [N]	error	F [N]	error
Experimental	5.9	---	140.6	---	105.8	---
Equation (4)	6.3	6.8 %	160.0	13.8 %	108.3	2.4 %
FEM	5.8	1.7 %	143.3	1.9 %	104.8	0.9 %

By superimposing the curves obtained from the previous tests it is possible to compute from experimental results the value of constant K to be introduced into equation (2). A value $K = 1.525$ N mm^2/ A^2 was then used in the further parts of the work (Figure 10b).
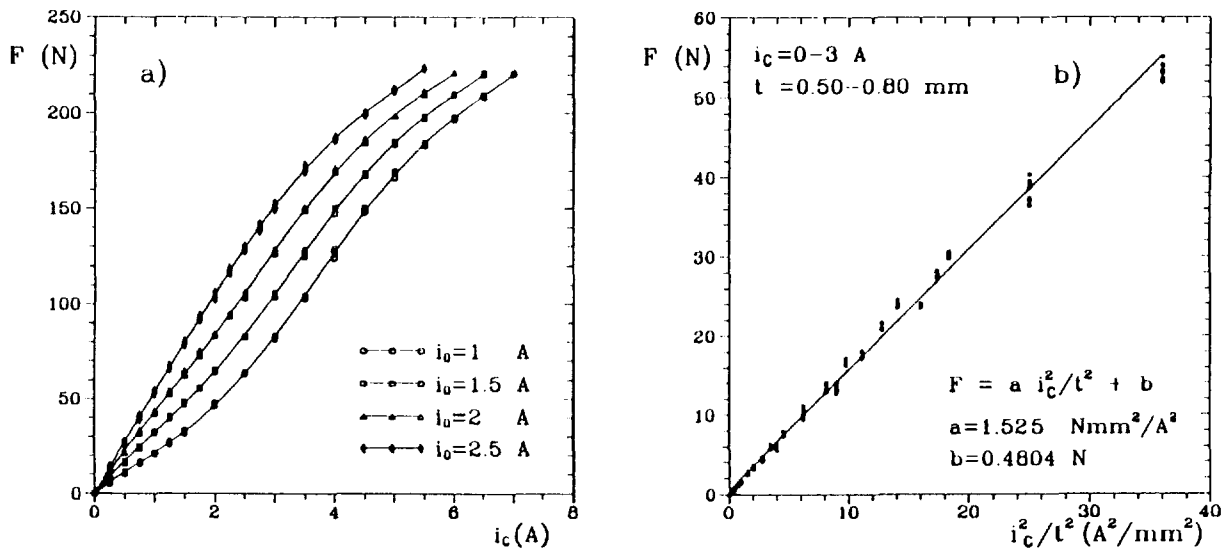
Figure 10. a) Results of the linearization tests for the radial bearing. Force versus control current at constant bias current. b) Force exerted by a pair of electromagnets versus parameter $(i/t)^2$, obtained by adding the experimental values of the previous tests.

Before running the system, the natural frequencies of the suspended rotor were measured by exciting the system with an instrumented hammer and measuring the acceleration at midspan. The first 3 values are compared with the numerical results in [11].

A series of spin tests have been performed up to a speed of 21000 rpm, which is lower than the critical speed related to the first deformation mode (third critical speed), expected at 25780 rpm. The amplitude of the orbit at the sensor location was recorded as a function of the spin speed during free spin-down from the maximum speed. The amplitude of the orbit has been obtained directly from the output of the sensors, using their gains. The synchronous component of the amplitude in horizontal direction obtained from a frequency analyzer is plotted in Figure 11.

The maximum amplitude of about 54 μm is reached during the crossing of the two rigid-body critical speeds, while the amplitude in the supercritical range is lower than about 15 μm. The corresponding values measured by an accelerometer located on the stator are of 13 μm and 0.2 μm respectively. The latter accounts for the extremely smooth running of the machine.

The measured critical speeds at 3300 and 4020 rpm are close to the computed values of 2990 and 3880 rpm.

Several tests aimed to verify the stability of the system were performed introducing disturbances both in form of impulsive loads on the stator and added unbalances on the rotor. In all cases the system proved to be able to maintain stable working conditions and reject disturbances.
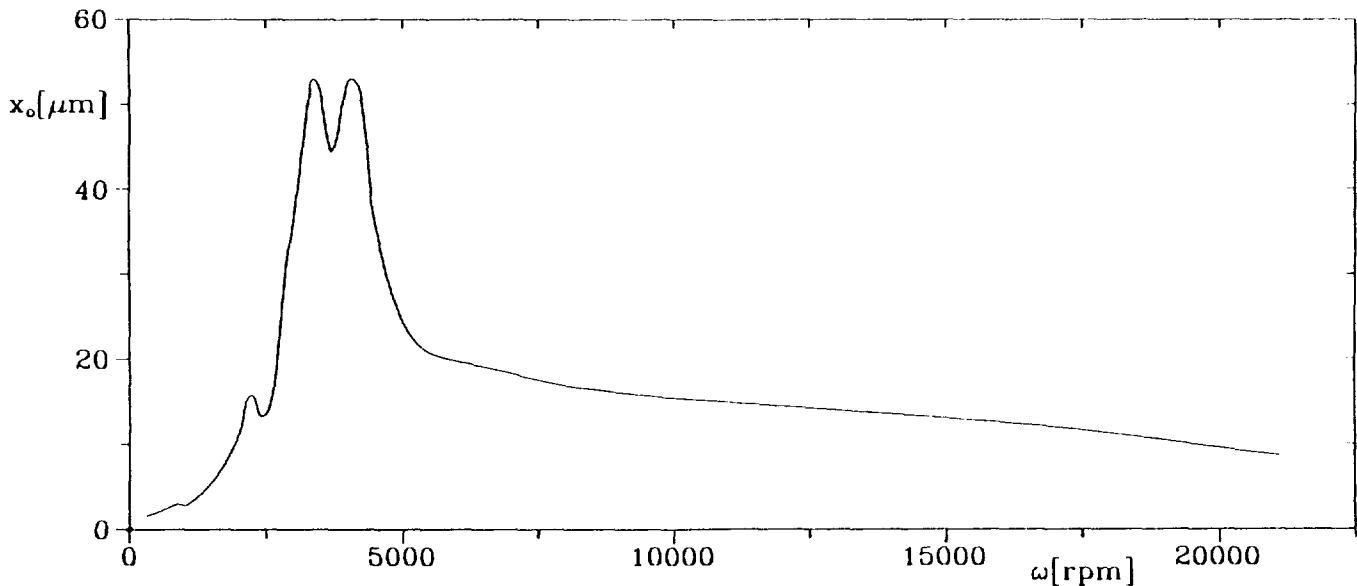
Figure 11. Results of a spin-down test: amplitude of the synchronous component of the displacement at one sensor location in horizontal direction versus spin speed.

CONCLUSIONS

The electric spindle supported by a five-active axes magnetic suspension built at the Department of Mechanics of Politecnico di Torino has been described in detail.

The machine has been tested thoroughly in the speed range up to the third critical speed, corresponding to the first deformation mode of the shaft. In this speed range it proved to be capable of stable operation even in presence of disturbances and to be extremely quiet and vibration free. Further tests aimed to exceed the third critical speed are planned; as numerical simulation shows that the amplitude in this condition is not small enough [11], suitable modifications to the controller are planned.

The device is now used as an experimental rig and as a teaching support.

A very interesting feature of the whole project is its low cost, which can effectively open new application areas to the active magnetic suspension technology.

REFERENCES

1.   Genta, G.; Mazzocchetti, L.; and Rava, E.: Magnetic Suspension for a Turbomolecular Pump. 2nd. International Symp. on MagneticBearings,Tokyo, July 1990, pp. 65-72.

2.   Genta, G.; Delprete, C.; Tonoli, A.; Rava, E.; and Mazzocchetti, L.: Study of the Geometry of a Passive Radial Magnetic Bearing for Application to a Turbomolecular Pump. MAG'92 Magnetic Drivers and Dry Gas Seals Conference & Exhibition, Alexandria, Virginia, July 1992, pp. 61-70.

3.   Delprete, C.; Genta, G.; Mazzocchetti, L.; Rava, E.; Ricca, A.; Ripamonti, G.; Santini, L.; Tonoli, A.; Varesi, A.; and Zannella, S.: High Speed Asynchronous Motor with High T_c Superconducting Bearings. 3rd. International Symp. on Magnetic Bearings, Alexandria, Virginia, July 1992, pp. 287-296.

4.   Schweitzer, G.; and Lange, R.: Characteristics of a Magnetic Rotor Bearing for Active Vibration Control. 1st. International Conf. on Vibrations in Rotating Machinery, Cambridge, September 1976, IMechE C239/76, pp. 1-6.

5.   Schweitzer, G.: Magnetic Bearings, Lecture Course "Rotordynamics - 2", CISM (Centre Int. Sciences Mech.), Udine, October 1985.

6.   Gondhalekar, V.; and Holmes, R.: Design of a Radial Electromagnetic Bearing for the Vibration Control of a Supercritical Shaft. Proc. IMechE 198C(16), 1984, pp. 235-242.

7.   Imlach, J.; Allaire, P.E.; Humphris, R.R.; and Barrett, L.E.: Magnetic Bearing Design Optimization. Proc. IMechE Vibrations in Rotating Machinery, Edinburgh, September 1988, pp. 53-60.

8.   Jeyaseelan, M.; Anand, D.K.; and Kirk, J.A.: A CAD Approach to Magnetic Bearing Design. Proc. 23nd IECEC Intersoc. Energy Conversion Eng. Conference, Denver, Colorado, July 1988, vol. 2, pp. 37-42.

9.   Maslen, E.H.; Allaire, P.E.; and Scott, M.A.: Magnetic Bearing Design for a High Speed Rotor. 1st International Symp. on Magnetic Bearing, Zurich, June 1988, pp. 137-148.

10.   Walowit, J.A.; and Pinkus, O.:Analytical and Experimental Investigation of Magnetic Support Systems. Part I: Analysis - Part II: Experimental Investigation. Trans. ASME J. Lubr. Tech., 1982, vol. 104, pp. 418-437.

11.   Genta, G.; Delprete, C.; and Carabelli, S.: Active Magnetic Bearing Control Loop Modeling for a Finite Element Rotordynamics Code. 2nd. International Symp. on Magnetic Suspension Technology, NASA CP3247, Seattle, Washington, August 1993.

EXPERIMENTAL MEASUREMENT AND CALCULATION OF LOSSES IN PLANAR RADIAL MAGNETIC BEARINGS

M. E. F. Kasarda, Research Associate
P. E. Allaire, Professor
R. W. Hope, Research Associate
R. R. Humphris, Research Professor
University of Virginia
Charlottesville, VA

ABSTRACT

The loss mechanisms associated with magnetic bearings have yet to be adequately characterized or modeled analytically and thus pose a problem for the designer of magnetic bearings. This problem is particularly important for aerospace applications where low power consumption of components is critical. Also, losses are expected to be large for high speed operation. The iron losses in magnetic bearings can be divided into eddy current losses and hysteresis losses. While theoretical models for these losses exist for transformer and electric motor applications, they have not been verified for magnetic bearings. This paper presents the results from a low speed experimental test rig and compares them to calculated values from existing theory. Experimental data was taken over a range of 90 to 2,800 rpm for several bias currents, and two different pole configurations. With certain assumptions agreement between measured and calculated power losses was within 16% for a number of test configurations.

NOMENCLATURE

B_{max} = Maximum Magnetic Flux Density
d = Lamination Thickness
D = Windage Drag Force on Rotor
E_k = Rotor Kinetic Energy
f = Frequency (Hz)
I = Current
J = Rotor Polar Moment of Inertia
L = Rotor Lamination Length
P_e = Eddy Current Power Losses
P_{ha} = Hysteresis Power Loss Due to Alternating Flux
P_{hr} = Hysteresis Power Loss Due to Rotating Flux

P_I = Iron Power Losses
P_k = Kinetic Power Loss
P_w = Power Loss Due to Windage
R = Rotor Lamination Radius
U = Surface Velocity of Rotor Laminations
t = Time
ρ = Material Resistivity
ρ_g = Gas Density
η = Hysteresis Coefficient
v = Gas Viscosity
ω = Rotor Angular Velocity (rad/sec)

INTRODUCTION

Magnetic bearings offer the designer of jet engines the ability to operate at much higher speeds than when conventional rolling element bearings are used. Because of the stiffness and damping properties of the magnetic bearings the squeeze film damper can be eliminated and the lubrication system is no longer necessary. In order to fully optimize the design of the engine the designer must account for losses in the bearings. While magnetic bearings do not have the kinds of losses associated with conventional bearing types, they do have several unique loss mechanisms that need to be quantified more accurately than they have been in the past.

The loss mechanisms in magnetic bearings may be classified in the categories of 1) coil losses, 2) iron losses, and 3) windage losses. The coil losses are the resistive losses due to current in the stator coils. They are relatively easily calculated by conventional I^2R formulas and are not discussed further here. The iron losses are the losses which occur in the stator and rotor of the magnetic bearings. Generally these have two components: eddy current losses and hysteresis losses. The rotor losses are the primary subject of this paper. The final category of losses is that of windage friction loss due to the gases or liquids surrounding the bearing rotor. While windage losses may be significant in some applications, they are a secondary subject of this paper.

The topic of magnetic core losses both in nonrotating devices, such as transformers, and rotating machines, such as electric motors, is a very complicated subject. Much of the early work on core losses, referred to as classical work in this paper, was done early in this century. It largely ignored the physics of the magnetic domain structure, but developed a series of relatively simple formulas for quantifying the losses. The iron losses were considered to be divided into two types: eddy current and hysteresis losses. Hysteresis losses were further sub-divided into alternating and rotational components. The more modern theory associates the losses with physical phenomena on a molecular level occurring with changing magnetism, called domain theory. All of the magnetic loss effects can be explained using the domain theory, but convenient formulas suitable for magnetic bearing design are not currently known to the authors.

This paper does not address the domain theory of losses but employs classical formulas to calculate some of the losses for comparison to the experimental run down test results. Iron losses in magnetic bearings, rather than in transformers and electric motors, began to be reported in the literature approximately 10 years ago. Yoshima [1] discussed an eddy current effect in magnetic bearings using a detailed finite element model to calculate the magnetic flux in the bearing. The effect of the induced opposing magnetic forces was studied, but losses were not quantified. Higuchi, et. al [2], and Higuchi, et. al [3] gave short reports on experimental studies of rotating losses in magnetic bearings. Matsumura, et. al [4] presented a fourier analysis of the distribution of the magnetic field for an alternating pole arrangement (NSNSNSNS) and a paired pole arrangement (NNSSNNSS). The paper gave a theoretical prediction of higher losses in the alternating pole arrangement. Experimental results show only a slight difference in the losses. At high speeds the loss plots are nearly identical while at lower speeds the alternating arrangement yields slightly higher losses.

Ueyama and Fujimoto [5] evaluated power losses in a magnetic bearing supported spindle test rig. Iron and windage loss effects were studied for an eight pole radial magnetic bearing of conventional design. Deceleration studies gave the iron losses for four materials when the chamber was placed in a

vacuum. A hysteresis coefficient and an eddy current coefficient were determined for the experimental results, but no comparison to theoretical predictions was presented. Measured and calculated windage losses were compared with good agreement for the turbulent flow calculation model. Matsumura and Hatake [6] conducted loss measurements using an eight pole radial magnetic bearing.

O'Kelly [7] has developed a model of nonlinear hysteresis BH effects in magnetic materials by employing a series of straight lines. Lin, et. al [8] formulated a numerical curve fitting BH routine for transformer coils and cores. Kasarda, et. al [9] presented measured losses with the journal at different eccentricities within the bearing stator and found this effect to be negligible for the test rotor under analysis.

The purpose of this paper is to measure the effect of both bias current and pole configuration on the power losses in a set of magnetic bearings and compare these results to theoretical predictions. Steady state bias currents directly affect the magnetic flux density so they are important. Two different pole configurations were studied: alternating poles (NSNSNSNS) vs. paired poles (NNSSNNSS). The measured results were then compared to calculated losses due to 1) eddy currents, 2) hysteresis, and 3) windage losses, from several existing theories. Calculations based upon iron losses in transformers and windage losses in annular clearances were employed.

EXPERIMENTAL PROCEDURE

A magnetic bearing test rig [10], illustrated in Figure 1, was set up for measurements of rotor run down time. The rotor consists of a 12.7 mm (0.50 inch) diameter shaft with three attached masses. The midspan disk measures 73.2 mm (2.88 inches) in diameter and 25.4 mm (1.0 inches) in length. The two outboard disks are the bearing journals, and measure 58.4 mm (2.3 inches) in diameter and 25.4 mm (1.0 inches) in length.
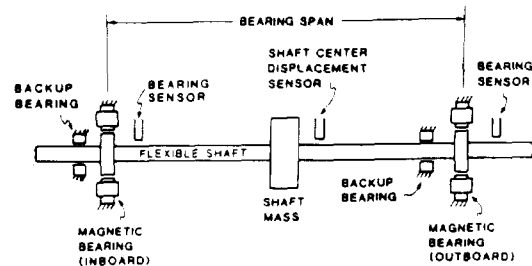
FIGURE 1 - Test Rotor Configuration

The magnetic bearings are eight pole radial bearings, shown in Figure 2. The leg width is 12.7 mm (0.50 inch) for each pole. The stators are constructed of solid soft magnetic iron and the journals are constructed of 0.18 mm (0.007 inch) laminations of non-oriented 3% silicon iron. The bearings have a 1.0 mm (0.039 inch) gap. The feedback system used an analog PD control with a linear power amplifier.

The rotor was decoupled from the electric motor, usually employed to drive the rig. This avoids the friction effects in the motor rolling element bearings. For each test run, a cord was wrapped
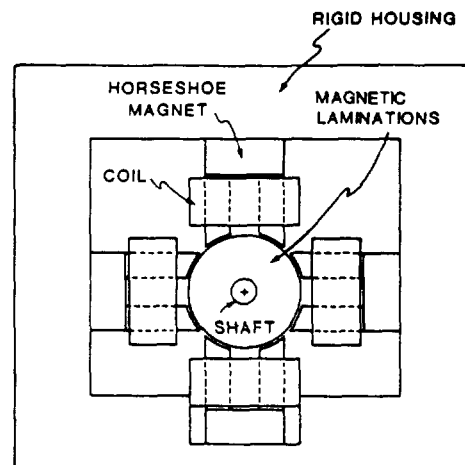
FIGURE 2 - Radial Magnetic Bearing Configuration

165

around the rotor shaft and then pulled off at a rapid rate. The rotor was thus accelerated to a speed somewhat above 2,800 rpm. Then the rotor was allowed to decelerate and measurements of speed vs. time were taken from 2,800 rpm to 90 rpm. Real time run down tests were made and data recorded on tape. From this data, decay rates were calculated and the corresponding total power loss, due to the conversion of kinetic energy of rotation into heat, determined.

No magnetic thrust bearing was used in the system, but reluctance centering due to end effects in the magnetic bearings was sufficient to keep the rotor axially centered. Small axial transients immediately present after a cord pull were manually damped out.

The kinetic energy of the rotor due to rotation is

$$E_k = \frac{1}{2} J \omega^2 \tag{1}$$

This kinetic energy was gradually converted to heat as the rotor decelerated. The power loss is the time derivative of the energy

$$P_k = \frac{\partial E_k}{\partial t} = \frac{\partial}{\partial t}\left(\frac{1}{2} J \omega^2\right) = J \omega \frac{\partial \omega}{\partial t} \tag{2}$$

The speed vs. time measurements were fit with a least squares polynomial of order 2

$$\omega = b_0 + b_1 t + b_2 t^2 \tag{3}$$

and the time derivative evaluated analytically. Time can be treated as a parameter and eliminated. Thus the change in energy vs. speed was calculated from Eq. (2).

EXPERIMENTAL RESULTS

A series of rotor run-down measurements was taken for two parameter studies: bias current effects and pole configuration effects.

Bias Current Effects

Steady state currents, called bias currents, are supplied to all coils in the bearings. Generally, the bias current allows control currents to add or subtract from the bias current and control the rotor dynamic forces. If there was no steady state load due to weight, all bias currents would be set equal and there would be no net steady state radial force acting on the journal. However, there is a vertical load due to the rotor weight so the upper magnets were set at a higher bias current than the lower vertical magnets. The side magnets were set at an equal intermediate bias current. The bias currents in each magnet can be varied within a certain range. Thus, the rotor laminations see a significant flux density change due to alternating N and S pole faces as they rotate. In between the pole faces the flux density is nearly zero. In

166

these tests, the bias currents were set at three different levels.

Figure 3 shows a plot of decay times for the rotor when the bearing was configured as a paired pole (NNSSNNSS) for three bias currents: 1.4, 1.6, and 1.8 amps/bearing axis. It is clear from this data that increasing the bias current increases the decay rate, indicating that the losses are higher. The total run-down time from 2,800 rpm to 90 rpm ranged from a high of approximately 558 sec for the 1.4 amp bias current setting to a low of 413 sec for the 1.8 amp bias current setting.
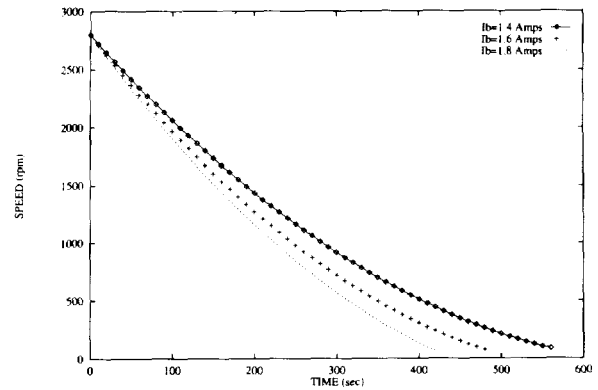
FIGURE 3 - Rotor Deceleration (Speed vs. Time), Paired Pole Configuration (NNSSNNSS)

Pole Configuration Effects

The power losses due to different pole winding patterns were examined. The bearings were configured with both alternating poles (NSNSNSNS) and paired poles (NNSSNNSS). Matsumura and Hataka [6] have measured data which indicated that the two configurations gave nearly the same losses for high speeds, ~ 3000 RPM, but somewhat different losses for lower speeds. The purpose of this test was to compare a different set of magnetic bearing results to their results, as well as to compare calculated losses to measured losses.

Figure 3, from the previous section, showed the run-down times for the bearings in the paired pole (NNSSNNSS) configuration. A second series of tests was run for the same bearing and bias settings with the alternating pole (NSNSNSNS) configuration. A comparison of these results is shown in Figure 4, for a bias current of 1.6 amps/axis. This data is presented in semi-log form to better demonstrate the differences at lower frequencies. It shows that there is essentially no difference between the decay rates in the higher frequency range and some minor, but decreasing, differences in the lower speed range, where the alternating pole configuration decays somewhat faster. The trends in these results agree well with results from Matsumura and Hatake [6].
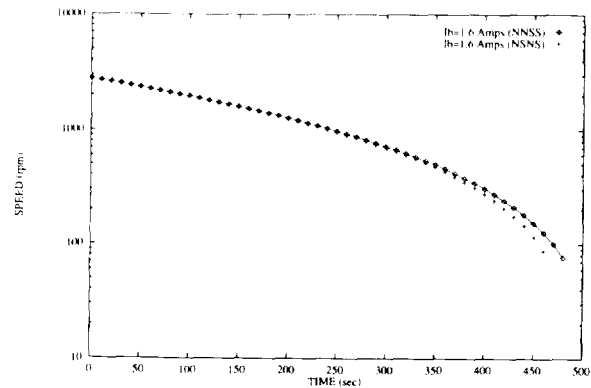
FIGURE 4 - Rotor Deceleration (Speed vs. Time), Paired Pole Configuration (NNSSNNSS) vs. Alternating Pole Configuration (NSNSNSNS)

167

THEORETICAL LOSS MODEL

Iron losses are the sum of two components: eddy current and both alternating and rotational hysteresis losses, which can be expressed as

$$P_I = P_e + P_{ha} + P_{hr} \qquad (4)$$

The individual formulas for these components are given in Appendices A and B.

It is difficult to quantify some of the input parameters to these formulas for the core losses. For example, the effective rotor lamination volume to be employed is not immediately obvious. Therefore it is probably impossible to calculate without a complete finite element analysis, and thus an estimate was made for this study. The numerical value may possibly be different for the hysteresis loss calculations as compared to the eddy current analysis. This is due to differences in the magnetic flux patterns in the rotor. Also the frequency to be employed is subject to much discussion, as is noted in the references. It depends upon the number of flux paths, number of pole faces, etc. The proper frequency might be $2f$, $4f$, or $16f$ (where f is the rotational frequency in Hz) for different loss formulas for the eight pole bearing.

An initial attempt is made in this paper to determine relatively accurate measures of the rotor properties to provide the best loss estimates for magnetic bearings by comparing theoretical formulas to measured data. A windage loss formula, based upon turbulent boundary layer theory, is given in Appendix C. This was employed to calculate the windage loss for the experimental geometry.

COMPARISON OF MEASURED AND CALCULATED LOSSES

The theoretical loss models were used to predict losses based upon several choices of frequencies and effective volumes. Table 1 presents the various calculated results and the measured data for a bias current of 1.6 amps per bearing axis.

All of the calculations in Table 1 were carried out using the equations from Appendices A, B, and C. The predicted power losses are given by

$$P_T = 2 P_e + 2 P_{ha} + 2 P_{hr} + P_w \qquad (5)$$

The factors of 2 are due to the two rotor lamination stacks, one for each bearing. P_w is the total windage loss for the rotor.

As noted earlier in this work, factors which are not easy to determine are the effective volume of magnetic material and the appropriate frequency components. For the iron losses, the volume used was based upon inspection of a finite element calculation of the magnetic flux penetration depth into a typical rotor lamination stack. All of the loss calculations were thus made with an estimate of effective volume equal to 23% of the total journal lamination volume. As seen in Table 1, the error is relatively small with this choice of effective volume.

Calculations were also carried out using the assumption of flux penetrating to a depth equal to the width of a leg. This yields an effective volume of 63% of the total volume, resulting in values which are significantly above the measured values, and are not presented.

Iron losses were evaluated with particular frequencies as well. From an examination of the flux-time patterns in each type of loss, it was believed for the eight pole bearing that the eddy current loss was dominated by a $16f$ component, the alternating hysteresis loss was dominated by a $4f$ component, and the rotating hysteresis was dominated by a $2f$ component (where f is the rotational frequency of the rotor). These values were employed in determining the results shown in Table 1.

A breakdown of the components of the calculated losses is shown in Figure 5 for the case when the bias current equals 1.6 amps per bearing axis. For the relatively low speeds of this experiment the dominant mechanisms are initially the rotating and alternating hysteresis losses. At higher speeds the windage and eddy current losses will dominate.

Figures 6, 7, and 8 show a comparison of the measured power loss for the paired pole configuration (NNSSNNSS) as determined from run-down data by the use of Eq. (2) along with a predicted total power loss for bias currents of 1.4, 1.6, and 1.8 amps/bearing axis in the bearings, respectively. For all three bias current settings the calculated losses were within 16% of the measured losses.

As shown in Figures 6-8 there is good overall correlation between the total calculated and measured power losses in the paired pole (NNSSNNSS) magnetic bearings with the calculated losses ranging between 84% and 101% of the measured power losses.

FIGURE 5 - Calculated Power Loss Components vs. Speed, Paired Pole Configuration (NNSSNNSS) with Bias Current at 1.6 Amps
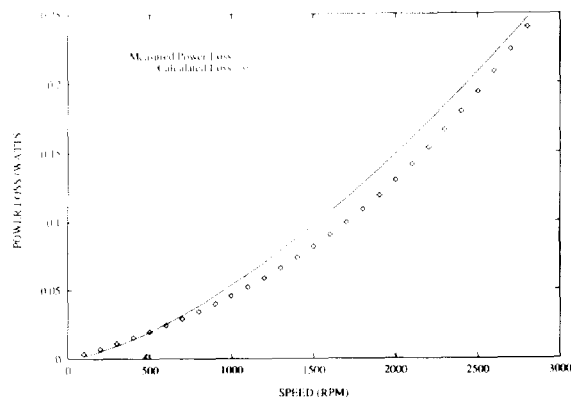
FIGURE 6 - Measured and Calculated Power Loss vs. Speed, Paired Pole Configuration (NNSSNNSS) with Bias Current at 1.4 Amps

Similar calculations were made for the case when the bearings are in the alternating pole (NSNSNSNS) configuration. However, the effective volume for this case is approximately 10% greater than the value used in the paired pole calculations. This is due to the fact that with the alternating pole arrangement, flux emanating from one pole will be attracted towards the opposite pole on the adjacent magnet pair. Therefore, the flux paths bulge towards the adjacent magnet pair and traverse a larger volume, as compared to the paired pole configuration. A comparison of measured and calculated power losses for the alternating pole (NSNSNSNS) configuration for a bias current of 1.6 amps is shown in Table 2. This comparison demonstrates good correlation between the calculated and measured power losses for the alternating pole (NSNSNSNS) configuration.

FIGURE 7 - Measured and Calculated Power Loss vs. Speed, Paired Pole Configuration (NNSSNNSS) with Bias Current at 1.6 Amps
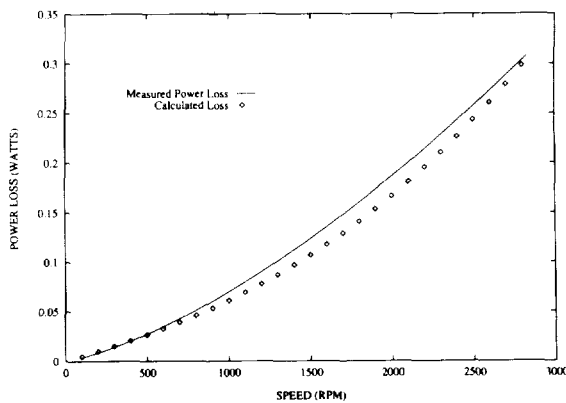
FIGURE 8 - Measured and Calculated Power Loss vs. Speed, Paired Pole Configuration (NNSSNNSS) with Bias Current at 1.8 Amps

LOSS CATEGORY	2500 RPM	1500 RPM	500 RPM
EDDY CURRENT	.0377	.0136	.0015
HYSTERESIS/ ALTERNATING	.0311	.0187	.0062
HYSTERESIS/ ROTATING	.0724	.0434	.0145
WINDAGE	.0763	.0183	.0008
TOTAL CALCULATED	.2175	.0940	.0230
MEASURED	.2376	.1121	.0231
% CALCULATED ERROR	8%	16%	<1%

TABLE 1 - Calculated and Measured Power Loss (watts) vs. Speed in Paired Pole (NNSSNNSS) Magnetic Bearing With Bias Current at 1.6 amps.

LOSS CATEGORY	2500 RPM	1500 RPM	500 RPM
EDDY CURRENT	.0415	.0150	.0017
HYSTERESIS/ ALTERNATING	.0342	.0206	.0068
HYSTERESIS/ ROTATING	.0796	.0477	.0160
WINDAGE	.0763	.0183	.0008
TOTAL CALCULATED	.2316	.1016	.0253
MEASURED	.2395	.1137	.0241
% CALCULATED ERROR	3%	11%	-5%

TABLE 2 - Calculated and Measured Power Loss (watts) vs. Speed in Alternating Pole (NSNSNSNS) Magnetic Bearings with Bias Current at 1.6 amps.

170

CONCLUSIONS

Power loss measurements were made, based on the deceleration rate of a rotor supported in magnetic bearings, for the variation of bias currents, and pole configurations. Measured losses were compared to calculated losses based on classical theory from transformer and electric motor analyses and showed good agreement, within 16%. Results of this study indicate that the proper application of classical power loss equations may adequately predict losses in magnetic bearings at low speeds. Future work includes high speed measurements in a vacuum chamber, further finite element analyses, and a more analytical method for determining the effective volumes and frequencies to use in the analysis.

ACKNOWLEDGMENTS

REFERENCES

1. Yoshimoto, T., "Eddy Current Effect in Magnetic Bearing Model," IEEE Transactions on Magnetics, Vol. MAG-19, No. 5, Sept. 1983.

2. Higuchi, T., Mizuno, T., and Miyake, S., "Experimental Study of Rotational Loss in Magnetic Bearings," Proc. Conf. IPE, Japan, Spring 1986, pp. 53-54.

3. Higuchi, T., et. al, "Experimental Estimation of Rotational Losses of Magnetic Bearings," Spring Conference of Precision, 1988, pp. 86-87.

4. Matsumura, F., Fujita, M., and Ozaki, Y., "Characteristics of Friction on Magnetic Bearings," Trans. IEE of Japan, 108-D, No. 5, 1988, pp 462-468.

5. Ueyama, H., and Fujimoto, Y., " Iron Losses and Windy Losses of Rotational Speed Rotor Suspended by Magnetic Bearings," Proceedings of 2nd International Symposium on Magnetic Bearings, July 12-14, 1990, Tokyo, Japan, pp. 237-242.

6. Matsumura, F., and Hatake, K., "Relation between Magnetic Pole Arrangement and Magnetic Loss in Magnetic Bearing," Proceedings of Third International Conference on Magnetic Bearings, July 29-31, 1992, Alexandria, Virginia, USA, pp. 274-283.

7. O'Kelly, D., "Simulation of Transient and Steady-State Magnetization Characteristics with Hysteresis," Proceedings of IEE, Vol 124, No. 6, June 1977.

8. Lin, C. E, Wei, J. B., and Huang, C. L., "A New Method for Representation of Hysteresis Loops," IEEE Transactions on Power Delivery, Vol. 4, No. 1, January 1989, pp. 413-419.

9. Kasarda, M.E., Allaire, P.E., Hope, R.W., and Humphris, R.R., "Measured and Predicted Losses in Planar Radial Magnetic Bearings," Proceedings of Mag '93, Alexandria, VA, July 1993.

10. Humphris, R. R., Allaire, P. E., and Lewis, D. W., "Design and Testing of Magnetic Bearings for Vibration Reduction," Detection, Diagnosis, and Prognosis of Rotating Machinery, Shives and Mertaugh, Cambridge Univ. Press, Proceedings of the 41st Meeting of the Mechanical Failures Prevention Group, Naval Air Station Test Center, Patuxent River, Md, October 28-30, 1986.

11. MIT Electrical Engineering Staff, Magnetic Circuits and Transformers, Wiley, 1943.

12. Cullity, B. D., Introduction to Magnetic Materials, Addison Wesley, 1972.

13. Matsch, L., Electromagnetic and Electromechanical Machines, Crowell Publishers, 1972.

14. Golding, E. W., Electric Measurements and Measuring Instrumentation, 4th Ed., Pitman Publishers, 1961.

15. Brailsford, F., "Rotational Hysteresis Loss in Electrical Shaft Steels," IEEJ, 1938, pp. 566-575.

16. Knowlton, Archer E., Editor-in-Chief, Standard Handbook for Electrical Engineers, McGraw-Hill Book Company, Inc. 1949.

17. K. Granger, Robert A., Fluid Mechanics, CBS College Publishing, 1985.

APPENDIX A - EDDY CURRENT LOSSES

A formula for the power loss due to eddy currents has been developed by Golding and others [11-14] by integrating ρI^2 over the volume of the magnetic material, where ρ is the material resistivity and I is the current due to the induced emf from the alternating flux. The loss formula for one rotor is

$$P_e = \frac{10^{-16} \pi^2 d^2 B_{max}^2 f^2}{6\rho} \left(watts/cm^3 \right) \tag{6}$$

Here d is the lamination thickness in cm, B_{max} is the flux density in gauss, f is the frequency in Hz, and ρ is in Ω-cm. This relation assumes that the permeability of the material is constant and that the lamination thickness is less than the penetration depth of the eddy currents (skin effects are neglected).

Eddy currents are dominated by the time rate of change in the magnetic field. Thus it is felt that the number of pole face edges that the rotor laminations pass per sec is the proper value for f, 16 times the rotation frequency for this case.

APPENDIX B - HYSTERESIS LOSSES

As noted in the text of the paper, hysteresis losses can be considered as two types: alternating and rotational. Alternating hysteresis loss occurs in iron when the magnetic field alternates at some frequency, from a maximum positive value to a maximum negative value and the loss is proportional to the enclosed area of the hysteretic loop. Rotational hysteresis occurs when the magnitude of the field is relatively constant but its direction changes with respect to the material in which losses are occurring.

The alternating component of the hysteresis losses in a magnetic material is due to the effects of traversing a complete cycle of the BH curve. This occurs in the rotor of a magnetic bearing as it passes the differently polarized pole faces. The kinetic energy of rotor rotation is converted into heat generation. The loss per cycle for one rotor lamination stack is given by the formula from Steinmetz [16]

$$P_{ha} = 10^{-7} \eta f B_{max}^{k} \left(watts / cm^3 \right)$$ (7)

Here the hysteresis coefficient η has a value of approximately 0.00046 for a good grade of silicon iron and the frequency f is in Hz. Also B_{max} is in gauss and k has the value of approximately 1.6 for flux densities in the range of 1500 and 12,000 gauss. It is felt that the proper frequency to use in this formula is the alternating frequency near the surface of the laminations, $4f$ for this eight pole bearing.

The rotational component of the hysteresis loss occurs when the magnitude of the magnetic field is relatively constant but its direction is changed within the rotating magnetic material. This situation occurs below the rotor surface in a magnetic bearing. This loss due to a rotational variation of the flux is different from the loss due to the alternating flux. Experimental curves have been generated [11,15]. For example, interpolation from a curve for a transformer silicon steel, at a flux density of 2000 gauss used in this work, gives, for one rotor lamination stack

$$P_{hr} = 3.60 x 10^{-5} \left(watts / cm^3 - Hz \right)$$ (8)

This value is then multiplied by the effective volume and frequency to obtain a power loss in watts. It is felt that the dominant frequency for this relation is based upon the number of magnetic field rotations experienced by the rotor per sec, 2 times the rotation frequency in this case.

APPENDIX C - WINDAGE LOSSES

Ueyama and Fujimoto [5] achieved good correlation to experimental data of windage loss calculations using a turbulent flow model. Therefore, windage losses on the rotor were calculated based upon the drag force on a turbulent boundary layer as developed by Von Karman and presented in Granger

[17]. For a fully turbulent boundary layer on a flat plate of length $2\pi R$ and width L, the drag force is

$$D = .072 \left(\rho_g \, 2\pi R \, U^2 L \right) \left(\frac{\nu}{2\pi RU} \right)^{0.2} \quad (9)$$

The surface speed, U, is given as $R\omega$, so this expression becomes

$$F_D = 0.144 \, \pi \rho_g \, R^3 L \left(\omega^2 \right) \left(\frac{\nu}{2\pi R^2 \omega} \right)^{0.2} \quad (10)$$

The windage power loss for each disk is

$$P_{w_1} = F_d U = .144 \rho_g \, L \, \pi R^4 \omega^3 \left(\frac{\nu}{2\pi R^2 \omega} \right)^{0.2} \quad (11)$$

and the total power loss is the sum of the losses on the two bearing journals and the midspan disk

$$P_w = 2 P_{Brgs} + P_{midspan\ disk} \quad (12)$$

174

Session 5b – Maglev

Chairman: Michael J. Goodyer
University of Southampton

FAULT TOLERANT COMPUTER CONTROL FOR A MAGLEV TRANSPORTATION SYSTEM*

Jaynarayan H. Lala, Gail A. Nagle
Advanced Computer Architectures Group
The Charles Stark Draper Laboratory
555 Technology Square, MS 73
Cambridge, MA 02139

George Anagnostopoulos, US Dept. of Transportation
Cambridge, MA 02142

SUMMARY

Magnetically levitated (Maglev) vehicles operating on dedicated guideways at speeds of 500 km/hr are an emerging transportation alternative to short-haul air and high-speed rail. They have the potential to offer a service significantly more dependable than air and with less operating cost than both air and high-speed rail. Maglev transportation derives these benefits by using magnetic forces to suspend a vehicle 8 to 200 mm above the guideway. Magnetic forces are also used for propulsion and guidance. The combination of high speed, short headways, stringent ride quality requirements, and a distributed offboard propulsion system necessitates high levels of automation for the Maglev control and operation. Very high levels of safety and availability will be required for the Maglev control system. This paper describes the mission scenario, functional requirements, and dependability and performance requirements of the Maglev command, control and communications system . A distributed hierarchical architecture consisting of vehicle on-board computers, wayside zone computers, a central computer facility, and communication links between these entities was synthesized to meet the functional and dependability requirements of the maglev. Two variations of the basic architecture are described: the Smart Vehicle Architecture (SVA) and the Zone Control Architecture (ZCA). Preliminary dependability modeling results are also presented.

I. INTRODUCTION

Magnetically levitated (Maglev) vehicles operating on dedicated guideways at speeds of 500 km/hr are an emerging transportation alternative to short-haul air and high-speed rail. They have the potential to offer a service significantly more dependable than air and with less operating cost than both air and high-speed rail. Maglev transportation derives these benefits by using magnetic forces to suspend a vehicle 8 to 200 mm above the guideway. Magnetic forces are also used for propulsion and guidance. A combination of factors such as high speed, short headways, stringent ride quality requirements, and a distributed offboard propulsion system make Maglev a unique mode of travel.

Maglev vehicles will travel at a much higher speed than conventional trains and at a significantly higher speed than conventional high speed rail. Although the higher speed increases transportation productivity, it implies more serious consequences if the control system fails to maintain safe train separation. Thus, the response time of the control system must be on a par with the response times of aircraft control systems. Furthermore, achieving a passenger load which makes the system economically viable, requires the shortest

---

headways possible within the limits of safe train separation. This conflict between capacity and safety can be mitigated by the use of a fully automated and validated control system which offers significantly faster response times than one using human operators.

The Maglev control system will be comprised of sensors, actuators, communication links, and computers whose collective activities will be coordinated and directed by control and decision making software. Maglev control systems are required to make many decisions in real-time. The consequences of an incorrect or late decision could be catastrophic. Since human safety is at risk, the automated control systems must work correctly and in a timely manner under all expected operating conditions. Furthermore, since the failure of one part of the system can disrupt travel along an entire route, the control system for Maglev must not only be safe but also highly available.

Since hardware and software are expected to fail at some time during the life of the system, the system must be able to tolerate these faults while maintaining normal operations or, in the exceptional, worst case scenario, fail in a safe manner. That is, the system should continue to function correctly as a whole even when parts have failed. This is referred to as fault-tolerant operation. If this is not possible, the system must be able to systematically shut down in a safe manner, i.e., fail-safe operation.

Under the sponsorship of the US Department of Transportation, a design-for-validation methodology previously developed by Draper Laboratory [1] has been applied to the design of the control computer system for a hypothetical US Maglev Transportation System [2]. Following the key steps prescribed by the methodology, the mission scenario, functional requirements, and dependability requirements of the Maglev command, control and communications system were developed. Performance requirements were then quantified with variations allowing for both electro-dynamic (EDS) and electro-magnetic (EMS) suspensions.

A distributed hierarchical architecture consisting of vehicle on-board computers, wayside zone computers, a central computer facility, and communication links between these entities was synthesized to meet the functional and dependability requirements of the Maglev. Two variations of the basic architecture were developed: in the Smart Vehicle Architecture (SVA) the on-board computer has the primary responsibility for train control and the wayside zone computers provide backup and consistency checking; in Zone Control Architecture (ZCA) these roles are reversed.

A set of qualitative and quantitative evaluation criteria for the Maglev control computer system were developed. A fail-safe communication protocol for the SVA was proposed and used to model and analyze the dependability characteristics of this architecture.

II. MAGLEV MISSION SCENERIO

The first step in the design-for-validation methodology is to develop a concept of operations which defines the mission scenario, including the method of operation and the operational environment, and specifies the computer control functional requirements. The concept of operations presented here is intended to produce a control system which can meet the most rigorously demanding operational requirements of an advanced and fully developed Maglev transportation system. Figure 1 shows various phases of operation of a typical Maglev vehicle during a 24-hour period.

During a stationary pre-run inspection in the maintenance phase, the vehicle performs internal self-checks on all its vital systems. Another use of the maintenance phase is to perform routine periodic maintenance. At this time, the maintenance crew inspects the vehicle, reviews fault logs and conducts the

scheduled diagnostic tests called for by the vehicle life-cycle maintenance program. The interval between these maintenance periods can be adjusted to meet the availability requirement of the vehicle. When necessary, the crew replaces components (Line Replaceable Modules or Line Replaceable Units) identified as faulty. If the testing and normally scheduled maintenance procedures do not identify any major repairs, the crew advances the vehicle to the normal operation phase. Otherwise, the vehicle is taken off-line and moved to a bay or a central repair facility for more extensive depot maintenance.

During normal operation, built-in-test (BIT) maintenance operations are conducted in the background and any detected faults are logged in non-volatile mass memory. The average duration of travel is two hours and twenty minutes, including station stops and post-mission maintenance, for a total of twenty-two hours daily. There is an average of three off-line station stops per mission. Station stops last an average of three minutes, during which time passengers board and leave the train, and additional BIT maintenance is performed. The vehicle has sufficient redundancy in all of its systems to allow it to be dispatched with faults, should those faults occur during normal operation. Of course, there is some minimum complement of components which must be functioning to allow the system to maintain the required level of reliability for a given mission. This is called the minimum dispatch complement (MDC). If faults accumulate such that the MDC is not functioning, the vehicle is not allowed to continue operation as this would expose the passengers and crew to an unacceptable risk of injury. At this point the vehicle would operate in a degraded mode, so as to be able to arrive at the next station for repairs. Redundancy which exceeds the system requirements for safe operation increases the availability of the system by allowing dispatch in the presence of failed components. Furthermore, additional redundancy also enhances the maintainability of the system by deferring repairs until they are normally scheduled to take place in a maintenance facility.

The capacity of each vehicle is 120 passengers. The line speed between stations is 500 km/hour. Vehicles will be dispatched so as to allow a volume of 4,000 to 12,000 passengers per hour to travel along the route. At peak capacity, the headway for each vehicle is approximately 36 seconds or 4 kilometers at 400 km/hour.

Off-line stations offer significant advantages in terms of capacity and flexible schedules required by the inter-city transportation market in the US . An off-line station is essentially a section of guideway built parallel to the main line. A specialized section of the guideway, called the switch, allows a vehicle to be diverted to either the main line or the off-line sections. Navigation of the switch may be accomplished in two ways, referred to as active or passive switching. In so-called passive switching, the guideway simply forms a Y-shape and the vehicle negotiates a route down one fork or the other. In an active switch, a flexible section of guideway is moved from one position to the other, thereby altering the route the vehicle follows. In either case, switching poses a significant burden on the control system both for safety and performance.

The final parameters which can have a significant impact on the architecture of the Maglev control computer system are the ride quality and passenger comfort and the number and distance between wayside zone controllers and safe stopping areas.

The level of ride comfort for normal, non-emergency operations will meet the two hour reduced comfort limits stipulated by ISO-2631. For emergency situations, a deceleration range is allowed, depending on the severity of the situation. When conditions allow, a deceleration of not more than 0.25 g will be used. For extreme situations, for example, when necessary to decelerate to prevent or mitigate a sudden stop, decelerations of up to 0.5 g are allowed.

Between any two stations there are approximately forty wayside zone controllers. The distance between these wayside zones is 2 kilometers. The site of each wayside zone controller also serves as a safe stopping area between stations.
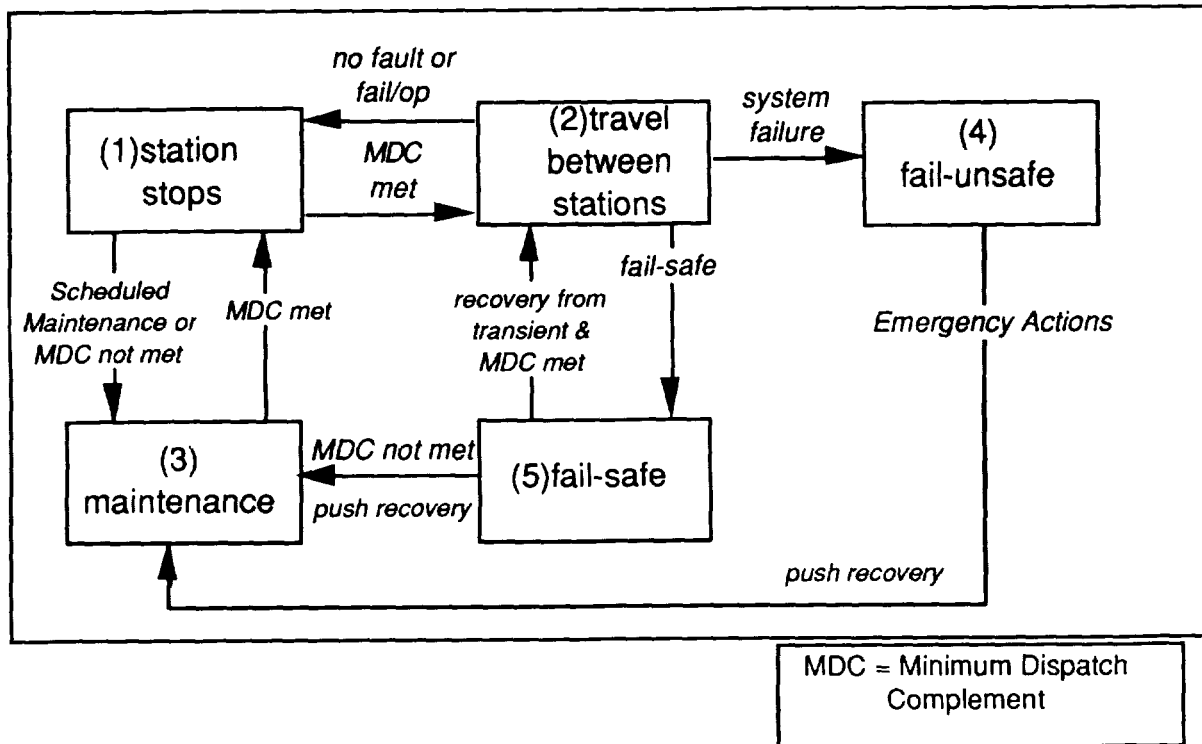
Figure 1. Maglev mission scenario vehicle state diagram.

III. MAGLEV FUNCTIONAL REQUIREMENTS

In order to determine the detailed computational requirements of the complete Maglev system, a set of functional requirements must be specified. Computational requirements include throughput, memory, processing lag, function iteration rate, order dependencies among functions, and I/O and inter-function communication rates. To fully specify the computer architecture for Maglev, constraints imposed on the control computer must also be provided, such as limitations on weight, power and volume.

Guided ground transportation control systems must perform three principal functions: control, protection, and supervision. In a fully automated system, these functions are performed by three main control system components: the onboard control computer, the wayside or zone control computer, and the central control computer. Each system component performs different aspects of each of the three principal functions. Historically, the vehicle control function has been performed by each individual train as it makes its way along the track. Wayside control has performed most of the functions pertaining to route integrity, such as operating the switching mechanisms and setting the maximum speed for a given section of track [4]. This division of tasks, which has been demonstrated to provide a reliable means of safe train separation, follows naturally from the fact the propulsion system which controls the velocity, acceleration, and braking of the vehicle is physically resident onboard the vehicle and the wayside has up-to-date knowledge of the track in its locale. However, the propulsion system for Maglev vehicles is *not* resident onboard the vehicle, but rather housed in stations distributed along the guideway. The design of the Maglev control system must reflect this important difference. The role of the central control computer is to perform the high level planning and coordination functions, such as setting up train arrival and departure schedules as well as scheduling maintenance operations. Central control also plays a role in coordinating the response of the system to an emergency situation. Some aspects of central control may actually be performed by computers located in stations.

Each of the three principal functions which must be performed by the Maglev control system, i.e. control, protection, and supervision, can be decomposed into several well-defined sub-functions. This purely functional analysis of the control system may be used as the basis for the design of a control architecture. By partitioning the sub-functions among the various control elements which make up the system, an optimal design for safety and reliability can be achieved. The functional decomposition of the Maglev control system is presented in Table 1. A quantitative analysis of the computational requirements of each function was performed and these results are summarized below.

Vehicle Control Functions

The vehicle state function is a sensing function which monitors the vehicle position, travel direction, speed, and acceleration. The velocity control function causes the speed and direction of travel of each vehicle to match the speed mandated by its travel profile (determined by the route planning and scheduling functions) in accordance with the existing conditions on the guideway. The velocity control must coordinate the activities of the individual propulsion power units in the guideway, which are nominally spaced at 2 km intervals along the guideway. Closer spacing of power units provides finer granularity of control for additional cost.

The levitation control for the EMS design consists of controlling the gap (about 8 mm) between the levitation magnets and the guideway at about 100 Hz. This is accomplished by controlling the current flow in the onboard electromagnets, which in turn determines the attractive magnetic force between the vehicle electromagnets and the guideway ferromagnets. For the EDS design, the gap does not require active control. However, the temperature of the superconducting onboard electromagnets needs to be carefully monitored and maintained at about 5° K. If the temperature rises above this value, quenching will occur leading to a loss of magnetic force.

Table 1. Maglev Control System Functions

CONTROL	PROTECTION	SUPERVISION
Vehicle State	Safe Vehicle Separation	Route Planning
Velocity Control	Vehicle Position Control	Route Scheduling
Levitation Control	Route Integrity	Dispatching
Lateral Position Control	Emergency Stopping	Maintenance Scheduling
Propulsion Control	Emergency Speed Control	Operator Interface
Secondary Suspension Control	Emergency Position Control	Status Displays
Route Control	Emergency Response	Passenger Supervision
Vehicle Systems Monitoring	Failure Management	
Vehicle Systems Control		
Environmental Monitoring		

For lateral position control (EMS design) the gap between the lateral guidance electromagnets and the guideway must be actively controlled in the same manner as for the levitation magnets. For the EDS design, the temperature of the superconducting guidance magnets must be maintained in the same manner as that of the temperature control of the levitation magnets.

Propulsion is achieved by the use of a linear synchronous motor made up of conducting windings, installed along the length of the guideway, and variable frequency converters which, together with the necessary switch gear, are located at sites distributed along the guideway. Each power unit can control the motion of a vehicle along a section of guideway called a zone. The speed of the vehicle within a zone is controlled by varying the frequency of a traveling electromagnetic field produced in the stator windings of the guideway by the power electronics system.

The purpose of the secondary suspension system is to provide a satisfactory level of ride comfort to passengers in the vehicle. EDS systems which possess a fairly stiff primary suspension require an actively controlled secondary suspension to achieve a satisfactory level of ride quality. For EMS systems, active control may not be necessary but could be provided to enhance the overall smoothness of the ride and offset jerk due to sudden accelerations and lateral motions induced by turns and cross-winds. The secondary suspension can be provided by a combination of actively controlled aerodynamic surfaces and actively or passively controlled dampers.

The route control function guides the vehicle through one of two possible paths at switching points in the guideway as indicated in the route profile. If an active switch is employed, the switching mechanism must be engaged at precisely the right moment to allow adequate time to detect a possible mechanical failure and safely stop an approaching vehicle. Designs of passive switches vary greatly but all require control of either an electrical or mechanical subsystem with similar timing and verification requirements to those of an active switch.

Onboard systems such as lighting, temperature, air flow, secondary braking capability, charge level of onboard batteries, and door position control are monitored and adjusted periodically. Environmental conditions such as the electromagnetic field strength at various positions in the coach, lateral wind speed and direction and external temperature are measured periodically. Advance weather information is collected.

Vehicle Protection Functions

These functions provide a fail-safe mode of operation. They can override the actions of the vehicle control functions and take control of a vehicle which has exceeded some safety threshold.

The safe separation function is responsible for ensuring that a minimum spacing of 4 km or 2 zones is maintained between any two consecutive vehicles on the guideway. The route integrity function monitors the integrity of the guideway and the propulsion and levitation coils. The guideway must remain properly aligned and free from hazards such as ice, litter, animals, etc. The emergency stopping function is employed when the primary braking capability of the linear synchronous motor provided by the guideway has failed. Secondary braking is accomplished by a combination of aerodynamic braking from either the trailing flap or a parachute, eddy currents, and friction after the vehicle has contacted the guideway.

The emergency speed control function is employed when the propulsive force provided by the guideway has failed. Sufficient energy must be available from batteries and the linear generators (which operate only while the train is moving) to control levitation, braking, and other loads. The vehicle is only allowed to stop at areas deemed safe stopping areas. A safe stopping area provides a means of safe evacuation of passengers from the vehicle. The emergency position control function determines the exact stopping point for a vehicle in an emergency stopping situation. Information about safe stopping points is maintained for each zone along the guideway.

182

Vehicle Supervision Functions

Supervision functions include route planning, scheduling and dispatching vehicles on these routes, displays of vehicle status, position, and velocity, weather displays, etc. A detailed discussion of these functions can be found in [2].

Computational Performance Requirements

A quantitative analysis of each of the computer control functions was performed to determine the computer performance required to do all of the Maglev functions. Estimates were made of such parameters as the iteration rate, throughput, memory, sensor data, frequency of reading sensors and outputting actuators, etc. for each function. These estimates were aggregated to help size the computer and communication links. A detailed discussion of the performance requirements is outside the scope of this paper due to space limitations but can be found in [2]. However, in summary, we can state that 10 to 15 MIPS throughput, 20 to 25 Mbytes of on-line memory, about 5 to 10 Mbits/sec of I/O bandwidth, and a 100 Hz iteration rate for the highest frequency control tasks would be sufficient to not only perform the functions identified here but also allow for about 50% growth margin. These requirements are well within the state-of-the-art of current microprocessors. If performance requirements were the only driver, the design of the Maglev control computer system would be a fairly straightforward task. However, it is the dependability dimension as well as validation of the system which makes the design a challenging task. These requirements are discussed next.

IV. MAGLEV DEPENDABILITY REQUIREMENTS

Dependability is defined as the trustworthiness of a computer system such that reliance can justifiably be placed on the service it delivers [5]. Reliability, availability, and safety are some of the attributes used to quantify the dependability of a system.

The reliability requirement, stated as a probability of failure, for the system control software, and presumably for the hardware upon which it executes, for commercial Maglev transportation, as specified in the draft Maglev System Parameters [3], is 10^{-9}. This requirement is based on the commercial transport flight control requirements mandated by the US Federal Aviation Administration (FAA). Those requirements pertain to a 10-hr commercial passenger flight.

It should be noted that for aircraft, the terms reliability and safety are used interchangeably as far as the flight-critical controls are concerned. This is due to the fact that the failure of a flight-critical computer is always assumed to result in a catastrophic aircraft failure if there is no backup system. In other words, for flight control computers, there is no fail-safe state. Hence, the reliability of the system, i.e. the probability that it will operate correctly over a given time interval, is equal to the safety of the system, which is the probability that it will operate correctly or fail in a safe manner. This is not necessarily the case for Maglev. If the control computer on-board the vehicle were to fail, it may not always lead to a catastrophic vehicle failure. For example, the computer may fail-stop and the vehicle may coast to a stop on the guideway. Or, the computer may cause the vehicle to exceed the speed limit which may be detected by a wayside computer which, in turn, may not turn the power on to the next section of the guideway resulting in the safe stopping of the vehicle. Thus, there are several alternatives available to bring a Maglev vehicle to a safe stop in the absence of a functioning on-board computer which are not available to an aircraft in flight. For these reasons, the safety and the reliability requirements for Maglev must be distinguished. In particular, the reliability requirement stated above for a commercial transport aircraft becomes the safety requirement for Maglev vehicles, which then may be specified as follows:

"The maximum acceptable probability of failure of the (safety-critical) computers is 10^{-10} per vehicle per hour of operation."

This requirement applies to the total computer system, including the hardware and software of the onboard vehicle, wayside and central control facility computers. The reliability requirement for Maglev relates to the probability of successfully completing a trip and a reasonable value for not completing a trip due to computer system malfunction is 10^{-6} per vehicle per hour.

The overall reliability and safety requirements for Maglev may be illustrated as follows. If 1 billion trips, each of 1 hour duration, were undertaken by a fleet of Maglev vehicles, then all except 1000 trips should be completed successfully. Of the 1000 trips in which the vehicles did not arrive at their destination without incident, only 1 would result in a catastrophic accident. If we assume that Maglev trains have the same number of scheduled departures per day as airplanes in the US, i.e. 14,000 per day, and that each trip averages one hour, these 1 billion trips will take approximately 195 years. Over that period of time, in a system which met the stated reliability and safety requirement, there would only be five incomplete trips per year and a total of one catastrophic accident attributable to the failure of the control computer system.

The availability of the Maglev transportation system is going to play a very important part in the public's acceptance of this mode of transportation. For the domestic US commercial airlines, the availability of the airliners approaches or exceeds 99 per cent. Less than 1 per cent of the flights are delayed or cancelled due to mechanical, electrical, hydraulic or other aircraft system related failures. It is obvious that the Maglev transportation system will have to match or exceed this level of dependability in order to be accepted by the public. A reasonable availability requirement for Maglev may be specified as follows:

" The maximum acceptable probability of not being dispatch ready for a trip for each Maglev vehicle will be 10^{-2}."

This requirement applies to all the subsystems on-board each vehicle. The unavailability apportionment for the control computer subsystem is assumed to be one tenth of this, or 10^{-3} per vehicle per trip. That is, only one tenth of the unavailable vehicles will be stuck due to on-board control computer system failures.

V. MAGLEV CONTROL SYSTEM ARCHITECTURE

Section III presented the principal functions to be performed by the Maglev computer control system: control, protection, and supervision. These functions can now be mapped to specific computation sites within the overall control computer architecture.

The overall Maglev control architecture is distributed and hierarchical. Its principal subsystems are an onboard vehicle computer system for each vehicle, a wayside zone computer system for each zone, and a central facility computer system as shown in Figure 2. Two basic architectures, which represent extremes of a continuum, are presented here.

In the Zone Control Architecture (ZCA), the primary responsibility for vehicle control rests with the wayside zone control computers, with the onboard system providing backup and consistency checking. Vehicle protection is distributed among the three subsystems. In the Smart Vehicle Architecture (SVA), the onboard computer has the primary responsibility for vehicle control, with the wayside zone computers providing backup and consistency checking. The functions relating to vehicle protection are again

distributed among the three subsystems. The function-subsystem mapping for these architectures is shown in Table 2. In this table, **P** signifies the primary assignment, **B** signifies the backup assignment used for verification and consistency checking, and **I** represents local access to information in a database.

In both architectures, the vehicle protection subsystem operates independently from the vehicle control functions, and therefore provides a fail-safe mode of operation. In cases where the speed or position of a vehicle exceeds safety thresholds, these protection functions can override the actions of the control functions and assume control of the vehicle. The supervision function is performed by the central facility computer system, which also includes major computing subsystems located in stations. However, the supervisory data such as the travel or route profile for a given vehicle which is needed by the primary control computer to adequately perform its function is transferred to that computer on at least a daily basis and may be updated more frequently. This form of operation views all normal train travel as planned in advance and all passengers riding in reserved seats. However, either architecture could be adapted to a demand driven schedule which requires more real-time planning capability.

In general, those functions which can best be performed in one site over another are assigned to those sites. For example, the control of levitation, guidance, secondary suspension, and onboard systems like air conditioning and lighting all require the control of onboard actuators. Furthermore, the sensors needed to obtain feedback information for these systems are also onboard. Hence, the control of these functions should be performed by an onboard computer. Other criteria used to assign functions to particular computational sites include minimization of communication and data latency, minimization of adverse effects of failures of communication links and processors, and ability to validate the architecture. Functions which can be performed by an onboard computer with a minimum of communication overhead is that of emergency stopping, emergency speed control, and emergency position control. The emergency which these functions are intended to address is the failure of the guideway propulsion and primary braking capability. The power for these emergency operations comes from batteries carried onboard for that purpose. The vehicle must be able to reduce its speed, continue onto a safe stopping area and stop there so that passengers can disembark safely from the vehicle and the elevated guideway.
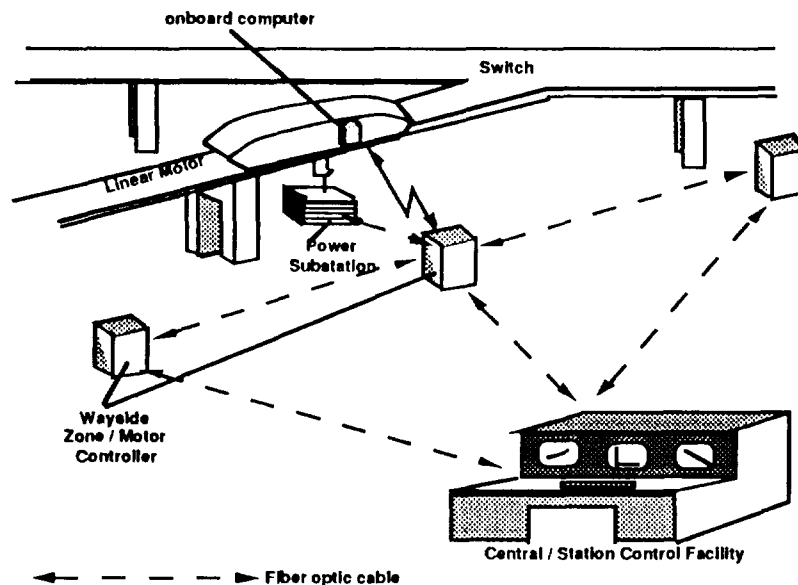
Figure 2. Maglev control computer architecture.

185

C-3

Table 2. Function Assignment for the Zone Control Architecture and the Smart Vehicle Architecture

	ZONE CONTROL ARCHITECTURE			SMART VEHICLE ARCHITECTURE		
	Onboard	Wayside	Central	Onboard	Wayside	Central
CONTROL						
Vehicle Location	B	P		P	B	
Velocity Control	B	P		P	B	
Levitation Control	P			P		
Lateral Position Control	P			P		
Propulsion Control		P			P	
Secondary Suspension Control	P			P		
Route Control	B	P		P	B	
Vehicle Systems Monitoring	P			P		
Vehicle Systems Control	P			P		
Environmental Monitoring	B	P		P	B	
PROTECTION						
Safe Vehicle Separation	B	P		P	B	
Vehicle Position	B	P		P	B	
Route Integrity	B	P		P	B	
Emergency Stopping	P	B		P	B	
Emergency Speed Control	P	B		P	B	
Emergency Position Control	P	B		P	B	
Emergency Response			P			P
Failure Management			P			P
SUPERVISION						
Route Planning		I	P	I		P
Route Scheduling		I	P	I		P
Dispatching		I	P	I		P
Maintenance Scheduling			P			P
Operator Interface	P		P	P		P
Status Displays	P		P	P		P
Passenger Supervision	B		P	B		P

The rationale behind the ZCA is that, unlike conventional transportation systems in which the mechanism for vehicle propulsion is resident onboard, the Maglev system is powered from the guideway. The propulsion control must be co-located with the power converters, i.e. within the same zone control computers, since the required iteration rate is so high as to preclude any communication latency. Since the wayside zone controllers must communicate with each other to coordinate the speed of the vehicle as it passes from one zone to the next, they can also perform the function of safe vehicle separation and vehicle position which are related to vehicle speed. The communication between wayside systems can be carried out through very reliable media such as redundant fiber optic links. By locating sensors in the guideway,

the vehicle location and route integrity functions can also be performed by the wayside using sensors embedded in or alongside the guideway for these purposes. Route control, or the direction of the vehicle through a switch, can also be performed from a wayside computer, especially if the switching mechanism is that of a moveable section of guideway. The ZCA most closely resembles conventional railway control systems without the attendant communication overhead that characterizes systems controlling onboard propulsion from the wayside [4].

The rationale behind the SVA is that an autonomous vehicle can most easily direct its own motion since it is in a position to obtain information about its own state and the state of its surroundings. It must be able to perform these functions for emergency purposes anyway. Hence, it may as well perform them for normal operations. It can easily communicate speed commands to wayside propulsion control systems using radio communication. Information about its speed, position, and acceleration are also easily obtained from a combination of a Global Positioning Satellite System and low cost Inertial Navigation Systems such as those based on micro-mechanical instruments, the technology for which will be available by the time the U.S. Maglev Transportation System reaches the prototype development stage. With information about its position and speed, it can perform the functions of safe vehicle separation and vehicle position control by communicating with vehicles both ahead of it and behind it on the guideway. By using onboard sensors, it can also perform route integrity checks both for alignment and obstacle detection. Furthermore, it can easily direct its movement through switches, i.e. perform route control operations, especially if the switches in use do not involve moveable sections of guideway but rather some vehicle-borne steering mechanism. The SVA most closely resembles the most advanced control systems being installed on conventional and high speed rail systems [4].

In order to determine the relative strengths and weaknesses of each architecture, a quantitative analysis must be performed. The dependability analysis of the onboard control computer for the SVA architecture is presented in the next section. The remaining analyses, namely the dependability analysis of the other components in the SVA and the ZCA and the performance analyses of both architectures, are planned for the next phase of this study. Additionally, life cycle cost also should be used as an evaluation criterion. Components contributing to life cycle cost include not only the initial acquisition cost of hardware and software but also the cost of validating and certifying the hardware and software for safety and the cost of maintaining the system over its life time.

VI. PRELIMINARY DESIGN SPECIFICATION OF THE SVA ONBOARD CONTROL COMPUTER

For the US Maglev Transportation System Onboard Control Computer (OCC), a baseline system using a Fault Tolerant Parallel Processor (FTPP) has been selected. The architecture of the Fault Tolerant Parallel Processor (FTPP) developed by Draper Laboratory was conceived to serve applications with requirements for ultra-high dependability and real-time performance. The FTPP architecture is described in references [6] and [7]. It is composed of many Processing Elements (PEs) and a few specially designed hardware components referred to as Network Elements (NEs). The multiple Processing Elements provide a parallel processing environment as well as components for hardware redundancy. The group of Network Elements acts as the intercomputer communications network and the redundancy management hardware. The FTPP architecture has been designed to accommodate up to 5 NEs and 40 PEs in a single cluster. PEs can be configured in triply or quadruply redundant virtual groups or virtual processors. Since a single state-of-the-art microprocessor provides adequate throughput for the present application, the FTPP is not used as a parallel processor here.

For the baseline OCC an FTPP with one triplex Virtual Processor (VP) and one simplex spare has been selected. The selection of this minimal system is based on the minimum redundancy level needed to mask hardware faults in real-time without suspending time-critical application tasks. If the baseline system falls short of the Maglev RMAS requirements presented in Section IV, additional processing elements

(PEs) and/or Network Elements (NEs) will be added as necessary. For the purpose of the present analysis, the processing elements will be Motorola 68040s which are directly compatible with the VMEbus-based network elements. This baseline system will be modeled for safety, reliability and availability in Section VII.

A brief review of the definitions of safety, reliability, availability, and related terms for the onboard computer is presented in Appendix I since they are particularly important to the following discussion and analysis.

OCC Functionality and Dependability Requirements

The functions performed by the onboard control computer were listed in Table 2. Although velocity and position of the vehicle are directly controlled by the wayside zone control computers (ZCCs), the vehicle itself monitors its precise position and velocity and determines its own speed profile based on existing conditions onboard, in its present zone, and in the system as a whole. The requested velocity is sent as a command via a radio communication link to the wayside zone control computer for the zone in which it is traveling. The iteration rates, throughput, memory, and I/O bandwidth requirements of the OCC ensemble of functions are well within the capabilities of the 68040-based processor board such as the MVME-167 with adequate margins allowed to perform operations for fault tolerance and redundancy management.

Since most of the functions performed by the onboard computer are safety-critical, the inability to perform these functions reliably constitutes an unsafe condition and requires that the vehicle be brought to a stop. However, the vehicle has no onboard mechanism which it can apply directly to stop itself in an emergency. Thus, it must communicate the command to stop to the wayside zone control computer (or the central control computer if the ZCC has failed), which can control the braking mechanism that can bring the vehicle to a stop. Every unsafe condition must be detected and cause a stop command to be issued. However, due to the redundant nature of the system, every fault does not create an unsafe condition. For example, as long as at least two channels of the OCC are operating correctly, safe operation of the onboard control computer is assured. Thus, if one of the three channels of a triplex OCC were to fail, the remaining two channels can continue to operate the vehicle safely.

A failure mode which poses a special problem for reliability (as distinct from safety) is the potential ability of a failed channel to generate an unnecessary stop command, a so-called false alarm. If safety were the only consideration, false alarms would not present a problem. However, false alarms drive down the reliability of the system by increasing the number of unsuccessful missions. In addition, false alarms also reduce the availability of the system as a whole. A disabled vehicle on the guideway renders the guideway unavailable to other traffic until it is removed. Such an event reduces the availability of the guideway.

What is needed is the guaranteed ability to stop safely when continued operation would be unsafe, as well as the ability to prevent false alarms from triggering unnecessary stops. The design discussed below operates in just that way.

OCC Architecture

Figure 3 shows a block representation of the FTPP-based onboard control computer. Three processing elements, designated T_A, T_B and T_C in the figure, form the fault tolerant virtual processor (VP) which conducts the onboard control functions. The fourth PE, designated S_1, acts as a spare. For simplicity, the four Network Elements (NEs) are not shown in the figure. Each Processing Element (PE) is connected to an I/O bus through a specialized interface called the monitor interlock. The redundant I/O

busses are identical. The sensors and actuators needed to perform all of the onboard control functions are attached to these busses, including the radio transmitter used to send velocity/stop commands to the wayside zone controller. Only one channel actually transmits a message to the zone controller. The VP decides which channel this will be.

The purpose of the monitor interlock is to prevent a channel or transmitter which has failed in an active manner from flooding the system with false messages, i.e. the monitor interlock transforms active faults into passive ones. It operates by turning off the power to the failed channel or to its I/O bus.
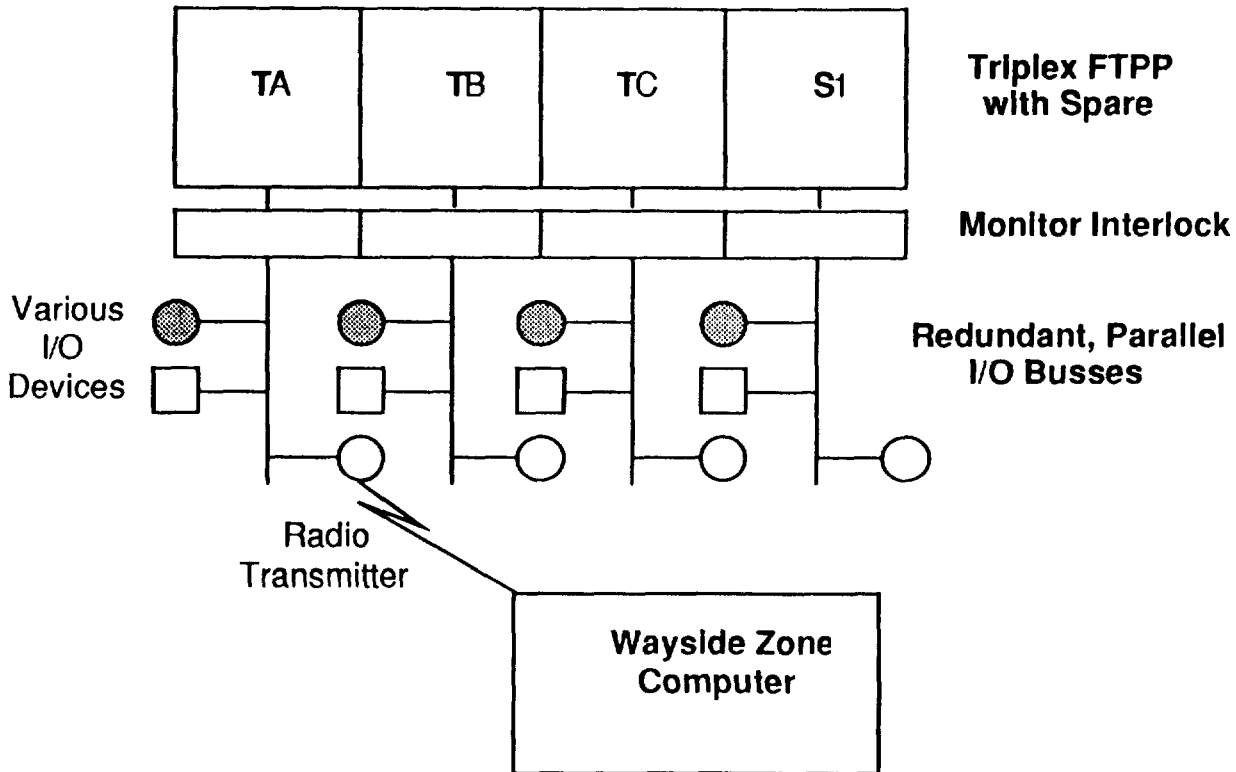
Figure 3. Block diagram of FTPP-based OCC architecture.

Spare PEs or NEs can be used in the OCC to increase availability. Activating a spare is a form of automated repair called reconfiguration. Although the time required to effect this type of automatic maintenance is only on the order of one second, it is still a relatively long period of time to suspend the vehicle control application which typically must execute every 10 milliseconds. Hence, for this analysis, it is assumed that reconfigurations of this type only occur when a vehicle is stopped at either a station or on the guideway following an emergency stop. If modelling shows the reliability of the triplex system is inadequate, the baseline system will be upgraded to a quadruplex FTPP (4 PEs) with 5 NEs and one spare PE.

OCC-Zone Controller Communication Protocol

The communication protocol followed by the onboard and wayside zone computers is designed to prevent false alarms while guaranteeing that every real alarm condition in the OCC results in the transmission of a stop command. It operates as follows. Periodically, the vehicle transmits a *well-formed*

message (WFM) to the wayside zone controller. The specification of a well-formed message is presented below. The maximum allowable time period between a vehicle's transmission of two consecutive well-formed messages is denoted τ_1 in Figure 4. If the zone controller receives a well-formed message from the vehicle, it replies with an acknowledgement within a bounded period of time. The maximum allowable time between a zone controller's reception of a WFM and the OCC's reception of the acknowledgement is denoted by τ_0 in the figure. Since the time between the transmission of a message by the OCC and its reception by the ZCC is very small relative to the values of τ_1 and τ_0, these events can be considered as occurring simultaneously.

These time-out periods are important because the absence of either an expected message or an acknowledgement by either side within the time-out period results in a corrective action. When the corrective actions do not produce the required response, a potentially unsafe condition exists and results in an emergency stop. Thus, if the ZCC does not receive a WFM within a small multiple of τ_1, it assumes that the OCC is in an unsafe condition and so performs an emergency stop. Similarly, if the OCC does not receive an acknowledgement from the ZCC within τ_0 after transmitting a WFM, it assumes that the outgoing message has been corrupted and performs some recuperative action such as switching to another transmitter and retransmitting the message.

The format of a well-formed message transmitted from an OCC to a ZCC is shown in Figure 5. The message consists of a data field and an authentication field. The data field carries the velocity command and other information which the zone controller uses to propel the vehicle at the indicated speed as well as some information specific to the fail-safe communication protocol. The authentication field consists of N 64-bit subfields whose value is uniquely determined as a function of the current message and the channel of the FTPP which generated the value. Each subfield is called the signature of its channel. Each channel of the FTPP is able to generate a unique, unforgeable signature for use by the wayside zone controller in authenticating a message, and, for a given message, no channel can generate the signature of another channel. Prior to transmitting the WFM to the ZCC, each non-faulty channel of the OCC signs the outgoing message and delivers it to the designated transmitter over the OCC's interchannel communication links. Since N is the redundancy level of the onboard VP, $3 \le N \le 5$. Thus for the baseline system N = 3. Details regarding the subfields in a WFM and their use in the protocol can be found in [2].

OCC-Zone Controller Communication Protocol Operation

One further aspect of the protocol involves the number of onboard radio transmitters and receivers which participate in message passing. While each I/O bus contains a radio transmitter, at any given time only one onboard transmitter is used to send a message. Hence, the wayside zone controller only needs to process a single message. To provide the designated transmitter channel with the capability to append the appropriate authentication fields to the message to be transmitted to the ZCC, each channel independently calculates its signature and provides it to the designated transmitter over the OCC's inter-channel communication links. However, the radio receivers in all onboard channels listen for the acknowledgement. If an acknowledgement is not received by a majority of the channels' receivers within a specified timeout period after transmission of a WFM, the message is retransmitted from another transmitter. Other fail-safe mechanisms are in place to deal with failures of the ZCC. These include the ability of neighboring ZCCs to act as backups for each other as well as the ability of the central control computer to bring any vehicle to a stop anywhere along the guideway. The details of these mechanisms are beyond the scope of this analysis but must be specified before the fail-safe design of the system can be considered complete. Similarly, if the zone controller does not receive a WFM from the onboard system within a specified timeout period (such as some multiple of τ_1 seconds), it initiates an emergency stop procedure.

190
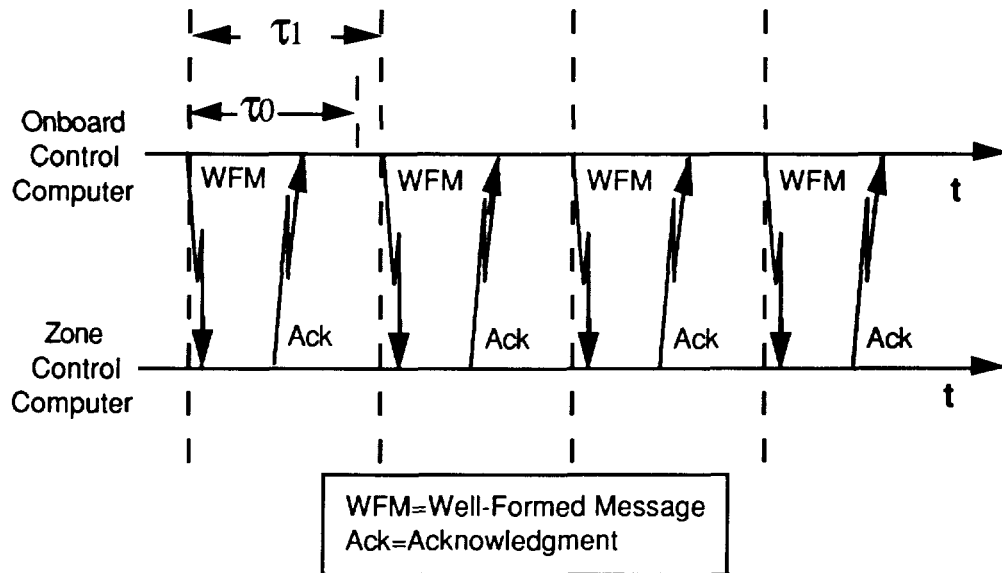
Figure 4. Timing relationships for fail-safe communication protocol.
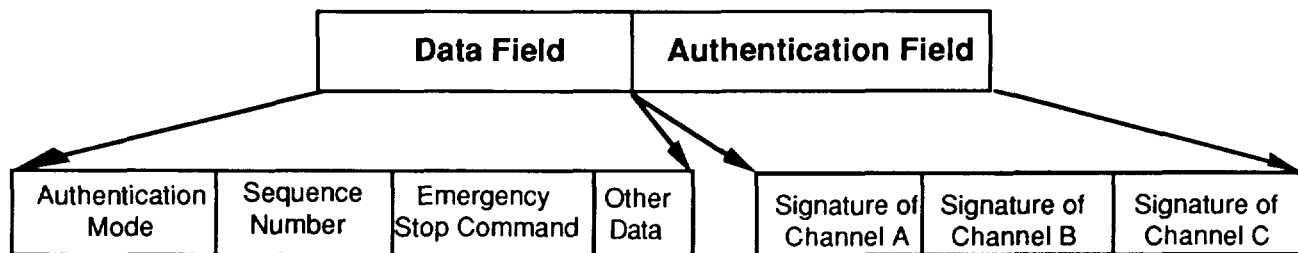
Figure 5. Format of a well-formed message for the fail-safe communication protocol.

To see how this works consider the following scenarios. Suppose that the onboard computer considers that channels A, B and C are working, and that the transmitter connected to channel C is designated to transmit radio messages to the ZCC. Thus, the message contains an authentication mode of ABC. Now suppose that C fails and transmits a stop command. The wayside zone controller would detect this as a false alarm since at most one authentication field (C's) would be valid. (Recall that C cannot forge the signatures of other channels.) This message will not be acknowledged by the ZCC within the timeout τ_0, causing the onboard computer to retransmit a message from another channel, channel B for example, which is not failed and which therefore does not contain a false emergency stop command. Note that this message contains valid digital signatures from channels A and B, thus meeting the requirements for a WFM emanating from a triplex OCC. Thus, the failure of one channel does not trigger an emergency stop. As long as two channels continue to operate, messages are authenticated with the valid signatures of the two working channels.

Furthermore, the OCC's local fault diagnosis function can now update the authentication mode in the first WFM which is sent after the failure is detected to indicate that the OCC is now operating in a duplex mode. Thus the authentication mode field now contains the value AB. Next suppose that channel B, the designated transmitter in this scenario, fails. Either B attempts to transmit messages that are not well-formed or ceases transmission altogether. In either event the ZCC will shut down the vehicle after expiration of the timeout. Alternatively, A can detect B's failure and send an emergency stop message.

Since this message has only one authentic signature, that of channel A, the vehicle is brought to a stop by the ZCC as required by the communication protocol. If, for some reason, A's message does not get through, the ZCC will not get a WFM, the timeout period will expire, and the vehicle will also be brought to a safe stop. Finally, if B fails such that it sends a "false-alarm" emergency stop message which has only one valid authentication signature and hence is not a WFM, the vehicle is again safely brought to a stop by the ZCC. Stopping at this point is a correct action since, by definition, B has failed leaving only a working simplex, namely channel A, in the system.

VII. SVA ONBOARD CONTROL COMPUTER DEPENDABILITY ANALYSIS

The primary objective of the dependability analysis is to produce a first order estimate of the safety, reliability, and availability of the baseline SVA Onboard Control Computer. Additionally, it is desirable to specify a system which is cost-effective by not allocating more redundancy than needed to meet the RMAS requirements, i.e. to determine the Minimum Dispatch Complement (MDC) and to determine the spare components needed to meet the availability requirement with a reasonable maintenance schedule.

The mission state diagram for the Maglev vehicle, shown in Figure 1, was used to construct a detailed Markov model for reliability and safety. Of special interest are the fail-safe and fail-unsafe states. There are only two events which can drive the system to a fail-unsafe state: coincident hardware faults and common mode failures. The probability of the former is addressed below. The probability of the latter cannot be stated with certainty; however, it can be reduced by various avoidance, removal and tolerances techniques. A system failure which results in a fail-safe state does not necessarily require push-recovery to rescue the vehicle. If the failure occurs as a result of a transient fault, which is by far the dominant failure mode, the system may be restarted and the mission completed, albeit not on schedule. It has been noted that the public can accept outage times of short duration (a few minutes), but outages longer than an hour have a very negative impact. Hence this ability to recover from transient faults is very important to public acceptance of Maglev.

The details of the Markov models, the underlying assumptions about component failure rates, fault detection and recovery rates, etc. as well as the dependability evaluations of all the configurations analyzed are beyond the scope of this paper. These details can be found in reference [2]. Only a summary of the results of the dependability modeling effort is presented here.

Reliability and Safety

The reliability and safety of the baseline triplex OCC as well as a quadruplex version, for a single mission, were evaluated with and without transient fault recovery. The advantage of not recovering from transient faults is that exposure to coincident faults during the transient recovery period is avoided. The disadvantage is that unreliability due to exhaustion of redundancy is not minimized. In the second policy, the OCC attempts recovery from transient faults, which reduces the unreliability due to exhaustion of redundancy but increases the exposure to coincident faults during the recovery period.

Two kinds of safe shutdowns are possible under a no-transient-recovery redundancy management policy: "soft" shutdown and "hard" shutdown. If a fault is transient, the vehicle is stopped, the OCC re-initializes itself and resumes operation as a fault tolerant controller, and the vehicle is restarted. This is a soft shutdown. Thus this state does not contribute to vehicle unreliability, although it will contribute to a late arrival at the destination station. In the hard shutdown states, the OCC has shut down due to permanent faults and cannot re-initialize itself and resume operation as a fault tolerant controller, so this state does contribute to vehicle unreliability. External activity such as a tow or physical replacement of an OCC component is required before the vehicle can be cleared from the guideway. Finally, in the "unsafe failure" category, the OCC is unable to safely control or shut down the vehicle.

The Markov models were evaluated for mission times ranging from 1 to 5 hours using the values for the failure and reconfiguration rates shown in Table 3. The results, for a mission time of 2.5 hours, are presented in Table 4.

Table 3. Failure and Reconfiguration Rates

Rate	Value
Permanent Failure Rate, λ_p	1×10^{-4} per hour (10,000 hours MTBF)
Transient Failure Rate, λ_t	1×10^{-3} per hour (1,000 hours MTBF)
Reconfiguration Rate From Permanent Faults, μ_p	5.5×10^6 per hour (20 msec)
Reconfiguration Rate From Transient Faults, μ_t	2.8×10^4 per hour (1 sec)

Table 4. Reliability and Safety of Triplex & Quadruplex OCC

Configuration	Probability of Soft Shutdown	Probability of Hard Shutdown	Probability of Unsafe Failure
No Transient Recovery			
Triplex	1.2×10^{-5}	2.5×10^{-6}	2.6×10^{-12}
Quadruplex	4.2×10^{-8}	9.9×10^{-10}	5.3×10^{-12}
With Transient Recovery			
Triplex	0	1.3×10^{-6}	4.7×10^{-10}
Quadruplex	0	3.5×10^{-10}	9.4×10^{-10}

When the triplex OCC is operated without transient fault recovery, the dominant failure mode is soft shutdown. Since soft shutdowns are caused by transient fault accumulation, the OCC can re-initialize from the transient faults after shutting down the vehicle, and subsequently restart and safely control the vehicle. Hard shutdowns are less likely than soft shutdowns, and are caused by permanent fault accumulation. Finally, the probability of unsafe failure is much less likely than either of the two safe shutdown modes. In this case, unsafe failure is primarily caused by a second fault occurring while the OCC is in the process of diagnosing and reconfiguring from a previous fault.

When the triplex OCC is operated with transient fault recovery, the soft shutdown failure mode is nonexistent. The probability of unsafe failure is higher by several orders of magnitude due to increased exposure to a second coincident fault during the transient recovery period.

The probability of unsafe shutdown for a quadruplex OCC is slightly higher than that of the triplex OCC because the quad's added hardware increases the overall failure rate and, consequently, the probability of coincident faults. However, the probability of both hard and soft shutdowns is significantly reduced due to the increased redundancy of the quadruplex.

As the above analysis shows, both the triplex and quadruplex OCC configurations exceed the safety requirement of 10^{-9} per hour. However, because the transient-recovery redundancy management options for both configurations result in unsafe failure probabilities which are uncomfortably close to the OCC's safety requirement, the no-transient-recovery option is preferable for safety reasons.

The triplex OCC without transient recovery marginally meets the OCC's reliability specification (i.e., probability of hard or soft shutdown) of 10^{-6} per hour, while the additional redundancy of a quadruplex OCC enables it to exceed this requirement with a wide margin. Because the triplex OCC only marginally meets the reliability requirement, this analysis leads to the selection of a quadruplex OCC operated without transient fault recovery as the baseline OCC configuration.

<center>Availability</center>

The OCC availability depends on the number of Fault Containment Regions (FCRs) in the OCC, the MDC, and the scheduled maintenance interval. The previous analysis indicates that the MDC must consist of four FCRs in order to meet the reliability and safety requirements. Availability of two OCC configurations was modeled: one with only the MDC, i.e., 4 FCRs, and another with a spare FCR, i.e., a total of 5FCRs. The scheduled maintenance interval is a free variable which can be determined based on the OCC's maximum allowable unavailability. The availability modeling results are presented in Table 5 for a maintenance interval of 200 hours (approximately 8 days).

<center>Table 5. Availability Analysis of OCC</center>

Configuration		MDC	Unavailability after 200 hours
5 FCRs	4		3.7×10^{-3}
4 FCRs	4		7.5×10^{-2}

The availability analysis indicates that 1 spare FCR yields an unavailability after 200 wall-clock hours of 3.7×10^{-3}, which slightly exceeds the OCC maximum unavailability requirement of 10^{-3}.

Further detailed analysis is necessary to perform some tradeoffs. For example, the maintenance interval can be decreased while maintaining a nominal configuration of 5 FCRs. The life-cycle costs of more frequent periodic maintenance must be compared to the savings accrued due to lower FCR hardware procurement costs. Or an additional FCR can be added to increase the nominal configuration to six FCRs. This would allow the maintenance interval to be stretched to 400 hours. The acquisition cost of the additional FCR hardware must be compared to the savings accrued by deferring periodic maintenance in a life cycle cost analysis to determine the cost-effectiveness of this strategy. Also, the failure rate of the OCC components can be decreased in a number of ways, such as reducing their complexity (while still meeting the required OCC functionality), exploiting advanced packaging (which may increase the OCC's cost), utilizing higher-quality components (which may also increase the OCC's cost), or housing the components in a more benign environment in order to reduce their failure rates.

IX. SUMMARY AND CONCLUSIONS

Magnetically levitated vehicles operating on dedicated guideways at speeds of up to 500 KM/HR are now being designed in the US, Europe and Japan. The operation and control of these vehicles will be totally automated. This paper has defined the functions that must be performed by the automated control computer system. Safety, reliability, and availability requirements for the control computer system were also defined. A distributed hierarchical architecture consisting of vehicle on-board computers, wayside zone computers, and a central computer facility was defined to meet the functional and dependability requirements of Maglev. Two variations of the basic architecture, the Zone Control Architecture and the Smart Vehicle Architecture, and their qualitative attributes were also discussed. An architecture for the control computer onboard the Maglev vehicle (OCC) for the SVA was presented along with a communication protocol which provides a fail-safe mode of operation without reducing mission reliability

or overall system availability. Detailed Markov reliability and availability models of the OCC in the SVA were constructed and used to analyze the safety, reliability, and availability of the OCC. Based on this analysis, a baseline configuration of the OCC was selected which meets its dependability and performance requirements in a cost effective and maintainable manner.

Future work includes modeling of other major components of the SVA such as the Zone Control Computers, the Central Computer, communication links and a similar detailed analysis of the ZCA, followed by a comparative life cycle cost analysis of the two alternative architectures.

ACKNOWLEDGEMENT

REFERENCES

[1] Lala, J.H., et al., Advanced Information Processing System for Advanced Launch System: Avionics Architecture Synthesis, NASA Contractor Report-187554, C. S. Draper Laboratory, Inc., Cambridge, MA, September 1991.

[2] Lala, J. H., Nagle, G. A., and R. E. Harper, "Verification Methodology for Fault-Tolerant Fail-Safe Computers Applied to Maglev Control Computer Systems," Final Report DOT/FRA/NMI-92/26, Contract DTFR 53-91-C-00043, US DOT, C. S. Draper Laboratory, May 1993.

[3] Final Report, National Maglev Initiative, Government-Industry Workshop, Argonne National Laboratory, Argonne, Illinois, November 1, 1990.

[4] Peterson, C., "Monorail Control System Safety," Journal of Electrical and Electronics Engineering, vol. 10, pp. 28-35, Sydney, Australia, March 1990.

[5] Dependability: Basic Concepts and Terminology, J. C. Laprie, Ed., vol. 5 of Dependable Computing and Fault-Tolerant Systems, Vienna, New York: Springer-Verlag, 1992, pp. 11–16.

[6] Harper, R., Lala, J., Deyst, J., "Fault Tolerant Parallel Processor Overview," 18th International Symposium on Fault Tolerant Computing, June 1988, pp. 252-257.

[7] Harper, R., Lala, J., "Fault Tolerant Parallel Processor," J. Guidance, Control, and Dynamics, V. 14, N. 3, May-June 1991, pp. 554-563.

APPENDIX I: DEFINITIONS

Mission: A *mission* is defined as a trip from one station to another, including departures and arrivals at stations.

Safety: A mission completes *safely* when one of two conditions is met: either (1) the mission completes successfully, i.e. the vehicle arrives at its destination without incident, or (2) the mission is not completed successfully but no one onboard is injured, i.e. when the vehicle stops safely at some intermediate point along the guideway.

Fail-Safe: The ability to bring the vehicle to a safe stop under all possible failure conditions is denoted as the *fail-safe* feature of the system.

Reliability: The probability that a trip completes successfully is defined as the *reliability* of the system. The reliability requirement is not as stringent as the safety requirement because of the existence of the fail-safe mode of operation.

Availability: The *availability* of the system is defined as the probability that a given vehicle is ready to depart for a mission on time, i.e., it has the minimum dispatch complement (MDC) operational.

SUPERCONDUCTING ELECTROMAGNETIC SUSPENSION (EMS) SYSTEM FOR GRUMMAN MAGLEV CONCEPT*

Swarn S. Kalsi
Grumman Corporation
Bethpage, New York

SUMMARY

Maglev vehicles normally employ one of the two types of Maglev suspension systems: Electrodynamic Suspension (EDS) and Electromagnetic Suspension (EMS). The EDS system provides suspension by a repulsive force between the magnets on the vehicle and the reaction magnets (or conductive metal sheets) on the guideway. On the other hand, the EMS system is based on an attractive force between electromagnets on the vehicle and iron rails on the track. Grumman has adopted the EMS for its Maglev. The Grumman Maglev system consists of superconducting C-iron cored magnets on the vehicle. They are attracted to iron rails mounted on the underside of the guideway. The magnets and rails are oriented in an inverted 'V' configuration in such a manner that the attractive force vectors between the magnets and the rails act through the center of gravity of the vehicle. These magnets simultaneously perform functions of vehicle levitation and propulsion. They are powered by NbTi superconducting coils operating at 4.2K. An electromagnet consists of a C-core, a superconducting (SC) coil on the back leg of the C-core and a normal control coil on each leg of the C-core. The SC coil provides the nominal lifting capability and the normal coils handle rapid variations in load with respect to the nominal value. The EMS system provides levitation at all speeds but the EDS only starts to levitate the vehicle at speeds above ¯ 60 m.p.h. Below this speed, the vehicle must be supported by wheels. In an EDS system, SC magnets are shielded from the harmonics of propulsion winding by an aluminum shield. The thickness of this shield is inversely proportional to the square-root of the frequency. At very low speeds, the frequency of harmonic fields generated by the traction winding is low and it is, therefore, difficult to attenuate them. These low frequency harmonic fields generate losses in the SC coils and often force them to go normal. However, in the EMS system, the whole flux mostly remains confined inside the iron-core at all speeds and therefore does not have the inherent shielding problem of the EDS system. Because of the iron in the EMS system, stray field in the passenger compartments is also well below the acceptable levels whereas in the EDS systems this field is usually too high in the passenger compartment and it must be reduced down to acceptable levels by introduction of shielding materials at additional cost/weight penalty. The EMS can use conventional rebar in the guideway but the EDS system must use non-magnetic non-conductive rebar.

The Grumman baseline magnet configuration was selected on the basis of extensive 2-D and 3-D magnetic analyses to meet the levitation and propulsion requirements. The selected magnetic system design employs 48 magnets, 24 on each side of a 100 passenger vehicle. The polepitch is 750 mm and the gap between the magnet poles and the rail is 40 mm. The NbTi SC coil has a modest ampere-turns

---

(50,000 AT) requirement, experiences a peak field of ~0.35 T and operates at 4.5 K. High temperature SC leads are specified for minimizing the helium boiloff. Because of the iron core the SC winding experiences little magnetic loads. The magnet is cooled with pool boiling liquid helium which is contained within the helium vessel of the coil. No helium refrigeration equipment is carried on-board the vehicle. Instead the boiled-off helium gas is compressed into a nitrogen cooled storage tank. Sufficient quantity of liquid helium is carried on-board for an uninterrupted 24 hour operation. At the end of a day, the gaseous helium is discharged at a central location for reliquefication and the liquid helium supply in the magnets is replenished.

INTRODUCTION

The important aspect of the Grumman Electromagnetic Suspension (EMS) system design [1] is the ability to levitate the vehicle, with a wide airgap 40 mm (1.6 inch), using iron cored SC magnets located along both sides of the vehicle's length. The magnetic field in the gap is also utilized to propel the vehicle at speeds up to 134 m/s using 3-phase propulsion coils embedded in the iron rail slots. The ability to accomplish this levitation and propulsion under a wide range of maneuvers, guideway irregularities and aero disturbances without saturating the iron is a complex task requiring extensive magnetic and control system analysis.

Figure 1 shows the baseline EMS magnet system consisting of an iron-cored magnet and a guideway iron rail. The laminated, iron-cored magnets and iron rails are oriented in an inverted "V" configuration (see [1] for details) with the attractive force between the magnets and rails acting through the vehicle's center of gravity (cg).
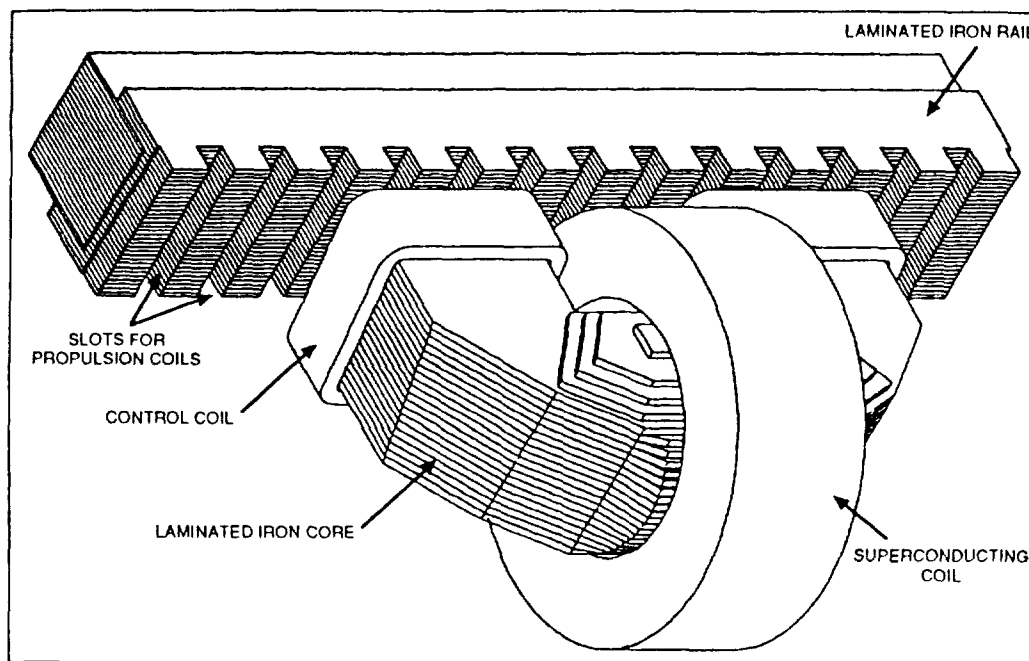

Figure 1. EMS Levitation and Propulsion Systems

The vertical control forces are generated by sensing the average gap clearance on the left and right side of the vehicle and adjusting the current in the control coils mounted on the magnet poles to maintain a constant 40 mm (1.6") gap. Lateral control is achieved by differential measurement of the gap clearance between the left and right sides of the vehicle. The corresponding magnet control currents are differentially driven for lateral control. In this manner, control of the vehicle relative to the rail is achieved in the vertical, lateral, pitch, and yaw directions. For roll control, the C-magnet assemblies are alternately off-set with respect to the rail width by 20 mm. With this arrangement, if the vehicle deviates from the nominal operating position, the lateral forces generated between the poles and the rails are such that they drive the system back to the equilibrium state. This process is further helped by sensing the vehicle's roll position relative to the rail and differentially driving the offset control coils to correct for roll errors. The iron rail on the guideway is laminated and carries 3-phase propulsion winding powered by a variable frequency ac source synchronized to the vehicle speed. Vehicle housekeeping power is inductively induced into coils mounted on the pole faces of each magnet.

REQUIREMENTS

The total weight of a 100 passenger fully-loaded vehicle is ˜ 60,000 Kg. The force generated by the magnet system must be 90% larger to provide lateral guidance in the inverted "V" configuration. The total baseline levitation and guidance force to be provided by the magnet system is 115,000 Kg. A load variation of +/- 45,000 Kg is required about the baseline value for rapid gap control. These and other baseline requirements are summarized in Table I. The vehicle has 18 m length available for accommodating the SC magnets and an airgap of 40 mm must be maintained between the levitation magnet pole faces and the rail. By reacting with 3-phase AC windings housed in the rails, these levitation magnets also generate a propulsion force of 6,000 Kg for nominal operation and 10,000 Kg for extended operation. The extended operation includes the requirements for accelerating on uphill grades, against head-wind, etc.

Table I. Maglev Vehicle Requirements

PARAMETER	UNIT	VALUE
Baseline levitation per vehicle	Kg	115,000
Load variation	Kg	45,000
Vehicle magnetic length	m	18
Airgap between poles and rail	mm	40
Propulsion force - nominal	Kg	6,000
- extended	Kg	10,000
Maximum vehicle speed	m/s	134

The levitation magnets must also generate sufficient lateral force to counter roll moments. Furthermore, the SC magnets must be designed for reliable operation and for easy maintenance.

BASELINE DESCRIPTION

Pole Configuration

The baseline C-magnet and rail configuration is shown in Fig. 2. The key parameters of the baseline magnet system are summarized in Table II. Each C-magnet assembly consists of a C-shaped iron core, a SC magnet located around the back leg of the iron core, and normal control coils around each pole of the iron core.
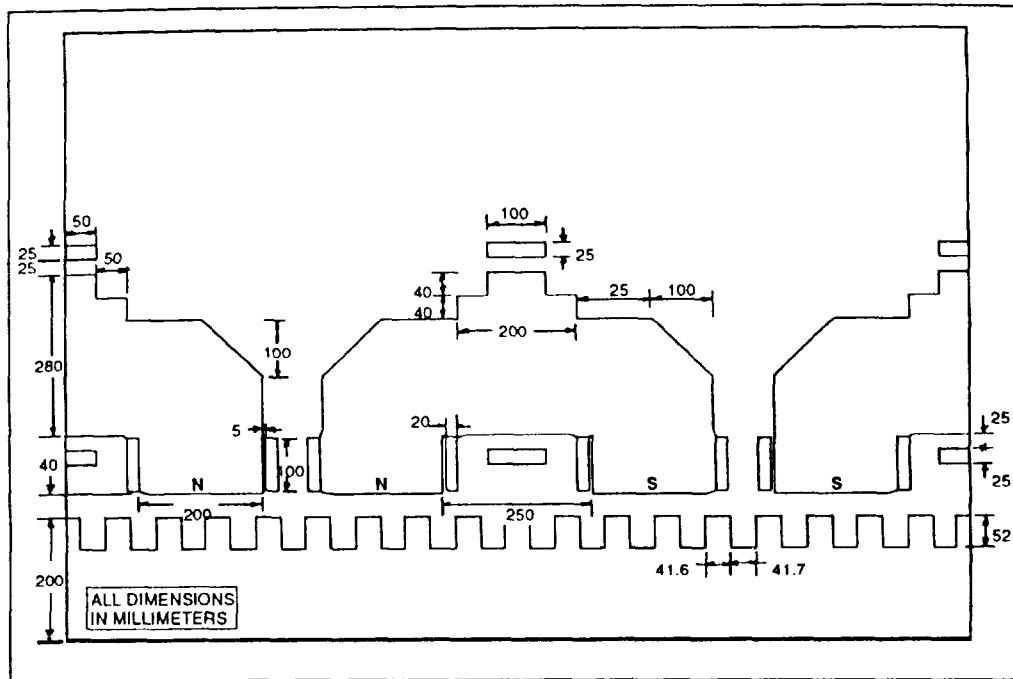
Figure 2. Baseline Pole and Rail Geometry

Table II. Baseline Levitation Magnet and Rail Parameters

PARAMETER	UNIT	VALUE
Lift capability per pole	Kg	2,400
Variation in lift capability	Kg	940
Pole pitch	mm	750
Number of poles		48
Airgap length	mm	40
Peak of sinusoidal field component in airgap	T	0.9
Operating frequency at rated speed	Hz	89
Nominal lift-to-weight ratio		6.4
Rail width	mm	200
Rail thickness	mm	200
Number of slots/pole in the rail		9

200

As shown in Fig. 2, the C-magnet assemblies are arranged such that the polarity of the poles of adjacent C-magnets is identical. Thus a pole (N or S) is formed by two legs of adjacent C-magnet assemblies. This arrangement of poles is the same as that accomplished with a continuous row of magnet poles on a single magnet core assembly. The baseline pole pitch is 750 mm.

Each pole face also has five slots (as shown in Fig. 3) for accommodating coils for inductive power generation on-board the vehicle for operating equipment and housekeeping services. These coils generate power at zero and low speeds by high frequency transformer action, and from airgap flux pulsations at high speeds. This power generation concept is described in [2]. The poles are skewed (Fig. 3) to minimize the effect of traction winding space harmonics on the traction force.
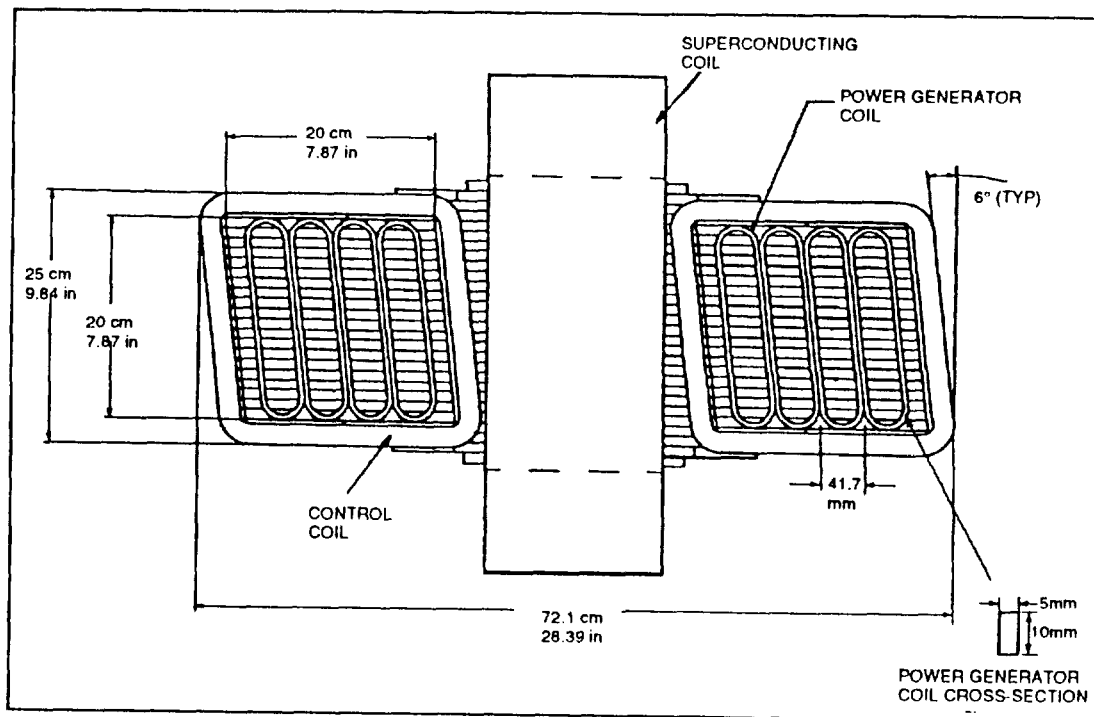
Figure 3. Skewed Magnet Poles with Power Generator Coils

Principle of Magnet System Operation

The SC magnet on a C-core operates in a quasi-steady state. During operation, any change in the size of the airgap tends to change the flux in the gap and in the core. When this happens, the current in the control coils is modulated to restore the flux in the airgap to its original value. This is accomplished with the help of a gap control system shown in Fig. 4 and is discussed below.

For reasons of SC coil stability and heat loads, the SC coil is supplied from a constant current source that has built-in capability to prevent current changes occurring faster than ⁻ 1 Hz. On the other hand, the airgap is expected to change at frequencies up to 10 Hz. The normal control coils develop self currents in response to these oscillations of gap length with an intent to restore the gap to its nominal

201

value. If a steady change in the gap is noticed (due to increased or decreased load), then the current in the SC coils is allowed to change so as to drive long-term currents in the normal coils to zero. It is possible to achieve a certain degree of damping with the shorted coils. But in a practical system, it is essential to dynamically control these coils to respond to gap variations resulting from passenger load changes, maneuvering around curves or during grade changes of a given route. For this purpose, the airgap is constantly monitored and current of appropriate polarity is supplied to each normal coil for maintaining the nominal gap. This concept is described in more detail in [3].
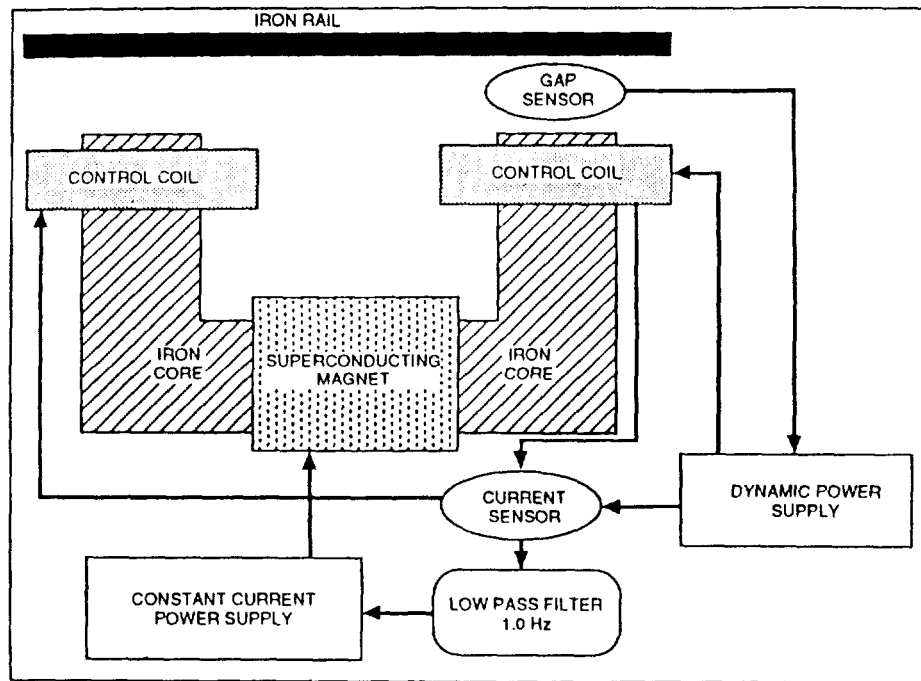
Figure 4. Magnet Control System

Effect of Normal Control Coils on the Levitation Force

The normal control coils are provided to compensate for fast changes in the required levitation capability. A set of calculations were performed to estimate the effect of control coil ampere-turns on the levitation force as a function of airgap length. Because of very high field levels in the iron core, it was decided to perform these calculations with 3-D codes (both TOSCA and ANSYS were used). Fig. 5 shows the combined lift and guidance force as a function of control coil current for constant gap lengths. The same data is presented in Fig. 6 but as a function of gap length for constant values of control coil currents. In both figures, the magnet is nearly a linear function of gap length and control coil current around the nominal operating point of a 40 mm gap and zero control coil current. When the core saturation increases, the relationship becomes non-linear. However, the important factor is to generate a sufficient amount of levitating force variation to maintain controllability of the vehicle and this objective has been achieved [4].

202

Figure 5. Levitation vs Control Coil Current for Constant Airgap Lengths

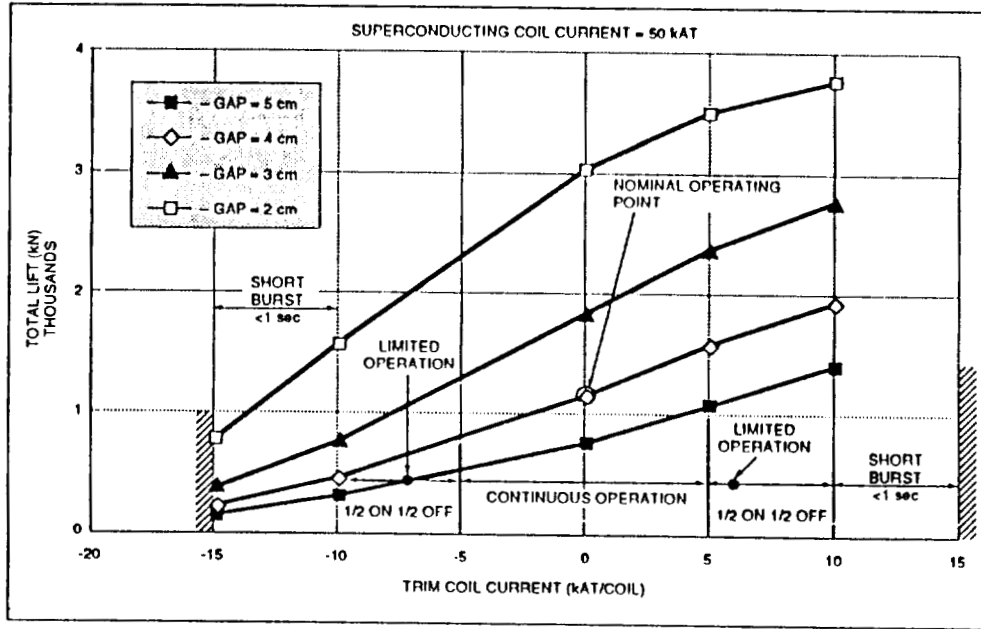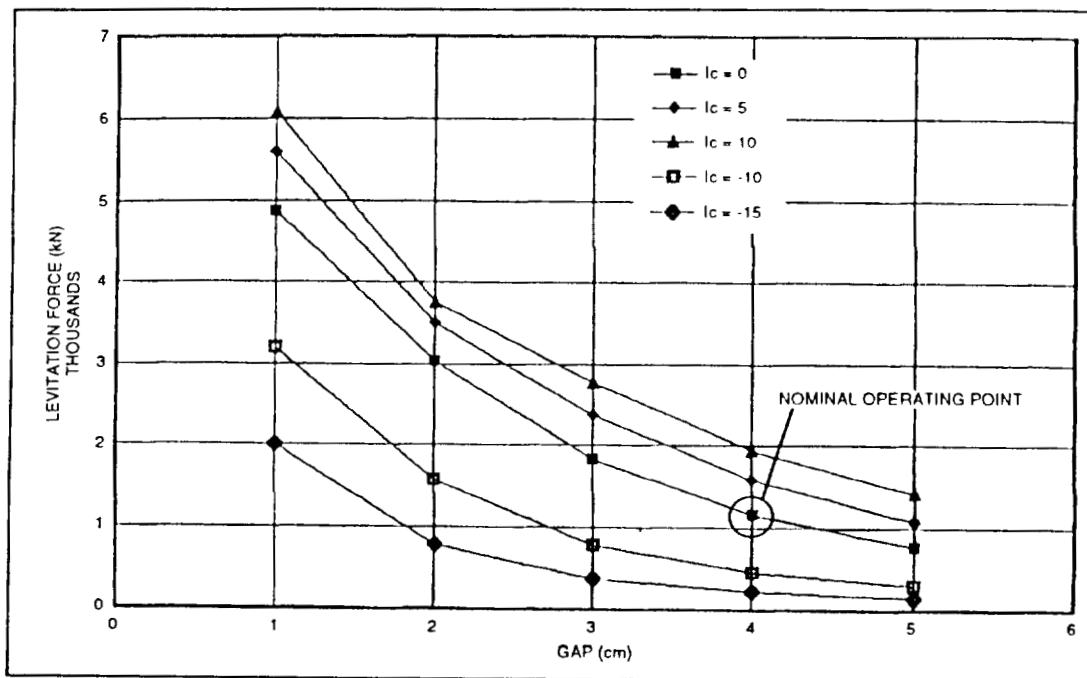Figure 6. Levitation vs Airgap Length for Constant Control Coil Current

Roll Control

The EMS maglev concept proposed here is inherently stable against roll rotation. This is achieved by off-setting C-magnet poles with respect to the rail. Two C-magnet assemblies are carried as a module. Alternate magnet modules are shifted laterally with respect to the rail by about 20 mm. As a result of this shift, a lateral force is generated between the poles and the rail. The total of forces on all poles sums to zero during normal operation. During a transient condition, if all poles move to one side with respect to the rail, the force decreases on poles that are getting aligned with the rail and the force increases for poles that are getting more misaligned. The net force always tends to return the system to the equilibrium state.

An estimate of the lateral restoring force was made with a 2-D finite element analysis. The lateral force as a function of misalignment is shown in Fig. 7. The permanent misalignment between the poles and rails is initially fixed at 20 mm. The restoring force for this misalignment is 890 N/pole; this is about 4% of the nominal levitation force and is considered adequate for most operating scenarios.

Figure 7: Lateral Restoring Force

Stray Magnetic Field Level

3-D magnetic field calculations were performed to estimate stray field in the passenger compartment and the surrounding areas. The flux density levels below the seat are less than 1 G, which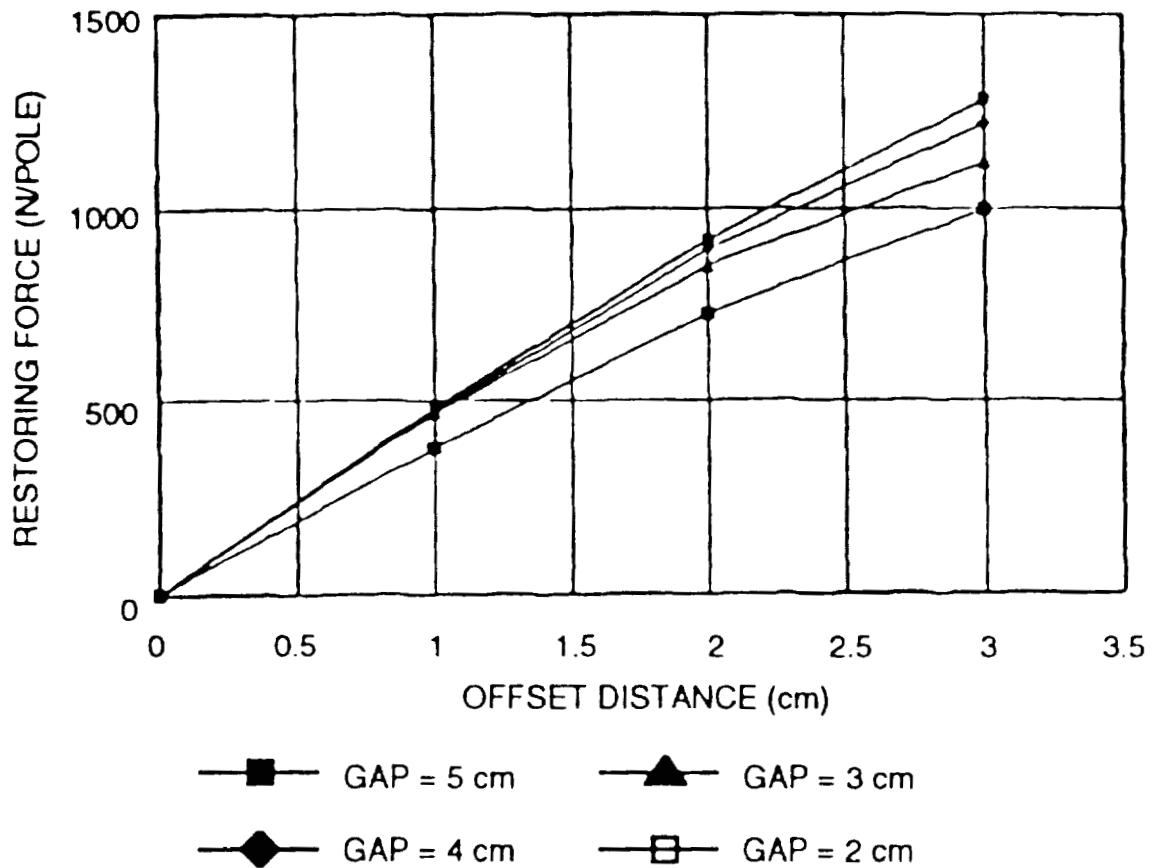 is very close to the ambient earth's field (0.5 G). On the platform, magnetic field levels do not exceed 5 G, which is considered acceptable in hospitals using magnetic resonant imaging (MRI) equipment. These results were obtained without any shielding. With a modest amount of shielding, these field levels could be further reduced should future studies indicate a need for lower values.

ESTABLISHING POLEPITCH

The sizing of both the depth of the rail guideway magnetic core and the core depth of the vehicle magnets is directly proportional to the polepitch. Thus the polepitch is the key factor in establishing overall system weight and steel materials cost.

The C-magnet and rail configuration of Fig. 2 was utilized for performing a parametric study to select an optimum polepitch that minimizes the overall cost of a Maglev system consisting of a double 300 mile track with 100 cars operating at any given time. The study was performed to satisfy requirements of Table I. The results of the study are summarized in Fig.8. As can be seen , the cost of the system continually increases with polepitch because a larger polepitch requires a deeper (thicker) rail to carry the magnetic field. A certain level of airgap field is required for the levitation capability, but it is not proportional to the polepitch because increasing the polepitch also improves the levitation efficiency of the magnet (large poleface to airgap length ratio). The lowest polepitch of 750 mm was selected on the basis of a volumetric constraint to accommodate the SC coil, its cryostat and the two normal control coils.
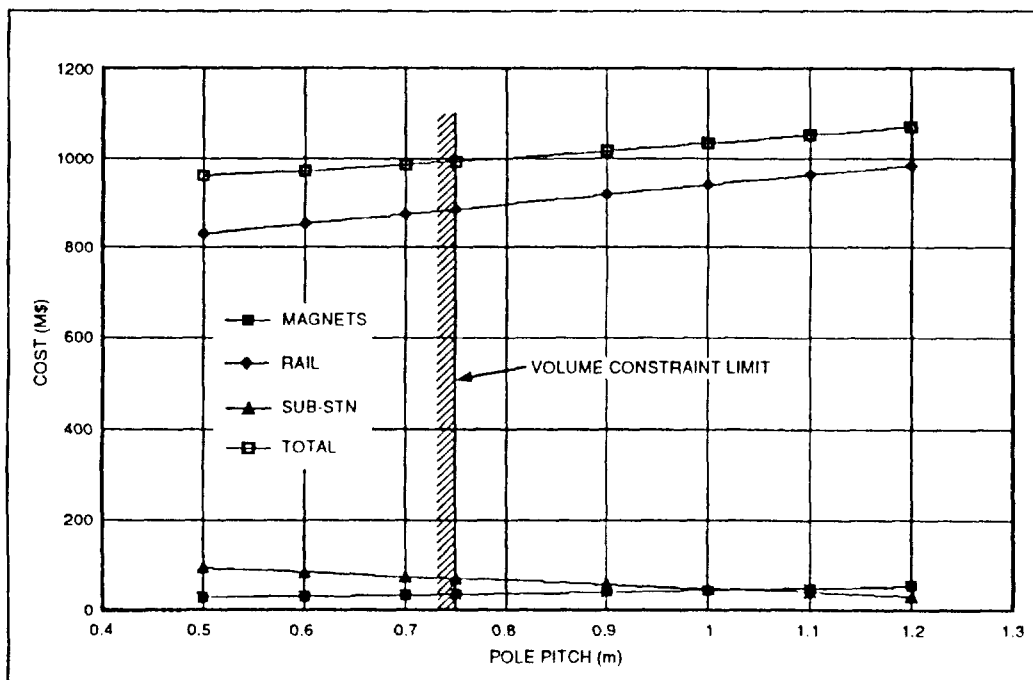

Figure 8. Maglev Levitation System Cost vs Polepitch

ESTABLISHING NUMBER OF MAGNETS REQUIRED

The 3-phase traction winding in the rail requires that the field produced by the excitation poles on the car (iron cored DC magnets) be sinusoidal in shape and its harmonic components be as small as possible for minimizing their deleterious effect on the traction force and eddy-current losses. The suspension magnets provide the key functions of levitation and propulsion simultaneously in the EMS system. Because of this constraint, a minimum number of poles are required for a given airgap magnetic field strength to accomplish the tasks of levitating and propelling the vehicle.

The analysis to determine the minimum number of poles follows. The levitation force generated by a sinusoidal field is given as:

$$F_l = 0.5 \, w \, \tau \, \{B_m{}^2/(2\mu_o)\} \, N_p \qquad\qquad (1)$$

where F_l = levitation force (N)

$\quad B_m$ = peak of the sinusoidal field (T)

$\quad w$ = width of the rail (m)

$\quad \tau$ = polepitch (m)

$\quad \mu_o$ = permeability of air = 4 p 10^{-7}

$\quad N_p$ = number of pole on a vehicle

Similarly the total traction force (N) per pole is:

$$F_t = 1.5 \, B_m \, I_m \, q \, w \, \eta K_d \, N_p \qquad\qquad (2)$$

where I_m = Peak of the sinusoidal current in traction winding (A)

$\quad q$ = slots per pole per phase in the rail

$\quad \eta$ = Efficiency of traction motor ~ 99%

$\quad K_d$ = Distribution for the traction winding

After eliminating B_m between (1) and (2), the equation for the number of poles is:

$$N_p = \{F_t{}^2/F_l\} \, \{\tau/(I_m{}^2 \, q^2 \, 9 \, \mu_o \, w)\}/(\eta^2 \, K_d{}^2) \qquad\qquad (3)$$

The baseline values for various variables are:

- F_t = 60 kN
- τ = 0.75 m
- q = 3
- η = 0.99

- F_l = 1,150 kN
- I_m = 1,900 A
- w = 0.2 m
- K_d = 0.96

With these values, the number of poles determined from Eq. (3) is 36. The baseline is fixed with 48 poles to provide redundancy.

MAGNET DESIGN

Magnetic Analysis

Initially a majority of calculations were performed with 2-D code (EMP, a commercial version of POISSON code) assuming a M43 iron core material. Fig. 9 shows field distribution calculated with the 2-D code in the airgap, pole and rail iron.

Table III. Comparison of Field Values Calculated with 2-D and 3-D Codes for the Baseline

LOCATION (SEE FIG. 9)	2-D FIELD (T) M43 IRON	3-D FIELD (T) M43 IRON	3-D FIELD (T) Permendur
A	1.21	2.45	2.47
B	0.89	1.73	1.2
C	0.8	0.87	0.88
D	1.33	1.52	1.45
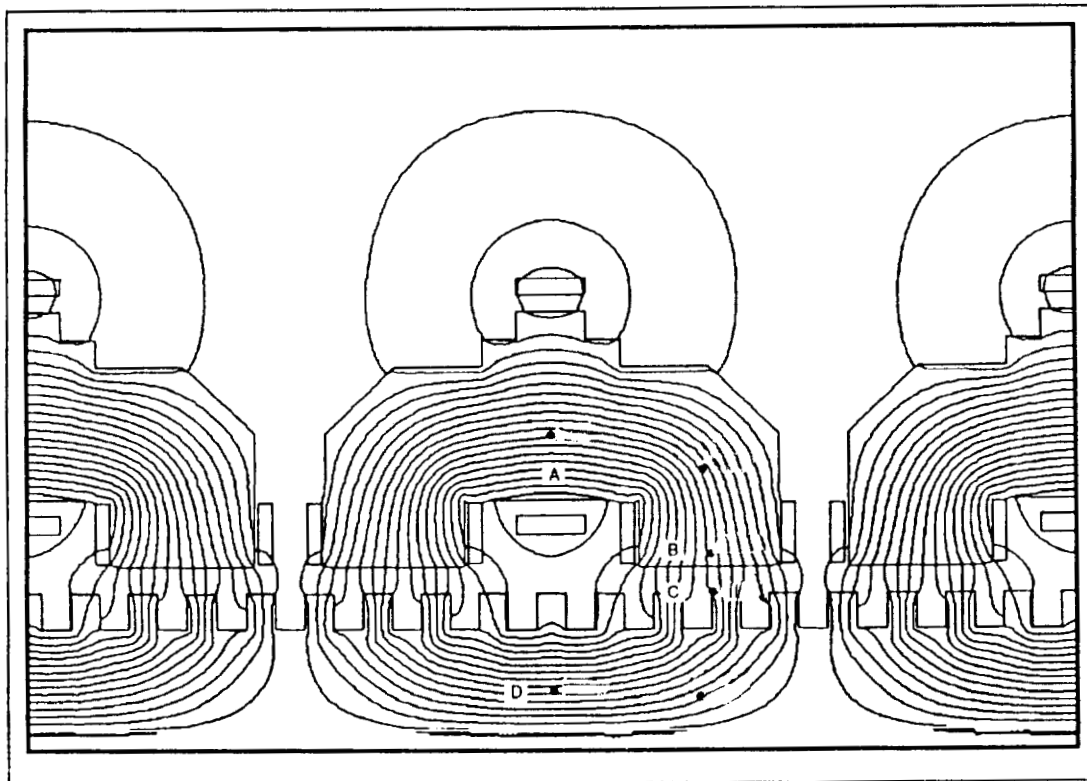
Figure 9: Baseline Magnetic Field Calculations with 2-D Code

Fig. 10 shows field distribution calculated with a 3-D code (TOSCA). The field distribution calculated by the two codes for the airgap is similar, but the 3-D calculation summarized in Table III shows a much higher degree of saturation of the pole-iron (in the vicinity of the SC coil). To reduce this saturation to a reasonable value, a permendur iron (2% vanadium, 49% iron, and 49% cobalt) was specified in place of the M43 material. Table III also compares the resulting field values for the M43 iron and the baseline permendur pole iron. The SC coil provides 54 kA-turns. Locations of field comparison are marked in Fig. 9. The penalty for selecting a permendur iron for the poles instead of M43 is approximately 7% of the vehicle cost.
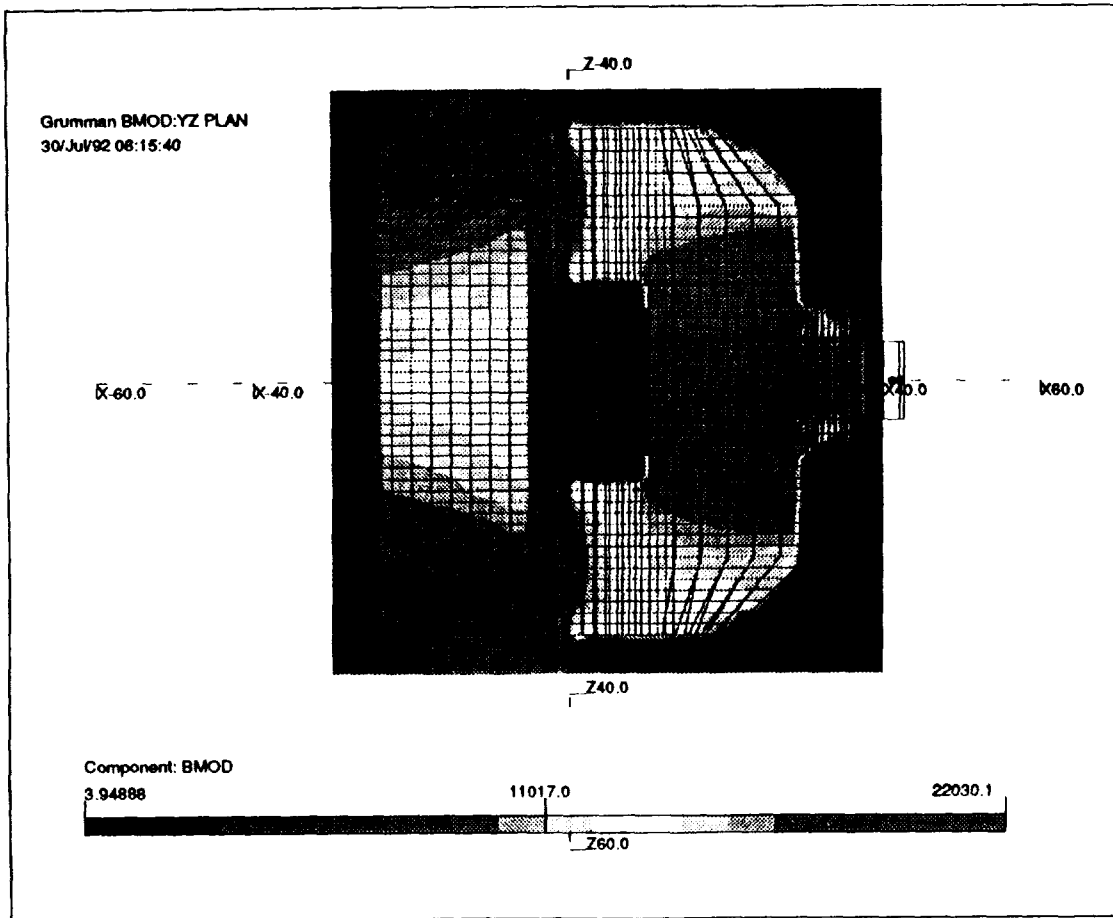
Figure 10: Baseline Magnetic Field Calculations with 3-D Code (Permendur Iron)

Sizing of SC Coil and Cryoplant

A cylindrical SC coil and cryostat were selected for each C-magnet assembly since they are easier to fabricate and are lighter in weight than non-cylindrical shapes. For this reason, the iron core cross-section under the magnet is made circular. The iron is built from 0.050 inch thick laminations (Permendur.)

208

The SC coil carries 54 kA-turns to produce the required field to simultaneously meet requirements of levitation and propulsion. The SC coil is designed by using a 0.65 mm diameter NbTi wire that has been developed by Brookhaven National Laboratory for their Relativistic Heavy Ion Collider (RHIC) dipole magnets. The key parameters for the SC coil are summarized in Table IV.

Table IV. SC Coil Parameters

| Parameter	Unit	Value
Ampere-turn rating of SC coil	kA-turn	54,000
Peak field at the SC coil	T	0.5
Operating current	A	53
Operating temperature	K	4.5
Number of turns		1,020
NbTi wire diameter - bare	mm	0.6477
Copper-to-superconductor ratio		2.2
Ratio of Operating to critical current		0.09
Temperature margin to current sharing	K	3.69

The SC coil has 1,020 turns; each turn carries 53 A to produce required 54 kA-turns. These turns are accommodated in a coil pack of 4 layers with 255 turns in each layer. The coil pack is epoxy impregnated to produce a monolith structure. No separate quench protection system is required because the energy stored in the magnet is very small. In the event of a quench, the magnet is disconnected from the supply and is shorted at its terminals.

The total heat load for the magnets on each car is 8 W. The weight and the cost of a cryogenic refrigeration plant would be 2,540 Kg and $110,000 respectively. It also will be necessary to supply ~16 kW of power to run the refrigerator plant. To mitigate the weight and operating power penalty a decision was made to employ a cryogenic storage system. The liquid helium cryogenic storage system consists of a small compressor operating at 350 psi that takes the gaseous helium boiloff and compresses it into a storage tank held at liquid nitrogen temperature. Sufficient helium inventory is carried in the magnet for a 24-hour continuous operation. The gaseous helium storage system is sized to accommodate helium boiloff over a 24-hour period. At the end of the 24-hour period, the gaseous helium is discharged at a central location and liquid helium is replenished in the magnets. Two cryogenic storage systems are provided for each 50 passenger module. The weight of each cryogenic system is 580 Kg which includes 180 Kg for a compressor and 400 Kg for the gaseous helium storage tank.

Potential of Using High Temperature Superconductors

The iron cored SC magnets of the Grumman concept are in the best position to take advantage of the new High Temperature Superconductor (HTS) technology. The peak field in the iron is greater than 2 T, but in the SC winding region it is less than 0.35 T. The superconductor is also required to supply a modest 54 kA-turns to generate the required field for vehicle levitation and propulsion.

Because of very small fields and forces experienced by the SC coil and recognizing rapidly advancing state-of-the-art of the HTS technology [5], Grumman considers that this Maglev concept is in a best position (relative to all other SC magnet Maglev concepts) to take advantage of the HTS technology. The following are the attractive features of the HTS magnet:

- Operation at liquid nitrogen temperature (77 K)
- No need for liquid helium compressor or storage tanks
- Simpler and lighter cryostat
- Lower weight and capital cost
- Lower manufacturing cost
- Lower operating and maintenance cost

The current state-of-the-art of HTS is sufficiently developed so that an HTS coil could be built for the Grumman Maglev. The HTS conductors [6] have acceptable current densities and are made in sufficiently long lengths to suit EMS magnet needs.

CONCLUSIONS

The Grumman developed EMS Maglev system has the following key characteristics:

- A large operating airgap - 40 mm
- Levitation at all speeds
- Both high speed and low speed applications
- No deleterious effects on SC coils at low vehicle speeds
- Low magnetic field at the SC coil - <0.35 T
- No need to use non-magnetic/non-metallic rebar in the guideway structure
- Low magnetic field in passenger cabin ˜ 1 G
- Low forces on the SC coil
- Employs state-of-the-art NbTi wire
- No need for an active magnet quench protection system
- Lower weight than a magnet system with copper coils

The EMS Maglev described in this paper does not require development of any new technologies. The system could be built with the existing SC magnet technology. The future work is planned to improve the design to minimize high magnetic fields in the iron core and to consider the possibility of replacing the helium cooled NbTi SC coils with nitrogen cooled High Temperature Superconductors.

REFERENCES

[1] M. Proise, et al. "System Concept Definition of the Grumman Superconducting Electromagnetic Suspension (EMS) Maglev Design", presented at the Maglev '93 Conference, Argonne National Laboratory, May 19-21, 1993.

[2] S. Kalsi, "On-vehicle Power Generation at all Speeds for Electromagnetic Maglev Concept", presented at the Maglev '93 Conference, Argonne National Laboratory, May 19-21, 1993.

[3] R. Hurbermann,"Self Nulling Hybrid Maglev Suspension System", presented at the Maglev '93 Conference, Argonne National Laboratory, May 19-21, 1993.

[4] R. Gran and M. Proise,"Five Degree of Freedom Analysis of the Grumman SC Maglev Vehicle Control/Guideway Interaction", presented at the Maglev '93 Conference, Argonne National Laboratory, May 19-21, 1993.

[5] P. Halder and L. Motowildo, "Recent Development in the Processing of High Jc Silver Clad Mono- and Multi-Filament (Bi, Pb)2Sr2Ca2Cu3O10 Wires and Tapes,"Journal of Metals, October 1992.

[6] P. Haldar, J. Hoehn, Jr., U. Balachandran, and L. Motowildo, "Processing and Transport Properties of High-Jc Silver-Clad Bi-2223 Tapes and Coils", Proceedings of the Symposium on High Temperature Superconductors, 1993 TSM Annual Meeting, Denver, CO, February 21-25, 1993.

NATIONAL MAGLEV INITIATIVE - CALIFORNIA LINE
ELECTRIC UTILITY POWER SYSTEM REQUIREMENTS

Phil Save
Southern California Edison Company
Rosemead, CA

SUMMARY

The electrical utility power system requirements were determined for a Maglev line from San Diego to San Francisco and Sacramento with a maximum capacity of 12,000 passengers an hour in each direction at a speed of 300 miles per hour, or one train every 30 seconds in each direction. Basically the Maglev line requires one 50-MVA Substation every 12.5 miles. The need for new power lines to serve these substations and their voltage levels are based not only on equipment loading criteria but also on limitations due to voltage flicker and harmonics created by the Maglev system. The resulting power system requirements and their costs depend mostly on the geographical area, urban or suburban with "strong" power systems, or mountains and rural areas with "weak" power systems. A reliability evaluation indicated that emergency power sources, such as a 10-MW battery at each substation, were not justified if sufficient redundancy is provided in the design of the substations and the power lines serving them. With a cost of $5.6 M per mile, the power system requirements, including the 12-kV DC cables and the inverters along the Maglev line, were found to be the second largest cost component of the Maglev system, after the cost of the guideway system ($9.1 M per mile), out of a total cost of $23 M per mile.

INTRODUCTION

Southern California Edison Company (SCE) has conducted a Study to determine the route and the electric utility power systems requirements for a Maglev line in California. This work was performed as an input to the Maglev System Concept Definition Final Report which was issued on September 30, 1992 by a team headed by Bechtel Corporation, under one of the four National Maglev Initiative Contracts.

MAGLEV LINE ROUTE

As shown by Figure 1, the route selected for the Maglev in California maximizes the potential ridership by connecting the largest urban areas which have the following population projections for year 2000, based on Reference 1 :

Urban Area	Population Projection (Year 2000)
Los Angeles	16.7 M
San Francisco	6.9 M
San Diego	3.0 M
Sacramento	1.8 M
Bakersfield	0.7 M
Fresno	0.7 M

Because Maglev can utilize elevated guideways installed on the median lane of existing freeways or highways, to minimize the need for land or right-of-way, the selected Maglev route follows Interstate 5 and Freeway 99 from San Diego to San Francisco and Sacramento, and Freeway 101 between San Francisco and San Jose, with two alternatives between the San Joaquin Valley and the San Francisco Bay area through the coastal mountains : the Altamont Pass Alternative on Freeway 480 and the Pacheco Pass Alternative on Highway 152.

MAGLEV SYSTEM DESIGN

The Maglev System, considered for the California line, is designed for the maximum capacity of 12,000 passengers an hour in each direction at a speed of 300 miles per hour, or one train every 30 seconds in each direction. The Maglev design characteristics, provided by Dr. Richard Thornton of MIT, are as follows :

The Maglev vehicles, which have been called "Boeing 737 without wings, tail, or engine", have a speed of up to 300 miles an hour, and are maintained by magnetic levitation at about 10 inches above a Guideway without physical contact. They do not require steel wheels and rails. Their propulsion system is of the repulsion or electrodynamic superconductive type; it consists in a Linear Synchronous three-phase AC Motor.

The stator coils, installed in the Guideway, create a magnetic field which moves along the Guideway at a speed which is a function of the AC frequency. The Rotor coils installed aboard the Maglev vehicle create another magnetic field. Interaction of the two magnetic fields provides propulsion and levitation. To minimize the weight of the rotor and maximize the gap between the Maglev vehicle and the Guideway the rotor coils are superconductive.

The resulting electric load requires a Substation every 12.5 miles along the route.

As shown by Figure 4, each Substation, served by the local electric utility AC power system, converts the AC to + - 12 kV DC with 12-pulse Transformer/Rectifiers . The DC power is delivered to two 12-kV DC cables which follow the Maglev line.

Every 2.5 miles, these 12-kV DC cables serve an Inverter which converts the DC back to AC, feeding the Stator coils of the Linear Synchronous Motor in the Guideway. The Inverter provides

214

adjustable frequency and voltage which control the speed of the Maglev vehicles. The Stator coils in the Guideway consist of independent 2.5-mile continuous blocks of coils, each served by an Inverter.

Each Substation has a peak balanced three-phase load of 60 MW (short time) and 50 MW (sustained), with power fluctuations of up to 40 MW every 30 seconds. These fluctuations are caused by the fact that the load of each Maglev vehicle is moving from one guideway stator coils block to the next. It should be noted that regenerative braking is possible with the regenerated power being delivered to the 12-kV DC Cables.

In addition to these power fluctuations, the Substation load includes voltage harmonics of 60 Hz, which are created by the rectifiers and inverters of the Maglev system and are propagated throughout the power system.

ELECTRIC UTILITY POWER SYSTEM REQUIREMENTS

All the electric utility power system requirements were based on Conceptual Planning, without benefit of computerized system simulations (load flow, short circuit, or stability), or detailed comparisons of alternatives, etc... However, this planning was done with the cooperation and the approval of the System Planning Departments of all Electric Utilities involved : San Diego Gas and Electric (SDG&E), Southern California Edison (SCE), Los Angeles Department of Water and Power (LADWP), and Pacific Gas and Electric (PG&E).

Reliabilty Criteria

The power system, required to serve the Maglev Substations, was designed to provide single contingency capability, with two lines on separate right-of-ways and two redundant transformer/ rectifiers.

With this design, the risk of losing service to a Maglev Substation is very low : once in 25 years for 14 to 22 minutes, as indicated by a reliability study which was conducted by using the outage rate frequency and duration method (Reference 3). The study was based on the results of a statistical analysis of a 17-year outage history of SCE Transmission and Transmission Systems, published in a 1980 IEEE Paper by P. Save de Beaurecueil (Reference 4).

Therefore, the single contingency criteria provides an acceptable level of reliability and use of emergency sources of power such as a 10-MW battery at each Substation is not justified, especially when considering the exorbitant costs of batteries of this size. (These batteries were initially considered to allow Maglev vehicles to operate at reduced speed and unload passengers at the next Station, following a power outage of several hours, which is extremely unlikely.)

Maglev Substation Design

The design of a Maglev Substation is shown by the schematic one line diagram in Figure 5. The Substation includes two redundant 50 MVA transformer/ rectifiers, each one with two 12-kV windings, wye and delta, serving two six-pulse rectifiers in series, equivalent to a 12-pulse rectifier. Having only one transformer/rectifier with a few mobile spare units on trailers for the total Maglev line was not selected because transportation and connection of a mobile unit would take more than a day, which is not acceptable. The Substation line and bus on the transmission or subtransmission side is a ring bus with two-line service and two double-breaker line positions.

The rectifiers are connected to the 12-kV DC cables with two 4000-A DC breakers. These breakers are normally closed.

All Maglev substations have an outdoor construction design except three Substations (Numbered 1, 42, and 52 in Figure 2), located in downtown areas of respectively San Diego, Sacramento, and San Francisco, which have an indoor SF6 gas insulated substastion (GIS) design.

Service to Maglev Substations

The 50-MW peak load of the Maglev Substation has the same order of magnitude as the load of typical Electric Utility Distribution Substations which are normally served from the Subtransmission System (66, 69, 115, or 138 kV). However, because the Maglev Substation load can experience periodic power fluctuations of up to 40 MW every 30 seconds, and includes voltage harmonics, special evaluations are required to ensure that the Electric Utility power systems are not adversely affected. As a result of these evaluations, service from higher voltage (230 kV) systems and harmonics filtering may be required. These evaluations were conducted at the conceptual level in the SCE Study presented later in this paper.

As required for Electric Utility distribution substations, the power factor of the Maglev Substation load should be unity. This requirement is especially important in areas where the utility power system is not strong such as in the mountains or the rural areas of the San Joaquin Valley.

Substations with 50-MW loads such as the Maglev Substations can be served from the Subtransmission (66, 69, 115, or 138-kV) systems when these systems are sufficiently strong, which is the case from San Diego through the Los Angeles Basin and in the San Francisco Bay Area.

However, in the coastal mountains north of Los Angeles, and some rural areas of the San Joaquin Valley, service from the 230-kV Transmission System is required. In these areas, also, the existing 230-kV system needs to be reinforced by forming new 230-kV lines or upgrading existing 230-kV lines.

216

The Maglev Line, and the locations of the Maglev Substations, numbered 1 through 61, are shown by an overall map in Figure 2 and one out of four detailed maps in Figure 3C. The maps show the 500-kV and 230-kV transmission systems in the vicinity of the Maglev Line, including the new and rebuilt 230-kV lines required to serve the Maglev Line. For the sake of clarity these Figures do not show the subtransmission line additions.

Service From the Subtransmission System

Typically, Subtransmission systems feeding a certain number (between 5 and 25) of subtransmission substations are interconnected. Each Subtransmission System is served by a "Source" Transmission Substation which is supplied from the Transmission System (at 230 or 500-kV).

When service to the Maglev Substations is provided from the Subtransmission System, to minimize the impact on the local subtransmission system, the Maglev Substations are served by two "Source" subtransmission single-circuit lines on separate right-of-ways, which are directly connected to the closest Transmission Substation, "Source" of the local subtransmission system.

The new subtransmission lines are connected to the subtransmission bus of the "Source" substation with two separate double-breaker positions. When more than one Maglev substation is connected to a "Source" Transmission Substation a new Standard 168/224/280-MVA Transmission Transformer Bank was added to meet the additional substation load at the subtransmission level. The Transformer Bank was connected to both transmission and subtransmission buses with double breaker positions.

In the Los Angeles Water and Power Department Service territory , because only distribution voltage of 33 kV is available at Velasco, Toluca, and Sylmar Substations, two 230-66-kV 50-MVA transformer banks were provided at each of these substations to serve the Maglev Substations at 66 kV, to maximize the short circuit duties (as required to minimize the effects of harmonics and power fluctuations).

In the San Diego Service territory additions of Maglev Substations require rebuilding the San Mateo-San Luis Rey 138-kV line.

To provide higher reliability and more acceptable visual impact, the new overhead subtransmission lines directly connected to the Maglev substations are on Steel Poles instead of wood poles or lattice towers.

In some areas underground Subtransmission lines were planned, wherever there is public opposition or impossibility of having new overhead subtransmission lines, such as Orange County, or Downtown areas of San Diego, Los Angeles, San Francisco bay area, and Sacramento.

Service From the 230-kV System

Service from the 230-kV System was required in the rural mountainous and the San Joaquin Valley, by forming the following new 230-kV single circuit lines :

SCE	Pardee-Magunden (68.7 mi.) looped into Substations 15 and 16
SCE	Magunden-Rector (83.1 mi.) looped into Substations 23 thru 26
PG&E	Bellota-Wilson (64.0 mi.) looped into Substations 34 thru 37
PG&E	Legrand-Los Banos (44.0 mi.) looped into Subs. 55, 56, and 57.(Pacheco Pass Alternative)

The following double circuit 230-kV lines need to be upgraded :

SCE	Rector-Big Creek 1 and 3 (64.3 miles)
PG&E	Legrand-Gregg 1 and 2 (32.0 miles)

To provide higher reliability and more acceptable visual impact, the new overhead transmission lines directly connected to the Maglev substations are on Steel Poles instead of wood poles or lattice towers.

Maglev Substation Load Fluctuations and Harmonics - Evaluation

Contrary to the conventional electric trains, which are single-phase loads, Maglev systems have the advantage of being balanced three-phase loads. However Maglev loads still have the problems created by harmonics and periodic power fluctuations which cause voltage flicker. Evaluation of these problems was conducted based on the criteria described below. Although this criteria is not a part of the official SCE Transmission Planning Guidelines (Reference 2), it is considered to be reasonable and sufficiently conservative, especially for a conceptual study.

Voltage Flicker Criteria

Voltage Flicker, caused by power fluctuations, is inversely proportional to the Short circuit duty, as shown in a later paragraph.

Guidelines for Voltage Flicker have been used in the Power Industry for more than 25 years. As shown by Figure 6, typically, these Guidelines include two curves defining voltage flicker limits in percent voltage dips as a function of the flicker frequency : a Lower Limit, the "Border Line of Visibility", and an Upper Limit, the "Border Line of Visual Irritation". It consists of three sections:

1.   Frequencies higher than 3 per minute : Border line of Visual Irritation.

2.   For frequencies between 3 per minute and 10 per hour : 1.5 percent.

218

3.   For frequencies lower than 10 per hour : 2 percent.

This criteria should be met at least at the Point of Connection with the Electric Utility during minimum short circuit duty conditions.

Harmonics Voltage Criteria

This Criteria,shown in Table 1, is derived from Guidelines used by the French Electric Utility E. D. F (Reference 5). It has been applied for the loads of electric trains which have been in service for more than 50 years. They have been applied in particular to the latest "TGV" trains which have loads similar to the Maglev loads in terms of magnitude and harmonics, since they use AC induction motors with adjustable speed drive systems (Reference 6).

For Transmission or Subtransmision loads the criteria is as follows :

1.   If the load creating voltage harmonics is below 1 percent of the minimum short circuit MVA duty at the point of connection with the Utility, it is acceptable and no further study or filtering is required.

2.   If the load creating voltage harmonics is 1 percent or more of the minimum short circuit MVA duty at the point of connection with the Utility, a harmonics study is required to determine the harmonics rates for each rank (multiple of the 60 Hertz fundamental frequency). If the rates are found to be exceeding the limits shown in Table 1, filtering should be provided to obtain voltage harmonics rates within these limits.

Application of Voltage Flicker and Voltage Harmonics Criteria

Using the above criteria, the impact of the Voltage Harmonics and the Voltage Flicker, caused by the Maglev Substations loads, was evaluated for each Connection Point of the Maglev Substations to the Electric Utility Systems.

For each Maglev Substation, served from the Subtransmission System, the Connection Point is the Subtransmission Bus at the "Source" Transmission Substation to which the two subtransmission lines, serving the Maglev Substation, are connected.

For the Maglev Substations, served from the Transmission System, the Connection Point is the 230-kV Bus of each of the two Transmission Substations where the 230-kV line serving one or more Maglev Substations is connected.

The minimum short circuit duty, required for the evaluation of both voltage harmonics and voltage flicker, as indicated above, was determined as follows : First, the maximum short circuit duty (MVA and angle) at each Connection Point was obtained from existing short circuit studies. The minimum short circuit duties were then estimated to be a fraction of the maximum duty.

For the Connection Points in the 230-kV system : 50 percent in the San Joaquin Valley and mountainous areas, and 60 percent in the Los Angeles Basin or the San Francisco Bay area. For the Connection Points in the Subtransmission System : 90 percent.

Harmonics Voltage Evaluation

The need for detailed Harmonics Analysis and possible filtering was identified whenever the Maglev Substation load is 1 percent or more of the minimum short circuit duty. For the recommended service voltage level, all Maglev Substations require Harmonics analysis and possible filtering, except 6 Maglev Substations out of a total of 52 for the Altamont Pass Alternative, or 55 for the Pacheco Pass Alternative.

These findings are confirmed by the fact that TGV traction systems, which are similar harmonics characteristics, are provided with harmonics filters as indicated in Reference 7.

Voltage Flicker Evaluation

The Maglev system considered for the California Line could be subjected to 40 MW power fluctuations, from 10 to 50 MW, every 30 seconds or twice per minute during maximum traffic conditions of 12,000 passengers an hour. To meet the above Criteria, as shown by Figure 6, for this frequency, the Voltage Flicker should be less than 1.5 percent.

The resulting percent Voltage Flicker can be estimated by using the following formula :

$$VOLTAGE\ FLICKER\ (\%) \approx 100 \times (\ IR\ \cos\varphi\ + IX\ \sin\varphi\ )$$

With :

MVA Base 100 *MVA*

$$I\ (\ p.u.\ ) = \frac{MVA\ Power\ Fluctuation}{MVA\ Base} = \frac{MVA\ Power\ Fluctuation}{100}$$

$$\cos\varphi = Load\ Power\ Factor = PF$$

$$\sin\varphi = \sqrt{1 - PF^2}$$

$Z = System\ Short\ Circuit\ Impedance\ in\ p.u.$

$$Z = \frac{MVA\ Base}{MVA\ System\ Short\ Circuit\ Duty} = \frac{100}{MVA\ System\ Short\ Circuit\ Duty}$$

$R = System\ Short\ Circuit\ Equivalent\ Resistance = Z\cos\delta$

$X = System\ Short\ Circuit\ Equivalent\ Reactance = Z\sin\delta$

$\delta = System\ Short\ Circuit\ Equivalent\ Impedance\ Angle$

It can be seen that the voltage flicker depends on the power factor of the Maglev Substation load and the angle of the System short circuit equivalent impedance at the point of connection.

A study was conducted to demonstrate the sensitivity of the voltage flicker at each connection point to the power factor of the Maglev Substation load, by considering the values of 1.0, 0.95, 0.90, and 0.85.

It was found that, at unity power factor the voltage flicker is minimum, in fact it is 0 when the System Short circuit equivalent Impedance has a 90 degree angle, which is the case at most point of connections located at the subtransmission side of the "Source" Transmission Substations. This is caused by the preponderance of the transformer impedance (11 percent on 150-MVA base) which has a high X/R ratio, typically more than 65 for transformers of this size (150 MVA).

It was also found that, if the power factor of the Maglev Substation load is less than unity, several Maglev Substations, which can be served at a Subtransmission voltage at unity power factor, would have to be served at 230 kV, because the voltage flicker would exceed 1.5 percent.

For instance, if the load power factor is 0.95, this would be the case for six Maglev Substations in the PG&E service territory, Substations 17, 18, 19, 38, 39, and 40, which would result in an additional cost of $71.5 M.

These findings, in addition to the need for adequate voltage support, show the importance of maintaining unity power factor at all Maglev Substations.

CONCLUSIONS

The total Cost estimates (1992 level) for the Electric Utility Power System requirements for the California Maglev Line are respectively $1.62 and $1.76 Billion, or an average of $2.7 and $2.8 M per mile of Maglev Line, for each Alternative: Altamont Pass and Pacheco Pass.

About 53.5 percent of these Total Costs are for the new Maglev Substations, 13.5 percent for additions at existing Substations, and 33.0 percent for Transmission and Subtransmission line work.

The cost of land associated with these facilities is respectively 12.4 and 15.9 percent of the Total Costs.

These large costs result from the magnitude of the project : respectively 590 and 628 miles of Maglev line, 52 and 55 Maglev Substations, and hundreds of miles of new or rebuilt Transmission and subtransmission lines, ranging from about 100 miles at 66 kV, 500 miles at 115 kV, to 340 miles at 230 kV.

These costs may be reduced by optimizing the system design, such as increasing the distance between the Maglev substations, or accepting the loss of one Maglev substation, which may result in higher costs for the transmission and subtransmission lines and the 12-kV DC cables along the Maglev line. Optimization will aslo be possible, during the next phase of the study, when detailed simulations of the Maglev system loads are available.

Together with the 12-kV DC cables and the inverters along the Maglev line, the power system requirements were found to have the second largest cost with $5.6 M per mile of Maglev line, out of a total of $23 M , after the guideway system ($9.1 M), as subsequently indicated in the Final Report of the National Initiative Bechtel Team (Reference 8).

To avoid even higher costs, the study indicated that unity power factor should be maintained and harmonics should be within criteria limits, for all Maglev Substation loads.

REFERENCES

1. Center for Continuous Study of the California Economy, California Population Characteristics, Report, Special Edition April 1990.

2. Southern California Edison Company, Transmission Planning Criteria and Guidelines, (Approved by the Plant Expenditure Review Committee in November 14, 1989).

3. Roy Billinton and Ronald Allan : Reliability Evaluation of Engineering Systems. Plenum Press, New York and London, 1983.

4. P. Save de Beaurecueil : Southern California Edison Company, Transmission Line Outages Statistical Analysis, 1980 Reliability Conference for the Electric Power Industry, Proceedings, Pages 27-38.

5. EDF Regional Systems Planning Guide - Systems Structures and Operation, Section 26, Article 262, Harmonics, dated 1/1/90.

6. Barnes, R. Wong, K. T : Unbalance and Harmonic Studies for the Channel Tunnel Railway System, IEE Proceedings Paper, Part B Electric Power Applications v 138 n 2 March 1991, p 41-50.

7. V. Sabate : Electric Disturbances generated by Electric Train Locomotives, Revue Technique GEC Alsthom No. 5 1991. (Paper describes harmonics filtering used for TGV systems)

8. National Maglev Initiative Bechtel Team, Maglev System Concept Definition Final Report, Prepared for the U.S. Department of Energy and the Federal Railroad Administration under Contract DTFR 53-92-C-00003, Dated September 30, 1992.

NATIONAL MAGLEV INITIATIVE

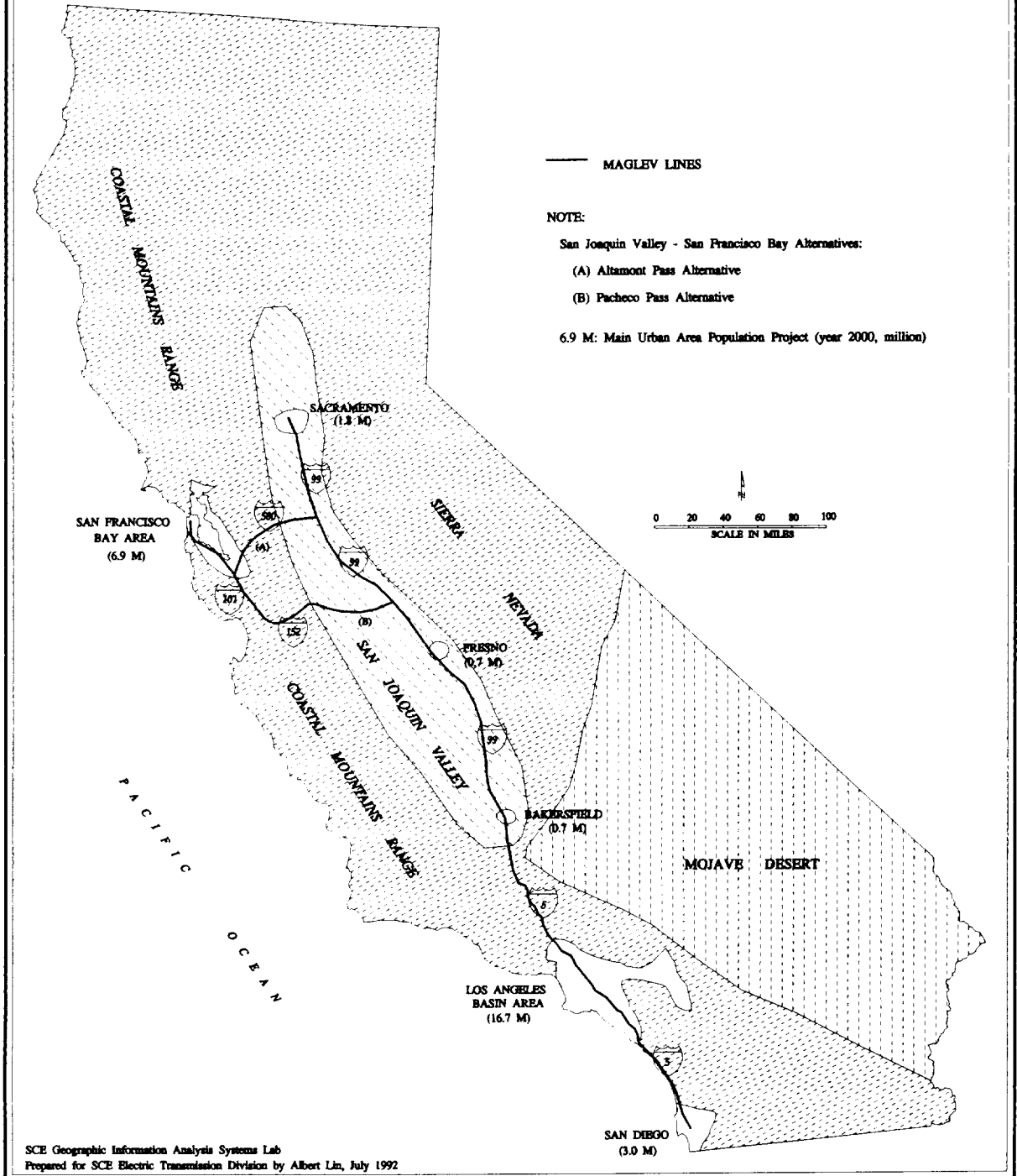**MAGLEV FEASIBILITY STUDY**

CALIFORNIA LINE GENERAL LOCATION

——— MAGLEV LINES

NOTE:

San Joaquin Valley - San Francisco Bay Alternatives:

(A) Altamont Pass Alternative

(B) Pacheco Pass Alternative

6.9 M: Main Urban Area Population Project (year 2000, million)

Figure 1. Maglev California line general location.

223

NATIONAL MAGLEV INITIATIVE
MAGLEV FEASIBILITY STUDY - CALIFORNIA LINE
MAGLEV SUBSTATIONS & UTILITY POWER SYSTEM (500 & 230KV)
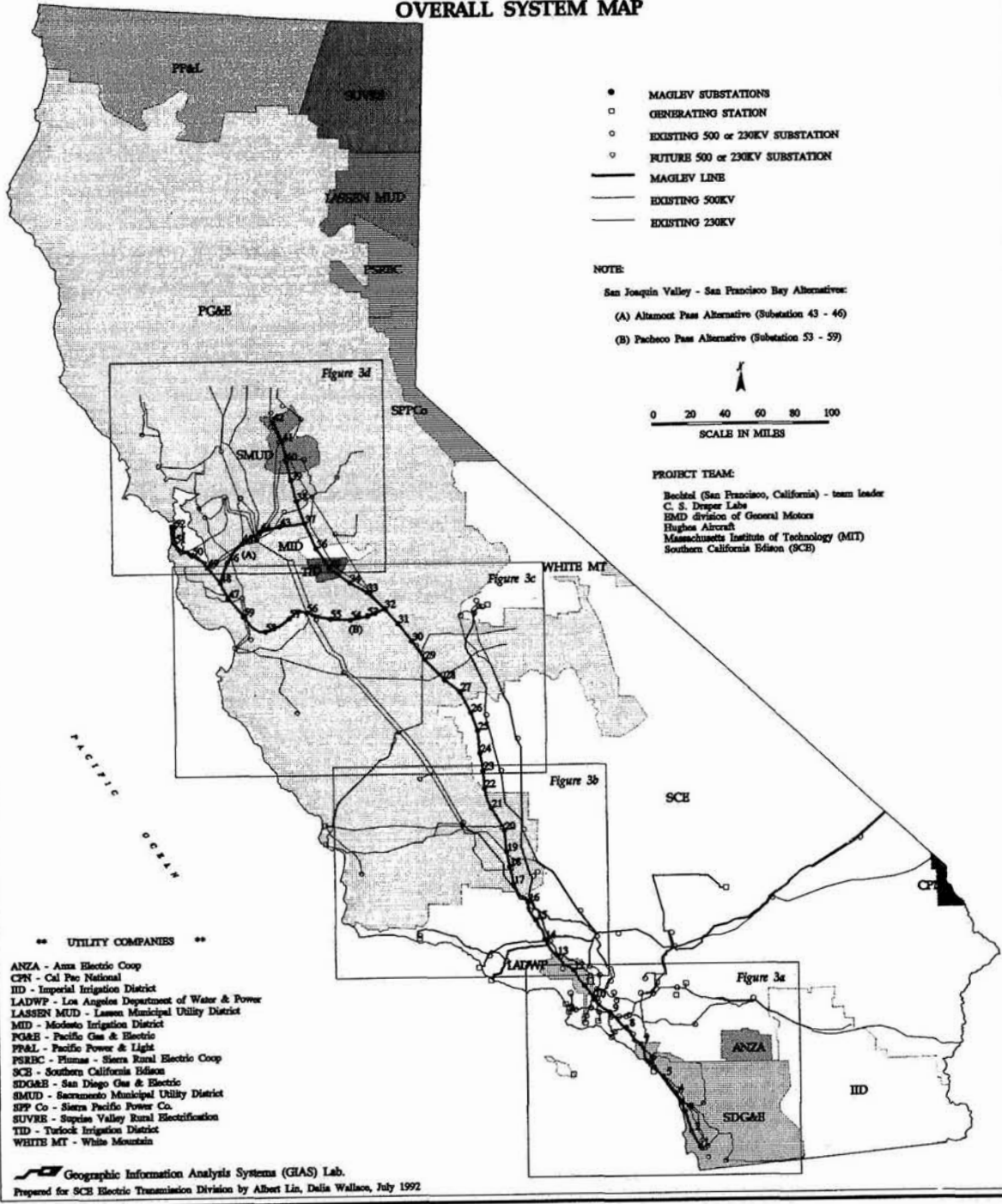## OVERALL SYSTEM MAP

Figure 2. Maglev California line overall system map.

224
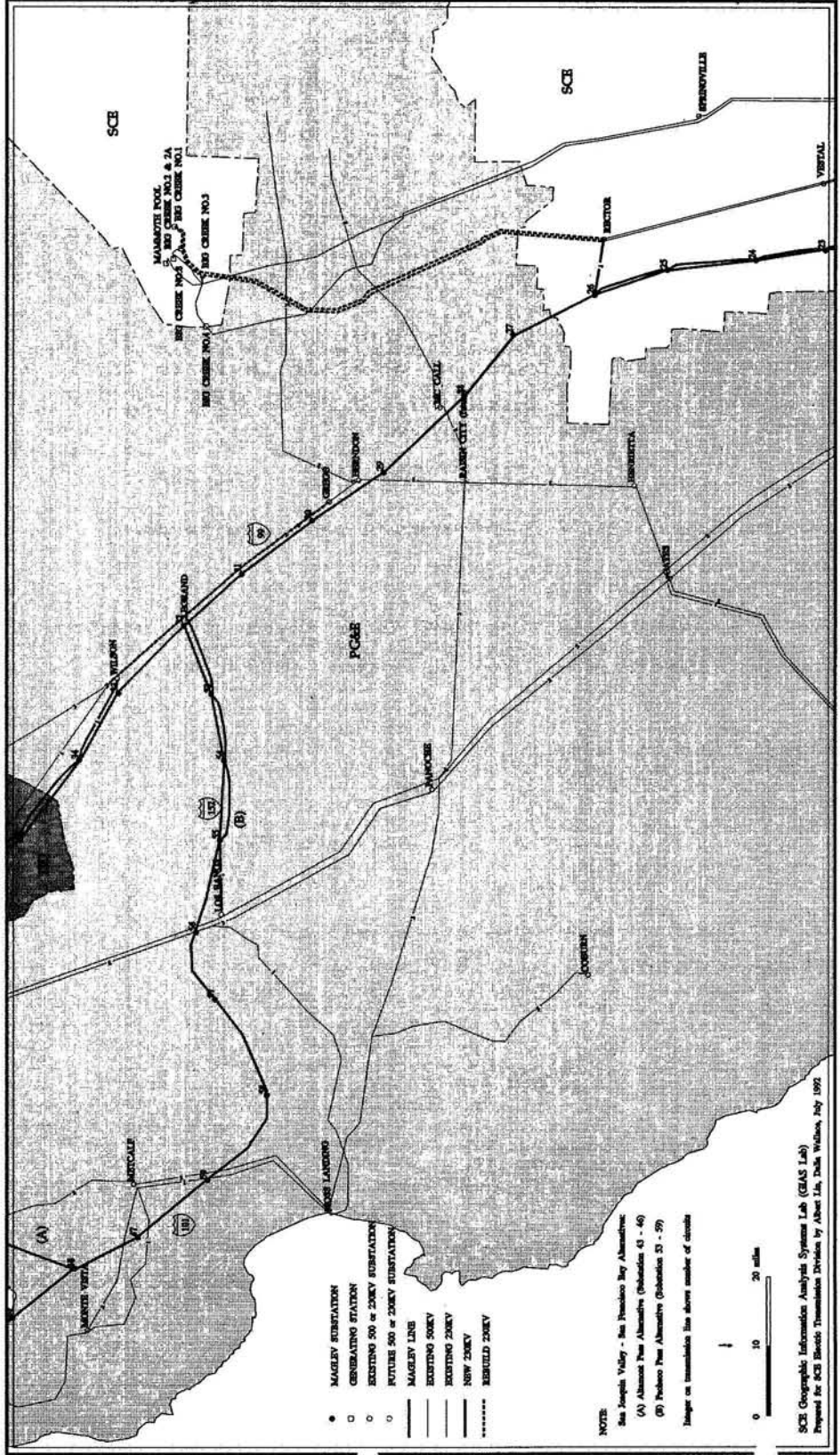
Figure 3. Maglev California line system map, Bakersfield-San Francisco section.
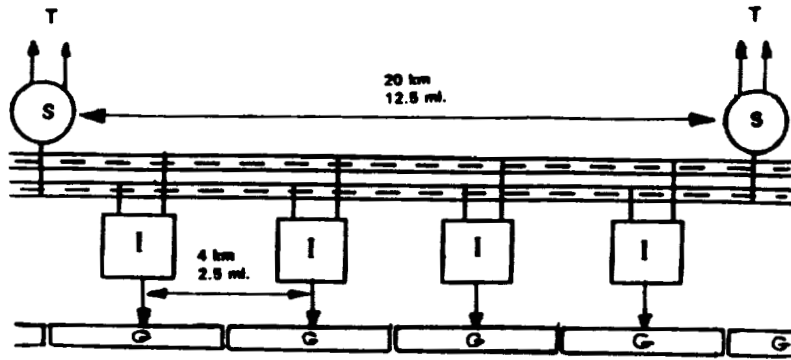
Figure 4. Maglev power supply system configuration between two consecutives maglev substations.
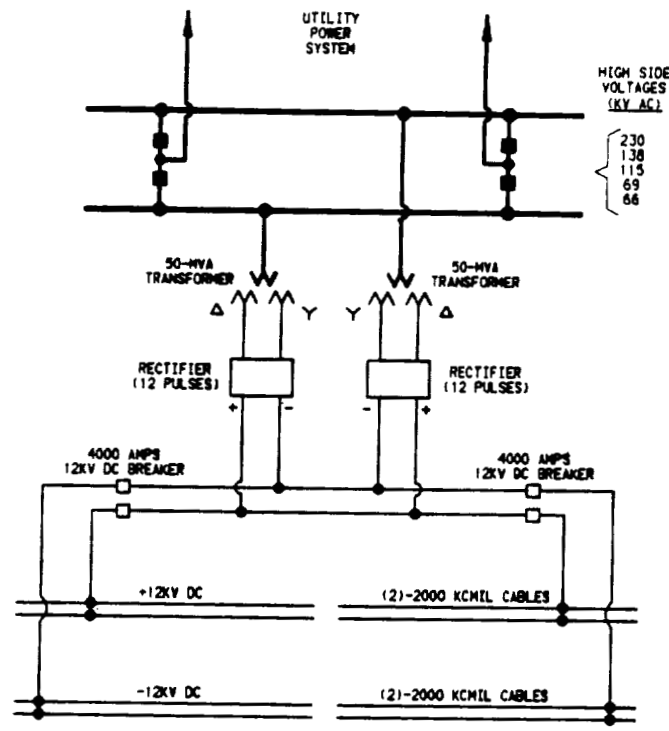

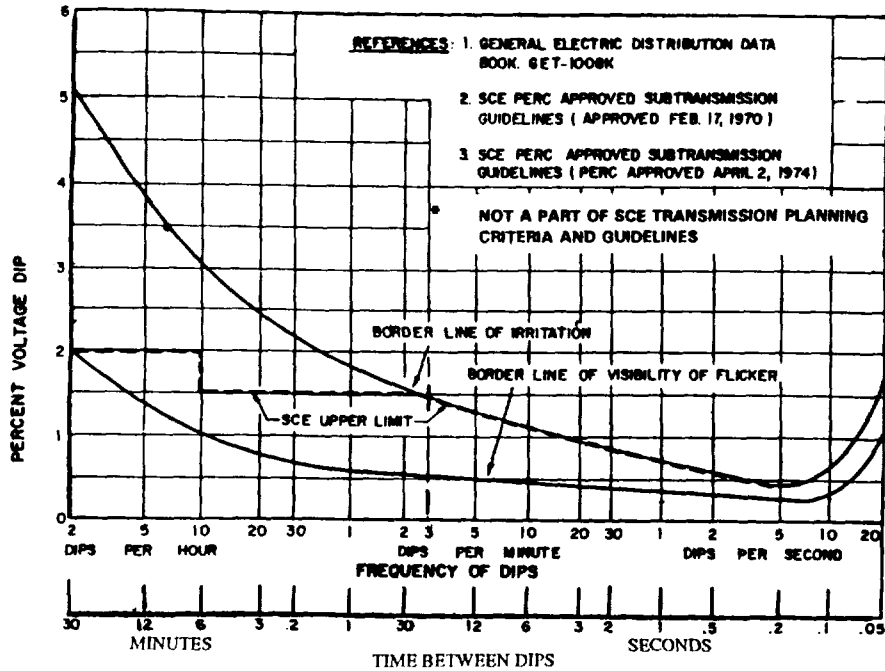Figure 5. Maglev substation schematic one line diagram.

Figure 6. Southern California Edison Company
Voltage fluctuation design limits.

Table 1. Limit harmonics rates, from EDF planning guide,
not part of SCE transmission planning criteria.

LIMIT HARMONICS RATES WHICH CAN BE CREATED ON SYSTEM BY ALL CUSTOMERS SERVED AT A GIVEN VOLTAGE LEVEL								
Odd Harmonics Non Multiples of 3			Odd Harmonics Multiples of 3			Even Harmonics		
Rank	Harmonics Voltage (Percent)		Rank	Harmonics Voltage (Percent)		Rank	Harmonics Voltage (Percent)	
n	Distrib.	Subtrans. & Trans.	n	Distrib.	Subtrans. & Trans.	n	Distrib.	Subtran & Trans
5	4.6	2	3	3.8	2	2	1.3	2.1
7	3.8	2	9	1.1	1	4	1	1.4
11	2.7	1.5	15	0.2	0.3	6	0.5	0.7
13	2.3	1.5	>21	0.2	0.2	8	0.2	0.3
17	1.5	1				10	0.2	0.3
19	1.2	1				>12	0.2	0.3
23	1.2	0.7						
25	1.2	0.7						
>25	0.15 + 10 / n	0.1 + 2.5 / n						

NOTES :
1. Harmonics Voltage (Percent) =
    (Harmonics Voltage of rank n) / (Normal Positive Sequence Voltage)

2. Distrib. = Distribution Voltage Levels (33, 16, 12, and 4 kV)

3. Subtrans. = Subtransmission Voltage Levels (138, 115, and 66 kV)

4. Trans. = Transmission Voltage Levels (500 and 230 kV)

Session 6a – Controls

Chairman: Roland Siegwart
MECOS Traxler

MICROGRAVITY ISOLATION SYSTEM DESIGN:
A MODERN CONTROL SYNTHESIS FRAMEWORK

R. D. Hampton, Research Associate
C. R. Knospe, Assistant Professor
P. E. Allaire, Professor
Department of Mechanical, Aerospace, and Nuclear Engineering
University of Virginia
Charlottesville, VA 22903

C. M. Grodsinsky
NASA Lewis Research Center
Cleveland, OH 44135

ABSTRACT

Manned orbiters will require active vibration isolation for acceleration-sensitive microgravity science experiments. Since umbilicals are highly desirable or even indispensable for many experiments, and since their presence greatly affects the complexity of the isolation problem, they should be considered in control synthesis. In this paper a general framework is presented for applying extended H_2 synthesis methods to the three-dimensional microgravity isolation problem. The methodology integrates control- and state frequency weighting and input- and output disturbance accommodation techniques into the basic H_2 synthesis approach. The various system models needed for design and analysis are also presented. The paper concludes with a discussion of a general design philosophy for the microgravity vibration isolation problem.

INTRODUCTION

Although many scientists have planned or conducted materials processes and fluid physics science experiments designed for a weightless environment, the currently available facilities have proved far from ideal. Evacuated drop towers can provide only a few seconds of "weightlessness" at levels on the order of 10^{-6} g_0 (where g_0 is the gravitational acceleration at sea level). Aircraft flying low-gravity parabolic trajectories can extend the time to about 15-20 seconds, and sounding rockets can provide several minutes of a microgravity environment, but the goal of providing days, or even hours, for microgravity research has proved elusive. It was once hoped that the Space Shuttle could provide the desired environment, but such factors as manned activity, machine and structural vibrations, and thruster firings for orientation or reboost have resulted in acceleration levels generally unsatisfactory for the designed experiments. (Background excitations have been measured in the milli-g range.) In fact, the data from many experiments have been found unacceptable due to the poor acceleration environment.

Due to the low frequencies of greatest concern (below about 10 Hz) the isolation problem is a largely unfamiliar one to vibration engineers; the requirement of a corner frequency of about 10^{-3} Hz is particularly vexing. Passive isolation is incapable of solving the isolation problem in this region, and even should a

sufficiently soft spring be physically realizable, it could not isolate against direct disturbances to the payload. If the payload is tethered (e.g., for evacuation, power transmission, cooling, or material transport), a passive isolator cannot provide isolation below the corner frequency imposed by the umbilical stiffness.

An active isolator (such as a magnetic suspension system) that merely possesses a low positive stiffness fares no better in the presence of an umbilical, for the same reasons. And if the control system seeks to lower the corner frequency by adding negative stiffness, to counteract the umbilical's stiffness, the system will (at best) possess almost no stability robustness. In the face of the usual umbilical nonlinearities and uncertainties, this situation is clearly unacceptable. At very low frequencies the rattlespace constraints become limiting (refs. 1, 2), so that any isolation system must have unit transmissibility in that region. In short, a microgravity isolator must be active, and it must be capable of dealing with the particular frequency-dependent complexities accompanying a tethered payload and a restrictive rattlespace.

The available acceleration data clearly point to a need for three-dimensional isolation (ref. 3). Classical control design methods are not well-suited for handling such problems; modern control methods provide a much more natural setting, opening up to the designer the power of the developing robust control synthesis and -analysis tools, along with a variety of well-tested and progressive computational software packages.

The well-known H_2 synthesis [i.e., LQR ("Linear Quadratic Regulator") or LQG("Linear Quadratic Gaussian")] methodology is one such modern control method. It can readily provide an optimal feedback controller for a linearized plant (i.e., payload plus umbilical) subject either to no exogenous input (LQR case) or to white noise disturbances only (LQG case). An optimal control found by H_2 synthesis minimizes a quadratic ("energy-type") cost function, or performance index. Such a performance index is quite appropriate for the microgravity isolation problem, since it allows penalizing both the control energy required for isolation and the vibrational energy of the payload. Unfortunately, however, the application of this synthesis method to practical problems has been plagued by robustness difficulties. Granted, the standard LQR solution provides excellent robustness guarantees for the single-input-single-output (SISO) problem (ref. 4, pp. 70-74) and also yields guarantees (though less useful) for the multiple-input-multiple-output (MIMO) problem (ref. 5). But the addition of a state observer to the controller (as is usually necessary for practical problems) removes these robustness guarantees (ref. 6). This fundamental practical concern has led to a common skepticism regarding H_2 synthesis.

There exist extensions to H_2 synthesis, however, which can resolve the robustness issues. The disturbance-accommodation and frequency-weighting techniques contributed, respectively, by C. D. Johnson (ref. 7, 1968; refs. 8 and 9, 1970; ref. 10, 1971) and N. K. Gupta (ref. 11, 1980) have proved to be highly useful in this regard. In fact, they provide the fundamental additional tools needed for solving practical controller design problems. These two extensions lead to augmented state equations which still allow for problem solution by the familiar H_2 synthesis machinery. Recent investigations have examined the effect of the frequency-weighting extension on system robustness (refs. 12, 13), and the dual relationship between frequency weighting and disturbance-accommodation (ref. 14). Additional extensions have also been proposed (ref. 15).

The utility of "extended H_2 synthesis" for the tethered microgravity vibration isolation problem has been clearly demonstrated by recent studies (refs. 16, 17). Extended H_2 synthesis has been used effectively to develop SISO and SIMO (single-input-multiple-output) controllers for a realistic one-dimensional microgravity vibration isolation problem, using a "smart" form of acceleration feedback. The

232

resulting closed-loop system exhibited excellent stability- and performance robustness guarantees, including a high degree of robustness to umbilical parametric uncertainty.

The present paper will give a general framework for controller design by the extended H_2 synthesis method, for the microgravity vibration isolation problem. Following a summary of the basic H_2 synthesis approach, the paper will describe how to incorporate the control- and state frequency weighting and input- and output disturbance accommodation extensions into the synthesis procedure. Control noise will also be included. General guidelines will be presented for effectively integrating these extensions into the design procedure.

The development below is specifically tailored to the microgravity isolation problem, but the mathematics are fully applicable to any problem that has the appropriate (very general) mathematical description. Four fundamental system models will be presented to aid the designer in visualizing the design effort. Only the synthesis procedure will be detailed here; the analysis techniques used for controller evaluation will be detailed in a later work.

BASIC H_2 SYNTHESIS REVIEW

A generic microgravity vibration isolation system is depicted below in Fig. 1. A payload, such as a microgravity science experiment, is acted upon by actuators (typically non-contacting) that are commanded by a control system. This control system uses measurements, such as payload positions and accelerations, to develop the control signals, typically currents or voltages. The objective of H_2 synthesis is to find a control signal that minimizes the weighted sum of the two-norm of the control energy and of the states, subject to the linearized system equations of motion. This control signal will be found to be dependent only on the past accumulative measurement information, for a system excited only by zero-mean white Gaussian noise.
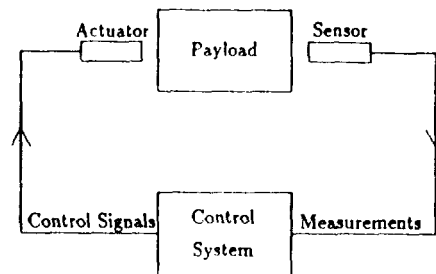

Figure 1. Vibration isolation system.

Specifically (and a bit more mathematically), to use H_2 synthesis the system equations of motion must first be linearized and expressed in the following (standard) state space form:

$$\dot{\underline{x}} = A\underline{x} + B\underline{u} + E_s\underline{w}_s, \qquad \underline{y} = C\underline{x} + D\underline{u}, \qquad \underline{z} = \underline{y} + E_n\underline{w}_n \qquad \text{(1a,b,c)}$$

$\underline{x}$ is the state vector, $\underline{y}$ is the output vector, $\underline{z}$ is the measurement vector, $\underline{u}$ is the control vector, E_s and E_n are selection matrices, and $\underline{w}_s$ and $\underline{w}_n$ are process- and sensor-noise vectors, respectively. For the microgravity vibration isolation problem, the process noise ($\underline{w}_s$) models the disturbances acting on the payload, either directly (e.g., air currents, fluid flow, or experiment-mounted rotating machinery) or indirectly (i.e., through the umbilicals). The sensor noise ($\underline{w}_n$) models the electrical or mechanical noise that contaminates the state measurements. In general, not all states will be measurable (i.e., rank $C \le$ dim $\underline{x}$).

Let the initial conditions on the state vector be $\underline{x}(0) = \underline{x}_0$ (although these intitial conditions will not appear in the final control solution); let $\underline{x}_0$, $\underline{w}_s$, and $\underline{w}_n$ be independent and bounded (as is reasonable, since unbounded states and infinitely large noise are not physically possible); and let $\underline{x}_0$ be Gaussian, and $\underline{w}_n$ and $\underline{w}_s$, zero-mean white Gaussian, for technical reasons. The power of the process- and sensor-noise vectors can be expressed mathematically by

$$\text{cov}[\underline{w}_s(t),\underline{w}_s(\tau)] = V_1\delta(t-\tau) \text{ and cov}[\underline{w}_n(t), \underline{w}_n(\tau)] = V_3\delta(t-\tau) \tag{2}$$

(ref. 18, p. 272). Assume that $\{A,B\}$ and $\{A,E_s V_1^{1/2}\}$ are stabilizable, where $V_1 = V_1^{1/2} V_1^{1/2*}$ (the asterisk here means "conjugate transpose"), and that $\{C,A\}$ is detectable (ref. 19, p. 226). These requirements mean, respectively, that a stabilizing controller exists, and that the available measurements are sufficient for its implementation. Let V_1 and V_3 be positive semidefinite (PSD) and positive definite (PD), respectively, for reasons of solution existence. That is, there need not be any process noise, but there must be at least some noise in all measurement channels (as there will be) if an optimal control solution is to exist.

The H_2 synthesis design method uses a quadratic performance index,

$$J = \lim_{T \to \infty} \frac{1}{2T} \int_0^T \mathcal{E}\left\langle \begin{bmatrix} \underline{x}^T & \underline{u}^T \end{bmatrix} \begin{bmatrix} W_1 & W_2 \\ W_2^T & W_3 \end{bmatrix} \begin{bmatrix} \underline{x} \\ \underline{u} \end{bmatrix} \right\rangle dt \tag{3}$$

where W_1, W_2, and W_3 are weighting matrices. These weighting matrices, assigned by the designer, allow him to place a relative importance on the two-norm of each state (using W_1) and of the control (using W_3). W_2 allows him to assign cross weightings. (These cross-weightings are not generally used for the basic H_2 synthesis problem, but they become important with some of the extensions.) W_1 is PSD and W_3 is PD (ref. 18; pp. 272, 276), again for reasons of solution existence. "$\mathcal{E}$" is the expected-value operator, needed since the system is excited stochastically by $\underline{w}_s$. The cost rate functional form for J (with "$\lim_{T \to \infty} \frac{1}{2T}$") is used to allow for the white noise disturbance $\underline{w}_s$. Otherwise the performance index would be infinite.

Let an admissible control $\underline{u}(t)$ be one that depends only on the past accumulative observation data. That is, $\underline{u}(t)$ has the form

$$\underline{u}(t) = \underline{u}[t,\underline{Z}(t)], \text{ where } \underline{Z}(t) = \{\underline{z}(\tau), 0 \le \tau \le t\}. \tag{4a,b}$$

(For more general conditions on admissibility, see ref. 18, p. 272.) The objective is to find an admissible control function $\underline{u}^*(t)$ which minimizes the cost J with respect to the set of admissible control functions $\underline{u}(t)$ subject to the dynamic constraint (1a,b,c). That is, the optimal control solution must exist and be realizable, must minimize the cost functional specified by the designer, and must take into consideration the system equations of motion.

The solution is well-known, and is summarized as follows:

$$\underline{u}^*(t) = -K\hat{\underline{x}}(t) \tag{5a}$$

where $\hat{\underline{x}}$ is an estimate of $\underline{x}$ using a Luenberger observer (ref. 18, pp. 288-289) having observer gain matrix L

$$K = W_3^{-1}\left(B^T P + W_2^T\right), \tag{5b}$$

P is the unique PD solution to the Algebraic Riccati Equation (ARE)

$$PA + A^T P - \left(PB + W_2\right)W_3^{-1}\left(PB + W_2\right)^T + W_1 = O, \tag{5c}$$

$$L = QC^T\left(E_n V_3 E_n^T\right)^{-1}, \tag{5d}$$

Q is the unique PD solution to the ARE

$$AQ + QA^T - QC^T\left(E_n V_3 E_n^T\right)^{-1} CQ + E_s V_1 E_s^T = O, \tag{5e}$$

234

P exists if $\{A,B\}$ is stabilizable and $\{C,A\}$ is detectable
or if the system is asymptotically stable, and

Q exists if $\{A, E_sV_1^{1/2}\}$ is stabilizable and $\{C,A\}$ is detectable
or if the system is asymptotically stable.

Note that this control signal is developed by simply applying constant (negative) feedback gains K to estimates of the system states. These estimates are themselves optimal in that they are the "closest" to the actual states, in terms of the expected value of the rms of the estimate error. They are produced in the controller from the control signal and the measurement vector, using constant observer gains L. Fig. 2 below presents this standard optimal controller (e.g., cf. ref. 20, pp. 356, 366) in block-diagram form.
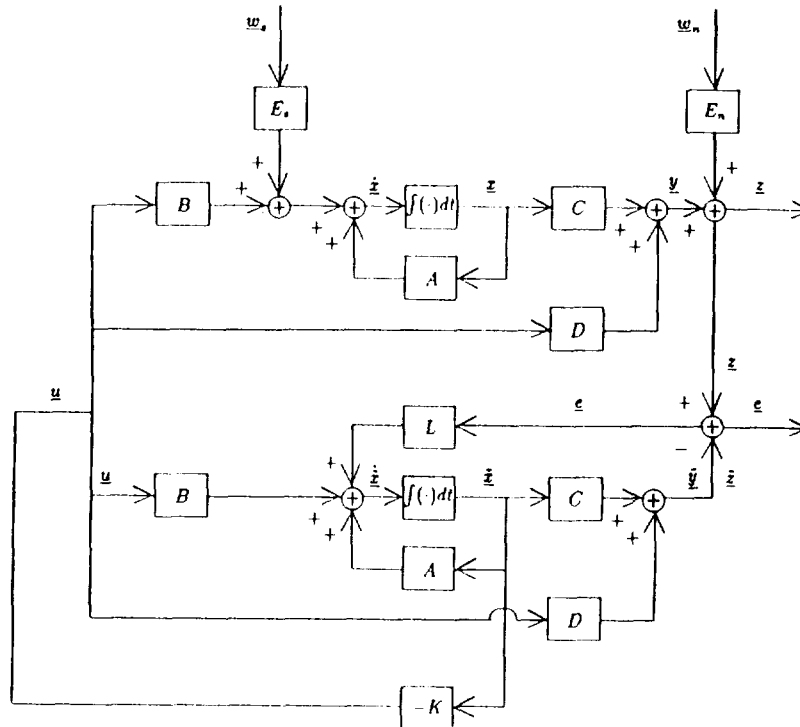

Figure 2. Block diagram of system with H_2-optimal controller.

EXTENSIONS TO H_2 SYNTHESIS

Frequency Weighting

For the active microgravity vibration isolation problem, payload accelerations are of much greater concern at some frequencies than at others. Accelerations at higher frequencies can be handled passively, and very low-frequency accelerations correspond to such large displacements that they are essentially unisolable, due to practical rattlespace constraints. Rattlespace constraints also require that the relative displacements between space platform and payload be kept to a minimum at low frequencies. Control is needed at lower frequencies, where the plant is best-known and where the major isolation effort is desired. At higher frequencies, however, excessive control can excite unmodeled higher modes of the plant. Consequently it is desirable, through the performance index, to be able to penalize control strategies in a frequency-dependent fashion. This can be achieved by weighting the states x and the control u in the cost

235

rate functional so that the weightings are frequency-dependent. The latter, extended, H_2 synthesis problem will be seen to have the same form as the former one. It will have the simple difference that the various system matrices now will be "augmented" to take into account the additional "pseudo" states required by the frequency-weighting extension.

Let $\underline{x}$ be considered to be the input to a filter $\mathcal{H}(s)$ of which $\bar{x}$ is the output, and let $\mathcal{H}(s)$ have a state-space representation defined by $\{A_I, B_I, C_I, D_I\}$.

That is, $\qquad \mathcal{H}(s) = C_I(sI-A_I)^{-1}B_I + D_I$. $\hfill (6)$

Then $\qquad \underline{\dot{z}}_I = A_I \underline{z}_I + B_I \underline{x}, \quad \bar{x} = C_I \underline{z}_I + B_I \underline{x}$ $\hfill (7a,b)$

expresses $\bar{x}$ in terms of $\underline{x}$, employing pseudostates $\underline{z}_I$. Similarly, if $\underline{u}$ is considered to be the input to a filter

$\mathcal{H}(s)$ of which $\bar{u}$ is the output, and if $\mathcal{H}(s)$ has a state-space representation defined by $\{A_2, B_2, C_2, D_2\}$, $\bar{u}$

can be expressed in terms of $\underline{u}$, employing pseudostates $\underline{z}_2$:

$$\underline{\dot{z}}_2 = A_2 \underline{z}_2 + B_2 \underline{u}, \qquad \bar{u} = C_2 \underline{z}_2 + D_2 \underline{u} \qquad (8a,b)$$

These *frequency-weighted* states ($\bar{x}$) and controls ($\bar{u}$) are now weighted (i.e., penalized) by constant

weighting matrices W_I and W_3, respectively. The resulting state equations and performance index are as follows:

$$^I\underline{\dot{x}} = {}^IA\,{}^I\underline{x} + {}^IB\underline{u} + {}^IF_s\underline{w}_s, \qquad y = {}^IC\,{}^I\underline{x} + Du, \qquad z = y + E_n\underline{w}_n \qquad (9a,b,c)$$

$$^IJ = \varepsilon\left\{ \lim_{T\to\infty} \frac{1}{2T}\int_0^T \left\langle \begin{bmatrix} {}^I\underline{x}^T & \underline{u}^T \end{bmatrix} \begin{bmatrix} {}^IW_I & {}^IW_2 \\ {}^IW_2^T & {}^IW_3 \end{bmatrix} \begin{Bmatrix} {}^I\underline{x} \\ u \end{Bmatrix} \right\rangle dt \right\} \qquad (9d)$$

where $\qquad {}^I\underline{x} = \begin{bmatrix} \bar{x} \\ z_I \\ z_2 \end{bmatrix}, \qquad {}^IA = \begin{bmatrix} A & O & O \\ B_I & A_I & O \\ O & O & A_2 \end{bmatrix}, \qquad {}^IB = \begin{bmatrix} B \\ O \\ B_2 \end{bmatrix}, \qquad {}^IC = \begin{bmatrix} C & O & O \end{bmatrix} \qquad (9e,f,g,h)$

$$^IF_s = \begin{bmatrix} F_s \\ O \\ O \end{bmatrix}, \quad {}^IW_I = \begin{bmatrix} D_I^T W_I D_I & D_I^T W_I C_I & O \\ C_I^T W_I D_I & C_I^T W_I C_I & O \\ O & O & C_2^T W_3 C_2 \end{bmatrix}, \quad {}^IW_2 = \begin{bmatrix} O \\ O \\ C_2^T W_3 D_2 \end{bmatrix}, \quad {}^IW_3 = \begin{bmatrix} D_2^T W_3 D_2 \end{bmatrix} \qquad (9j,k,m,n)$$

The optimal control $\underline{u}(t)$ will now minimize the weighted sum of the two-norm of the *frequency-weighted* control energy and states.

Input Disturbance Accommodation

In the basic H_2 problem it was assumed that the process noise $\underline{w}_s$ (i.e., the disturbance acting on the payload, whether directly, or indirectly via the umbilicals) is zero-mean white Gaussian. This, of course, will not generally be the case; the process noise will have some (known or unknown) non-white power spectrum. Let the process noise be modeled as f_s, where f_s is a stochastic disturbance with power spectral density $S_f(\omega) = S_f^{1/2}(j\omega) S_f^{1/2}(j\omega)$. Defining $H_f(j\omega)$ by $S^{1/2}(j\omega) V_f^{1/2}$, one can consider f_s to be the

density $S_f(\omega) = S_f^{1/2}(j\omega)\, S_f^{1/2}(j\omega)$. Defining $H_f(j\omega)$ by $S^{1/2}(j\omega)\, V_l^{1/2}$, one can consider f_s to be the output of a filter $H_f(s)$, excited by zero-mean white Gaussian noise $\underline{w}_s$ with power V_l (i.e., $\mathrm{cov}[\underline{w}_s(t), \underline{w}_s(\tau)] = V_l\,\delta(t-\tau)$).

In state-space form,
$$\underline{\dot\xi}_l = A_s\underline{\xi}_l + B_s\underline{w}_s, \qquad \underline{f}_s = C_s\underline{\xi}_l + D_s\underline{w}_s \tag{10a,b}$$

such that
$$H_f(s) = C_s(sI - A_s)^{-1}B_s + D_s \tag{10c}$$

Incorporating these new pseudostates (ξ_l) into the state equations and performance index yields the further augmented H_2 synthesis problem given below:

$$^2\underline{\dot x} = {}^2A\,^2\underline{x} + {}^2B\underline{u} + {}^2E_s\underline{w}_s, \qquad \underline{y} = {}^2C\,^2\underline{x} + D\underline{u}, \qquad \underline{z} = \underline{y} + E_n\underline{w}_n \tag{11a,b,c}$$

$$^2J = \varepsilon\left\{ \lim_{T\to\infty}\frac{1}{2T}\int_0^T \left\langle \begin{bmatrix} ^2\underline{x}^T & \underline{u}^T \end{bmatrix} \begin{bmatrix} ^2W_1 & ^2W_2 \\ ^2W_2^T & ^2W_3 \end{bmatrix} \begin{Bmatrix} ^2\underline{x} \\ \underline{u} \end{Bmatrix} \right\rangle dt \right\} = {}^1J \tag{11d}$$

where
$$^2\underline{x} = \begin{Bmatrix} {}^1\underline{x} \\ \underline{\xi}_l \end{Bmatrix}, \qquad {}^2A = \begin{bmatrix} A & O & O & E_sC_s \\ B_l & A_l & O & O \\ O & O & A_2 & O \\ O & O & O & A_s \end{bmatrix}, \qquad {}^2B = \begin{bmatrix} B \\ O \\ B_2 \\ O \end{bmatrix} \tag{11e,f,g}$$

$$^2C = [C\ O\ O\ O], \qquad {}^2E_s = \begin{bmatrix} E_sD_s \\ O \\ O \\ B_s \end{bmatrix} \tag{11h,j}$$

$$^2W_1 = \begin{bmatrix} D_l^TW_1D_l & D_l^TW_1C_l & O & O \\ C_l^TW_1D_l & C_l^TW_1C_l & O & O \\ O & O & C_2^TW_3C_2 & O \\ O & O & O & O \end{bmatrix}, \qquad {}^2W_2 = \begin{bmatrix} O \\ O \\ C_2^TW_3D_2 \\ O \end{bmatrix} \tag{11k,m}$$

$$^2W_3 = \begin{bmatrix} D_2^TW_3D_2 \end{bmatrix} \tag{11n}$$

The optimal-control solution to this problem will minimize the frequency-weighted cost functional as before, with the plant now considered to be subject to the specified colored noise disturbance.

In actual space applications the power spectrum of the process noise may not be known. Fortunately, orbiter spectral vibration information need not be available for disturbance accommodation to be used. The disturbances can be assumed to have whatever form the designer finds useful. For example, if he desires the controller not to respond to process noise above some frequency range, he might choose to model $H_f(s)$ as a lowpass filter.

Output Disturbance Accommodation

The same procedure can be employed to incorporate colored sensor noise into the extended H_2 synthesis problem. No sensor will have the white-noise contamination assumed by the basic H_2 problem. And the designer may even find it useful to shape the sensor noise filter in some non-physical way. For example, if payload acceleration measurements are known to be more accurate in one frequency range, and relative position measurements in another, he might choose his sensor noise filters appropriately to

237

"inform" the observer of these facts. The resulting observer would tend to rely more heavily on the more accurate measurement(s) in a particular frequency range, in its state-reconstruction process.

Let the sensor noise vector be f_n, with selection matrix E_n, where f_n is a stochastically modeled disturbance with power spectral density $S_n(j\omega) = S_n^{1/2}(j\omega)\,S_n^{1/2*}(j\omega)$. As with the input disturbance f_s, f_n can be considered to be the output of a filter $H_n(s)$ excited by zero-mean white Gaussian noise w_n with power V_3 (i.e., $\mathrm{cov}\!\left[w_n(t), w_n(\tau)\right] = V_3 \delta(t - \tau)$). In state-space form,

$$\dot{\xi}_2 = A_n \xi_2 + B_n w_n , \qquad f_n = C_n \xi_2 + D_n w_n , \quad \text{such that} \quad H_n(s) = C_n\!\left(sI - A_n\right)^{-1} B_n + D_n \qquad (12a,b,c)$$

For the extended H_2 synthesis problem with state- and control frequency weighting (pseudostates z_1 and z_2, respectively), and with input- and output disturbance accommodation (pseudostates ξ_1 and ξ_2, respectively), the augmented state equations and the performance index are as follows:

$$^4\dot{\underline{x}} = {}^4A\,{}^4\underline{x} + {}^4B\underline{u} + {}^4E_s\,{}^4\underline{w}_s , \qquad z = {}^4C\,{}^4\underline{x} + {}^4D\underline{u} + {}^4E_n\,{}^4\underline{w}_n \qquad (13a,b)$$

$$^4J = \mathcal{E}\left\{ \lim_{T\to\infty} \frac{1}{T} \int_0^T \left\langle \begin{bmatrix} {}^4\underline{x}^T & \underline{u}^T \end{bmatrix} \begin{bmatrix} {}^4W_1 & {}^4W_2 \\ {}^4W_2^T & {}^4W_3 \end{bmatrix} \begin{Bmatrix} {}^4\underline{x} \\ \underline{u} \end{Bmatrix} \right\rangle dt \right\} \qquad (13c)$$

$$\text{where} \quad {}^4\underline{x} = \begin{Bmatrix} \underline{x} \\ \underline{z}_1 \\ \underline{z}_2 \\ \underline{\xi}_1 \\ \underline{\xi}_2 \end{Bmatrix}, \quad {}^4A = \begin{bmatrix} A & O & O & E_sC_s & O \\ B_1 & A_1 & O & O & O \\ O & O & A_2 & O & O \\ O & O & O & A_s & O \\ O & O & O & O & A_n \end{bmatrix}, \quad {}^4B = \begin{bmatrix} B \\ O \\ B_2 \\ O \\ O \end{bmatrix} \qquad (13d,e,f)$$

$$^4C = \begin{bmatrix} C & O & O & O & E_nC_n \end{bmatrix}, \qquad {}^4D = D, \qquad {}^4E_s = \begin{bmatrix} E_sD_s & O \\ O & O \\ O & O \\ B_s & O \\ O & B_n \end{bmatrix} \qquad (13g,h,j)$$

$$^4\underline{w}_s = \begin{Bmatrix} w_s \\ w_n \end{Bmatrix}, \qquad {}^4\underline{w}_n = \{w_n\}, \qquad {}^4E_n = \begin{bmatrix} E_nD_n \end{bmatrix} \qquad (13k,m,n)$$

$$^4W_1 = \begin{bmatrix} D_1^T W_1 D_1 & D_1^T W_1 C_1 & O & O & O \\ C_1^T W_1 D_1 & C_1^T W_1 C_1 & O & O & O \\ O & O & C_2^T W_3 C_2 & O & O \\ O & O & O & O & O \\ O & O & O & O & O \end{bmatrix}, \quad {}^4W_2 = \begin{bmatrix} O \\ O \\ C_2^T W_3 D_2 \\ O \\ O \end{bmatrix} \qquad (13p,q)$$

$$^4W_3 = \begin{bmatrix} D_2^T W_3 D_2 \end{bmatrix} \qquad (13r)$$

$$^4V_1 = \begin{bmatrix} V_1 & O \\ O & V_3 \end{bmatrix} \quad \text{is the autocorrelation matrix for } {}^4\underline{w}_s, \qquad (13s)$$

$$^4V_2 = \begin{bmatrix} V_2 \\ V_3 \end{bmatrix} \quad \text{is the cross-correlation matrix between} \begin{Bmatrix} w_s \\ w_n \end{Bmatrix} \text{ and } \underline{w}_n, \qquad (13t)$$

and $^4V_3 = V_3$ is the autocorrelation matrix for $\underline{w}_n$. $\qquad (13u)$

Control Noise

The active microgravity vibration isolation system must perform well even when the actual system dynamics are less than perfectly described by the system model. One way to improve the isolation system's robustness to parameter changes at the control inputs (i.e., to uncertainties in the actuator or plant model) is to add a process noise input ($\underline{w}_c$) to the model's control signal (ref. 21, p. 1-48). Recall that the H_2 synthesis machinery seeks to minimize the rms of the observation error. It does this by finding an observer gain matrix L that will optimally trade off the measurement uncertainties against the plant model uncertainties, in the state reconstruction process. Control noise will reduce the observer's "confidence" in the plant model, so that the observer will "trust" its measurement data more and its plant model less. The resulting gain matrix L will sacrifice a degree of observation quality for improved observer robustness to plant model inaccuracies. The controller gain matrix K will be unaffected.

Under these circumstances the state equations of motion, unaugmented by frequency weighting or disturbance accommodation, become

$$\dot{\underline{x}} = A\underline{x} + B(\underline{u} + \underline{w}_c) + E_s\underline{f}_s, \qquad \underline{y} = C\underline{x} + D(\underline{u} + \underline{w}_c), \qquad \underline{z} = \underline{y} + E_n\underline{f}_n \qquad (14a,b,c)$$

where $\underline{f}_s$ and $\underline{f}_n$ can be represented by filters in state-space form with white-noise inputs, as noted previously. Assume no cross-correlation between $\underline{w}_c$ and $\underline{w}_s$, or between $\underline{w}_c$ and $\underline{w}_n$, and let

$$cov\left[\underline{w}_c(t), \underline{w}_c(\tau)\right] = V_c \delta(t - \tau). \qquad (15)$$

Using now the pre-superscript designator "5" to indicate the appropriate state-space augmentation, the system equations change as follows:

$$^5\underline{x} = {}^4\underline{x}, \qquad (16a)$$

$$^5A = {}^4A, \; ^5B = {}^4B, \; ^5C = {}^4C, \; ^5D = {}^4D, \qquad (16b)$$

$$^5W_1 = {}^4W_1, \; ^5W_2 = {}^4W_2, \; ^5W_3 = {}^4W_3 \qquad (16c)$$

$$^5E_s = \begin{bmatrix} B & E_sD_s & O \\ O & O & O \\ B_2 & O & O \\ O & B_s & O \\ O & O & B_n \end{bmatrix}, \; ^5\underline{w}_s = \left\{ \begin{matrix} \underline{w}_c \\ \underline{w}_s \\ \underline{w}_n \end{matrix} \right\}, \; ^5\underline{w}_n = \left\{ \begin{matrix} \underline{w}_c \\ \underline{w}_n \end{matrix} \right\}, \; ^5E_n = \begin{bmatrix} D & E_nD_n \end{bmatrix} \qquad (16d,e,f,g)$$

$$^5V_1 = \begin{bmatrix} V_c & O & O \\ O & V_1 & O \\ O & O & V_3 \end{bmatrix}, \; ^5V_2 = \begin{bmatrix} V_c & O \\ O & V_2 \\ O & V_3 \end{bmatrix}, \; ^5V_3 = \begin{bmatrix} V_c & O \\ O & V_3 \end{bmatrix} \qquad (16h,j,k)$$

The basic tools are now in place for practical microgravity vibration isolation system design, by extended H_2 synthesis.

SYSTEM MODELING

The H_2 synthesis problem is actually a two-fold design problem; the designer must determine a regulator gain matrix K, and also an observer gain matrix L, which together are used to comprise the optimal controller. The full augmented state vector must be used for the regulator sub-design problem,

but pseudostates z_1 and z_2 (which occur due to frequency weighting) need not be reconstructed by the observer. They can simply be developed by passing the reconstructed state vector $\underline{x}$ and the control vector $\underline{u}$, respectively, through the appropriate frequency-weighting filters. Consequently the observer sub-design problem can (though need not) be one of reduced order. It is helpful, then, to have different mathematical models for conceptualizing these two sub-problems. These models will also differ, in general, from the basic plant model, which depicts the "actual" linearized plant (i.e., the system without the controller) in state space form. This model will not include the frequency-weighting and disturbance-accommodation augmentations of the former. In addition to these three conceptual models of the system, there is a fourth model, which more properly falls under the category of analysis but should be kept in mind during the synthesis procedure. This "nominal analysis model" depicts the linearized and unaugmented plant with the synthesized controller attached. It is used, with various modifications, to analyze closed-loop system performance.

Basic Plant Model

The basic plant model (shown schematically in Fig. 3) simply presents the linearized differential equations of motion in a state space form useful to the H_2 synthesis machinery. Such a representation is given below.

$$\underline{\dot{x}} = A\underline{x} + B\underline{u} + E_s\underline{f}_s \,, \qquad \underline{y} = C\underline{x} + D\underline{u} \,, \qquad \underline{z} = \underline{y} + E_n\underline{f}_n \qquad (17a,b,c)$$

No performance index is needed at this stage, since it is the *frequency-weighted* states and control which will be weighted relative to each other for the actual controller synthesis. For the microgravity vibration isolation problem a useful choice for the state vector would include relative displacements, relative velocities, and accelerations. Weighting an acceleration more heavily in a frequency range would correspond roughly to a demand to increase the associated effective mass (or inertia) of the system. A similar correspondence can be drawn between relative-displacement weighting and the effective relative stiffness, and between relative-velocity weighting and the effective relative damping.
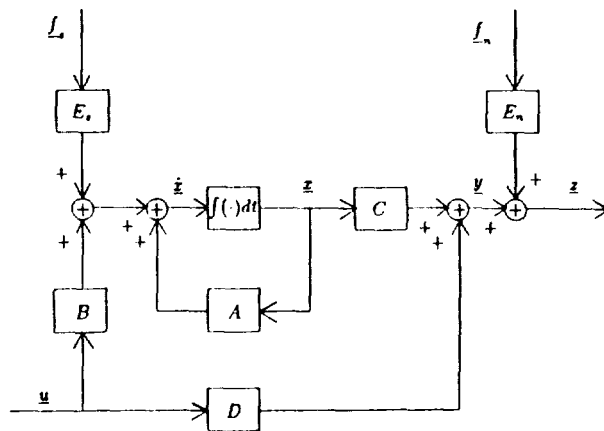

Figure 3. Basic plant model.

Regulator Synthesis Model

The regulator synthesis model adds frequency weighting and disturbance accommodation weighting filters to the basic plant model, and is the model actually used by the extended H_2 synthesis machinery in

designing the regulator. Fig. 4 portrays this model in block diagram form. Note that it has a similar form to the basic plant model, but that now augmented A, B, C, E_s, E_n, W_1, W_2 and W_3 matrices are used, as indicated by the pre-superscripts. These matrices were defined previously (16b through 16g). Also note that white noise vector $\underline{w}_s$ replaces f_s, since the process noise power spectral information is now contained in matrices ^5A and ^5E_s.

The regulator synthesis model shows the system as viewed by the extended H2 machinery in determining the matrix ^5P. This matrix is the unique positive definite solution to the following ARE,

$$^5P\ ^5A + ^5A^T\ ^5P - \left(^5P\ ^5B + ^5W_2 \right) ^5W_3^{-1} \left(^5P\ ^5B + ^5W_2 \right)^T + ^5W_1 = O \tag{18}$$

^5P is used to find the regulator feedback gains. This model is typically used only in determining the regulator gains - ^5K. It is not generally used for the design of observer gains $^{(\cdot)}L$ (although it could be), since that design problem can be reduced to one of lower order, as noted before.
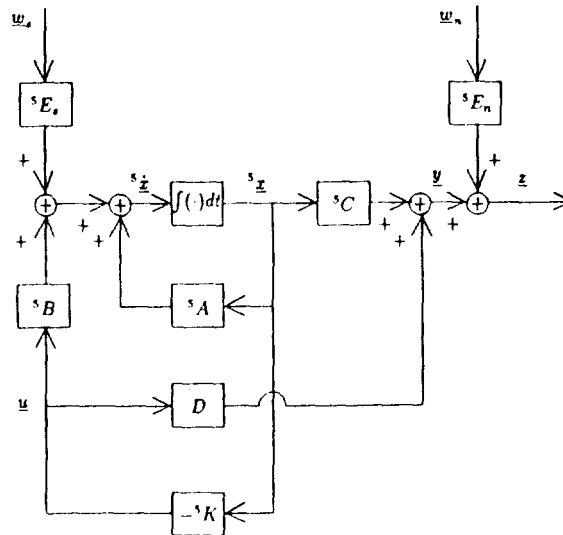

Figure 4. Regulator synthesis model.

Observer Synthesis Model

The observer uses the measurement vector $\underline{z}$ (e.g., measured relative positions and accelerations) and the control vector $\underline{u}$ as inputs to produce observations of the state vector. (In general an observer is needed to estimate the unmeasurable system states. Only rarely will all system states actually be available for measurement, and never will the disturbance-accommodation pseudostates actually be capable of measurement.) Kalman-Bucy filter design uses knowledge of process noise and sensor noise covariance matrices (and, if necessary, cross-correlation matrices) to produce optimal observer gains $^{(\cdot)}L$, in the sense of optimality previously discussed. If the complete augmented state vector $^5\underline{x}$ is to be observed, then an appropriate observer synthesis model would be as depicted in Fig. 5. ^5L would be found from the equation

$$^5L = \left(^5Q\ ^5C^T + ^5E_s\ ^5V_2\ ^5E_n^T \right)\left(^5E_n\ ^5V_3\ ^5E_n^T \right)^{-1} \tag{19a}$$

where ^5Q is the unique PD solution to the following ARE,

$$^5\tilde{A}\ ^5Q + ^5Q\ ^5\tilde{A}^T - ^5Q\ ^5C^T\left(^5E_n\ ^5V_3\ ^5E_n^T \right)^{-1}\ ^5C\ ^5Q + ^5E_s\ ^5\tilde{V}_1\ ^5E_s^T = O \tag{19b}$$

and where

$$^5\tilde{A} = ^5A - \left(^5E_s\ ^5V_2\ ^5E_n^T \right)\left(^5E_n\ ^5V_3\ ^5E_n^T \right)^{-1}\ ^5C \tag{19c}$$

$$^5\tilde{V}_1 = ^5V_1 - ^5V_2\ ^5E_n^T\left(^5E_n\ ^5V_3\ ^5E_n^T \right)^{-1}\ ^5E_n\ ^5V_2^T \tag{19d}$$

and $\quad ^5V_1, ^5V_2, ^5V_3,$ and ^5E_s are as defined previously.

Equations (19b, c, d) reduce to the form

$$^5A\,^5Q + ^5Q\,^5A^T - \left(^5Q\,^5C^T + ^5E_s\,^5V_2\,^5E_n^T\right)\left(^5E_n\,^5V_3\,^5E_n^T\right) + \left(^5Q\,^5C^T + ^5E_s\,^5V_2^T\,^5E_n^T\right)$$
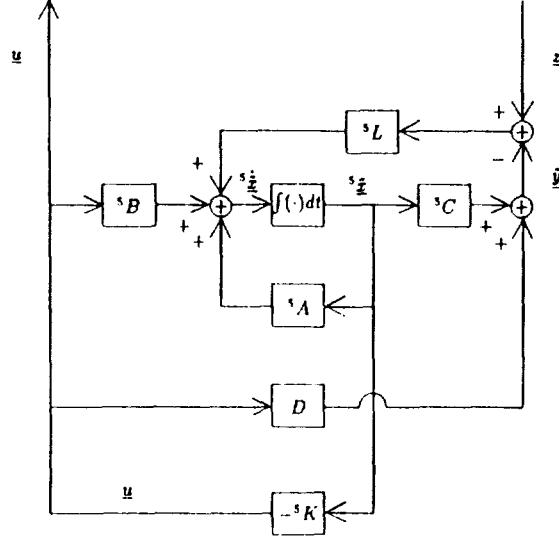
$$+^5E_s\,^5V_1\,^5E_s^T = O \tag{19e}$$

Figure 5. Observer synthesis model, observing all states and pseudostates.

However, as noted previously, the observer does not need to reconstruct the frequency-weighting pseudostates z_1 and z_2. This fact will permit an observer of smaller dimension. In this case Fig. 6 will be an appropriate observer synthesis model, with pertinent matrices defined as follows. ^6L would be found from the equation

$$^6L = \left(^6Q\,^6C^T + ^6E_s\,^6V_2\,^6E_n^T\right)\left(^6E_n\,^6V_3\,^6E_n^T\right)^{-1} \tag{20a}$$

where ^6Q is the unique PD solution to the following ARE,

$$^6\tilde{A}\,^6Q + ^6Q\,^6\tilde{A}^T - ^6Q\,^6C^T\left(^6E_n\,^6V_3\,^6E_n^T\right)^{-1}\,^6C\,^6Q + ^6E_s\,^6\tilde{V}_1\,^6E_s^T = O, \tag{20b}$$

and where

$$^6\tilde{A} = ^6A - \left(^6E_s\,^6V_2\,^6E_n^T\right)\left(^6E_n\,^6V_3\,^6E_n^T\right)^{-1}\,^6C \tag{20c}$$

$$^6\tilde{V}_1 = ^6V_1 - ^6V_2\,^6E_n^T\left(^6E_n\,^6V_3\,^6E_n^T\right)^{-1}\,^6E_n\,^6V_2^T \tag{20d}$$

$$^6V_1 = ^5V_1, \qquad ^6V_2 = ^5V_2, \qquad ^6V_3 = ^5V_3 \tag{20e,f,g}$$

$$^6E_s = \begin{bmatrix} B & E_sD_s & O \\ O & B_s & O \\ O & O & B_n \end{bmatrix}, \quad ^6A = \begin{bmatrix} A & E_sC_s & O \\ O & A_s & O \\ O & O & A_n \end{bmatrix}, \quad ^6C = \begin{bmatrix} C & O & E_nC_n \end{bmatrix} \tag{20h,j,k}$$

Equations (20b,c,d) reduce to the form

$$^6A\,^6Q + ^6Q\,^6A^T - \left(^6Q\,^6C^T + ^6E_s\,^6V_2\right)^6V_3^{-1}\left(^6Q\,^6C^T + ^6E_s\,^6V_2\right)^T + ^6E_s\,^6V_1\,^6E_s^T = O \tag{20m}$$
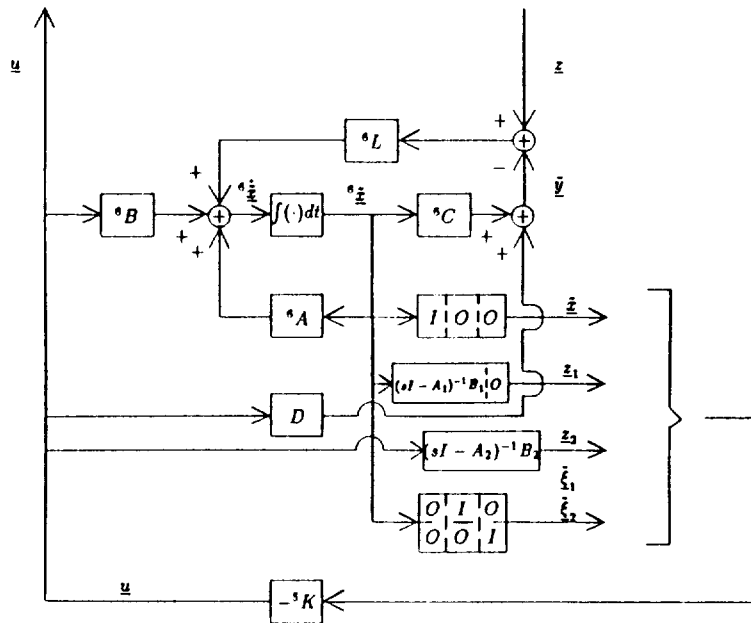
Figure 6. Reduced observer synthesis model.

Nominal Analysis Model

Once the active vibration-isolation controller has been designed, it can usually be reduced in size by modal truncation and/or balance-and-truncate ("Moore's method," ref. 22). Then the closed loop system can be evaluated, with the controller applied to the actual plant.

Letting the state space system $\{A_{F/B}, B_{F/B}, C_{F/B}, D_{F/B}\}$ represent the feedback controller, a nominal analysis model can be portrayed as in Fig. 7. Checks on nominal stability can be made by simple eigenvalue
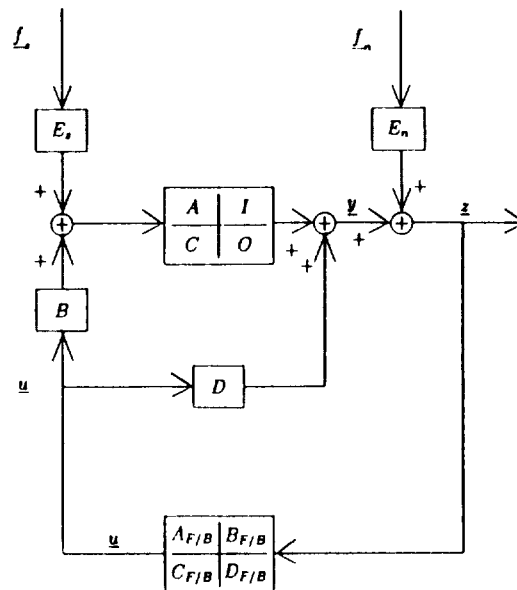
Figure 7. Nominal analysis model.

243

checks of this closed-loop system. Nominal performance can also be conducted readily using this model. With the appropriate placement of complex Δ-blocks to represent system uncertainties, one can also evaluate the system for robust stability and robust performance guarantees, using the powerful methods of mu-analysis (ref. 23).

DESIGN PHILOSOPHY FOR THE MICROGRAVITY ISOLATION PROBLEM

With the synthesis framework now in place, as presented above, the designer must choose a reasonable strategy in order to use his H_2 synthesis tools with skill. He must determine what states to use, what frequency-weighting and disturbance-accommodation filters (if any) to employ, the relative weightings of the resultant frequency-weighted states and control, and the relative weightings of the various noise vectors in his system model. The designer must also decide which measurements to make, whether to use the full- or the reduced observer synthesis model, and whether to conduct the regulator- and observer-gain sub-problems in sequence or in combination.

One primary goal in controller design should be *simplicity*. The construction of the controller will be easiest, and its speed of operation fastest, if its complexity (i.e., the number of controller states) is kept to a minimum. To accomplish this aim, the authors recommend that the engineer seek to design the controller by starting with basic (unextended) H_2 synthesis and adding complexity "one layer at a time." For example, he might first determine if basic LQG is adequate, and then add appropriate frequency weighting and disturbance accommodation step by step, evaluating after each addition whether or not the design is acceptable. If not, the next layer of complexity could be added based on the present design inadequacies. Once an adequate design has been found, it is recommended that the controller order (i.e., number of states) be reduced by using modal reduction and /or balance-and-truncate. This "step-up, step-down" philosophy should keep controller complexity to a minimum.

A second fundamental goal should be *intuitiveness*. Unless the problem is posed in such a way as to employ the designer's intuition, he will find it very difficult, especially with a three-dimensional problem, to proceed with any degree of speed. The single most important step toward an intuitive problem is the proper choice of plant states. For the microgravity vibration isolation problem, the authors believe that a reasonably physical choice is payload relative position, payload relative velocity, and payload acceleration. A heavier weighting on payload relative position (in the cost functional matrix W_j), for example, signals the H_2 machinery to attempt to increase system stiffness. Similar analogues exist for the other two suggested states, as noted before. And at least two of these states are readily measurable for microgravity systems. Such state choices, then, allow the designer to assign his weightings with a degree of "physical feel," so that extended H_2 synthesis becomes more of a craftsman's design tool, rather than a black box for use in a time-consuming trial-and-error approach.

The designer must also decide whether or not to conduct the regulator- and observer-gain design problems independently. The well-known "separation principle" guarantees that for a perfectly known system the regulator gains K and the observer gains L can be designed independently. One approach, then, would be first to design the regulator to meet the design goals, and then to design the observer to produce a state-vector estimate that is "accurate enough" over a "sufficient" bandwidth. The frequency-weighting and disturbance-accommodation extensions, however, affect the state observations in such a manner that "accurate enough" and "sufficient" are quite difficult terms to define. The closed-loop system must be analyzed as a whole for this purpose. The existence of an observer bandwidth can also be used to enhance overall system performance, so that a full-state-feedback system with inadequate performance can actually

perform quite well when the observer is added. Since the system stability- and performance robustness must ultimately be evaluated for the total closed-loop system, it is recommended that the entire controller (i.e., the observer-plus-regulator) be designed as a unit, rather than in parts.

For the microgravity vibration isolation problem, studies to date indicate that H_2 synthesis extensions are necessary, if one is to produce a practical control (ref. 16). This being so, there are certain frequency weightings that are very reasonable choices to use. At very low frequencies, indirect disturbances (i.e., orbiter positional deviations from a perfectly elliptical orbit), will be much larger than rattlespace constraints will allow. In the low-frequency region, then, the payload relative displacement should be weighted heavily, and the payload acceleration, lightly. These weighting choices could reasonably be expected to call for a controller producing unit transmissibility between orbiter and payload, at low frequencies. In the intermediate frequency range, where payload acceleration is of most concern, that state should be weighted heavily. At higher frequencies, where the plant model is not well known, high control weightings and low state weightings should be used to call for reduced control.

Certain disturbance-accommodation filters, as well, will be appropriate for the problem, while others will be inadvisable. From a physical perspective, a more massive experiment would be less susceptible either to direct or to indirect disturbances. One could expect, then, that an input disturbance filter which models a large direct disturbance would call for a controller tending to make the system seem more massive (electronically). On the other hand, an indirect disturbance alone (i.e., acting through the umbilical) could be attenuated effectively either by a greater system effective mass or by a reduced system effective stiffness. The latter means of disturbance attenuation is ineffective for direct disturbances. It also tends to reduce the stability robustness of the system. Hence, the designer should be wary of having too large an indirect disturbance model.

Output disturbance accommodation and control noise should be included in the system model only if necessary. Research to date does not indicate that either is needed for microgravity vibration isolator design. Again, the goal is to achieve a satisfactory controller that is as simple as possible.

Observer design involves the numerical solution of an ARE. An ARE involving matrices of smaller dimension will be less susceptible to the numerical difficulties which sometimes attend such solution procedures. It is preferable, then, to use the reduced rather than the full observer synthesis model.

CONCLUDING REMARKS

Active vibration isolation of microgravity science experiments is a three-dimensional, MIMO design problem requiring sophisticated design- and analysis tools. Modern control methods provide the most natural setting for handling this problem, and with a suitable choice of states, modern-control design can be conducted in a relatively intuitive fashion. The H_2 synthesis approach can be extended, using frequency weighting and disturbance accommodation techniques, to give the designer great flexibility in building a suitable controller. Implementation of these extensions involves a straightforward augmentation of various system matrices, so that the ARE-based solution methods of LQG synthesis can be readily applied. Extended H_2 synthesis provides the necessary tools for the design of a robust isolation system. This paper has provided a general framework for using extended H_2 synthesis to design the controller for such a system.

In addition to the basic plant model, there are three complementary system models that are of use in conceptualizing the synthesis problem. Observer synthesis requires fewer pseudostates than regulator synthesis, so two respective system models are needed to reflect this difference. The controller model is developed by combining the observer and regulator models, followed by reduction of the controller dimensionality. Attachment of this controller to the basic plant model produces an analysis model that can be used, with mu-analysis methods, to evaluate the closed-loop system in terms of its stability- and performance robustness.

This paper has also suggested a general design philosophy for applying the extended H_2 synthesis machinery to the particular design problem at hand. In addition to an overall design strategy, reasonable state choices were suggested, and basic practical guidelines were given for the effective use of frequency-weighting and disturbance-accommodation techniques.

ACKNOWLEDGMENTS

REFERENCES

1. Knospe, C.; and Allaire, P.: Limitations on Vibration Isolation for Microgravity Space Experiments. *Journal of Spacecraft and Rockets*, Vol. 27, No. 6, Nov.-Dec. 1990, pp. 642-646.

2. Knospe, C. R.; and Allaire, P. E.: Limits on the Isolation of Stochastic Vibration for Microgravity Space Experiments. *Journal of Spacecraft and Rockets*, Vol. 28, No. 2, March-April 1991, pp. 229-237.

3. Nelson, Emily S.: An Examination of Anticipated g-Jitter on Space Station and Its Effects on Materials Processes. *NASA TM-103775*, April 1991.

4. Anderson, Brian D. O.; and Moore, John B.: *Linear Optimal Control*. Englewood Cliffs, New Jersey: Prentice Hall, Inc., 1971.

5. Safonov, M. D.; and Athans, M.: Gain and Phase Margins for Multiloop LQG Regulators. *IEEE Transactions on Automatic Control*, April 1977, pp. 173-179.

6. Doyle, J. C.: Guaranteed Margins for LQG Regulators. *IEEE Transactions on Automatic Control*, Vol. AC-23, 1978, pp. 756-757.

7. Johnson, C. D.: Optimal Control of the Linear Regulator with Constant Disturbances. *IEEE Transactions on Automatic Control*, Vol. AC-13, August 1968, pp. 416-421.

246

8. Johnson, C. D.: Further Study of the Linear Regulator with Disturbances--The Case of Vector Disturbances Satisfying a Linear Differential Equation. *IEEE Transactions on Automatic Control* (Short Papers), Vol. AC-15, April 1970, pp. 222-228.

9. Johnson, C. D.: Further Comments on "Optimal Control of the Linear Regulator with Constant Disturbances." *IEEE Transactions on Automatic Control*, Vol. AC-15 August 1970, pp. 516-518.

10. Johnson, C. D.: Accommodation of External Disturbances in Linear Regulator and Servomechanism Problems. *IEEE Transactions on Automatic Control*, Vol. AC-16, December 1971, pp. 635-644.

11. Gupta, N. K.: Frequency-Shaped Cost Functionals: Extension of Linear-Quadratic-Gaussian Design Methods. *AIAA Journal of Guidance and Control*, November-December 1980, pp. 529-535.

12. Anderson, B. D. O.; and Mingori, D. L.: Use of Frequency Dependence in Linear Quadratic Control Problems to Frequency-Shape Robustness. *Journal of Guidance, Control, and Dynamics*, Vol. 8, No. 3, May-June 1985, pp. 397-401.

13. Teo, C. L.; and Tomizuka, M.: Frequency-Shaped Cost Functionals: Output or Input Weighting. *Proceedings of the 28th Conference on Decision and Control*, Tampa, Florida, December 1989, pp. 2389-2390.

14. Sievers, Lisa A.; and Von Flotow, Andreas H.: Comparison of Two LQG- Based Methods for Disturbance Rejection. *Proceedings of the 28th Conference on Decision and Control*, Tampa, Florida, December 1989, pp. 483-485.

15. Hampton, R. D.; and Knospe, C. R.: Extended H_2 Synthesis for Multiple-Degree-of- Freedom Controllers. *Proceedings of the International Symposium on Magnetic Suspension Technology*, Hampton, Virginia, August 19-23, 1991, sponsored by NASA Langley Research Center.

16. Hampton, R. D.; Knospe, C. R.; and Grodsinsky, C. M.: Controller Design for Microgravity Vibration Isolation Systems (IAF-92-0969). World Space Congress 1992, Washington, D.C., August 28 - September 5, 1992.

17. Hampton, R. D.: Controller Design for Microgravity Vibration Isolation Systems. Ph.D. dissertation, University of Virginia, Charlottesville,Virginia, 1993.

18. Sage, A. P.; and White, C. C., III: *Optimum Systems Control*, 2nd ed. Englewood Cliffs, New Jersey: Prentice Hall, Inc., 1977.

19. Maciejowski, J. M.: *Multivariable Feedback Design*. Wokingham, England: Addison-Wesley Publishing Company, Inc., 1989.

20. Chen, Chi-Tsong: *Linear System Theory and Design*. New York: Holt, Rinehart and Winston, Inc., 1985.

21. Grace, A.; Laub, A. J.; Little, J. N.; and Thompson, C.: *MATLAB User's Guide: Control System Toolbox*. October 30, 1990, p. 1-48.

22. Moore, B. C.: Principal Component Analysis in Linear Systems: Controllability, Observability, and Model Reduction. *IEEE Transactions on Automatic Control*, Vol. AC-26, 1981, pp. 17-32.

23. Dailey, R. Lane: Lecture Notes for the Workshop on H_∞ and μ Methods for Robust Control. Seattle, Washington: The Boeing Company. Presented at the 1990 American Control Conference, San Diego, California, May 21-22, 1990.

FUZZY SELF-LEARNING CONTROL FOR MAGNETIC SERVO SYSTEM

J.H. Tarn   L.T. Kuo   K.Y. Juang   C.E. Lin

Institute of Aeronautics and Astronautics
National Cheng Kung University
Tainan, Taiwan

ABSTRACT

It is known that an effective control system is the key condition for successful implementation of high-performance magnetic servo systems. Major issues to design such control systems are nonlinearity; unmodelled dynamics, such as secondary effects for copper resistance, stray fields and saturation; and that disturbance rejection for the load effect reacts directly on the servo system without transmission elements. One typical approach to design control systems under these conditions is a special type of nonlinear feedback called gain scheduling. It accommodates linear regulators whose parameters are changed as a function of operating conditions in a preprogrammed way.

In this paper, an on-line learning fuzzy control strategy is proposed. To inherit the wealth of linear control design, the relations between linear feedback and fuzzy logic controllers have been established. The exercise of engineering axioms of linear control design is thus transformed into tuning of appropriate fuzzy parameters. Furthermore, fuzzy logic control brings the domain of candidate control laws from linear into nonlinear, and brings new prospects into design of the local controllers.

On the other hand, a self-learning scheme is utilized to automatically tune the fuzzy rule base. It is based on network learning infra-structure; statistical approximation to assign credit; animal learning method to update the reinforcement map with a fast learning rate and temporal difference predictive scheme to optimize the control laws. Different from supervised and statistical unsupervised learning schemes, the proposed method learns on-line from past experience and information from the process and forms a rule base of an FLC system from randomly assigned initial control rules.

INTRODUCTION

Interest in research on large-gap magnetic suspension systems began in the early 1960's. The principal goal was the elimination of aerodynamic support interference in wind tunnel testing. In early 1970's the interest extended to small-gap systems. The first system developed was the Annular Momentum Control Device (AMCD) with applications to the stabilization and control of spacecraft [1]. This research was continued with the Annular Suspension and Pointing System (ASPS) which provides orientation, mechanical isolation, and fine pointing of space experiments [2,3]. For decades, Magnetic suspension technologies (MST) have demonstrated their capabilities in many fields, from

industrial compressors, high-speed milling and grinding spindles, magnetically levitated trains, and control wheel suspension for spacecraft to rocket propulsion turbomachinery. Important features of the magnetic suspension and actuator systems are:

(1) Versatility of the Electromagnetic Forces

The physical force of a magnetic circuit to a high-permeable armature is called the Maxwell-force. Contrary to this commonly used force, the reaction force of a conductor carrying a current in a magnetic field is called the Lorentz-force. Successful integration of these physical effects and the constructed electromagnetic subsystem can be utilized as a rotary motor, linear actuator, radial bearing, thrust bearing, etc.

(2) Molecule-size Resolution

One problem of electric-motors is the ripple of motion at low-speed operating regions due to the finite pole effect. The rotor always rests at the finite circumference positions which have the minimum magnetic flux (potential energy). Thus there are inherited limitations for resolution of control. The non-pole magnetic field provided by a coil, on the other hand, sets no resolution limitation. The resolution limit, in turn, is set by sensors, instrumentation and control strategies. Magnetic suspension systems provide a promising approach for achieving positioning with nanometer resolution.

In this paper, a linear positioning system with a linear force actuator and magnetic levitation is to be designed. By locating a permanently magnetized rod inside a current-carrying solenoid, the axial force is achieved by boundary effect of magnet poles and utilized to power the linear motion, while the force for levitation is provided by magnetic bearing and governed by maximum linkage principle. With the levitation in a radial direction, there is no friction between the rod and solenoid. The demand of high speed motion can hence be achieved . Under the proposed arrangement, the axial force act on the rod is a smooth function of rod position, so the system can provide nanometer-resolution linear positioning to the molecule size. It is known that an effective control system is the key condition for successful implementation of high-performance magnetic levitated positioning systems. Major issues for design of such control systems are:

(1) Nonlinearity

By assuming that the complete energy of the magnetic field is concentrated within the air gap. The basic mathematical models of active magnetic bearing are obtained from Maxwell's laws. The input-output relations are highly nonlinear despite the variables defined.

(2) Unmodelled Dynamics

Secondary effects such as copper resistance, stray fields and saturation are neglected.

(3) Disturbance Rejection

Because the load effect reacts directly on the servo system without transmission elements, the capability of "disturbance rejection" is also required.

With the above considerations, a fuzzy logic controller with PD type rule-base is utilized. A self-learning scheme for a fuzzy logic controller is used to form a proper rule-base for FLC. The characteristics of this self-learning FLC are as follows:

(1) It is based on the adaptive neuron-like element concepts, statistical approximation, animal learning and temporal difference predictive method [4].

(2) The scheme can get a quick learning rate by using the animal learning method.

(3) It is different from the supervised learning. Without knowing the system dynamics, this learn-

250

ing scheme can learn from past experience to form a rule-base for fuzzy logic controllers.

(4) It is different from the statistical unsupervised learning scheme. Conventionally, the statistical unsupervised learning scheme learns from the fail experiences, so it belongs to off-line learning. In contrast, this scheme is an on-line learning scheme by getting information from the control process.

(5) As the rule-base formed, a fuzzy logic controller can work independently without a learning mechanism.

Effectiveness of the control systems are illustrated by numerical simulation results.

SYSTEM DYNAMICS

System Configuration

Consider a magnetic servo system shown in Figure 1, where r_1 is 1.1 cm, r_2 is 1.0 cm and the length of the rod is 1.0 cm; the length of the solenoid is 10 cm. The current supplied to the solenoid will generate a magnetic field around the rod and result in a linear motion. To achieve the function of levitation, the current in the solenoid must be kept in the direction that can maintain the stability of radial motion. Under such condition, the axial motion is unstable, i.e., the magnetic force in axial direction tends to push the rod away from the center of the solenoid. Hence the spring is required to supply the force in the opposite direction. Also, the spring must be precompressed to avoid an uncontrollable equilibrium point. The additional magnetic bearing system is used to keep the moving part balanced in axial direction. With a biased current fed to the solenoid, the magnetic force in radial direction is utilized to suspend the moving part, while, with the controlled current, the axial motion is governed by the force caused by a non-uniform magnetic field in the boundary.
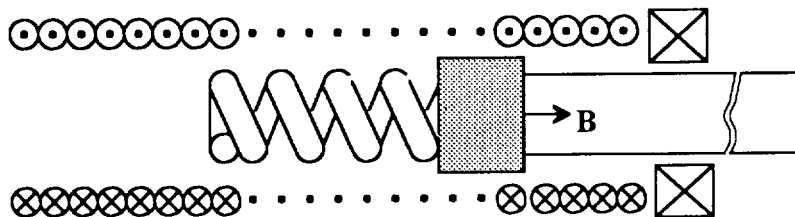

Figure 1 The configuration of a magnetic levitated linear positioning system

251

The magnetic force induced by the current in the solenoid is a nonlinear function of the position. The dynamic equation of the servo system can be expressed as

$$\dot{x}_1 = x_2$$

$$\dot{x}_2 = -\frac{1}{m}[K_1 \cdot (x_1 + x_p) + K_2(x_1) \cdot (i + i_b)]$$

where

x_1, x_2 = position and velocity of the rod respectively, cm, cm/sec
K_1 = stiffness of the spring, N/cm
$K_2(x)$ = current controlled stiffness of solenoid-rod configuration, N/A
x_p = pre-compressed length of the spring, cm
i_b = biased current for levitation, A
i = controlled current, A
m = mass of the moving part includes the load, kg

$K_2(x_1)$ is the input gain of the system, which is the nonlinear function of rod position described in Figure 2. In short, the system can be simplified as the configuration in Figure 3, where K_2 is a nonlinear current controlled stiffness spring.
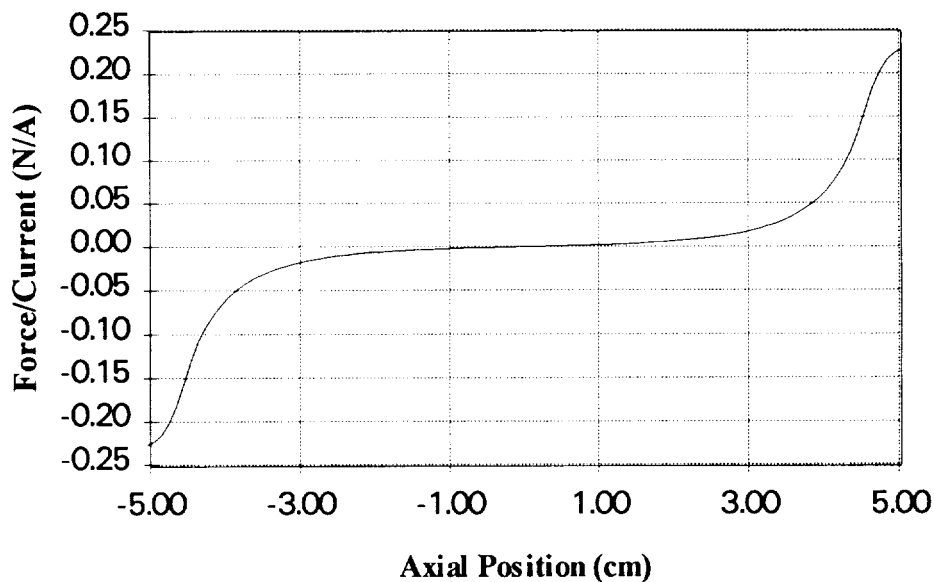
Figure 2 Force-position relation in axial motion.
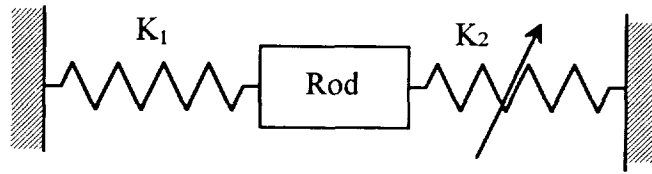
Figure 3 Simplified model of axial motion.

SELF-LEARNING FUZZY LOGIC CONTROLLER

Architecture of Self-Learning FLC

In a Fuzzy Logic Controller designing process, we use a self-learning scheme to form a proper control rule-base automatically from past control actions and experiences. After the rule-base has been formed, an FLC can work independently to control the magnetic suspension system.

The architecture of the self-learning FLC is shown in Figure 4. To achieve the on-line learning purpose, a performance evaluator (called Critic element) is needed to determine the system performance and to react to the environment changes at the end of each learning period. This unit produces an external reinforcement signal, R, to provide information for the learning mechanism to learn from. While receiving the reinforcement, the external information is evaluated and an internal reinforcement, $\hat{r}$, is sent to the next unit by the adaptive critic unit (ACU). This signal helps to judge the necessary changes of the control rules. The associative search unit (ASU) searches a proper control force location in the rule space for each control rule in the rule-base of FLC according to the internal reinforcement and system status. After the rules are changed, this rule-base is held over next learning period to show its control effects and to accumulate its experiences. At the end of the next learning period, an external reinforcement, R, is evaluated again and the learning process is continued recurrently. It is shown that all firing strengths of control rules are sent to both ACU and ASU to assist these mechanisms to accumulate past experience.

More distinctly, our learning process introduced above is implemented following the steps below:

(1) At time instance k, the firing strength μ_i, the control action u_i in each rule, and the system output y(k) are available.

(2) Critic element determines external reinforcement, R

(3) ACU evaluates internal reinforcement, $\hat{r}$

(4) ASU updates control rules, u_i

(5) FLC calculates the current action, f, by fuzzy inference

(6) Send the action to system, repeat steps (4) and (5) over this learning period
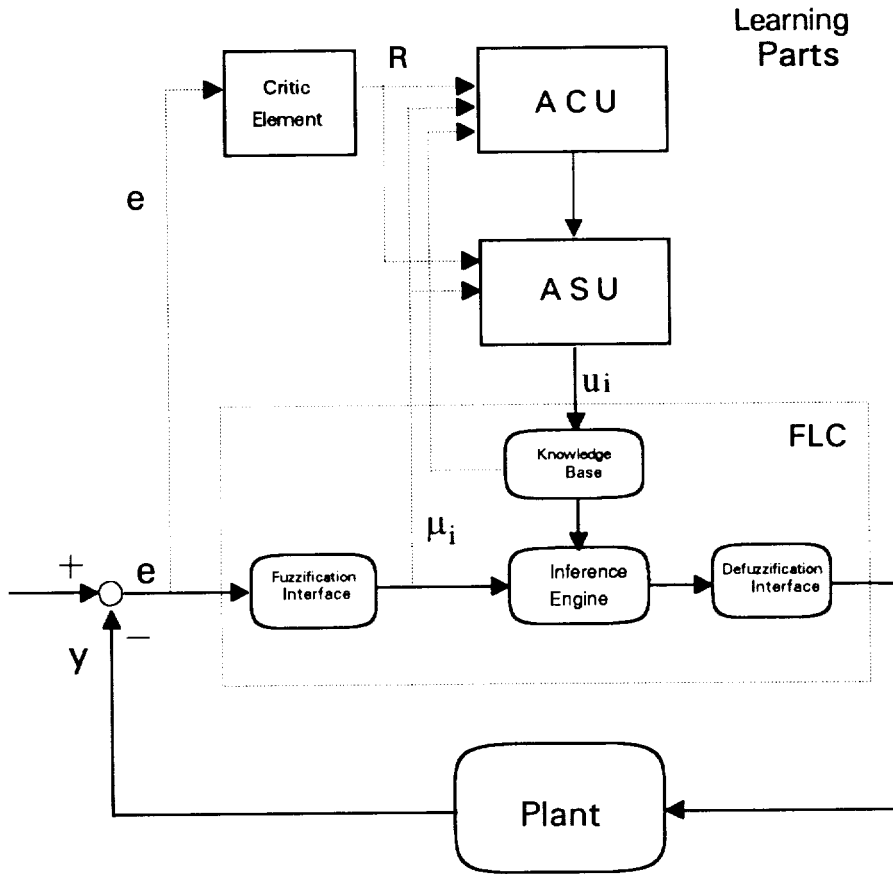
(7) Repeat step (1) at next learning period

Fig 4 : The Architecture of The Self-learning Fuzzy Logic Controller

A Self-Learning Scheme for **FLC**

The learning algorithms are described as follows :
* The critic element :

$$R = -\frac{1}{\max(|a|,|b|)}(\frac{1}{N}\Sigma_{k=1}^{N} \ |E(kT)|)$$

* The adaptive critic unit (ACU) :

$$p(t) = \Sigma_{i=1}^{n} v_i(t)\mu_i(t)$$

$$\hat{r} = \gamma p(t) - p(t-1) \qquad ; \qquad 0 \le \gamma \le 1$$

$$v_i(t+1) = v_i(t) + \beta R\hat{\mu}_i(t) \qquad ; \qquad 0 < \beta \le 1$$

$$\hat{\mu}_i(t) = \lambda\hat{\mu}_i(t-1) + (1-\lambda)\mu_i(t) \qquad ; \qquad 0 \le \lambda < 1$$

* The associative search unit (ASU) :

$$u_i = FL \times \tanh(Kw_i)$$
$$e_i(t) = \delta e_i(t-1) + (1-\delta)\mu_i(t)u_i(t) \quad , \qquad\qquad 0 \le \delta < 1$$
$$w_i(t+1) = w_i(t) + \alpha sign(E)\left|e_i(t)(R+\hat{r})\right|$$

where R is the external reinforcement signal; N is the sampling numbers in a learning period; T is the sampling period; the working range of error is [a,b]; u_i is the control force of i-th rule; μ_i is the firing strength of i-th rule; e_i is called eligibility of the i-th rule; $\hat{r}$ is the internal reinforcement evaluated by ACE; α is the learning rate and δ is the forgetting factor.

Simulation Result

In the simulation, the fuzzy logic controller reads the input terms "error", "change in error" and concludes the output term "change in control force". The term "error" is defined in [-3,3] and is partitioned into 9 equal-space intervals; the membership of each interval is of isosceles triangle form. The term "change in error" is the measurement of the velocity, which is defined in [-50,50] and is partitioned into 7 equal-space intervals. The geometry of its membership is also an isosceles triangle. The 63 rules are initialized with random number and trained with algorithms described in the previous section for 500 training process from initial condition 4.0 to setpoint 2.5. The simulation result is given as Figure 5. In this figure, the results of the trained controller applied to different operating points are also demonstrated.

CONCLUSION

From the results, the effectiveness of the learning scheme and the robustness of fuzzy logic controllers are shown. It works well, though the input gain of the system varies with the operating point significantly. Such capability is achieved by the nonlinearity of the fuzzy logic controller.

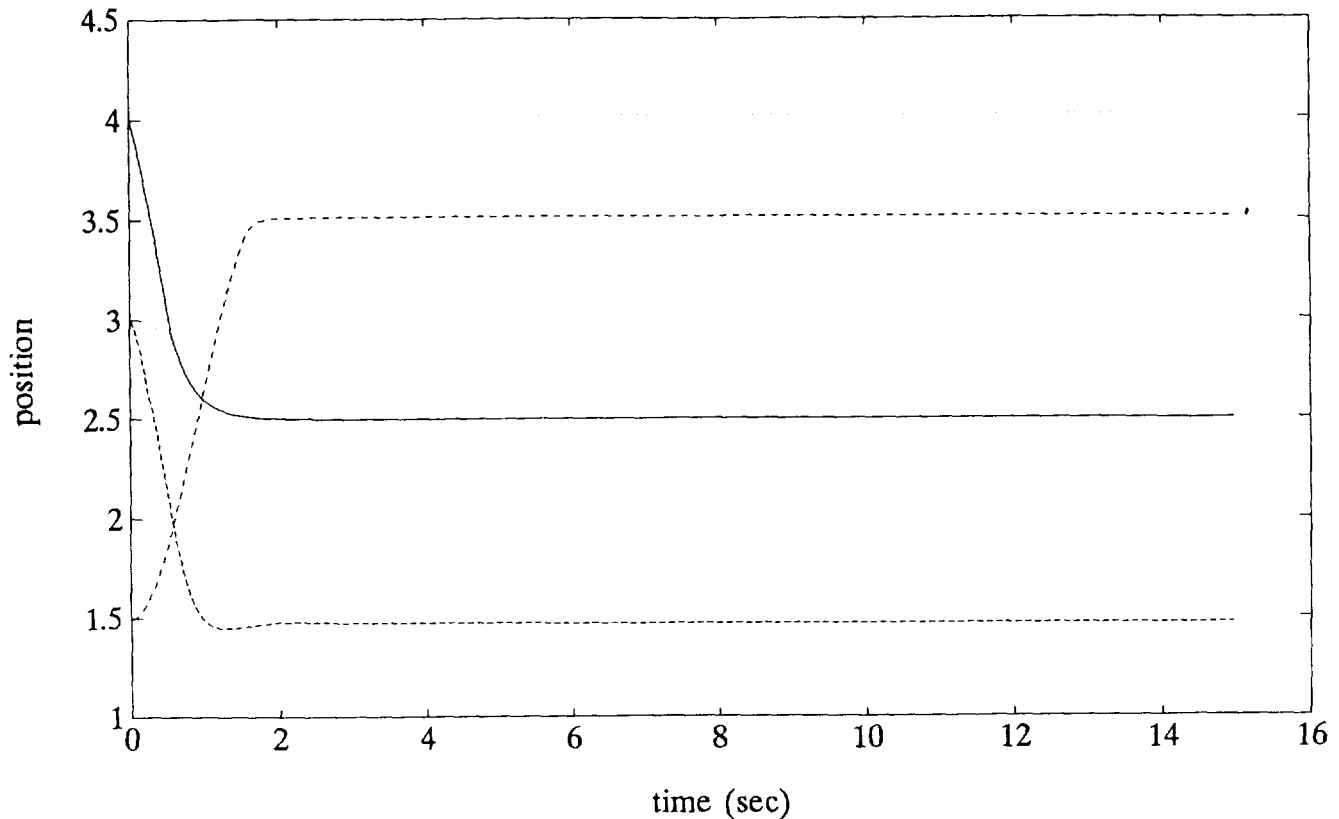out responses with different set point and initial condition

Figure 5 Simulation results with fuzzy logic controller.

REFERENCE

[1] Anderson, Willard W. and Groom, Nelson J., "The Annular Momentum Control Device (AMCD) and Potential Applications," NASA TN D-7866, 1975.

[2] Anderson, Willard W. and Joshi, Suresh M., "The Annular Suspension and Pointing (ASP) System for Space Experiments and Predicted Pointing Accuracies," NASA TR R-448, 1975.

[3] Anderson, Willard W. ; Groom, Nelson J. and Woolley, Charles T., "The Annular Suspension and Pointing System," Journal of Guidance and Control, Vol. 2, No. 5, 1979, pp. 367-373.

[4] R.S.Sutton, "Learning to Predict by the Methods of Temporal Difference", Machine Learning 3, pp. 9-44.

IMPLEMENTATION OF A DECOUPLED CONTROLLER FOR A MAGNETIC SUSPENSION SYSTEM USING ELECTROMAGNETS MOUNTED IN A PLANAR ARRAY

D. E. Cox   N. J. Groom

NASA Langley Research Center

Hampton, VA

Abstract

An implementation of a decoupled, single-input/single-output control approach for the Large Angle Magnetic Suspension Test Fixture is described. Numerical and experimental results are presented. The experimental system is a laboratory model large gap magnetic suspension system which provides five degree-of-freedom control of a cylindrical suspended element. The suspended element contains a core composed of permanent magnet material and is levitated above five electromagnets mounted in a planar array.

1   INTRODUCTION

A research effort is underway at NASA Langley Research Center to demonstrate the magnetic suspension, positioning, and maneuvering of objects over wide ranges of attitudes. Future applications of this technology range from magnetic suspension of wind tunnel models to advanced spacecraft experiment isolation and pointing systems. As part of this effort, a Large Angle Magnetic Suspension Test Fixture (LAMSTF) has been designed and built. The LAMSTF is a small scale laboratory model of a Large Gap Magnetic Suspension System (LGMSS) which provides five degree-of-freedom control of a cylindrical suspended element that contains a core composed of permanent magnet material. The suspended element is levitated above five electromagnets mounted in a planar array. The LGMSS is a conceptual design of a ground based experiment which is to be used to investigate the technology issues associated with: magnetic suspension at large gaps, accurate suspended element control at large gaps, and accurate position sensing at large gaps [1]. The objectives of the LAMSTF effort were to investigate the feasibility of the LGMSS concept and to provide a test fixture for developing and demonstrating control approaches. A description of the LAMSTF and some of the control approaches which have been investigated are presented in [2]. LAMSTF suspended element parameters and the field components generated by the electromagnets at the centroid of the suspended element are given in the Appendix to this paper.

This paper presents the implementation of a single-input/single-output (SISO) control approach for the LAMSTF with numerical and experimental results. The control approach

which was implemented was developed in [3] using the extended linearized model developed in [4]. The control approach is proportional-derivative (PD), where the command torques and forces are functions of positions and derivatives of position. The design technique provides a dynamic compensator given the desired pole locations of the closed-loop system. Numerical results are obtained which compare the desired poles to the actual coupled pole locations for a candidate design. Experimental responses are also obtained on the LAMSTF testbed and compared to simulation results.

2 EQUATIONS OF MOTION

The equations of motion for the LAMSTF were developed in [4]. The LAMSTF configuration consists of five electromagnets mounted in a planar array. Figure 1 is a schematic representation of the LAMSTF configuration and defines the coordinate systems. The suspended element coordinate system consists of a set of orthogonal $\bar{x}, \bar{y}, \bar{z}$ body-fixed axes which define the motion of the suspended element with respect to inertial space. The suspended element coordinate system is initially aligned with an orthogonal x, y, z system fixed in inertial space. The open-loop equations of motion are determined by evaluating the forces
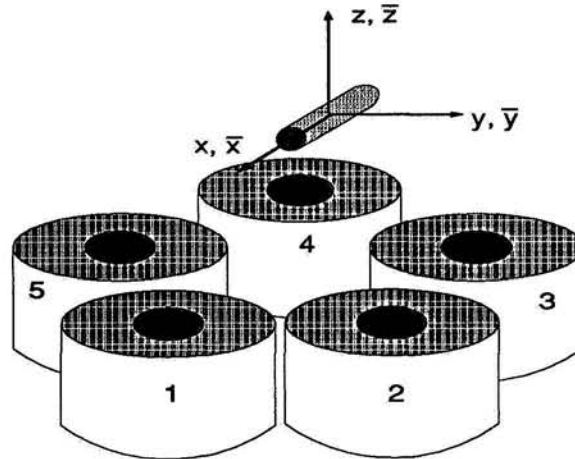
Figure 1: LAMSTF Configuration

and torques produced on the permanent magnet core by the magnetic fields [5]. They can be written as,

$$\dot{X} = f(X, I) \qquad (1)$$

where

$$X = \begin{bmatrix} \Omega_{\bar{y}} & \Omega_{\bar{z}} & V_{\bar{x}} & V_{\bar{y}} & V_{\bar{z}} & \theta_y & \theta_z & x & y & z \end{bmatrix}^{\mathrm{T}}$$

and

$$I = \begin{bmatrix} I_1 & I_2 & I_3 & I_4 & I_5 \end{bmatrix}^{\mathrm{T}}$$

In the state vector, θ_y and θ_z are rotations about the y and z axis called pitch and yaw, respectively. The translations are x, y, and z, and Ω and V are time derivatives of the

258

corresponding positions. The input to the system are the five coil currents, denoted by I. In order to generate a linear model these equations are expanded about the nominal operating point X_o, I_o using a Taylor series expansion and simplified using small angle approximations. Higher order terms are neglected in the expansion and motion about the uncontrolled axis (x) is assumed to be zero. Details of the linearization are presented in [4]. The linearized equations have the form

$$\delta \dot{X} = \mathcal{A}\delta X + \mathcal{B}\delta I \qquad (2)$$

where

$$\mathcal{A} = \left.\frac{\partial \dot{X}}{\partial X}\right|_{X_o, I_o} \quad \text{and} \quad \mathcal{B} = \left.\frac{\partial \dot{X}}{\partial I}\right|_{X_o, I_o}$$

Expanding these equations yields,

$$I_c \dot{\Omega}_{\bar{y}} = vM_{\bar{x}}\left(-B_x\theta_y - B_{xz}x - B_{yz}y - B_{zz}z\right) - vM_{\bar{x}}\mathbf{K}_z I \qquad (3)$$

$$I_c \dot{\Omega}_{\bar{z}} = vM_{\bar{x}}\left(-B_x\theta_z + B_{xy}x + B_{yy}y + B_{yz}z\right) + vM_{\bar{x}}\mathbf{K}_y I \qquad (4)$$

$$m_c \dot{V}_{\bar{x}} = vM_{\bar{x}}\left(-B_{xz}\theta_y + 2B_{xy}\theta_z + B_{xxx}x + B_{xxy}y + B_{xxz}z\right) + vM_{\bar{x}}\mathbf{K}_{xx} I \qquad (5)$$

$$m_c \dot{V}_{\bar{y}} = vM_{\bar{x}}\left(B_{yz}\theta_y + (B_{yy} - B_{xx})\theta_z + B_{xyx}x + B_{xyy}y + B_{xyz}z\right) + vM_{\bar{x}}\mathbf{K}_{xy} I \qquad (6)$$

$$m_c \dot{V}_{\bar{z}} = vM_{\bar{x}}\left((B_{xx} - B_{zz})\theta_y + B_{yz}\theta_z + B_{xzx}x + B_{xzy}y + B_{xzz}z\right) + vM_{\bar{x}}\mathbf{K}_{xz} I \qquad (7)$$

where the B terms describe components and spatial derivatives of the magnetic field vector at the equilibrium point. The first subscript of B refers to a unit vector direction, while additional subscripts imply partial derivatives with respect to the coordinate system. The K coefficients are row vectors which define the fields produced by each coil per amp of current. I_c and m_c are inertia and mass of the core respectively, and $vM_{\bar{x}}$ is the product of the core's volume and magnetization. The first terms on the right in equations (3)-(7) are the torques and forces generated on the core due to perturbations in X, evaluated in the presence of the uncontrolled fields and gradients produced by the constant bias currents required to provide equilibrium suspension. The second terms are the torques and forces generated on the core by controlling the coil currents about the suspension currents. The controlled torques and forces can be written as,

$$\begin{bmatrix} \bar{T}_c \\ \bar{F}_c \end{bmatrix} = \tilde{\mathcal{B}} I \qquad (8)$$

where

$$\tilde{\mathcal{B}} = vM_{\bar{x}} \begin{bmatrix} -\mathbf{K}_z \\ \mathbf{K}_y \\ \mathbf{K}_{xx} \\ \mathbf{K}_{xy} \\ \mathbf{K}_{xz} \end{bmatrix} \qquad (9)$$

For the LAMSTF configuration $\tilde{\mathcal{B}}$ is full rank and the currents required to produce given

command torques and forces become

$$I = \tilde{B}^{-1} \begin{bmatrix} T_{\bar{y}c} \\ T_{\bar{z}c} \\ F_{\bar{x}c} \\ F_{\bar{y}c} \\ F_{\bar{z}c} \end{bmatrix} \qquad (10)$$

For equilibrium suspension the torques and forces produced on the suspended element must be zero, except to counteract the effect of gravity. Therefore at equilibrium the suspension currents are

$$I_o = \tilde{B}^{-1} \begin{bmatrix} 0 \\ 0 \\ 0 \\ 0 \\ m_c g \end{bmatrix} \qquad (11)$$

Although $\tilde{B}^{-1}$ decouples the five degrees of freedom in terms of force commands, the system dynamics are still highly coupled through the destabilizing bias terms in equations (3)-(7). The bias currents, I_o, are used to calculate the values of the bias fields and gradients presented in the Appendix. Many of these terms can be shown to be zero due to symmetry of the five-coil planar array. Referring to Figure 1, it can be seen that coil 1 is located symmetrically about the x, z plane and so cannot produce field components in this plane which are along the y axis. Furthermore, coils 2 and 5, and coils 3 and 4 form symmetric pairs about the x, z plane. These coil pairs have equal bias currents; therefore the projection along the y axis of fields from each pair is also zero throughout the x, z plane. This means that at X_o, the y component of the field is zero and all of its derivatives with respect to x and z are zero. Similar arguments can be used to show that B_{yy} and B_{zz} are also zero. Considering these zero terms, and making the additional approximation $B_{xxz} \simeq 0$ and $B_{xzx} \simeq 0$, equations (3)-(7) become,

$$\begin{align}
I_c \dot{\Omega}_{\bar{y}} &= -K B_x \theta_y - K B_{xz} x + T_{\bar{y}c} & (12) \\
I_c \dot{\Omega}_{\bar{z}} &= -K B_x \theta_z + T_{\bar{z}c} & (13) \\
m_c \dot{V}_{\bar{x}} &= K B_{xxx} x - K B_{xz} \theta_y + F_{\bar{x}c} & (14) \\
m_c \dot{V}_{\bar{y}} &= K B_{xyy} y + F_{\bar{y}c} & (15) \\
m_c \dot{V}_{\bar{z}} &= K B_{xzz} z + F_{\bar{z}c} & (16)
\end{align}$$

where the KB terms are constants equal to the product of $vM_{\bar{x}}$ and the corresponding field or gradient value evaluated at X_o, I_o. From these equations, it can be seen that the dynamics in y, z and θ_z are uncoupled and can be analyzed as single degree-of-freedom systems. The dynamics in θ_y and x, however, remain coupled. The strength of this interaction and its effect on SISO control design will be addressed in the next section.

The term KB_x in equations (12) and (13) is negative and causes open-loop instability. These terms cause high frequency unstable modes referred to as compass needle modes. Compass needle modes occur because, with the LAMSTF configuration, in order to achieve gradients which generate the vertical suspension force, the core's magnetization vector must

be aligned 180 degrees from the suspension field vector. These modes dominate the dynamics in pitch and yaw. The bias terms KB_{xxx} and KB_{xyy} also cause unstable dynamics. These terms are similar to the unstable bias flux stiffness terms encountered with small gap magnetic bearings that use permanent magnet bias flux [6, 7]. The terms KB_{xz} and KB_{xzz} cause stable coupling between x and θ_y, and stable oscillations in z. Eigenvalues for the LAMSTF open-loop system are presented in Table 1.

Mode	Eigenvalue	
Compass needle	-58.7793	
	58.7793	
Compass needle	-57.8061	
	57.8061	
y Translation	9.7764	
	-9.7764	
Stable Coupling	0.0000	+ 7.9697i
	0.0000	- 7.9697i
z Translation	0.0000	+ 0.9556i
	0.0000	- 0.9556i

Table 1: Eigenvalues of the open-loop system

3 CONTROL SYSTEM EQUATIONS

The control design technique allows the designer to directly place the poles of the closed loop system for each degree of freedom. Damping ratios and frequencies can be chosen to provide adequate response to disturbance inputs. The position of the suspended element is assumed to be known and is measured on the LAMSTF system by a set of five shadow sensors. As mentioned earlier, the control approach is PD, where the command torques and forces are functions of positions and derivatives of position. The command torques and forces can be written as

$$T_{\bar{y}c} = -\left(P_{\theta_y} + sR_{\theta_y}\right)\theta_y \tag{17}$$

$$T_{\bar{z}c} = -(P_{\theta_z} + sR_{\theta_z})\theta_z \tag{18}$$

$$F_{\bar{x}c} = -(P_x + sR_x)x \tag{19}$$

$$F_{\bar{y}c} = -(P_y + sR_y)y \tag{20}$$

$$F_{\bar{z}c} = -(P_z + sR_z)z \tag{21}$$

Position and rate gains are denoted P and R, respectively, for each degree of freedom. Control of pitch rotation and x translation will be examined first since these are the only suspended element motions which are coupled. The approach is to close the loop around each axis independently and to determine the effect of the cross-coupling on the performance of the resulting system. Equations (17) and (19) can be written in matrix form as

$$\begin{bmatrix} T_{\bar{y}c} \\ F_{\bar{x}c} \end{bmatrix} = -G_F \begin{bmatrix} \theta_y \\ x \end{bmatrix} \qquad (22)$$

where G_F is the forward-loop transfer function matrix,

$$G_F = \begin{bmatrix} P_{\theta_y} + sR_{\theta_y} & 0 \\ 0 & P_x + sR_x \end{bmatrix} \qquad (23)$$

Taking the Laplace transform of system equations (12) and (14) and putting them in matrix form results in

$$\begin{bmatrix} s^2 I_c \theta_y \\ s^2 m_c x \end{bmatrix} = \begin{bmatrix} -KB_x & -KB_{xz} \\ -KB_{xz} & KB_{xxx} \end{bmatrix} \begin{bmatrix} \theta_y \\ x \end{bmatrix} + \begin{bmatrix} T_{\bar{y}c} \\ F_{\bar{x}c} \end{bmatrix} \qquad (24)$$

Substituting for $T_{\bar{y}c}$ and $F_{\bar{x}c}$ in (24) and collecting terms results in

$$\begin{bmatrix} I_c s^2 + R_{\theta_y} s + P_{\theta_y} + KB_x & KB_{xz} \\ KB_{xz} & m_c s^2 + R_x s + P_x - KB_{xxx} \end{bmatrix} \begin{bmatrix} \theta_y \\ x \end{bmatrix} = 0 \qquad (25)$$

The characteristic equation becomes

$$\begin{vmatrix} I_c s^2 + R_{\theta_y} s + P_{\theta_y} + KB_x & KB_{xz} \\ KB_{xz} & m_c s^2 + R_x s + P_x - KB_{xxx} \end{vmatrix} = 0 \qquad (26)$$

Expanding the determinant yields

$$\left(s^2 + \frac{R_{\theta_y} s}{I_c} + \frac{P_{\theta_y} + KB_x}{I_c} \right) \left(s^2 + \frac{R_x s}{m_c} + \frac{P_x - KB_{xxx}}{m_c} \right) - \frac{(KB_{xz})^2}{I_c m_c} \qquad (27)$$

where the system's characteristic equation has been factored into two decoupled second order terms and a single coupling term. The coupling term in equation (27) is similar in form to the natural frequencies of the second order terms; however, it does not depend upon the feedback gains. It is possible to make this term negligible by increasing the position gains on the x and θ_y degrees of freedom. Ignoring the coupling term, the closed loop natural frequencies and damping for the θ_y mode can be written as

$$\omega_{\theta_y} = \sqrt{\frac{P_{\theta_y} + KB_x}{I_c}} \qquad \zeta_{\theta_y} = \frac{R_{\theta_y}}{2\sqrt{\left(P_{\theta_y} + KB_x \right) I_c}} \qquad (28)$$

Similarly for the x control loop

$$\omega_x = \sqrt{\frac{P_x - KB_{xxx}}{m_c}} \qquad \zeta_x = \frac{R_x}{2\sqrt{(P_x - KB_{xxx}) m_c}} \qquad (29)$$

Solving these equations for P and R yields design equations which allow for pole placement

$$P_{\theta_y} = \omega_{\theta_y}^2 I_c - KB_x \qquad R_{\theta_y} = 2\zeta_{\theta_y}\omega_{\theta_y} I_c \qquad (30)$$

$$P_x = \omega_x^2 m_c + KB_{xxx} \qquad R_x = 2\zeta_x \omega_x m_c \qquad (31)$$

The coupling term in equation (27) can only be ignored if the position gains are large, which implies that the SISO pole placement will be accurate only for sufficiently high frequencies. On the LAMSTF system this requirement was easily achieved. Table 2 shows design versus actual closed loop eigenvalues when the pitch and x loops are closed independently then analyzed as a coupled system. In each case the desired pole locations for the pitch and x modes were equal. Table 2 shows that the pole placement is inaccurate for low frequencies, but is reasonably accurate for frequencies above 75 rad/s, as expected. The table also shows very little variation between design and actual pole location for changes in damping.

SISO design poles		Coupled poles	
Frequency, rad/s	Damping	Frequency, rad/s	Damping
10.000	0.707	19.402	0.364
		22.117	1.000
30.000	0.707	34.299	0.618
		24.971	0.849
75.000	0.707	76.820	0.690
		73.133	0.725
100.000	0.707	101.372	0.697
		98.608	0.717
150.000	0.707	150.918	0.702
		149.075	0.711
75.000	0.100	76.820	0.097
		73.133	0.102
75.000	0.300	76.820	0.292
		73.133	0.307
75.000	0.500	76.820	0.488
		73.133	0.512
75.000	0.700	76.820	0.683
		73.133	0.717
75.000	0.900	76.820	0.878
		73.133	0.923

Table 2: Effect of coupling on accuracy of SISO pole placement

The characteristic equations for the remaining degrees of freedom can be obtained in a manner similar to the pitch and x loops. Since these loops are uncoupled, the design equations are exact. The compensator parameters as a function of damping ratios and natural frequencies are given by,

$$P_{\theta_z} = \omega_{\theta_z}^2 I_c - K B_x \qquad R_{\theta_z} = 2\zeta_{\theta_z}\omega_{\theta_z} I_c \qquad (32)$$

$$P_y = \omega_y^2 m_c + K B_{xyy} \qquad R_y = 2\zeta_y\omega_y m_c \qquad (33)$$

$$P_z = \omega_x^2 m_c + K B_{xzz} \qquad R_z = 2\zeta_z\omega_z m_c \qquad (34)$$

4 IMPLEMENTATION

The design method generates compensators which achieve approximate pole placement in the closed-loop system. The goal was to stabilize the experimental system and be able to maintain stability in the presence of disturbance forces. Poles were chosen to yield a system with a stiff response to disturbances and adequate damping to limit overshoot and oscillations.

As a design example the natural frequency of each closed-loop pole pair was set to 75 rad/s and the damping ratio of each was set to 0.707. Using equations (30)-(34) and parameters of the LAMSTF system, the position and rate gains were calculated. These gains are listed in Table 3. In the implementation of the PD controller it is desirable to

$$
\begin{array}{llll}
P_{\theta_y} & = 4.94 \times 10^{-2} & \mathrm{Nm/rad} & R_{\theta_y} & = 5.84 \times 10^{-4} & \mathrm{Nms/rad} \\
P_{\theta_z} & = 4.98 \times 10^{-2} & \mathrm{Nm/rad} & R_{\theta_z} & = 5.84 \times 10^{-4} & \mathrm{Nms/rad} \\
P_x & = 1.25 \times 10^2 & \mathrm{N/m} & R_x & = 2.35 & \mathrm{Ns/m} \\
P_y & = 1.25 \times 10^2 & \mathrm{N/m} & R_y & = 2.35 & \mathrm{Ns/m} \\
P_z & = 1.25 \times 10^2 & \mathrm{N/m} & R_z & = 2.35 & \mathrm{Ns/m}
\end{array}
$$

Table 3: Position and rate gains for example design

limit the high frequency gain to minimize the effects of noise. Therefore, each PD loop was implemented as the following lead network,

$$
\frac{P_i + sR_i}{s/\omega_r + 1} \tag{35}
$$

where the roll-off frequency, ω_r, is greater than the bandwidth of interest. In practice this was chosen to be 750 rad/second, an order of magnitude above the desired pole locations. A state-space model of the fully coupled system was developed and combined with the dynamic compensator to generate a continuous closed-loop system model. The damping ratios and natural frequencies of the poles of the closed-loop system are shown in Table 4. The frequencies are higher than designed due to the effects of the roll-off pole in the implementation.

The compensator designed above has been successfully implemented on the LAMSTF testbed. The suspended element position was derived from a set of five optical sensors arranged as shown in Figure 2. The sensors are based on power loss due to a shadowing of a collimated beam. The five measurements of the suspended element's position were sufficient to calculate the position and orientation in five degrees-of-freedom. The sensors are accurate to about 10 microns and have a linear range of about ± 1 mm. Dynamics from the sensor electronics are negligible.

An EISA-class 486 personal computer was used to implement the controller. Data acquisition, computation, and analog output were all handled by this computer. The controller was implemented as a set of discrete state space equations. The SISO continuous transfer functions were combined into a state space model and mapped into the discrete domain using a zero order hold transformation. The controller was implemented at a sample rate

264

Freq (rad/sec)	Damping
85.39	0.648
76.91	0.730
81.48	0.703
81.09	0.669
81.50	0.703
635.2	1.000
635.3	1.000
635.4	1.000
641.4	1.000
641.4	1.000

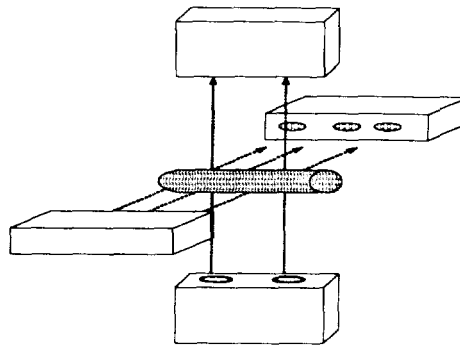Table 4: Natural frequencies and damping of closed-loop poles

Figure 2: Geometry of shadow sensor system

of 1 kHz. A computational delay of 0.43 msec separated the input sampling and analog output times. Performance of the controller was demonstrated by subjecting the suspended element to equivalent pulse disturbance forces. Actuator currents corresponding to a given disturbance force or torque are calculated for each degree of freedom using $\tilde{B}$. These disturbances are implemented by adding these inputs to the closed-loop coil currents. Since the system has a nonzero steady-state error, the position of the suspended element tracks the input disturbance. Position of the element and the input torques and forces are plotted in Figure 3. The system remains stable and generally has a well damped response to the disturbances. Response in the yaw, x, y, and z degrees-of-freedom are all similar and consistent with design expectations. The response in pitch, however, contains slightly more overshoot and more oscillation than the other degrees-of-freedom. The cause of the underdamped response in pitch is currently being investigated and may be related to unmodeled dynamics from eddy current loops in the aluminum baseplate of the system. Additional testing and system identification are being performed to verify this hypothesis. A simula-
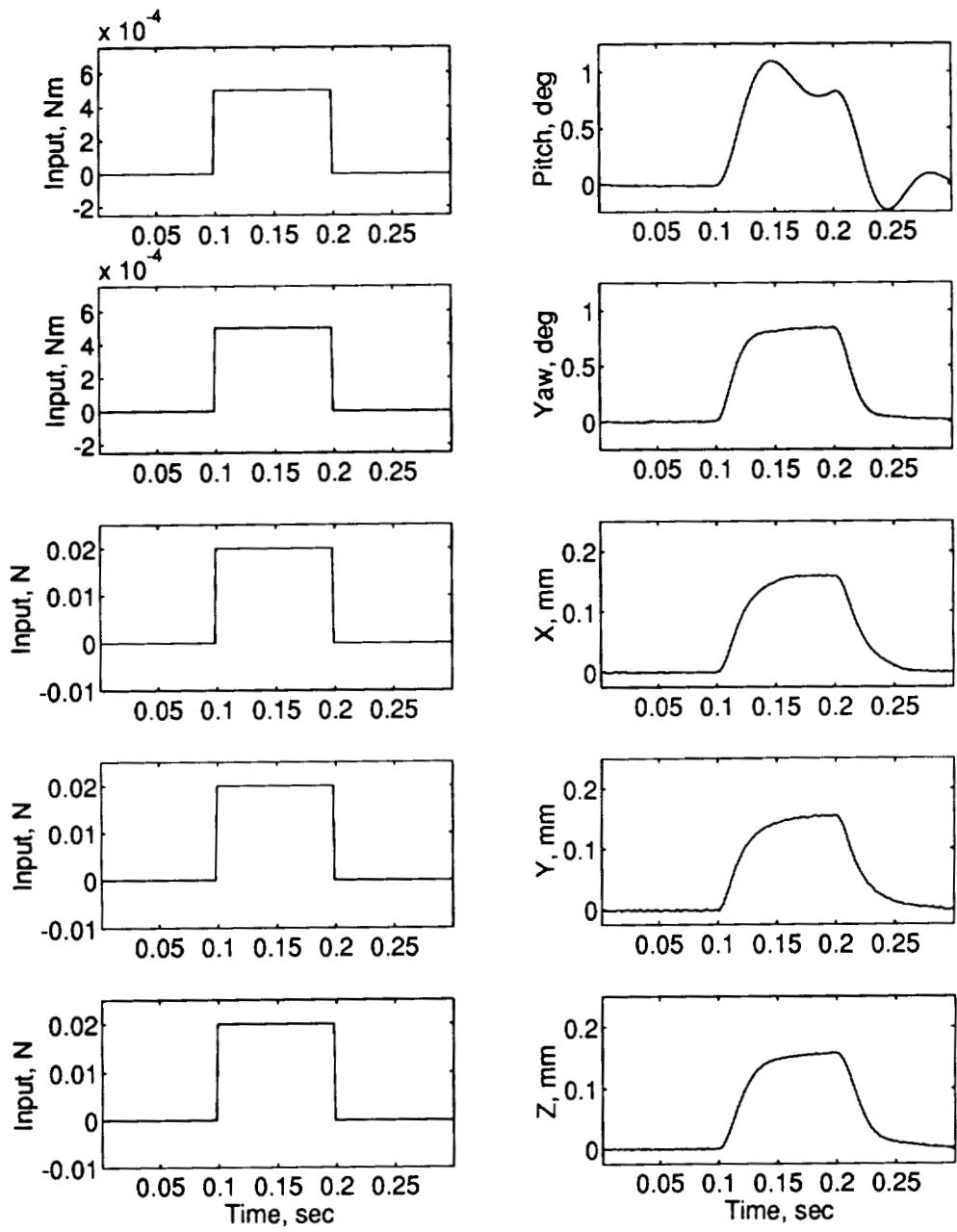
Figure 3: Experimental response to disturbance input

tion of the closed-loop system was developed with MATLAB's Simulink package [8]. The simulation models the continuous dynamics of the plant and considers the effect of sampling and computational delay in the implementation of the discrete controller. Figure 4 is a block diagram of the system as implemented in Simulink.
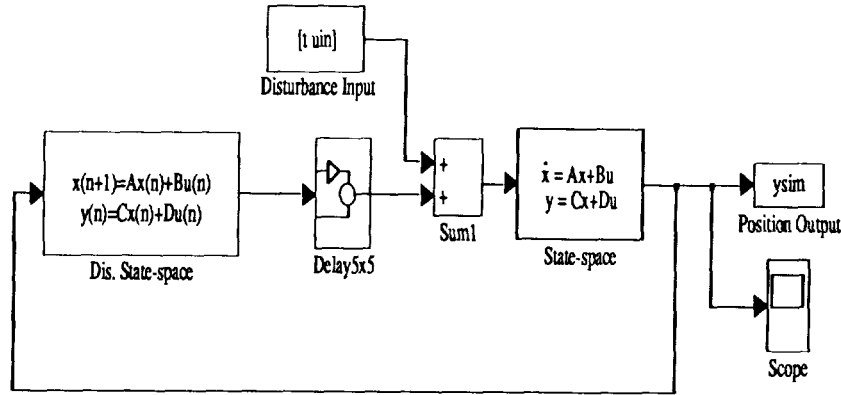
Figure 4: Block diagram of Simulink system simulation

Although the sampling frequency of 1 kHz is well above the closed loop dynamics, it was discovered that a pure analog analysis produced different responses than a simulation which considered the digital implementation. Figure 5 compares the full simulation, the experimental data, and an analog simulation. Response in pitch is underdamped experimentally, and the difference with respect to simulation can be easily seen. For the other degrees-of-freedom the digital simulation and actual response match quite well. The analog simulation, however, predicts a faster rise time and more overshoot in each case. A discrepancy between the frequency response of the continuous and discrete controllers was also noticed and appeared to be related to the high gain of the controller at the Nyquist frequency. Since the controller design was defined in the continuous domain, the differences between the digital and analog simulations are important to note.

5 CONCLUDING REMARKS

A decoupled control approach for a large gap magnetic suspension system has been presented. The magnetic suspension system is a planar array of electromagnets which provides levitation and five degree-of-freedom control of a cylindrical permanent magnet. The control approach assumes decoupled models for each degree of freedom. Position and rate gains for a dynamic compensator are computed based on desired pole locations. In the actual system, however, the system's dynamics remain coupled through bias terms resulting from the bias currents required to produce equilibrium suspension. The closed-loop performance, therefore, must be verified by applying the compensator to the coupled system model.

This technique provides the control designer simple and intuitive parameters to adjust in order to achieve closed-loop performance. In order to investigate the effects of coupling
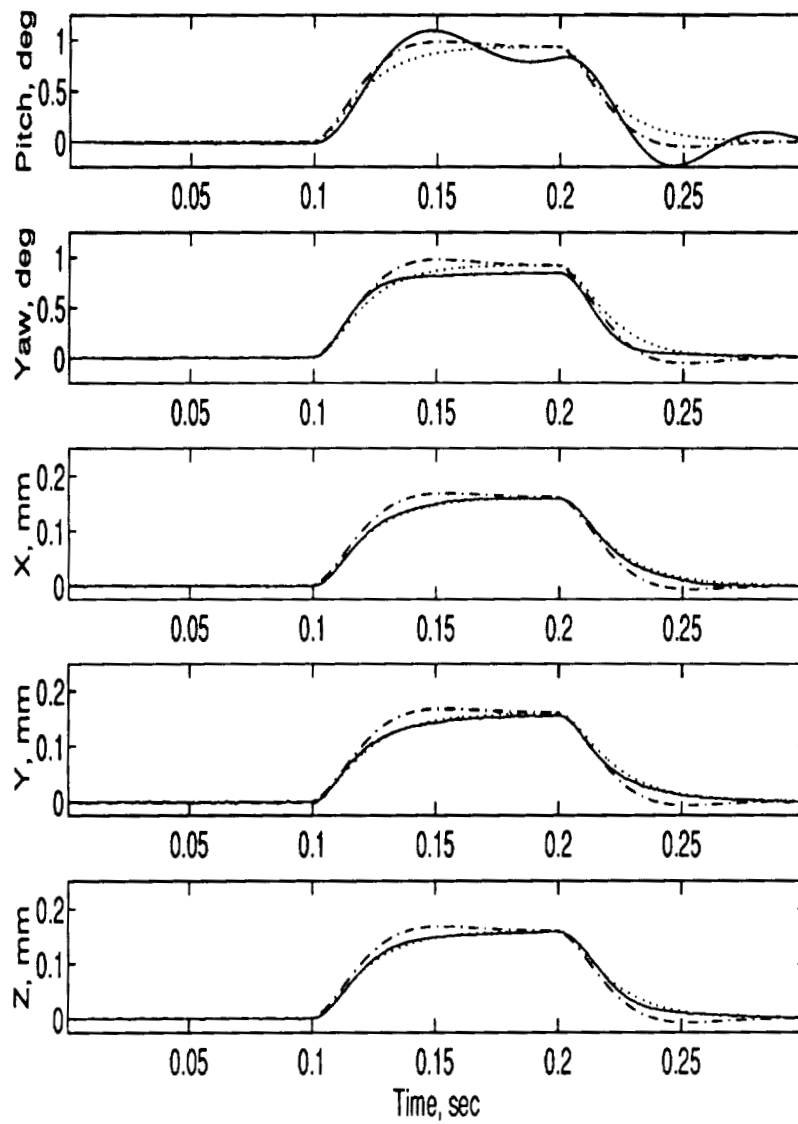
Figure 5: Comparison of experimental response (solid), digital simulation (dotted), and analog simulation (dash-dot)

between pitch and x translation, an example design was performed using the parameters of the Large Angle Magnetic Suspension Test Fixture (LAMSTF). Results of the design indicate that the damping ratios and natural frequencies of the coupled axes differ only slightly from design values. The control approach has been experimentally demonstrated on the LAMSTF system. Transient responses to pulse inputs compare favorably with simulations of the closed-loop system.

References

[1] Groom, N. J.: *Description of the Large Gap Magnetic Suspension System (LGMSS) Ground Based Experiment.* NASA CP-3109, Vol. 2, March 1991, pp. 365-377.

[2] Groom, N. J.; and Britcher, C. P.: *A Description of a Laboratory Model Magnetic Suspension Test Fixture with Large Angular Capability.* Proceedings of the First IEEE Conference on Control Applications, September 13-16, 1992, Dayton, Ohio, Vol. 1, pp.454-459.

[3] Groom, N. J.: *A Decoupled Control Approach for Magnetic Suspension Systems Using Electromagnets Mounted in a Planar Array.* NASA TM-109011, August 1993.

[4] Groom, N. J.; and Britcher, C. P.: *Open-Loop Characteristics of Magnetic Suspension Systems Using Electromagnets Mounted in a Planar Array.* NASA TP-3229, November 1992.

[5] Groom, N. J.: *Analytical Model of a Five Degree-of-Freedom Magnetic Suspension and Positioning System.* NASA TM-100671, July 1990.

[6] Groom, N. J.: *Analytical Model of an Annular Momentum Control Device (AMCD) Laboratory Test Model Magnetic Bearing Actuator.* NASA TM-80099, August 1979.

[7] Groom, N. J.; Woolley, C. T.; and Joshi, S. M.: *Analysis and Simulation of a Magnetic Bearing Suspension System for a Laboratory Model Annular Momentum Control Device.* NASA TP-1799, March 1981.

[8] Matlab 4.0 Users Manual, The Mathworks Inc. August 1992.

[9] The VF/GFUN Reference Manual, VF068894. Vector Fields Limited, June 1988.

A APPENDIX

This appendix presents, in the form of tables, LAMSTF suspended element parameters, electromagnet parameters, and components of fields and gradients (including second-order gradients) generated by the LAMSTF electromagnets at the centroid of the suspended element. The LAMSTF contains a planar array of five room-temperature electromagnets, with iron cores, mounted in a circular configuration. The configuration is shown schematically in Figure 1. For a more detailed description of the LAMSTF see [2]. The fields and gradients were calculated using VF/GFUN [9], including the pre- and post-processor OPERA, with all iron cores modeled. Physical parameters of the LAMSTF are presented in table A1. Electromagnet fields and first-order gradients generated by the suspension currents at the equilibrium point are presented in table A2. The fields, first-order gradients and second-order gradients generated by each coil at the equilibrium point are presented in table A3. It should be noted that only non-zero terms are included and the full set of components is not listed in the tables since $B_{ij} = B_{ji}$ and $B_{ijk} = B_{ikj}$.

Core diameter	8.509×10^{-3} m
Core length	5.08×10^{-2} m
Suspended element mass, m_c	22.124×10^{-3} kg
Suspended element inertia, I_c	5.508×10^{-6}
Core volume, v	2.889×10^{-6} m^3
Core magnetization, $M_{\bar{x}}$	7.785×10^5 A/m
Suspension height	0.1 m
Electromagnet outer radius	0.0825 m
Electromagnet inner radius	0.0475 m
Electromagnet height	0.105 m
Iron core radius	0.038 m
Location radius*	0.1375 m

* Distance from center of array to axis of given coil

Table A1: Physical parameters of LAMSTF

Component	Field strength, Tesla
B_x	-8.1863e-03
B_{xz}	9.6504e-02
B_{xxx}	4.9139e-01
B_{xxz}	-2.4689e-04
B_{xyy}	9.4051e-01
B_{xzz}	-8.9865e-03

Table A2: Values of bias fields and gradients at suspension point

270

Component	Fields, Tesla/Amp				
	Coil 1	Coil 2	Coil 3	Coil 4	Coil 5
K_x	2.3100e-04	7.1000e-05	-1.8700e-04	-1.8700e-04	7.1000e-05
K_y	0	2.2000e-04	1.3600e-04	-1.3600e-04	-2.2000e-04
K_z	-9.4000e-05	-9.4000e-05	-9.4000e-05	-9.4000e-05	-9.4000e-05
Component	First-order field gradients, Tesla/m/Amp				
	Coil 1	Coil 2	Coil 3	Coil 4	Coil 5
K_{xx}	2.1790e-03	-1.5030e-03	7.7200e-04	7.7200e-04	-1.5030e-03
K_{xy}	0	1.1960e-03	-1.9360e-03	1.9360e-03	-1.1960e-03
K_{xz}	-2.7230e-03	-8.4100e-04	2.2030e-03	2.2030e-03	-8.4100e-04
K_{yy}	-1.8920e-03	1.7900e-03	-4.8500e-04	-4.8500e-04	1.7900e-03
K_{yz}	0	-2.5900e-03	-1.6000e-03	1.6000e-03	2.5900e-03
K_{zz}	-2.8700e-04	-2.8700e-04	-2.8700e-04	-2.8700e-04	-2.8700e-04
Component	Second-order field gradients, Tesla/m^2/Amp				
	Coil 1	Coil 2	Coil 3	Coil 4	Coil 5
K_{xxx}	3.4340e-03	-1.8276e-02	1.6559e-02	1.6559e-02	-1.8276e-02
K_{xyx}	0	-1.4560e-02	1.3733e-02	-1.3733e-02	1.4560e-02
K_{xzx}	-5.3466e-02	1.6371e-02	-2.6790e-02	-2.6790e-02	1.6371e-02
K_{xyy}	-2.1916e-02	-1.1938e-02	2.2896e-02	2.2896e-02	-1.1938e-02
K_{xyz}	0	8.7350e-03	-1.4134e-02	1.4134e-02	-8.7350e-03
K_{xzz}	2.5400e-04	7.8000e-05	-2.0500e-04	-2.0500e-04	7.8000e-05

Table A3: Field and gradient values for each coil, Tesla/Amp

Session 6b – MSBS

Chairman: Colin P. Britcher
Old Dominion University

STATUS OF MSBS STUDY AT NAL

Hideo Sawada and Hisashi Suenaga
National Aerospace laboratory
7-44-1 Jindaijihigashi-machi Chofu-shi Tokyo
182, Japan

Takayuki Suzuki and Nobukazu Ikeda
Musashi Institute of Technology
1-28-1 Tamatutumi Setagayaku Tokyo
Japan

SUMMARY

Two Magnetic Suspension and Balance Systems (MSBS) at the National Aerospace Laboratory (NAL) in Japan are introduced. They are 10cm MSBS and 60cm MSBS. They have 10cm × 10cm and 60cm × 60cm test sections. The control of suspending a model at the 10cm MSBS is the 6 degrees of freedom including the rolling moment control. The model for the rolling moment control has two pairs of small extra permanent magnets at both its ends plus a main cylindrical magnet. The rolling moment is generated by the magnetic forces acting on the extra magnets by controlled current passing through the four side coils independently. Test results show the roll angle of the model is controlled in this way. The dynamic calibration test was carried out at the MSBS in 5 degree of freedom without the rolling moment control. The model is a simple cylindrical magnet magnetized along its axis. The obtained results show that the dynamic calibration with measured magnetic field intensity is much superior to that with the coil currents. The 60cm MSBS was designed with some data obtained at the 10cm one. It is fundamentally proportional to the 10cm one in size and coils position. The measured magnetic field intensity is not so strong as expected at design. It was operated first in 1993. The control is 3 degree of freedom in the longitudinal direction. The size of it is the largest one in the world presently.

INTRODUCTION

The MSBS is a very attractive instrument of the wind tunnel testing technologies because it can provide the support interference free test data and so on. However, only several MSBS's have been operated in the wind tunnel tests in some countries (ref. 1). The maximum one was the 40 cm × 60 cm in its test section at Russia (ref. 2). Primitive study was started at NAL about 8 years ago to build a practical sized MSBS in the future. The 10cm MSBS was built in 1985 and was operated first in 1987 (ref. 3). It has been improved in many points since that time. The purposes of the 10cm MSBS were to examine the way of designing it and to get a way of designing a larger one and to gain experience in operating it. Some fundamental data relating to

the MSBS have been obtained with it. The 60cm MSBS was designed and built with the data. It has been operated in the 3 degree of freedom since March in 1993. It is the largest one in the world in size as shown in Figure 1. The two MSBS's and some test results which have been obtained through the study of them are introduced in this paper.
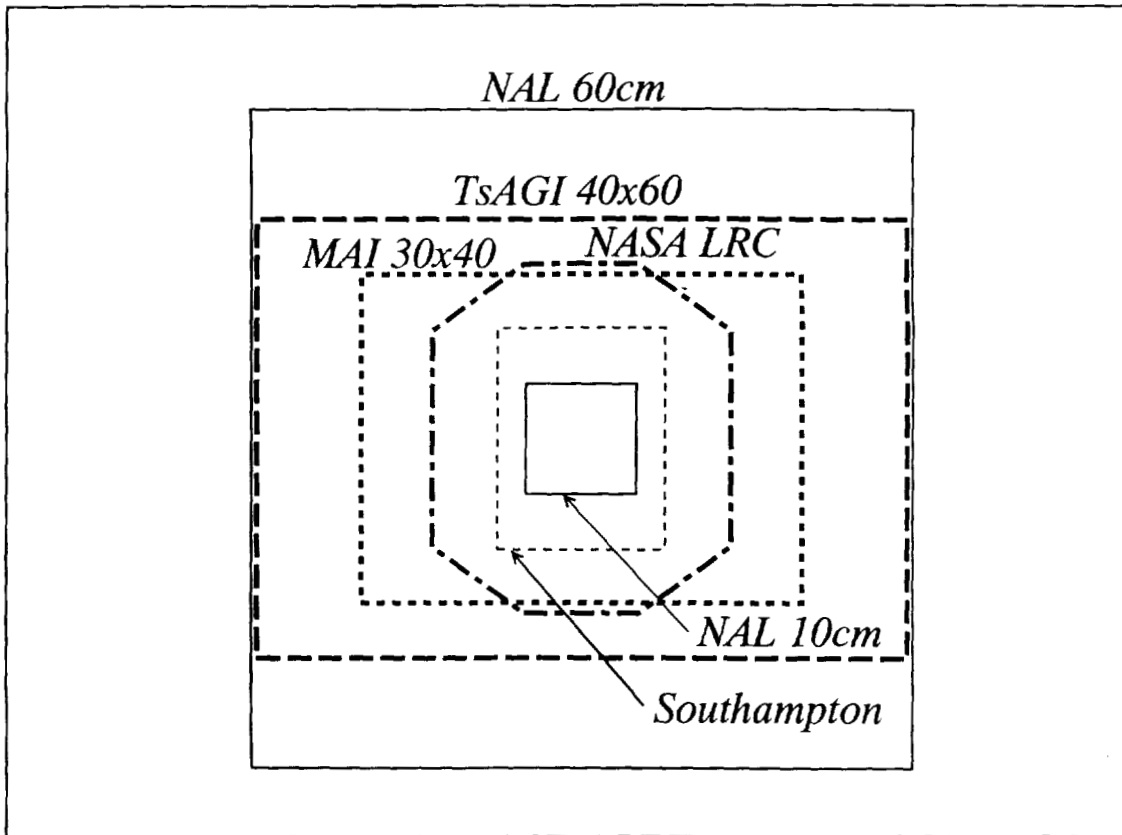

Figure 1. Test section size of large MSBS's

Symbols

H magnetic field intensity. (H_x, H_y, H_z)
H_z ave.   averaged H_z

m_i magnetic charge. (i = 1, ..., 8) See Figure 5.
mt magnetic moment of extra magnets. See Figure 5.
r distance to the extra magnets from model center. See Figure 5.
w distance to coil end from x axis. See figure 5.
x coordinate in the direction of centerline of test section. The x axis is on the horizontal plane. See Figure 2
y coordinate in the perpendicular to xz plane. See Figure 2.
z coordinate in the normal direction to the horizontal plane.
(x,y,z) coordinate system. Origin is located at the point across the symmetrical plane of the MSBS and the x axis.
ϕ roll angle of model. See Figure 5.
mg gravity force acting on a model.

276

System Description

Coil Arrangement

The 10cm MSBS has 8 iron cored coils and 2 air cored coils as shown in Figure 2. The 8 coils are arranged in the axial symmetry with respect to the x axis. All coils are placed symmetrically with respect to the yz plane at x = 0. The coils are numbered as shown in the figure and identified with their number in this paper. The dimensions of the coils are listed in Table I. A wind tunnel test section is placed through the two air cored coils along the x axis. A part of the section wall is made of transparent plastic. The position of a model inside it can be measured with the model position sensor through this part as shown in the figure.
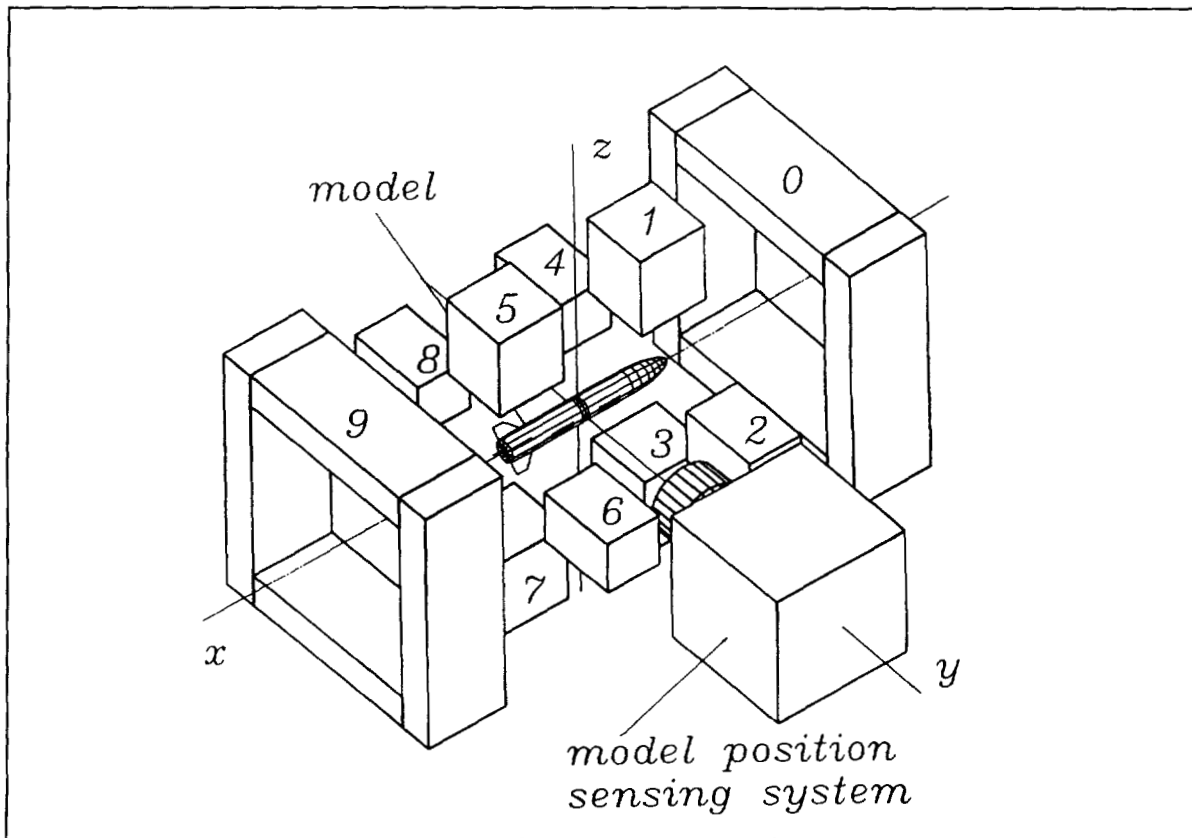
Figure 2. Coil arrangement at the NAL's MSBS's

The two air cored coils generate $\partial H_x/\partial x$. The magnetic force in the x direction (drag) acts on a permanent magnet magnetized in the x direction with the $\partial H_x/\partial x$. They are called drag coils for their purpose in this paper. Similarly, the coils of 1, 3, 5 and 7 are called lift coils. The coils of 2, 4, 6 and 8 are also called side coils in this paper. Currents passing through the lift coils generate H_z. The $\partial H_z/\partial x$ generates the magnetic force in the z direction (lift) acting on the model magnetized uniformly in the x direction. The averaged H_z on the

model generates the magnetic moment about the y axis (pitching moment) acting on the model. The $\partial H_y/\partial x$ and the averaged H_y on the model generate the magnetic force in y direction (side force) and moment about the z axis (yawing moment) acting on the model. The magnetic moment about the x axis (rolling moment) will not be generated with the model magnetized in x direction. Some extra magnets magnetized perpendiculars to the model axis are attached for the rolling moment at the 10cm MSBS.

coil No.	turns	core size(mm)	purpose
0, 9	240	120 x 120 air cored	drag force
1, 3, 5, 7	200	50 x 50 iron cored	lift force pitching moment
2, 4, 6, 8	100	40 x 40 iron cored	side force yawing moment rolling moment

Table I. Dimensions of coils of the 10cm MSBS

Models

Each model for the 10cm MSBS has a cylindrical permanent magnet in it along its center line at least. The magnet is magnetized in its axial direction. Almost all magnets which have been used at the 10cm MSBS are Alnico. Models with a cylindrical magnet inside are controlled in the 5 degree of freedom without the rolling moment control. Two pairs of extra small magnets are placed at the main cylindrical magnet ends as shown in Figure 3. One pair of them is rotated by 90 degrees about the model axis to the other one. Two magnets of each are placed in the way of facing with the same kind of the pole. As a result, the extra magnets are Sm-Co ones to keep their high intensity of magnetization.
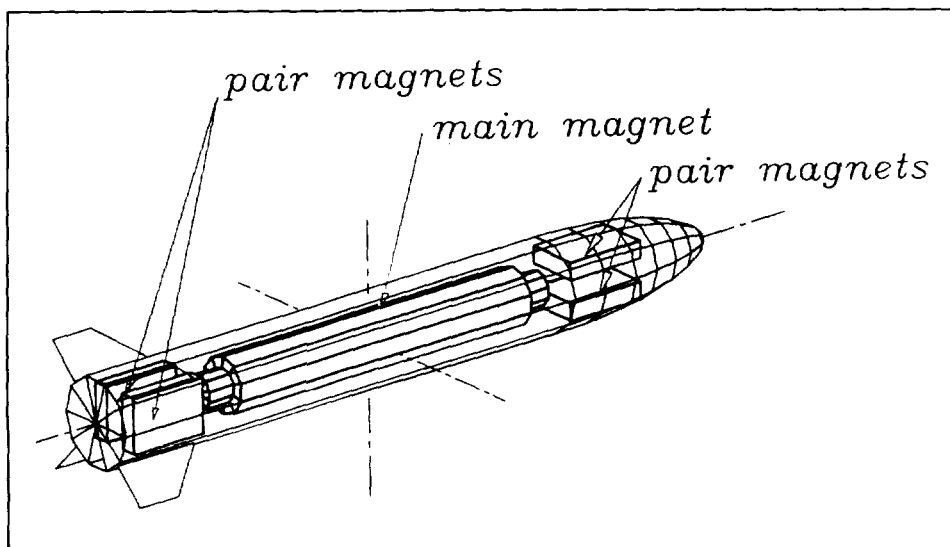
Figure 3. Magnet arrangement inside a model for rolling moment control

Besides those models, small simple cylindrical magnet models are tested at the 10cm MSBS to examine the control ability. The smallest one is 50 mm long and 6 mm in its diameter. The tested cored magnets and models are listed in Table II. The model length is limited by the measurable range of the model position sensing system.

shape	diameter	length	control	core magnet
Rocket type	16	150	6 degree	Alnico-5+Sm-Co
Rocket type	16	100	6 degree	Alnico-5+Sm-Co
cylinder	16	80	5 degree	Ferrite
cylinder	10	125	5 degree	Alnico-5
cylinder	8	80, 60, 50	5 degree	Alnico-5
cylinder	6	80, 60, 50	5 degree	Alnico-5

Table II. List of models at the 10cm MSBS

Model Position Sensing System

The model position sensors are developed at NAL. The features are reflection type and its rapid measurement. The image of a model is focused on a screen in the system with a lens. The model is painted in white and some marks are written on it in black. Three one dimensional CCD array sensors are placed in the letter H. The image of the model makes some dark and bright parts on the sensors according to the model position. The model position can be estimated accurately by counting the positions of the boundaries between the dark and bright parts on the arrays. The detail of the sensor is described in reference 4.

This system gives a feature to both MSBS's at NAL. It is in operation with the system. The model position can be controlled arbitrarily by changing the system position while it is kept at a constant position with respect to the system.

Power Supply

The power supply consists of 10 bipolar current control mode power units. The maximum current of the units is 15 A. The 2 units for the drag coils are different from the others a little. The maximum voltage of them is 20 V but that of the other ones is 18 V. All coils are provided with current by their independent power units. The power units are controlled by voltage signals from 10 DA converters. DC outputs for the current monitors in the units are available. Their accuracy is within 30 mA at most in their full range. The side coils are controlled with independent DA converters. The signals to control them are calculated to control the y direction translation, yawing motion, and rotation of the model.

Controller

The MSBS is controlled by a personal computer with Intel 486 of 20 MHz. The cycle of feedback control is 397 Hz and its timing signal is generated accurately by a crystal oscillator. The control algorithm is

the PI control plus double phase advance like the MSBS in reference 5. The coefficients of these control elements can be changed during its operation. The model position is displayed graphically in real time. A setpoint of it can also be changed both in step-like and continuous ways. The sinusoidal motion of the model is available. This mode was used in the dynamic calibration test.

Data Acquisition

Another personal computer is used for the data acquisition. The controller generates an interrupt signal to the data acquisition computer and also sends the model position data to it. The computer measures the current monitor output of the power units synchronistically with the controller. All data are stored in its memory in real time.

Measured Magnetic Field

The minimum distance between the two facing iron cored coils in the 10cm MSBS was 120 mm but it is 130 mm presently. The change was carried out in 1992 to make the test section removal easier. The distance between the drag coils became shorter by 40 mm to improve its drag force generation ability. The magnetic field intensity was measured in detail before the improvement. The whole magnetic field inside the 10cm MSBS is shown in Figure 4 although the measurement was carried out before the modification. It shows the well controlled magnetic field is generated in it.
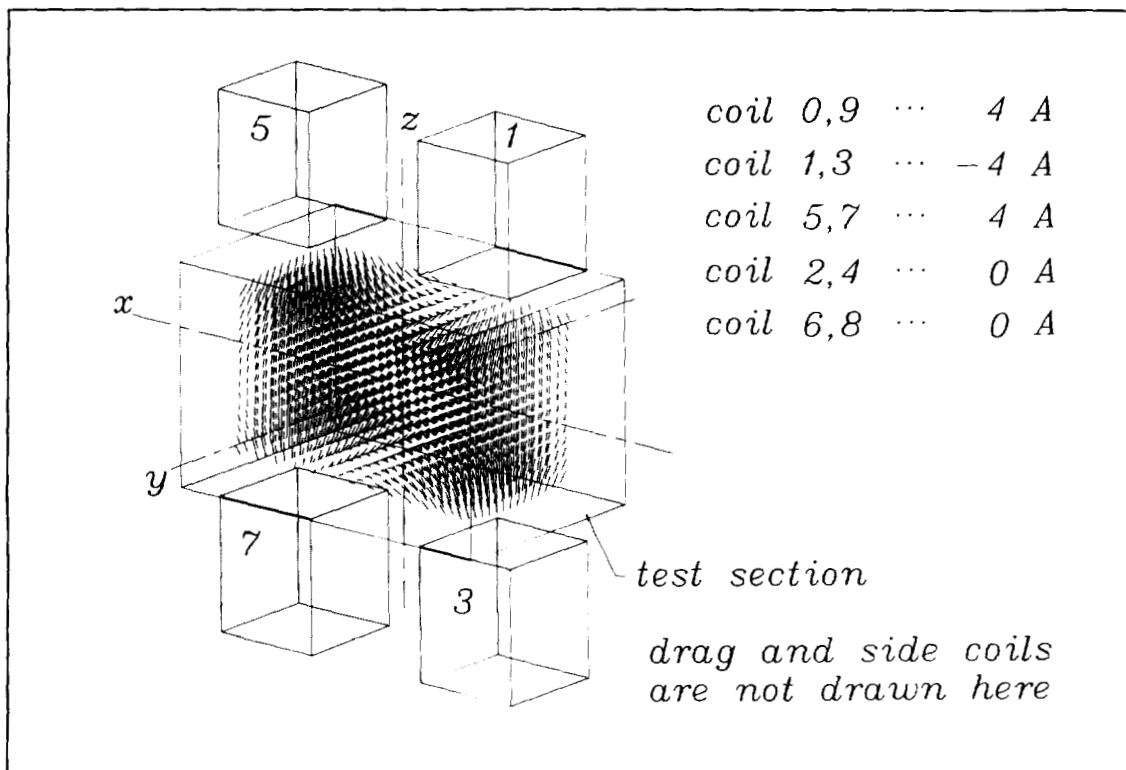
Figure 4. Measured magnetic field inside the 10cm MSBS

Wind Tunnel

A small supersonic wind tunnel of the blow down type was reformed as a wind tunnel for the MSBS. The test section size is 10 cm x 10 cm. A downstream part of the old contraction was replaced by a new one made of aluminum. The test section is also made of aluminum. Two windows are equipped on the side walls for the model position measurement. The maximum available flow speed is about 60 m/s. The flow uniformity in 60mm x 60 mm about the center line is good and its deviation is less than 1 % at x = 0. The turbulence intensity measured at the center with a hot wire is within 0.5% when the flow speed is less than 36 m/s. But the flow angle uniformity was found to be poor. As a result, this tunnel is used for examining the model suspension ability in the flow but not for measuring any aerodynamic test data.

Rolling Moment Control

Principle

The rolling moment can be controlled at the MSBS when a special model is used. The model contains the two pairs of extra magnets at both ends of a main magnet. The two magnets of each pair and the four iron cored coils surrounding an end of the model can be replaced by two magnetic moments and four magnetic charges in their effects as shown in Figure 5. Analytical estimation (ref. 6) shows that pure rolling moment acts on the model by placing the same polar magnetic charge at the two side magnet positions. The other forces and moments do not act on it. The estimated magnitude of the rolling moment is shown in Figure 6. The pair magnets do not generate any rolling moment in the uniform magnetic field in any direction. As a result strong coupling among the controls of forces and moments is not expected.
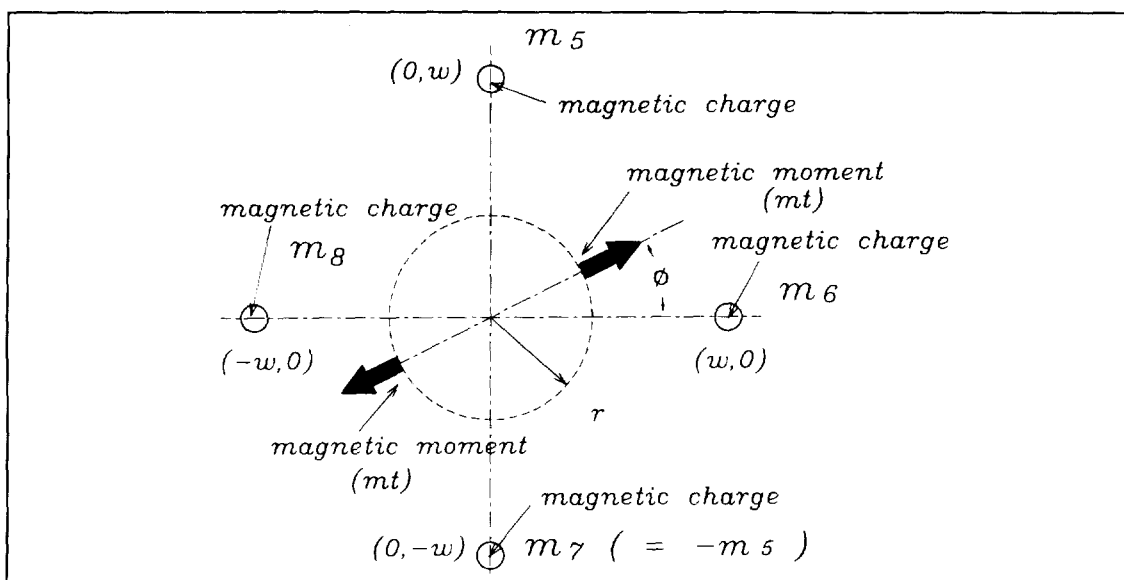
Figure 5. A model of rolling moment generation

$r/w = 0.058$
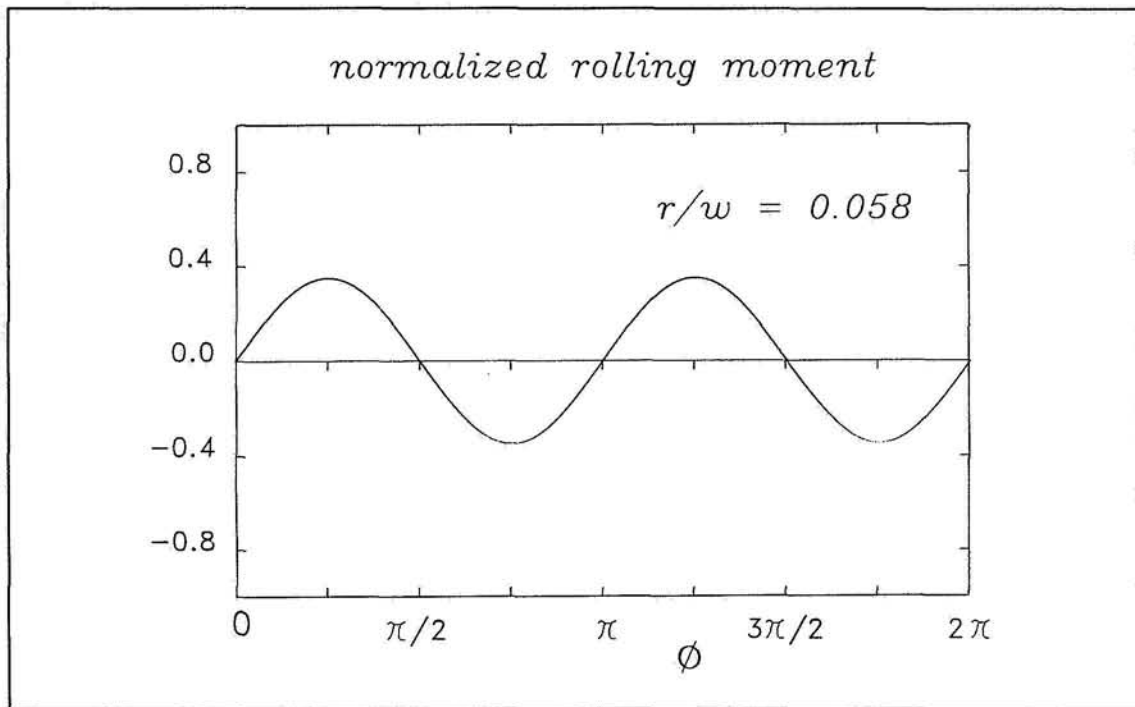
Figure 6. Estimated result
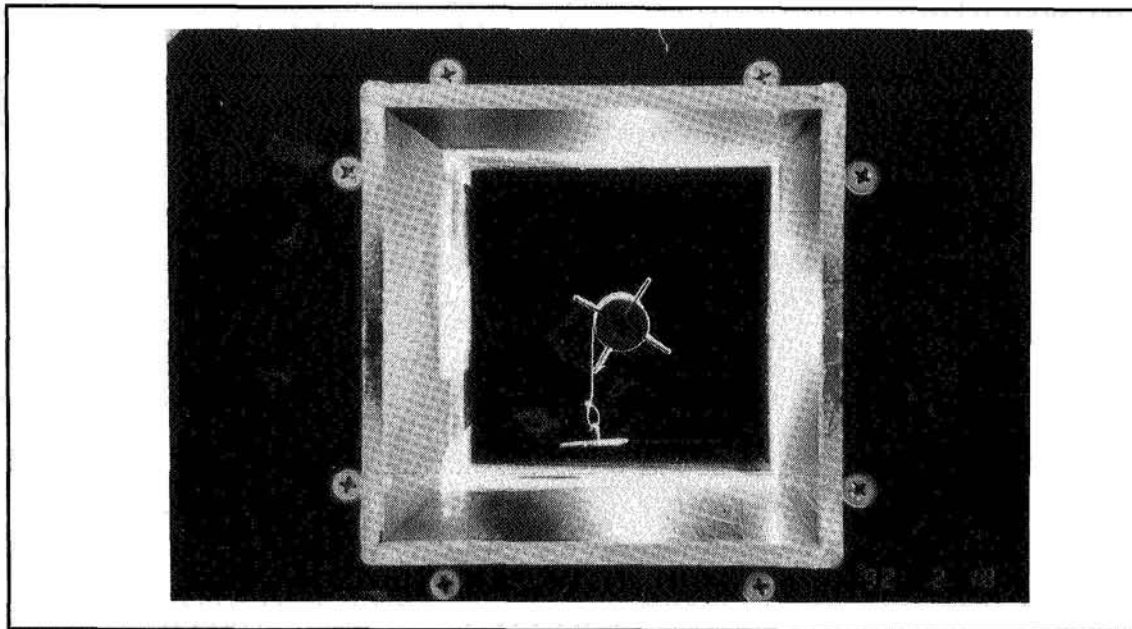
Figure 7. A model during the rolling moment calibration test

Test Results

Tests were conducted two times with different models. The model of the first test is shown in Figure 7. The model of the second test is different in the size and shape of the pair magnets. A part of the test results is shown in Figure 8. The rolling moment is controlled well. According to the figure, the relation between the rolling moment magnitude and the current for generating it are the same as expected

C-4.

by the principle. Besides, the roll angle effects on the other forces and moments are also small as shown in Figure 9. Both test results look very similar to each other. As a result they show the principle of generating the rolling moment right.
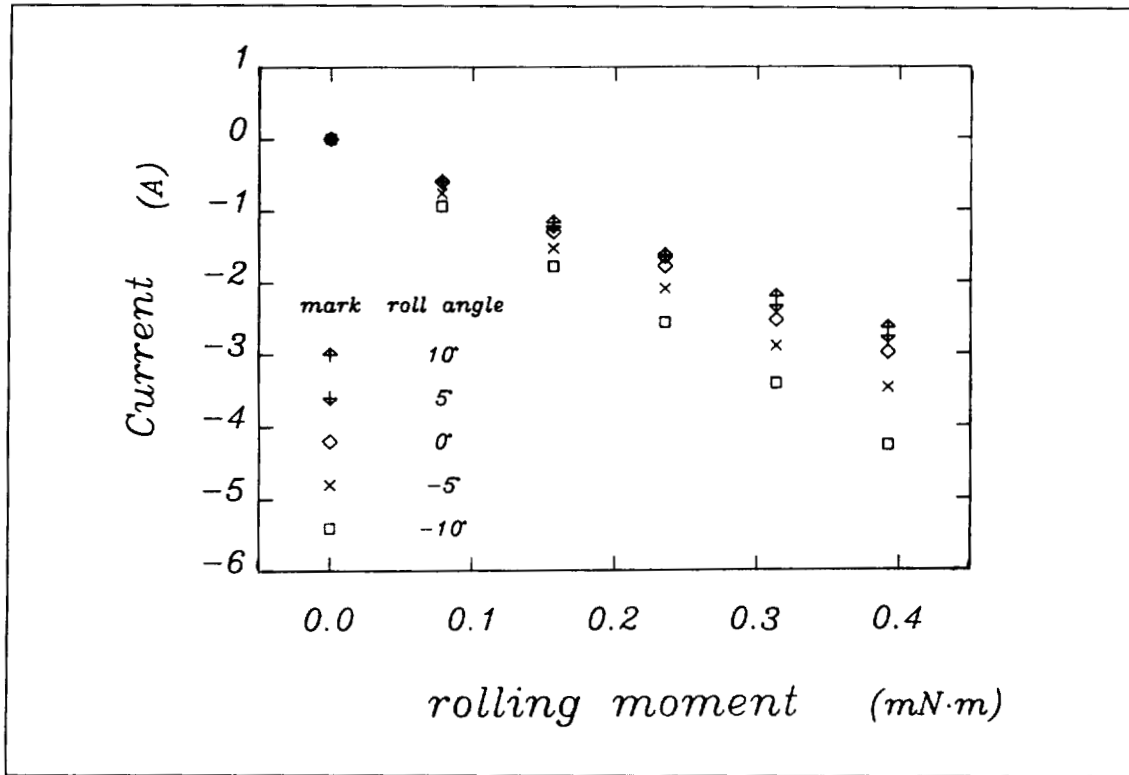
Figure 8. Rolling moment calibration test results
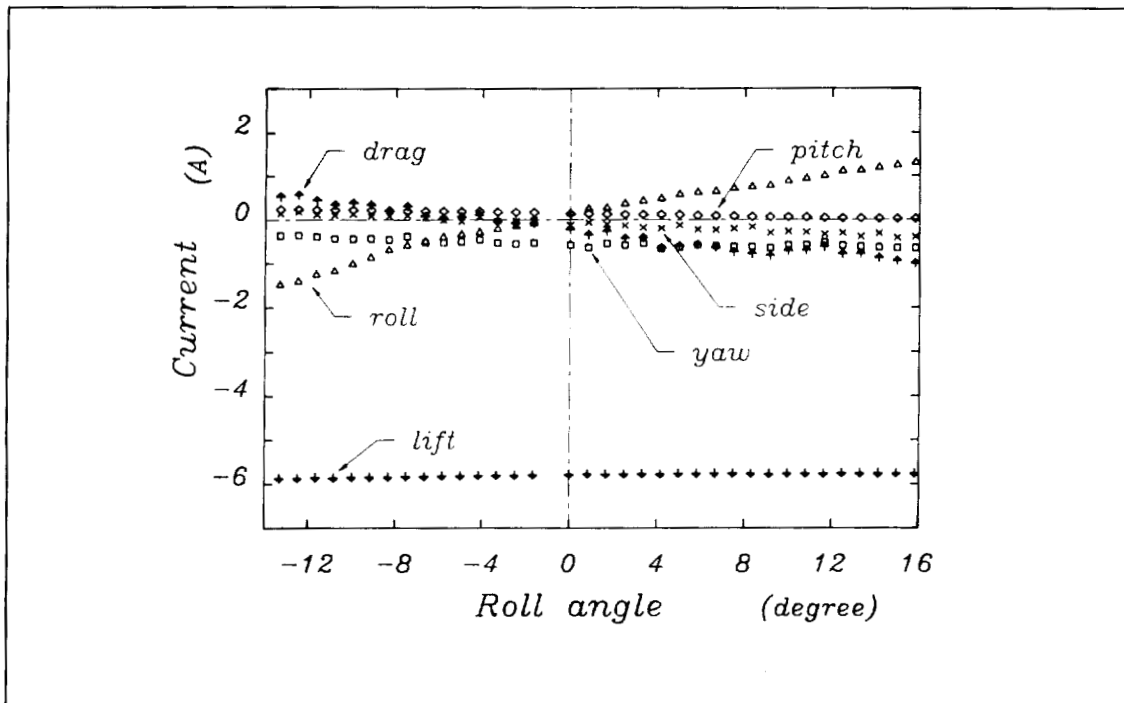
Figure 9. Coupling effects among forces and moments

Dynamic Calibration Analysis

Dynamic calibration is a very attractive way of calibrating the balance function in the MSBS. Static calibration of the MSBS is expected to be very elaborate if the model is in various attitudes. The principle of the dynamic calibration is simple. The practice of the calibration is much easier than the static one. But the obtained results do not show good accuracy compared with those by the static calibration presently. A preliminary dynamic calibration test was carried out with the 10cm MSBS.
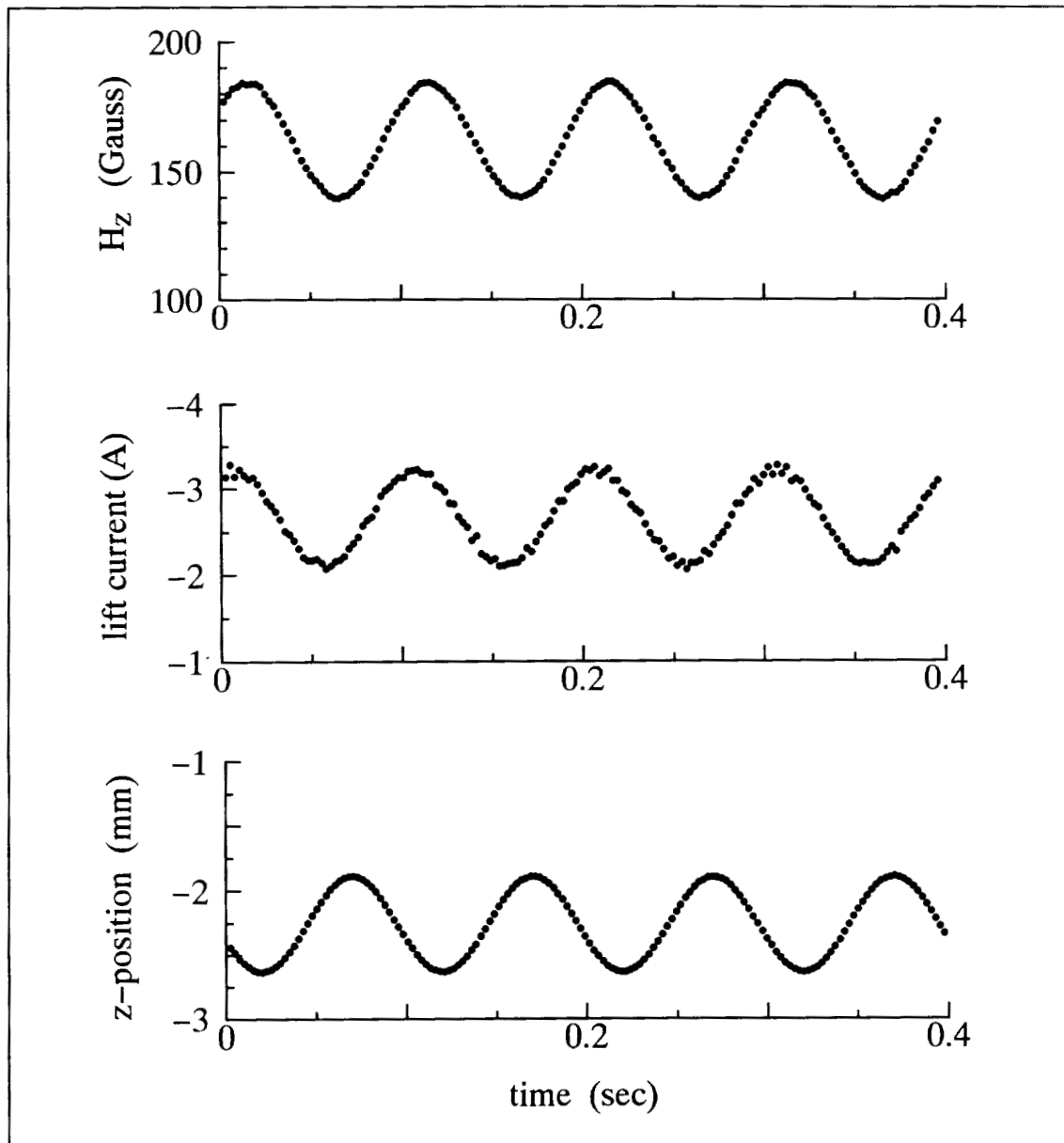
Figure 10. Measured z position and lift current
at 10 Hz heaving motion

Current passing through each coil and the model position and H_z just below the coil 5 were measured in real time during a model heaving at various speeds. The model is a simple cylindrical magnet with a sheet of white paper.The magnet is 125 mm long and 10 mm in its diameter. The weight of it is 72.8 g. The control frequency is 397 H_z. The lift current is defined here as a half sum of both currents passing coils 1 and 5. The lift current does not lie on the 10 Hz sinusoidal wave so accurately as the measured z-position and H_z in Figures 10. Besides the difference in phase between z-position and the current is much larger than between z-position and H_z.

The estimated force/current constant is affected by the frequency as shown in Figure 11. The resuls looks similar to the those in reference 7. On the contrary, the force/H_z constant looks constant when the frequency is larger than 9 Hz. The static results are estimated from the model mass and the averaged measured H_z at each frequency. The static ones are very near the constant value of the dynamic results although there still exists a little difference between the two constants. This fact means that measuring the magnetic field intensity is superior to measuring the coil currents *for the magnetic balance.* Although only one H_z was measured in this preliminary test, it is more desirable to measure the magnetic field intensity at many points on the test section walls near the coils.
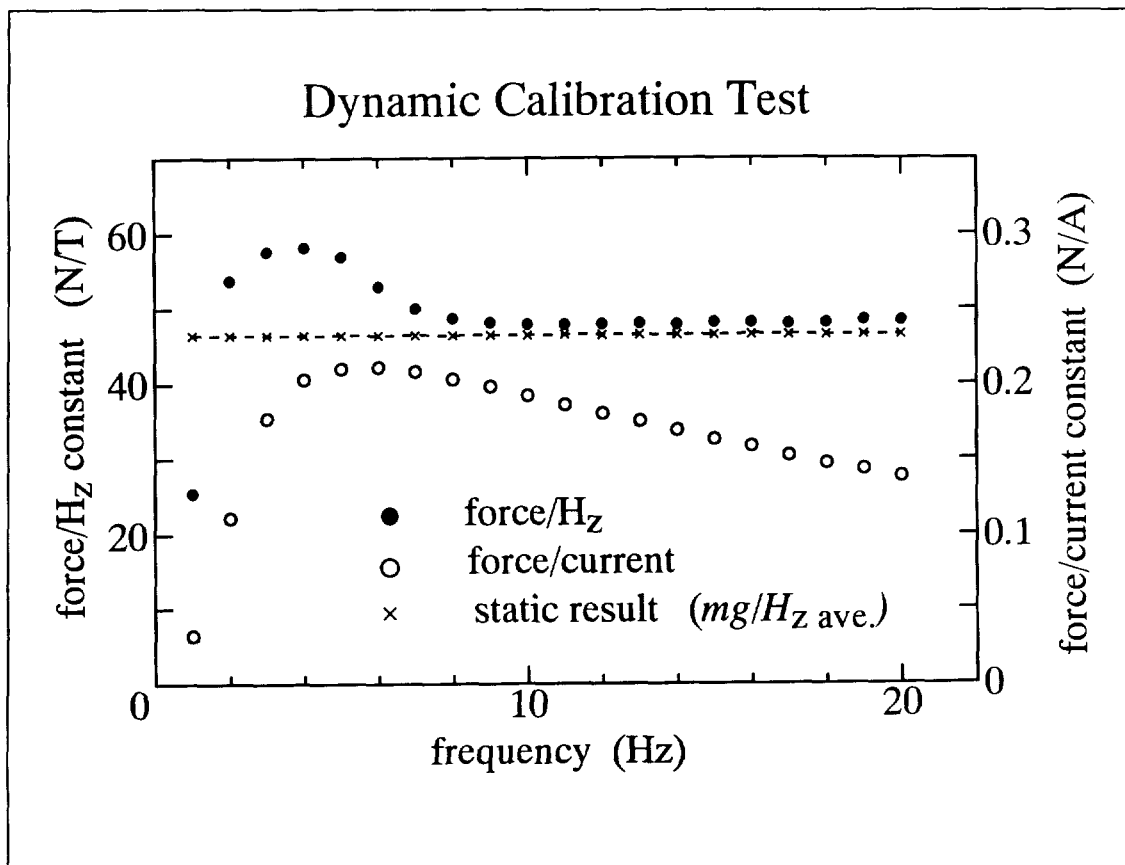
Figure 11. Dynamic calibration test results
with sinusoidal motion in z

System Description

Coil Arrangement

The 60cm MSBS has 8 iron cored coils and 2 air cored coils as the 10cm MSBS. The four lift coils are subdivided into two parts in each. Constant current passes through the half part of each lift coil to generate the constant large $\partial H_z/\partial x$. The turns and sizes of the coils are listed in Table III. The assembled coils are shown in Figure 12. The positions of the coils are a little different from those of the 10cm MSBS. The drag coils are closer to each other than in the 10cm MSBS to get good efficiency of generating large $\partial H_x/\partial x$. The two sets of four iron coils at front and rear positions are closer to each other than in the 10cm MSBS. The test section of the 60cm MSBS is the largest in the world as shown in Figure 1.

coil No.	turns	core size(mm)	purpose
0, 9	50	620 x 620 air cored	drag force
1, 3, 5, 7	97+97	200 x 200 iron cored	lift force pitching moment
2, 4, 6, 8	100	200 x 200 iron cored	side force yawing moment rolling moment

Table III. Dimensions of coils of the 60cm MSBS
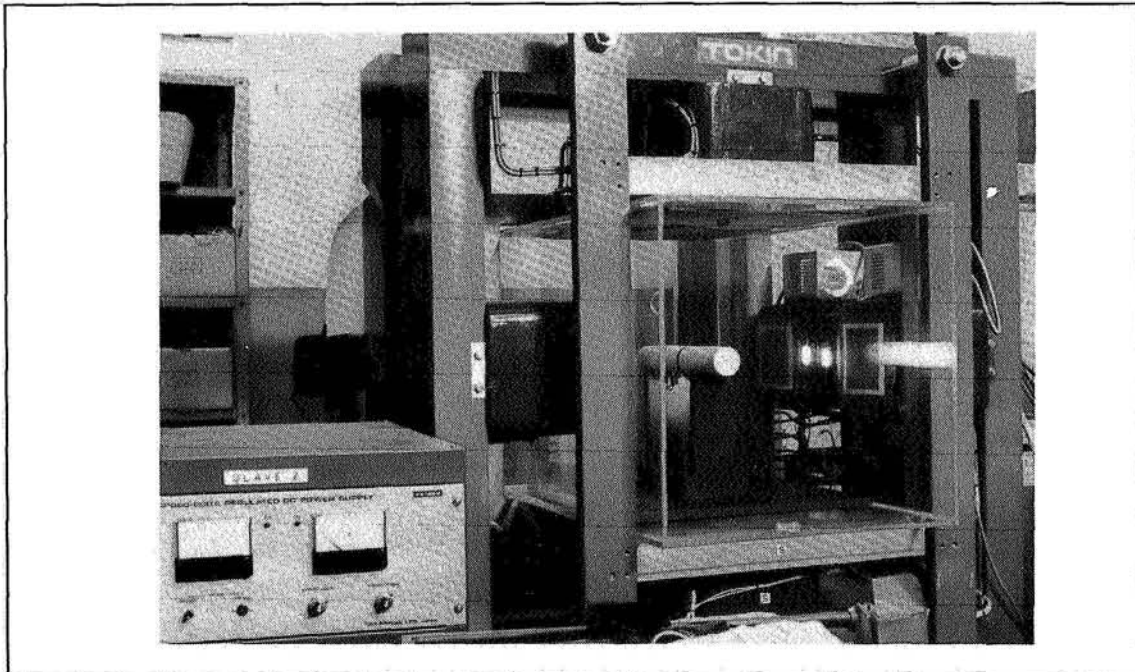
Figure 12. Assembled coils at the 60cm MSBS

Models

There is only one magnetic core for two models at the 60 cm MSBS. One model is 461.5 mm long and 60 mm in its diameter and about 1.3 kg in its weight without the magnet. It has a large room inside it for mounting some instruments. The other model is 381 mm long and 55 mm in its diameter and about 500 g in its weight. It looks similar to the other one but is much lighter. It does not have much room inside it. The permanent magnet is cylindrical and 50 mm in its diameter and 300 mm in length. The material is Fe-Ni-Co magnet and the flux of magnetic induction is 0.00238 Wb.

Model Position Sensor

The model position sensor at the 60 cm MSBS is similar to the one at 10cm MSBS. But it has a zoom lens system and adjusts the size of the image on its screen. The image size is about 1/3 of the model size. Analytical estimation shows the accuracy of the sensor does not vary with the image size except in the y position.
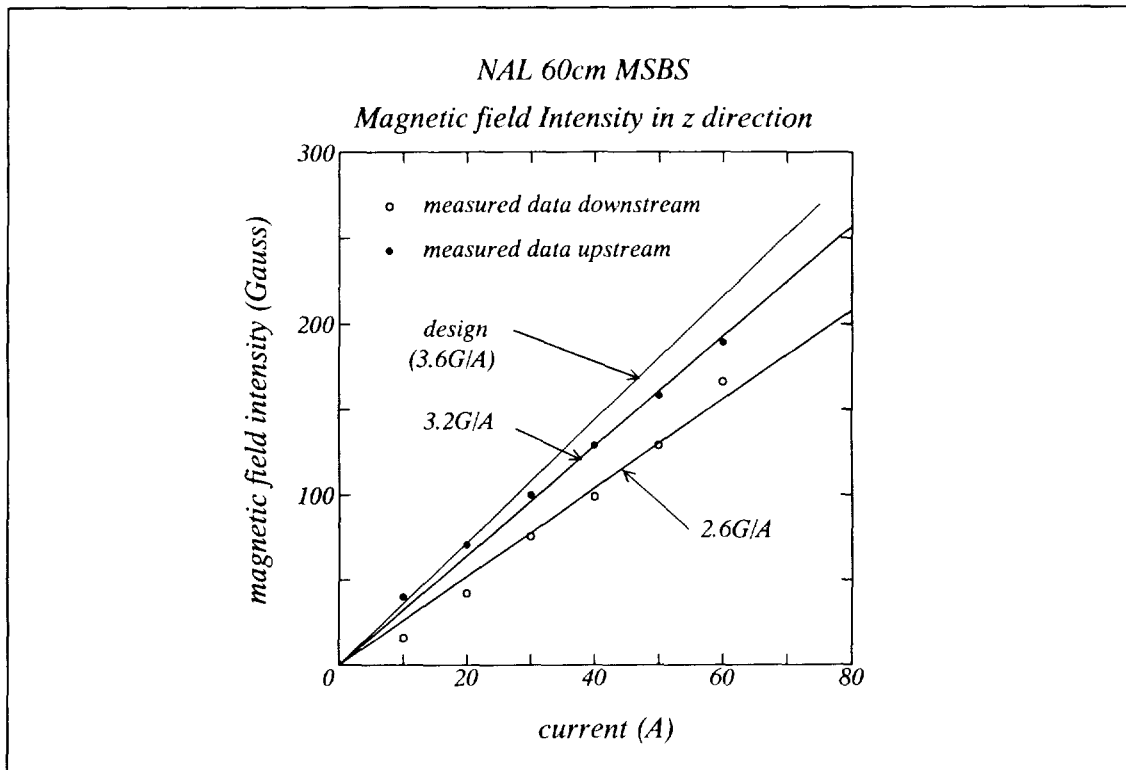
Figure 13. Measured Hz at the 60cm MSBS
Measured Magnetic Field

Power Supply

The power supply for the MSBS consists of five bipolar current control mode power units and two uni-polar power units for bias coils. The maximum current and voltage of the units are 75 A and 60 V. The forward lift coils 1 and 3 are connected to each other and are provided with current by a power unit. The pairs of coils (5,7), (2,4),

(6,8) and (0,9) are also connected in one respectively in a similar way. The 5 degree control in freedom will be available with this power supply. An extra two power units will make the control be available in 6 degrees of freedom at the MSBS as at the 10cm MSBS. The power units are controlled by voltage signals from five DA converters and monitor DC outputs of the units are available as in the 10cm MSBS. Those power units are linear. The error is within 0.1% of their full range.

Controller

The MSBS is controlled by a personal computer as in the 10 cm MSBS. The feedback control speed is 248 Hz. The control algorithm is the same as in the 10cm MSBS. There is no data acquisition computer but the model position and signal outputs for the power units are stored in its memory in real time.

The generated magnetic field intensity is weaker than that designed in the z direction by 30 %. Figure 13 shows the measured one.
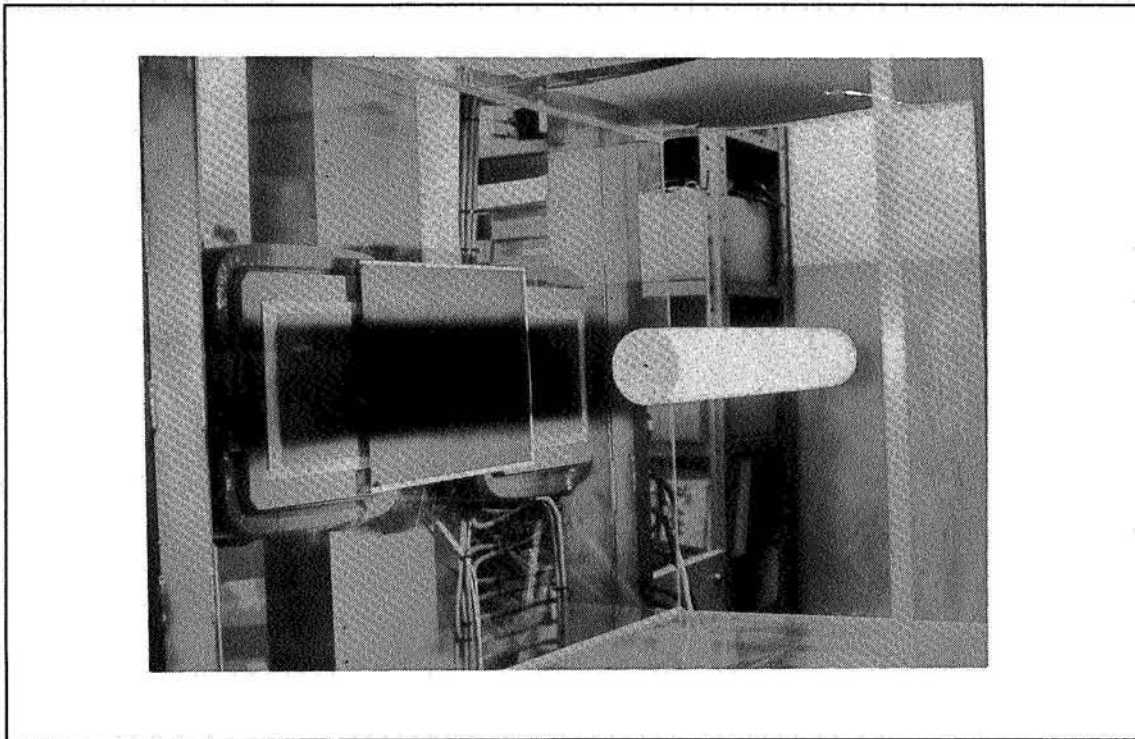
Figure 14. A suspended model at the 60cm MSBS.
Some Suspension Results

The larger model was suspended in the 60 cm MSBS in 3 degrees of freedom in the longitudinal direction. The four side coils generate the magnetic field to put the model along the center line. Figure 14 shows the model in suspension. The pitch angle and z location of the model were changed by moving and rotating the model position sensing system. The system is mounted on a stage. The stage is composed of two substages which are used for rotation and for translation in z. The system position in pitch angle and in heaving can be changed by controlling the substages independently. These tests were carried out in a very primitive sense.

REMARKS

The two magnetic suspension and balance systems are in operation at NAL. The smaller one, the 10cm MSBS, was first operated in 1987. The examination of MSBS design method and study of MSBS operation have been carried out with this MSBS. A model with two pairs of extra magnets plus a main magnet inside it can be suspended in the 6 degrees of freedom. The way of rolling moment control was examined two times with different models and the results show the way is right. A preliminary dynamic calibration test was carried out. The dynamic force calibration with the coil currents looks poor in accuracy as well as in reference 7. But the calibration with measured magnetic field intensity is very superior to that.

The larger one, the 60cm MSBS, was designed with obtained test results and experiences with the 10cm MSBS and first operated in 1993. A model with a cylindrical magnet can be suspended in the 60 cm MSBS in 3 degrees of freedom in the longitudinal direction. The measured magnetic field intensity in z direction was less than the designed one by about 30% in its magnitude. The system has 5 power supply units and it can potentially suspend a model with a cylindrical magnet in the 5 degrees of freedom. The size of it is the largest in the world.

REFERENCES

1. Kilgore, R: MSBS Newsletter, number 9, May, 1992, pp. 14
2. Kuzin, A.V.; and Vyshkov, Y.D., eds.: PROGRESS OF MAGNETIC SUSPEN-SION AND BALANCE SYSTEMS FOR WIND TUNNELS IN THE USSR, NASA CP 3152, August, 1991, pp. 765-774
3. Sawada, H.; and Kanda, H., eds.: Study of the 0.1m x 0.1m Magnetic Suspension and Balance System. NAL TM-623, June, 1990
4. Sawada, H.; and Kanda, H., eds.: THE 10CM X 10CM MAGNETIC SUSPEN-SION AND BALANCE SYSTEM AT THE NATIONAL AEROSPACE LABORATORY. AIAA 91-0397, Jan., 1991
5. Britcher,C.P.; and Goodyer,M.J., eds.: DIGITAL CONTROL OF WIND TUNNEL MAGNETIC SUSPENSION AND BALANCE SYSTEM, ICIASF'87 RECORD pp .334-341, June, 1987
6. Sawada, H.; and Suenaga, H., eds.: Rolling Moment Control in the NAL 10 cm x 10 cm Magnetic Suspension and Balance System. NAL TR-1164, June, 1992
7. Eskins, J; AN INVESTIGATION INTO FORCE/MOMENT CALIBRATION TECH-NIQUES APPLICABLE TO A MAGNETIC SUSPENSION AND BALANCE SYSTEM, NASA CR 181695, August, 1988

THE SIMULATION OF A PROPULSIVE JET AND FORCE MEASUREMENT USING A MAGNETICALLY SUSPENDED WIND TUNNEL MODEL

K.S.Garbutt and M.J.Goodyer
The University of Southampton, England

SUMMARY

Models featuring the simulation of exhaust jets were developed for magnetic levitation in a wind tunnel. The exhaust gas was stored internally producing a discharge of sufficient duration to allow nominal steady state to be reached. The gas was stored in the form of compressed gas or a solid rocket propellant. Testing was performed with the levitated models although deficiencies prevented the detection of jet-induced aerodynamic effects. Difficulties with data reduction led to the development of a new force calibration technique, used in conjunction with an exhaust simulator and also in separate high incidence aerodynamic tests.

INTRODUCTION

The aerodynamics of base flows are particularly subject to support interference and it is desirable for the Magnetic Suspension and Balance System (MSBS) to be capable of such investigations. The influence of the propulsion system on flight vehicle base flows leads to the conclusion that a commercial wind tunnel equipped with an MSBS should be capable of propulsion simulation tests. Performing these tests with a magnetically suspended model presents a particular challenge, given the complexities of achieving such simulation, of inlet and exhaust flows simultaneously for some models, even in a conventional wind tunnel.

The aim of the work outlined in this paper was to address the issue of providing an exhaust flow from a magnetically suspended model free from an umbilical. The overriding design consideration for this simulation, as no support exists through which to supply a gas, became the need to incorporate a gas generator within the levitated model.

An evaluation of exhaust flow simulators was undertaken as a cooperative venture between Physical Sciences Inc. (PSI) of Andover, Mass. and the University of Southampton, England, funded under the NASA LRC SBIR scheme NAS1-17496. In terms of hardware PSI contributed a complete model for the work described in this paper, based on the use of stored liquid CO_2 as a gas source, while the University provided a model featuring a solid propellant gas source, the magnetic suspension system and associated wind tunnel.

The wind tunnel is horizontal and its magnetic suspension system comprises a set of ten actively controlled copper wire electro-magnets, some with air and some with iron cores, positioned around the test section, acting upon a magnetised model. The coil and model geometries allow the control of up to six degrees of freedom. The system is stabilised by the action of an optical system which senses model

position and attitude, feeding to digital control software in control loops which generate demands for current from individual power supplies for each electro-magnet. The computer allows also the control of position and attitude by change of set point. A schematic of the magnets and model is shown on figure 1. The test section is 7 inches across and allows the testing of models of length about 5 to 8 inches depending on angle of attack. The role of the electro-magnets is to magnetise the model, support its weight and resist aerodynamic and propulsive system force and moment components. The sum of each of the force and moment components acting on the model during a test is measured by establishing a relationship between them and the set of currents, by means of calibration.
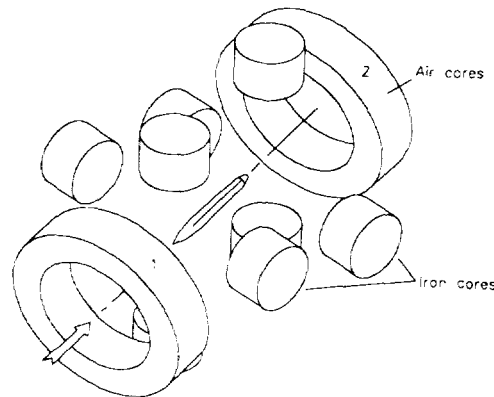
Figure 1. Wind tunnel magnetic suspension and balance system.
Array of electro-magnets around the test section.

Prior practice had been to levitate model designs comprising a non-magnetic outer aerodynamic shell normally containing permanent magnets, although we had experience in suspending models with iron cores and also a superconducting core. In view of the demands of the propulsion simulation experiments, namely a need to withstand a reasonably high force, to provide gas storage space, a nozzle and perhaps controls, it was decided to avoid the non-magnetic shell and instead to use iron for the whole of the model to easily allow a complex internal geometry, the maximum magnetisable volume and a high force capability provided the model was well magnetised. Essentially the model would be axi-symmetric and therefore need active control in only five degrees of freedom, rolling being prevented passively by an offset centre of gravity.

MODIFICATIONS TO THE SOUTHAMPTON MSBS TO ALLOW PROPULSION SIMULATION

The major change required was provision for the magnetisation of ferrous models, by means of current components in appropriate electro-magnets. The magnetisation method was novel in that the magnetisation vector was rotated to match the instantaneous angle of attack of the model. This was the first use of an adaptive magnetisation procedure, allowing the suspension of iron models over the full angle of attack range available with the Southampton MSBS[1].

Normally the streamwise position of the model is monitored with a laser light beam directed across the base of the model. This region was now to be occupied, at least in part, by exhaust gas which we could not be sure would not affect the beam. Therefore this component of model position was monitored

at the nose, requiring a software trigger to be installed to switch off electrical power to the electro-magnets when the model was absent.

EXHAUST SIMULATOR SPECIFICATION

The notional design would comprise a gas generator, controls and rear-mounted nozzle all contained in iron. The propulsive force vector would be along the model axis and generally horizontal, resisted partly by the air-cored electromagnet pair 1,2 on figure 1. Force capability was limited by current to about 1 lb. The good resolution of forces and moments required, in our experience, a steady model and currents. Good resolution was necessary if the aerodynamic effects of exhaust flows were to be separated. A minimum thrust-on duration was therefore set by the need to allow time for model motion transients to die away following firing. The model position control system had a natural frequency of order 10Hz with fairly good damping not far short of critical and therefore as a minimum the thruster needed to run steadily for about a half-second for the model to steady with another half second or so to allow data sampling and averaging.

Exhausts are often characterised by nozzle pressure ratio. The ratio of specific heats of the jet γ is also an important parameter[2]. The importance of other jet properties such as temperature, pressure, Mach number and Reynolds number depends on the particular propulsion simulation test to be attempted, which typically might be a rocket or jet engine exhaust. The test engineer is forced to compromise, selecting a small number of parameters to be correctly scaled for each investigation. Reference 3 is a review of requirements. Thrust duration and time profile were the main design drivers in this exploratory work.

A review of safety, cost and convenience issues eventually narrowed down the several options for on-board gas generator and led to the use of two commercially available generators. In turn this decision introduced constraints on the available generator size and therefore total mass of stored gas. The combination of design considerations led to the use of small diameter exhaust jets in relation to the body diameter, compared with many flight vehicles.

CARBON DIOXIDE THRUSTER

A compressed gas thruster was selected by PSI for proof of concept propulsion simulation trials. The decision to develop the compressed gas thruster was based on the perceived simplicity[4]. In the absence of any source of heating this type of thruster would by its nature generate a low temperature jet in comparison with many engines, but could be fairly representative in terms of γ and jet Mach number.

A thruster was proposed containing a small disposable CO_2 bottle, the contents of which could be exhausted via a nozzle. The major difference between the initial proposal and the design eventually tested was that the initial proposal incorporated a control valve to regulate gas flow. However no fast-acting valve was commercially available to match the small scale of the model and PSI were forced to omit a valve from the final design. Figure 2 is a simplified sketch of the layout of the model showing the important components. To initiate the gas discharge a laser beam was shone into a window on the forward

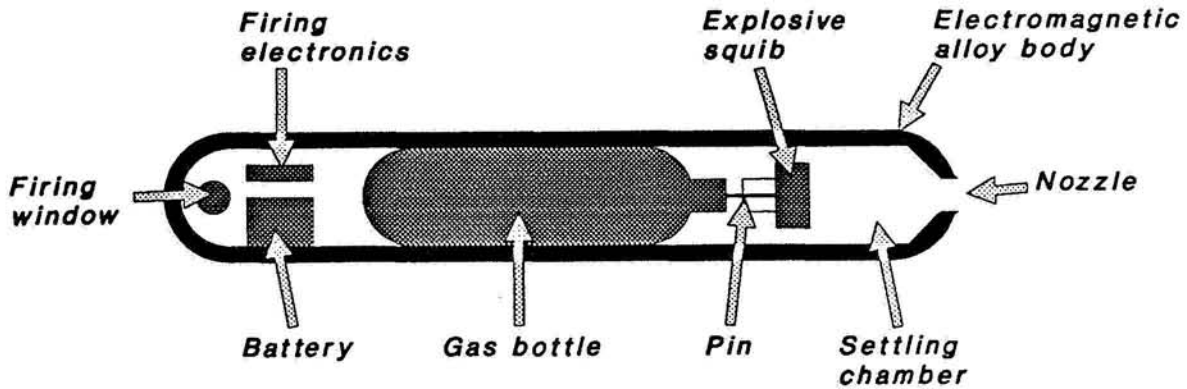part of the model, firing a squib to puncture the bottle.

Figure 2. Schematic of compressed gas exhaust simulator model.

Thruster Performance

In the design study for the small scale carbon dioxide propulsion simulator[4], PSI envisaged a stepped (or top-hat) thrust profile of two to three seconds duration. Such a profile would have been suitable for exhaust simulation in the Southampton MSBS. A typical profile from the actual thruster is shown in Figure 3. A peak corresponding to puncturing the gas bottle is followed by an almost exponential decay in thrust over a period of around one second.
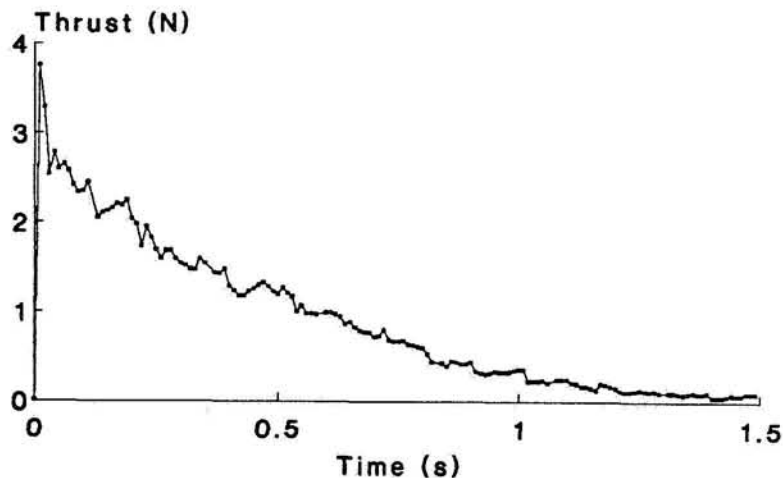
Figure 3. Thrust profile produced by the compressed gas exhaust jet simulator.

The critical factor leading to the discrepancy between the expected and actual thruster behaviour was the assumption that the propulsion simulator model had enough thermal mass to maintain the temperature of the carbon dioxide bottle and contents during a firing. The observed thrust decay is a result of rapid cooling of the thruster as the carbon dioxide absorbs heat for vaporisation and expansion from the model structure. This cooling reduces the vapour pressure and consequently the rate of CO_2 vaporisation.

294

The ultimate aim of the wind tunnel tests conducted using the suspended CO$_2$ thruster was to measure the difference in drag coefficient caused by the presence of an exhaust plume. To make this measurement it was expected that the following three parameters would be evaluated:

1. Installed thrust: Probably inferred from bench tests of the thruster.
2. Total external force: This comprises thrust and drag, and for tests at incidence also includes effects of lift and pitching moment.
3. Zero-thrust total external force: Aerodynamic loads alone.

Thrust was found to be sensitive to the initial temperature of the model and to attitude, factors which contributed to inconsistencies in the thrust. The resulting unsuitable thrust-time profile combined with the unsatisfactory repeatability of this thruster caused severe control and data interpretation problems. In the form tested the small-scale CO$_2$ thruster was judged as being poorly suited to the needs of exhaust simulation in the MSBS.

However once it had been shown that the capability of the MSBS to apply static axial force to the compressed gas exhaust simulator exceeded the level of the expected thrust peak, a series of firings of the thruster in suspension proceeded at zero angle of attack. The thrust peak tended to cause a large transient axial motion of the model. A large peak would often cause the model to move out of range of the axial position sensor. This event usually caused a loss of control. If the initial disturbance did not exceed the allowable limits, the MSBS was generally able to regain control of the thruster[1].

The MSBS with CO$_2$ model was calibrated statically for three components. The aim was to use the results of the calibration, that is the variation of system current with lift, drag, and pitching moment, to allow the extraction of these components from run-data obtained during thruster trials in suspension.

In view of the relatively violent motions of the model following its firing, a new computer program, TRANSIENT, was developed to deduce the forces and moments acting on the model from the observed changes in system current and model position. The aim was to derive the time history of the heave force, axial force and pitching moment from recorded data, the analysis accounting for inertia and acceleration[5]. The results obtained were generally disappointing. The axial force extracted from a wind-*off* thruster firing should have resembled a typical thrust profile such as that of figure 3. However, the output of the analysis appeared badly corrupted, as shown in Figure 4. A number of position-dependent factors were thought to have combined to denigrate the results. Some of these factors were identified and modifications made in attempts to reduce their effects but without a satisfactory outcome.
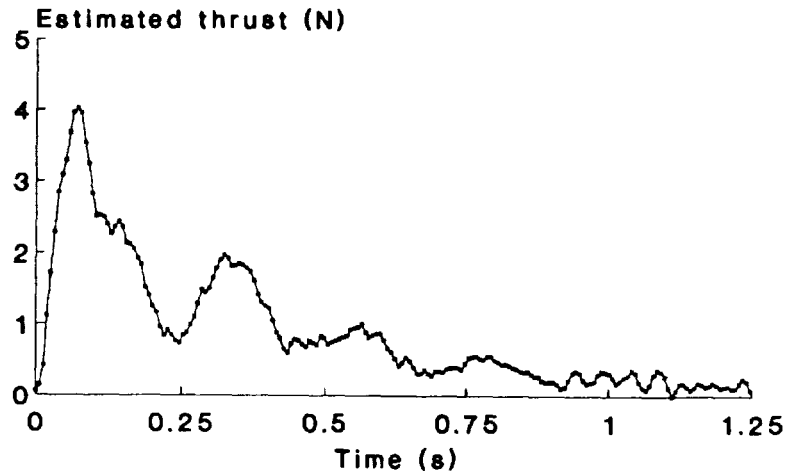
Figure 4. A typical thrust history calculated from position and current data.

It became clear that given the available apparatus, two of the parameters introduced above, whose evaluation would allow measurement of a change in thruster drag coefficient, could not be accurately assessed. The thrust level (1) was uncertain and variable for this model, while as described above, attempts to extract three force and moment components simultaneously were not successful. This prevented accurate assessment of parameter (2). Parameter (3) could be found with more confidence.

Further investigations into the subject of the transient-dependence of the analysis were not deemed worthwhile. The performance of the compressed gas propulsion simulator was considered to be so far removed from that of a device acceptable for use in production wind tunnel testing as to draw into question the benefit of the further development of strategies to cope with its unpredictable and peaky thrust profile.

The disappointing results helped prompt a review of force measurement practices employed with MSBS facilities. This led directly to the development of the DFM technique described later in this paper.

SOLID ROCKET PROPELLANT

The use of a solid rocket grain to generate an exhaust plume in an MSBS was first considered by PSI in their initial proposal to NASA for the propulsion simulation contract[4]. The idea was rejected but doubt arose later over the objections in the light of the availability of small solid propellant motors from various sources, including rockets from hobby shops for use in model rockets and aircraft. It was decided to pursue the solid rocket option at Southampton.
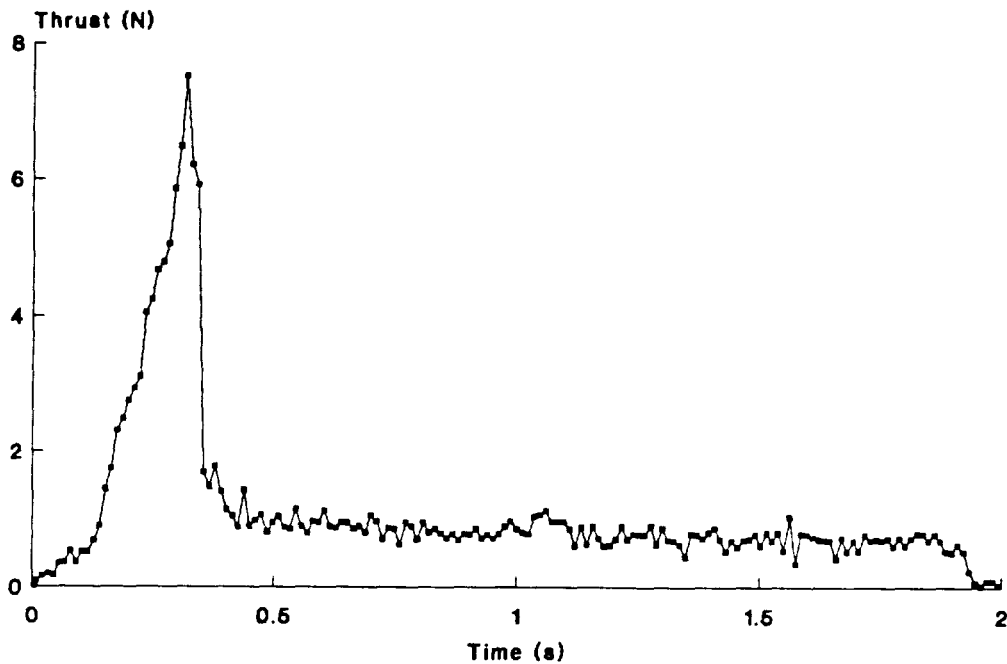
Figure 5. Thrust profile for solid propellant rocket motor

Hobby rocket motors generally have a peaky thrust profile. Figure 5 shows a typical profile featuring a substantial boost peak followed by a cruise phase. This same source of rocket motor was developed to a form more suitable for use for propulsion simulation with an MSBS. The development paid particular attention to the ignition and burn-out phases[1]. Figure 6 shows the performance of the same grain material but developed for this application and is typical of the developed performance. The profile is essentially top-hat as desired, of sufficient duration and suitable maximum thrust. The only criticism of the profile is the time variation of thrust, small but still judged to be too high, and a variability between motors which seems inevitable, discovered later during the test series.
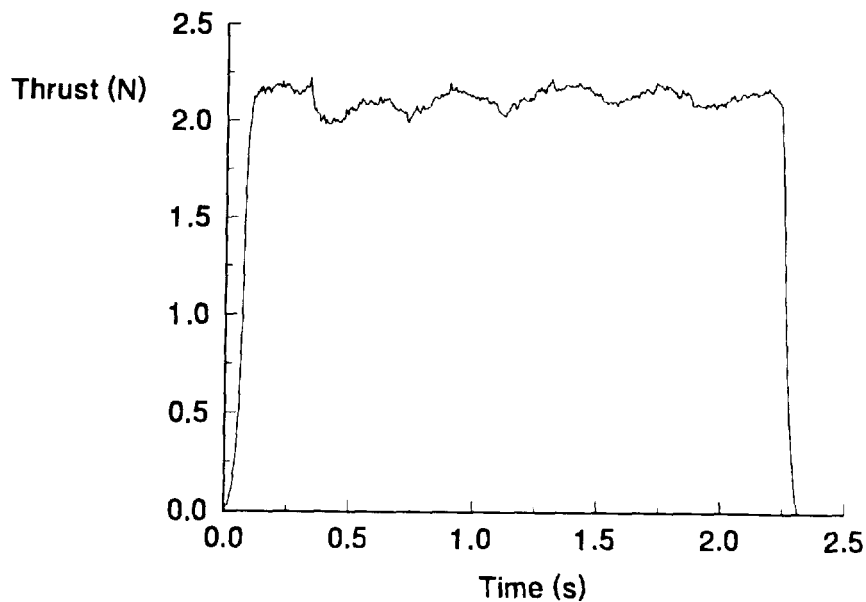
Figure 6. Thrust profile of improved solid propellant generator and model

Figure 7 is a sketch of the solid propellant cartridge and mild steel model designed for it. The settling chamber and nozzle diameters were 0.5 and 0.165 inches respectively.
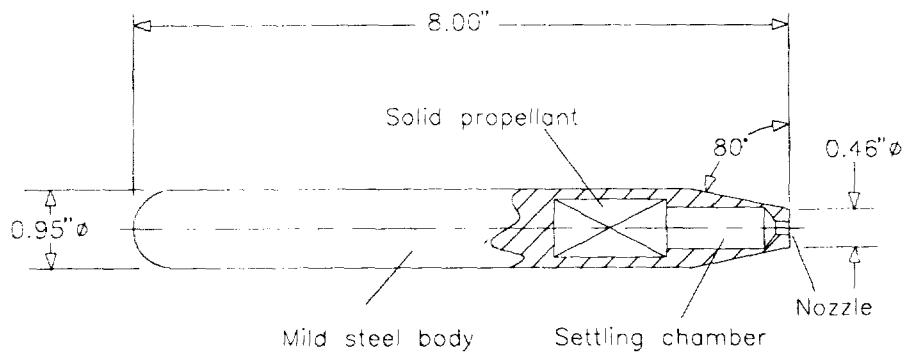
Figure 7. Solid propellant gas generator model

Rocket Exhaust Pressure Measurement

To allow a comparison of rocket thrusters with other propulsion simulation techniques and full scale exhaust flows, it was necessary to more completely characterise the exhaust. Parameters such as ratio of specific heats of the exhaust and density of the propellant (used to estimate mass flow rate from thrust duration) were available from data published by the manufacturer, given the commonality of propellants. One of the remaining characteristics which had to be measured directly was exhaust stagnation pressure, information not common with the off-the-shelf rockets because we removed the standard nozzle and provided our own as part of the model. A pressure measurement would also make possible the estimation of Mach number. It was decided also to try to relate thrust to another measurable, pressure being an obvious candidate.

Measurements of stagnation pressure during bench tests of using a pitot probe positioned in the exhaust plume close to the nozzle and a static tapping in the settling chamber downstream of the motor gave similar readings. For practical reasons the static tapping became the preferred method.

Figure 8 shows settling chamber pressure plotted against thrust for the rocket bench test of Figure 6. The data for the full-thrust period, concentrated in the upper right hand corner of the figure, suggests that thrust is linearly related to static pressure during nominal steady running. The mean chamber pressure, at about 1.3 bar gauge, would give an ideal exit Mach number of about 1.2 from a convergent-divergent nozzle. This introduces the possible alternative to the development of a thruster with a highly reliable and repeatable thrust profile. A propulsion simulator could be developed with pressure telemetry yielding an instantaneous thrust signal. An infra-red pressure telemetry system has been developed for the NASA Langley 13-inch MSBS[6], as a refinement of the radio telemetry techniques used at Farnborough in the 1960's. Pressure measurement could prove to be an attractive method for acquiring more precise data on installed thrust.
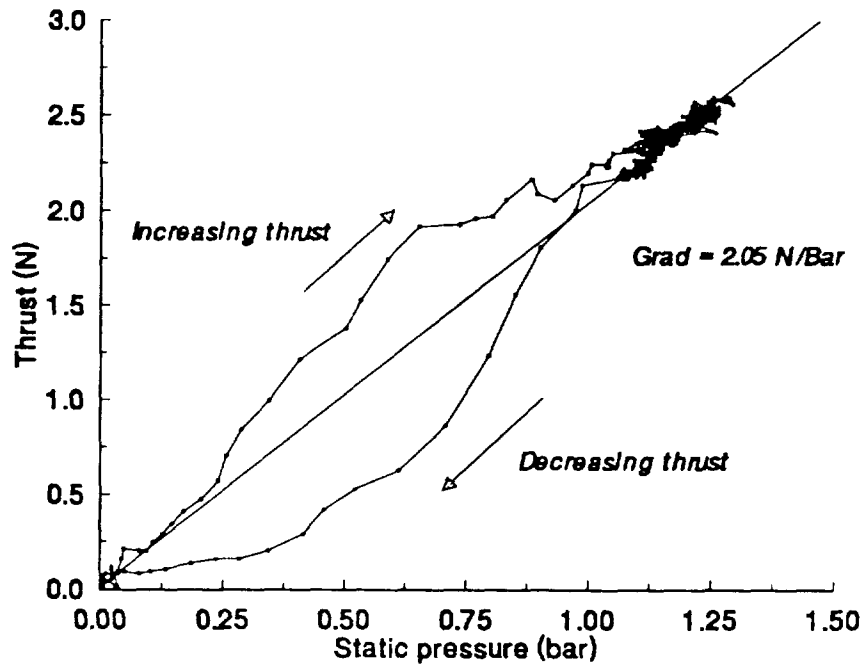
Figure 8. Chamber static pressure and thrust for solid propellant model

Rocket Thruster in Suspension

A typical axial position response to the 'top hat' thrust profile is shown in Figure 9. The start and finish of the rocket firing, at times 0.2 and 2.3 seconds, provoke a similar but opposite transient response in axial position, that is movement of the model away from its datum axial position, as the control system compensates for the changes. Once the starting response is damped out by the controller, the desired condition of a stationary model with the thruster firing is achieved in the interval 1.5 to 2.3 seconds. The electro-magnet current shown on this figure is the source of axial force data available from the MSBS. The evident transients are similar in character to the bench calibration of figure 6. A feature of these motors is the production of considerable solids and smoke which could constitute a problem in a closed circuit wind tunnel.

The external vertical heave force, axial force, and pitching moment experienced by the model were measured by the DFM rig described below. These components represent the summation of the instantaneous aerodynamic loads, motor thrust and model weight. As these tests were conducted wind-*off* at zero incidence, it was expected that motor thrust alone would dominate as the applied external axial force. The loads experienced during the firing illustrated in Figure 9 are shown in figure 10. The axial force recorded between 1.5 and 2.3 seconds is around 2.25 N, in good agreement with the levels of motor thrust measured during bench tests, figure 6. Much smaller levels of heave force and essentially zero pitching moment were recorded, as would be expected.
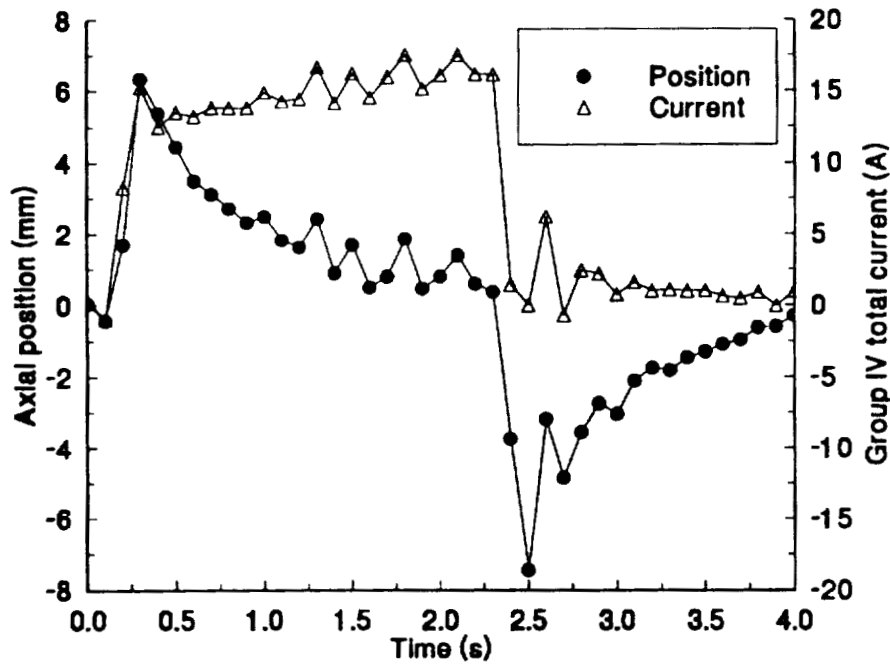
Figure 9. Responses to firing levitated solid propellant model
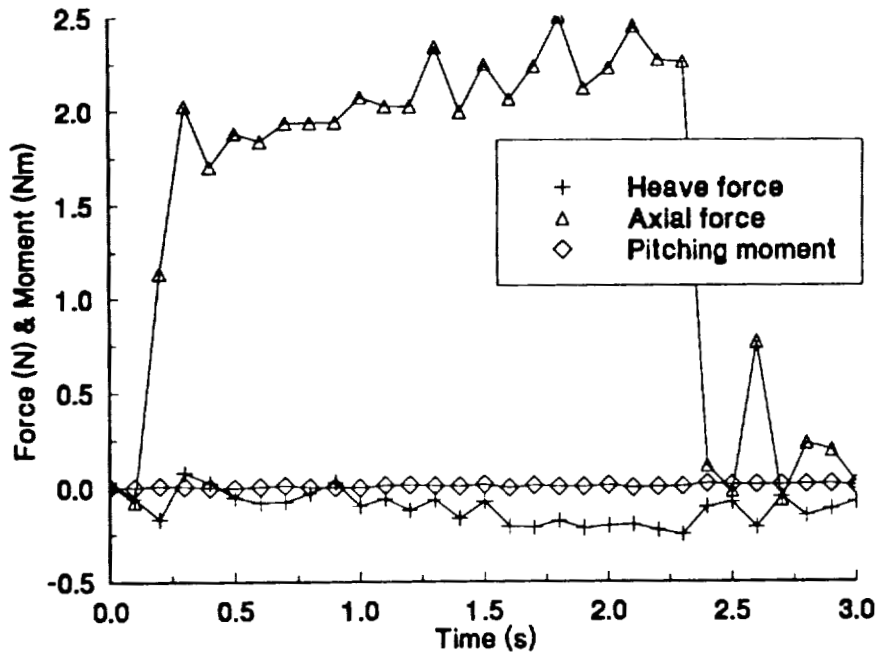

Figure 10. Measured loads on solid propellant thruster in suspension

Solid rocket cartridges have proved a moderately successful gas source for simulating an engine exhaust for a model in a small MSBS. There remains a number of aspects of their performance which need to be addressed before firm conclusions can be drawn as to the suitability of this simulation

technique for use in a larger facility. The areas of question include safety, thrust profile, repeatability and smoke reduction. There are other sources of solid motor which might overcome some restrictions and offer a higher specific impulse. This, combined with the elimination of the separate motor case feature of model rockets, which is entirely feasible, could lead to a useful increase in jet diameter but in turn would require modifications to the MSBS equipment.

LOAD MEASUREMENT

Introduction

For an MSBS to be effective as an aid to wind tunnel testing, it is vitally important for it to be able to perform its 'Balance' function. The aim is to convert run-time coil currents into loads. The tradition has been to pre-calibrate a model/coil array by applying known loads to the model wind-off and recording current sets to allow calibration constants to be derived for the subsequent analysis of wind-on data. The evaluation of multiple force and moment components for a model suspended in an arbitrary position can, however, involve a particularly time consuming calibration procedure. Each of the force and moment components, six in all, is dependent on the currents in each of the ten electro-magnets of our suspension array, also on the position and attitude of the model and on the type and geometry of magnetic core inside the model. There can be appreciable non-linearities.

Simplifications are adopted because complete pre-calibration is too daunting a prospect for contemplation even for the case of one model core. For example the calibration matrix is reduced by using integrators in the control system to return the model to its nominal position following changes of applied load. Previous MSBS experience had demonstrated that the accurate assessment of aerodynamic loads by pre-calibration is straightforward for simple cases such as the measurement of a single force component applied to a centrally suspended model, and is possible in a reasonable time for up to three load components.

A review of the available load-extraction techniques[7] identifies five categories: (1) static or (2) dynamic pre-calibration of the MSBS load-current relationship, direct measurement of aerodynamic load using (3) an internal or (4) an external balance, and (5) calculation of the loads from first principles. The latter is quite impractical to the precision required for aerodynamic testing when using iron cores, but is attractive otherwise because the operation does not demand tunnel time. This is a feature it shares with (3), a method in which the model contains a balance[8] telemetering directly the force and moment data. The internal volume of the model occupied by the balance, processing electronics and telemetry compromises the maximum force capability. In contrast the other calibration methods (1), (2) and (4) do require tunnel occupancy time but with no compromise on model design. Dynamic calibration (2) involves the deliberate oscillation of the model to allow currents to be related to inertia forces and aside from avoiding the friction which might be associated with static calibration, it has no operational advantage.

The issue of tunnel occupancy for calibration purposes must be considered during studies into the appropriate measurement techniques for a commercial MSBS. The external balance notion (4) is a compromise solution much reducing the tunnel time devoted to calibration.

Previous research into external balances has been of limited scope, the major example being the construction of a force balance for use with an MSBS by Vlajinac[9]. He designed a rig to support a model in air bearings. Force and moment components in six degrees of freedom were deduced from air pressure measured inside the bearings. A static calibration of the rig away from the tunnel related bearing pressure to applied load. This rig appears to have performed well, exhibiting good linearity between load and pressure.

Since this work, miniature force transducers have become available, giving an electrical signal in response to load and it was decided to adopt this approach in a similar calibration rig, the Direct Force Measurement (DFM) rig. The notion was to carry out a wind tunnel test, recording all data as usual, then to extract the load information post-test. This would be by means of mounting the rig in the tunnel, with the model mechanically fixed to it at the proper position and attitude, then to play back the electro-magnet currents and record actual forces and moments.

DFM Rig Design

A DFM rig for use in a commercial MSBS was conceived as a starting point for the design of the new equipment, with the emphasis on automation[1], but was simplified to a three-component rig for the purposes of the actual demonstrator.
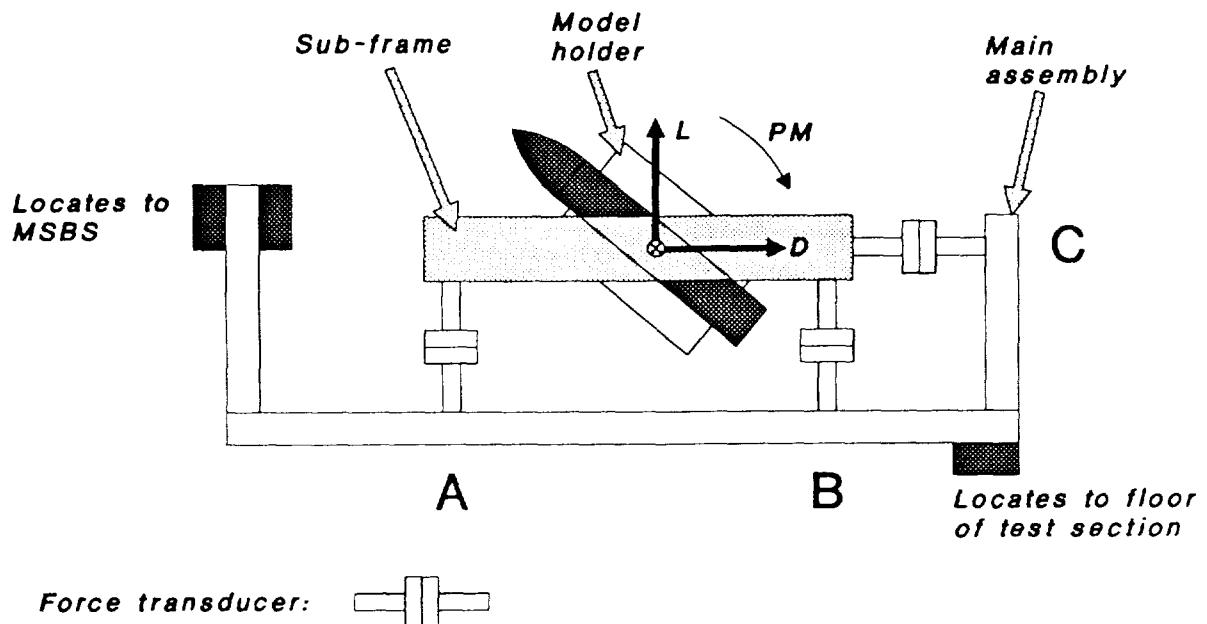
Figure 11. DFM rig schematic

A schematic of the DFM rig produced is shown in Figure 11. Layout was partly dictated by the need for compatibility with the position sensing system. The structural materials were primarily

aluminium and brass. A model restraining yoke allowed micro-adjustment of position and attitude which were checked by play-back of the recorded optical system data. Between the yoke and ground is a set of three pre-calibrated force transducers. Support electronics, software and test procedures were developed in parallel with the design and construction of the rig. Play-back of the currents then yielded the history of variation of the loads. Lift force and pitching moment are available from the sum and difference of outputs from transducers A and B, and drag force directly from C. The transducers have an accuracy of ±2%, adequate for a first build but not of a satisfactory standard for normal aerodynamic measurements.

DFM Applications

This equipment came along too late to be widely used in the propulsion demonstrator work but its usefulness was exploited several other ways, two of which are outlined below.

The DFM rig was used to improve the way force and moment components are generated by the MSBS. The new equipment allowed us to measure the effectiveness of the electromagnet array in influencing a model, whereas to this point we had relied only on estimates. The results were used to improve the ability of the controller to generate decoupled forces and moments.

At the beginning of this research program no practical method had existed for using the high angle of attack capability of our MSBS. The unique potential of this facility to investigate high alpha aerodynamics free from support interference remained unrealised. Having improved the quality of control it was possible to apply the new balance capabilities to such an aerodynamic investigation. The low speed high alpha behaviour of an ogive cylinder model was studied. This work is of interest because the advent of digital flight control systems coupled with developments in aerodynamics has allowed controlled flight at incidences beyond the stall. This in turn has led to a resurgence of interest in the aerodynamic behaviour of a cylinder-nose combination at high angles of attack.
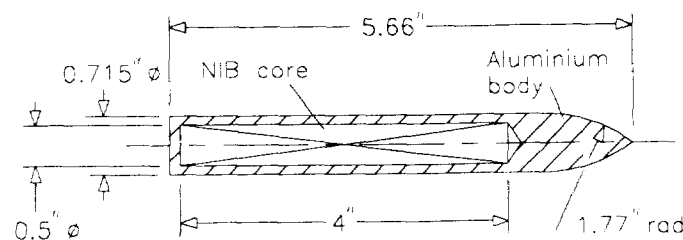

Figure 12. Ogive-cylinder model

The model's outline is shown on figure 12. This simple axi-symmetric shape contains a permanent magnet and was controlled in all degrees of freedom except roll. Tests were conducted over the incidence range -5 to +95 degrees. The DFM rig was used to reduce the wind tunnel test data yielding lift, drag and pitching moment coefficients. Examples for the complete angle of attack range are shown on figure 13.

Unsteady loads sometimes were experienced during high alpha tests with this model, the loads appearing to be periodic and predominately in the lateral direction. The model is likely to have been subject to periodic vortex shedding and the result was pronounced lateral motions, sometimes coupling

into roll due to asymmetries, which points to a need for an overall improvement in the tightness of control. Airspeed was restricted in these circumstances to avoid losing the model.
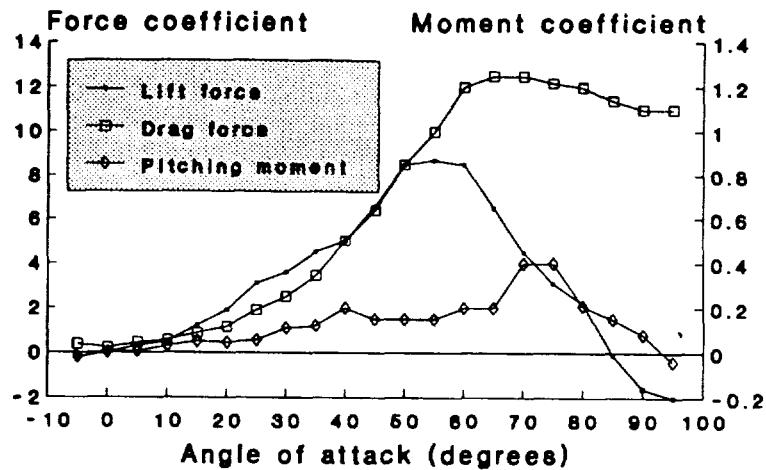

Figure 13. Variation of force and moment coefficients with incidence.
Ogive-cylinder model at Mach 0.1, atmospheric tunnel.
Coefficients are based on frontal area.

CONCLUSIONS

In relation to the simulation of an exhaust jet from a magnetically levitated wind tunnel model:

• Propulsion exhaust simulation experiments are feasible in an MSBS wind tunnel.
• Simple software algorithms can achieve satisfactory control.
• A peak thrust greater than the maximum restraint is rarely acceptable.
• A steady thrust period should exist to permit satisfactory model control and data acquisition.
• The thrust profile must be compatible with the MSBS hardware limitations.
• Pressure telemetry might be desirable to monitor thrust variations.
• Improvements are possible from the use of a higher specific impulse grain and other refinements.
• No separation of jet effects on base flow proved possible.
• Stored CO_2 is an inappropriate gas source unless, perhaps, the flow is regulated and controlled in temperature.

And in relation to Direct Force Measurement:

• The rapid assessment of aerodynamic loads is possible using a DFM rig post-test.
• The equipment may be used to improve the generation of force components by the control system.
• Pre-calibration of model cores could be simplified by this technique.
• Interference-free, high α wind tunnel tests may be performed.

304

REFERENCES

1. Garbutt, K.S.: University of Southampton Ph.D. Thesis, 1992

2. Fuhs, A.E.: Nozzles and Inlet Testing in Transonic Flight Regime

3. Ferri, A.: Review of the Conclusions of the AGARD Ad-Hoc Committee on Engine Airplane Interference and Wall Corrections in Transonic Wind Tunnel tests. AGARD Propulsion and Energetics Panel, Sandefjord, Norway, Sept. 1971, AGARD CP-91-71

4. Joshi, P.B.; Beerman, H.P.; Chen, J.; Krech, R.H.;Lintz, A.L.; and Rosen, D.I.:Propulsion Simulator for Magnetically Suspended Wind Tunnel Models. Phase 1 final report. Physical Sciences Inc., Andover MA, Aug. 1988

5. Joshi, P.B.; Malonson, M.R.;Sacco, G.B.;Goldey, C.L.; Garbutt, K.S.; and Goodyer, M.J.:Propulsion Simulator for Magnetically Suspended Wind Tunnel Models. NASA CR-189560, Jan. 1992

6. Tcheng, P.;Schott, T.D.; and Bryant, E.L.: A Miniature, Infrared Pressure Telemetry System. 34th International Instrumentation Symposium, Albuquerque, New Mex., May 1988

7. Eskins, J.: An Investigation into Force/Moment Calibration Techniques Applicable to a Magnetic Suspension and Balance System. University of Southampton M.Phil. Thesis, also NASA CR-181695, Aug. 1988

8. Roberts, P. W..; and Cheng, P.: Strain Gage Balance Calibration of a Magnetic Suspension and Balance System. Paper at 12th International Congress on Instrumentation in Aerospace Simulation Facilities, ICIASF, June 1987

9. Vlajinac, M.: A Pneumatic Calibration Rig for Use with a Magnetic Suspension and Balance System. MIT-TR-159, Jan. 1970

A Dynamic Method for Magnetic Torque Measurement

C. E. Lin   H. L. Jou

Institute of Aeronautics and Astronautics

National Cheng Kung University

Tainan, Taiwan, China

SUMMARY

In a magnetic suspension system, accurate force measurement will result in better control performance in the test section, especially when a wider range of operation is required. Although many useful methods were developed to obtain the desired model, however, significant error is inevitable since the magnetic field distribution of the large-gap magnetic suspension system is extremely nonlinear. This paper proposed an easy approach to measure the magnetic torque of a magnetic suspension system using an angular photo encoder. Through the measurement of the velocity change data, the magnetic torque is converted. The proposed idea is described and implemented to obtain the desired data. It is useful to the calculation of a magnetic force in the magnetic suspension system.

INTRODUCTION ·

In a large-gap magnetic suspension system, an adequate magnetic force model determines the accuracy of force measurement within the test section, such as wind tunnel applications. Many useful methods have been developed to obtain the desired model. However, the magnetic field distribution of the large-gap magnetic suspension system results in significant model error. From the force model, the velocity change of the suspended model implicitly contains the force model. It is obvious that the applied force on the suspended model leads to more direct and accurate information to look into the force model, if the velocity data can be obtained.

From Newton's Second Motion Law, the magnitude of acceleration in motion refers to the applied force or torque to the object. This is also useful to motion objects in a magnetic field to measure magnetic force or torque. However, the measurement of acceleration is difficult using conventional methods. The results are obtained from a first or second derivative from the velocity or position data, respectively. It requires an extreme effort to identify measured data under noisy conditions.

The torque model to describe the magnet suspending in the space magnetic field is expressed by:

$$\vec{T} = \int_v \vec{M} \times \vec{B} dv. \tag{1}$$

Assume the magnet is very small comparing relatively in the magnetic field space to cause little influence. Then the force model equation is approximated into:

$$\vec{T} = vol(\vec{M} \times \vec{B}) \tag{2}$$

[1]. This equation does not contain an integration, and is very simple in real time calculation. However, errors may exist.

Since the proposed method uses the dynamic measurement method to obtain the force model data, the results are free from the influence of magnetic field distribution. The proposed dynamic measurement method is applied to calibrate the approximate force model.

In this paper, the experimental setup is presented with test procedures based on the proposed measurement concept. A real time data acquisition system for position data measurement from an angular photo encoder with a data processing personal computer is established for the experiments. The obtained torque model is used in a large-gap magnetic suspension system.

TORQUE MEASUREMENT

Figure 1 shows the experimental setup of this study. A permanent magnet is fixed to become a single pendulum. The pendulum is attached to an angular photo encoder. The angular position change data are measured from the encoder, and are transmitted to PC-AT via an interface I/O card. The angular change data are real time acquired and displayed on the monitor. The pendulum with

magnet is located on the top of a circular electromagnetic axis. When the electromagnet is energized or excited, the magnetic force exerting on the permenant magnet will be measured from the locus of the pendulum. During the measurement process, the exerting force on the magnet includes the magnetic force and gravitation force. The former is desired, while the latter should be eliminated. Considering the damping condition, the equation of motion is expressed:

$$\ddot{\theta} = \frac{mgl}{I}\sin\theta + b\dot{\theta},\qquad\qquad(3)$$

where $I = 0.0005165 Kg \cdot m^2, m = 0.033 Kg, l = 0.115m$. Assume b = 0.5; solve the above equation to obtain the angular position and velocity. In Figure 2, a computational result expressed in a solid line and the experimental result expressed in a dashed line are shown with good agreement.

From the results, the resulting data through two differencing processes of the measurement data from an angular photo encoder contain some acceptable noise. Because the sampling rate in this test is 100 Hz to match the low angular change rate, the error resulting from difference amplification is still tolerable. When testing a higher speed angular change rate, a higher sampling rate may required to result in noisy conditions. The noise and signal may combine together.

$B\hat{E}ZIER$ B-SPLINE CURVE FITTING

Taking care of the problem of difference amplification of the noise, a curve fitting method to smooth the obtained data is applied before signal differencing, in order that continuity be maintained after the differencing process. The algorithm is termed as $B\hat{e}zierB - spline$ curve fitting [2]. The advantage of B-spline curve fitting is to fit a possible inclination of the data curve, instead of including all the control points. The B-spline curve method is not so sensitive as to change the rate in comparison to the cubic spline method, is simpler by calculation in comparison to the iteration algorithms, results in a much closer curve to all changes, and is free from the limitation of control points comparing to the Bezier curve fitting. If there are more than 10 control points, the Bezier curve fitting will become very high order, making it difficult to calculate.

Before applying curve fitting, all the ill data points, such as data jumps, should be filtered. If the control points fall on the ill data, a great fitting error may result. The number of control points also determines the change rate of the fitting curve. The more control points

that are included, the faster the fitted curve change rate might be obtained. It is a trade-off consideration to determine the control points, curve change rate, and possible oscillation after differencing processes.

MAGNETIC TORQUE MEASUREMENT AND CALCULATION

Figure 3 shows the process of measurement of acceleration to obtain magnetic torque. Fig. 3(a) shows the measured angular change; Fig. 3(b) shows the obtained angular velocity by the difference of angular change in a solid line, and by the Bizier B-spline curve fitting in a dashed line; Fig. 3(c) shows the angular acceleration after the linear difference from the fitted angular velocity of the above dashed line and the result subtracted from the gravity effect in the solid line and dashed line; Fig. 3(d) shows the magnetic torque by multiplying the angular acceleration and the inertia moment with respect to the angular data.

Figure 4(a) shows a magnetic field measurement in a pendulum locus; the solid line shows the axial magnetic field data, while the dashed line shows the radial magnetic field data. According to the magnetic torque equation,

$$\vec{T} = vol(\vec{M} \times \vec{B}), \tag{4}$$

to calculate the magnetic torque as shown in Fig. 4(b), where $\vec{M}$ is the magnetization vector of the permenant magnet, and B is the space magnetic flux density obtaining from Fig. 4(a). Comparing the theoretical result in Fig. 4(b) and the experimental result in Fig. 3(d), the difference is significant by about 3 times.

DISCUSSIONS

From the measurement results, the theoretical results and the experimental results of the magnetic torque distribution are shown in Figures 3 and 4 for comparison. The differences between those two results are significant as compared with about 3 times difference. Because of the many calibrations and recalculations, the differences in the results are difficult to see. At present, we are still working on the identification of the proper explanation of the obtained results. More detailed discussions will be presented in the revised paper which will be included in the conference proceedings.

ACKNOWLEDGEMENT

REFERENCES

1. Groom, N.J.:*Analytical Model of a Five Degree-of-Freedom Magnetic Suspension and Positioning system.* NASA TM-100671, March 1989.

2. D. Kahaner, Cleve Moler, Stephen Nash, *Numerical Methods and Software*, Prentice-Hall Inc, New York, 1989, pp. 132.
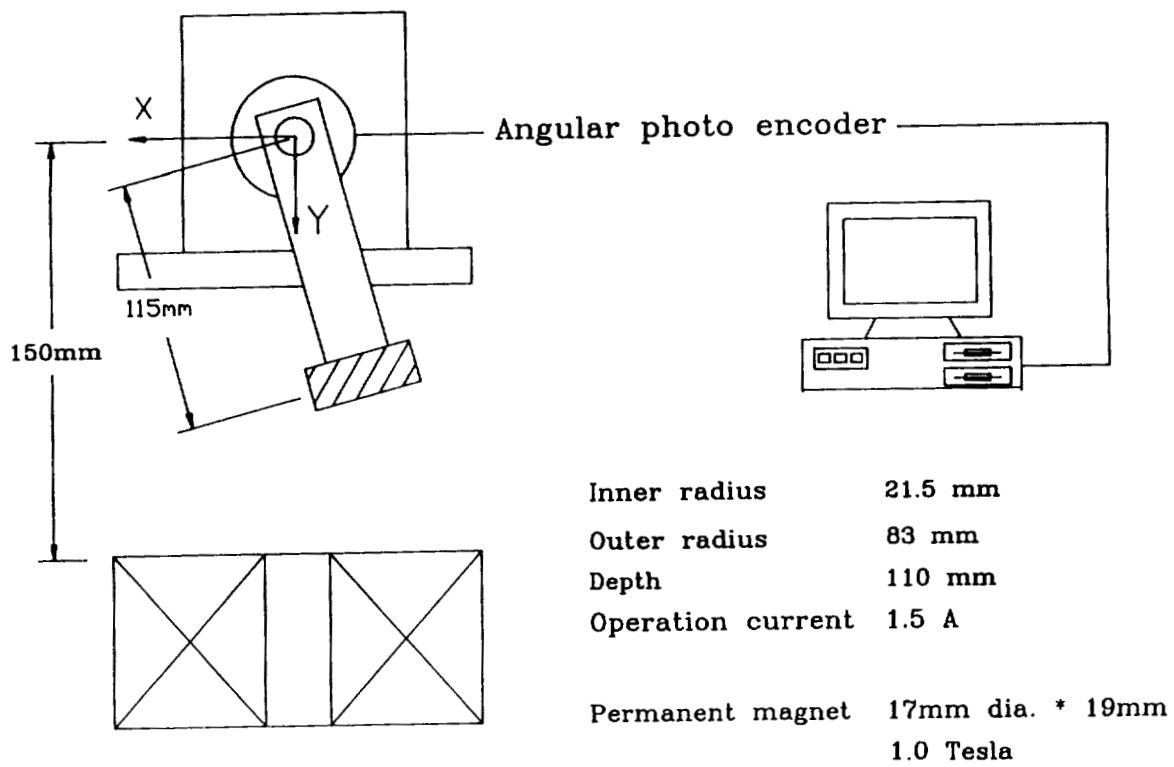
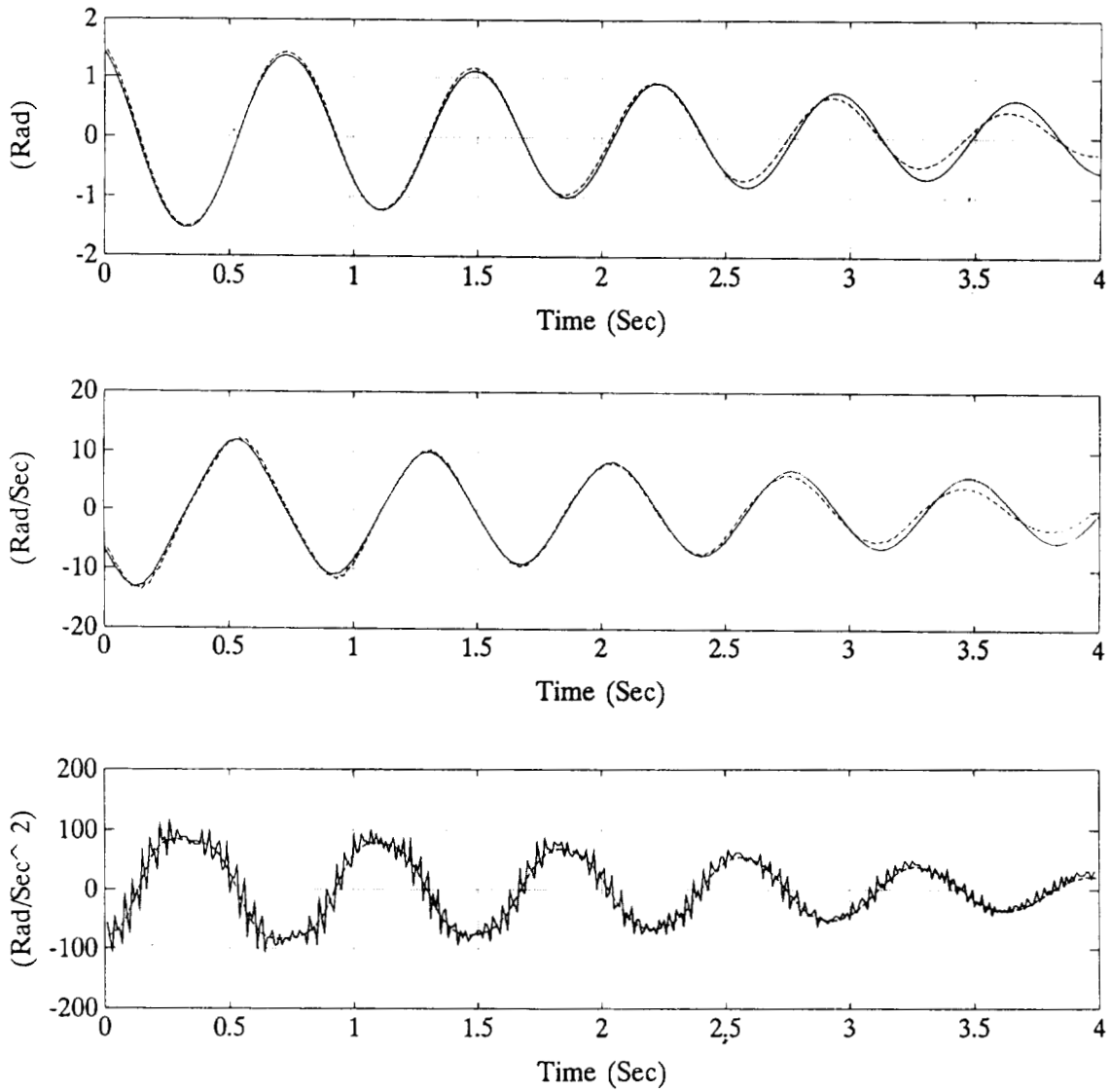Figure 1. Configuration of the Experimental Set-up.

Inner radius	21.5 mm
Outer radius	83 mm
Depth	110 mm
Operation current	1.5 A
Permanent magnet	17mm dia. * 19mm
	1.0 Tesla

Figure 2. Experimental and Simulational Results in Pendulum Motion.
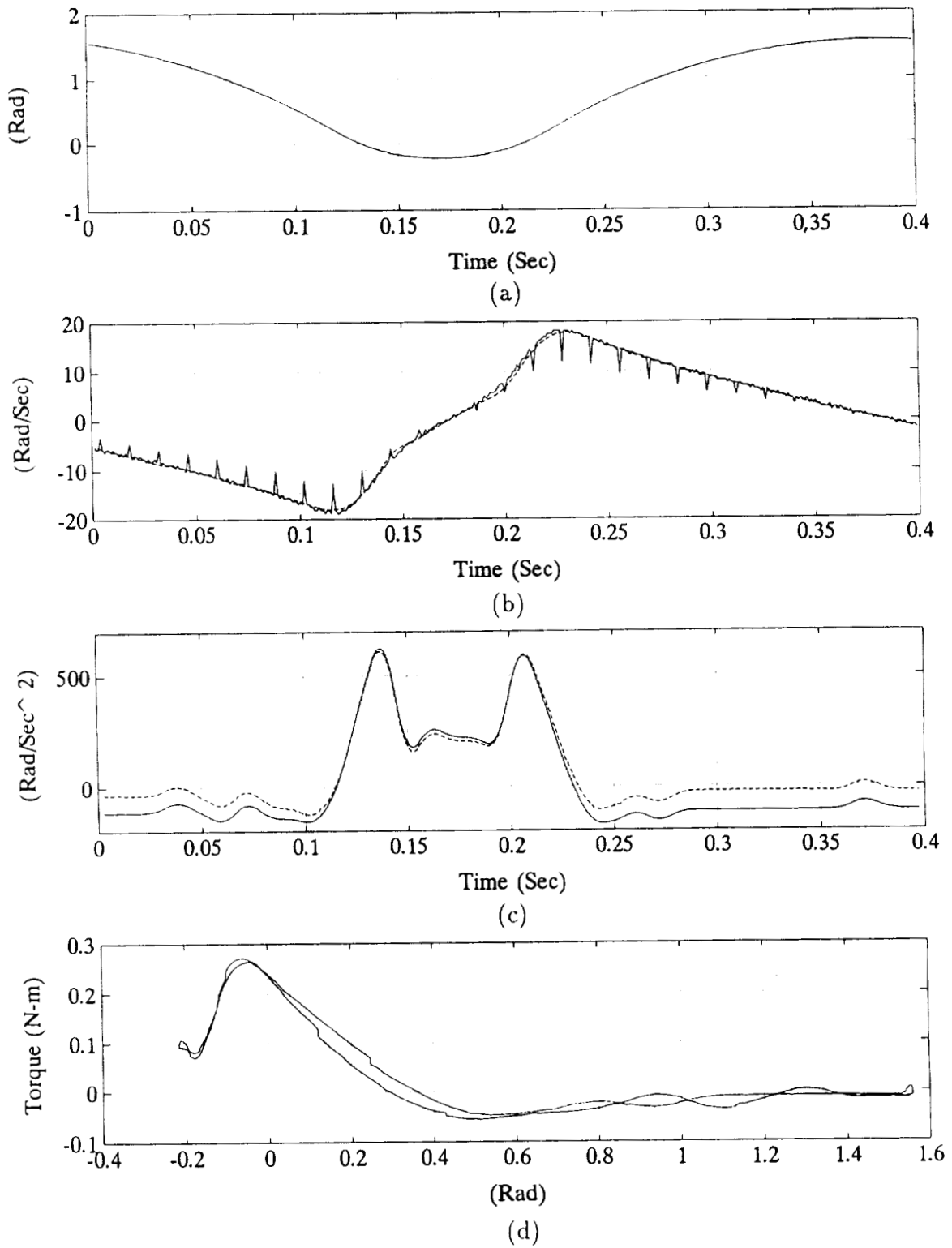
Figure 3. Pendulm Motion in Magnetic field: (a) Angular Change, (b) Angular Velocity and Fitting Line, (c) Corrective Angular Acceleration, (d) Magnetic Torque.
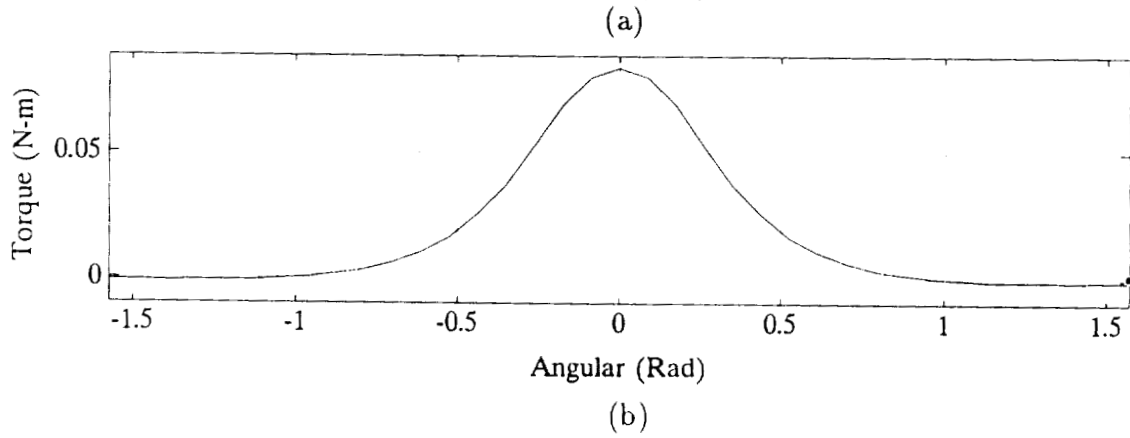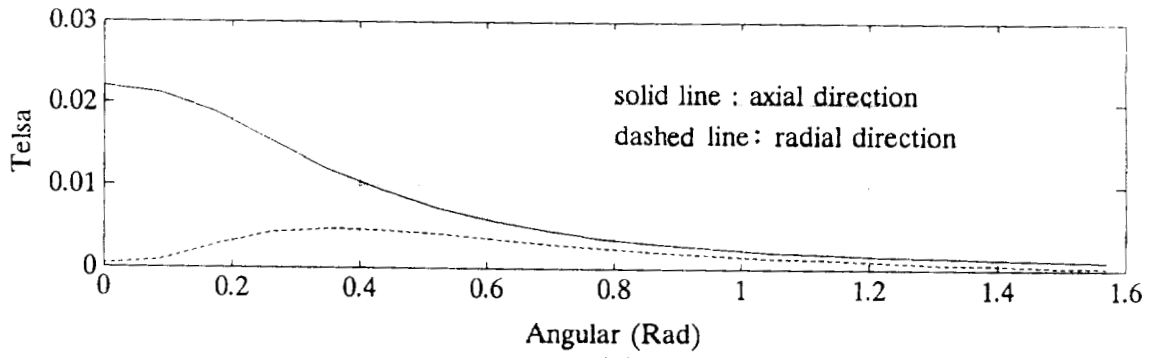
Figure 4. (a) Magnetic Field in the Pendulum Locus, (b) Magnetic Torque Obtained from the Formula $\vec{T} = vol(\vec{M} \times \vec{B})$.

Session 7a – Bearing Modeling

Chairman: Hideo Sawada
National Aerospace Laboratory

ACTIVE MAGNETIC BEARING CONTROL LOOP MODELING

FOR A FINITE ELEMENT ROTORDYNAMICS CODE

Giancarlo Genta, Cristiana Delprete
Dipartimento di Meccanica, Politecnico di Torino
Torino, Italy

Stefano Carabelli
Dipartimento di Automatica e Informatica, Politecnico di Torino
Torino, Italy

SUMMARY

A mathematical model of an active electromagnetic bearing which includes the actuator, the sensor and the control system is developed and implemented in a specialized finite element code for rotordynamic analysis. The element formulation and its incorporation in the model of the machine are described in detail. A solution procedure, based on a modal approach in which the number of retained modes is controlled by the user, is then shown together with other procedures for computing the steady-state response to both static and unbalance forces. An example of application shows the numerical results obtained on a model of an electric motor suspended on a five active-axis magnetic suspension. The comparison of some of these results with the experimental characteristics of the actual system shows the ability of the present model to predict its performance.

INTRODUCTION

DYNROT is a specialized finite element code for rotordynamic analysis developed at the Department of Mechanics of Politecnico di Torino during the last 15 years. Its main features are the use of complex co-ordinates for the rotor degrees of freedom linked with flexural behaviour and the subsequent use of mean and deviatoric matrices in all cases in which some parts of the machine lack axial symmetry.

The theoretical bases on which the code is founded have been summarized by the authors in many papers (from [1] to [8]). The latest code release (4.1) is based on the only assumption of uncoupling between flexural, axial and torsional behaviour of the whole machine; other assumptions as linearity or axial symmetry, which were postulated in earlier versions, are no more required. However, the code cannot account for a lack of symmetry which interests simultaneously parts of the machine spinning at different speeds: this would make it impossible to write the mathematical model in the form of differential equations with constant coefficients and would prevent from obtaining exact solutions even in the case of linear systems.

The code is implemented in MATLAB (trademark of The MathWorks, Inc.); this allows us to deal with complex arithmetic in a straightforward way and improves the portability of the code, including its graphic parts, on any hardware (personal computers or mainframes) for which a version of MATLAB exists.

Aim of the work here described is to develop a "finite element" able to simulate active radial magnetic bearings together with their control systems and to implement the solution routines to plot the Campbell diagram, the eigen loci and the unbalance response of rotating machinery employing such bearings. This allows us to study the effects of the various design parameters of control systems, actuators and sensors on the dynamic behaviour of the system. As no assumption on the relative positions of actuators and sensors is done, it is possible to study also the dynamic effects of the collocation of such elements.

MATHEMATICAL MODEL OF THE ROTOR

Assume that a fixed co-ordinate system xyz is placed with z-axis along the spin axis of the rotor and define a set of complex co-ordinates for flexural behaviour as described in [1]. The equation of motion of a linear rotating system made by a "rotor" whose spin speed is ω and a nonrotating "stator", is

$$
\begin{aligned}
&[M]_m\{\ddot{q}\} + ([C]_m - j\omega\,[G])\{\dot{q}\} + ([K]_m - j\omega\,[C_r]_m)\{q\} + \\
&+[M_n]_d\left\{\ddot{\overline{q}}\right\} + [M_r]_d e^{2j\omega t}\left(\left\{\ddot{\overline{q}}\right\} + 2j\omega\left\{\dot{\overline{q}}\right\}\right) + [C_n]_d\left\{\dot{\overline{q}}\right\} + [C_r]_d e^{2j\omega t}\left\{\dot{\overline{q}}\right\} + \\
&+[K_n]_d\{\overline{q}\} + ([K_r]_d + j\omega\,[C_r]_d)e^{2j\omega t}\{\overline{q}\} = \{F_c\} + \{F_n\} + \omega^2\{F_r\}e^{j\omega t}
\end{aligned}
\tag{1}
$$

where subscripts m and d designate respectively mean and deviatoric matrices; n and r designate nonrotating and rotating parts of the system [2] and $\{\overline{q}\}$ is the complex conjugate of $\{q\}$.

As the main aim of the present work is the study of the stability "in the small" of the system, nonlinearities are not introduced into the model. This is consistent also with the fact that nonlinearities are usually introduced in rotordynamics by rolling element or hydrodynamic bearings which are not present in the case of rotors running on magnetic bearings. However, if deviations from linearity are present, the system is linearized about an equilibrium position.

The forces exerted by the electromagnetic actuators are introduced in equation (1) through vector $\{F_c\}$. Such forces are function of the displacement vector $\{q\}$ owing to the presence of the control system and to the characteristic of the actuator itself. They are present also in the study of the free behaviour.

If the whole system is isotropic with reference to the rotation axis, the free circular whirling can be obtained by introducing into the homogeneous equation of motion, which includes the forces due to the actuators, a solution of the type

$$
\{q\} = \{q_o\}e^{j\lambda t} \quad , \tag{2}
$$

where λ is the complex whirl pulsation: its real part is the actual frequency of the whirl motion while its imaginary part is the decay rate that must be positive to insure stability.

The steady-state response to nonrotating forces, as self-weight, can be obtained by introducing a constant displacement $\{q_o\}$ into equation (1) in which rotating forces $\{F_r\}$ have been neglected. The steady-state response to rotating forces, as unbalance, can be obtained by introducing a constant displacement vector

$$\{q\} = \{q_o\}e^{j\omega t} \quad , \tag{3}$$

into equation (1) in which only rotating forces $\{F_r\}$ are included together with the forces due to the actuators. There is no difficulty to extend the above mentioned solutions to cases in which either the stator or the rotor lack axial symmetry, following the lines shown in [2].

By introducing the mentioned solution vectors $\{q\}$ into the equation of motion, it can be readily transformed into an algebraic equation. Note that equation (1) does not include hysteretic damping. Although it is possible to introduce all the relevant changes to take it into account, this would compel us to solve the eigenproblem linked with free whirling a number of times for each spin speed. In order to avoid this complication, an "equivalent" viscous damping obtained from the modal analysis of the linear, isotropic, natural system will be introduced. Alternatively hysteretic damping can be neglected. This is justified also by the reason that hysteretic damping is usually quite small, particularly if compared with the damping introduced by the control system, and some approximations on its modelling can be accepted.

MATHEMATICAL MODEL OF ACTIVE RADIAL ELECTROMAGNETIC BEARINGS

Nodes and Degrees of Freedom

A magnetic bearing element of the simplest type must at least include four nodes (Figure 1). Nodes k and l are respectively placed at the location of the actuator, the first one on the rotor, the second one on the stator. Similarly, nodes p and q are placed at the location of the sensor. If the stator of the machine is not introduced into the model, only nodes k and p are included: the actuator is in this case more similar to a compliant constraint than to a "spring" element. Note that the co-ordinates of nodes k and l must coincide; the same holds for nodes p and q. Each node can be assumed to have only one complex degree of freedom related to displacements in direction perpendicular to the spin axis. The complex displacement and the corresponding force acting on the node are

$$\vec{z} = x + jy \quad ; \qquad \vec{F} = F_x + jF_y \quad . \tag{4}$$
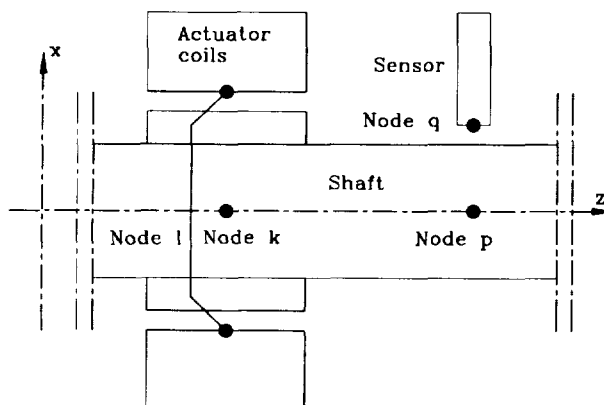

Figure 1. Sketch of the magnetic bearing element with its four nodes.

This type of element does not consider the bending torque which can result when the shaft is not aligned with the bearing. It can be subdivided into several components: force actuator with power amplifier, position transducer and controller [10].

Actuator, transducer and controller

The actuator is physically made by a magnetic circuit equivalent to four electromagnets, placed at angles of 90° from each other. A pair of electromagnets is assumed to be located along x-direction, while the other is in y-direction. Their characteristics are assumed to be all equal and the shaft is assumed to be centred in a reference position.

The force exerted on the shaft by each electromagnet can be expressed by the following function of the current i and air gap t

$$F = K \left(\frac{i}{t} \right)^2 \quad . \tag{5}$$

Constant K can be either computed using simplified formulae or finite element simulation, or measured experimentally. Equation (5), which does not include the saturation of the pole pieces, is strongly nonlinear. To linearize its behaviour it is customary to supply the electromagnets with a constant bias current i_o to which a control current i_c is superimposed [1], [9].

Assuming that the shaft is centred in the reference position with constant clearance c, the force supplied by the pair of electromagnets controlling the position along x-axis is

$$F_x = K \left(\frac{i_o - i_c}{c - x} \right)^2 - K \left(\frac{i_o + i_c}{c + x} \right)^2 \quad . \tag{6}$$

Equation (6) can be linearized for small displacements x and small values of the control current i_c as

$$F_{x_{lin}} = \frac{\partial F_x}{\partial i_c} i_c + \frac{\partial F_x}{\partial x} x = -4K \frac{i_o}{c^2} i_c + 4K \frac{i_o^2}{c^3} x \quad . \tag{7}$$

The equation linking the stator-rotor interaction force at the actuator location (nodes k and l) with the displacements at the same nodes is then

$$\begin{Bmatrix} F_{x_k} + j F_{y_k} \\ F_{x_l} + j F_{y_l} \end{Bmatrix} = -4K \frac{i_o}{c^2} \begin{Bmatrix} 1 \\ -1 \end{Bmatrix} (i_{c_x} + j\, i_{c_y}) + 4K \frac{i_o^2}{c^3} \begin{bmatrix} 1 & -1 \\ -1 & 1 \end{bmatrix} \begin{Bmatrix} x_k + j y_k \\ x_l + j y_l \end{Bmatrix} \quad . \tag{8}$$

The second term at the right hand side describes the behaviour of a spring element with negative stiffness and is linked with the unstable behaviour of the uncontrolled magnetic bearing.

322

The actuator is driven by a power amplifier modulated by the controller output signal. In practice, as commonly found in magnetic bearing applications, a transconductance amplifier with current feedback is used. It provides the control current i_c to the inductive load constituted by the pair of electromagnets.

The resulting transfer function between the controller output signal v_u and the control current i_c is

$$\frac{i_c(s)}{v_u(s)} = G_a(s) = \frac{k_a}{s\tau_a + 1} \quad , \tag{9}$$

where k_a is the stationary gain and $1/\tau_a$ is the power amplifier bandwidth.

The rotor displacements are detected by inductive proximity probes. The transfer function between the displacement from the reference position of the rotor and the sensor output signal v_x, including the conditioning circuitry, is

$$\frac{v_x(s)}{x(s)} = G_s(s) = \frac{k_s}{s\tau_s + 1} \quad , \tag{10}$$

where k_s is the stationary gain and $1/\tau_s$ is the sensor bandwidth.

The transducer dynamics as well as those of the power amplifier should be considered as parasitic phenomena and should be placed as high as possible with respect to the desired closed loop system bandwidth.

The controller is a linear filter and can be given with a fixed Proportional-Integral-Derivative (PID) form or with a user defined transfer function. The transfer function of a realistic PID in parallel form is

$$PID(s) = k_c \left(1 + \frac{1}{sT_i} + \frac{sT_d}{s\tau_d + 1} \right) \quad , \tag{11}$$

where k_c is the stationary gain, T_i is the reset time, T_d is the prediction time and τ_d is the time constant of the causal pole of the derivative term (certainly present due to the parasitic capacitances in the operational amplifiers).

If $T_i \gg T_d > \tau_d$, the previous parallel form can be well approximated by the following series form

$$PID(s) \approx \frac{k_c}{T_i} \frac{sT_i + 1}{s} \frac{sT_d + 1}{s\tau_d + 1} \quad . \tag{12}$$

It is easily noticed that if the extra-pole $1 / \tau_d$ may be arbitrarily adjusted then the PID controller can be conveniently thought of as the series of a PI and a lead network. In this way it is possible to adjust the attenuation of high frequency disturbances.

When the controller is defined by the user with an arbitrary transfer function the latest has to be expressed in the following polynomial form

$$C(s) = \frac{b_m s^m + \ldots\ldots + b_1 s + b_o}{s^n + a_{n-1} s^{n-1} + \ldots\ldots + a_1 s + a_o} \quad , \qquad \text{with } m \leq n \quad . \tag{13}$$

The user defined transfer function can be used either alone or in series with the *PID* controller.

STATE SPACE EQUATIONS IN MODAL FORM

Modal equations of the mechanical subsystem

The equation of motion of the mechanical subsystem is equation (1); all matrices which are included in it are symmetrical: the complex co-ordinate approach leads to symmetrical gyroscopic and rotating damping matrices. It can be transformed in modal form by resorting to the eigenvector matrix $[\Phi]$ of the undamped, natural, axi-symmetrical system: i.e. the matrix of the eigenvectors of matrix $[M]_m^{-1}[K]_m$. This modal transformation is always possible and does not introduce approximations in itself but is unable to uncouple the equations of motion. Actually it leads to diagonal mean mass and stiffness matrices while damping; gyroscopic and all deviatoric matrices are not diagonal and couple the equations of motion.

A further coupling can come from the fact that when using magnetic bearings the rotor is usually unsupported by other means, the only exception being that of hybrid bearing systems. The stiffness matrix of the mechanical subsystem is then singular and the first two whirl frequencies are equal to zero. The corresponding eigenvectors are usually neither orthogonal with respect to the mass nor orthogonal with respect to the stiffness matrix but are linear combinations of vectors which have these properties. The consequence is that, ordering the eigenvalues in ascending order, elements in position 1,2 and 2,1 of the modal stiffness and mass matrices do not vanish. Although there is no difficulty to substitute the first two columns of the matrix of the eigenvectors with their linear combinations having the required orthogonality properties, the fact that the first two (rigid body) modes do not uncouple is not considered important and the eigenvectors are used as directly obtained.

The size of the problem can be reduced in two different ways: by reducing the original, non modal formulation using Guyan reduction or by performing the modal transformation using a reduced set of eigenvectors. Both reduction schemes yield approximated results that can be quite close to those of the original problem if the reduction is performed carefully.

The strategy here considered is to start with Guyan reduction to reduce the size of the eigenproblem needed to perform the modal transformation. Since Guyan reduction is standard in DYNROT code [1], it will not be dealt with here any further.

The use of a reduced set of eigenvectors can give way to the usual spillover problems and must be performed with care. Here the modes are not only coupled by the control system, as usual, but also by the characteristics of the mechanical elements and, in particular, by the gyroscopic matrix and, if the system has no axial symmetry, by the deviatoric matrices. Several tests performed using a different number of eigenvectors did show that very accurate results can be obtained by using a number of modes slightly higher than the number of critical speeds of the free-rotor system encountered within the working range of the machine.

When in doubt, the user can perform the computation retaining a different number of modes and compare the results obtained.

The state equations are here obtained in explicit form only for the case of an isotropic machine; their extension to the more general case is straightforward.

By neglecting the deviatoric matrices and introducing explicitly the forces $\{F_c\}$ exerted by the actuators, equation (1) yields the following modal equation

$$[\overline{M}]\{\ddot{\eta}\} + ([\overline{C}] - j\omega[\overline{G}])\{\dot{\eta}\} + ([\overline{K}] - j\omega[\overline{C}_r])\{\eta\} =$$
$$= \{\overline{F}_c\} + \{\overline{F}_n\} + \omega^2\{\overline{F}_r\}e^{j\omega t} \quad , \tag{14}$$

Vector $\{\eta\}$ is the modal complex co-ordinates vector ($\{\eta\} = [\Phi]\{q\}$); its real part refers to the xz-plane, while its imaginary part to the yz-plane.

The mass and stiffness matrices ($[\overline{M}] = [\Phi]^T[M][\Phi]$ and $[\overline{K}] = [\Phi]^T[K][\Phi]$) are diagonal and coincide with the conventional modal matrices linked with the vibration of the system in the xz-plane.

The damping matrices (global damping $[\overline{C}] = [\Phi]^T[C][\Phi]$ and rotating damping $[\overline{C}_r] = [\Phi]^T[C_r][\Phi]$) are not diagonal except for the case of generalized proportional damping. However, as usually the mechanical subsystem is lightly damped, they can be approximated by simply neglecting their elements outside the main diagonal.

The gyroscopic matrix ($[\overline{G}] = [\Phi]^T[G][\Phi]$) is not diagonal and, except for the case of very slender rotors which exhibit a very small gyroscopic effect, cannot be approximated by simply neglecting the elements outside the main diagonal.

Vectors $\{\overline{F}_n\}$ and $\{\overline{F}_r\}$ are respectively the complex modal force vectors linked with stationary and unbalance forces. Their real parts refer to the xz-plane (stationary reference system or rotor-fixed reference respectively), while their imaginary parts refer to the yz-plane.

Vector $\{\overline{F}_c\}$ is the complex modal control force vector ($\{\overline{F}_c\} = [\Phi]^T[S_c]\{F_c\}$). Vector $\{F_c\}$ contains the control forces in complex modal form: the real part refers to the xz-plane, the imaginary part refers to the yz-plane; the number of its elements is equal to the number of actuators. Matrix $[S_c]$ has a number of lines equal to the number of degrees of freedom of the system and a number of columns equal to the number of nodes related to the actuators. All its elements are zero except for the elements in the column related to each bearing and the line related to the degree of freedom of the rotor at the actuator location (displacement at the k-th or l-th node, see Figure 1) whose value is 1.

Expressing the force vector $\{F_c\}$ as a function of the control currents and displacements through equation (8), the modal control force vector $\{\overline{F}_c\}$ can be written as

$$\{\overline{F}_c\} = -[\Phi]^T[S_c][K_i]\{i_c\} - [\Phi]^T[S_c][K_u][\Phi]\{\eta\} = -[\overline{K}_i]\{i_c\} - [\overline{K}_u]\{\eta\} \quad , \tag{15}$$

where $[K_i]$ is a matrix with a number of rows equal to the number of nodes related to the actuators and a number of columns equal to the number of the latter; it is simply obtained from the first term at right hand

side of equation (8). In a similar way, $[K_u]$ is a square matrix with the same number of rows as $[K_i]$ obtained from the second term at the right hand side of equation (8); it is nonpositive defined and expresses the open loop negative stiffness of the actuators.

Equation (14) can thus be expressed in the form

$$\{\ddot{\eta}\} + [\overline{M}]^{-1}([\overline{C}] - j\omega[\overline{G}])\{\dot{\eta}\} + [\overline{M}]^{-1}([\overline{K}] + [\overline{K}_u] - j\omega[\overline{C}_r])\{\eta\} =$$
$$= -[\overline{M}]^{-1}[\overline{K}_i]\{i_c\} + [\overline{M}]^{-1}\{\overline{F}_n\} + \omega^2[\overline{M}]^{-1}\{\overline{F}_r\}e^{j\omega t} \quad . \tag{16}$$

The complex output vector $\{y_s\}$ containing the displacements at the sensor locations can be expressed as a function of the modal co-ordinates as

$$\{y_s\} = [S_s][\Phi]\{\eta\} \quad , \tag{17}$$

where matrix $[S_s]$ has a number of lines equal to the number of sensors and a number of columns equal to the number of degrees of freedom of the system. All its elements are zero except for the elements in the row related to each sensor and the column related to the degree of freedom of the rotor at the sensor location (displacement at the p-th node, see Figure 1) whose value is 1 and to that in the same row and the column related to the degree of freedom of the stator at the sensor location, if any (displacement at the q-th node), whose value is -1.

Open loop state space equation

By introducing a state vector including the modal velocities and displacements, the open loop state equation of the mechanical sub-system is

$$\begin{cases} \{\dot{z}\} = [\mathcal{A}]\{z\} + [B_c]\{i_c\} + [B_n]\{\overline{F}_n\} + \omega^2[B_r]\{\overline{F}_r\}e^{j\omega t} \\ \{y_s\} = [C]\{z\} + [\mathcal{D}]\{i_c\} \quad , \end{cases} \tag{18}$$

where

$$\{z\} = \begin{Bmatrix} \{\dot{\eta}\} \\ \{\ddot{\eta}\} \end{Bmatrix} \quad , \qquad [\mathcal{A}] = \begin{bmatrix} -[\overline{M}]^{-1}([\overline{C}] - j\omega[\overline{G}]) & -[\overline{M}]^{-1}([\overline{K}] + [\overline{K}_u] - j\omega[\overline{C}_r]) \\ [I] & [0] \end{bmatrix} \quad , \tag{19}$$

$$[B_c] = \begin{bmatrix} -[\overline{M}]^{-1}[\overline{K}_i] \\ [0] \end{bmatrix} \quad , \qquad [B_n] = [B_r] = \begin{bmatrix} [\overline{M}]^{-1} \\ [0] \end{bmatrix} \quad , \qquad [C] = \begin{bmatrix} [0] & [S_s][\Phi] \end{bmatrix} \quad , \qquad [\mathcal{D}] = [0] \quad .$$

The manipulable command signal $\{i_c\}$ and the non manipulable signals $\{\overline{F}_n\}, \omega^2\{\overline{F}_r\}e^{j\omega t}$ can be organized in a unique term. In this way equation (18) can be rewritten in the following more compact form

326

$$\begin{cases} \{\dot{z}\} = [\mathcal{A}]\{z\} + [\mathcal{B}]\{u\} \\ \{y_s\} = [C]\{z\} + [\mathcal{D}]\{i_c\} \quad , \end{cases} \tag{20}$$

where

$$\{u\} = \begin{Bmatrix} \{i_c\} \\ \{\overline{F}_n\} \\ \omega^2\{\overline{F}_r\}e^{j\omega t} \end{Bmatrix} \quad , \qquad [\mathcal{B}] = \begin{bmatrix} [B_c] & [B_n] & [B_r] \end{bmatrix} \quad . \tag{21}$$

Note that the dynamic matrix of the system and all vectors are complex. An equivalent formulation employing real co-ordinates is possible, but it would involve matrices of double size.

Closed loop state space equation

While the (linearized) force actuator is already taken into account in the open loop state equation of the isotropic machine, the controller, the power amplifier and the position transducer are usually described as single-input single-output transfer functions in the frequency domain. Thus the Laplace domain descriptions given in the previous section must be converted to a time domain form to be compatible with the rotor model equation (1) and open loop state equations (20). The desired form is the state space formulation obtained by a minimal realization (of equations from (9) to (13)) in the controllable canonical form.

Since the open loop state variable is in complex form also, the single-input single-output realization for the controller, the power amplifier and the position transducer should be thought of accordingly. It is to be noted that the controller may be directly designed as a multiple-input multiple-output system (i.e. by pole placement techniques) and represented in complex matrix form.

Given the state equation (20) of the plant and given the state space realization of controller, actuator and transducer with the following quadruples

$$\begin{bmatrix} [\mathcal{A}] & [\mathcal{B}] \\ [C] & [\mathcal{D}] \end{bmatrix} \quad , \quad \begin{bmatrix} [\mathcal{A}_c] & [\mathcal{B}_c] \\ [C_c] & [\mathcal{D}_c] \end{bmatrix} \quad , \quad \begin{bmatrix} [\mathcal{A}_a] & [\mathcal{B}_a] \\ [C_a] & [\mathcal{D}_a] \end{bmatrix} \quad , \quad \begin{bmatrix} [\mathcal{A}_t] & [\mathcal{B}_t] \\ [C_t] & [\mathcal{D}_t] \end{bmatrix} \quad , \tag{22}$$

the closed loop equations are obtained through standard series and then feedback connections as shown in Figure 2.
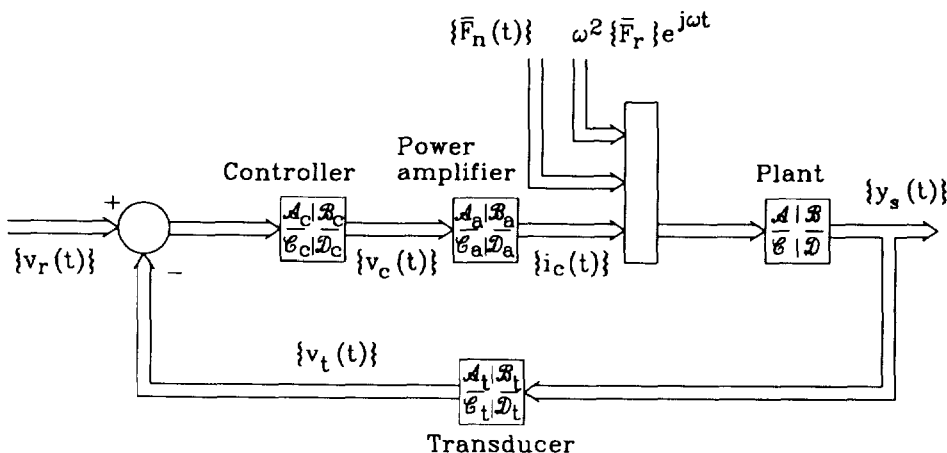
Figure 2. Closed loop blocks and signals diagram.

Here $\{v_r(t)\}$ is the position reference signal, $\{v_c(t)\}$ the command signal to the power amplifier, $\{i_c(t)\}$ the control current (then force), $\{\overline{F}_n\}$, $\omega^2\{\overline{F}_r\}e^{j\omega t}$ the rotor stationary and unbalance modal forces, $\{y_s(t)\}$ the displacements at sensor location and $\{v_t(t)\}$ the sensors output.

In the regulation problem the reference signal may be put to zero and the closed loop system output $\{y_s(t)\}$ expressed in function of the rotor stationary force $\{\overline{F}_n\}$ and rotor unbalance modal force $\omega^2\{\overline{F}_r\}e^{i\omega t}$

$$\begin{cases} \{\dot{\zeta}\} = [\mathcal{A}_{CL}]\{\zeta\} + [\mathcal{B}_{CL}]\begin{Bmatrix} \{\overline{F}_n\} \\ \omega^2\{\overline{F}_r\}e^{j\omega t} \end{Bmatrix} \\ \{y_s\} = [C_{CL}]\{\zeta\} + [\mathcal{D}_{CL}]\begin{Bmatrix} \{\overline{F}_n\} \\ \omega^2\{\overline{F}_r\}e^{j\omega t} \end{Bmatrix} \end{cases} , \tag{23}$$

where $\{\zeta\}$ is an extended state vector containing all modal states $\{z\}$ of the system plus the realized state of the control loop.

Campbell diagram and eigen loci

The Campbell diagram and the velocity eigen locus are two ways of representing in graphic form the variation of the whirl frequencies and decay rates when the spin speed changes. They are essentially equivalent but, as the first is more common with rotordynamics specialists while the second with control scientists, the DYNROT code is designed to supply both.

Usually when computing the Campbell diagram the solution of the equation of motion is assumed to be of the type (2) and consequently the whirl frequency is the real part of λ while the decay rate is its imaginary part. The real and imaginary parts are plotted separately as functions of the spin speed ω.

When plotting the velocity eigen locus a solution of the type

$$\{q\} = \{q_o\}e^{st} \tag{24}$$

is assumed: the whirl frequency is thus the imaginary part of s while the decay rate is its real part changed of sign. The imaginary part is then plotted as a function of the real part in the complex plane (ω does not appear explicitly).

As the system is assumed to be linear, the Campbell diagram depends neither on unbalance nor on static external forces. By introducing the solution (24) into the closed loop state equation in modal form (23), in which the external forcing functions have been neglected, it is readily transformed into the algebraic equation

$$\left([\mathcal{A}_{CL}] - s[I]\right)\{\zeta_o\} = \{0\} . \tag{25}$$

328

Matrix $[\mathcal{A}_{CL}]$ is in this case complex and, as a consequence, the eigenvalues are not conjugate. This feature, which is uncommon in the solution of the eigenproblem related to state equations, is directly linked with the use of complex co-ordinates and with their physical meaning: the real and imaginary parts are the generalized displacements (or modal displacements) in xz- and yz- planes and the sign of the imaginary part of s has a physical meaning, indicating whether the circular whirling occurs either in forward or in backward direction. As a consequence of the gyroscopic effect the whirl speeds for forward and backward whirling are different and the solutions for s cannot be conjugate. A different situation occurs in the case of unsymmetrical systems: elliptical whirling is here obtained as the combination of a forward and a backward circular whirling at the same frequency, and then solutions with an equal imaginary part but with an opposite sign must be present.

Apart from plotting the Campbell diagram and the decay rate plot as a function of the speed and the velocity eigen locus at varying speeds, a routine which computes the closed loop eigen locus at fixed speed with varying the overall gain of the feedback loop has been developed.

Steady-state response

The response to unbalance and to constant nonrotating forces can be computed as

$$\left(j\omega[I] - [\mathcal{A}_{CL}] \right)\{\zeta_o\} = \omega^2[B_r]\{\overline{F}_r\} \quad , \qquad -[\mathcal{A}_{CL}]\{\zeta_o\} = [B_n]\{\overline{F}_n\} \quad . \tag{26}$$

For each value of the speed spin ω, equation (26) can be readily solved in $\{\zeta_o\}$. After applying the inverse modal transformation the same solutions yield the response of the system. Note that in general and also in the case of response to static forces the dynamic matrix of the system depends on the spin speed.

NUMERICAL EXAMPLE

The five-active axes magnetic suspension described in [11] was used as a test case for the present mathematical model and then for the code used to implement it.

The rotor has been modelled with 22 beam elements and 3 concentrated mass elements. Two magnetic bearing elements have been added and the stator was considered as a rigid body. Consequently the nodes of the type l and q of Figure 1 were directly grounded. The model has a total number of 46 degrees of freedom, reduced to 23 by using the Guyan algorithm considering as master degrees of freedom all complex translations. The damping of the material constituting the shaft has been neglected in the model.

A first analysis of the open loop system was performed. The first 4 modes corresponding to the critical speeds are reported in Figure 3b together with a sketch of the model of the shaft (Figure 3a). The first two modes are rigid-body modes and the other two correspond to critical speeds at 25780 and 54890 rpm.

The computation was repeated using a *PID* controller on each axis; the results for the first 6 modes are reported in Figure 3c. Here the first two modes are rigid-body modes at 2990 and 3880 rpm. They are well damped, the decay rates being 17.4 and 28.9 1/s, respectively. Two additional modes linked with the control system can then be found at 7290 and 7350 rpm; they are however very much damped, with a decay rate of 20930 1/s and cannot be expected to be seen experimentally. The first two deformation modes of the rotor occur at 25860 and 54810 rpm, essentially unaffected by the presence of the controller.
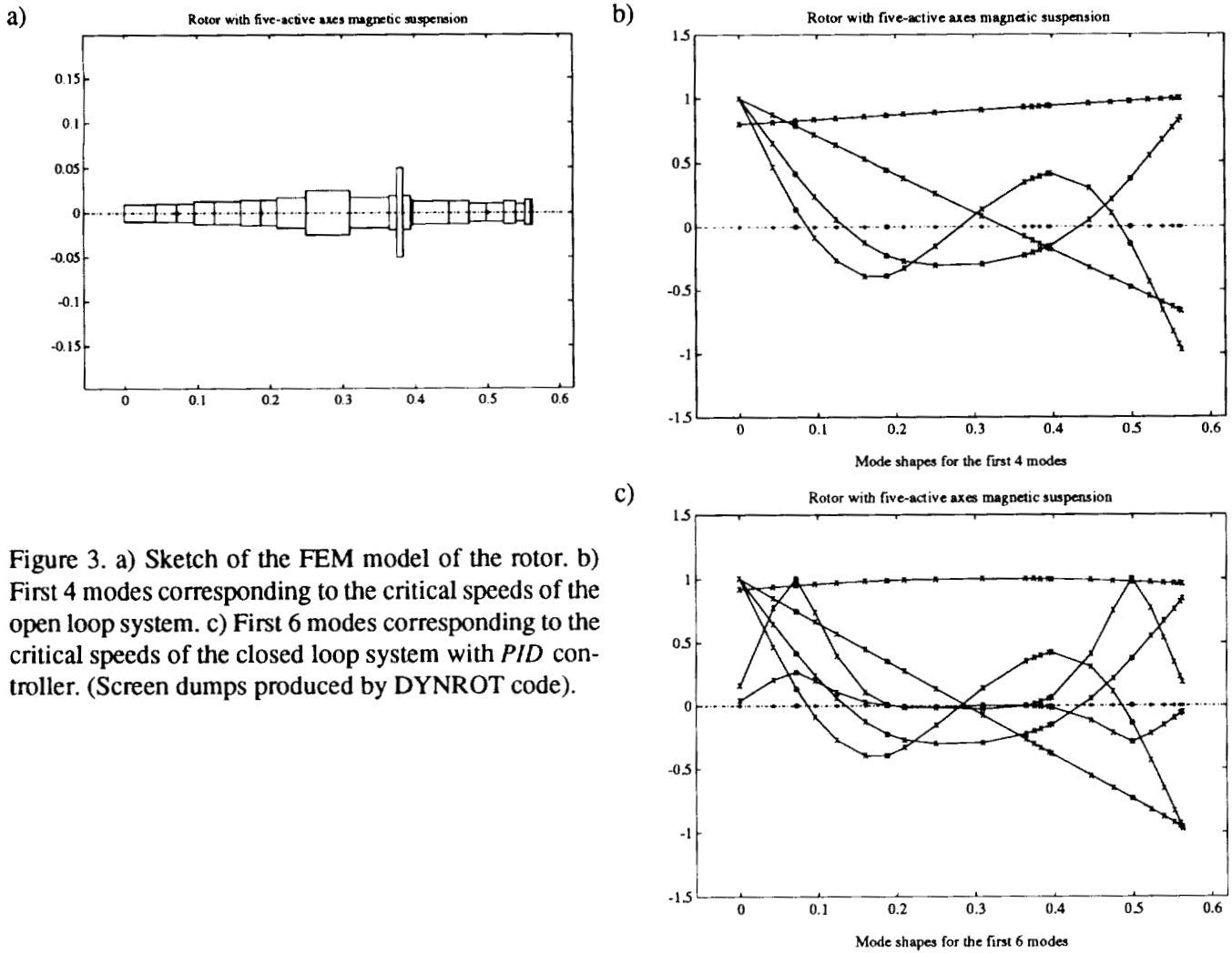
329

Figure 3. a) Sketch of the FEM model of the rotor. b) First 4 modes corresponding to the critical speeds of the open loop system. c) First 6 modes corresponding to the critical speeds of the closed loop system with *PID* controller. (Screen dumps produced by DYNROT code).
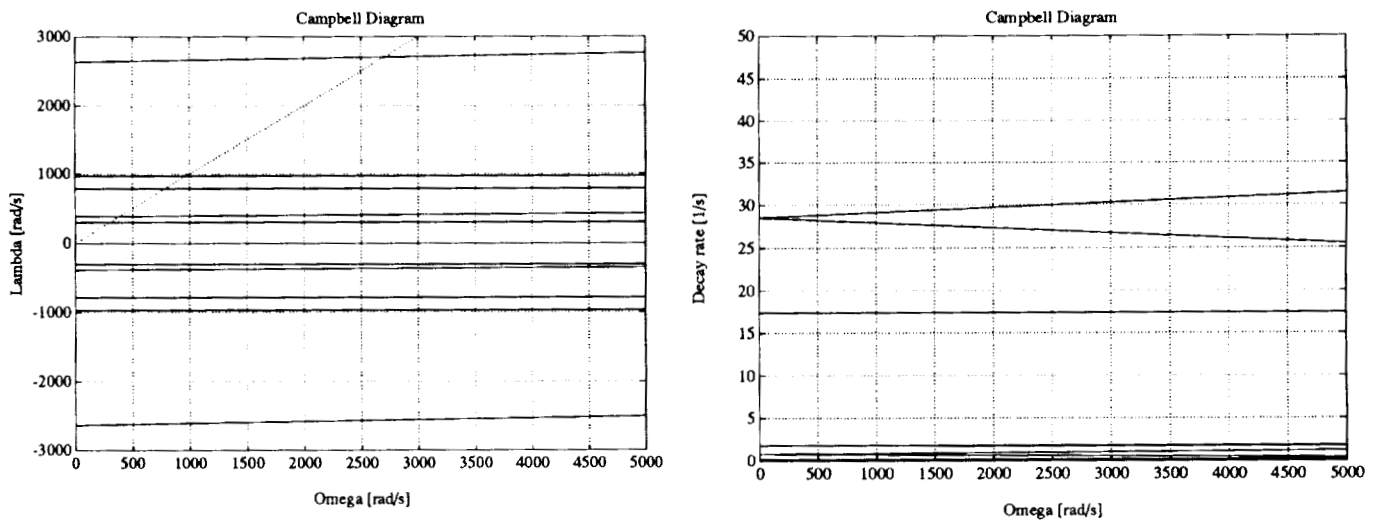

Figure 4. Campbell diagram: whirl speed and decay rate as functions of the spin speed. (Screen dumps produced by DYNROT code).
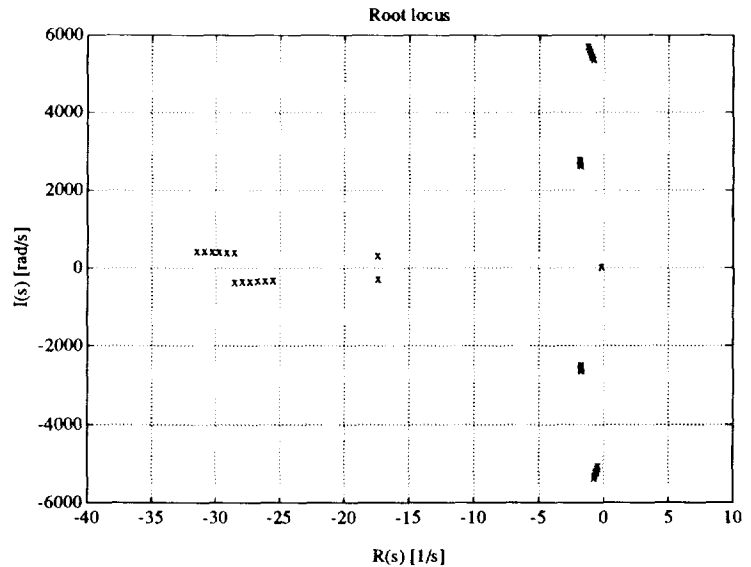
330

Figure 5. Velocity eigen loci at varying spin speed in the range 0 - 5000 rad/s. (Screen dump produced by DYNROT code).

The decay rate corresponding to the last two modes is still positive but quite small (1.86 and 1.34 1/s). Other critical speeds, well outside the working range, have negative decay rates showing that at those speeds the system would be unstable.

The Campbell diagram is shown in Figure 4. It has been obtained by considering only 5 modes as adding further modes would not change the results in the field of speeds and frequencies of interest. Note that the whirl frequencies are not much influenced by the spin speed, as was easily predictable from the geometrical configuration of the rotor. Actually in the case of rotors with small gyroscopic effects as the present one the whirl frequencies can be assumed to be independent from ω and the information gained from the Campbell diagram is not as important. A greater dependence from the spin speed is shown by the decay rate. The controller modes mentioned above are reported in the plot of the whirl frequencies but not in that of the decay rate, as they are out of scale.

The velocity eigen loci at varying spin speeds are shown in Figure 5. The plot has been obtained for speeds ranging from 0 to 5000 rad/s, with increments of 1000 rad/s: a finer pitch is considered useless as the results are not much affected by the spin speed. Note that in the present case the velocity eigen loci are not symmetrical with respect to the real axis: in the present case, negative values of the imaginary part of s designate backward whirling and positive values of s indicate forward whirling. They are always different even if in the present case, owing to the low gyroscopic effect, this difference is not great.

The unbalance response has then been computed. An eccentricity of 1 μm of rotor of the electric motor has been assumed, which corresponds to a quality balancing grade G 3.6 at 35000 rpm, following the ISO 1925 standard.

The amplitude of the orbit at the location of the motor (node 5) and of the sensor of the radial bearing at the right in Figure 3a (node 16) are shown in Figure 6. The amplitude at the rigid-body critical speeds is far smaller than that at the first deformation mode; the two controller modes are completely damped out. At the motor location the two rigid-body critical speeds are well separated and an ample zone in which the amplitude is very small is visible between the rigid-body and the deformation critical speeds. Self-centring occurs in most of the working range above the rigid-body modes, except near the third critical speed. The response at the sensor location shows slightly different patterns: the rigid body critical speeds are not well separated, tending to merge into a single peak.

331
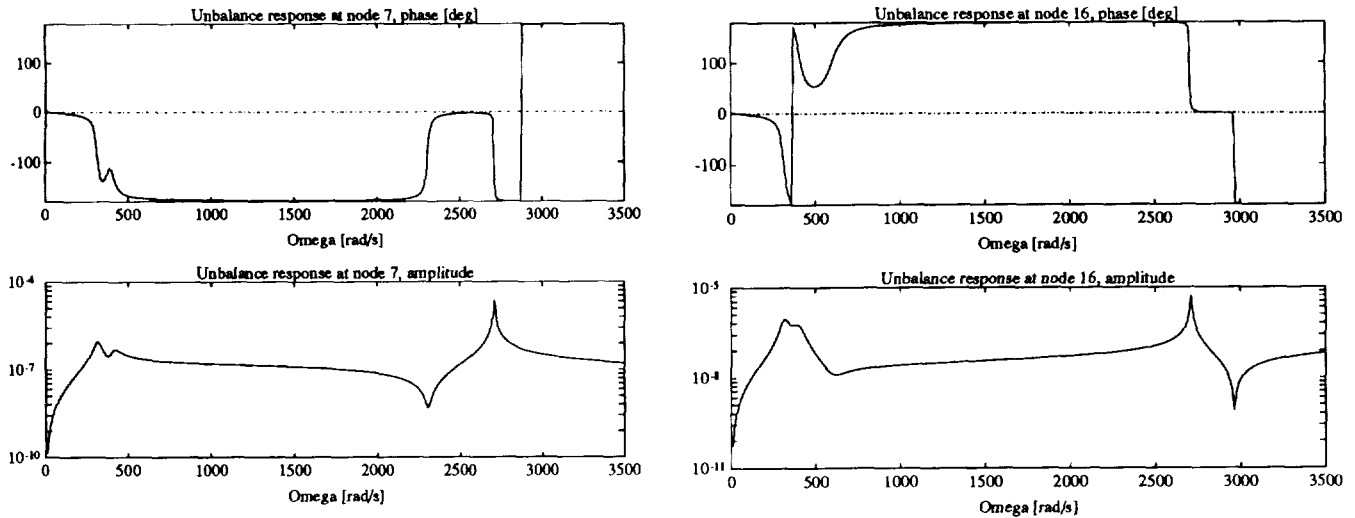
Figure 6. Unbalance response. Amplitude of the orbits (in m) at the centre of the motor (node 7) and at the sensor of the bearing at the right (node 16) caused by an eccentricity of 1 μm of the rotor of the motor (balancing quality grade G 3.6 at 35000 rpm). (Screen dumps produced by DYNROT code).

The natural frequencies of the system at standstill obtained from the Campbell diagram of Figure 4 are compared in Table I with the experimental values obtained by exciting the system with an instrumented hammer at the centre of the shaft and measuring the acceleration in the same point. The values obtained from the Campbell diagram in correspondence with the frequencies due to the controller have not been reported.

The accordance is very good, particularly considering that the comparison has not been made between exactly correspondent quantities. The experimental values correspond to the peaks of the impulse response while the numerical ones are the damped eigenvalues of the system. While in the case of lightly damped modes no noticeable difference exists between them; in the case of modes with higher damping, the comparison can be at best indicative. The first two natural frequencies merge into a single value; a similar effect can be seen in the numerical results of Figure 6.

Table I. Experimental Values of the Lowest Natural Frequencies (Hz) Compared with the Values Obtained from the Campbell Diagram of Figure 4 at Standstill

Experimental	57		420	884
Numerical	47.9	60.8	419	855

CONCLUSIONS

A mathematical model for the dynamic simulation of rotating machines with active electromagnetic bearings based on the FEM and the use of complex co-ordinates has been described in detail. The main aim of the model and of the code based on it is the computation of the Campbell diagram to study the stability in the small and of the steady-state responses to unbalance and static forces.

At present the model is limited to machines possessing axial symmetry; however, this limitation is not intrinsic to the model used and can be easily avoided by simple changes to the solution algorithms. Another limitation which can be easily eliminated is the assumption that the controller operates on the two axes of each bearing and on the various bearings as a number of separated SISO units. There is no difficulty in introducing a complex transfer function to allow coupling between the control in xz- and yz- planes or to couple together the various controllers.

An assumption which on the contrary is actually needed is that of linearity. It can be dropped by introducing nonlinear elements but this would make it impossible to obtain Campbell diagrams or eigen loci and the only possible computation would then be that of the unbalance response. However, the small values of the amplitudes which can be obtained using magnetic bearings guarantee that the system remains in most cases within limits in which the linearity of the model does not introduce unacceptable approximations.

The possibility of introducing an accurate modelization of complex rotors allows us to obtain accurate results for practical cases and in particular allows us to study the effects of the relative position of the sensors and the actuators (collocation problem).

An example has shown the types of results which can be obtained from the routines developed from the equations here described and incorporated in the DYNROT finite element code. The comparison with some experimental results shows that a very good accuracy can be obtained.

REFERENCES

1. Genta, G.: *Vibration of structures and machines*. Springer, New York, 1993.
2. Genta, G.: Whirling of unsymmetrical rotors: a Finite Element Approach Based on Complex Co-ordinates. *J. Sound and Vibration*, vol.124, no. 1, 1988, pp. 27-53.
3. Genta, G.; and Gugliotta, A.: A Conical Element for Finite Element Rotor Dynamics. *J. Sound and Vibration*, vol. 120, no. 2, 1988, pp. 175-182.
4. Genta, G.; and Vatta, F.: A Lubricated Bearing Element for FEM Rotor Dynamics. IX IMAC, Firenze, April 1991.
5. Genta, G.; and De Bona, F.: Unbalance Response of Rotors: a Modal Approach with some Extensions to Damped Natural Systems. *J. Sound and Vibration*, vol. 140, no. 1, 1990, pp. 129-153.
6. Genta, G.; Repaci, A.; and Briacca, I.: Iterative Techniques for Computation of the Unbalance Response of Multi-degrees of Freedom Nonlinear Rotors. III International Conf. Rotordynamics, Lyon, September 1990.
7. Genta, G.; Delprete, C.; Tonoli, A.; and Vadori, R.: Conditions for Noncircular Whirling of Nonlinear Isotropic Rotors. *J. Nonlinear Dynamics*, vol. 4, 1993, pp. 153-181.
8. Genta, G.: A Fast FEM Technique for the Computation of the Campbell Diagram of Multi-Degrees of Freedom Rotors. *J. Sound and Vibration*, vol. 155, no. 3, 1992, pp. 385-402.
9. Schweitzer, G.; and Lange, R.: Characteristics of a Magnetic Rotor Bearing for Active Vibration Control. 1st. International Conf. on Vibrations in Rotating Machinery, Cambridge, September 1976, IMechE C239/76, pp. 1-6.
10. Maslen, E.H.; and Bielk, J.R.: A Stability Model for Flexible Rotors With Magnetic Bearings. Trans. ASME Journal of Dynamics Systems, Measurement, and Control, vol. 114, 1992, pp. 172-175.
11. Delprete, C.; Genta, G.; and Carabelli, S.: Design, Construction and Testing of a five-active axes magnetic bearing system. 2nd. International Symp. On Magnetic Suspension Technology, NASA CP-3247, Seattle, Washington, August 1993.

$P_{}$ 18

Modelling and Control of a Rotor Supported by Magnetic Bearings

R. Gurumoorthy*   A. K. Pradeep[†]

July 20, 1993

Abstract: *In this paper we develop a dynamical model of a rotor and the active magnetic bearings used to support the rotor. We use this model to develop a stable state feedback control of the magnetic bearing system.*

We present the development of a rigid body model of the rotor, utilizing both Rotation Matrices (Euler Angles) *and* Euler Parameters (Quaternions). *In the latter half of the paper we develop a stable state feedback control of the actively controlled magnetic bearing to control the rotor position under imbalances. The control law developed takes into account the variation of the model with rotational speed. We show stability over the whole operating range of speeds for the magnetic bearing system. Simulation results are presented to demonstrate the closed loop system performance. We develop the model of the magnetic bearing, and present two schemes for the excitation of the poles of the actively controlled magnetic bearing. We also present a scheme for averaging multiple sensor measurements and splitting the actuation forces amongst redundant actuators.*

1 Introduction

Several representations of rigid body rotations, including *Rotation Matrices, Cayley -Kline parameters, Euler Parameters & Spinors* ([K.W86] [PP80] [OB79]) have been developed. Conventional methods of deriving rigid body dynamics utilize the Euler angle parametrization of the space of orientations of the rigid body. Such a parametrization of $SO(3)$ suffers from coordinate singularities. The singularities are entirely a result of the choice of parametrization. A parametrization that is globally nonsingular is the parametrization utilizing Euler parameters (unit quaternions). In this paper we develop the dynamical equations describing the rigid body model of a rotor supported by actively controlled magnetic bearings, using rotation matrices (parametrized by euler angles) and using euler parameters.

We begin this paper by giving a brief description of the various mathematical terms and ideas that will be used in defining *rotation matrices* and *euler parameters* [YCBDB82]. We present some of the properties of *rotation matrices* and *quaternions*. We derive the dynamical equations of the rotor supported by active magnetic bearings using both *rotation matrices* and *quaternions*. We present the development of a stable state feedback control law and simulation results of the system when controlled by this state feedback control law. Most magnetic bearing systems are comprised of redundant sensors and actuators. We present a linear algebraic technique utilizing the method of least squares to average multiple measurements and split the actuation forces amongst redundant actuators.

2 Preliminaries

The magnetic bearing system utilizes many frames of reference, in which various quantities such as positions, velocities and angles are described. In this section we will set out the notation by which we will refer to the various quantities. Also we will present some of the definitions and facts necessary for the derivation of the dynamical equations.

*Electronic Technologies Laboratory, Corporate Research and Development, General Electric Company. Schenectady NY 12301

[†]Control Systems Laboratory, Corporate Research and Development, General Electric Company. Schenectady NY 12301

2.1 Notation

In this section we will set out the notation by which we will refer to the various quantities.

- Vectors will be referred to by lower case letters, with an arrow on top. Position vectors will be represented in either Cartesian or spherical coordinate systems. Representation of vectors in Cartesian coordinate systems will be the $\vec{X}, \vec{Y}, \vec{Z}$ components of the vector. Vectors would also be represented as column matrices. The components of the column matrix would not contain an arrow.

Example 2.1 *The vector $\vec{a}$ would be represented in either of the two ways.*

$$\vec{a} = a_x\vec{X} + a_y\vec{Y} + a_z\vec{Z}$$

$$\vec{a} = \begin{bmatrix} a_x \\ a_y \\ a_z \end{bmatrix}$$

The components of a vector would be written without the arrow on top.

- Matrices and tensors will be referred to by upper case letters. Dimensions and components of the matrix will always accompany the notation. Example: $A \in \Re^{3 \times 3}$

- Variables and constants will be denoted by lower case letters, and will be accompanied by a statement concerning their dimension. Example: $\theta \in S$.

- When referring to variables, which are described in a frame of reference, the subscript of the variable will refer to the frame of reference. Example: $\vec{\omega}^{rotor}_{inertial}$

- We will use three frames of reference primarily.

  1. The first frame of reference is the fixed inertial frame of reference. This frame will be referred to as the **inertial frame**, and the subscript *inertial* will accompany variables described in this frame of reference. The orthonormal coordinate vectors of this reference frame will be denoted as $\vec{X}_{inertial}, \vec{Y}_{inertial}, \vec{Z}_{inertial}$.

  2. The second frame of reference is rigidly attached to the center of mass of the rotor, and moves with the rotor. This frame will be referred to as the **rotor based reference frame**, and the subscript *rotor* will accompany variables described in this frame of reference. The orthonormal coordinate vectors of this reference frame will be denoted as $\vec{X}_{rotor}, \vec{Y}_{rotor}, \vec{Z}_{rotor}$. The orientation of the rotor frame is along the principal axes of inertia of the rotor. The origin of the rotor frame is at the center of mass of the rotor.

  3. The third frame of reference is attached to the center of the magnetic bearing. We will say more about this frame later. The origin of this frame is coincident with the center of the bearing. This frame will be referred to as the **bearing based reference frame**, and the subscript *bearing* will accompany variables described in this reference frame. The orthonormal coordinate vectors of this reference frame will be denoted as $\vec{X}_{bearing}, \vec{Y}_{bearing}, \vec{Z}_{bearing}$.

- Rotation matrices relate the orientation of vectors in one frame relative to another. The convention we employ through this report would be as follows.

$$\begin{bmatrix} \vec{X} \\ \vec{Y} \\ \vec{Z} \end{bmatrix}_{frame-1} = R^{frame-2}_{frame-1} \begin{bmatrix} \vec{X} \\ \vec{Y} \\ \vec{Z} \end{bmatrix}_{frame-2} \tag{1}$$

where $R^{frame-2}_{frame-1}$ is a rotation matrix that expresses the basis vectors of $frame - 2$ in terms of the basis vectors of $frame - 1$. The rotation matrix can be expressed as a combination of basis vectors of both the frames in the following manner. Given that the basis vectors of frames 1 and 2 are represented with the appropriate subscript,

$$R^{frame-2}_{frame-1} = \begin{bmatrix} \vec{X}_{frame-2} \cdot \vec{X}_{frame-1} & \vec{Y}_{frame-2} \cdot \vec{X}_{frame-1} & \vec{Z}_{frame-2} \cdot \vec{X}_{frame-1} \\ \vec{X}_{frame-2} \cdot \vec{Y}_{frame-1} & \vec{Y}_{frame-2} \cdot \vec{Y}_{frame-1} & \vec{Z}_{frame-2} \cdot \vec{Y}_{frame-1} \\ \vec{X}_{frame-2} \cdot \vec{Z}_{frame-1} & \vec{Y}_{frame-2} \cdot \vec{Z}_{frame-1} & \vec{Z}_{frame-2} \cdot \vec{Z}_{frame-1} \end{bmatrix} \tag{2}$$

- Position vectors of objects will be referred to in the following manner.

$$\vec{r}^{object}_{frame} = \begin{bmatrix} r^{object}_{x-frame} \\ r^{object}_{y-frame} \\ r^{object}_{z-frame} \end{bmatrix} \tag{3}$$

336

- The cross product form of a vector is referred to as $S(\cdot)$. That is

$$\vec{a} \times \vec{b} = S(a)b$$

$$S(a) = \begin{bmatrix} 0 & -a_z & a_y \\ a_z & 0 & -a_x \\ a_y & a_x & 0 \end{bmatrix}$$

$$\vec{a} = \begin{bmatrix} a_x \\ a_y \\ a_z \end{bmatrix}$$

$$\vec{b} = \begin{bmatrix} b_x \\ b_y \\ b_z \end{bmatrix}$$

- A unit vector in the direction of an object will be represented as

$$\vec{u}_{frame}^{object} = \begin{bmatrix} u_{x-frame}^{object} \\ u_{y-frame}^{object} \\ u_{z-frame}^{object} \end{bmatrix} \tag{4}$$

$$= \frac{\vec{r}_{frame}^{object}}{\|\vec{r}_{frame}^{object}\|_2} \tag{5}$$

$$\|\vec{r}_{frame}^{object}\|_2 = \sqrt{[r_{x-frame}^{object}]^2 + [r_{y-frame}^{object}]^2 + [r_{z-frame}^{object}]^2} \tag{6}$$

- By norm, we refer to the Euclidean norm of the vector throughout this report.
- If the object being referred to is the origin of a coordinate frame, it will be referred to as $\vec{r}_{frame-1}^{frame-2-origin}$.

To set the ideas clear, consider the following examples.

Example 2.2 *The origin of the rotor coordinate frame, as observed in an inertial reference frame would be represented as*

$$\vec{r}_{inertial}^{rotor-origin} = \begin{bmatrix} r_{x-inertial}^{rotor-origin} \\ r_{y-inertial}^{rotor-origin} \\ r_{z-inertial}^{rotor-origin} \end{bmatrix} \tag{7}$$

We tag the word origin when we explicitly refer to the origin of a coordinate frame.

- ## Homogenous Transforms

Mappings between points in the Euclidean group $SE(3)$ to points in $SE(3)$ are represented as 4×4 matrix transformations that map a position and orientation of a frame to another position and orientation. Such mappings are termed *homogenous transforms*, and in coordinates are specified as follows.

$$T_{frame-1}^{frame-2} : SE(3) \to SE(3)$$

$$\begin{bmatrix} \vec{X}_{frame-1} \\ \vec{Y}_{frame-1} \\ \vec{Z}_{frame-1} \\ 1 \end{bmatrix} = T_{frame-1}^{frame-2} \begin{bmatrix} \vec{X}_{frame-2} \\ \vec{Y}_{frame-2} \\ \vec{Z}_{frame-2} \\ 1 \end{bmatrix}$$

$$T_{frame-1}^{frame-2} = \begin{bmatrix} R_{frame-1}^{frame-2} & \begin{bmatrix} r_{x-frame-1}^{frame-2-origin} \\ r_{y-frame-1}^{frame-2-origin} \\ r_{z-frame-1}^{frame-2-origin} \end{bmatrix} \\ [\; 0 \quad 0 \quad 0 \;] & 1 \end{bmatrix}$$

The inverse of a homogenous transform $T_{frame-1}^{frame-2}$ is represented and given as follows.

$$[T_{frame-1}^{frame-2}]^{-1} = T_{frame-2}^{frame-1}$$

$$= \begin{bmatrix} [R_{frame-1}^{frame-2}]^T & -[R_{frame-1}^{frame-2}]^T \begin{bmatrix} r_{x-frame-1}^{frame-2-origin} \\ r_{y-frame-1}^{frame-2-origin} \\ r_{z-frame-1}^{frame-2-origin} \end{bmatrix} \\ [\; 0 \quad 0 \quad 0 \;] & 1 \end{bmatrix}$$

Example 2.3 *The homogenous tranformation tranforming coordinates of the origin of the bearing coordinate frame as observed in the inertial coordinate frame to the same coordinates as observed from the rotor reference frame would be represented as follows.*

$$\begin{bmatrix} r_{x-rotor}^{bearing-origin} \\ r_{y-rotor}^{bearing-origin} \\ r_{z-rotor}^{bearing-origin} \\ 1 \end{bmatrix} = T_{rotor}^{inertial} \begin{bmatrix} r_{x-inertial}^{bearing-origin} \\ r_{y-inertial}^{bearing-origin} \\ r_{z-inertial}^{bearing-origin} \\ 1 \end{bmatrix} \tag{8}$$

$$= \begin{bmatrix} R_{rotor}^{inertial} & \begin{bmatrix} r_{x-rotor}^{inertial-origin} \\ r_{y-rotor}^{inertial-origin} \\ r_{z-rotor}^{inertial-origin} \end{bmatrix} \\ \begin{bmatrix} 0 & 0 & 0 \end{bmatrix} & 1 \end{bmatrix} \begin{bmatrix} r_{x-inertial}^{bearing-origin} \\ r_{y-inertial}^{bearing-origin} \\ r_{z-inertial}^{bearing-origin} \\ 1 \end{bmatrix} \tag{9}$$

2.2 Definitions

We will use the properties of linear vector spaces, quaternions and quaternion algebra. In this section we begin by defining vector spaces and algebras. We then proceed to state/derive the properties of rotation matrices and euler parameters (quaternions and quaternion algebra) [L.A79] [AR88] [AR89] [RA87] [K.W86].

Groups: A *group* is a set X with an internal operation $X \times X \to X$, such that

- the operation is associative

  $$(xy)z = x(yz) \quad \forall \, x, y, z \in X,$$

- there is an element $e \in X$ called the identity such that

  $$xe = ex = x \quad \forall \, x \in X,$$

- for each $x \in X$ there is an element of X called the inverse of x (written x^{-1}), such that

  $$x^{-1}x = xx^{-1} = e.$$

Usually this group operation is referred to as multiplication. If the operation is commutative then it is referred to as addition and the group is called an *Abelian Group*.

Ring: A *ring* is a set X with two internal operations called multiplication and addition, such that

- X is an abelian group under addition,

- multiplication is associative and distributive with respect to addition.

If the group has an element $e \in X$ such that $ex = xe = x \; \forall \, x \in X$ it is called a *ring with identity*. Also, if $x \in X$ has an inverse, then it is said to be *regular*.

Field: A *field* is a ring with identity, all the elements of which (except zero, the additive identity) are regular.

Module: A *module* X over a ring R is an abelian group X with an external operation, called scalar multiplication, such that

$$\begin{aligned} \alpha(x+y) &= \alpha x + \alpha y \\ (\alpha + \beta)x &= \alpha x + \beta x \\ (\alpha\beta)x &= \alpha(\beta x) \end{aligned}$$

for all $\alpha, \beta \in \Re$ and $x, y \in X$.

Algebra: An *algebra* A is a module over a ring R with identity with an internal operation called multiplication such that

- A is a ring,

- the external operation $(\alpha, x) \to \alpha x$ is such that

  $$\alpha(xy) = (\alpha x)y = x(\alpha y).$$

Vector Spaces: A *vector or linear space* is a module for which the ring of operators is a field. Its elements are called vectors.

Quaternion: Quaternions can be viewed in many ways. A *quaternion* is defined as an operator with a scalar q_0 and a vector part $\vec{q}$, expressed either as a sum of its parts,

$$\mathbf{q} = \{q_0 + \vec{q}\}$$

or as a four dimensional vector,

$$\mathbf{q} = \begin{bmatrix} q_0 \\ \vec{q} \end{bmatrix}.$$

If $q_0 = 0$ then the quaternion is called a *vector quaternion*, and if $\vec{q} = \vec{0}$ then it is said to be a *scalar quaternion*. In this paper we notate the *quaternions* by boldface letters.

2.3 Properties of Rotation Matrix

The rotation matrix that relates the orientation of one frame relative to another requires the specification of three angles, and can be parametrized in a number of ways. We now indicate two commonly utilized parametrizations.

- **Fixed Axis Rotations:** Let $frame - 1$ and $frame - 2$ be coincident to begin with.

  - Rotate $frame - 2$ through an angle θ_x about the vector $\vec{X}_{frame-1}$.
  - Rotate $frame - 2$ through an angle θ_y about the vector $\vec{Y}_{frame-1}$.
  - Rotate $frame - 2$ through an angle θ_z about the vector $\vec{Z}_{frame-1}$.

The resulting rotation matrix, relating the coordinate vectors of $frame - 2$ to the coordinate vectors of $frame - 1$ can be given as

$$R^{frame-2}_{frame-1} = \begin{bmatrix} \cos\theta_z & -\sin\theta_z & 0 \\ \sin\theta_z & \cos\theta_z & 0 \\ 0 & & 1 \end{bmatrix} \begin{bmatrix} \cos\theta_y & 0 & \sin\theta_y \\ 0 & 1 & 0 \\ -\sin\theta_y & 0 & \cos\theta_y \end{bmatrix} \begin{bmatrix} 1 & 0 & 0 \\ 0 & \cos\theta_x & -\sin\theta_x \\ 0 & \sin\theta_x & \cos\theta_x \end{bmatrix}$$

Comment 2.1 Note that as the successive rotations are performed about the fixed axes, the rotation matrices are premultiplied in the order in which the rotations are performed.

$$R^{frame-2}_{frame-1} = \begin{bmatrix} \cos\theta_z\cos\theta_y & \cos\theta_z\sin\theta_y\sin\theta_x - \sin\theta_z\cos\theta_x & \cos\theta_z\sin\theta_y\cos\theta_x + \sin\theta_z\sin\theta_x \\ \sin\theta_z\cos\theta_y & \sin\theta_z\sin\theta_y\sin\theta_x + \cos\theta_z\cos\theta_x & \sin\theta_z\sin\theta_y\cos\theta_x - \cos\theta_z\sin\theta_x \\ -\sin\theta_y & \cos\theta_y\sin\theta_x & \cos\theta_y\cos\theta_x \end{bmatrix} \tag{10}$$

$$\begin{bmatrix} \vec{X} \\ \vec{Y} \\ \vec{Z} \end{bmatrix}_{frame-1} = R^{frame-2}_{frame-1} \begin{bmatrix} \vec{X} \\ \vec{Y} \\ \vec{Z} \end{bmatrix}_{frame-2} \tag{11}$$

- **Moving Axis Rotations:** Let $frame - 1$ and $frame - 2$ be coincident to begin with.

  - Rotate $frame - 2$ through an angle θ_z about the vector $\vec{Z}_{frame-2}$.
  - Rotate $frame - 2$ through an angle θ_y about the vector $\vec{Y}_{frame-2}$.
  - Rotate $frame - 2$ through an angle θ_x about the vector $\vec{X}_{frame-2}$.

The resulting rotation matrix, relating the coordinate vectors of $frame-2$ to the coordinate vectors of $frame-1$ can be given as

$$R^{frame-2}_{frame-1} = \begin{bmatrix} \cos\theta_z & -\sin\theta_z & 0 \\ \sin\theta_z & \cos\theta_z & 0 \\ 0 & & 1 \end{bmatrix} \begin{bmatrix} \cos\theta_y & 0 & \sin\theta_y \\ 0 & 1 & 0 \\ -\sin\theta_y & 0 & \cos\theta_y \end{bmatrix} \begin{bmatrix} 1 & 0 & 0 \\ 0 & \cos\theta_x & -\sin\theta_x \\ 0 & \sin\theta_x & \cos\theta_x \end{bmatrix}$$

Comment 2.2 Note that as the rotations are performed about the moving axes, the rotation matrices are post-multiplied in the order in which the rotations are performed.

$$R^{frame-2}_{frame-1} = \begin{bmatrix} \cos\theta_z\cos\theta_y & \cos\theta_z\sin\theta_y\sin\theta_x - \sin\theta_z\cos\theta_x & \cos\theta_z\sin\theta_y\cos\theta_x + \sin\theta_z\sin\theta_x \\ \sin\theta_z\cos\theta_y & \sin\theta_z\sin\theta_y\sin\theta_x + \cos\theta_z\cos\theta_x & \sin\theta_z\sin\theta_y\cos\theta_x - \cos\theta_z\sin\theta_x \\ -\sin\theta_y & \cos\theta_y\sin\theta_x & \cos\theta_y\cos\theta_x \end{bmatrix} \tag{12}$$

$$\begin{bmatrix} \vec{X} \\ \vec{Y} \\ \vec{Z} \end{bmatrix}_{frame-1} = R^{frame-2}_{frame-1} \begin{bmatrix} \vec{X} \\ \vec{Y} \\ \vec{Z} \end{bmatrix}_{frame-2} \tag{13}$$

We now note three important properties of rotation matrices.

$$\dot{R}^{frame-2}_{frame-1} = S(\vec{\omega}^{frame-2}_{frame-1})R^{frame-2}_{frame-1} \tag{14}$$

$$\frac{d}{dt}[R^{frame-2}_{frame-1}]^T = -[R^{frame-2}_{frame-1}]^T S(\vec{\omega}^{frame-2}_{frame-1}) \tag{15}$$

$$S(R^{frame-2}_{frame-1}a) = R^{frame-2}_{frame-1}S(a)R^{frame-1}_{frame-2} \tag{16}$$

We will now derive expressions for angular velocity of the object as a function of the derivatives of the parametrizations of the orientation angles. We will now derive the derivatives of the elementary rotation matrices.

$$R(\theta_x) = \begin{bmatrix} 1 & 0 & 0 \\ 0 & \cos\theta_x & -\sin\theta_x \\ 0 & \sin\theta_x & \cos\theta_x \end{bmatrix} \tag{17}$$

$$\frac{d}{dt}R(\theta_x) = \begin{bmatrix} 1 & 0 & 0 \\ 0 & -\sin\theta_x & -\cos\theta_x \\ 0 & \cos\theta_x & -\sin\theta_x \end{bmatrix}\dot{\theta}_x \tag{18}$$

$$= \begin{bmatrix} 0 & 0 & 0 \\ 0 & 0 & -\dot{\theta}_x \\ 0 & \dot{\theta}_x & 0 \end{bmatrix}\begin{bmatrix} 1 & 0 & 0 \\ 0 & \cos\theta_x & -\sin\theta_x \\ 0 & \sin\theta_x & \cos\theta_x \end{bmatrix} \tag{19}$$

$$= S(\dot{\theta}_x)R(\theta_x) \tag{20}$$

$$\frac{d}{dt}R(\theta_y) = S(\dot{\theta}_y)R(\theta_y) \tag{21}$$

$$\frac{d}{dt}R(\theta_z) = S(\dot{\theta}_z)R(\theta_z) \tag{22}$$

For the case of fixed axis rotations, we note that

$$R^{frame-2}_{frame-1} = R(\theta_z)R(\theta_y)R(\theta_x) \tag{23}$$

$$\frac{d}{dt}R^{frame-2}_{frame-1} = [\frac{d}{dt}R(\theta_z)]R(\theta_y)R(\theta_x) + R(\theta_z)[\frac{d}{dt}R(\theta_y)]R(\theta_x) \tag{24}$$

$$+R(\theta_z)R(\theta_y)[\frac{d}{dt}R(\theta_x)] \tag{25}$$

$$\frac{d}{dt}R^{frame-2}_{frame-1} = S(\dot{\theta}_z)R(\theta_z)R(\theta_y)R(\theta_x) + R(\theta_z)S(\dot{\theta}_y)R(\theta_y)R(\theta_x) \tag{26}$$

$$+R(\theta_z)R(\theta_y)S(\dot{\theta}_x)R(\theta_x) \tag{27}$$

$$\frac{d}{dt}R^{frame-2}_{frame-1} = S(\dot{\theta}_z)R(\theta_z)R(\theta_y)R(\theta_x) \tag{28}$$

$$+R(\theta_z)S(\dot{\theta}_y)R^T(\theta_z)R(\theta_z)R(\theta_y)R(\theta_x) \tag{29}$$

$$+R(\theta_z)R(\theta_y)S(\dot{\theta}_x)[R(\theta_z)R(\theta_y)]^T R(\theta_z)R(\theta_y)R(\theta_x) \tag{30}$$

$$\frac{d}{dt}R^{frame-2}_{frame-1} = [S(\dot{\theta}_z) + S(R(\theta_z)\dot{\theta}_y) + S(R(\theta_z)R(\theta_y)\dot{\theta}_x)]R^{frame-2}_{frame-1} \tag{31}$$

$$S(\vec{\omega}^{frame-2}_{frame-1})R^{frame-2}_{frame-1} = [S(\dot{\theta}_z) + S(R(\theta_z)\dot{\theta}_y) + S(R(\theta_z)R(\theta_y)\dot{\theta}_x)]R^{frame-2}_{frame-1} \tag{32}$$

$$S(\vec{\omega}^{frame-2}_{frame-1}) = S(\dot{\theta}_z) + S(R(\theta_z)\dot{\theta}_y) + S(R(\theta_z)R(\theta_y)\dot{\theta}_x) \tag{33}$$

We simplify the above expression to get,

$$S(\vec{\omega}^{frame-2}_{frame-1}) = \begin{bmatrix} 0 & -\dot{\theta}_z & 0 \\ \dot{\theta}_z & 0 & 0 \\ 0 & 0 & 0 \end{bmatrix} \tag{34}$$

$$+\begin{bmatrix} 0 & 0 & \cos\theta_z\dot{\theta}_y \\ 0 & 0 & \sin\theta_z\dot{\theta}_y \\ -\cos\theta_z\dot{\theta}_y & -\sin\theta_z\dot{\theta}_y & 0 \end{bmatrix} \tag{35}$$

$$+\begin{bmatrix} 0 & \sin\theta_y\dot{\theta}_x & \cos\theta_y\sin\theta_z\dot{\theta}_x \\ -\sin\theta_y\dot{\theta}_x & 0 & -\cos\theta_y\cos\theta_z\dot{\theta}_x \\ -\cos\theta_y\sin\theta_z\dot{\theta}_x & \cos\theta_y\cos\theta_z\dot{\theta}_x & 0 \end{bmatrix} \tag{36}$$

$$= \begin{bmatrix} 0 & \omega^{frame-2}_{z-frame-1} & \omega^{frame-2}_{y-frame-1} \\ \omega^{frame-2}_{z-frame-1} & 0 & -\omega^{frame-2}_{x-frame-1} \\ -\omega^{frame-2}_{y-frame-1} & \omega^{frame-2}_{x-frame-1} & 0 \end{bmatrix} \tag{37}$$

$$\begin{bmatrix} \omega^{frame-2}_{x-frame-1} \\ \omega^{frame-2}_{y-frame-1} \\ \omega^{frame-2}_{z-frame-1} \end{bmatrix} = \begin{bmatrix} \cos\theta_y \cos\theta_z \dot{\theta}_x - \sin\theta_z \dot{\theta}_y \\ \cos\theta_y \sin\theta_z \dot{\theta}_x + \cos\theta_z \dot{\theta}_y \\ \dot{\theta}_z - \sin\theta_y \dot{\theta}_x \end{bmatrix} \tag{38}$$

$$= \begin{bmatrix} \cos\theta_y \cos\theta_z & -\sin\theta_z & 0 \\ \cos\theta_y \sin\theta_z & \cos\theta_z & 0 \\ -\sin\theta_y & 0 & 1 \end{bmatrix} \begin{bmatrix} \dot{\theta}_x \\ \dot{\theta}_y \\ \dot{\theta}_z \end{bmatrix} \tag{39}$$

Note from equation (39) that determinant of the matrix relating the angular velocities of $frame-2$ and the derivatives of the parametrization $\cos\theta_y$. Therefore, the matrix is invertible for small values of the angle θ_y.

2.4 Properties of Quaternions

We will present here the properties of quaternion algebra that we use in this paper [1] [K.W86] [OB79]. We will also derive the derivatives of quaternions.

Quaternion addition: The sum of two quaternions x and y is given by

$$\mathbf{x} + \mathbf{y} = \begin{bmatrix} x_0 + y_0 \\ \vec{x} + \vec{y} \end{bmatrix}.$$

Quaternion product: The product of two quaternions x and y is given by

$$\mathbf{xy} = \begin{bmatrix} -\vec{x}^T & x_0 \\ x_0 \vec{1} + \vec{x}\times & \vec{x} \end{bmatrix} \mathbf{y} = \begin{bmatrix} x_0 y_0 - \vec{x} \cdot \vec{y} \\ x_0 \vec{y} + y_0 \vec{x} + \vec{x} \times \vec{y} \end{bmatrix}.$$

Quaternion conjugate: The conjugate of a quaternion q is given by

$$\mathbf{q}^* = \begin{bmatrix} q_0 \\ -\vec{q} \end{bmatrix}.$$

Quaternion norm: The norm of a quaternion q is defined to be

$$||\mathbf{q}||^2 = \mathbf{q}^*\mathbf{q} = q_0^2 + \vec{q} \cdot \vec{q}.$$

This is analogous to the euclidean vector norm of a four dimensional vector.

Quaternion Inverse: The inverse of a quaternion q is defined as

$$\mathbf{q}^{-1} = \frac{1}{||\mathbf{q}||^2} \mathbf{q}^*.$$

It can be verified that this inverse has the property that

$$\mathbf{q}^{-1}\mathbf{q} = \mathbf{q}\mathbf{q}^{-1} = 1.$$

Rotation operation: A rotation of a vector $\vec{x}$ by θ about an axis $\vec{n}$ is given by

$$\mathbf{q}\vec{x}\mathbf{q}^*$$

where q is the quaternion given by

$$\mathbf{q} = \begin{bmatrix} \cos(\frac{\theta}{2}) \\ \sin(\frac{\theta}{2})\vec{n} \end{bmatrix}$$

The derivatives of the *Quaternion* representing a rotation operation are given by

$$\dot{\mathbf{q}} = \mathbf{q}\{\frac{1}{2}\vec{w}\}$$

$$\ddot{\mathbf{q}} = \mathbf{q}\{\frac{1}{2}\vec{w}\} + \mathbf{q}\{\frac{1}{2}\vec{w}\}\{\frac{1}{2}\vec{w}\}$$

where $\vec{w}$ is the angular velocity and $\vec{\dot{w}}$ is the angular acceleration.
The angular velocity and angular accelerations are given in terms of the quaternions through the following relations:

$$\vec{w} = 2\mathbf{q}^*\dot{\mathbf{q}}$$

$$\vec{\dot{w}} = 2\mathbf{q}^*\ddot{\mathbf{q}} + 2\dot{\mathbf{q}}^*\dot{\mathbf{q}}$$

---

[1] Boldface letters represent *quaternions*

Let us now calculate the derivative of the conjugate of the quaternion. As the quaternions representing a rotation operation are *unit quaternions* (unity norm), the inverse is the conjugate. Hence

$$1 = qq^*$$
$$0 = \dot{q}q^* + q\dot{q}^*$$
$$\dot{q}^* = -q^{-1}\dot{q}q^*$$
$$= -q^*\dot{q}q^*$$
$$= -q^*q\{\frac{1}{2}\vec{w}\}q^*$$

2.5 Relation between Rotation Matrices & Euler Parameters

The operation of rotation by an angle θ about an axis $\vec{n}$ can be represented by both a rotation matrix (R) and euler parameters (q) as

$$R = \cos(\theta)\vec{1} + (1 - \cos(\theta))\vec{n}\vec{n}^T + \sin(\theta)\vec{n}\times$$

$$q = \left[\begin{array}{c} \cos(\frac{\theta}{2}) \\ \sin(\frac{\theta}{2})\vec{n} \end{array} \right]$$

These two representations can be related as follows:

$$R = (q_0{}^2 - \vec{q}^T\vec{q})I_{3\times3} + 2\vec{q}\vec{q}^T + 2q_0\vec{q}\times$$

3 · Dynamical Equations of the Rotor

In this section we derive the equations of motion of the rigid body rotor supported by active magnetic bearings. We begin this section, with a derivation using rotation matrices, and then proceed to do the same using euler parameters (quaternions).

3.1 Dynamical Equations using *Rotation Matrices*

To eliminate ambiguity regarding the specification of reference frames, we will primarily work in the rotor reference frame, and finally transform the coordinates to the inertial reference frame. We derive the dynamic equations of the magnetic bearing in a systematic manner. For an excellent exposition on kinematics, refer to [RS94].

Step 1.
We compute the angular momentum of the rotor about the origin of the rotor reference frame, denoted as $\vec{H}_{rotor}^{rotor}$ as

$$\vec{H}_{rotor}^{rotor} = I_{rotor}^{rotor}\vec{\omega}_{rotor}^{rotor} \tag{40}$$

Step 2.
We utilize the principle of torque balance to relate the rate of change of angular momentum to the net torque. We note here that by net torques (T^{rotor}) we refer to the summation of the applied torques (τ^{rotor}, and the moments of the applied forces ($\vec{F}^i$) about the origin of the rotor reference frame. It is to be understood of course that the quantities on either side of the equality will be referenced in one coordinate frame. Indeed to avoid ambiguity, we will henceforth refer to each of the aforementioned quantities in a single coordinate frame. Expressing all quantities in the inertial reference frame, we get

$$\vec{H}_{rotor}^{rotor} = I_{rotor}^{rotor}R_{rotor}^{inertial}\vec{\omega}_{inertial}^{rotor}$$

Step 3.
We utilize Newton's torque balance equations to derive the following.

$$T_{rotor}^{rotor} = \frac{d}{dt}[\vec{H}_{rotor}^{rotor}]$$

$$\vec{\tau}_{rotor}^{rotor} + \sum_{i=1}^{n}\vec{r}_{rotor}^i \times \vec{F}_{rotor}^i = I_{rotor}^{rotor}\dot{\vec{\omega}}_{rotor}^{rotor} + \vec{\omega}_{rotor}^{rotor} \times \vec{H}_{rotor}^{rotor}$$

$$R_{rotor}^{inertial}\vec{\tau}_{inertial}^{rotor} + \sum_{i=1}^{n}\vec{r}_{rotor}^i \times R_{rotor}^{inertial}\vec{F}_{inertial}^i = I_{rotor}^{rotor}\dot{\vec{\omega}}_{rotor}^{rotor}$$

$$+R^{inertial}_{rotor}\,\vec{\omega}^{rotor}_{inertial} \times R^{inertial}_{rotor}\,R^{rotor}_{inertial}\,\vec{H}^{rotor}_{rotor}$$

$$R^{inertial}_{rotor}\,\vec{\tau}^{rotor}_{inertial} + \sum_{i=1}^{n}\vec{r}^{i}_{rotor} \times R^{inertial}_{rotor}\,\vec{F}^{i}_{inertial} \quad = \quad I^{rotor}_{rotor}\,\dot{\vec{\omega}}^{rotor}_{rotor}$$

$$+R^{inertial}_{rotor}(\vec{\omega}^{rotor}_{inertial} \times R^{rotor}_{inertial}I^{rotor}_{rotor}R^{inertial}_{rotor}\,\vec{\omega}^{rotor}_{inertial})$$

$$R^{inertial}_{rotor}\,\vec{\tau}^{rotor}_{inertial} + \sum_{i=1}^{n}S(\vec{r}^{i}_{rotor})R^{inertial}_{rotor}\,\vec{F}^{i}_{inertial} \quad = \quad I^{rotor}_{rotor}\,\dot{\vec{\omega}}^{rotor}_{rotor}$$

$$+R^{inertial}_{rotor}\,S(\vec{\omega}^{rotor}_{inertial})R^{rotor}_{inertial}I^{rotor}_{rotor}R^{inertial}_{rotor}\,\vec{\omega}^{rotor}_{inertial}$$

where $\vec{r}^{i}_{rotor}$ is the point of application of the force $\vec{F}^{i}_{inertial}$, and is given as

$$\begin{bmatrix} r^{i}_{x-rotor} \\ r^{i}_{y-rotor} \\ r^{i}_{z-rotor} \\ 1 \end{bmatrix} \quad = \quad T^{inertial}_{rotor}\begin{bmatrix} r^{i}_{x-inertial} \\ r^{i}_{y-inertial} \\ r^{i}_{z-inertial} \\ 1 \end{bmatrix} \tag{41}$$

$$= \quad \begin{bmatrix} R^{inertial}_{rotor} & -R^{inertial}_{rotor}\begin{bmatrix} r^{rotor-origin}_{x-inertial} \\ r^{rotor-origin}_{y-inertial} \\ r^{rotor-origin}_{z-inertial} \end{bmatrix} \\ \begin{bmatrix} 0 & 0 & 0 \end{bmatrix} & 1 \end{bmatrix}\begin{bmatrix} r^{i}_{x-inertial} \\ r^{i}_{y-inertial} \\ r^{i}_{z-inertial} \\ 1 \end{bmatrix} \tag{42}$$

We now compute $\dot{\vec{\omega}}^{rotor}_{rotor}$ in the following manner utilizing (14) - (16)

$$\dot{\vec{\omega}}^{rotor}_{rotor} \quad = \quad \frac{d}{dt}[R^{rotor}_{inertial}]^{T}\,\vec{\omega}^{rotor}_{inertial} \tag{43}$$

$$= \quad [R^{rotor}_{inertial}]^{T}\,\dot{\vec{\omega}}^{rotor}_{inertial} - [R^{rotor}_{inertial}]^{T}S(\vec{\omega}^{rotor}_{inertial})\vec{\omega}^{rotor}_{inertial} \tag{44}$$

$$= \quad [R^{rotor}_{inertial}]^{T}\,\dot{\vec{\omega}}^{rotor}_{inertial} \tag{45}$$

$$= \quad R^{inertial}_{rotor}\,\dot{\vec{\omega}}^{rotor}_{inertial} \tag{46}$$

Substituting the expression for $\dot{\vec{\omega}}^{rotor}_{rotor}$ from equation(46) in the torque balance equation, we get

$$R^{inertial}_{rotor}\,\vec{\tau}^{rotor}_{inertial} + \sum_{i=1}^{n}S(\vec{r}^{i}_{rotor})R^{inertial}_{rotor}\,\vec{F}^{i}_{inertial} \quad = \quad I^{rotor}_{rotor}R^{inertial}_{rotor}\,\dot{\vec{\omega}}^{rotor}_{inertial}$$

$$+R^{inertial}_{rotor}\,S(\vec{\omega}^{rotor}_{inertial})R^{rotor}_{inertial}I^{rotor}_{rotor}R^{inertial}_{rotor}\,\vec{\omega}^{rotor}_{inertial}$$

We now recast the above equation in the following form

$$\dot{\vec{\omega}}^{rotor}_{inertial} \quad = \quad [I^{rotor}_{rotor}R^{inertial}_{rotor}]^{-1}[R^{inertial}_{rotor}\,\vec{\tau}^{rotor}_{inertial} + \sum_{i=1}^{n}S(\vec{r}^{i}_{rotor})R^{inertial}_{rotor}\,\vec{F}^{i}_{inertial}] \tag{47}$$

$$-[I^{rotor}_{rotor}R^{inertial}_{rotor}]^{-1}[R^{inertial}_{rotor}\,S(\vec{\omega}^{rotor}_{inertial})R^{rotor}_{inertial}I^{rotor}_{rotor}R^{inertial}_{rotor}\,\vec{\omega}^{rotor}_{inertial}] \tag{48}$$

$$\dot{\vec{\omega}}^{rotor}_{inertial} \quad = \quad R^{rotor}_{inertial}[I^{rotor}_{rotor}]^{-1}[R^{inertial}_{rotor}\,\vec{\tau}^{rotor}_{inertial} + \sum_{i=1}^{n}S(\vec{r}^{i}_{rotor})R^{inertial}_{rotor}\,\vec{F}^{i}_{inertial}] \tag{49}$$

$$-R^{rotor}_{inertial}[I^{rotor}_{rotor}]^{-1}R^{inertial}_{rotor}\,S(\vec{\omega}^{rotor}_{inertial})R^{rotor}_{inertial}I^{rotor}_{rotor}R^{inertial}_{rotor}\,\vec{\omega}^{rotor}_{inertial} \tag{50}$$

Step 4.

We derive the force balance equations by first calculating the expression for the linear momentum of the rotor in the following manner.

$$\vec{L}^{rotor}_{rotor} \quad = \quad m^{rotor}\,\vec{v}^{rotor}_{rotor}$$

$$= \quad m^{rotor}\,R^{inertial}_{rotor}\,\vec{v}^{rotor}_{inertial}$$

Step 5

Newton's law asserts that the rate of change of linear momentum equals the applied force. That is,

$$R^{inertial}_{rotor}\sum_{i=1}^{n}\vec{F}^{i}_{inertial} \quad = \quad \frac{d}{dt}[\vec{L}^{rotor}_{rotor}] \tag{51}$$

$$= \quad m^{rotor}\,\dot{\vec{v}}^{rotor}_{rotor} + \vec{\omega}^{rotor}_{rotor} \times \vec{L}^{rotor}_{rotor} \tag{52}$$

$$= \quad m^{rotor}\,\dot{\vec{v}}^{rotor}_{rotor} + S(R^{inertial}_{rotor}\,\vec{\omega}^{rotor}_{inertial})m^{rotor}\,R^{inertial}_{rotor}\,\vec{v}^{rotor}_{inertial} \tag{53}$$

We now compute $\dot{\vec{v}}^{rotor}_{rotor}$ in (53) in the following manner utilizing (14) - (16).

$$\dot{\vec{v}}^{rotor}_{rotor} = \frac{d}{dt}[R^{rotor}_{inertial}]^T \vec{v}^{rotor}_{inertial} \tag{54}$$

$$= [R^{rotor}_{inertial}]^T \dot{\vec{v}}^{rotor}_{inertial} - [R^{rotor}_{inertial}]^T S(\vec{\omega}^{rotor}_{inertial}) \vec{v}^{rotor}_{inertial} \tag{55}$$

$$= R^{inertial}_{rotor} \dot{\vec{v}}^{rotor}_{inertial} - R^{inertial}_{rotor} S(\vec{\omega}^{rotor}_{inertial}) \vec{v}^{rotor}_{inertial} \tag{56}$$

Substituting the expression for $\dot{\vec{v}}^{rotor}_{rotor}$ from equation (56) in the force balance equation (53), we recast the force balance equation as,

$$R^{inertial}_{rotor} \sum_{i=1}^{n} \vec{F}^i_{inertial} = m^{rotor} R^{inertial}_{rotor} \dot{\vec{v}}^{rotor}_{inertial} - m^{rotor} R^{inertial}_{rotor} S(\vec{\omega}^{rotor}_{inertial}) \vec{v}^{rotor}_{inertial} \tag{57}$$

$$+ m^{rotor} S(R^{inertial}_{rotor} \vec{\omega}^{rotor}_{inertial}) R^{inertial}_{rotor} \vec{v}^{rotor}_{inertial} \tag{58}$$

$$\tag{59}$$

We now rewrite the force equation (58) in the following form

$$\dot{\vec{v}}^{rotor}_{inertial} = \frac{1}{m^{rotor}} \sum_{i=1}^{n} \vec{F}^i_{inertial} + S(\vec{\omega}^{rotor}_{inertial}) \vec{v}^{rotor}_{inertial} \tag{60}$$

$$- R^{rotor}_{inertial} S(R^{inertial}_{rotor} \vec{\omega}^{rotor}_{inertial}) R^{inertial}_{rotor} \vec{v}^{rotor}_{inertial} \tag{61}$$

Note that the last term in equation (61) may be simplified in the following manner.

$$R^{rotor}_{inertial} S(R^{inertial}_{rotor} \vec{\omega}^{rotor}_{inertial}) R^{inertial}_{rotor} \vec{v}^{rotor}_{inertial} = R^{rotor}_{inertial} S(\vec{\omega}^{rotor}_{rotor})[R^{rotor}_{inertial}]^T \vec{v}^{rotor}_{inertial} \tag{62}$$

$$= S(R^{rotor}_{inertial} \vec{\omega}^{rotor}_{rotor}) \vec{v}^{rotor}_{inertial} \tag{63}$$

$$= S(\vec{\omega}^{rotor}_{inertial}) \vec{v}^{rotor}_{inertial} \tag{64}$$

Substituting the expression in equation (64) in equation (61), we arrive at the force balance equations,

$$\dot{\vec{v}}^{rotor}_{inertial} = \frac{1}{m^{rotor}} \sum_{i=1}^{n} \vec{F}^i_{inertial} + S(\vec{\omega}^{rotor}_{inertial}) \vec{v}^{rotor}_{inertial} - S(\vec{\omega}^{rotor}_{inertial}) \vec{v}^{rotor}_{inertial} \tag{65}$$

$$= \frac{1}{m^{rotor}} \sum_{i=1}^{n} \vec{F}^i_{inertial} \tag{66}$$

Collecting the force and torque balance equations, we write the dynamic equations of the magnetic bearing as follows.

$$\dot{\vec{\omega}}^{rotor}_{inertial} = R^{rotor}_{inertial}[I^{rotor}_{rotor}]^{-1}[R^{inertial}_{rotor} \vec{\tau}^{rotor}_{inertial} + \sum_{i=1}^{n} S(\vec{r}_{rotor}) R^{inertial}_{rotor} \vec{F}^i_{inertial}] \tag{67}$$

$$- R^{rotor}_{inertial}[I^{rotor}_{rotor}]^{-1} R^{inertial}_{rotor} S(\vec{\omega}^{rotor}_{inertial}) R^{rotor}_{inertial} I^{rotor}_{rotor} R^{inertial}_{rotor} \vec{\omega}^{rotor}_{inertial} \tag{68}$$

$$\dot{\vec{v}}^{rotor}_{inertial} = \frac{1}{m^{rotor}} \sum_{i=1}^{n} \vec{F}^i_{inertial} \tag{69}$$

3.2 Dynamical Equations using *Quaternions*

As we saw in the previous section in equation 69 the force balance equations essentially are a restatement of $F = ma$ in the inertial coordinates. So we will only consider the angular momentum equations.

$$T^{rotor}_{rotor} = \frac{d}{dt}[\vec{H}^{rotor}_{rotor}] \tag{70}$$

$$\vec{\tau}^{rotor}_{rotor} + \sum_{i=1}^{n} \vec{r}_{rotor} \times \vec{F}^i_{rotor} = I^{rotor}_{rotor} \dot{\vec{\omega}}^{rotor}_{rotor} + \vec{\omega}^{rotor}_{rotor} \times \vec{H}^{rotor}_{rotor}$$

Let us look at the first term on the right hand side of 71 initially.

$$I^{rotor}_{rotor} \dot{\vec{\omega}}^{rotor}_{rotor} = I^{rotor}_{rotor} \frac{d}{dt}(q^{inertial}_{rotor} \vec{\omega}^{rotor}_{inertial} q^{inertial *}_{rotor})$$

$$= I^{rotor}_{rotor}(\dot{q}^{inertial}_{rotor} \vec{\omega}^{rotor}_{inertial} q^{inertial *}_{rotor} + q^{inertial}_{rotor} \dot{\vec{\omega}}^{rotor}_{inertial} q^{inertial *}_{rotor}$$

344

$$+q_{rotor}^{inertial}\,\vec{\omega}_{inertial}^{rotor}\,\dot{q}_{rotor}^{inertial*})$$

$$= I_{rotor}^{rotor}(q_{rotor}^{inertial}\{\frac{1}{2}\vec{\omega}_{inertial}^{rotor}\}\vec{\omega}_{inertial}^{rotor}q_{rotor}^{inertial*} + q_{rotor}^{inertial}\,\vec{\omega}_{inertial}^{rotor}q_{rotor}^{inertial*}$$

$$-q_{rotor}^{inertial}\,\vec{\omega}_{inertial}^{rotor}q_{rotor}^{inertial*}q_{rotor}^{inertial}\{\frac{1}{2}\vec{\omega}_{inertial}^{rotor}\}q_{rotor}^{inertial*})$$

$$= I_{rotor}^{rotor}(q_{rotor}^{inertial}\{\frac{1}{2}\vec{\omega}_{inertial}^{rotor}\}\vec{\omega}_{inertial}^{rotor}q_{rotor}^{inertial*} + q_{rotor}^{inertial}\,\dot{\vec{\omega}}_{inertial}^{rotor}q_{rotor}^{inertial*}$$

$$-q_{rotor}^{inertial}\,\vec{\omega}_{inertial}^{rotor}\{\frac{1}{2}\vec{\omega}_{inertial}^{rotor}\}q_{rotor}^{inertial*})$$

$$= I_{rotor}^{rotor}(q_{rotor}^{inertial}\,\dot{\vec{\omega}}_{inertial}^{rotor}q_{rotor}^{inertial*})$$

Substituting this back into 71 we get

$$\vec{\tau}_{rotor}^{rotor} + \sum_{i=1}^{n}\vec{r}_{rotor}^{i} \times \vec{F}_{rotor}^{i} = I_{rotor}^{rotor}(q_{rotor}^{inertial}\,\dot{\vec{\omega}}_{inertial}^{rotor}q_{rotor}^{inertial*}) + \vec{\omega}_{rotor}^{rotor} \times \vec{H}_{rotor}^{rotor} \tag{71}$$

$$q_{rotor}^{inertial}\,\vec{\tau}_{inertial}^{rotor}q_{rotor}^{inertial*} + \sum_{i=1}^{n}(q_{rotor}^{inertial}\,\vec{r}_{inertial}^{i}q_{rotor}^{inertial*} \times q_{rotor}^{inertial}\,\vec{F}_{inertial}^{i}q_{rotor}^{inertial*})$$

$$= I_{rotor}^{rotor}(q_{rotor}^{inertial}\,\dot{\vec{\omega}}_{inertial}^{rotor}q_{rotor}^{inertial*}) + q_{rotor}^{inertial}\,\vec{\omega}_{inertial}^{rotor}q_{rotor}^{inertial*} \times q_{rotor}^{inertial}\,\vec{H}_{inertial}^{rotor}q_{rotor}^{inertial*} \tag{72}$$

$$\dot{\vec{\omega}}_{inertial}^{rotor} = q^{inertial}rotor^{*}[I_{rotor}^{rotor}]^{-1}[q_{rotor}^{inertial}\,\vec{\tau}_{inertial}^{rotor} + \sum_{i=1}^{n}(q_{rotor}^{inertial}\,\vec{r}_{inertial}^{i}q_{rotor}^{inertial*} \times q_{rotor}^{inertial}\,\vec{F}_{inertial}^{i})$$

$$-q_{rotor}^{inertial}\,\vec{\omega}_{inertial}^{rotor}q_{rotor}^{inertial*} \times q_{rotor}^{inertial}\,\vec{H}_{inertial}^{rotor}] \tag{73}$$

Comparing equations 68 and 73 we see the equivalence of both these derivations.

We have briefly derived the dynamics equations of the magnetic bearing system using euler parameters, as they have many advantages. Euler Parameters are defined everywhere and they have a nonsingular mapping with the rotational velocity $\vec{w}$. Using Quaternion algebra the above expressions can be further simplified. Simple expressions for all composite rotations and rotating reference frames can be developed [K.W86]. Euler parameters have also been shown to be as efficient computationally as rotation matrices and more compact in storage [JR90].

4   Small Angle Assumption

We have derived a detailed nonlinear model of the rotor supported by active magnetic bearings. We will now present the standard assumptions made in deriving the dynamical equations of the magnetic bearing and the simplification achieved on the nonlinear model [FK90].

In the magnetic bearing system, let the spin axis be x and the pitch and yaw axes be y and z axes. Let the spin angle, pitch and yaw angles be $\theta_x, \theta_y, \theta_z$. Usually we assume that the angles θ_y, θ_z are very small so that $\cos(\theta_y), \cos(\theta_z) \approx 1$, $\sin(\theta_y), \sin(\theta_z) \approx 0$. Also we can reasonably assume that the product of velocities and angular velocities are small and can be ignored. The external forces acting on the system are the forces at the two radial bearing systems F_y^1, F_z^1 and F_y^2, F_z^2; the force at the axial bearing F_x and the external torque τ_{motor} applied along the spin axis. With these assumptions the equations of motion of a rotor supported by magnetic bearings reduce to

$$\begin{bmatrix} \dot{x} \\ \dot{y} \\ \dot{z} \\ \dot{\theta_x} \\ \dot{\theta_y} \\ \dot{\theta_z} \\ \ddot{x} \\ \ddot{y} \\ \ddot{z} \\ \ddot{\theta_x} \\ \ddot{\theta_y} \\ \ddot{\theta_z} \end{bmatrix} = F \begin{bmatrix} x \\ y \\ z \\ \theta_x \\ \theta_y \\ \theta_z \\ \dot{x} \\ \dot{y} \\ \dot{z} \\ \dot{\theta_x} \\ \dot{\theta_y} \\ \dot{\theta_z} \end{bmatrix} + G \begin{bmatrix} F_x \\ F_y^1 \\ F_y^2 \\ F_z^1 \\ F_z^2 \\ \tau_{motor} \end{bmatrix}$$

where $F \in \Re^{12 \times 12}$ and $G \in \Re^{12 \times 6}$.

$$F = \begin{bmatrix} 0_{6 \times 6} & I_{6 \times 6} \\ & \begin{matrix} 0 & 0 & 0 & 0 & 0 & 0 \\ 0 & 0 & 0 & 0 & 0 & 0 \\ 0 & 0 & 0 & 0 & 0 & 0 \\ 0 & 0 & 0 & 0 & 0 & 0 \\ 0 & 0 & 0 & 0 & 0 & -\omega a \\ 0 & 0 & 0 & 0 & \omega a & 0 \end{matrix} \end{bmatrix}$$

where $a \in \Re^+$ is a constant dependent on the inertias J_x, J_y.

$$G = \begin{bmatrix} & & & 0_{6 \times 6} & & & \\ \frac{1}{M} & 0 & 0 & 0 & 0 & 0 \\ 0 & \frac{1}{M} & \frac{1}{M} & 0 & 0 & 0 \\ 0 & 0 & 0 & \frac{1}{M} & \frac{1}{M} & 0 \\ 0 & 0 & 0 & 0 & 0 & \frac{1}{J_x} \\ 0 & 0 & 0 & -\frac{l_1}{J_y} & \frac{l_2}{J_y} & 0 \\ 0 & \frac{l_1}{J_y} & -\frac{l_2}{J_y} & 0 & 0 & 0 \end{bmatrix}$$

5 Feedback control of the rotor motion

The rotor system motion is decoupled between the spin axes and its pitch and yaw axes. Hence for the design of a linear state feedback controller we shall consider the dynamical equations of only the pitch and yaw axes motions of the rotor system, given by

$$\dot{\vec{x}} = \begin{bmatrix} 0_{4 \times 4} & I_{4 \times 4} \\ 0_{4 \times 4} & A[\omega] \end{bmatrix} \vec{x} + \begin{bmatrix} 0_{4 \times 4} \\ B \end{bmatrix} u \tag{74}$$

where $\vec{x} = [x_1^1 x_1^2 x_1^3 x_1^4 x_2^1 x_2^2 x_2^3 x_2^4]^T \in \Re^8$, $u = [u^1 u^2 u^3 u^4]^T \in \Re^4$, $A : \Re^+ \to \Re^{4 \times 4}$, $B \in \Re^{4 \times 4}$.

$$A[\omega] = \begin{bmatrix} 0 & 0 & 0 & 0 \\ 0 & 0 & 0 & 0 \\ 0 & 0 & 0 & -\omega a \\ 0 & 0 & \omega a & 0 \end{bmatrix} \& B = \begin{bmatrix} \frac{1}{M} & \frac{1}{M} & 0 & 0 \\ 0 & 0 & \frac{1}{M} & \frac{1}{M} \\ 0 & 0 & -\frac{l_1}{J_y} & \frac{l_2}{J_y} \\ \frac{l_1}{J_y} & -\frac{l_2}{J_y} & 0 & 0 \end{bmatrix} \tag{75}$$

Note that the x_1^1, x_2^1 subsystem and x_1^2, x_2^2 subsystem form two decoupled 2×2 systems, while $x_1^3, x_1^4, x_2^3, x_2^4$ form a coupled 4×4 system. Let us choose the control

$$u = B^{-1} \begin{bmatrix} -k_1^1 x_1^1 - k_2^1 x_2^1 \\ -k_1^2 x_1^2 - k_2^2 x_2^2 \\ -k_1^3 x_1^3 - k_2^3 x_2^3 \\ -k_1^4 x_1^4 - k_2^4 x_2^4 \end{bmatrix} \tag{76}$$

such that $k_i^j > 0$ for $i = 1, 2 : j = 1 \cdots 4$. We can now show that this control stabilizes the $x_3^1, x_3^2, x_4^1, x_4^2$ system at all speeds ω.

Theorem 5.1

Given *(G1) The system given by equation 74*

(G2) Feedbacks u given by equation 76

Then *(T1) u^1, u^2 stabilize the system at all speeds ω.*

Proof: ♠ ▷ Let us choose a Lyapunov function candidate V as follows:

$$V = \frac{\sum_{j=1}^{j=4} k_1^j {x_1^j}^2 + {x_2^j}^2}{2}$$

Taking the derivative of the Lyapunov function we get

$$\dot{V} = \sum_{j=1}^{j=4} k_1^j x_1^j x_2^j - k_1^j x_1^j x_2^j - k_2^j {x_2^j}^2$$

$$- \omega a x_2^3 x_2^4 + \omega a x_2^3 x_2^4$$

$$= \sum_{j=1}^{j=4} -k_2^j {x_2^j}^2$$

$$< 0 \quad if x_2^j \neq 0 \, for j = 1 \cdots 4$$
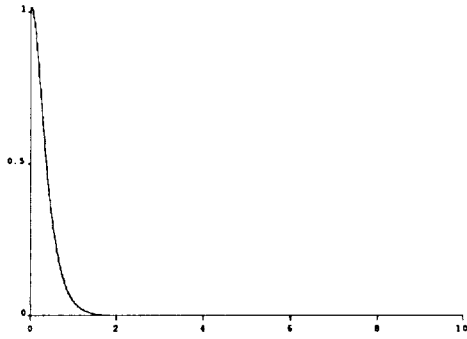
Figure 1: y vs time : w = 0
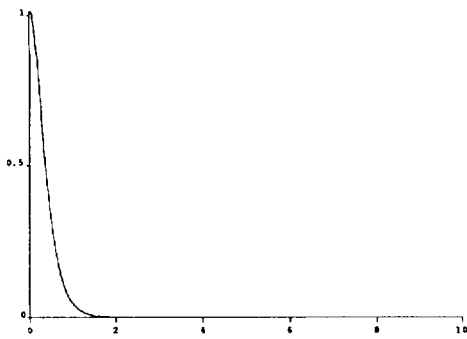
Figure 2: θ_y vs time : w = 0

Hence by Lyapunov theorem x_2^j converge to 0 for $j = 1 \cdots 4$. As the maximum invariant set containing the set $x_2^j = 0$ is $x_1^j = 0$, by LaSalle theorem [M.V78] x_1^j also converges to 0. Hence the system is stable at all ω. ◁♠

5.1 Simulation Results

We simulate this system using the control system simulation package *SIMNON*. We present the simulation results of applying the state feedback control given by equation 76 to the magnetic bearing system. We simulate the system response y and θ_y under the feedback when there is no spin (Figures 1,2) and with a spin of $100 rad/sec$ (Figures 3, 4).
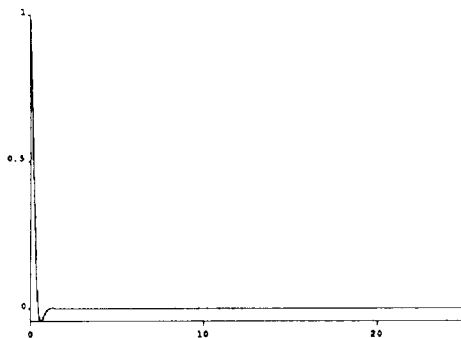
Figure 3: y vs time : w = 100

347
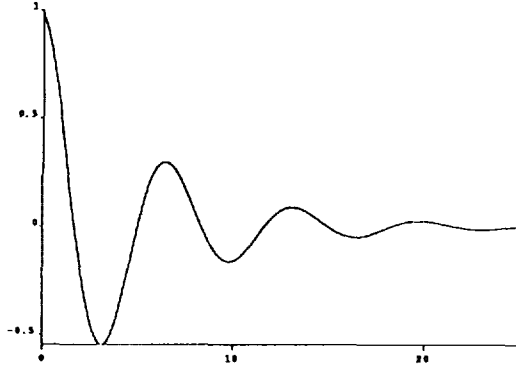
Figure 4: θ_y vs time : w = 100

5.2 Magnetic Bearing Model

In this section we present the basic equations for a single axis magnetic bearing, and two associated pole excitation schemes. The dynamical equations of the magnetic bearing may be written as follows.

$$\dot{\phi}_0 = u_0 \tag{77}$$

$$\dot{\phi}_\pi = u_\pi \tag{78}$$

where

$$\phi_0 \in \Re \quad \text{flux at pole location } 0 \tag{79}$$

$$\phi_\pi \in \Re \quad \text{flux at pole location } \pi \tag{80}$$

$$u_0 \in \Re \quad \text{Control at pole location } 0 \tag{81}$$

$$u_\pi \in \Re \quad \text{Control at pole location } \pi \tag{82}$$

Let the control force F generated by the magnetic bearing be the net force produced by the bearing elements at the angles 0 and π (the positive and negative poles in a pair). Indeed,

$$F = F_0 - F_\pi \tag{83}$$

We shall design the feedback control of the rotor using the net force as the control actuation. Treating this requisite force as the commanded output of the magnetic bearing subsystem described by equations 77,78, we design the flux feedback as a deadbeat controller. Inherent in this approach is the assumption that the flux feedback loop would be run at a much faster rate than the bandwidth of the force feedback system.

Discretizing the flux equations in the following manner.

$$\begin{bmatrix} \phi_0(k+1) \\ \phi_\pi(k+1) \end{bmatrix} = \begin{bmatrix} \phi_0(k) \\ \phi_\pi(k) \end{bmatrix} + \begin{bmatrix} Tu_0(k) \\ Tu_\pi(k) \end{bmatrix} \tag{84}$$

where

$$u_0(k) = \text{is the net control voltage at pole } 0 \tag{85}$$

$$u_\pi(k) = \text{is the net control voltage at pole } \pi \tag{86}$$

We now note the relation between force and flux is given the following form

$$F(k+1) = K_{force-flux}[\phi_0^2(k+1) - \phi_\pi^2(k+1)] \tag{87}$$

where the magnetic constant $K_{force-flux} \in \Re$ relating the forces produced due to fluxes applied is assumed to be known. Choose the control inputs in equation (84) to be of the following form.

$$u_0(k) = \frac{-\phi_0(k) + v_0(k)}{T} \tag{88}$$

$$u_\pi(k) = \frac{-\phi_\pi(k) + v_\pi(k)}{T} \tag{89}$$

348

where

Substituting equations (88) and (89) in (84), we get,

$$\begin{bmatrix} \phi_0(k+1) \\ \phi_\pi(k+1) \end{bmatrix} = \begin{bmatrix} v_0(k) \\ v_\pi(k) \end{bmatrix} \quad (92)$$

Substituting equation (92) in (87), we get,

$$F(k+1) = K_{force-flux}[v_0^2(k) - v_\pi^2(k)] \quad (93)$$

We consider the following choices for choosing the control inputs $v_0(k)$ and $v_\pi(k)$.

5.2.1 Mutually Exclusive Scheme

Choose the control to be

$$w(k) = \frac{-F(k+1)}{K_{force-flux}} \quad (94)$$

Now choose the controls $v_0(k)$ and $v_\pi(k)$ in the following manner.

$$w(k) > 0 \quad \longrightarrow \quad \left\{ \begin{array}{l} v_0(k) = \sqrt{w(k)} \\ v_\pi(k) = 0 \end{array} \right. \quad (95)$$

$$w(k) < 0 \quad \longrightarrow \quad \left\{ \begin{array}{l} v_0(k) = 0 \\ v_\pi(k) = \sqrt{|w(k)|} \end{array} \right. \quad (96)$$

5.2.2 Biasing Scheme

Choose the following structure for the controls $v_0(k)$ and $v_\pi(k)$.

$$v_0(k) = v_{bias} + v_{variable}(k) \quad (97)$$

$$v_\pi(k) = v_{bias} - v_{variable}(k) \quad (98)$$

where

$v_{bias} \in \Re$ is a constant biasing input (99)

$v_{variable} \in \Re$ is a varying control input (100)

Note that such a structure for $v_0(k)$ and $v_\pi(k)$ implies that

$$\begin{aligned} K_{force-flux}[v_0^2(k) - v_\pi^2(k)] &= K_{force-flux}[(v_{bias} + v_{variable}(k))^2 - [(v_{bias} - v_{variable}(k))^2] \\ &= K_{force-flux}[4v_{bias}v_{variable}k] \end{aligned} \quad (101)$$

We now choose the control $v_{variable}(k)$ to be

$$v_{variable}(k) = \frac{F(k+1)}{K_{force-flux}v_{bias}} \quad (102)$$

where the control F is chosen to stabilize the rotor motion.

Both these excitation schemes have their advantages and disadvantages. In the *constant biasing* scheme, we note that the force to flux equations become linear. Also by choosing as the control is scaled by v_{bias}, change in force (or equivalently currents) required for a certain net force can be reduced. But maintaining a constant biasing voltage may increase the losses. An alternative might be to use permanent magnets to provide the bias voltage. In the mutually exclusive scheme we provide a force (or current) in only one pole, from a pair, at any time. On the other hand, the force to flux relations are nonlinear.

6 Multiple Sensors & Redundant Actuators

In many situations, we measure the same output with multiple sensors and the measurements have to be averaged in some manner. Similarly, in the case when we have redundant actuators (more than the necessary three orthogonal pairs), we need to apportion the actuation forces in an optimal sense, between all the actuators. Linear least squares theory provides us with a method for doing these [RH88] [Aub79] [J.L55]. In this section we will look at using the least squares estimation schemes for averaging measurements from multiple sensors and splitting the forces among redundant actuators.

6.1 Linear Least Squares

Definition 6.1 *A complete inner product space X is called a Hilbert space.*

Definition 6.2 *Given a Hilbert space X, and a subset $U \in X$, the orthogonal complement of U, denoted by $U^\perp$ is defined as follows.*

$$U^\perp = \{x \in X :< x, u >= 0 \; \forall \; u \in U\} \tag{103}$$

That is, the orthogonal complement of a set $U \in X$ is the set of all vectors in X that are orthogonal to every vector in U.

Theorem 6.1 *Projection Theorem*

Given *(G1) A Hilbert space X.*

If *(I1) $U \in X$ is a closed subspace of X.*

Then *(T1) The Hilbert space X can be decomposed into the direct sum,*

$$X = U \oplus U^\perp \tag{104}$$

Definition 6.3 *Let $U \in X$ be a closed subspace of a Hilbert space X. Decompose a vector $\vec{x} \in X$ into the direct sum $\vec{x} = \vec{x}_0 + \vec{x}_1$ where $\vec{x}_0 \in U$ and $\vec{x}_1 \in U^\perp$. Then $\vec{x}_0$ is called the orthogonal projection of the $\vec{x} \in X$ onto the subspace $U \in X$.*

Theorem 6.2 *Projection Theorem*

Given *(G1) A Hilbert space X.*

G(2) A direct sum decomposition of $X = U \oplus U^\perp$.

G(3) A vector $\vec{x} \in X$.

If *(I1) $\vec{x}_0$ is the orthogonal projection of $\vec{x}$ onto the closed subspace $U \in X$.*

Then *(T1) $\vec{x} - \vec{x}_0$ is the orthogonal projection of $\vec{x}$ onto the close subspace $U^\perp$*

Theorem 6.3 *Minimum Norm*

Given *(G1) A Hilbert space X, and a vector $\vec{x} \in X$.*

(G2) A closed subspace $U \in X$.

If *(I1) $\vec{x}_0$ is the orthogonal projection of $\vec{x}$ onto the subspace U.*

Then *(T1) For each $\vec{u} \in U$,*

$$||\vec{x} - \vec{x}_0|| \leq ||\vec{x} - \vec{u}|| \tag{105}$$

Given two Hilbert spaces X, Y, let the operator A be such that $A : X \to Y$. We now make the following definitions.

Definition 6.4 *The range of $A : X \to Y$ denoted as $\mathcal{R}(A) = \{A[x] \in Y \; \forall \; x \in X\}$.*

Note that the range of A is the set of all vectors in Y that are obtained by the action of the operator A on every element in X. That is, $\mathcal{R}(A) \subset Y$.

Definition 6.5 *The null space of $A : X \to Y$ denoted $\mathcal{N}(A) = \{x \in X : \; A[x] = 0_Y\}$*

Note that the null space of A is the set of all vectors in X that are mapped by A into the zero element of Y. It is clear that $\mathcal{N}(A) \subset X$.

Definition 6.6 *The adjoint of a linear operator $A : X \to Y$, denoted as A^*, is defined as follows.*

- $A^* : Y \to X$
- $< A[x], y >_Y = < x, A^*[y] >_X \; \forall \; x \in X, \; y \in Y$.

where $< \cdot >_X$ is the inner product defined in space X, and $< \cdot >_Y$ is the inner product defined in space Y.

The usefulness of the adjoint operator will become evident in the solution of linear equations. The following properties of the adjoint operator are vital to its use.

- Given an operator on a Hilbert space $A : X \to Y$, and its adjoint $A^* : Y \to X$, it can be shown that
  1. $\mathcal{N}(A) = \mathcal{N}(A^*A)$
  2. $\mathcal{R}(A) = \mathcal{R}(AA^*)$
- Given an operator on a Hilbert space $A : X \to Y$, and its adjoint $A^* : Y \to X$, it can be shown that there exist orthogonal direct sum decompositions of Hilbert spaces X and Y of the following form.
  1. $X = \mathcal{R}(A^*) \oplus \mathcal{N}(A)$
  2. $Y = \mathcal{R}(A) \oplus \mathcal{N}(A^*)$

6.2 Least Squares Solution of $y = A[x]$

Given a linear operator on the Hilbert space $A : X \to Y$, and a specific $y_1 \in Y$, we define the solution of the linear equation $y_1 = A[x]$ as $\{x \in X : y_1 = A[x]\}$.

There are three cases that merit consideration.

- If the operator $A : X \to Y$ is such that the $\mathcal{R}(A) = Y$ and the $\mathcal{N}(A) = \{0_X\}$, then the solution of $y_1 = A[x]$ exists and is unique. The solution is given as $x = A^{-1}[y_1]$. Note that the inverse $A^{-1} : Y \to X$ exists. Such a solution corresponds to a system of linear equations with as many equations as there are unknowns.

- If the operator $A : X \to Y$ is such that the $\mathcal{R}(A) \subset Y$ and the $\mathcal{N}(A) = \{0_X\}$, then we note the following,

$$
\begin{aligned}
y_1 &= A[x] \\
A^*[y_1] &= A^*[A[x]] \\
A^*[y_1] &= A^*A[x]
\end{aligned}
$$

where the operator $A^*A : X \to X$. Note that $\mathcal{N}(A^*A) = \mathcal{N}(A) = \{0_X\}$. This implies that the inverse $(A^*A)^{-1} : X \to X$ exists. The solution therefore can be written as

$$x = (A^*A)^{-1}A^*y_1 \tag{106}$$

There is a simple geometric interpretation of the above result. Given $y_1 \in Y$, there is a unique direct sum decomposition of y_1 as, $y_1 = (y_{11} \in \mathcal{R}(A)) \oplus (y_{12} \in \mathcal{N}(A^*))$. That is, the vector in $\mathcal{R}(A)$ closest to y is the vector $y - y_{12}$. Indeed, the best one could do is to find a solution $x \in X$ such that $A[x] = y - y_{12} = y_{11}$. So we attempt the following solution,

$$
\begin{aligned}
y_1 - y_{12} &= A[x] \\
A^*[y_1 - y_{12}] &= A^*A[x] \\
A^*[y_1] - A^*[y_{12}] &= A^*A[x] \\
A^*[y_1] - 0_Y &= A^*A[x] \\
A^*[y_1] &= A^*A[x] \\
x &= (A^*A)^{-1}A^*[y_1]
\end{aligned}
$$

The solution (106) is called the least-squares solution of the linear equation $y_1 = A[x]$. Such a solution corresponds to an overdetermined set of linear equations.

- Given a linear operator $A : X \to Y$ is such that the $\mathcal{R}(A) = Y$ and the $\{0_X\} \subset \mathcal{N}(A)$, we follow the geometric intuition as follows.

  – Solutions exist as $\mathcal{R}(A) = Y$.

  – Consider any solution $x_i \in X : y_1 = A[x_i]$. This solution has a unique direct sum decomposition of the form $x_i = (x_{i1} \in \mathcal{R}(A^*)) \oplus (x_{i2} \in \mathcal{N}(A))$. Indeed, there is no contribution of $x_{i2} \in \mathcal{N}(A)$ to the solution of $y_1 = A[x]$. Furthermore, as $x_{i1} \in \mathcal{R}(A^*)$, it is true that there exists $w \in Y$ such that $x_{i1} = A^*[w]$. Note that

$$
\begin{aligned}
y_1 &= A[x_i] & (107) \\
&= A[x_{i1} + x_{i2}] & (108) \\
&= A[x_{i1}] & (109) \\
&= A[A^*[w]] & (110) \\
&= AA^*[w] & (111)
\end{aligned}
$$

Now note that $AA^* : Y \to Y$. Also $\mathcal{R}(AA^*) = \mathcal{R}(A) = Y$. This implies that $\mathcal{N}(AA^*) = 0_Y$. This guarantees that $(AA^*)^{-1}$ exists. We therefore solve for w in equation (111) as

$$w = (AA^*)^{-1}y_1 \tag{112}$$

Note that the minimum norm solution is certainly one that does not include elements from $\mathcal{N}(A)$. Therefore, the minimum norm solution of $y_1 = A[x]$ is $x_{i1} = A^*[w] = A^*(AA^*)^{-1}y_1$. This solution corresponds to an underdetermined set of linear equations.

6.3 Least squares solution to multiple sensors and redundant actuators

Let us consider the case when there exists a multiplicity of sensors for the same measurement. Let the actual measurement we are looking for be x and the multiple sensor measurements be $y = Ax$. Then, to get a mean measurement, with minimum error to the actual measurement, corresponds to exactly the overdetermined case in the least squares estimation. The measurement is then given by

$$x = (A^*A)^{-1}A^*[y_1]$$

This $(A^*A)^{-1}A^*$ is indeed the pseudoinverse of the A matrix.

Now consider the case when we have redundant sensors and we are looking for a force split that minimizes the norm of the total force applied. Given forces x produced by the redundant actuators, the net force applied is given by $y = Bx$. Now, given a force to be applied y, splitting it among the redundant actuators with minimum norm, is exactly the underdetermined case derived in the least squares estimation. The solution is given by

$$x = B^*[w] = B^*(BB^*)^{-1}y$$

Note that $B^*(BB^*)^{-1}$ is the pseudoinverse of B.

7   Summary

In this paper we have developed the detailed dynamical equations of a rigid body rotor supported by actively controlled magnetic bearings. We have done this using both *Rotation Matrices* and *Quaternions* to see the equivalence. Quaternions are more convenient to use, as they provide a nonsingular (invertible) transformation to the angular velocity $\vec{w}$. Also euler parameters are computationally as efficient and more compact in storage than rotation matrices. In addition, in developing the model of the magnetic bearing system, we have considered two schemes for pole excitation.

We notice that the model of the bearing system depends on the angular velocity in the spin direction. We have developed a state feedback controller that stabilizes the system for all speeds of rotation. We also note that this controller essentially decouples the system into 2×2 subsystems. We have presented simulation results showing the performance of the controller.

Finally we also present a least squares scheme for minimizing the residual in measurements of output with multiple sensors, and for minimizing the norm of the actuation forces when there are redundant actuators.

References

[AR88]   R.Mukundan A.K.Pradeep, P.J.Yoder and R.J.Schilling. Crippled motion in robots. *IEEE Transactions on Aerospace and Electronic Systems*, 24(1):2–14, 1988.

[AR89]   P.J.Yoder A.K.Pradeep and R.Mukundan. Dual matrix exponentials in robotic kinematics. *International Journal of Robotics Research*, 8(5):57–66, 1989.

[Aub79]   Jean-Pierre Aubin. *Applied Functional Analysis*. Wiley, 1979.

[FK90]   M.Fajita F.Matsumura and K.Okawa. Modelling and control of magnetic bearing systems achieving a rotation around axis of inertia. *Proceedings of 2nd international symposium on magnetic bearing*, 1990.

[J.L55]   J.L.Kelley. *General Topology*. Springer-Verlag, 1955.

[JR90]   R.H.Taylor J.Funda and R.P.Paul. On homogeneous transforms, quaternions and computational efficiency. *IEEE Transactions on Robotics and Automation*, 6(3), 1990.

[K.W86]   K.W.Spring. Euler parameters and the use of quaternion algebra in the manipulation of finite rotations: A review. *Mechanism and Machine Theory*, 21(5):365–373, 1986.

[L.A79]   L.A.Pars. *A Treatise on Analytical Dynamics*. Ox Bow Press, 1979.

[M.V78]   M.Vidyasagar. *Nonlinear Systems Analysis*. Prentice-Hall Electrical Engineering Series. Prentice-Hall, Inc., Englewood Cliffs, N.J., 1978.

[OB79]   O.Bottema and B.Roth. *Theoretical Kinematics*. North-Holland, 1979.

[PP80]   P.Kelland and P.Q.Tait. *Introduction to Quaternions*. Macmillan, 1880.

[RA87]   R.Mukundan and A.K.Pradeep. Comments on the computational aspects of matrix exponentials and their use in robotic kinematics. *IEEE Transactions on automatic control*, AC32(11), 1987.

[RH88]   R.J.Schilling and H.Lee. *Engineering Analysis*. Wiley Interscience, 1988.

[RS94]   Z.Li R.M.Murray and S.S.Sastry. *A mathematical introduction to robotic manipulation*. CRC Press, To appear 1994.

[YCBDB82] C. D. Morette Y. C. Bruhat and M. Dillard-Bleick. *Analysis, Manifolds And Physics*. Elsevier Science Publishers, 1982.

DYNAMIC ANALYSIS OF A MAGNETIC BEARING SYSTEM
WITH FLUX CONTROL

Josiah Knight

Thomas Walsh

Lawrence Virgin

Department of Mechanical Engineering
and Materials Science
Duke University
Durham, NC

SUMMARY

Using measured values of two-dimensional forces in a magnetic actuator, equations of motion for an active magnetic bearing are presented. The presence of geometric coupling between coordinate directions causes the equations of motion to be nonlinear. Two methods are used to examine the unbalance response of the system: simulation by direct integration in time; and determination of approximate steady state solutions by harmonic balance. For relatively large values of the derivative control coefficient, the system behaves in an essentially linear manner, but for lower values of this parameter, or for higher values of the coupling coefficient, the response shows a split of amplitudes in the two principal directions. This bifurcation is sensitive to initial conditions. The harmonic balance solution shows that the separation of amplitudes actually corresponds to a change in stability of multiple coexisting solutions.

INTRODUCTION

In the short time since the introduction of practical magnetic levitation for rotating shafts, significant progress has been made in designing and modelling the performance of magnetic bearings, to the point where they are practical for a variety of applications. These include machine tool spindles, pumps, compressors, gyroscopes and momentum wheels [1]. Some applications, those with significant rotor flexibility and coordinate cross coupling, present difficult challenges, however. In this category fall some pumps and many compressors and turbines, including gas turbines. Recent papers, such as those of Williams, et al. [2], Lee and Kim [3], and Nonami, et al.[4] have confronted limitations of vibration control at high speeds for flexible rotors using magnetic bearings. Rotor dynamic stability and robust vibration control in these machines will increasingly depend on an understanding of the system dynamics that goes beyond traditional linear models.

This paper presents equations of motion and simulations of a two-degree-of-freedom system subject to forces from an actively controlled magnetic actuator, where the control is linear but the forces from the actuator include coordinate coupling of a form found in experimental measurements. The resulting equations are nonlinear and coordinate-coupled, and the response contains several features found only in nonlinear systems.

ACTUATOR FORCES

A schematic of an active magnetic bearing is shown in Figure 1. It consists of two opposed pairs of electromagnets arranged around a shaft. Each of the magnet pairs will be controlled independently. The control is linear, taking as input the shaft displacement along the

axis of the magnet pair, and producing as output a variation of the magnetic flux B. This type of control is an idealization from the practical case, where control is more easily exerted on either the current or the voltage applied to the magnet coils.
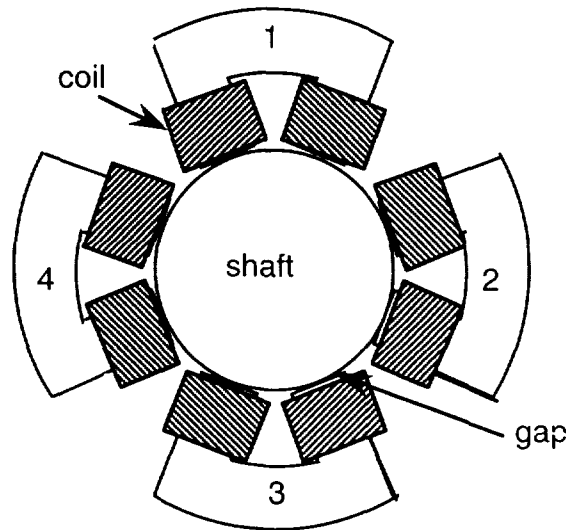
Figure 1. Magnetic bearing actuator. Sensors and control not shown.

The force between a magnet and a ferromagnetic part is the negative of the derivative of magnetic field energy with respect to virtual displacement of the part. The traditional model for forces from a magnetic actuator in a magnetic bearing is based on one-dimensional magnetic circuit theory, in which it is assumed that the lines of magnetic flux cross the air gaps of the bearing in straight lines. It is generally assumed that the direction of the force is along the axis of symmetry of the magnet. In a previous paper [5] measurements were described in which the forces from a magnet with curved pole faces acting on a circular shaft had both an attractive component and a component normal to the axis of the magnet when the shaft was given a displacement away from this symmetry axis. The ratio of forces was found approximately proportional to the normal coordinate.

In the calculations that follow, both principal forces and normal forces are assumed to act. The principal force from each magnet is modelled by this one-dimensional circuit theory, in which

$$F_p = \frac{aB^2}{\mu_o}$$ (1)

where   a = pole cross section area
             B = magnetic flux

             μ_o = permeability of free space

Often the flux is written as a function of the coil current i, wire turns N and gap h, leading to

$$F_p = \frac{\mu_o(Ni)^2 a}{4h^2}$$ (1a)

354

In the present work, the controlled quantity is assumed to be the flux B, so Equation (1) will be used to model the attractive force between each magnet and the shaft

Based on the measurements of [5], the normal force is considered to be

$$F_n = \alpha F_p \qquad (2)$$

where the coupling parameter α is empirical. The directions p,n correspond to directions x,y or y,x as appropriate for each magnet.

Linear Flux Control

Consider the case in which a point mass is acted on by two opposed magnet pairs, shown schematically in Figure 1. In an attempt to linearize the system so that the mass effectively is subject to a linear restoring force like a spring stiffness, a large bias flux B_b is introduced in each magnet gap, and a control flux B_c is superposed. If the bias flux is equal in both magnets of the vertically oriented pair

$$B_{1b} = B_{3b} = B_b \qquad (3)$$

This constitutes the special case in which the bearing is not required to support a steady load, as in a vertically oriented machine.

If the control flux is made equal in magnitude but opposite in sign in the two magnets

$$B_{1c} = -B_{3c} = B_c \qquad (4)$$

then the resultant force in the y direction

$$F_{y\,(1,3)} = \frac{a}{\mu_o}\left[(B_{1b} + B_{1c})^2 - (B_{3b} + B_{3c})^2\right] \qquad (5)$$

is linear in the control flux

$$F_{y\,(1,3)} = \frac{4a}{\mu_o} B_b B_c \qquad (6)$$

Coordinate Coupling

The approach above ignores the normal force found by experiment and calculation. This normal force results in the need for control in the x direction as well. Suppose that an additional magnet pair is placed on the x axis, subject to the same bias and control flux as the y-direction pair. For instance, let the control flux in each magnet be proportional only to the distance from that magnet, neglecting for the present any derivative control. That is

$$B_c = - \kappa B_b x_p \qquad (7)$$

where the subscript p denotes the principal axis, the axis of symmetry of the magnet.

Then, adding all the forces in the x direction

$$F_x = \frac{-4aB_b^2}{\mu_o}\left[\kappa x - \frac{\alpha}{2}x\left(1 + \kappa^2 y^2\right)\right]$$

(8)

Similarly, the y direction force is

$$F_y = \frac{-4aB_b^2}{\mu_o}\left[\kappa y - \frac{\alpha}{2}y\left(1 + \kappa^2 x^2\right)\right]$$

(9)

It is seen that the coordinate coupling embodied in the parameter α has two effects: it obviously yields a force normal to the displacement, but it also attenuates the restoring force, reducing the effective stiffness. Both these effects occur even though the independent-axis control algorithm is assumed perfect in its ability to give a linear stiffness characteristic in the principal direction.

The forces given by Equations (8) and (9) are derivable from a potential energy function

$$v = \frac{4aB_b^2}{\mu_o}\left[\left(\frac{\kappa}{2} - \frac{\alpha}{4}\right)\left(x^2 + y^2\right) - \frac{\alpha}{4}\kappa^2 x^2 y^2\right]$$

(10)

This quantity may be rendered dimensionless

$$V = \left(\frac{K}{2} - \frac{A}{4}\right)\left(X^2 + Y^2\right) - \frac{A}{4}K^2 X^2 Y^2$$

(10a)

using the parameters

$$K = \kappa c \qquad\qquad A = \alpha c$$

$$X = x/c \qquad\qquad Y = y/c$$

(11)

$$V = v\,\frac{\mu_o}{4aB_b^2 c}$$

Figure 2 contains plots of the dimensionless potential energy at different levels of the coupling parameter A [6]. The attenuation of principal stiffness with increasing A is evidenced by the decrease in amplitude of the potential, and the normal forces are evidenced by the tendency of the potential surface to sag along lines at 45° to the principal axes. One way to consider the implications of these plots is to visualize them as solid surfaces upon which a mass in the shape of a small sphere might roll if given an initial velocity and/or displacement from the origin. This is a physical analog to the free vibration of a mass subject to the force equations given above.

356
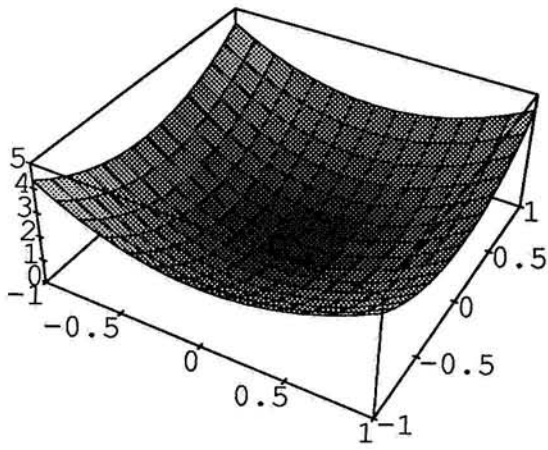
K=5, A=0.1
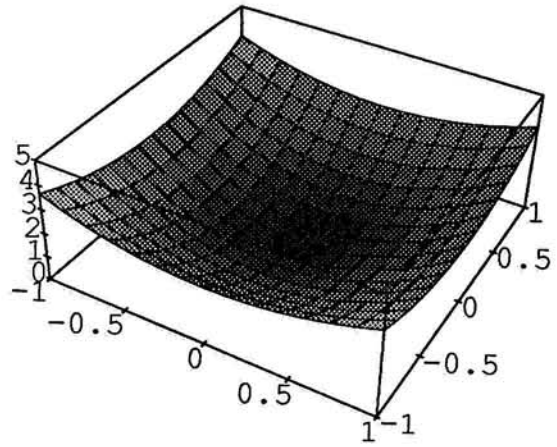
K=5, A=0.2
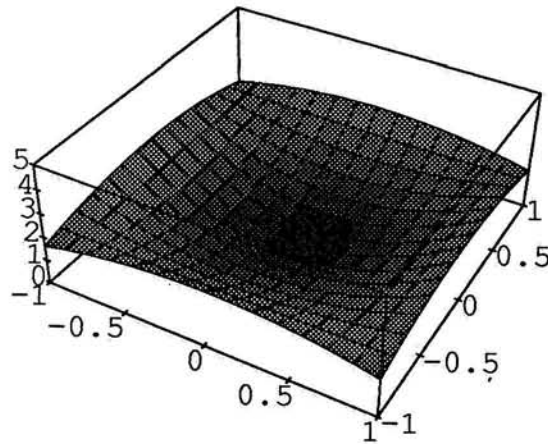
K=5, A=0.5

Figure 2. Potential energy for different degrees of coupling.

357

FORCED RESPONSE

If a derivative feedback is added to the proportional feedback

$$B_c = -\kappa B_b x_p - \gamma B_b \dot{x}_p \tag{12}$$

the force equations

$$F_x = \frac{2aB_b^2}{\mu_o}\left[-2\kappa x + \alpha x\left(1 + \kappa^2 y^2\right)\right] - 2\gamma\dot{x} + 2\alpha\kappa\gamma x y\dot{y} + \alpha\gamma^2 x\dot{y}^2 \tag{13}$$

$$F_y = \frac{2aB_b^2}{\mu_o}\left[-2\kappa y + \alpha y\left(1 + \kappa^2 x^2\right)\right] - 2\gamma\dot{y} + 2\alpha\kappa\gamma y x\dot{x} + \alpha\gamma^2 y\dot{x}^2 \tag{14}$$

show a coupling of the proportional and derivative terms in each coordinate, as well as a coupling of both these terms to the other position coordinate.

Consider a mass m subject to the above actuator forces in addition to an unbalance forcing function. Newton's second law is written for each of the coordinate directions, with the resulting equation of motion in x as

$$m\ddot{x} = \frac{-4aB_b^2}{\mu_o}\left[\kappa x - \frac{\alpha}{2}x\left(1 + \kappa^2 y^2\right) + \gamma\dot{x} - \alpha\kappa\gamma x y\dot{y} - \frac{1}{2}\alpha\gamma^2 x\dot{y}^2\right] + me\omega^2\cos\omega t \tag{15}$$

or

$$m\ddot{x} = \frac{-4aB_b^2}{\mu_o}\left[\kappa x + \gamma\dot{x} - \frac{\alpha}{2}x\left(1 + \kappa^2 y^2 + \alpha\kappa\gamma y\dot{y} + \frac{1}{2}\alpha\gamma^2\dot{y}^2\right)\right] + me\omega^2\cos\omega t \tag{16}$$

and in y

$$m\ddot{y} = \frac{-4aB_b^2}{\mu_o}\left[\kappa y + \gamma\dot{y} - \frac{\alpha}{2}y\left(1 + \kappa^2 x^2 + \alpha\kappa\gamma x\dot{x} + \frac{1}{2}\alpha\gamma^2\dot{x}^2\right)\right] + me\omega^2\sin\omega t \tag{17}$$

By choosing the additional nondimensional parameters

$$K = \kappa/c \qquad\qquad E = e/c$$

$$T = t\omega_n \qquad\qquad \Gamma = \gamma c\omega_n$$

$$\Omega = \omega/\omega_n \qquad\qquad \omega_n = \sqrt{\frac{4a\kappa B_b^2}{m\mu_o}} \tag{18}$$

the system of equations can be nondimensionalized. Here, ω_n is the natural frequency the system would have if there were no coupling present ($\alpha = 0$). As Equation (10) indicates, for any positive value of α, the actual natural frequency will be reduced from this value.

358

The nondimensional forms of the equations are

$$X'' = -\frac{1}{K}\left(KX + \Gamma X' - \frac{A}{2}X\left(1 + K^2 Y^2 + 2K\Gamma YY' + \Gamma^2 Y'^2 \right)\right) + E\Omega^2 \cos\Omega T \qquad (19)$$

$$Y'' = -\frac{1}{K}\left(KY + \Gamma Y' - \frac{A}{2}Y\left(1 + K^2 X^2 + 2K\Gamma XX' + \Gamma^2 X'^2 \right)\right) + E\Omega^2 \sin\Omega T \qquad (20)$$

where $'$ and $''$ indicate differentiation with respect to dimensionless time T. These equations may be integrated in time after assigning values to the system parameters K, Γ, A and E, along with appropriate initial conditions for all of the quantities X, Y, X' and Y'. It should also be noted that the forms of the forcing function in the final terms of Equations (19) and (20) also constitute initial conditions, in the form of an assumed phase angle for the forcing function at T = 0.

ANALYSIS

Two methods are used to examine the response of the system to unbalance forcing: numerical integration from arbitrary initial conditions using a fourth-order Runge-Kutta algorithm: and approximate calculation of steady state solutions by the harmonic balance method.

Natural Frequency

Because the potential energy of the system as shown in Figure 2 is not described by a surface of revolution, the natural frequency of the system depends on the initial conditions. If initial conditions of finite displacements and zero velocities are chosen, the period of oscillation in free vibration is a function of the displacements, or alternatively, of the radius and angle of the initial conditions. Figure 3 indicates this dependence. The results were obtained by direct numerical integration, and dissipation was not included. Part (a) shows the period as a function of radius for a fixed angle from the x-axis (22.5°) and part (b) shows the effect of the angle of the initial condition for a fixed radius (0.5). The two periods both increase with radius, a characteristic of systems with softening stiffness. The period in Y is different from that in X because the path of the oscillation does not in general pass through the origin. There is a single period only when the initial conditions lie along a line at 45° to the two axes, as shown in Figure 3b.

(a) Fixed angle from x axis   (b) Fixed radius
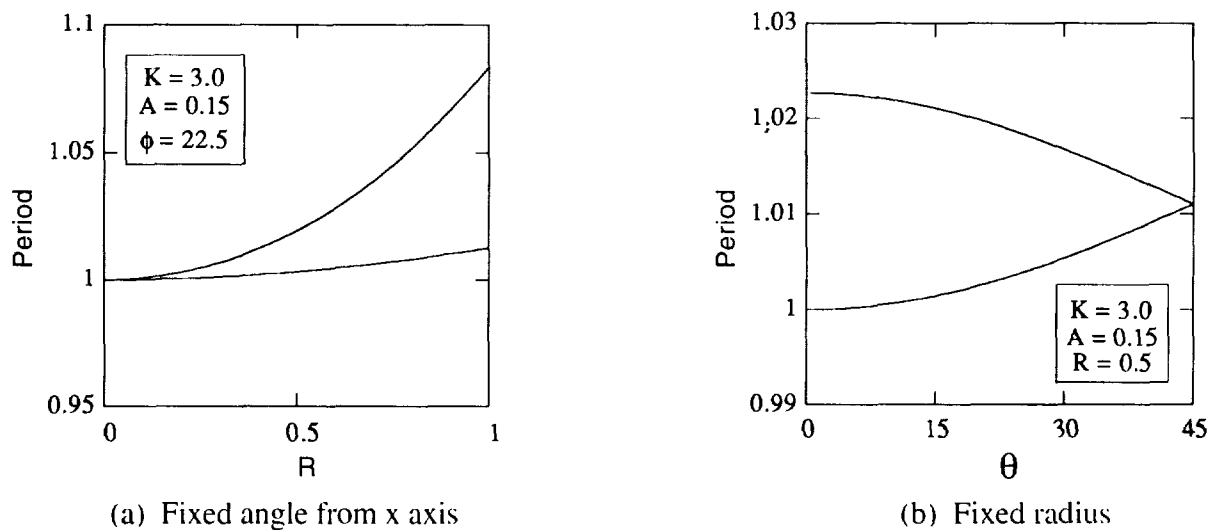
Figure 3. Effect of Initial Conditions on Natural Period

When the derivative control coefficient Γ is made finite so the system dissipates energy, the response of the system to unbalance forcing can be calculated. The effects of three parameters are examined: K, Γ, and A.

The proportional control coefficient K determines how rapidly the flux, and thereby the force, from a magnet is reduced as the shaft approaches that magnet. A value of K=1 would cause the flux to be reduced to zero at contact (not counting the contribution from the derivative control coefficient Γ). Larger values of K would correspond to "stiffer" bearings. Because of the form of nondimensionalization of Equations (19) and (20), however, an increase in K while holding Γ constant causes a decrease in the effective dissipation coefficient, by virtue of a change in the natural frequency. This must be considered when interpreting the results of parametric studies, since a straightforward increase in the dimensional quantity κ (1/m) would not affect the dissipation, or derivative control, coefficient. The fact that K cannot be eliminated from the equations of motion is a result of the essential nature of nonlinear systems.

The measurements of [5] indicate that A=0.15 is a reasonable value for the coordinate coupling coefficient A. In the calculations below, A is varied from 0.05 to 0.25.The values of Γ were chosen to provide dissipation of the same order as in a linear system having damping ratios between 0.1 and 0.3 . In all the results presented here, the unbalance magnitude is E=0.1 .

Studies examining large ranges of parameter combinations are planned but are beyond the scope of the present work. Nevertheless, much can be learned from a limited parametric study.

Figure 4 shows the effect of increasing the coefficient K from 1.0 in part a to 3.0 in part b to 5.0 in part c. As noted above, increasing K alone results in a smaller value of the derivative control coefficient. With this in mind, Figure 4 still indicates an important feature of the system: that for some combinations of parameters, the response exhibits a split, with the motion on one axis having a much higher amplitude than that on the other axis. Associated with this split is a sudden jump in one of the amplitudes as the frequency is increased. In fact, one of the solutions of Figure 4c extends beyond an eccentricity of 1.0, which in the physical case would result in solid contact. At some frequencies near the natural frequency, however, two solutions exist that are both within the physical bounds of the system. Furthermore, the solutions are dependent on the initial conditions. For the case shown, the integration begins with both shaft position and velocity equal to zero. The numerical integration proceeds until all transients have decayed and the peak amplitudes in the two directions are sampled. The forcing function, the final terms in Equations (19) and (20), also imposes an implicit initial condition by virtue of its assumed phase. In fact, the cosine portion of the forcing function begins with a step imposition of force at time t=0, although all transients associated with this discontinuity have decayed before the amplitudes are sampled. If, however, the cosine and sine parts of the force are exchanged, the solutions for X and Y are also found to have exchanged places. This is in marked contrast to a linear system, where the amplitude is unique after transients have decayed.
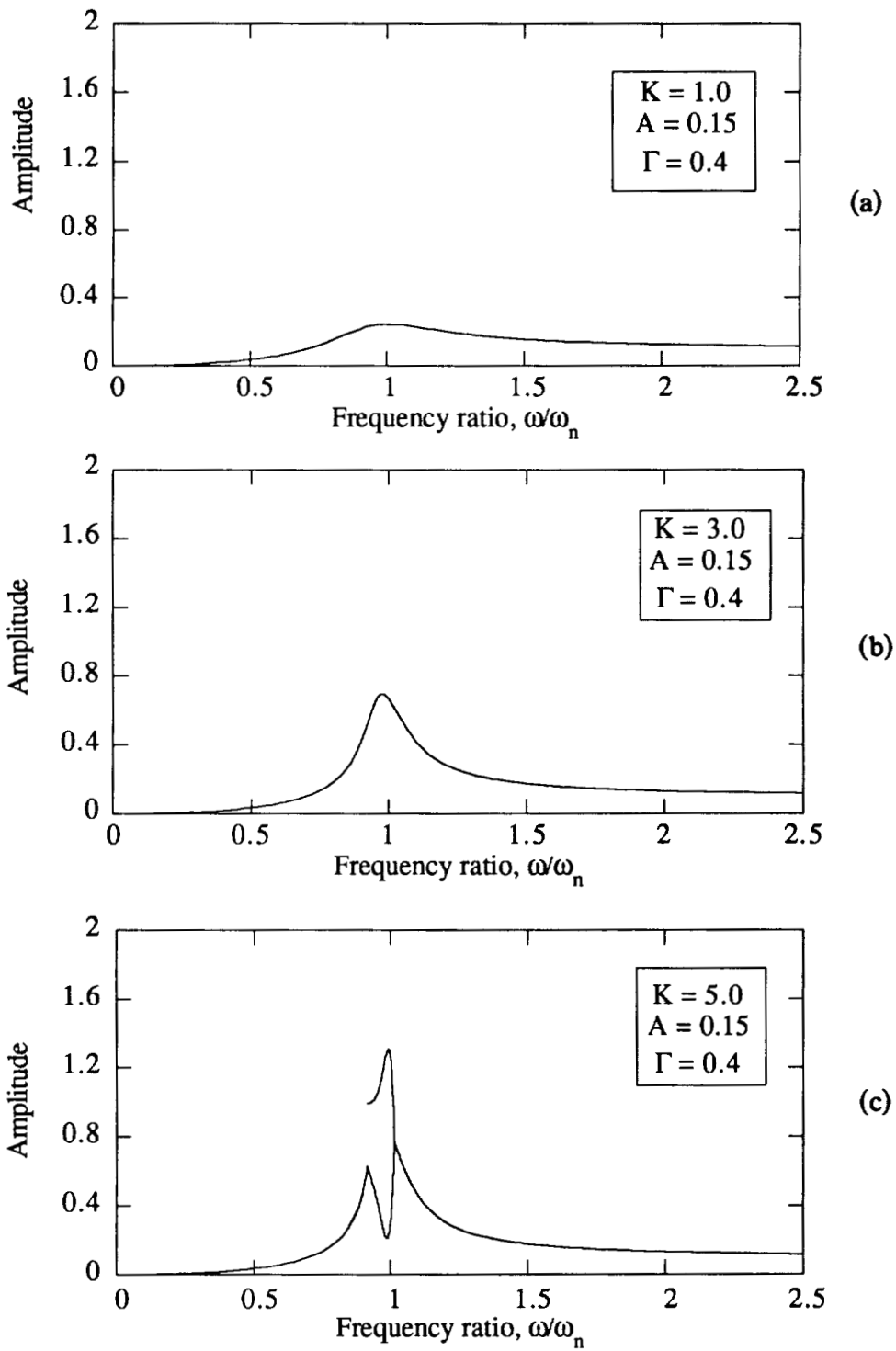
Figure 4. Effect of variation in dimensionless proportional control coefficient K.

The effect of the coupling parameter can also be examined. Figure 5 illustrates the effect of increasing the value of A, while K is held constant at 0.3. The values of all parameters except A are equal to those of the case shown in Figure 4b. As A is increased beyond a threshold value, between 0.15 and 0.25, multiple solutions appear near the natural frequency. In this set of plots, the natural frequency is a constant, making this parametric variation somewhat easier to interpret than the previous one.

Reduction of the derivative control coefficient Γ can also bring about a situation with multiple solutions, as shown in Figure 6, as can an increase of the unbalance eccentricity, not shown.

Thus, the bifurcation seems mostly to be an amplitude-driven phenomenon, such that when a critical amplitude is exceeded, the solutions split. In all cases, the split is initial-condition-dependent.

Solution by Harmonic Balance

Another approach to examining the steady-state response of a nonlinear system is the harmonic balance method, which is approximate but analytical rather than numerical. It has the advantage that both stable and unstable solutions can be located, whereas numerical integration can locate only stable solutions.

The method consists of assuming steady solutions of the form

$$X = C \cos\Omega T + D\sin\Omega T \tag{21}$$

$$Y = G \cos\Omega T + H\sin\Omega T \tag{22}$$

where C, D, G, and H are to be determined. Equations (21) and (22) are differentiated and substituted into the equations of motion. The resulting powers of trigonometric functions are expanded using trig identities, after which the harmonics higher than 1 are neglected. Because the truncation of higher harmonics is not performed until after the powers of trig functions are expanded, the solution retains its nonlinear character, although the equations have been approximated. The resulting four algebraic equations for the constants C, D, G, and H are coupled and highly nonlinear and must themselves be solved by a numerical Newton-Raphson iteration [6]. When the constants are found, the steady amplitudes can be calculated readily.

Figure 7 shows the amplitudes obtained by harmonic balance for the case corresponding to Figure 5a. These results indicate that in the neighborhood of the natural frequency, four solutions actually exist. (Two are identical.) Two of the solutions are apparently unstable, but the harmonic balance method does not yield stability characteristics. Based on the results of numerical integration, however, it appears that the solutions corresponding to equal amplitudes for X and Y are unstable when they lie between the unequal solutions. Thus the jump in one of the amplitudes stems from a change in that solution's stability. Where the equal-amplitude solutions lie below the unequal solutions, they are the stable ones. The unequal solutions are believed to exist at all frequencies, but are difficult to locate by Newton-Raphson beyond the range that is shown.
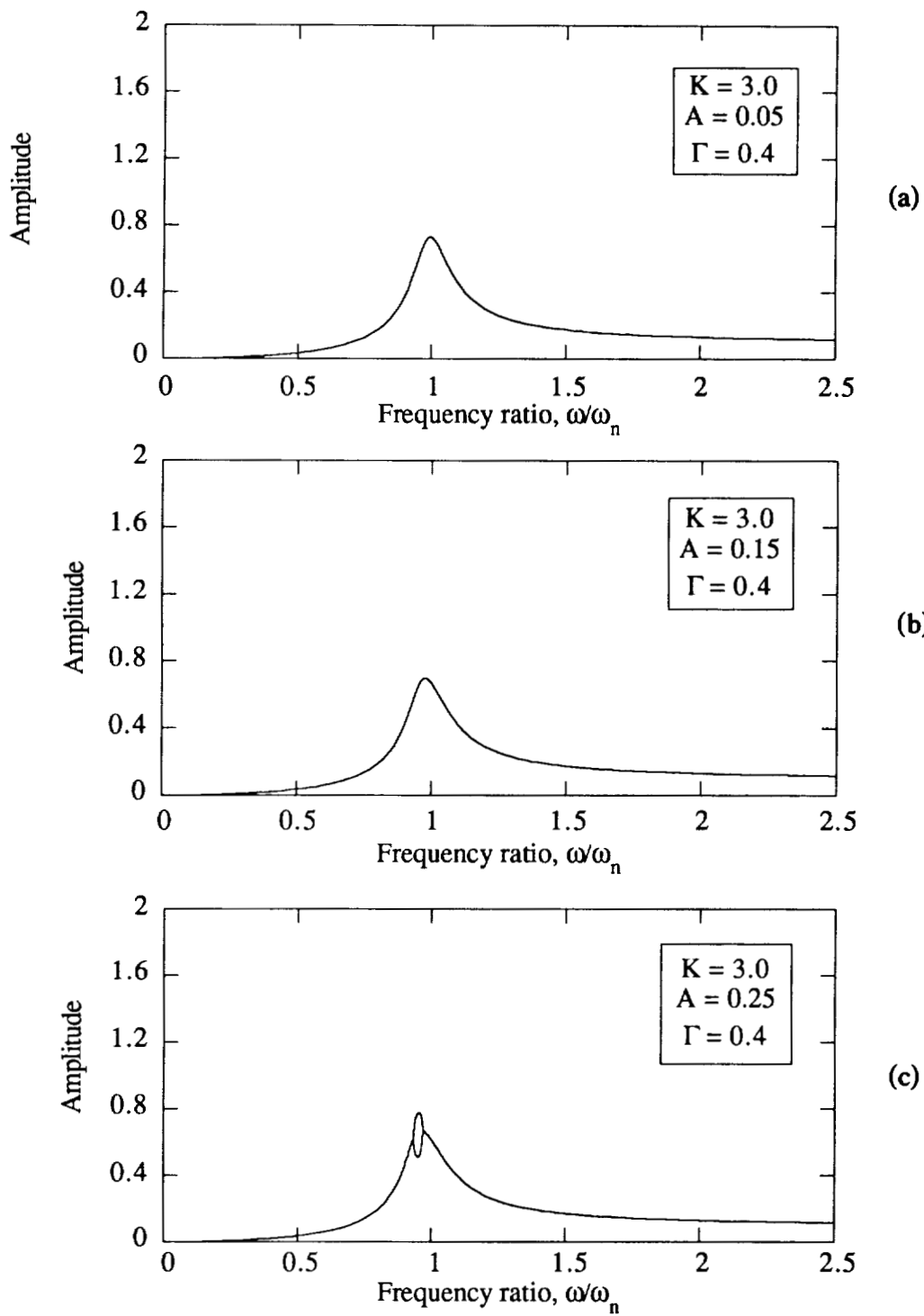
Figure 5. Effect of variation in coupling parameter A.
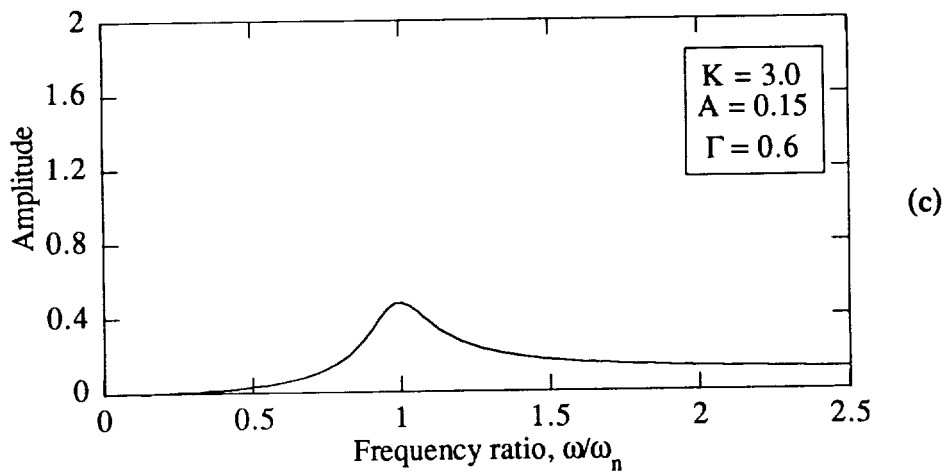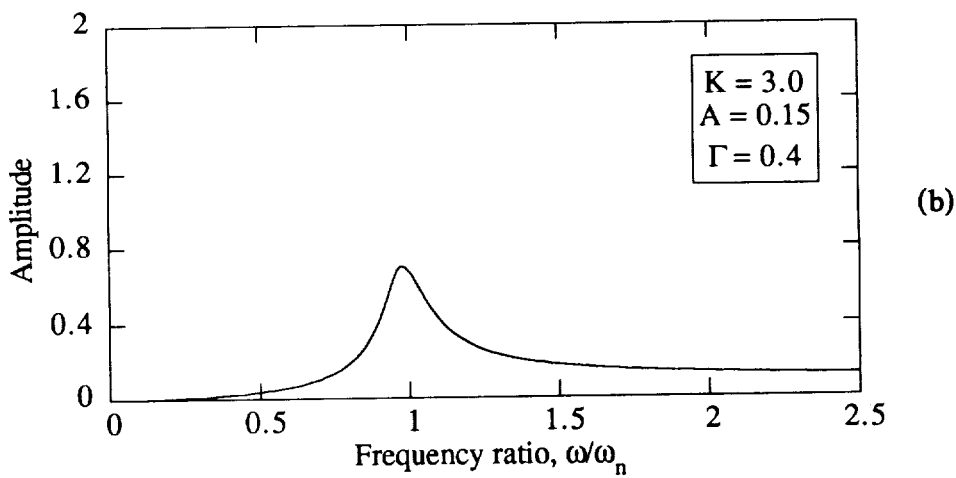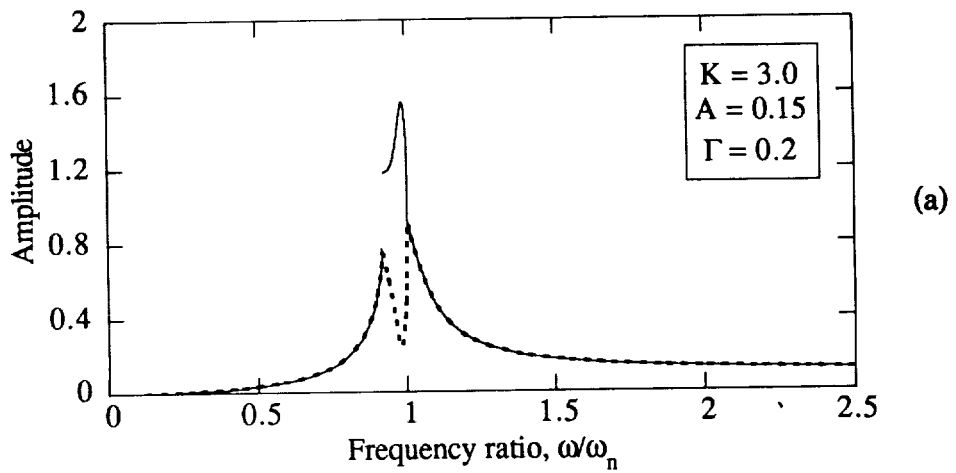
Figure 6. Effect of variation in derivative control coefficient Γ.
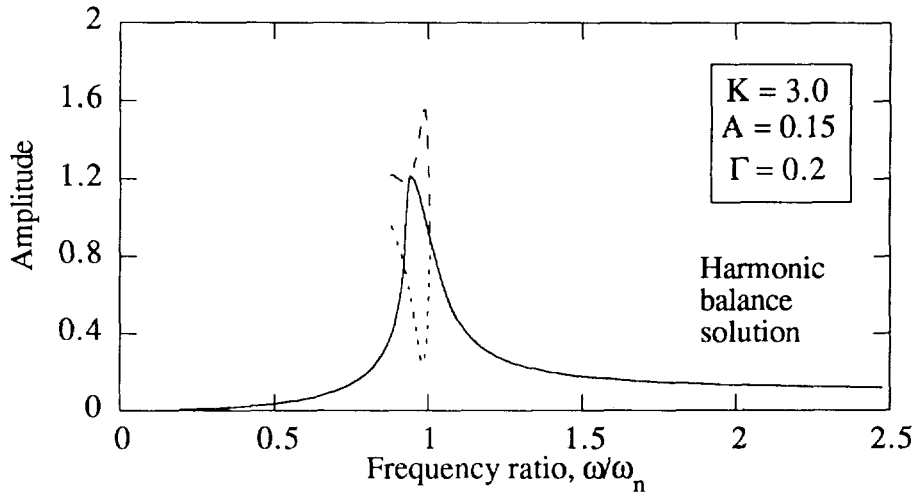
Figure 7. Multiple coexisting solutions by harmonic balance method.

The close correspondence between the numerical and analytical results supports the validity of both methods. Neither method alone is sufficient for a complete understanding, however, because the numerical solutions are dependent on initial conditions, and the analytical solutions provide no information on stability.

The numerical integration can in fact be used to track the unstable solutions to a very limited extent by careful choice of initial conditions, as shown in Figure 9 by the parts of the curves labelled "alternate solution". These initial conditions are based on the harmonic balance results, and tend further to support the validity of both methods.
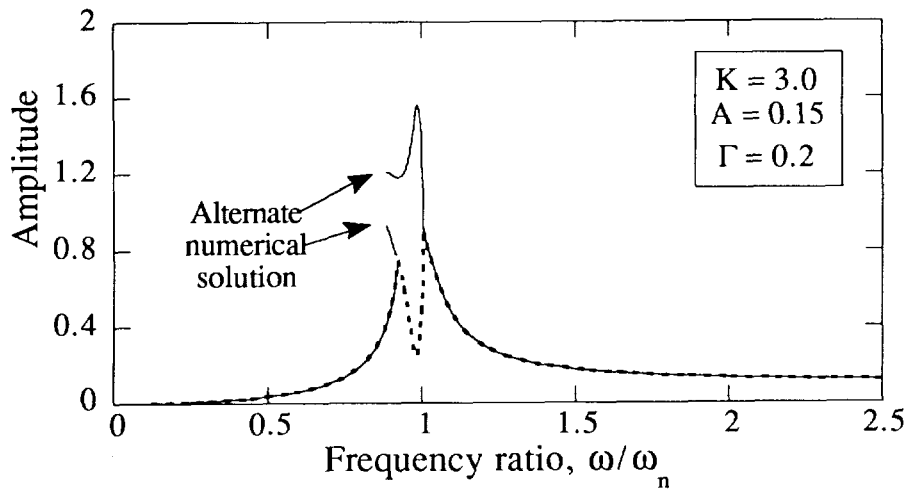
Figure 8. Limited unstable solution-following by numerical integration.

CONCLUSIONS

Equations of motion and limited parametric studies are presented for the case of a magnetic bearing subject to flux control, with geometric coordinate coupling. There are two effects of the coupling parameter on the system potential energy: a reduction of the principal stiffness, and introduction of a nonlinear normal stiffness.

The equations of motion are nonlinear and exhibit behavior that is distinctly different from that of linear systems. In forced response, the amplitudes of the system show bifurcations that are the result of changes in stability of multiple coexisting solutions. The stability seems mostly to be amplitude dependent, and the critical amplitude is a function of several parameters: K, Γ, and A.

In the long term, successful implementation of magnetic bearings where large eccentricities may be encountered will depend on a deeper understanding of the nonlinear characteristics of the combined rotor-actuator-control system.

REFERENCES

1. O'Connor, L. "Active Magnetic Bearings Give Systems a Lift'" Mechanical Engineering, V. 114, No. 7, pp. 52-57.

2. Williams, R. D., Keith, F. J., and Allaire, P. E., "A Comparison of Analog and Digital Controls for Rotor Dynamic Vibration Reduction through Active Magnetic Bearings," Journal of Engineering for Gas Turbines and Power, V. 113, No. 4, pp.535-543.

3. Lee, C. W., and Kim, J. S., "Modal Testing and Suboptimal Vibration Control of Flexible Rotor Bearing System by Using a Magnetic Bearing," Journal of Dynamic Systems, Measurement, and Control, V. 114, No. 2, pp. 244-252.

4. Nonami, K., Yamanaka, T., and Tominaga, M., "Vibration and Control of a Flexible Rotor Supported by Magnetic Bearings," JSME International Journal, Series III, V. 33, No. 4, pp. 475-482.

5. Knight, J. D., Xia, Z., and McCaul, E. B., "Forces in Magnetic Journal Bearings: Nonlinear Computation and Experimental Measurement," Proceedings of 3rd International Symposium on Magnetic Bearings, Alexandria, VA, 1992, P. E. Allaire, ed.

6. Walsh, T. F., "Nonlinear Dynamic Analysis of a Magnetic Bearing System with Flux Control: The Effects of Coordinate Coupling'" M. S. Thesis, Duke University, 1993.

SOME FURTHER DEVELOPMENTS IN THE
DYNAMIC MODELLING AND CONTROL OF THE
LARGE ANGLE MAGNETIC SUSPENSION TEST FIXTURE

Colin P. Britcher, Lucas E. Foster

Department of Aerospace Engineering

Old Dominion University

Norfolk, VA

SUMMARY

A small-scale laboratory magnetic suspension system, the Large Angle Magnetic Suspension Test Fixture (LAMSTF) has been constructed at NASA Langley Research Center. This paper first presents some recent developments in the mathematical modelling of the system, particularly in the area of eddy current effects. It is shown that these effects are significant, but may be amenable to modelling and measurement. Next, a theoretical framework is presented, together with a comparison of computed and experimental data. Finally, some control aspects are discussed, together with illustration that the major design objective of LAMSTF - a controlled 360° rotation about the vertical axis, has been accomplished.

INTRODUCTION

In order to explore and develop technology required for the magnetic suspension of objects over large ranges of orientation, a small-scale laboratory development system, the Large Angle Magnetic Suspension Test Fixture (LAMSTF) has been constructed at NASA Langley Research Center. Possible applications for magnetic suspension systems of this general class include space payload pointing and manipulation, microgravity vibration isolation and wind tunnel model suspension [1]. An important objective of this particular project is to investigate the dynamic modelling of large-gap magnetic suspension systems, so that future systems can be designed with higher confidence levels.

HARDWARE DESCRIPTION

The general configuration [2] is illustrated in Figures 1,2. An array of five, room temperature, copper electromagnets are equally spaced on a 13.77 cm radius. The coils are wound with 509 turns of AWG 10 enamelled copper wire on bakelite forms, with mild steel cores. The electromagnets are mounted on an aluminum plate 1.27 cm thick. Each electromagnet is driven by a transistor switching power amplifier, rated at ±150 V and ±30 A continuous, with four-quadrant operation.

The suspended element consists of 16 wafers of Neodymium-Iron-Boron permanent magnet material, each 0.851 cm in diameter and 0.3175 cm thick, epoxied into an aluminum tube, 5.32 cm long and 0.9525 cm outside diameter. The total mass of the suspended element is 22.5 grams and the moment of inertia about tranverse axes

is 5.5×10^{-6} kg.m^2. The direction of magnetization is along the axis of the cylinder, which is horizontal when suspended. The nominal magnetization is 954,930 A/m (1.2 Tesla), although measurements have indicated a slightly lower working value. The suspension height is 0.1m, measured from the axis of the suspended element to the top plane of the electromagnet conductor.

The position sensing system consists of multiple light beams, arranged in the vertical and horizontal planes, partially interrupted by the suspended element. The light sources are miniature infra-red light-emitting diodes, intended for use with fiber-optics, with collimating lenses added. The light receivers are matching infra-red phototransistors, with focussing lenses added. The complete sensor system is mounted on a framework which can be rotated by hand about a vertical axis. A schematic diagram of the sensor assembly is shown in Figure 3.

Several different control systems have been developed and demonstrated, including a simple analog version with phase-advance ("lead") compensation [2], a first-generation digital controller, generated using the bilinear (Tustin's) transformation [3,4], a decoupled PD controller [5], and LQR and LQG designs [4].

EDDY CURRENT EFFECTS IN LAMSTF

Introduction

Whenever a time-varying magnetic flux penetrates a conducting medium, eddy-currents will be generated. In the case of LAMSTF, the principal time variation is due to the necessary control forces and torques being generated by fluctuating electromagnet currents, since the system is open-loop unstable. In the original design, eddy-current circuits were deliberately introduced in three main areas, as illustrated in Figure 4 :

1) Position sensor structure,   2) Electromagnet cores,   3) Aluminum baseplate

This was done so that it would be necessary to measure, analyze and model the eddy current effects, rather than attempting to avoid their influence, as is the usual practice. The fact that stable suspension was initially achieved rather easily [2] was taken to indicate that the eddy current effects were not very significant. However, a consistent discrepancy has been found in the dynamic behaviour in the "pitch" degree-of-freedom, illustrated in Figure 5 [3,4]. In consequence, an analysis and modelling effort has now been undertaken.

Eddy Current Modelling

A simplified analysis can be employed to assess the effects of eddy currents in LAMSTF. The two key assumptions are some a priori knowledge of the geometry of the eddy current circuit and that the circuit geometry be independent of frequency. The first assumption might require that the eddy currents be constrained to flow around well-defined paths, such as the position sensor structure here, rather than through large plates or shells of conducting material. Alternatively, the circuit geometry must be relatively simple and predictable. The second assumption requires that the "skin depth" be much greater than the local material thickness. The skin depth is given by the following formula [6] :

$$d = \sqrt{\left(\frac{2}{\mu_o \, \mu_r \, \sigma \, \omega} \right)} \quad \text{or} \quad \sqrt{\left(\frac{2 \, \rho}{\mu_o \, \mu_r \, \omega} \right)} \quad \text{- (1)}$$

- where d = Skin depth, μ = Permeability, $\rho = 1/\sigma$ = Resistivity, ω = angular frequency. In the case of LAMSTF, the natural frequencies of the suspended element are rather low, of the order of 10Hz or less. For an aluminum conductor, the value at 10Hz would be around 28mm, much greater than the typical material thickness in LAMSTF. The only exceptions are the iron electromagnet cores, although it is found later that their influence is confined to higher frequencies.

If both of the above assumptions are satisfied, the resulting model corresponds to that commonly described in literature as the Single Time Constant Model. The derivation resembles the analysis of a transformer with a shorted secondary, as illustrated in Figure 6 :

$$V = IR + L\frac{dI}{dt} + L_{m_1}\frac{dI_{e_1}}{dt} + L_{m_2}\frac{dI_{e_2}}{dt} + \cdots \qquad -(2)$$

$$0 = I_{e_1}R_{e_1} + L_{e_1}\frac{dI_{e_1}}{dt} + L_{m_1}\frac{dI}{dt} \qquad -(3)$$

- where R_{e_n}, L_{e_n} are the resistance and inductance of the n'th eddy current circuit and L_{m_n} is the mutual inductance between the primary (the electromagnet coil) and the eddy current circuit. Note that mutual inductances between multiple eddy current circuits are neglected. The terminal characteristics of the primary (driven coil) can be found by combining these two equations :

$$\frac{I}{V} = \left(\frac{1}{(R + Ls) - \dfrac{(L_{m_1}s)^2}{R_{e_1} + L_{e_1}s} - \cdots} \right) \qquad -(4)$$

One special case is of interest here. Suppose that :

$$L = \alpha L_{e_1} \ (\ 0 \leq \alpha \leq \infty \ ) \quad \text{and} \quad L_{m_1} = \beta \sqrt{(L \ L_{e_1})} \ \ (\ 0 \leq \beta \leq 1) \qquad -(5)$$

then :
$$\frac{I}{V} = \left(\frac{1}{(R + Ls) - \dfrac{\beta^2\alpha \ (L_{e_1}s)^2}{R_{e_1} + L_{e_1}s} - \cdots} \right) \qquad -(6a)$$

but if $R_{e_1} \rightarrow 0$ or $s \rightarrow \infty$:
$$\frac{I}{V} = \left(\frac{1}{R + Ls \ (1\text{-}\beta^2)} \right) \qquad -(6b)$$

This indicates that a non-dissipative (reactive) secondary effectively "turns off" part of the primary inductor. Continuing, the field components generated (at the suspended object) can be expressed as :

$$B_j = K_jI + K_{e_1}I_{e_1} + \cdots = K_jI\left(1 - \frac{K_{e_1} L_{m_1} s}{K_j \ (R_{e_1} + L_{e_1}s)} - \cdots \right) \qquad -(7)$$

where K_j, K_{e_n} are constants representing the field generated at the suspension location by the electromagnet and the n'th eddy current respectively. Now the factor K_{e_n} will, in general, be different for each field component, that is each individual eddy current will

affect each field component by a different proportion. Therefore the eddy current effects in a system involving several electromagnets and eddy current circuits should be represented as follows :

$$[B_j] = [K_j] \, [I] + [K_{j_e}] \, [I_e] \qquad - (8)$$

- where $[B_j] = (B_x \; B_y \; B_z \; B_{xx} \cdots)^T$, $[I]=(I_1 \; I_2 \cdots)^T$, $[K_j]$ is a rectangular matrix of field coefficients and $[K_{j_e}]$ is similar, though possibly of differing dimension. It is presumed that $[I_e]$ can be derived from $[I]$, following equations 2,3.

Alternatively, if the eddy current circuit has similar geometry to the primary (for example the induced current in electromagnet cores), it can be argued that the relative effect on all field and field gradient components at the suspended object will be similar. In this case, the representation can be considerably simplified by invoking a false current as shown :

$$I' = \left(1 \; - \; \frac{K_{e_1} \, L_{m_1} \, s}{K_j \, (\, R_{e_1} + L_{e_1} s \,)} \; + \cdots \right) I \; , \quad \text{where } B_j = K_j I' \qquad - (9)$$

It should be noted that the change in electromagnet terminal characteristics and the change in field at the model are two separate effects and should be modelled as such.

Determination of Parameters

The question now is, can the parameters K_{e_n}, L_{e_n}, R_{e_n} and L_{m_n} be estimated and/or measured with sufficient accuracy? First the problem of estimation is addressed.

Calculations have been carried out using the finite element computer code VF/GFUN, by Vector Fields Inc.. It should be noted that this code is magnetostatic and has no capability for direct eddy current calculations, although such codes are available (for instance ELEKTRA, by the same supplier). Instead, the code is used to calculate flux linkages, hence inductances, using :

$$\phi_{ij} = \sum_{j=1}^{n} L_{ij} \, I_j \qquad - (10)$$

VF/GFUN calculates the field on a grid representing the linkage plane of the eddy current circuit. The field normal to the plane is then numerically integrated (by the OPERA pre- and post-processor) to yield the flux linkage term. Figure 7 illustrates the general arrangement. The calculation of the K_{e_n} terms is straightforward.

By way of example, a series of calculations has been made for a single LAMSTF electromagnet with a representation of one part of the position sensor assembly mounted on the same axis, as illustrated in Figure 8. The required parameters were predicted (or previously measured) to be :

$$L = 0.0275 \text{ H} \qquad\qquad R = 0.74 \ \Omega$$
$$L_e = 6.69 \times 10^{-7} \text{ H} \qquad\qquad R_e = 2.243 \times 10^{-4} \ \Omega$$
$$L_m = 1.0998 \times 10^{-5} \text{ H}$$

$$K_z = 3.495 \times 10^{-4} \text{ T} \qquad K_{z_e} = 4.369 \times 10^{-6} \text{ T}$$

Incorporating these values in equation 7, and examining the axial (z-axis) field component, gives :

$$B_z = K_z I \left(1 - \frac{6.13 \times 10^{-4} \text{ s}}{1 + 2.983 \times 10^{-3} \text{s}} \right) \qquad - (11)$$

It is seen that the reasonant frequency of this eddy current circuit is around 53Hz, significantly higher than LAMSTF open-loop natural frequencies, but still well within the range of interest.

Experimental Verification

Actual measurements of the current to field transfer function, corresponding to equation 7, were made with an experimental set-up as described above, and later with LAMSTF. Field components were measured with a F.W. Bell Model 9903 Hall-effect gaussmeter. Electromagnet currents were measured using a current shunt. The transfer function was measured directly with a Schlumberger Model SI 1250 analyzer, with sine-sweep excitation. The results for an air-cored electromagnet with no eddy current circuits are shown in Figure 9, and are taken to represent the probe + instrument + data acquisition system response. These results are subtracted from all subsequent measurements. Figure 10 shows the measured transfer function for B_z, together with the predictions from equation 11. The agreement is thought to be satisfactory. The values of most parameters could be adjusted (refined) to give a better agreement, as shown in Figure 11. The only significant residual discrepancies are seen to occur at higher frequencies where the validity of the Single Time Constant Model is questionable.

The adjusted form of equation 11 is :

$$B_z = K_z I \left(1 - \frac{7.591 \times 10^{-4} \text{ s}}{1 + 2.934 \times 10^{-3} \text{s}} \right) \qquad - (11b)$$

More Complex Cases

If the electromagnet is mounted on the aluminum plate, a second eddy current circuit is added; when the iron core is inserted, a third is added. Figure 12 shows the comparison between experimental and computed responses. Again, the agreement is fair, although capable of improvement by refinement of parameter estimates, also shown in Figure 12. Note that, even if refinement of parameters is undertaken, the model does not correctly predict the high frequency behaviour, particularly where the iron core is present. This is due to the iron core becoming highly dissipative at these frequencies, due to its small skin depth.

An additional series of calculations and measurements has been made for the vertical field component generated at the centroid of the suspended element due to a LAMSTF electromagnet at the design location, i.e. with the sensor ring off-axis relative to the electromagnet. The geometry is illustrated in Figure 13 and typical computed and measured responses are shown in Figure 14. It is clear that the model is progressively less suitable for progressively more complex geometries.

Measurements have also been made with the full LAMSTF sensor frame in place. Examples are shown in Figure 15. Due to the geometrical complexity, with multiple interlocking eddy current paths, it has not yet been possible to compute resonable estimates by the methods shown. It should be noted, however, that another assumption inherent in the form of the model previously chosen has been violated, that is the lack of interaction between separate eddy circuits. If these circuits are physically and electrically connected, this is clearly not reasonable.

Terminal Characteristics

It appears to be possible to experimentally estimate certain important parameters without direct measurement of magnetic fields. Figure 16 shows a comparison of measured and computed terminal characteristics for the single LAMSTF electromagnet mentioned above. The agreement is not perfect, but sufficient to validate the approach and can, of course, be improved by adjustment of parameters.

PART 2 - IMPLEMENTATION of LARGE ANGULAR ROTATION

Linear Modelling

A portion of the development of the idealized governing equations for LAMSTF will be briefly reviewed here. Further details are given in References 7,8. The magnetic forces and moments acting on a magnetized core in a "large-gap" magnetic suspension system can be approximated as follows :

$$\vec{F}_c \simeq \Psi(\vec{M}.\nabla\vec{B}_o) \qquad \vec{T}_c \simeq \Psi(\vec{M} \times \vec{B}_o) \tag{12}$$

- where $\vec{M}$ represents the magnetization of the magnetic core in A/m, $\vec{B}$ the applied magnetic field in Tesla, Ψ is the volume of the magnetic core in m^3, and the subscript o indicates that the field or field gradient is evaluated at the centroid of the magnetic core. Now, following the detailed development presented in reference 9, the effect of changes in relative orientation between the magnetic core and the electromagnet array can be incorporated as follows :

$$\vec{\bar{F}}_c = \Psi\ [T_m][\partial B][T_m]^{-1}\ \vec{\bar{M}} \tag{13}$$

$$\vec{\bar{T}}_c = \Psi\ \vec{\bar{M}} \times \left([T_m]\ \vec{\bar{B}} \right) \tag{14}$$

Where a bar over a variable indicates magnetic core coordinates, $[\partial B]$ is a matrix of field gradients and $[T_m]$ is the coordinate transformation matrix from electromagnet coordinates to suspended element (magnetic core) coordinates. The axis systems and some nomenclature are clarified in Figure 17.

The fields and field gradients are created by an array of n electromagnets. Thus we can write :

$$\vec{B} = [\ K_B\ ]\frac{\vec{I}}{I_{max}} \tag{15}$$

- where $\vec{I} = (I_1,\ I_2,\ \cdots\ ,\ I_n)^T$ and $[\ K_B\ ]$ represents a matrix of field coefficients. Similarly, each element of $[\partial B]$ can be written :

$$\partial B_{ij} = [\, K_{\partial B_{ij}} \,] \frac{\vec{I}}{I_{max}} \tag{16}$$

At this stage, the equations are quite general, but will now be considerably simplified for the LAMSTF application. First, the magnetization of the suspended element is assumed to be along its principal ($\overline{x}$) axis :

$$\vec{M} = (\, M_{\overline{x}} \,, 0 \,, 0 \,) \tag{17}$$

Continuing, the only large rotation of the suspended element is assumed to take place about the z axis, so $[T_m]$ becomes :

$$[T_m] = \begin{bmatrix} \text{Cos } \theta_z & \text{Sin } \theta_z & 0 \\ -\text{Sin } \theta_z & \text{Cos } \theta_z & 0 \\ 0 & 0 & 1 \end{bmatrix} \tag{18}$$

Substituting, expanding and collecting terms :

$$\begin{bmatrix} T_{\tilde{y}} \\ T_{\tilde{z}} \\ F_{\tilde{x}} \\ F_{\tilde{y}} \\ F_{\tilde{z}} \end{bmatrix} = \begin{bmatrix} [\, KT \,] \\ [\, KF \,] \end{bmatrix} \vec{I} \tag{19}$$

- where :

$$[\, KT \,] = \begin{bmatrix} -\lfloor K_z \rfloor \\ -\text{Sin } \theta_z \lfloor K_x \rfloor + \text{Cos } \theta_z \lfloor K_y \rfloor \end{bmatrix} \tag{20}$$

$$[\, KF \,] = \begin{bmatrix} \text{Cos}^2 \theta_z \lfloor K_{xx} \rfloor + 2 \, \text{Cos } \theta_z \, \text{Sin } \theta_z \lfloor K_{xy} \rfloor + \text{Sin}^2 \theta_z \lfloor K_{yy} \rfloor \\ -\text{Cos } \theta_z \, \text{Sin } \theta_z \lfloor K_{xx} \rfloor + (\text{Cos}^2 \theta_z - \text{Sin}^2 \theta_z) \lfloor K_{xy} \rfloor + \text{Cos } \theta_z \, \text{Sin } \theta_z \lfloor K_{yy} \rfloor \\ \text{Cos } \theta_z \lfloor K_{xz} \rfloor + \text{Sin } \theta_z \lfloor K_{yz} \rfloor \end{bmatrix}$$
$$- (21)$$

Now there are two related problems to solve. Firstly, the equilibrium currents required to support the weight of the suspended element may be found by using :

$$F_z = F_{\tilde{z}} = m_c \, g = \forall \, M_{\tilde{x}} \, B_{\tilde{x}\tilde{z}}$$
$$T_{\tilde{y}} = T_{\tilde{z}} = F_{\tilde{x}} = F_{\tilde{y}} = 0$$
$$- (12)$$

- where m_c is the mass of the suspended element. Equation 19 can now be solved for

required currents as a function of yaw orientation θ_Z. As a point of interest :

$$B_{\bar{x}\bar{z}} = \frac{m_c \, g}{\forall \, M_{\bar{x}}} = 0.0962 \text{ Tesla/m in this case} \qquad - (13)$$

Secondly, a decoupling matrix is required so that the conroller can call for the appropriate combination of electromagnet currents to create the required forces and moments. This can be found by direct inversion of the [KT/KF] matrix from Equation 19, giving :

$$\vec{I}_{\text{demand}} = \begin{bmatrix} [\, KT \,] \\ [\, KF \,] \end{bmatrix}^{-1} \begin{bmatrix} T_{\bar{y}} \\ T_{\bar{z}} \\ F_{\bar{x}} \\ F_{\bar{y}} \\ F_{\bar{z}} \end{bmatrix}_{\text{demand}}$$

Note that the [KT/KF] matrix is a function of θ_Z. Initially, it has been found convenient to normalize the inverted [KT/KF] matrix column-by-column, with the normalization factor being incorporated into the loop gain.

The variable decoupling matrix is incorporated into the controller in the following way. Matrices are calculated at frequent intervals (6° presently) and stored in memory. The controller interpolates in real-time between these matrices. The first three matrices, individually normalized, are shown here for reference :

$$\vec{I}_{\text{demand}_{\theta=0^\circ}} = \begin{bmatrix} 0.7713 & 0 & 1 & 0 & -1 \\ 1 & 1 & -0.8091 & 0.6182 & -0.3092 \\ 0.8584 & 0.6178 & 0.3091 & -1 & 0.8092 \\ 0.8584 & -0.6178 & 0.3091 & 1 & 0.8092 \\ 1 & -1 & -0.8091 & -0.6182 & -0.3092 \end{bmatrix} \begin{bmatrix} T_{\bar{y}} \\ T_{\bar{z}} \\ F_{\bar{x}} \\ F_{\bar{y}} \\ F_{\bar{z}} \end{bmatrix}_{\text{demand}}$$

$$\vec{I}_{\text{demand}_{\theta=6^\circ}} = \begin{bmatrix} 0.7637 & -0.1069 & 1 & -0.2091 & -1 \\ 0.9695 & 0.9340 & -0.6841 & 0.7474 & -0.409 \\ 0.8728 & 0.6841 & 0.1068 & -1 & 0.7472 \\ 0.8234 & -0.5112 & 0.5112 & 0.8708 & 0.8708 \\ 1 & -1 & -0.9339 & -0.4091 & -0.209 \end{bmatrix} \begin{bmatrix} T_{\bar{y}} \\ T_{\bar{z}} \\ F_{\bar{x}} \\ F_{\bar{y}} \\ F_{\bar{z}} \end{bmatrix}_{\text{demand}}$$

$$
\vec{I}_{\text{demand}_{\theta=12°}} = \begin{bmatrix} 0.7655 & -0.2091 & 0.9339 & -0.409 & -1 \\ 0.9405 & 0.8708 & -0.5111 & 0.8708 & -0.5112 \\ 0.8916 & 0.7472 & -0.1068 & -1 & 0.6841 \\ 0.7958 & -0.409 & 0.6840 & 0.7472 & 0.9339 \\ 1 & -1 & -1 & -0.209 & -0.1069 \end{bmatrix} \begin{bmatrix} T_{\bar{y}} \\ T_{\bar{z}} \\ F_{\bar{x}} \\ F_{\bar{y}} \\ F_{\bar{z}} \end{bmatrix}_{\text{demand}}
$$

For this interpolation, the controller must have information as to the actual yaw orientation of the suspended element. It was realised that under certain circumstances this information could be deduced in near real-time from the observed behaviour of the suspended element, rather than by direct global measurement of the suspended element orientation, in at least two ways.

A. Yaw Error Tracking

Suspension is established at a known reference orientation. If the sensor framework is now rotated (by hand) through some small angle, the suspended element will tend to become misaligned relative to the sensors. This yaw error signal is filtered to remove the effects of noise and the natural motion of the suspended element in response to small disturbances. Once the filtered error reaches a preset threshold, the controller steps through the array of decoupling matrices in an attempt to drive the yaw error back to zero. This method is rather crude, but has proven to be unexpectedly reliable.

B. Current Distribution Analysis

The predicted current distributions required to suspend at various yaw orientations, together with actual measurements, are shown in Figure 18. It should be noted that the distributions are almost perfectly sinusoidal in nature. By straightforward analysis of an observed current distribution, again with some filtering to remove the effects of noise and so forth, it is possible to deduce the orientation of the suspended element.

In both cases, the algorithm cannot accommodate a steady-state applied yaw torque. Nevertheless, the fact that the position sensor framework does not require any form of angular orientation sensor is a great practical advantage. A sequence of photographs showing the system in operation is shown as Figure 19.

DISCUSSION

The simple eddy current model proposed appears to be satisfactory in the case of large eddy current circuits in conducting, non-magnetic material. Relatively simple computations are capable of providing reasonable estimates of important parameters, with the option of refinement based on measurements of magnetic field or electromagnet terminal characteristics. In the case of the iron electromagnet cores, or at higher frequencies, more elaborate models have been proposed (for instance [9]), but these have one potentially serious drawback. This is that the greater the elaboration in the eddy current model, the more complex the overall suspension system model becomes, and the greater the potential difficulty in manipulating this model in the

process of controller synthesis using modern model-based design methods. In some applications, the simple model proposed, with parameter adjustment, may adequately describe the eddy current influence on the dynamic behaviour, hence control performance, of the system. Discrepancies at frequencies well outside (above) the controller bandwidth would be of no consequence.

CONCLUSIONS

A simple model for the effect of eddy currents in the metallic structure of LAMSTF has been proposed and validated by experiment. However, it has not yet been possible to fully describe the eddy currents in the position sensor framework due to the geometric complexity involved.

Eddy currents have been shown to seriously affect field and field gradient components in the frequency range of interest, such that they must be incorporated into a system dynamic model if modern control synthesis techniques are to be fully successful.

The principal design objective of LAMSTF, the 360° rotation about the vertical axis, has been achieved.

ACKNOWLEDGEMENTS

376

REFERENCES

1. Britcher, C.P.: Large-Gap Magnetic Suspension Systems. International Symposium on Magnetic Suspension Technology. NASA Langley Research Center, August 1991. NASA CP-3152

2. Britcher, C.P.; Ghofrani, M.; Britton, T.; Groom, N.J.: The Large-Angle Magnetic Suspension Test Fixture. International Symposium on Magnetic Suspension Technology. NASA Langley Research Center, August 1991. NASA CP-3152

3. M. Ghofrani, Approaches to Control of the Large-Angle Magnetic Suspension Test Fixture. NASA CR-191890, December 1992.

4. Groom, N.J.; Britcher, C.P.: A Description of a Laboratory Model Magnetic Suspension Test Fixture with a Large Angular Capability. 1st IEEE Conference on Control Applications, Wright-Patterson AFB, September 1992.

5. Cox, D.; Groom, N.J.: A Decoupled Control Approach for a Large-Gap Magnetic Suspension System. 2nd International Symposium on Magnetic Suspension Technology, Seattle, WA, August 1993.

6. Stoll, R.L.: The Analysis of Eddy Currents. Clarendon, 1974

7. Groom, N.J.: Analytical Model of a Five Degree of Freedom Magnetic Suspension and Positioning System. NASA TM-100671, March 1989.

8. Groom, N.J.; Britcher, C.P.: Open-Loop Behaviour of Magnetic Suspension Systems Using Electromagnets Mounted in a Planar Array. NASA TP-3229

9. Buntenbach, R.W.: Improved Circuit Models for Inductors Wound on Dissipative Magnetic Cores. 2nd Asilomar Conference on Corcuits and Systems, 1968.
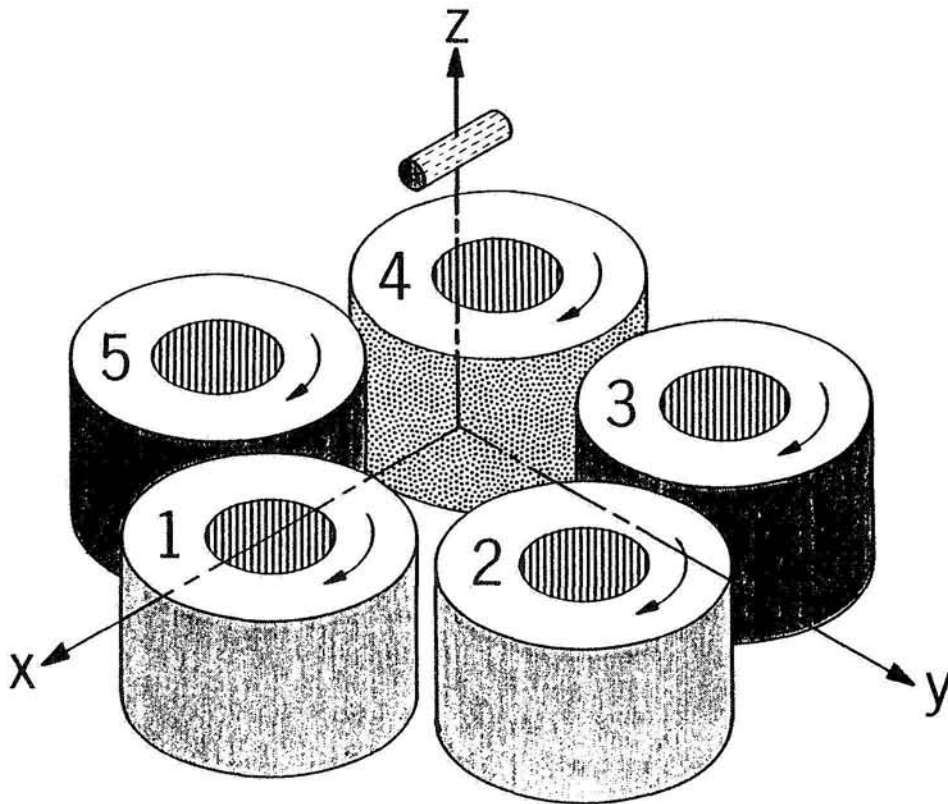
Figure 1 - General Arrangement of the Large Angle Magnetic Suspension Test Fixture
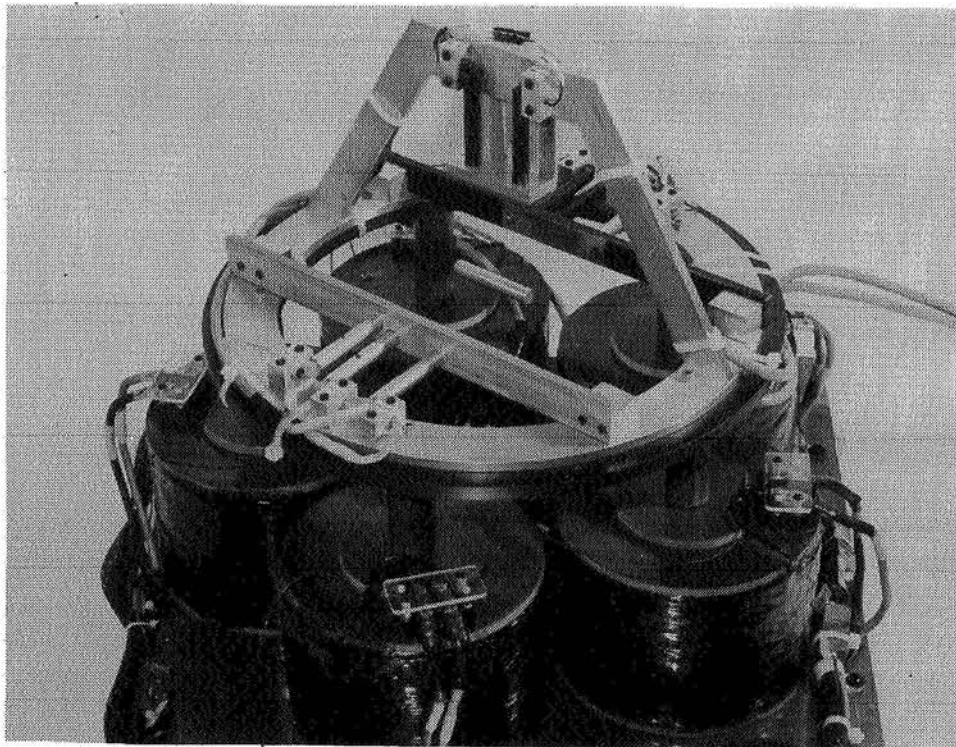
Figure 2 - The Large Angle Magnetic Suspension Test Fixture

378
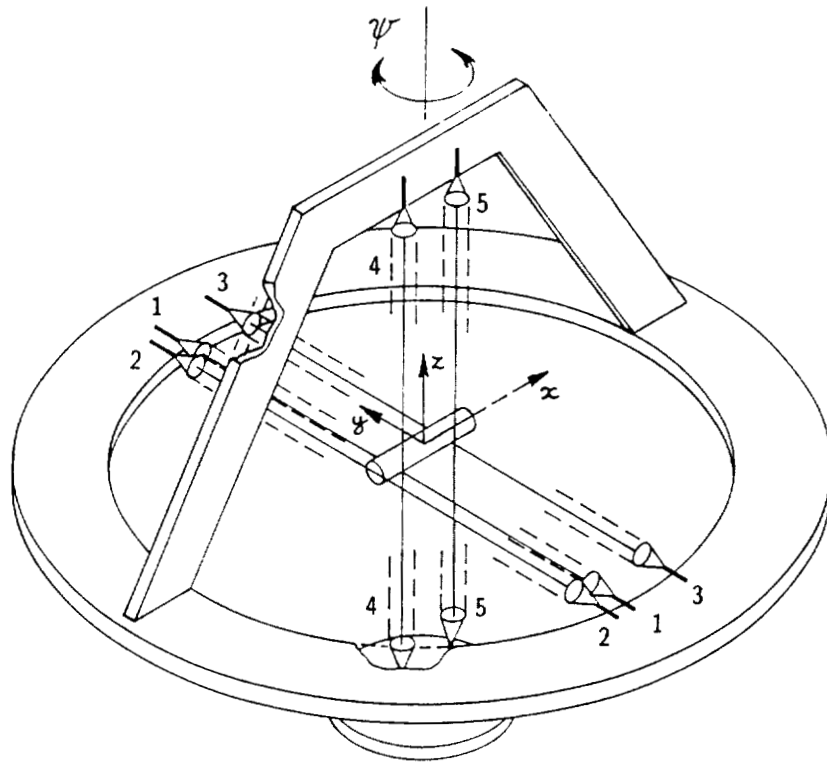
Figure 3 - Schematic Diagram of Optical System
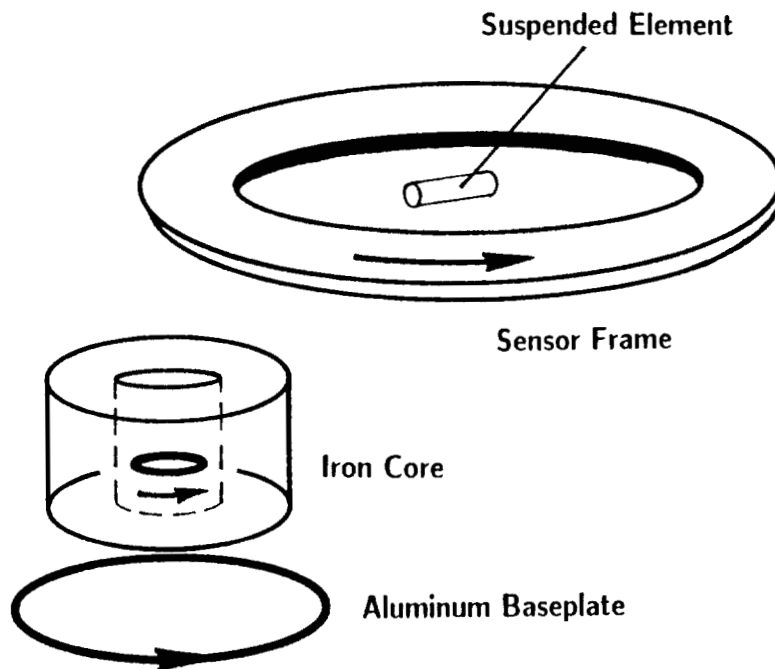
Figure 4 - Schematic Diagram of Eddy Current Circuits in LAMSTF
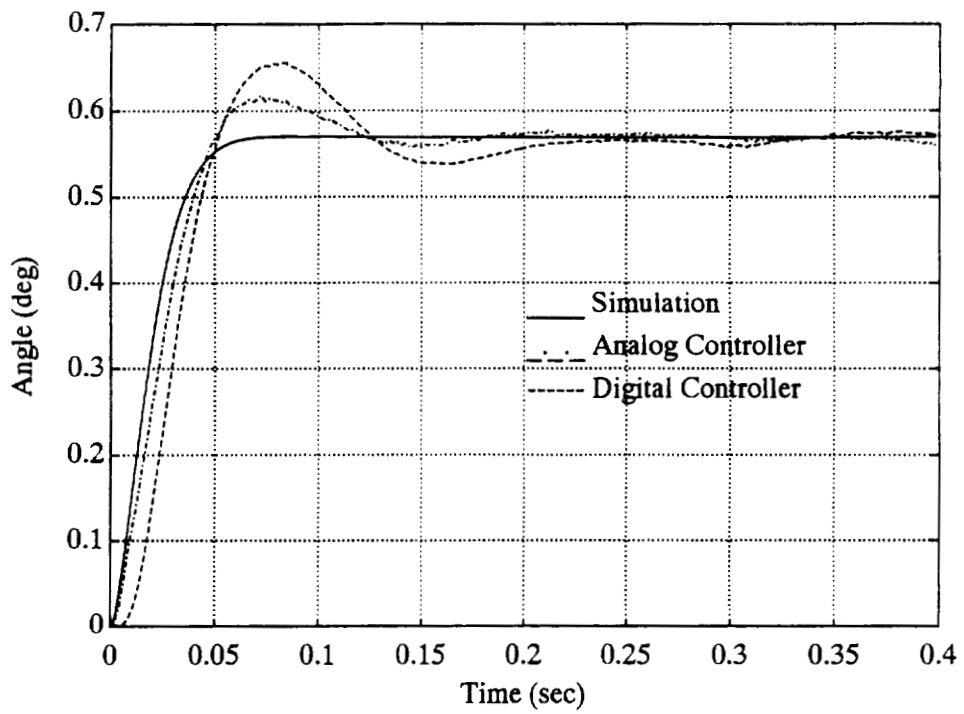
Figure 5 - Initial Discrepancy in Dynamic Response in Pitch (θ_y)
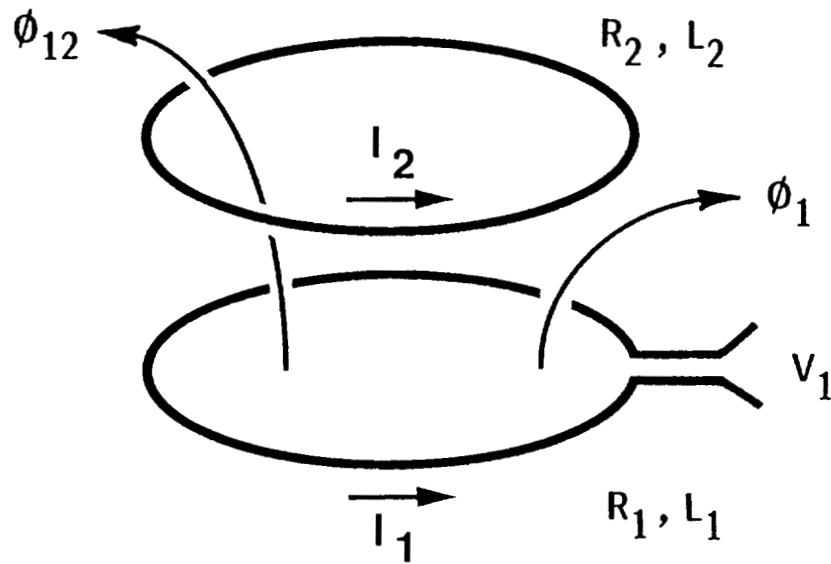
Figure 6 - Schematic of Circuit Model for Primary to Secondary Coupling
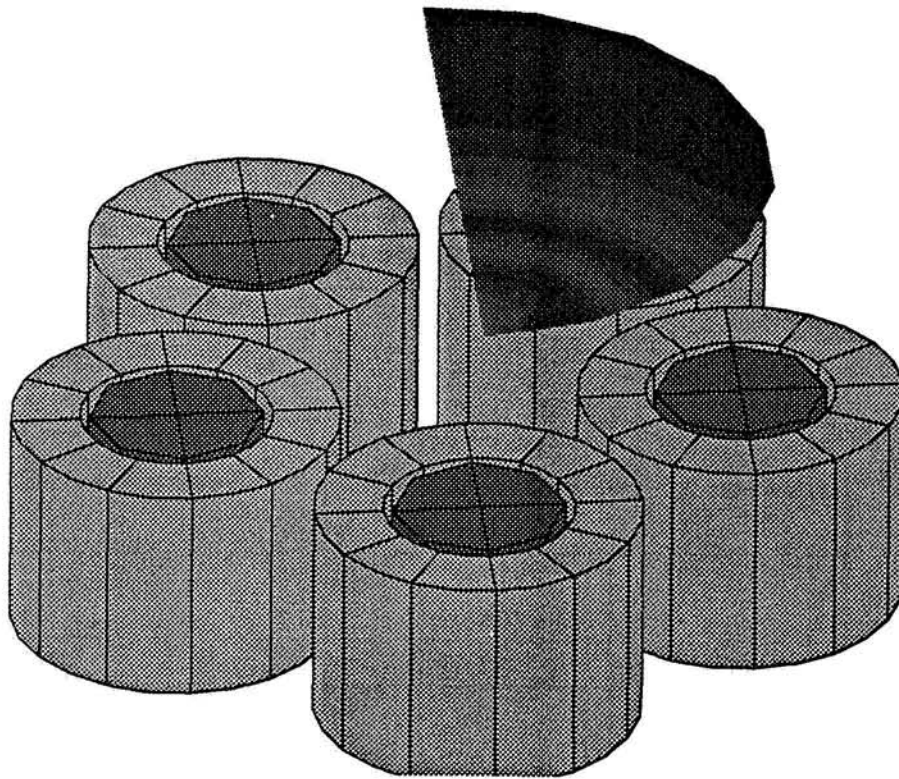
Figure 7 - Illustration of OPERA Flux Linkage Computation (B_z shown)
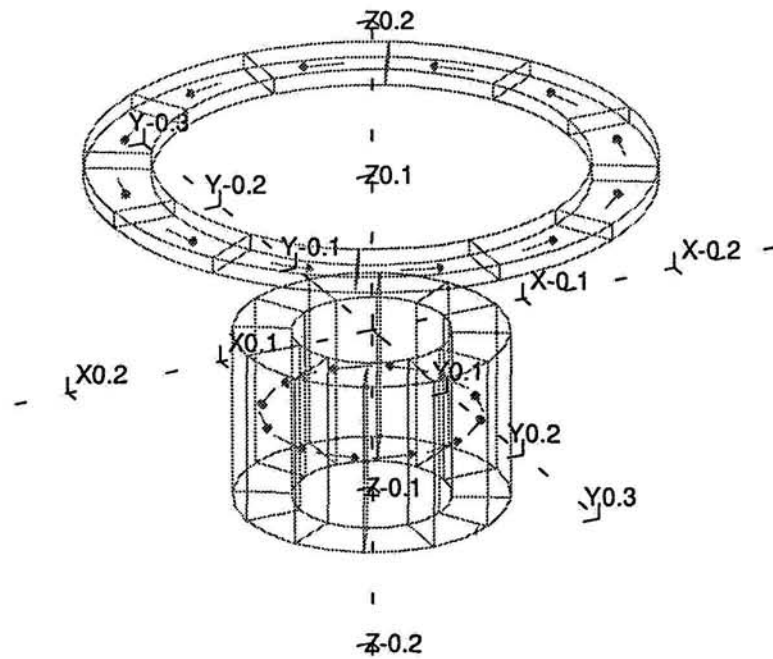
Figure 8 - Simplified Eddy Current Test Set-Up
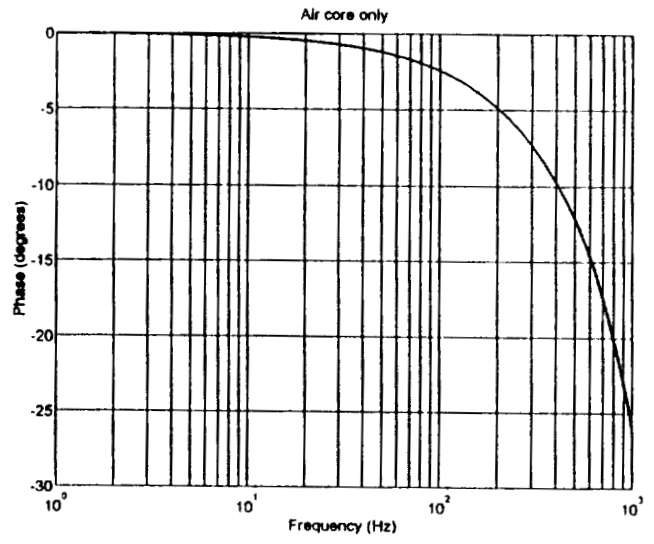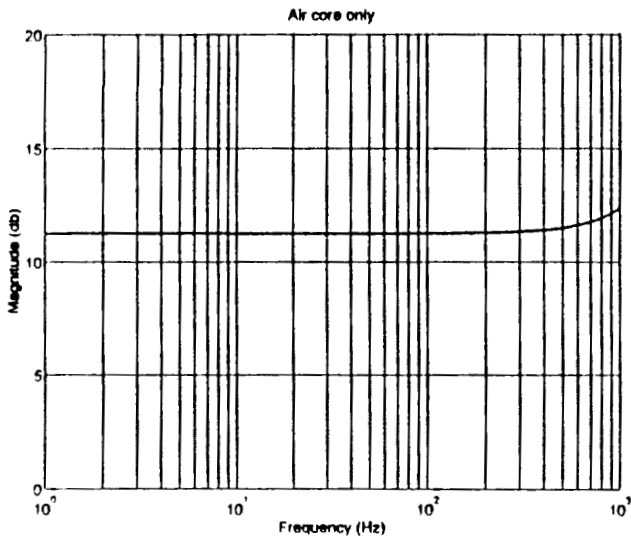
Figure 9 - Gaussmeter Probe Response
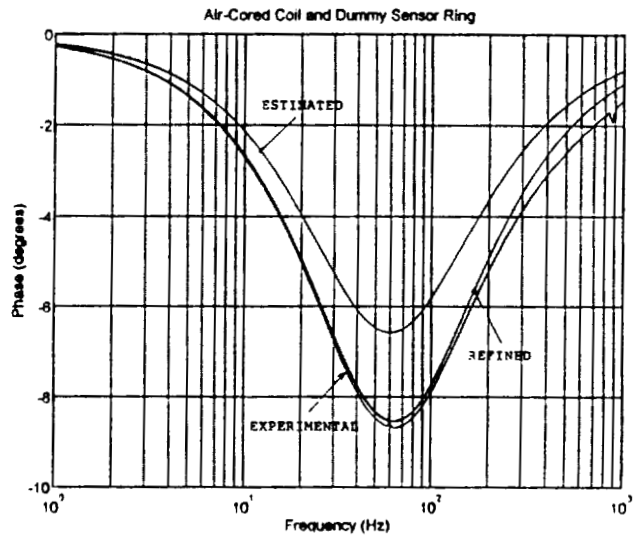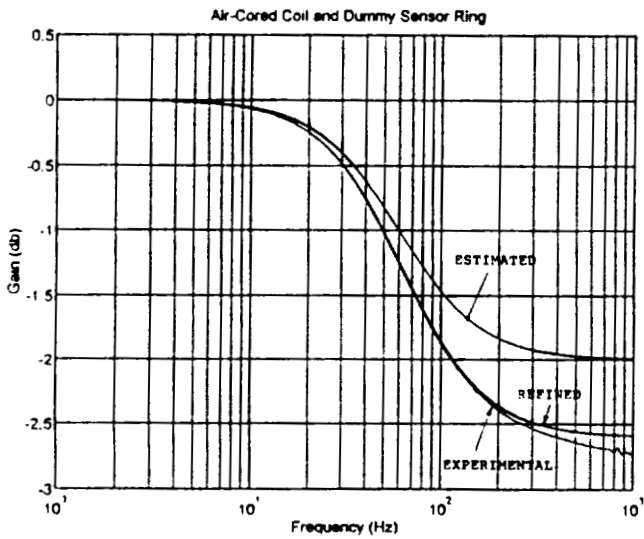
Figure 10 - Axial Field for Air-Cored Electromagnet and Dummy Sensor Ring

382
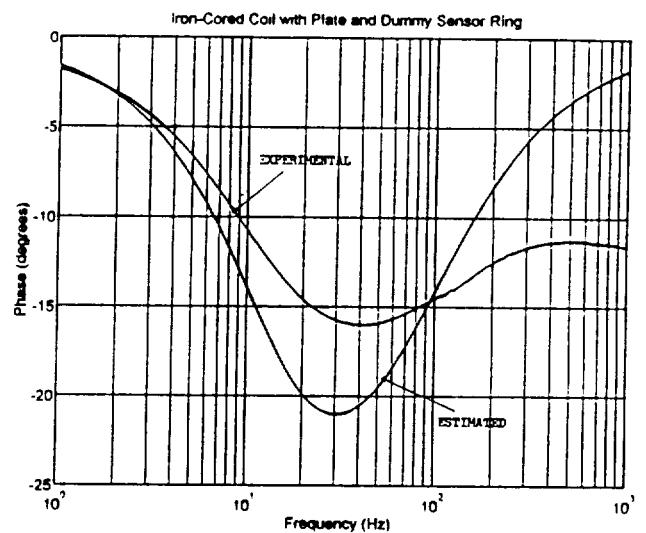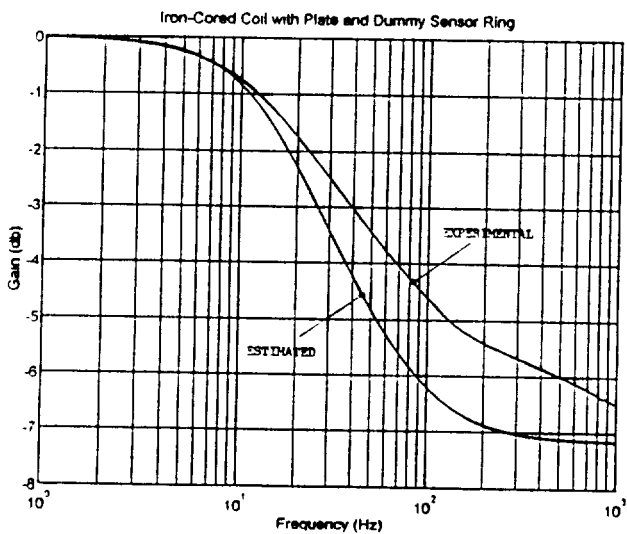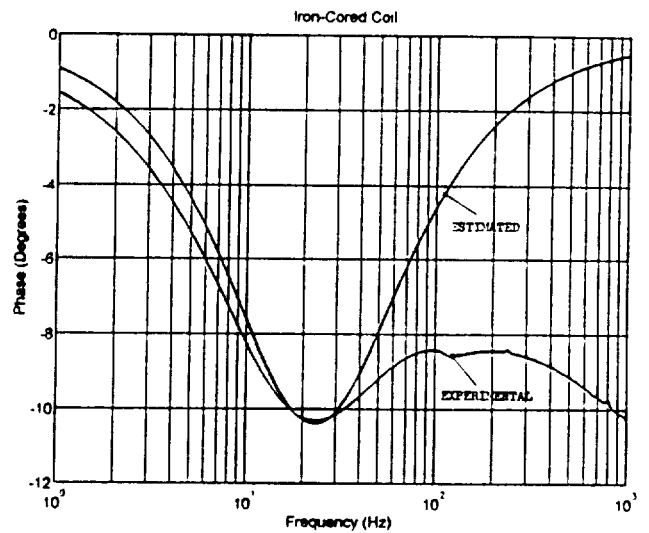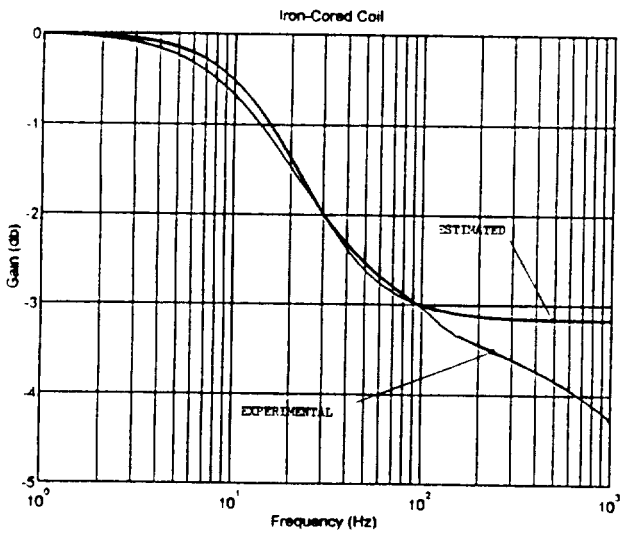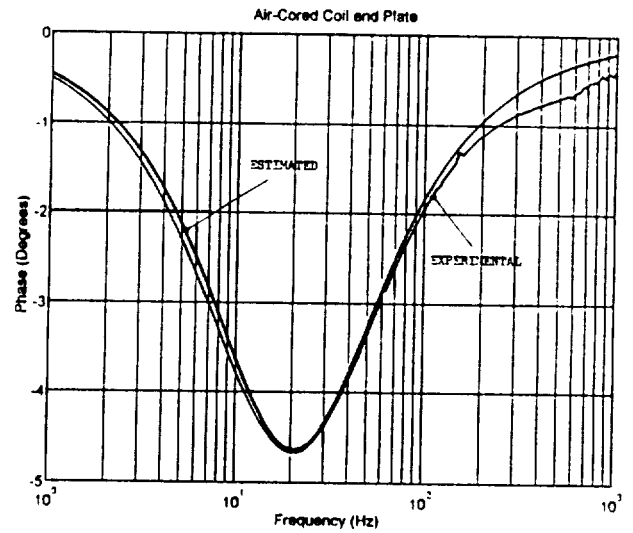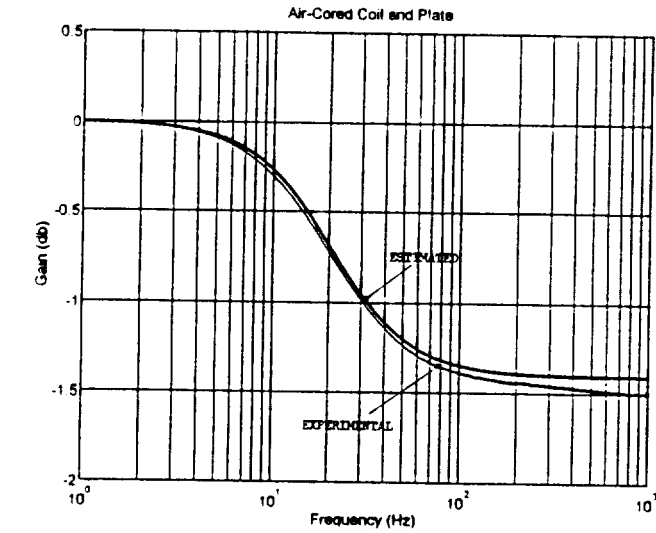
Figure 11 - Axial Field with Iron Core and Alloy Plate Added
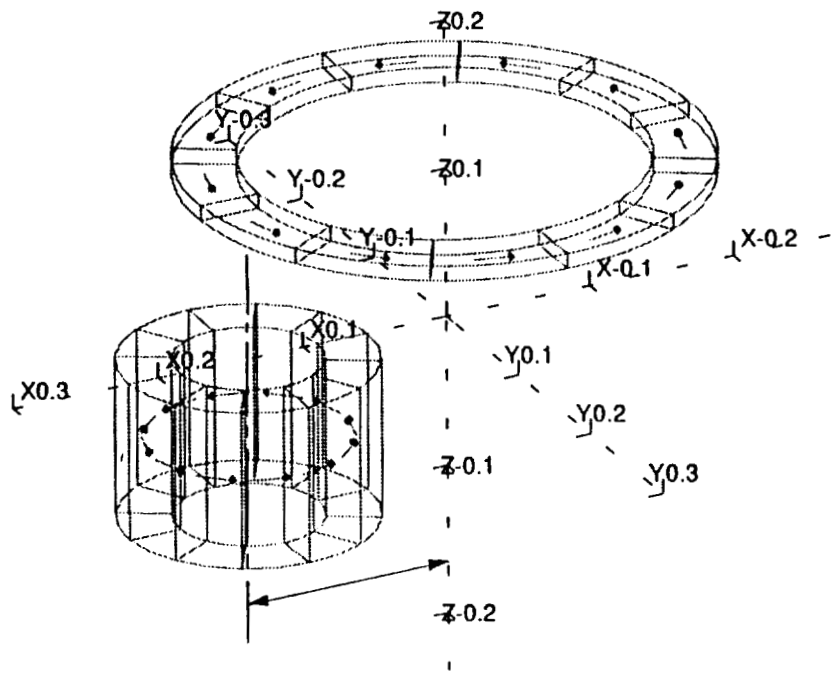
Figure 12 - Off-Axis Test Geometry
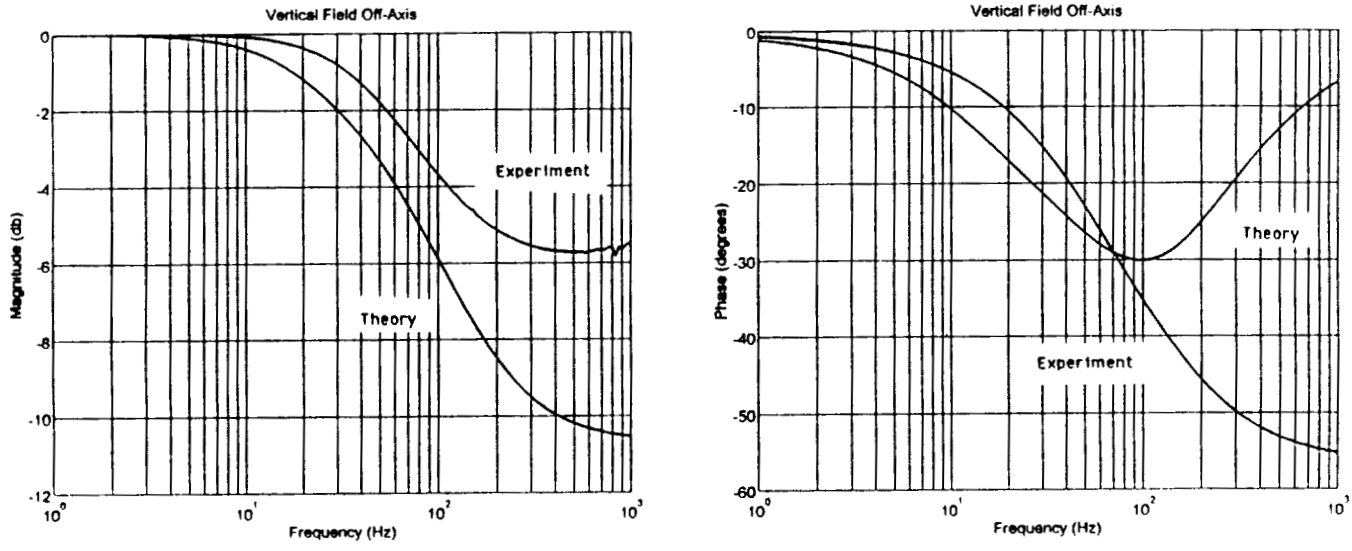
Figure 13 - Vertical Field with Off-Axis Test Set-Up
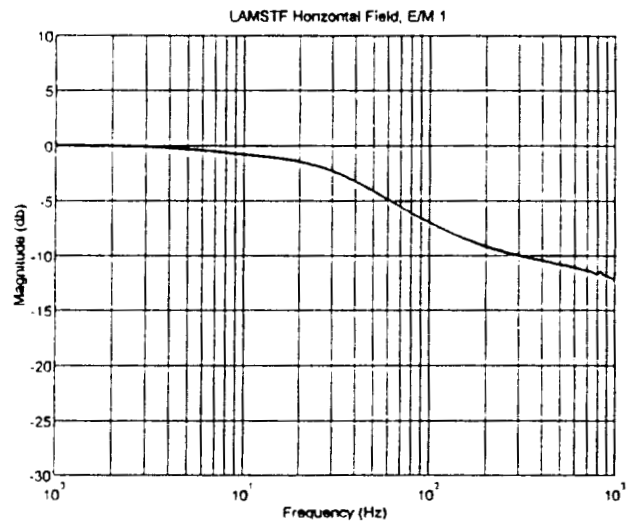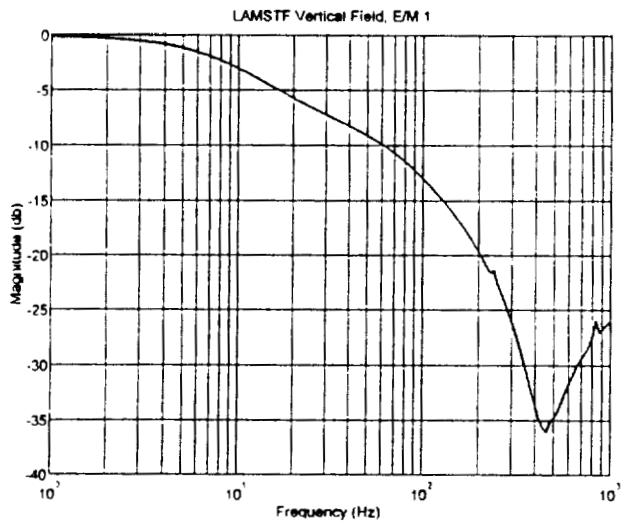
Figure 14 - Typical Field at Suspended Element with Full (Aluminum) Sensor Frame
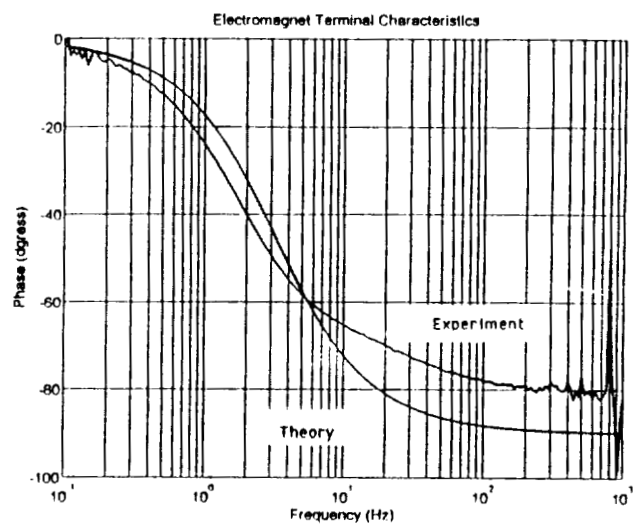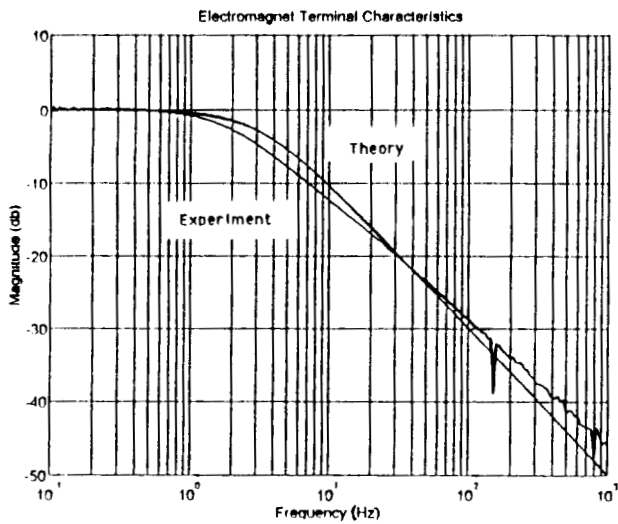
Figure 15 - Electromagnet Terminal Characteristics
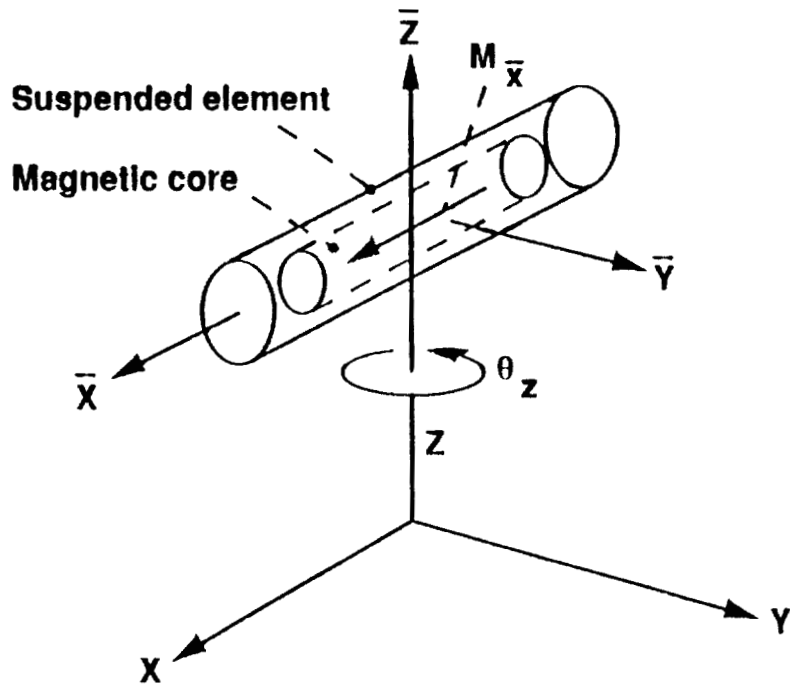
Figure 16 - Axis Systems and Nomenclature
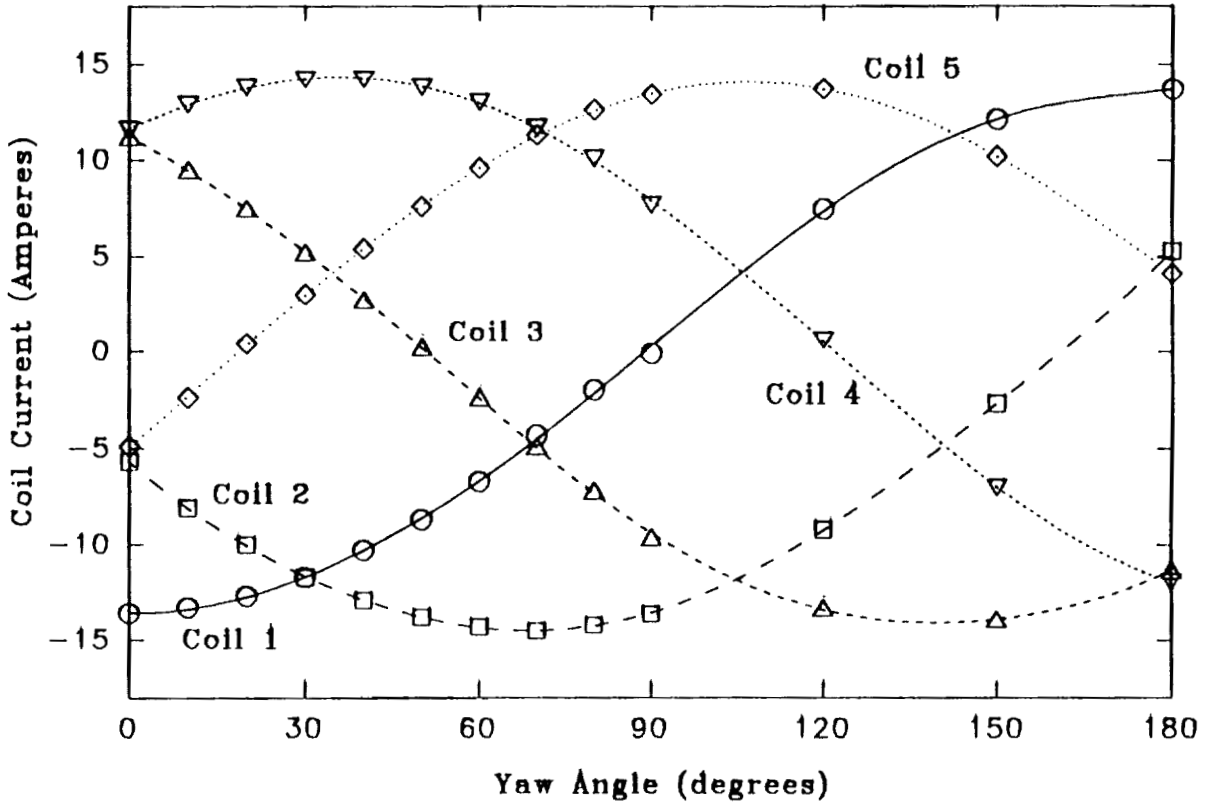
Figure 17 - Predicted Current Distributions for 180° Rotation
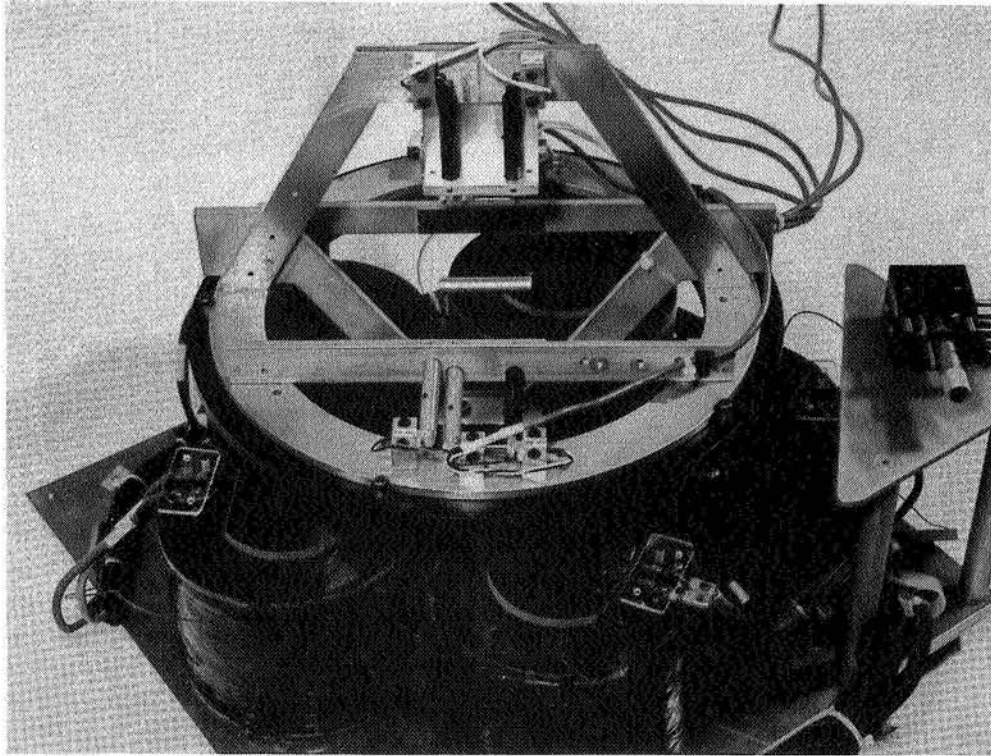
Practical Demonstration of Large Angular Rotation (0°)
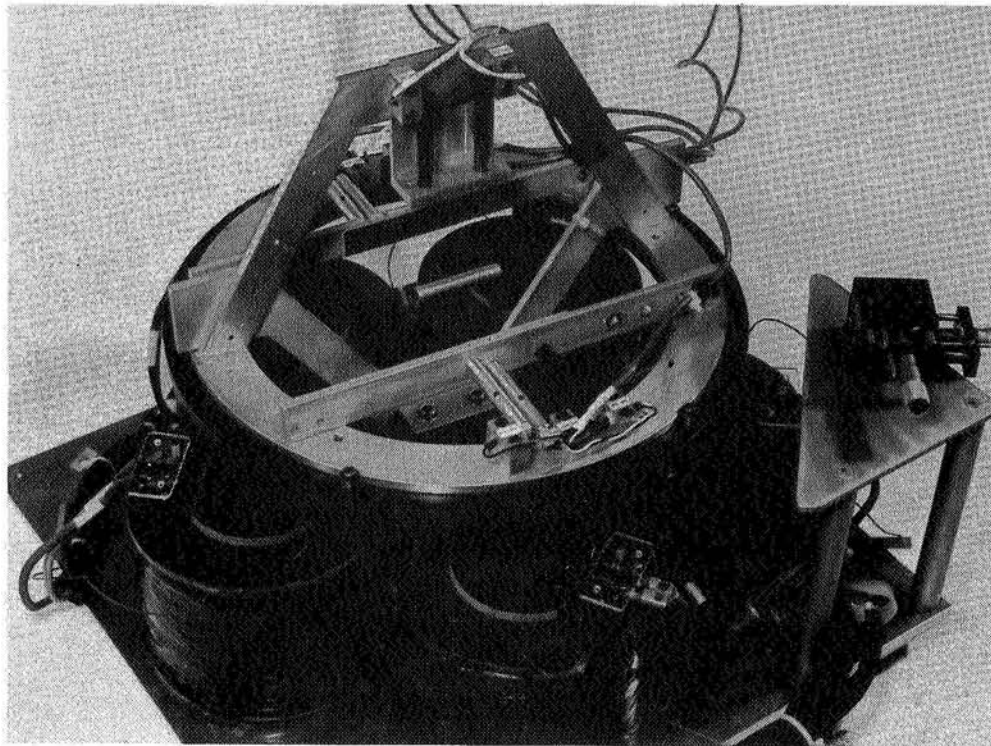
Figure 18 - Practical Demonstration of Large Angular Rotation (30°)
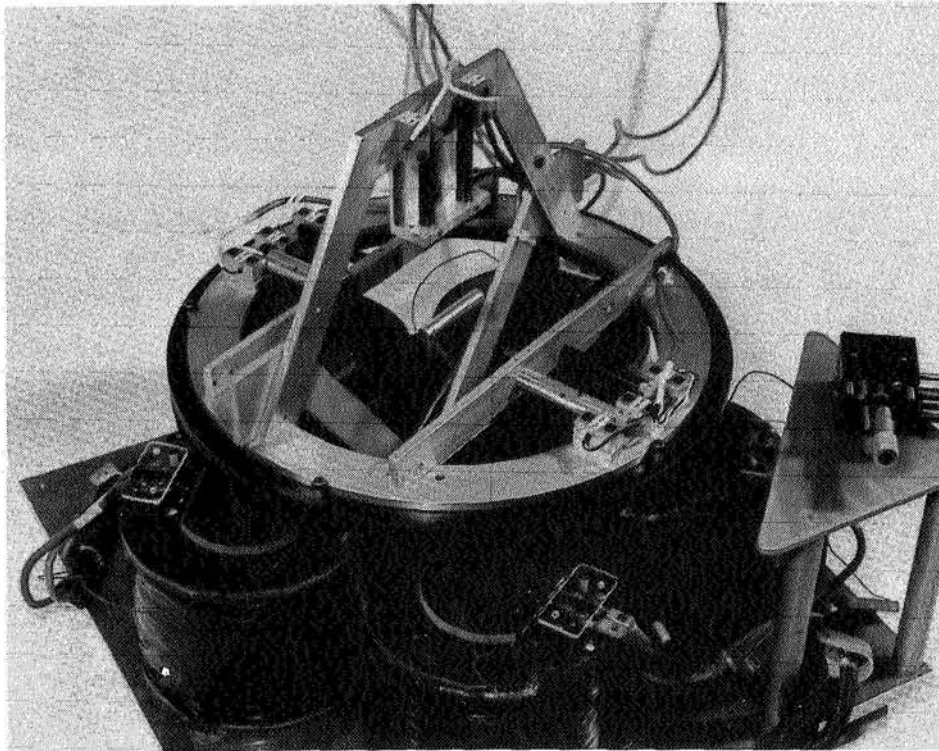
Practical Demonstration of Large Angular Rotation (60°)
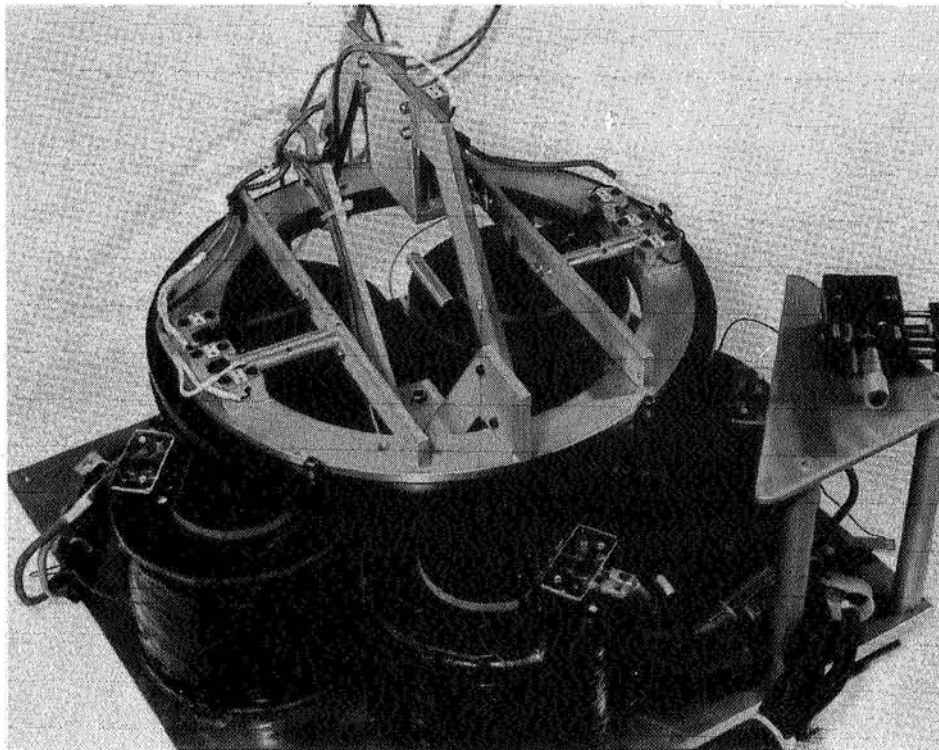
Figure 18 (concluded) - Practical Demonstration of Large Angular Rotation (120°)

388

Session 7b – Controls

Chairman: Claude R. Keckler
NASA Langley Research Center

NEURAL NETWORK CONTROLLER DEVELOPMENT FOR A MAGNETICALLY SUSPENDED FLYWHEEL ENERGY STORAGE SYSTEM

Roger L. Fittro
University of Virginia
Charlottesville, VA

Da-Chen Pang
Davinder K. Anand
University of Maryland
College Park, MD

ABSTRACT

A neural network controller has been developed to accommodate disturbances and nonlinearities and improve the robustness of a magnetically suspended flywheel energy storage system. The controller is trained using the back-propagation-through-time technique incorporated with a time-averaging scheme. The resulting nonlinear neural network controller improves system performance by adapting flywheel stiffness and damping based on operating speed. In addition, a hybrid multi-layered neural network controller is developed off-line which is capable of improving system performance even further. All of the research presented in this paper was implemented via a magnetic bearing computer simulation. However, careful attention was paid to developing a practical methodology which will make future application to the actual bearing system fairly straightforward.

INTRODUCTION

Artificial neural networks are massively parallel systems of densely interconnected simple processing elements which work together to adaptively produce a complex input/output functional relationship through a learning process. Since they were developed based on the understanding of how the human brain functions, physically neural networks can be visualized as a very simple model of the massive interconnections of neurons which make up the human brain.

Neural networks have been developed over the past 40 years. In the 1950's, research was carried out utilizing neural networks composed of individual neurons (nodes) called perceptrons. A considerable amount of progress was made with these networks and associated learning algorithms; however, they were only capable of learning linear relationships [1,2]. Because the ability to learn and represent nonlinear relationships is highly desirable, in ensuing years many researchers pursued methods to surpass the capabilities of perceptrons. In the 1960's, for example, Bernard Widrow developed networks composed of adalines and madalines which improved the overall capabilities of neural networks even in the area of representing nonlinear functions [1]. However, a practical, universally applicable network and training scheme which could accurately learn highly nonlinear relationships alluded Widrow and others. It was not until 1974 that the long awaited breakthrough was made by Werbos [3]. His work was popularized by Rumelhart, et al. [4] in 1986 and is now commonly know as back-propagation. Since that time,

many researchers have made further advancements in artificial neural networks. Numerous new network configurations and training algorithms have evolved as well as countless practical applications [1,2].

The building blocks (nodes) of all artificial neural networks perform a very simple two-step procedure. First, the inputs to a node are multiplied by independent weighting factors and then added together. Second, this weighted sum is passed through some sort of function, usually a nonlinear sigmoid function (see Figure 1). By connecting a large number of these elements together and choosing the correct weighting factors, very complex input/output relationships can be represented. However, to successfully achieve this goal, an appropriate network configuration and training algorithm are necessary.

Primarily there have been two main neural network configurations which have developed over the years. First, there are feed-forward networks which are composed of nodes fully interconnected from one layer to the next, beginning with the input and culminating at the output layer (see Figure 2a). Recurrent networks are the second predominant type of network configuration. In these networks, all or a portion of the nodes are fully interconnected to every other node and a few or all of the nodes are chosen as inputs and/or outputs (see Figure 2b).

In order to choose the proper weighting values to correctly represent a given relationship, a network learning technique is necessary. Neural network learning algorithms can also be broken down into two main categories: supervised and unsupervised. In supervised learning, desired input/output pairs are provided and the network adapts in such a way as to learn the associated relationship. Unsupervised learning, on the other hand, does not have desired input/output pairs available to learn from. Instead, a performance criterion is utilized to judge whether the correct relationship has been learned to a desired accuracy.

NEURAL NETWORK CONTROL SYSTEMS

Neural networks have been successfully implemented as system controllers in a number of different ways. Primarily, existing control system designs have been utilized with neural networks replacing various system components. For example, neural networks have been used as inverse plant controllers, self-tuning regulators, and as part of model reference adaptive control systems [5-7]. For this research, the existing PD controller in the magnetic bearing system was chosen to be replaced with a neural network. A PD-like neural network control system can be developed by feeding time-delayed inputs and direct inputs into the input nodes of a neural network. With these inputs, a derivative can be developed as well as a nonlinear proportionality resulting in a PD-like controller configuration.

Specific research in the area of neural network controller development for magnetic bearings has been limited to date. The main contribution has come from the Swiss Federal Institute of Technology. Researchers there have completed two stages of research. First, they have successfully developed a neural network controller capable of suspending a one degree-of-freedom iron sphere computer simulation. Second, they have experimentally suspended a single degree-of-freedom floating ball using a control system consisting of a standard linear controller and a neural network running in parallel [8]. This research produced significant results and provided the motivation to pursue further developments in this area. There are, however, a number of limitations in this research that need to be overcome. First, only a very small scale application was dealt with (i.e. mass = 0.013 kg). Second, only self-suspension was investigated. Rotation, especially at high speeds, produces a great deal of complications. And third, inefficient training algorithms based on random adaptation methods were used. The inherent instability of magnetic bearings makes these methods much less than ideal. Therefore, in order to address these areas and

pursue the development of a neural network controller for magnetic bearings further, a more thorough analysis is considered in this research.

MAGNETIC BEARING FLYWHEEL ENERGY STORAGE SYSTEM

The University of Maryland has developed a combination electro/permanent magnet bearing system for use in flywheel energy storage. The design consists of a motor/generator sandwiched between two pancake magnetic bearings which support a composite flywheel (see Figure 3). Each degree of freedom in the system is controlled by an independent controller, and a SISO model of the pancake magnetic bearing and control system is shown in Figure 4. In the bearing, a position transducer senses the position of the flywheel and generates a control signal to drive the electromagnetic coils producing the appropriate stabilizing force. Unfortunately from a system design standpoint, the resulting control and stabilization of the system based on linear control theory is not robust due to a number of nonlinearities and disturbances [9]. The following nonlinearities and disturbances were incorporated into the magnetic bearing computer simulation which was developed using Butcher's fifth-order Runge-Kutta method [10]. First, the nonlinearity associated with the power amplifier saturation was included. The nonlinear relationship (K_i) between the current supplied to the electromagnets and the resulting corrective force (F_c) was also taken into account in the analysis. (see Figure 5) And finally, the nonlinearity associated with the touch-down gap due to the back-up mechanical bearing was considered. The disturbances included in this research are those resulting from the mass imbalance of the flywheel, geometric error due to manufacturing and assembly tolerances, and error attributable to the sensors.

NEURAL NETWORK CONTROLLER TRAINING TECHNIQUE

Out of all of the numerous training techniques developed for neural networks, only a fraction of them are capable of addressing the unique problems encountered in controller training. A number of candidates were evaluated [2], and the back-propagation-through-time method was chosen because of its relative simplicity and proven performance.

The Back-propagation-through-time technique is based on the well documented learning algorithm: back-propagation [1,2,4]. Back-propagation is a supervised training technique which performs a gradient descent search for the optimal network weights. In control system applications, the proper input/output relationship necessary to produce the desired response of the plant is to be learned. Since back-propagation is a supervised learning technique which requires sample input/output pairs of this unknown relationship, it cannot be used directly as a controller training method.

In D.H. Nguyen and B. Widrow's paper [5], the following two-step procedure was outlined to circumvent this problem. First, a neural network is trained to emulate the plant. To train this network, appropriate plant input/output pairs need to be developed. Using these pairs, the network can very easily be trained via back-propagation or some other technique. This procedure closely parallels the plant identification procedure commonly performed in linear control system design. The second step of the procedure is developing a relationship between the plant output error and the error in the control signal. Because the plant emulator is a neural network, the error associated with the plant output can be back-propagated through it. This back-propagated error produces the desired relationship between the output and the control signal errors. The control signal error in turn can be back-propagated through the controller and used to adapt the controller weights

393

appropriately (see Figure 6). Because the plant output error cannot be back-propagated through the plant, the neural network emulator had to be developed.

The exact step by step desired plant output is not known for the magnetic bearing system. Therefore, an operating range is used as a more general system constraint in this work. The neural network controller and plant are allowed to progress unaltered for a predetermined period of time or until the operating range is exceeded. After this time, a performance criterion is calculated and used to back-propagate the associated plant error through the neural network emulator and controller. Since the controller and plant progressed through a number of time steps before resulting in the output error and since the final controller output is not solely responsible for the final state of the plant, this back-propagation procedure is continued through as many time iterations as the system progressed in the forward mode. In this way, there is an error and weight update associated with each controller output. It is this back-propagation of the output error through numerous time steps that gives back-propagation-through-time its name. A graphical representation of this procedure can be seen in Figure 7, where the C's, E's, and P's represent the neural network controller, emulator, and plant respectively.

MAGNETIC BEARING SYSTEM IMPLEMENTATION

For the magnetic bearing system, the plant was defined as the power amplifier, voltage supply, actuator coils, flywheel dynamics, and position transducer (see Figure 4). The remainder of the system was replaced by the neural network controller.

Emulator Development

The first step in the back-propagation-through-time technique is the training of a neural network plant emulator. In order to train the emulator, the appropriate inputs and outputs for modeling the plant need to be determined. Utilizing discrete linear control system design representation, the plant's dynamics in state-space notation can be expressed as:

$$x(k+1)=Ax(k) + Bu(k). \tag{1}$$

Utilizing this representation, the present state of the plant and the plant inputs were chosen as the inputs to the neural network emulator. The network outputs were chosen to be the future states of the plant. The appropriate plant states were determined to be the coil current and the position and velocity of the flywheel as sensed by the position transducer. The control signal and disturbance force were chosen as the plant inputs. The corresponding inputs to the emulator are the control signal, disturbance force, and present states of the plant (coil current, position, and velocity). The outputs are the resulting states of the plant one time step later.

Because the magnetic bearing system is inherently unstable, it is not practically possible to obtain the sample input/output pairs necessary for training the emulator without having a controller in place. It would also be very expensive and impractical to build a controller just to obtain the data necessary to develop another control system. Therefore, an alternate method of training the emulator is necessary. One of the practically useful characteristics of the back-propagation-through-time technique is its relatively high tolerance to emulator error. Because it is a one-step predictor, as opposed to a multi-step predictor, it only requires relatively accurate modeling over one time step. Linearization of a system over a single time step produces satisfactory accuracy in most cases. Therefore, sample I/O pairs were generated based on an easily developed linearized model of the plant. Following this approach, a suitable magnetic bearing emulator was trained. A

conjugate gradient learning algorithm was used for training the emulator instead of back-propagation because of its superior speed and accuracy. These advantages can be demonstrated by comparing the results obtained from learning a sine wave. The conjugate gradient method learned the proper relationship approximately 17 times faster while achieving an RMSE value one order of magnitude better than the back-propagation routine. When applied to training the emulator, the conjugate gradient method achieved an RMSE value of 3.17×10^{-8} on a training set consisting of 600 I/O pairs. The resulting network was subsequently testing on a set of 400 I/O pairs producing a comparable RMSE value of 3.94×10^{-8}.

Controller Training

Because network training is a trial and error procedure and the magnetic bearing is an inherently unstable system, bearing damage is very possible due to excessive failures. To overcome this problem, a two-stage training procedure was implemented. The first stage was to train the network to perform self-suspension. Once this was accomplished, the bearing was allowed to rotate at increasingly higher speeds while the controller continued to learn. If the speed is not increased too quickly and appropriate operating ranges are chosen, learning is able to continue without any failures taking place after self-suspension is accomplished. This is because learning takes place when the designated operating range is exceeded; and if this range is chosen carefully, the system will remain stable throughout this phase of training.

Before this two-stage training procedure was started, one more concern was dealt with. Neural networks produce an instantaneous response while a time delay exists in the actuator coil. This combination results in an overly sensitive controller which in turn causes system instability. The neural network continually attempts to instantaneously bring the system to a point of equilibrium without being influenced in any way by previous outputs. Therefore, the network does not allow sufficient time for the actuator to respond properly to counteract the destabilizing force before a new and possibly contradictory command is given.

Based on this insight, a time-averaging scheme for the neural network control signal was developed. This time-averaging method takes the instantaneous output of the network and averages it with previous outputs over a specified time period. This produces a control signal which takes into account previous outputs and also causes a smooth signal to result. As long as the time-averaging period is chosen appropriately, this technique tends to produce a stable system (see Table I).

A number of different network configurations were successfully trained using the modified back-propagation-through-time technique. The performance criterion (E) used during training was

$$E = \alpha_1 x + \alpha_2 x; \qquad (2)$$

where α_1 and α_2 were calculated based of the emulator such that the position and velocity of the flywheel had comparable effects on the weight updating procedure. The values calculated were as follows: $\alpha_1 = 1.0$ and $\alpha_2 = 0.00036$ [2].

In the first stage of controller training, self-suspension, the networks learned quickly allowing less than ten failures on average. The operating range specified for this stage was the entire touch-down gap (0.00015 m). The resulting neural networks were capable of controlling the system at 1000 rpms. Operating at this speed, the networks went through an additional training procedure, after which the weights were fixed. For this stage of training, an operating range of 0.00002 m

was specified in conjunction with a moderate mass imbalance corresponding to a sinusoidal disturbance of 10 Newtons. A summary of the training run for the network with the best performance is shown in Table II.

The best performing controller unexpectedly turned out to be a single-layer network. Even though theoretically a nonlinear controller should be able to produce better results than a linear controller, this is only true if the proper nonlinear function is developed. It turns out that an optimal control system for a magnetic bearing has a nonlinear relationship with respect to flywheel rotational speed. This means that in order for a controller training algorithm to produce an appropriate nonlinear network, a relationship involving the rotational speed of the plant needs to be included. This was not the case for this training procedure; therefore, the resulting nonlinear relationships developed by the multi-layered neural networks cannot be expected to be correct, and neither can they be expected to out perform a single-layer network. This analysis is also confirmed by the results of Krodiewski, et al [11].

In addition to the training of these networks using back-propagation-through-time, a hybrid multi-layered neural network controller was developed off-line utilizing experimental results of the previously trained networks. In this network (see Figure 8), the speed of the flywheel and a + 1 bias act as the only inputs. Experimentally determined controller stiffness and damping factors appear as weights in the second layer. These cause the effective stiffness and damping values to vary based on the speed of the flywheel (see Figure 9). The outputs of the third layer of nodes are the effective stiffness and damping for the given speed. In the fourth layer of nodes, these values are taken as inputs in addition to the flywheel's position and velocity. This layer of nodes is made up of two product units which multiply the inputs together rather than calculating a weighted sum. Finally, the outputs of these two nodes are fed into the fifth layer of nodes producing the control signal (v_o).

Performance Results

Comparison of the best performing trained neural network controller (NN) and the linear control system (LCS) produced another unexpected result. As can be seen from Figure 10, the performance envelopes for the linear controller and the neural network are very similar in the low to mid-speed range. However, in the higher speed range, the neural network performance far exceeds that of the linear controller. A single-layer neural network is only capable of producing a linear relationship; therefore, the question as to why it is able to outperform a linear control system design needs to be answered. Upon closer analysis, it turns out that the neural network in conjunction with the time-averaging scheme is able to produce a nonlinear relationship with respect to the rotational speed of the flywheel. At low speeds, the time-averaging period is negligible compared to the time period associated with the mass imbalance. However, as the flywheel speed increases, the time period of the mass imbalance related disturbance force decreases. Meanwhile, the time-averaging period remains fixed. As the speed of the flywheel increases above a certain level, the time-averaging period becomes significant and causes lower effective controller stiffness and damping. This phenomenon becomes more pronounced as the flywheel speed increases, and results in the desired nonlinear control system relationship necessary to improve performance. Hence, the combination of the trained single-layer neural network controller and the time-averaging technique actually results in a nonlinear rather than a linear controller. Further performance improvements can be seen to be achieved through the use of the hybrid multi-layered neural network controller (HMLNN).

The disturbance force due to a mass imbalance can be written in the form:

$$F_d = m \, e \, \omega^2 \sin(\omega t); \tag{3}$$

where m is the mass of the flywheel and e is the mass imbalance distance. Using this relationship, new performance curves can be generated. As can be seen from Figure 11, performance measured by this new index is also improved through the use of the neural network controllers. This result is very significant because it demonstrates that the neural network is much more likely to be able to control the system at higher speeds. It also suggests that comparable performance can be obtained with a neural network controlled system subjected to reduced manufacturing tolerances and a system using a linear controller and much tighter tolerances.

CONCLUSIONS/RECOMMENDATIONS

In this research, the historical developments and basic operating principles of artificial neural networks have been discussed. The back-propagation-through-time technique has been described and modified to produce a very practical controller training technique for the magnetic bearing system. The training procedure has been implemented on a computer simulation, and the neural network controllers were successfully trained. The resulting system performance characteristics were compared with those of the existing linear control system. Significantly improved performance was achieved for both the single-layer and hybrid multi-layered neural network controllers. These improvements demonstrate the advantages of using neural networks in control system design especially when the desired controller response is nonlinear.

In order to produce even better performing nonlinear controllers, the developments of this research can be extended. The on-line training technique could be modified to include the rotational speed of the flywheel as a training parameter so that the appropriate nonlinear relationship would be learned by a multi-layered neural network. The inclusion of the coil current as an input to the control system should also be investigated. This added input may be able to improve controller performance for both standard linear control systems and neural networks. In addition, an even more accurate computer simulation could be developed. The simulation used in this research includes most of the important system characteristics. However, there are a few areas that still need to be addressed [9]. At high speeds, a number of factors begin to play a significant role. For example, gyroscopic effects at high speeds make the assumption of independent control axes incorrect. Material deformation at high speeds also alters system performance due to growth of the air gap. Additionally, magnetic material properties alter due to eddy currents and hysteresis. Therefore, all of these characteristics need to be taken into account in order to obtain an accurate model. However, no simulation is ever perfect. Therefore, controller training should be performed on the actual magnetic bearing flywheel energy storage system in order to practically prove and improve on the results obtained through simulation.

REFERENCES

1. Dayhoff, J., Neural Network Architectures: An Introduction, Van Nostrand Reinhold, 1990.

2. Fittro, R., "Neural Network Controller Design for a Magnetic Bearing Flywheel Energy Storage System", Master's Thesis, University of Maryland, College Park, MD, 1993.

3. Werbos, P., "Beyond Regression: New Tools for Prediction and Analysis in the Behavioral Sciences", Ph.D. Thesis, Harvard University, Cambridge, MA, 1974.

4. Rumelhart, D., Hinton, G., Williams, R., "Learning Internal Representation by Error Propagation", In Rumelhart, D., McClelland, J., editors, <u>Parallel Distributed Processing - Explorations in the Microstructure of Cognition</u>, chapter 8, pp. 318 - 362, MIT Press, 1986.

5. Nguyen, D., Widrow, B., "Neural Networks for Self-Learning Control Systems", IEEE Control Systems Magazine, April, 1990.

6. Chen, F., "Back Propagation Neural Networks for Nonlinear Self-Tuning Adaptive Control", IEEE Control System Magazine, April, 1990.

7. Narendra, K., Parthasarathy, K., "Identification and Control of Dynamical Systems Using Neural Networks", IEEE Trans. on Neural Networks, Vol. 1, No. 1, 4 - 27, March 1990.

8. Bleuler, H., Diez, D., Lauber, G., Meyer, U., Zlatnik, D., "Nonlinear Neural Network Control with Application Example", International Neural Network Conference (INNC), 1990.

9. Johnson, R.G., Pang, D., Kirk, J.A., Anand, D.K., "Physical Modeling of High Speed Magnetic Bearing Systems", International Symposium on Magnetic Bearings, 1992.

10. Chapra, Canale, <u>Numerical Methods for Engineers with PC Applications</u>, McGraw Hill, 1985.

11. Krodiewski, J., Zmood, R., Kirk, J., Lashley, C., "Influence of Magnetic Bearing Operating Constraints on Rotor-Bearing System Performance", Proc. of the 27th Intersociety Energy Conversion Engineering Conference, Vol. 4, pp. 15 - 22, 1992.
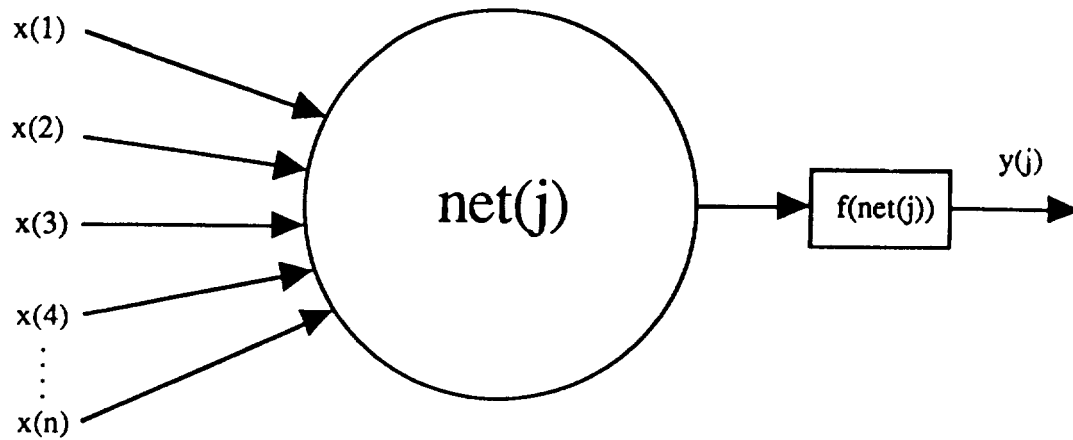
$$net(j) = \sum_i w(i,j)\, x(i)$$

$$y(j) = f(net(j))$$

Figure 1. Single neural network node and equations.
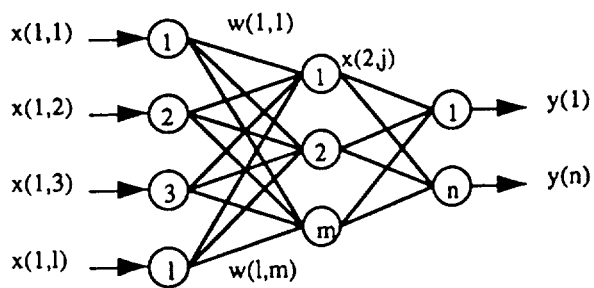
Figure 2a. Feed-forward network.
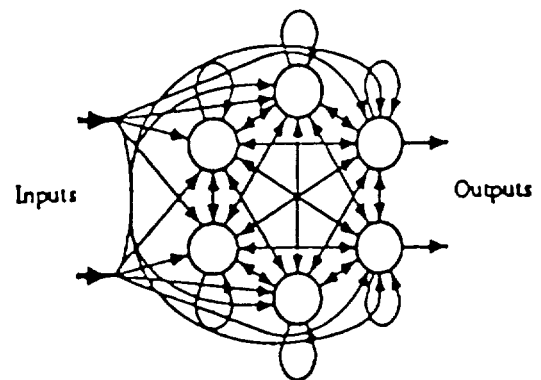
Figure 2b. Recurrent network.
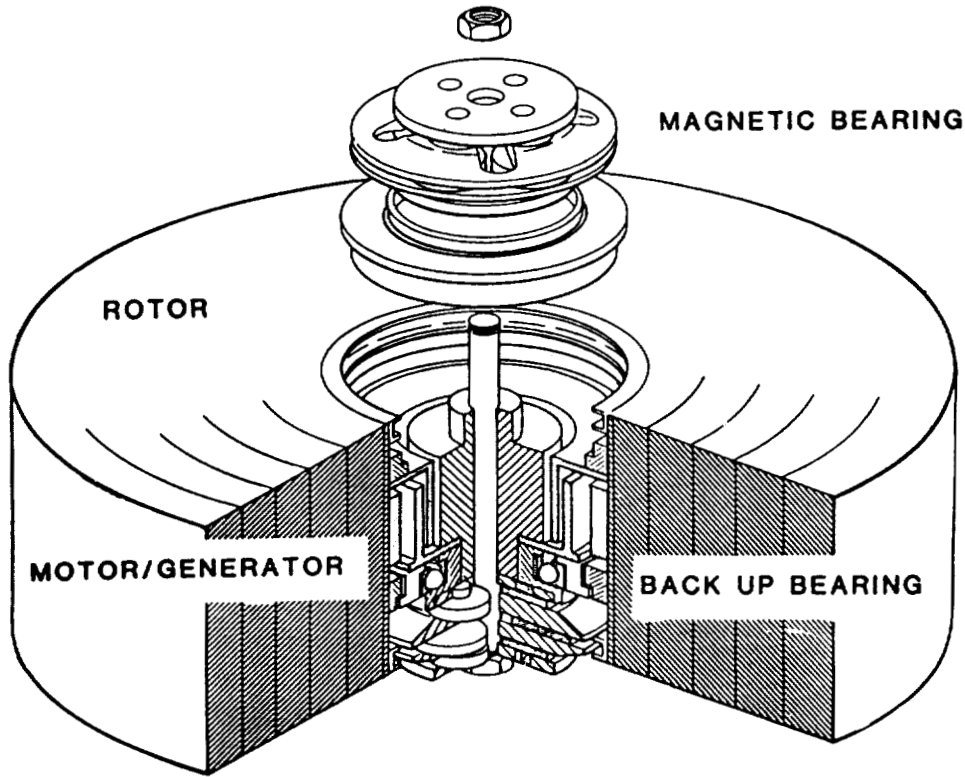
Figure 3. Stack design magnetic bearing flywheel energy storage system.
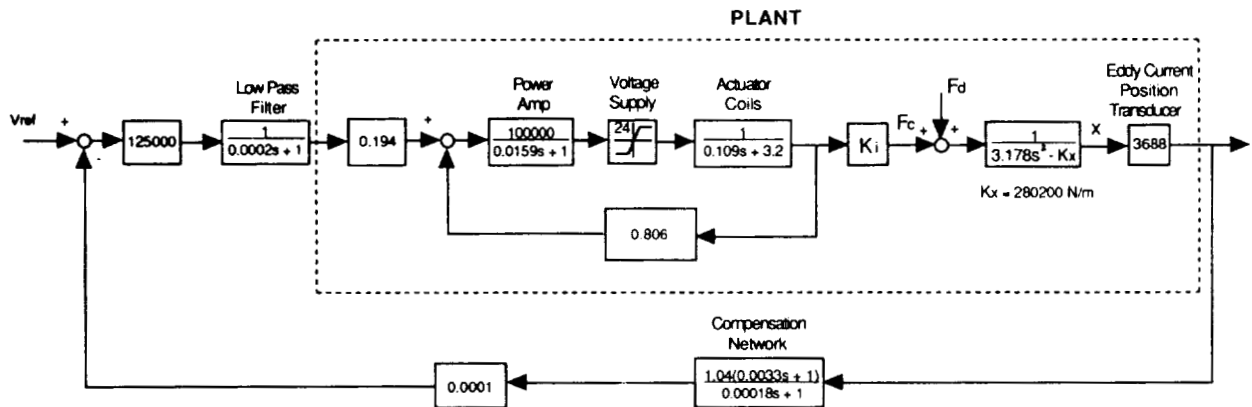
Figure 4. Nonlinear pancake bearing system block diagram.
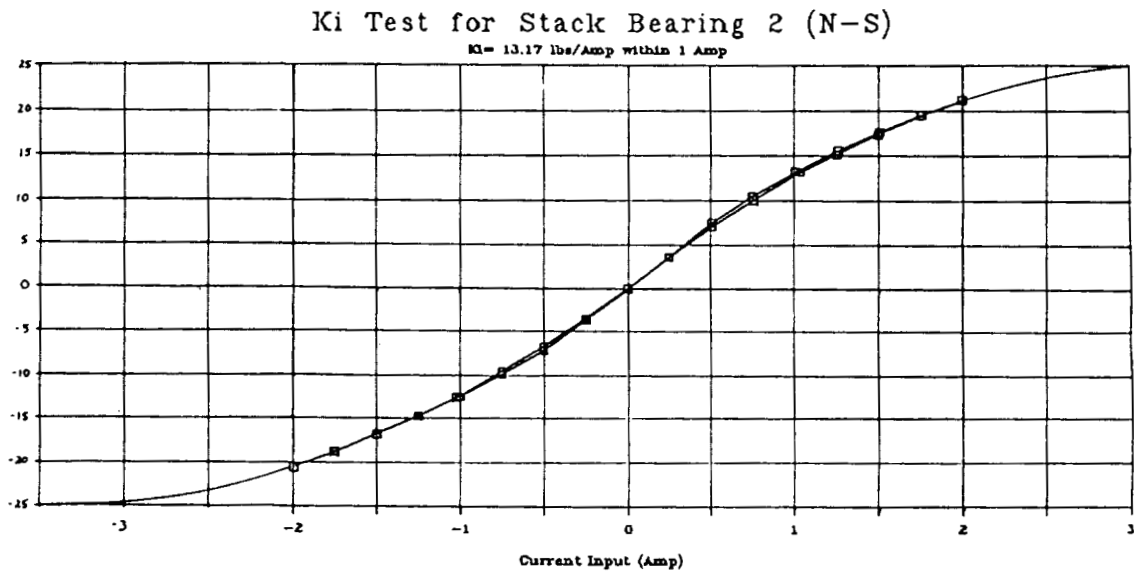
Figure 5. Current/Force Sensitivity.
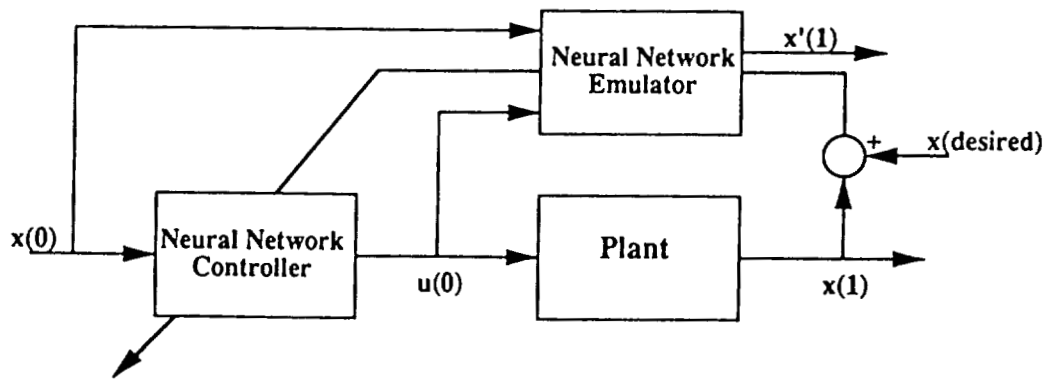
Figure 6. Single step of the back-propagation-through-time procedure.
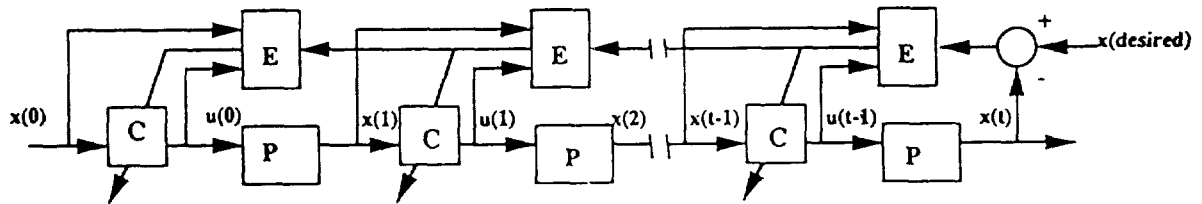
Figure 7. Back-propagation-through-time procedure.

Table I. Time-averaging Period Results

Time-averaging Period	Results
0.0002 sec.	unstable
0.0005 sec.	stable - better performance at low to medium speeds
0.0010 sec.	stable - better performace at higher speeds

Table II. Neural Network Controller Training Results

Training	Network weights (normalized)	Adjusted weights
Self-suspension	$w(1,1) = -0.636254$ $w(1,2) = -0.455918$	$w'(1,1) = -6.36254$ $w'(1,2) = -0.022796$
1000 rpm	$w(1,1) = -1.31773$ $w(1,2) = -0.777021$	$w'(1,1) = -13.1773$ $w'(1,2) = -0.038851$
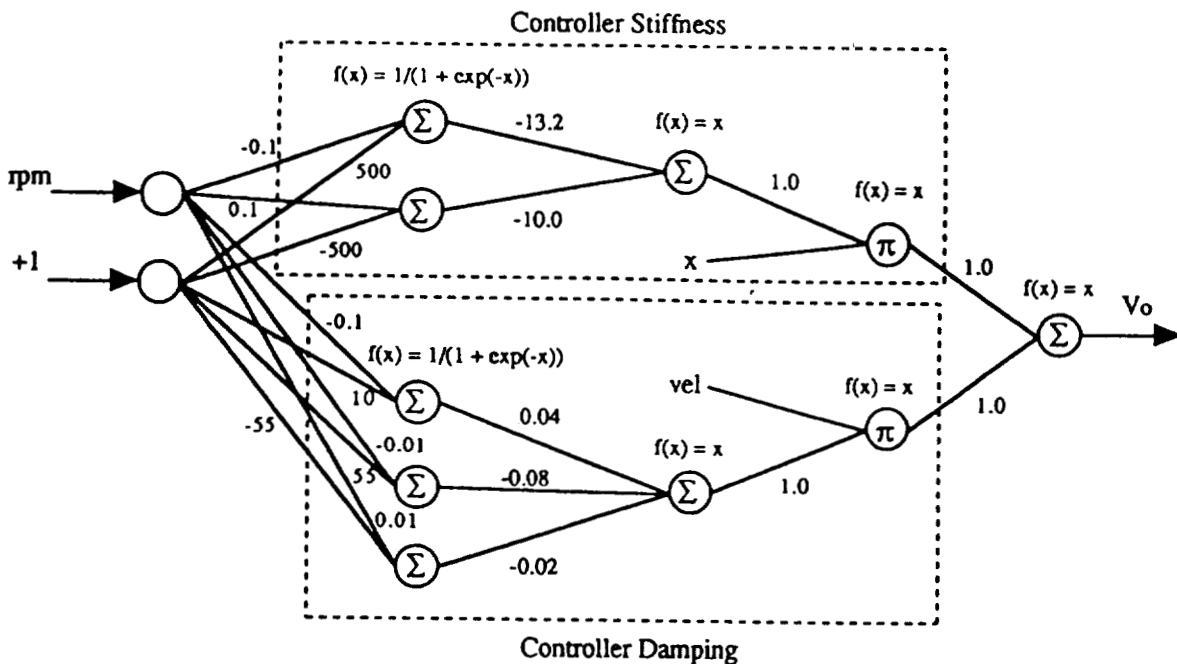
Figure 8. Hybrid multi-layered neural network controller.
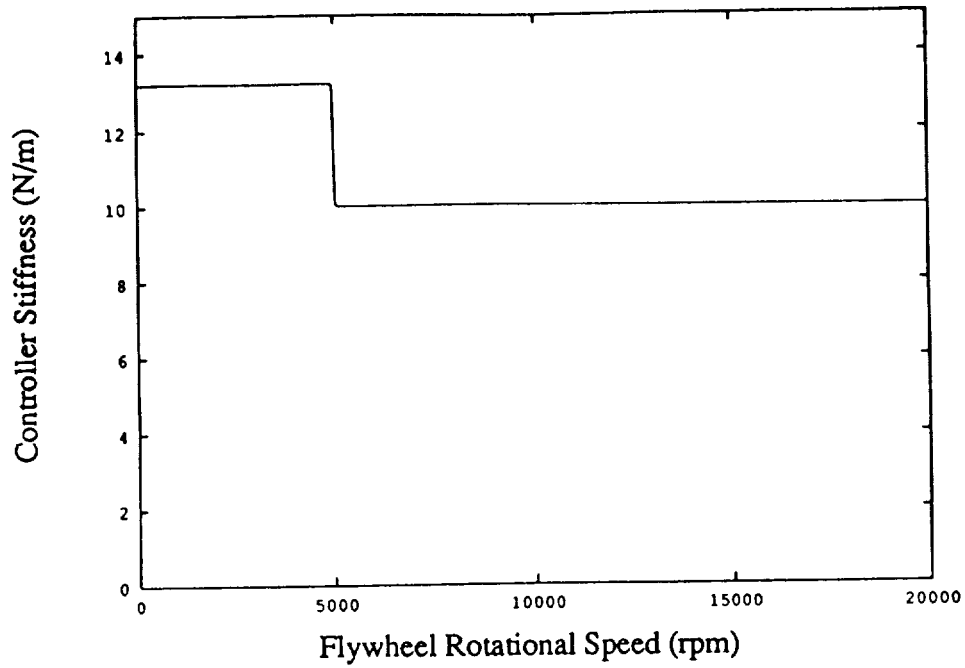
Figure 9a. Neural network controller stiffness.
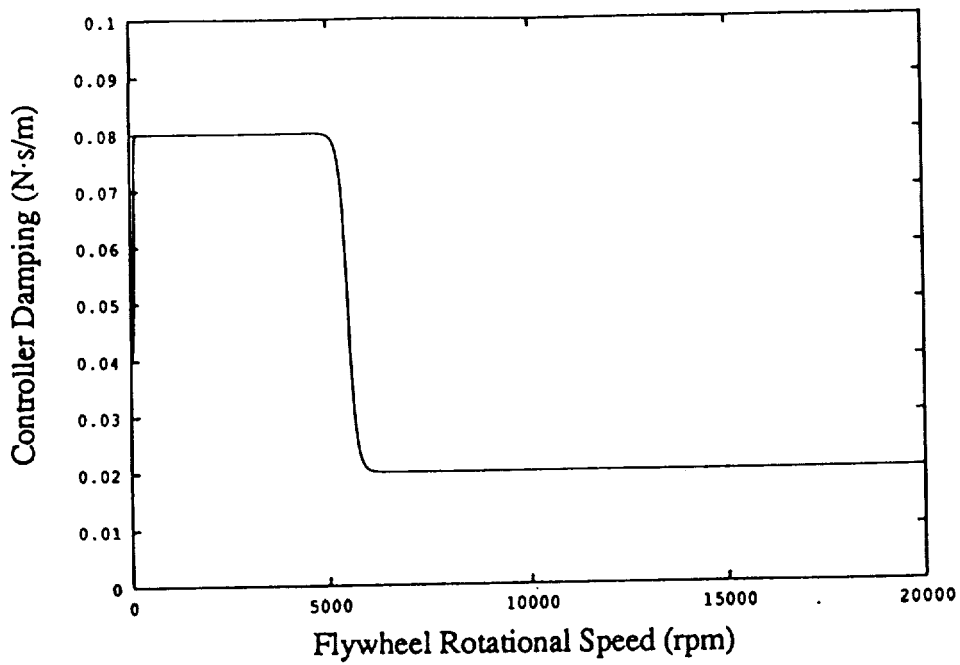
Figure 9b. Neural network controller damping.
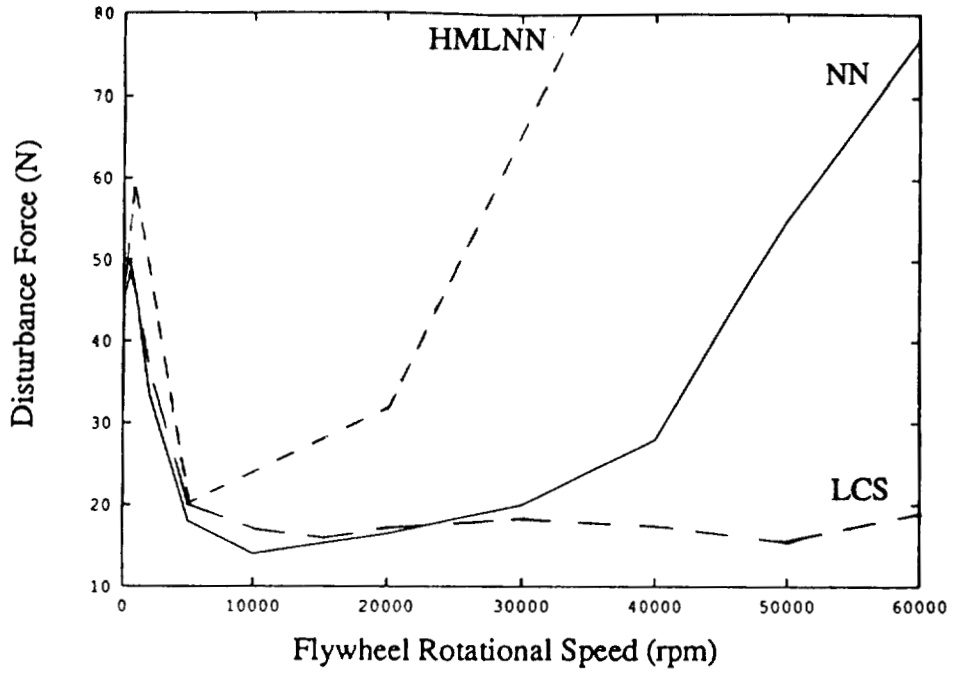
Figure 10. Control system performance.
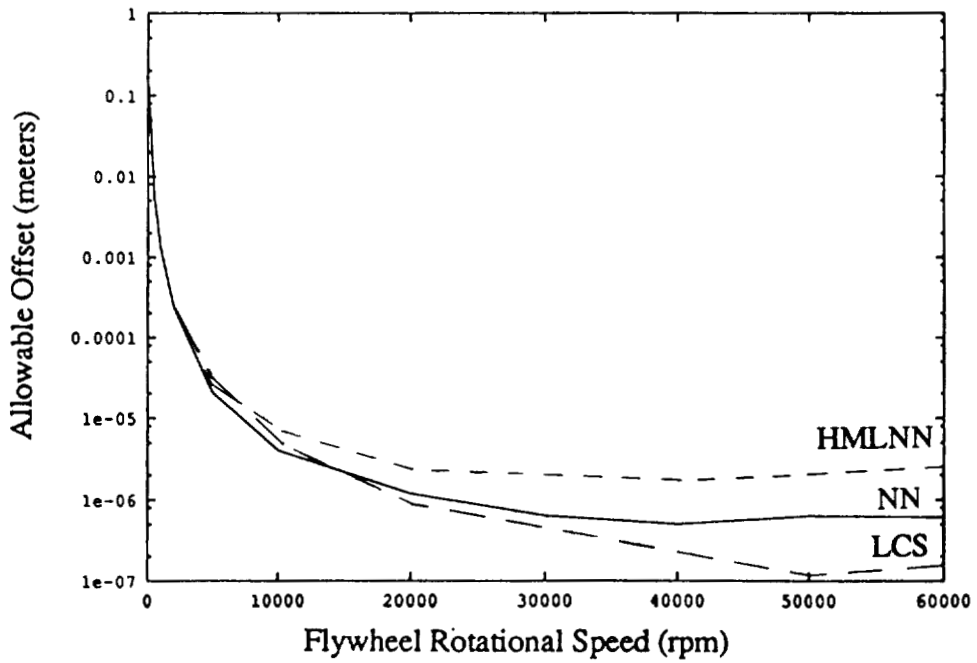
Figure 11. Control system performance.

TIME-DELAY CONTROL OF A MAGNETIC LEVITATED LINEAR POSITIONING SYSTEM

J.H.Tarn   K.Y. Juang   C.E. Lin
Institute of Aeronautics and Astronautics
National Cheng Kung University
Tainan, Taiwan

$$p. 14$$

ABSTRACT

In this paper, a high accuracy linear positioning system with a linear force actuator and magnetic levitation is proposed. By locating a permanently magnetized rod inside a current-carrying solenoid , the axial force is achieved by the boundary effect of magnet poles and utilized to power the linear motion, while the force for levitation is governed by Ampere's Law supplied with the same solenoid. With the levitation in a radial direction, there is hardly any friction between the rod and the solenoid. The high speed motion can hence be achieved. Besides, the axial force acting on the rod is a smooth function of rod position, so the system can provide nanometer resolution linear positioning to the molecule size. Since the force-position relation is highly nonlinear, and the mathematical model is derived according to some assumptions, such as the equivalent solenoid of the permanently magnetized rod, so there exists unknown dynamics in practical application. Thus "robustness" is an important issue in controller design. Meanwhile the load effect reacts directly on the servo system without transmission elements, so the capability of "disturbance rejection" is also required. With the above consideration, a time-delay control scheme is chosen and applied. By comparing the input-output relation and the mathematical model, the time-delay controller calculates an estimation of unmodeled dynamics and disturbances and then composes the desired compensation into the system. Effectiveness of the linear positioning system and control scheme are illustrated with simulation results.

INTRODUCTION

Interest in research on large-gap magnetic suspension systems began in the early 1960's. The principal goal was the elimination of aerodynamic support interference in wind tunnel testing. To early 1970's the interest extended to small-gap ones. The first system developed was the Annular Momentum Control Device (AMCD) with applications to the stabilization and control of spacecraft [1]. This research was continued with the Annular Suspension and Pointing System (ASPS) which provides orientation, mechanical isolation, and fine pointing of space experiments[2][3]. For decades, Magnetic suspension technologies (MST) have demonstrated their capabilities in many fields, from industrial compressors, high-speed milling and grinding spindles, magnetically levitated trains, control wheel suspension for

PAGE 406 INTENTIONALLY BLANK

spacecraft to rocket propulsion turbomachinery. Important features of the magnetic suspensions and actuator systems are:

(1) Versatility of the Electromagnetic Forces

The physical force of a magnetic circuit to a high-permeable armature is called the Maxwell-force. Contrary to this commonly used force, the reaction force of a conductor carrying a current in a magnetic field is called the Lorentz-force. By successful integration of these physical effects, the constructed electromagnetic subsystem can be utilized as a rotary motor, linear actuator, radial bearing, thrust bearing, etc.

(2) Molecule-size Resolution

One problem of electric motors is the ripple of motion at low-speed operating regions due to the finite pole effect. The rotor always rests at the finite circumference positions which have the minimum magnetic flux (potential energy). Thus there are inherited limitations for resolution of control. The non-pole magnetic field provided by a coil, on the other hand, sets no resolution limitation. The resolution limit, in turn, is set by sensors, instrumentation and control strategies. Magnetic suspension systems provide a promising approach for achieving positioning with nanometer resolution.

In this paper, a linear positioning system with a linear force actuator and magnetic levitation is to be designed. By locating a permanently magnetized rod inside a current-carrying solenoid, the axial force is achieved by the boundary effect of magnet poles and utilized to power the linear motion, while the force for levitation is provided by the magnetic bearing and governed by the maximum linkage principle. With the levitation in a radial direction, there is no friction between the rod and solenoid. The demand of high-speed motion can hence be achieved. Under the proposed arrangement, the axial force acting on the rod is a smooth function of rod position, so the system can provide nanometer-resolution linear positioning to the molecule size. It is known that an effective control system is the key condition for successful implementation of high-performance magnetic levitated positioning systems. Major issues for design of such control systems are:

(1) Nonlinearity

By assuming that the complete energy of the magnetic field is concentrated within the air gap. The basic mathematical models of active magnetic bearings are obtained from Maxwell's laws. The input-output relations are highly nonlinear despite the variables defined.

(2) Unmodelled Dynamics

Secondary effects such as copper resistance, stray fields and saturation are neglected.

(3) Disturbance Rejection

Because the load effect reacts directly on the servo system without the transmission elements, the capability of "disturbance rejection" is also required.

With the above considerations, a time-delay control scheme with the properties of "robustness" and "disturbance rejection" is utilized[4][5]. By comparing the input-output relation and the mathematical model, the time-delay controller calculates an estimation of unmodeled dynamics and disturbances and then composes the desired compensation into the system. Effectiveness of the linear positioning and control systems is illustrated by numerical simulation results.

SYSTEM DYNAMICS

System Configuration

The configuration of the proposed magnetic levitated linear positioning system is shown in Figure 1. To achieve the function of levitation, the current in the solenoid must be 'kept in the direction that can maintain the stability of radial motion. Under such condition, the magnetic force in the axial direction tends to push the rod away from the center of the solenoid. Hence a spring is required to supply the force in the opposite direction. Also, the spring must be precompressed to avoid an uncontrollable equilibrium point. The additional magnetic bearing system is used to keep the moving part balanced in the axial direction. With a biased current fed to the solenoid, the magnetic force ($F = I \times B$) in the radial direction is utilized to suspend the moving part, while, with the controlled current, the axial motion is governed by the force caused by the non-uniform magnetic field in the boundary.
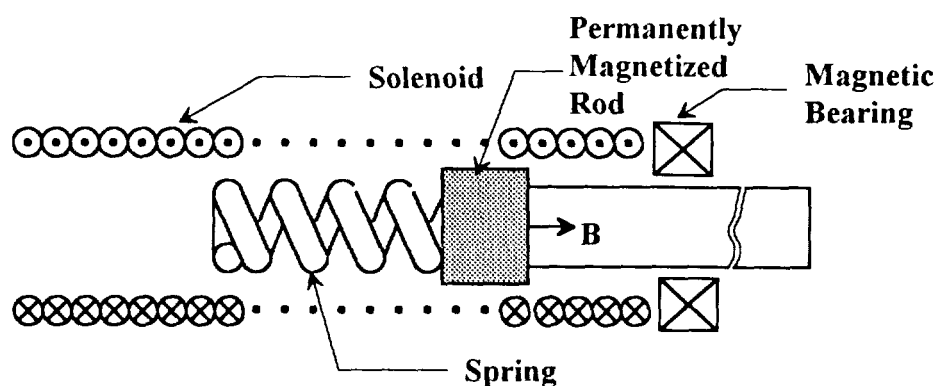
Figure 1 The configuration of magnetic levitated linear positioning system

Dynamics in Axial Motion

To derive the dynamics, a solenoid is employed to produce the equivalent magnetic field **B** of the permanently magnetized rod and thus simplify the calculation of the force-position relationship. With such an arrangement, the solenoid-rod configuration can be approximated as depicted in Figure 2. The force acting on the inner coil due to the current in the outer coil can then be found with Ampere's Law.
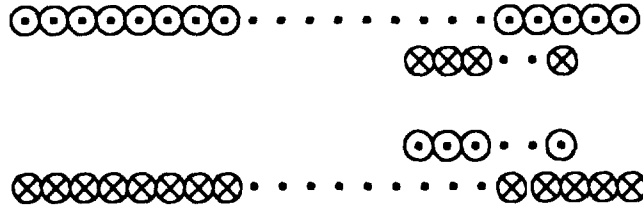
Figure 2 Equivalent configuration

Consider two current-carrying elements as shown in Figure 3. The force between the two current-carrying elements is[6]

$$dF = \frac{\mu_0 I_2 I_1}{4\pi r^2} \hat{a}_1 \times (\hat{a}_2 \times \hat{r}) dl_2 dl_1$$

where
dF = force on element 1 due to current in element 2, N
μ_0 = permeability of air, Hm^{-1}
dl_1, dl_2 = lengths of current-carriyng elements 1 and 2, respectively, m
I_1, I_2 = currents in elements 1 and 2, respectively, A
r = distance between elements, m
$\hat{a}_1$ = unit vector in direction of current in element 1, dimensionless
$\hat{a}_2$ = unit vector in direction of current in element 2, dimensionless
$\hat{r}$ = unit vector in radial direction(from element 2 to 1), dimensionless

Applying the force-position relation to the equivalent model, it can be found that the force acting on the inner coil with radius r_2 at position x_2 due to the current-carrying outer coil with radius r_1 at position x_1 is given by the following equation:

$$dF = \frac{\mu_0 I_1 I_2 r_1 r_2 d\theta_1 d\theta_2}{4\pi \left[(x_1 - x_2)^2 + (r_1\sin\theta_1 - r_2\sin\theta_2)^2 + (r_1\cos\theta_1 - r_2\cos\theta_2)^2 \right]^{3/2}} \cdot \left[\cos\theta_2 \vec{j} - \sin\theta_2 \vec{k} \right]$$

$$\times \left\{ \left[\cos\theta_1 \vec{j} - \sin\theta_1 \vec{k} \right] \times \left[(x_2 - x_1)\vec{i} + (r_2\sin\theta_2 - r_1\sin\theta_1)\vec{j} + (r_2\cos\theta_2 - r_1\cos\theta_1)\vec{k} \right] \right\}$$

Hence the force in the axial direction can be expressed as

$$dF_x = \frac{-\mu_0 I_1 I_2 r_1 r_2 (x_2 - x_1)(\cos\theta_1\cos\theta_2 + \sin\theta_1\sin\theta_2)}{4\pi \left[(x_1 - x_2)^2 + (r_1\sin\theta_1 - r_2\sin\theta_2)^2 + (r_1\cos\theta_1 - r_2\cos\theta_2)^2 \right]^{3/2}} d\theta_1 d\theta_2,$$

with the numerical calculation, the force-position relation of the rod, with 5000 Gauss of flux density at one end on the axis shown in Figure 4, where r_1 is 1.1 cm, r_2 is 1.0 cm, the length of the rod is 1.0 cm, and the length of the solenoid is 10 cm. The result indicates that the solenoid-rod configuration operates as a current-controlled stiffness nonlinear spring, so the model of axial motion can be simplified and shown in Figure 5, where K_1 is the preload spring, and K_2 is the equivalent model of the solenoid-rod configuration.

410
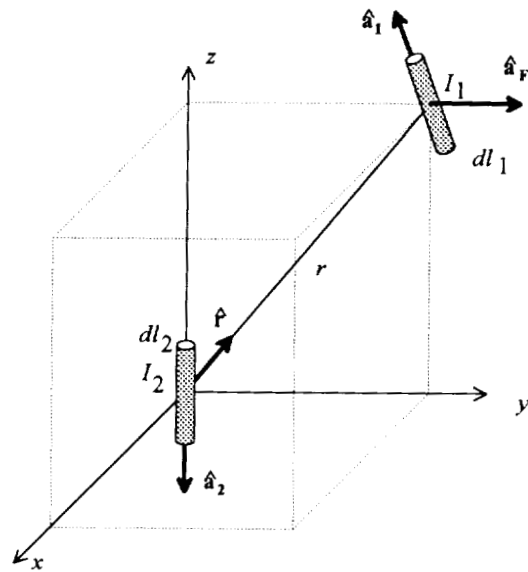
Figure 3 Geometry of short current-carrying elements for finding force between them.
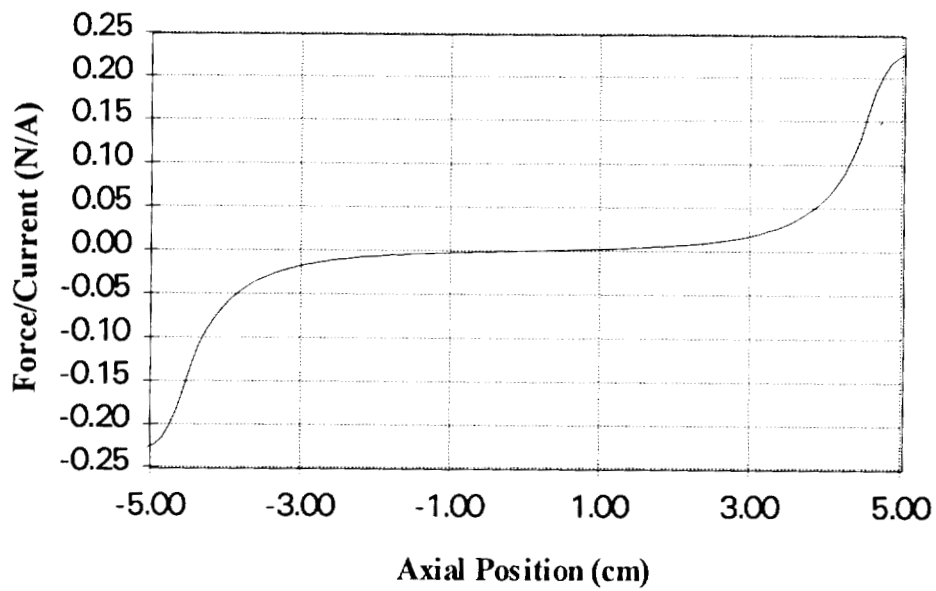
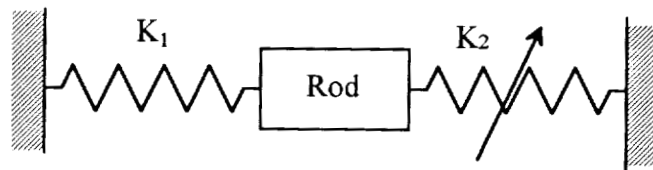Figure 4 Force-position relation in axial motion.

Figure 5 Simplified model of axial motion.

The dynamic equation in axial motion can then be modeled as

$$\dot{x}_1 = x_2$$

$$\dot{x}_2 = -\frac{1}{m}[K_1 \cdot (x_1 + x_p) + K_2(x_1) \cdot (i + i_b)]$$

where

x_1, x_2 = position and velocity of the rod respectively, cm, cm/sec

K_1 = stiffness of the spring, N/cm

$K_2(x)$ = current controlled stiffness of solenoid-rod configuration, N/A

x_p = pre-compressed length of the spring, cm

i_b = biased current for levitation, A

i = controlled current, A

m = mass of the magnetic rod, kg

Dynamics of Radial Motion

To verify the function of levitation of the proposed mechanism, the dynamics of radial motion is taken into consideration. Imagine a small deviation of the rod position in radial direction y_2, then the radial force can be modeled as

$$d\mathbf{F}_y = \frac{\mu_0 I_1 I_2 r_1 r_2 [r_2 \sin\theta_2 (\cos\theta_1 \cos\theta_2 + \sin\theta_1 \sin\theta_2) + (y_2 \sin\theta_1 - r_1)\sin\theta_2]}{4\pi \left[(x_1 - x_2)^2 + (y_2 + r_1\sin\theta_1 - r_2\sin\theta_2)^2 + (r_1\cos\theta_1 - r_2\cos\theta_2)^2 \right]^{3/2}} d\theta_1 d\theta_2,$$

From the calculation, the result is shown in Figure 6. It is clear that, with positive current, the force tends to force the rod staying in the central axial position. Any deviation in radial direction will cause a force in the opposite direction to push it back. Hence the function of levitating is achieved. In this paper, the motion in the radial direction is not controlled.

Since the system is passive and motion in the radial direction is confined, the open loop in the radial direction poses no stability problem.
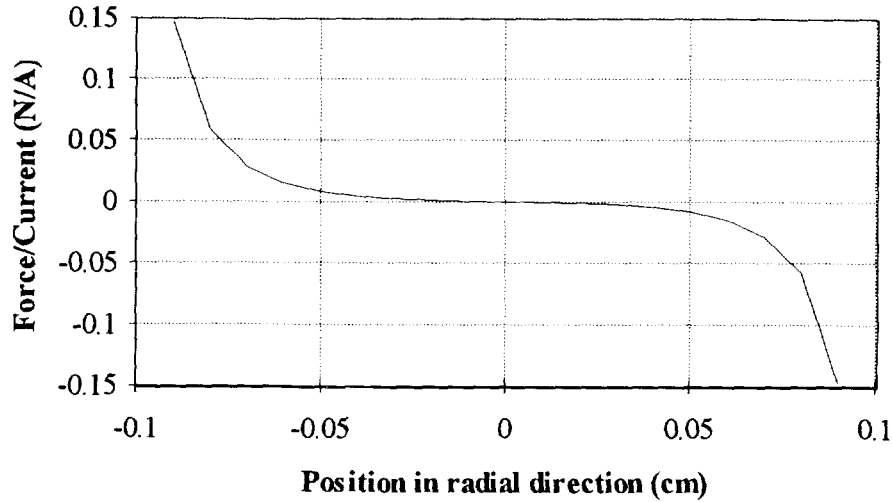
Figure 6 Axial force-position relation.

CONTROLLER DESIGN

Time Delay Controller

Since the magnetic levitated positioning system is subjected to the load effect directly, the controller must be good at disturbance rejection. Besides, the force-position relation is highly nonlinear. Hence the Time-Delay Controller (TDC) design method proposed by Youcef-Toumi [3] is applied to control the rod position.

Consider the axial motion to be controlled as

$$\dot{x} = f(x, t) + h(x, t) + B(x, t)u + d(t)$$

where

x = an $n \times 1$ plant state vector,

$f(x,t)$ = an $n \times 1$ nonlinear vector represents the known dynamics,

$h(x,t)$ = an $n \times 1$ nonlinear vector represents the unknown dynamics,

$B(x,t)$ = an $n \times r$ control distribution matrix with rank r,

$d(t)$ = an $n \times 1$ unknown disturbance function.

Define the linear time-invariant reference model as

$$\dot{x}_m = A_m x_m + B_m r$$

413

and the error between the model and the plant as

$$\mathbf{e} = \mathbf{x}_m - \mathbf{x}.$$

The objective of the control scheme is to make the error behave as the desired dynamics

$$\dot{\mathbf{e}} = \mathbf{A}_e\mathbf{e} = (\mathbf{A}_m + \mathbf{K})\mathbf{e}$$

Combined with the plant dynamics and reference model dynamics, the error dynamics can be formulated as

$$\dot{\mathbf{e}} = \mathbf{A}_e\mathbf{e} + [-\mathbf{f} - \mathbf{h} - \mathbf{d} + \mathbf{A}_m\mathbf{x} + \mathbf{B}_m\mathbf{r} - \mathbf{B}\mathbf{u} - \mathbf{K}\mathbf{e}]$$

To satisfy the desired error dynamics, the control input **u** must be functioned to make

$$[-\mathbf{f} - \mathbf{h} - \mathbf{d} + \mathbf{A}_m\mathbf{x} + \mathbf{B}_m\mathbf{r} - \mathbf{B}\mathbf{u} - \mathbf{K}\mathbf{e}] = 0$$

Observe the above equation; only **h** and **d** are unknown. They can be estimated from the measured information at time $t - L$, with

$$\hat{\mathbf{h}}(\mathbf{x}, t) + \mathbf{d}(t) \cong \hat{\mathbf{h}}(\mathbf{x}, t - L) + \mathbf{d}(t - L) \cong \dot{\mathbf{x}}(t - L) - \mathbf{f}(\mathbf{x}, t - L) - \mathbf{B}(\mathbf{x}, t - L)\mathbf{u}(t - L).$$

Then the TDC control law is

$$\mathbf{u}(t) = \mathbf{B}^+(t)[\mathbf{f}(\mathbf{x}, t - L) - \dot{\mathbf{x}}(t - L) + \mathbf{B}(\mathbf{x}, t - L)\mathbf{u}(t - L) - \mathbf{f}(t) + \mathbf{A}_m\mathbf{x}(t) + \mathbf{B}_m\mathbf{r}(t) - \mathbf{K}\mathbf{e}(t)]$$

Rewrite the dynamics equation of the magnetic levitated linear positioning system as

$$\dot{x}_1 = x_2$$
$$\dot{x}_2 = -\frac{1}{m}\left\{[K_1 \cdot (x_1 + x_P)] + \left[K_2(x_1) \cdot (i + i_b) + m\hat{b}i\right]\right\} + \hat{b}i$$

and let

$$\mathbf{f}(\mathbf{x}) = \begin{bmatrix} x_2 \\ -K_1 \cdot (x_1 + x_P)/m \end{bmatrix}, \quad \mathbf{h}(\mathbf{x}) = \begin{bmatrix} 0 \\ -K_2(x_1) \cdot (i + i_b)/m - \hat{b}i \end{bmatrix} \text{ and } \mathbf{B} = \begin{bmatrix} 0 \\ \hat{b} \end{bmatrix}$$

then by choosing the reference model as

$$\begin{bmatrix} \dot{x}_1 \\ \dot{x}_2 \end{bmatrix} = \begin{bmatrix} 0 & 1 \\ -100 & -20 \end{bmatrix} \begin{bmatrix} x_1 \\ x_2 \end{bmatrix} + \begin{bmatrix} 0 \\ 100 \end{bmatrix} i$$

and $\mathbf{K} = 0$, then the control force is

414

$$i(t) = \hat{b}^{-1}\left\{K_1[x_1(t-L)-x_1(t)]/m - \dot{x}_2(t-L) + \hat{b}(t-L)i(t-L) - 100x_1(t) - 20x_2(t) + 100r(t)\right\}$$

The simulation results are shown in Figure 7 and Figure 8. In the simulation, the control force is limited with a saturation bound [-3.5, 10] and $\hat{b}$ is chosen to be a constant 10. Under the case in Figure 7, the linear positioning system is subjected to a step disturbance in the axial direction at time $t = 0.5$ sec, whose amplitude is -0.1. For the case in Figure 8, the system is utilized to move a load with mass equals to 5 m, the mass of the moving part.
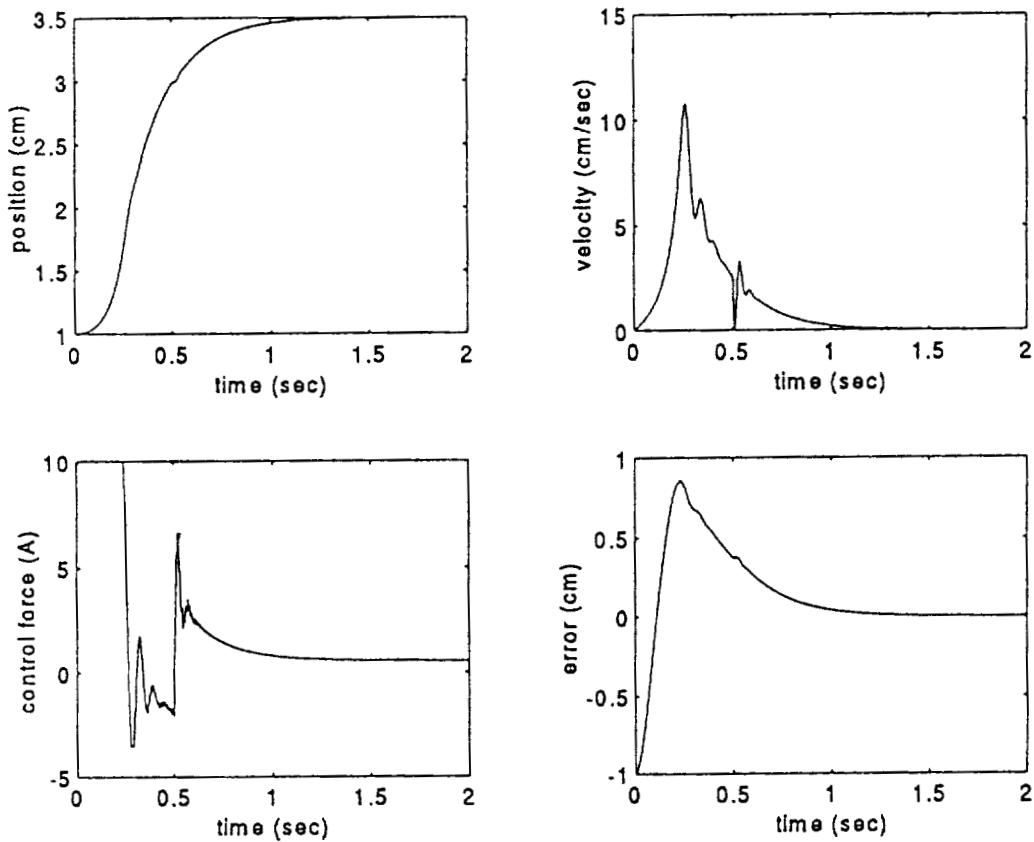
Figure 7 Simulation result with Time Delay Controller.
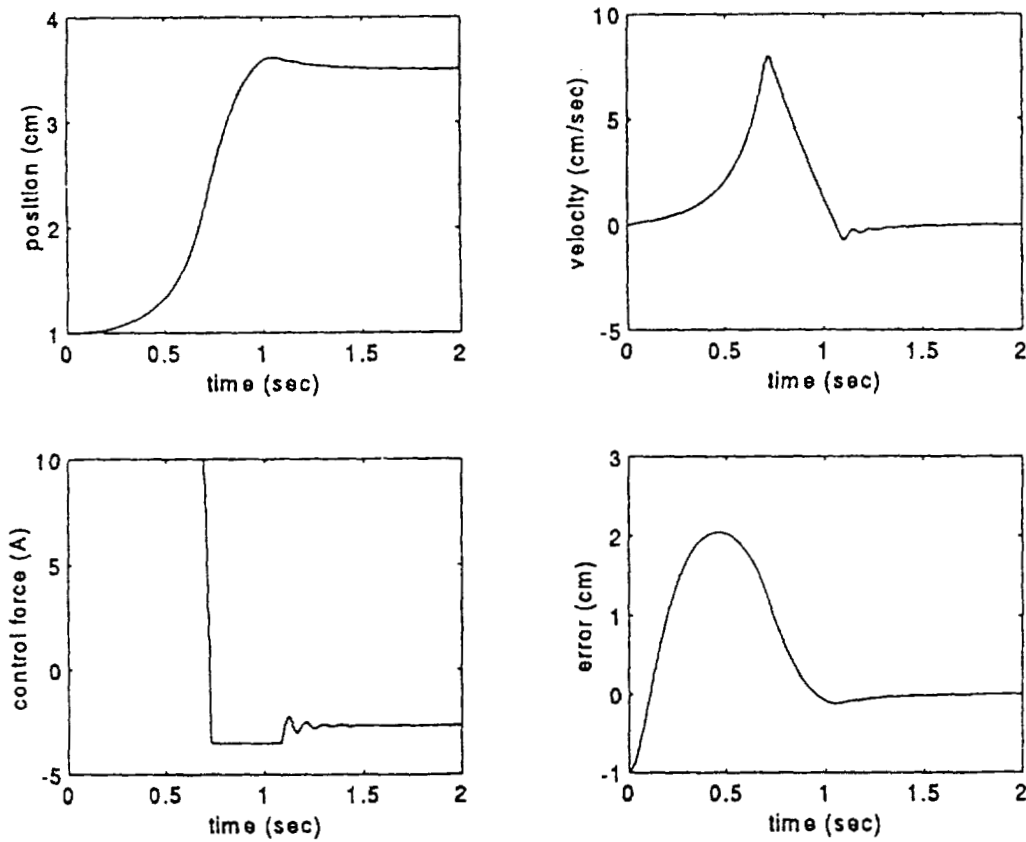
Figure 8 Simulation result of TDC

Time Delay Controller with Mean Value Theorem

The method described in the previous section requires the measurement of $\dot{x}_2$. It means that the designer must take care of either the noise induced by numerical derivativeness or the setting up of the accelerometer. An alternative scheme is introduced by Youcef-Toumi[4] with the application of the mean-value theorem as follows:

Define the unmodeled dynamics $\Psi = h + d$; the error dynamics can be written as

$$\dot{e} = A_e e + [-f - \Psi + A_m x + B_m r - Bu - Ke]$$

Integrate the equation at both sides to get

$$e(t) = \Phi(t, t_0)e(t_0) + \int_{t_0}^{t} \Phi(t, \tau) [A_m x(\tau) + B_m r(\tau) - f(\tau) - \Psi(\tau) - Bu(\tau) - Ke(\tau)]d\tau \qquad \forall t \geq t_0$$

416

where

$$\Phi(t, \tau) = e^{A_e(t-\tau)}$$

Then

$$\int_{t_0}^{t} \Phi(t, \tau)\Psi(\tau)d\tau = \Phi(t, t_0)e(t_0) - e(t) + \int_{t_0}^{t} \Phi(t, \tau) [A_m x(\tau) + B_m r(\tau) - f(\tau) - Bu(\tau) - Ke(\tau)]d\tau$$

Utilizing the mean-value theorem approximation, the above equation can be approximated by

$$\left[\int_{t_0}^{t} \Phi(t, \tau) d\tau\right]\hat{\Psi}(t) = \Phi(t, t_0)e(t_0) - e(t) + \int_{t_0}^{t} \Phi(t, \tau) [A_m x(\tau) + B_m r(\tau) - f(\tau) - Bu(\tau) - Ke(\tau)]d\tau$$

Thus the control force can be found as

$$u = B^{+}\left[A_m x + B_m r - f - \hat{\Psi} - Ke\right]$$

With the same choice of reference model in the previous section, the simulation result with step disturbance in axial force is given in Figure 9. Figure 10 demonstrates the result of load effect.
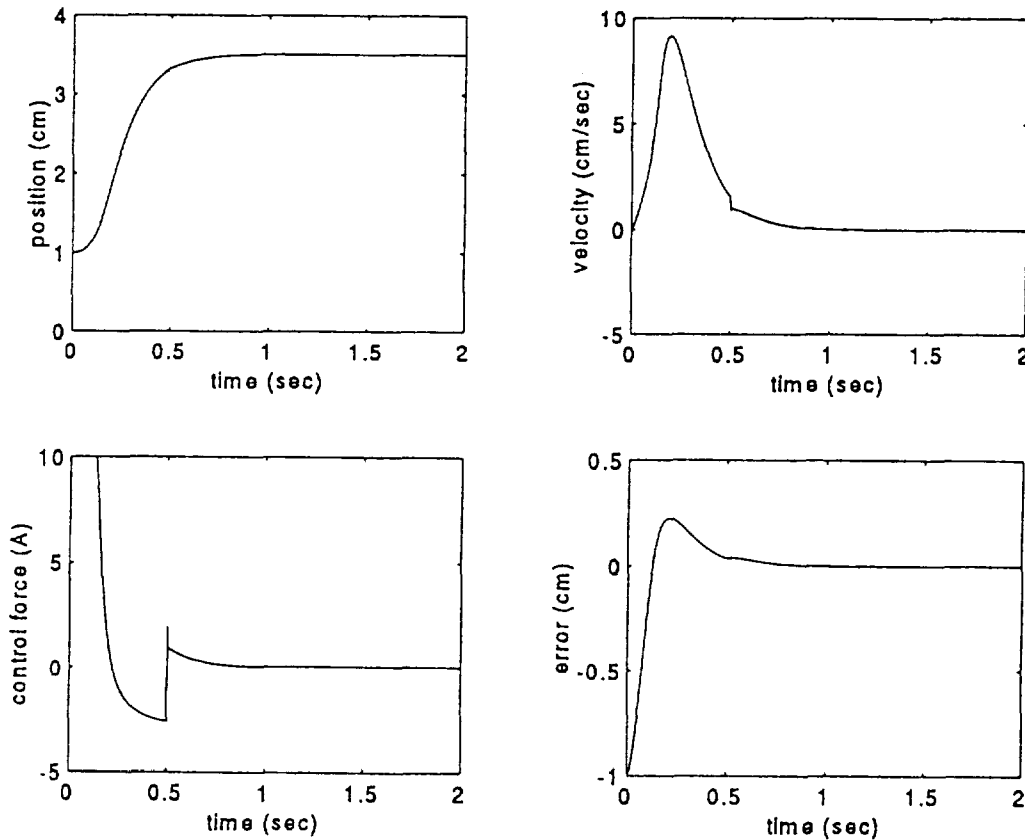
Figure 9 Simulation result with modified Time Delay Controller (I)
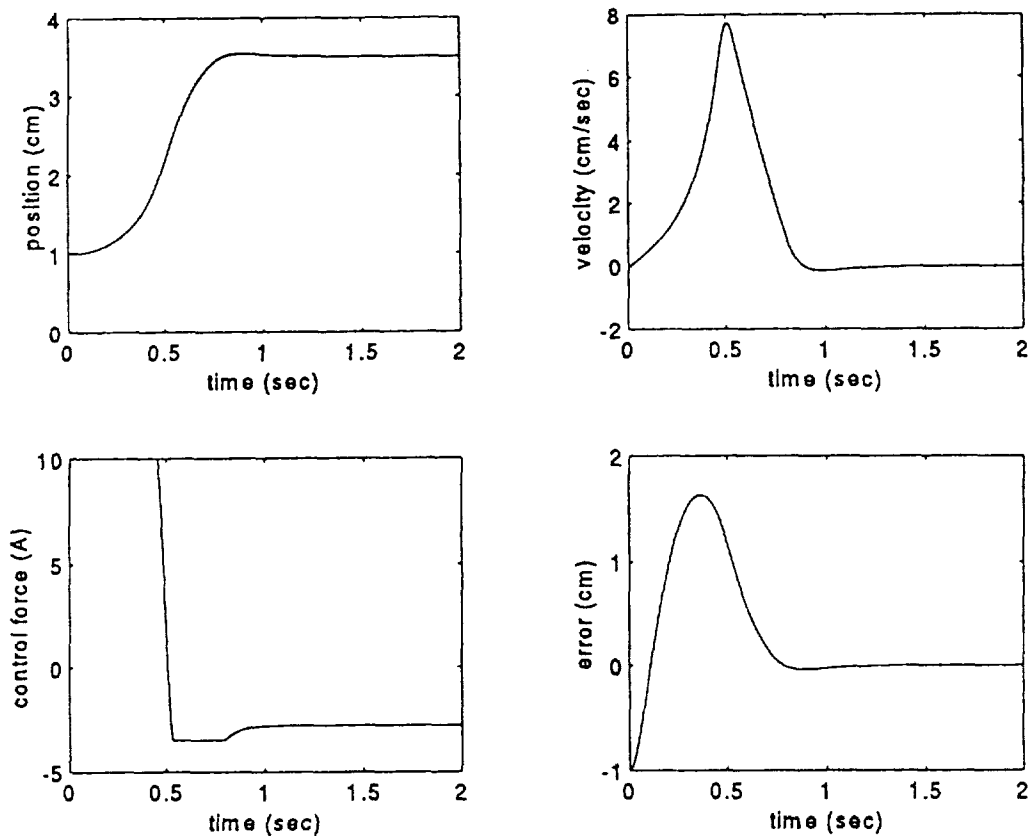
Figure 10 Simulation result with modified Time Delay Controller (II)

Discussions

From the simulation results, the property of "disturbance rejection" of Time Delay Controllers is demonstrated. Due to the saturation constraint in the control force, the controller can perform well with limited external load. With the mean-value approximation, the performance is improved. But it requires a higher sampling rate to gather more information in the delay time.

During the design stage, the choice of parameter $\hat{b}$ plays an important role. In general, if we know more about the nonlinear dynamics of the system to be controlled, we can have a better choice of $\hat{b}$. Under the situation that no information is given for the unknown dynamics, we usually choose $\hat{b}$ as a constant value. From simulation results shown in Figure 11, we conclude that the larger $\hat{b}$ provides more guarantee on the "disturbance rejection", but has poorer performance. But, the larger $\hat{b}$ drives the control force to the saturation bound easily and consequently the system fails to work.

418
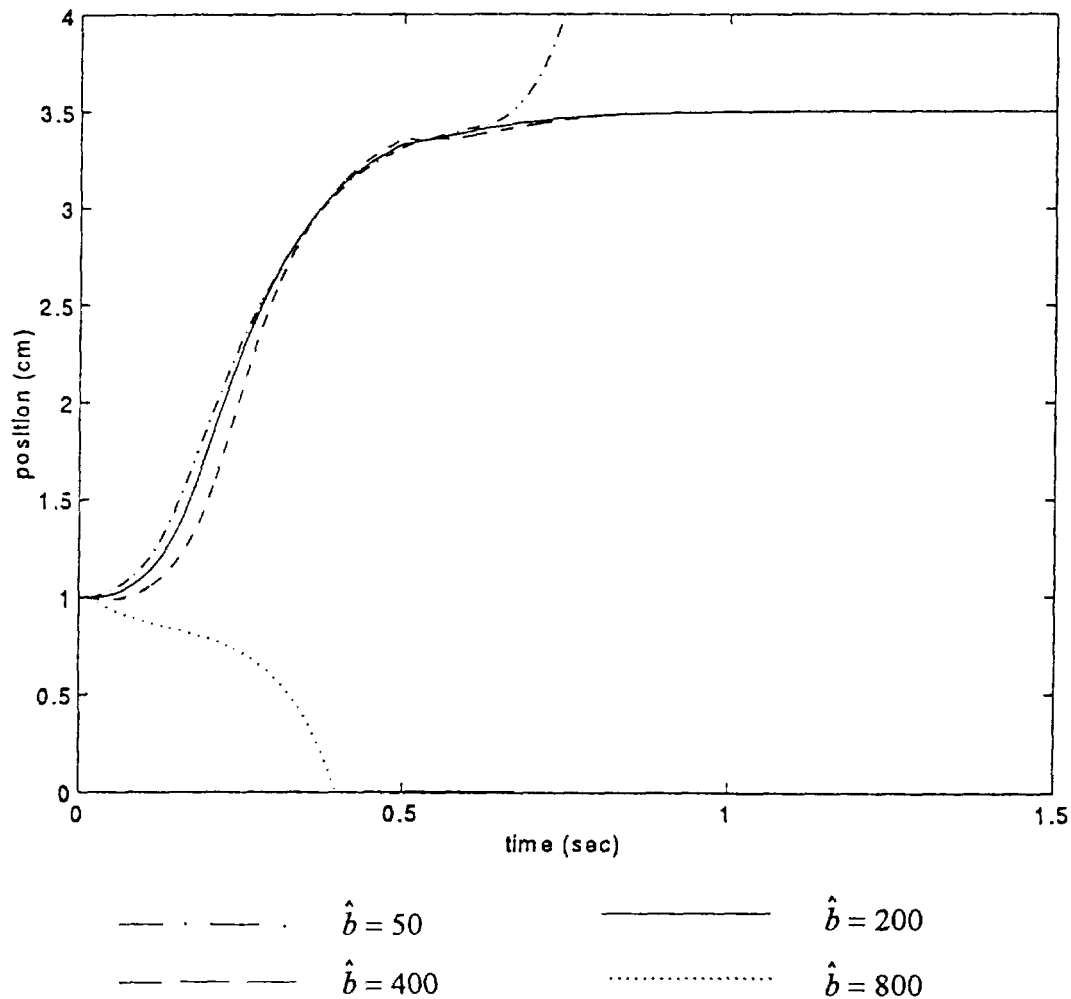
Figure 11 Response under different choices of $\hat{b}$.

CONCLUSION

Applying the equivalent magnetic flux density between the solenoid and permanently magnetized rod, a method of modeling the force-position relation in the solenoid-rod configuration is proposed. Based on the model, a "current controlled stiffness" spring serves as a low friction linear positioning system. Two kinds of Time Delay Control schemes are applied to control the system. The Time Delay Controller is a fast adaptive control scheme without identification of the dynamics of the plant to be controlled, so it can be easily implemented. From the simulation results, the property of disturbance rejection is demonstrated.

REFERENCES

[1] Anderson, Willard W. and Groom, Nelson J., "The Annular Momentum Control Device (AMCD) and Potential Applications," NASA TN D-7866, 1975.

[2] Anderson, Willard W. and Joshi, Suresh M., "The Annular Suspension and Pointing (ASP) System for Space Experiments and Predicted Pointing Accuracies," NASA TR R-448, 1975.

[3] Anderson, Willard W.; Groom, Nelson J. and Woolley, Charles T.,"The Annular Suspension and Pointing System," Journal of Guidance and Control, Vol. 2, No. 5, 1979, pp. 367-373.

[4] Youcef-Toumi, K. and Wu, S.-T., 1992, "Input/Output Linearization Using Time Delay Control," ASME Journal of Dynamic Systems, Measurement, and Control, March issue, 1992.

[5] Youcef-Toumi, K. and Reddy, S., "Analysis of Linear Time Invarient Systems with Time Delay," ASME Journal of Dynamic Systems, Measurement, and Control, December issue, 1992.

[6] Kraus, J. D."Electromagnetic," 3rd Edition, McGraw-Hill.

[7] Youcef-Toumi, K. and Ito, O., "A Time Delay Controller for Systems With Unknown Dynamics," ASME Journal of Dynamic Systems, Measurement, and Control, Vol. 112, Mar 1990, pp.133-142.

[8] Youcef-Toumi, K., "Fast Adaptive Control Algorithms In Precision Motion Control Systems," Proceedings of 1993 National Symposium on Automatic Control, pp. 59-149.

420

THIRD ORDER LPF TYPE COMPENSATOR FOR FLEXIBLE ROTOR SUSPENSION

Osami Matsushita
The National Defense Academy

Naohiko Takahashi
Tsuchira Works, Hitachi, Ltd.

Michiyuki Takagi
Mechanical Engineering Research Laboratory, Hitachi, Ltd.

ABSTRACT

The tuning job of the compensator for levitating flexible rotors supported by active magnetic bearings (AMB) concerns providing a good damping effect to the critical speed modes while avoiding the spillover problem on the instability of higher bending modes. In this paper, an idea for design of the control law of the compensator based on utilizing a third order low pass filter (LPF) is proposed to essentially enable elimination of the spillover instability. According to the proposed design method, good damping effects for the critical speeds are obtained by the usual phase lead/lag function. Stabilization for all of higher bending modes is completed by the additional function of the 3rd order LPF due to its phase lag approaching about -270 degrees in the high frequency domain. This idea is made clear by experiments and simulations.

INTRODUCTION

To design control network driving active magnetic bearings (AMB) for flexible rotor levitation, it is important to consider rigid mode levitation, controllability of flexible modes at critical speeds and a stability margin for high frequency bending modes. For instance, a design of super critical compressors supported by AMBs illustrates this point. In the first design phase, rigid mode levitation performance is determined. Next, the well damping ratio of the first bending mode necessary to pass the critical speed is determined according to Q-value criteria. Finally, the PID controller transfer function is tuned so as to satisfy these two requirements and so as to avoid higher frequency instability beyond 2nd bending modes. It is called a spillover problem.[1]

Usually, the PID control law with optional notch filters and/or low pass filters is used for tuning. Otherwise, the increase of the internal damping of the rotor is improved. However, this design method based upon the phase lead/lag function is not free from the spillover problem. However, the presented method can provide a highly robust control system for the higher modes and satisfactory performance for the controlled modes. It is possible to skillfully combine the commonly used phase lead/lag function with the 3rd order LPF. How to design the 3rd order LPF is a main point of this paper.

The phase lead/lag function can possibly provide enough damping performance to the rigid and first bending modes. It can be done by placing these critical speeds in the phase lead domain. If a flexible rotor system requires higher damping than one provided by the phase lead function, some

optional function can be used just for passing the bending critical speeds. According to our experiences, an optional network, called N-CROSS, is recommended.[2] It works only around the critical speeds of the shaft bending modes during the rotor rotation. Then, the problem is how to design the compensator featuring no spillover to potentially stabilize all the eigen modes.

The proposed design method features the addition of the 2nd order LPF to the usual PID compensator in order to realize this 3rd order LPF. The center frequency of the 2nd order LPF coincides with the eigen frequency of the rotor restricted by pin-pin boundary at AMB portions. This eigen frequency is equal to the anti-resonance frequency located between the 1st and 2nd bending modes. Since the total function of the controller network becomes a 3rd order LPF, the phase lag forwards to -270 degrees, i.e., a 90 degree phase lead, in the high frequency domain. Therefore, all the higher natural frequencies beyond the 2nd bending mode are essentially stable, i.e., completely free from the spillover problem.

This idea is theoretically explained for a rotor system with one AMB support. The effectiveness of this design method is proven by numerical simulations and experimental results. The rotation test is done with a low enough Q-value to pass the rigid and first bending critical speed without the high frequency instability. The generalization of this design concept is finally proposed for the flexible rotor borne by two AMBs.

A FLEXIBLE ROTOR WITH ONE ACTIVE MAGNETIC BEARING

A flexible rotor shown in Fig.1 is selected for explaining the fundamental idea of the design method of AMB compensator. The rotor is supported by a ball bearing at the right end and by an AMB at the other. The ball bearing placed here is represented by the pin boundary condition to explain the idea clearly. The problem then focuses on to how to design the compensator driving the AMB at the left side.

rotor weight = 18 DN

Free-free natural frequency =

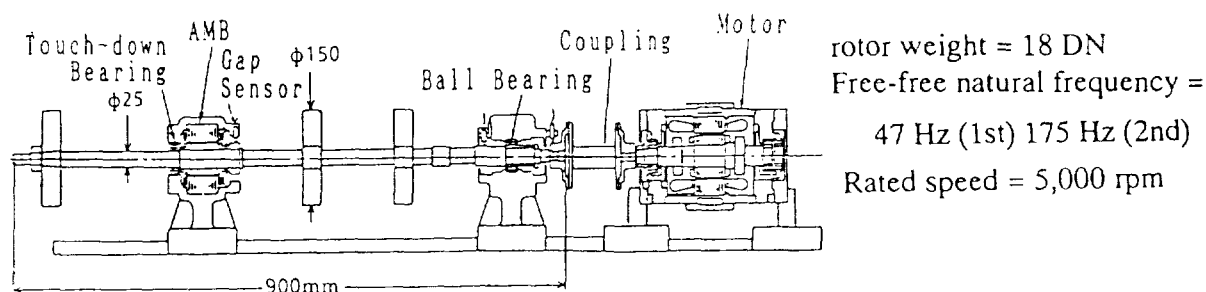47 Hz (1st) 175 Hz (2nd)

Rated speed = 5,000 rpm

Fig.1 Experimental test rig

A gap sensor placed at the left side detects the rotor radial displacement which feeds its signal to the controller. The signal from the controller drives the magnetic bearing force through the power amplifier having a transfer function of unity. The rotor is connected to a motor with a flexible coupling. The flexible coupling is flexible enough to satisfy the free boundary condition at the right end of the rotor as shown Fig.2(a). Gyroscopic effects are neglected here.

The displacement vector is noted by $X=[X_1^t,X_2]$: X_2 for the rotor displacement at the AMB portion and X_1 for the displacements of all portions of the rotor except the AMB portion. The former is called the boundary displacement and the latter called the inner displacement vector. In the AMB

servo-control system, the boundary displacement X_2 is measured and the AMB force U acts upon the rotor according to a control law. Then, the equation of motion of the rotor-bearing system can be written in matrix form as follows:

$$\begin{bmatrix} M_1 & \\ & M_2 \end{bmatrix} \begin{bmatrix} \ddot{X}_1 \\ \ddot{X}_2 \end{bmatrix} + \begin{bmatrix} K_{11} & K_{12} \\ K_{12}^t & K_{22} \end{bmatrix} \begin{bmatrix} X_1 \\ X_2 \end{bmatrix} = \begin{bmatrix} 0 \\ 1 \end{bmatrix} U \qquad (1)$$

where M_i and K_{ij} (i,j=1,2) indicate mass and stiffness matrices of the rotor system, respectively, noted by 1 for the inner portion and by 2 for the boundary AMB portion.

Any damping factors, e.g., shaft material damping, mechanical dampers, are neglected. In the authors' opinion, the consideration of such system damping factors, in addition, will potentially destroy the realization of practical robust control. Rotordynamics designers want to consider the compensator design for the AMB, similarly, the design for oil-film bearings, i.e., neglecting any system damping.

(c) Reduced Model

(a) Rotor System with an AMB

Deflection Mode

Bending Mode

(b) Transformation modes
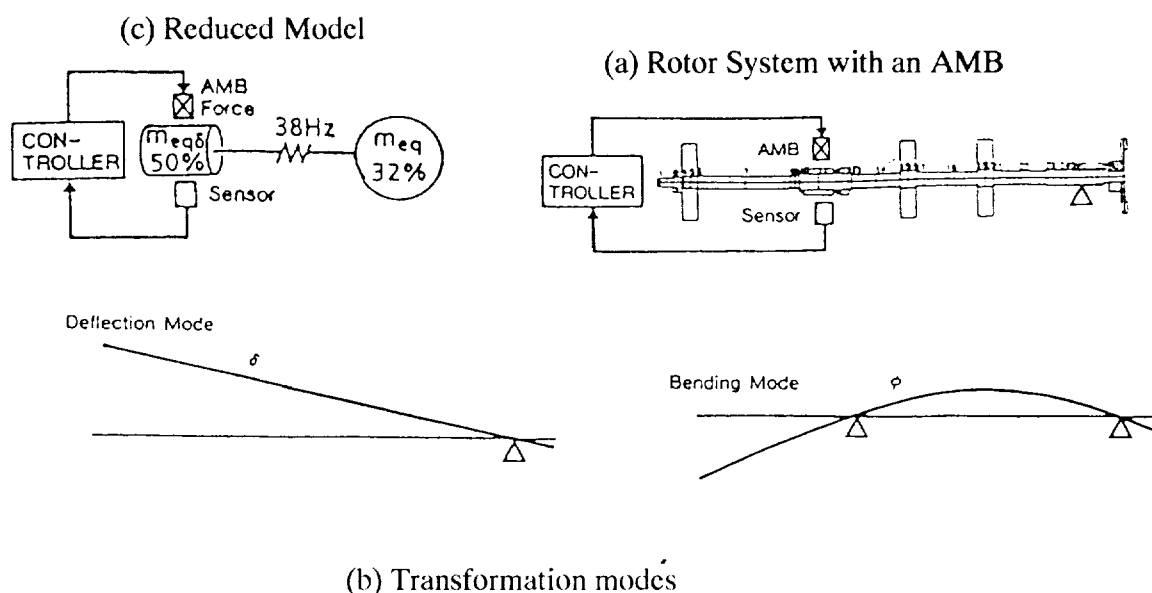
Fig.2 Modelling by quasi-modal transformation

SYSTEM MODELLING

The equation of motion (1) of the rotor is formulated in FEM matrix forms on meshing by the shaft beam element. The quasi-modal system reduction in a category of the modal synthesis is applied to the original system.[3] The quasi-modal transformation modes are determined by two kinds of modes as shown in Fig.2(b):

(1) Pure bending mode ϕ obtained by eigen mode of the rotor if the pin condition is imposed at the AMB portion.

(2) Rigid mode δ obtained by deflection mode if the rotor is lifted to give the unit displacement at the AMB portion.

The quasi-modal transformation is defined by the following equation:

$$X = \begin{bmatrix} X_1 \\ X_2 \end{bmatrix} = \begin{bmatrix} \phi & \delta \\ 0 & 1 \end{bmatrix} \begin{bmatrix} s \\ X_2 \end{bmatrix} \tag{2}$$

where the variable s is a weighting value indicating the magnitude of the pure bending mode obtained in the rotor bending critical speed mode.

From the result of the transformation, the following equation of motion of the reduced model having 2 degrees of freedom is completed:

$$\begin{bmatrix} m^* & m_c \\ m_c & m_\delta \end{bmatrix} \begin{bmatrix} \ddot{s} \\ \ddot{x}_2 \end{bmatrix} + \begin{bmatrix} k^* & \\ & 0 \end{bmatrix} \begin{bmatrix} s \\ x_2 \end{bmatrix} = \begin{bmatrix} 0 \\ 1 \end{bmatrix} u, \tag{3}$$

where $m^* = \phi^t M_1 \phi$, $m_c = \phi^t M_1 \delta$, $m_\delta = M_2 + \delta^t M_1 \delta$, $k^* = m^* \omega_P^2$ and

ω_P = the natural frequency of the pure bending mode under the pin

boundary condition at the AMB portion.

This equation of motion having the mass interaction between the pure bending mode and the rigid mode is equivalently converted to the spring interaction. This conversion is possible to provide the reduced vibrating model visually composing the mass-spring connection, if a new absolute displacement x* is introduced as s=a(x* - x_2):

$$a = m_c / m^* = \phi^t M_1 \delta / \phi^t M_1 \phi \tag{4}$$

$$\begin{bmatrix} m_{eq} & \\ & m_{eq\delta} \end{bmatrix} \begin{bmatrix} \ddot{x}^* \\ \ddot{x}_2 \end{bmatrix} + \begin{bmatrix} k_{eq} & -k_{eq} \\ sym. & k_{eq} \end{bmatrix} \begin{bmatrix} x^* \\ x_2 \end{bmatrix} = \begin{bmatrix} 0 \\ 1 \end{bmatrix} u, \tag{5}$$

where $m_{eq} = a^2 m^*$, $m_{eq\delta} = m_\delta - m_{eq}$, $k_{eq} = m_{eq} \omega_P^2$ and $a = m_c / m^* = \phi^t M_1 \delta / \phi^t M_1 \phi$

The obtained model is illustrated in Fig.2(c). The masses of meq δ and meq indicate the equivalent masses of the rigid mode and the pure bending mode, respectively.

CONVENTIONAL DESIGN CONCEPT FOR COMPENSATOR

The negative spring effect exhibited by the AMB is neglected. It can be easily compensated by certain gain of the proportional action. The equation of motion (5) of the model is rewritten by the state equation form as follows:

$$\dot{X} = AX + bu$$
$$y = cX \tag{6}$$

where

$$
X = \begin{bmatrix} x_2 \\ x^* \\ \dot{x}_2 \\ \dot{x}^* \end{bmatrix}, \quad
A = \begin{bmatrix} 0 & 0 & 1 & 0 \\ 0 & 0 & 0 & 1 \\ -k_{eq}/m_{q5} & k_{eq}/m_{q5} & 0 & 0 \\ k_{eq}/m_{eq} & -k_{eq}/m_{eq} & 0 & 0 \end{bmatrix}, \quad
b = \begin{bmatrix} 0 \\ 0 \\ 1/m_{q5} \\ 0 \end{bmatrix} \quad \text{and}
$$

$$ c = \begin{bmatrix} 1 & 0 & 0 & 0 \end{bmatrix} $$

The controller design based upon the modern control theory combining the full order observer and the optimum feedback gain due to LQR is applied to the model in the manner as shown in Fig.3. [4]

One example of the transfer function of the compensator itself is obtained as shown in Fig.4. The overall configuration of the transfer function is fundamentally similar to PID action, but down slope gain of 1st order LPF at the high frequency domain.

The free-free eigen frequency is indicated by the bottom points of the dotted curve. Therefore, the damping ratio of the rigid and first bending mode of the global system can be well provided. However, higher bending modes than the 2nd will be easily unstable due to the phase lag at this high frequency domain.

In fact, the phase curve on the Bode diagram changes from the phase lead region to the phase lag region beyond the peak portion of the gain curve. This phase lag forwarding to -90 degrees provides a negative damping effect for high frequency eigen modes of the global system. This is the reason why the spillover instability is induced.
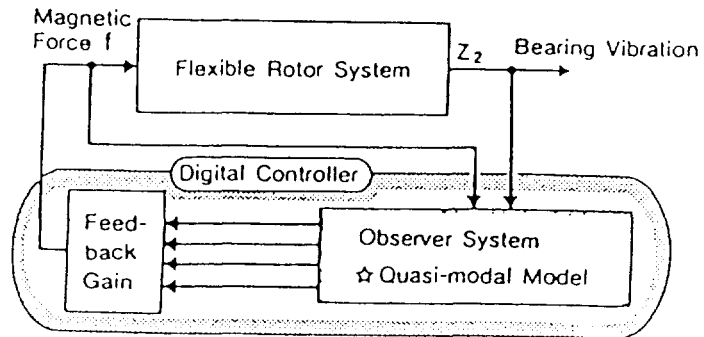
Fig. 3 Conventional control layout
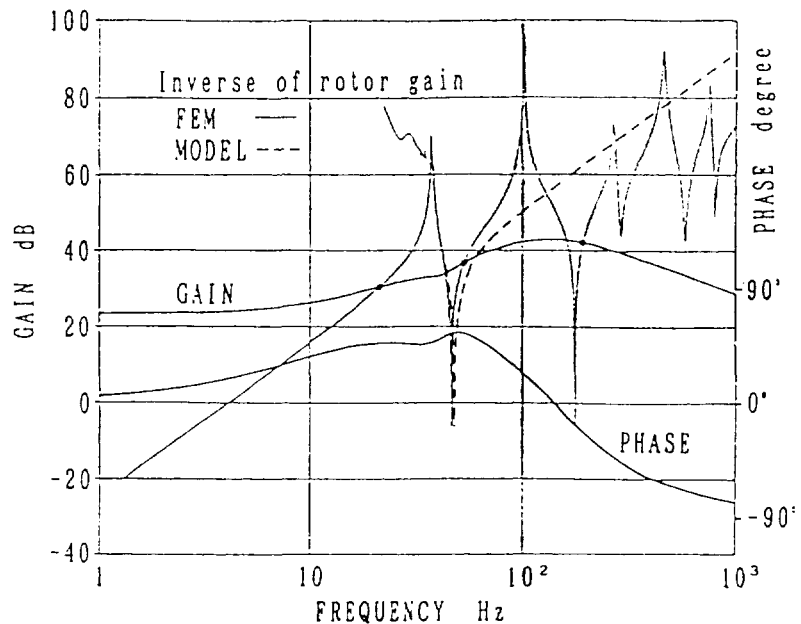
Fig.4 Controller transfer funnction (Conventional design)

PROPOSED DESIGN CONCEPT FOR COMPENSATOR

The idea of the new design comes from the fact that if this phase lag forwards to -270 degrees instead of -90 degrees, the compensator can provide the positive damping to the system even in the high frequency domain.[5] This idea can be realized by replacing the behavior of the 1st order LPF of the conventional compensator by one of the 3rd order LPF. In other words, it is easily completed by the cascade combination of the present type plus a 2nd order LPF as shown in Fig.5.

The type of the 2nd order LPF that must be added is now discussed. It is recommended that the center frequency of the 2nd order LPF is tuned with the anti-resonance frequency, i.e., the eigen frequency of the pure bending mode. This is because the rotor does not react to the resonance of the 2nd order LPF in the control network.

If the LQR method stated in the APPENDIX is applied to a control objector, composing the rotor and this 2nd order LPF, the required compensator is automatically designed. One of the transfer functions of the proposed compensator is shown in Fig.6 including the 2nd order LPF. The dotted curve indicates the inverse function of rotor response against force input, called the rotor gain. The peak of the dotted curve indicates the anti-resonance frequency in which the amplitudes of the corresponding AMB portions are zero, i.e., nodes on the pin-pin eigen modes.

In this figure, the phase lead covers the natural frequency of the rigid and first bending modes to provide the well damping effects at the critical speeds. The phase lag starts beyond 80 Hz, but it quickly passes -180 degrees before the 2nd bending mode and it finally moves forward to -270 degrees. Therefore, positive damping is provided to all bending modes of the global system beyond the 2nd mode, ensuring stability. As obviously shown in this phase curve, all of the higher frequency modes are definitely stable. There is no spillover problem. This controller will be robust from the practical viewpoint of the AMB compensator design.

The result of the eigenvalue of the global system is shown in Table 1. Clearly all modes are completely stabilized even with no material damping.
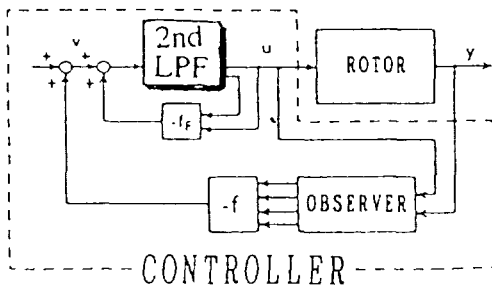
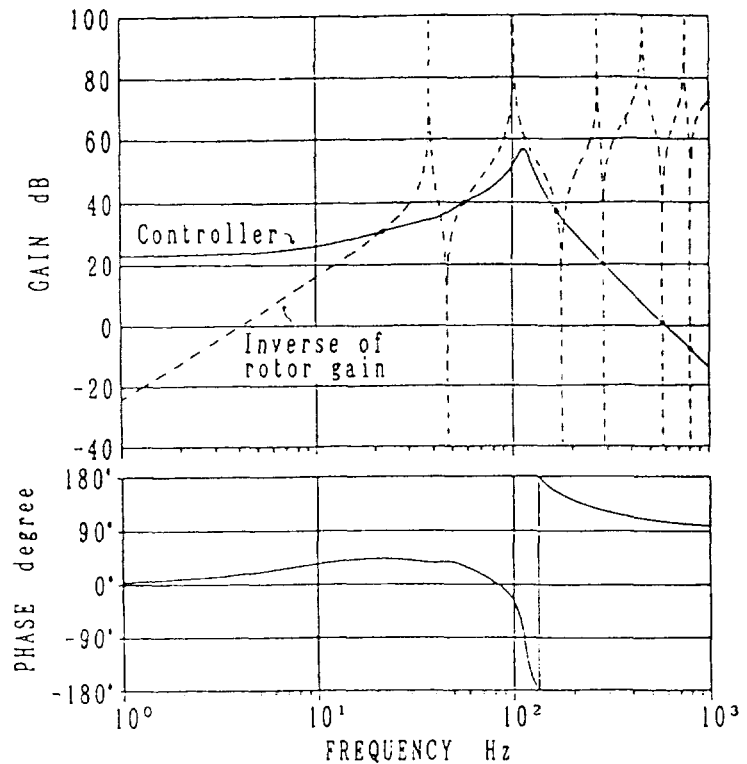

Fig. 5 Control layout
(Proposed design)

Fig.6 Controller transfer function
(Proposed design)

Table 1. Eigenvalue of the Flexible Rotor

Mode	0rpm eigen value (ζ %, Hz)	
	Open loop	Closed loop
Rigid mode	0, 0	61.65038, 20
1st bending mode	0, 47	16.24556, 48
2nd bending mode	0, 175	2.82522, 169
3rd bending mode	0, 285	0.05888, 285
4th bending mode	0, 374	0.00009, 374

EXPERIMENTAL RESULTS

A control law is made by digital means with the following specifications:
- Bilinear S-Z transformation used for digitalization,
- 8 KHz for sampling frequency and
- DSP board (type ADSP320 made by Chubu Denki)

In the experiment, the integral action is added for statically levitating the rotor. A proportional action is also included in addition, for cancelling the negative spring effect in the AMB.

For experimentally checking the stability of the developed control law of the 3rd order LPF, it is compared with the commonly used PID control law as shown in Fig.7. In the case of the PID control, depending on the increase of the feedback loop gain, the instability of the 5th bending mode appears when the natural frequency of the rigid mode reaches 13 Hz. However, in the case of the 3rd LPF control, even if the rigid mode natural frequency is increased to 24 Hz, the bending mode instability does not appear. This proposed controller is thus very robust.
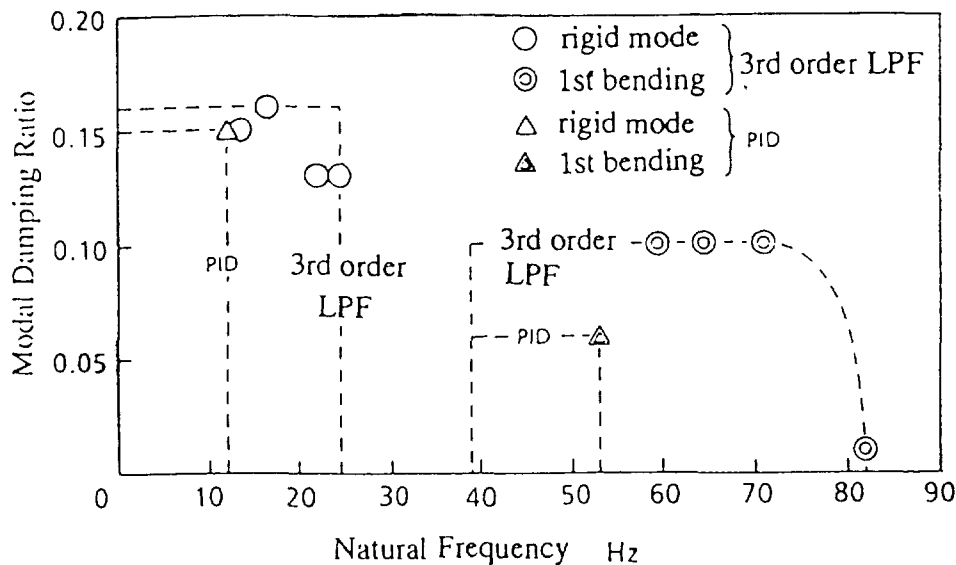
Fig. 7 Comparison of improvement of system damping by tuning

As shown in Fig.8, the vibration response curves are measured. Compared with the PID, enough damping effect is provided by the proposed controller for the rigid and first bending modes at the critical speeds. Small peak amplitudes are obtained compared with the conventional type.
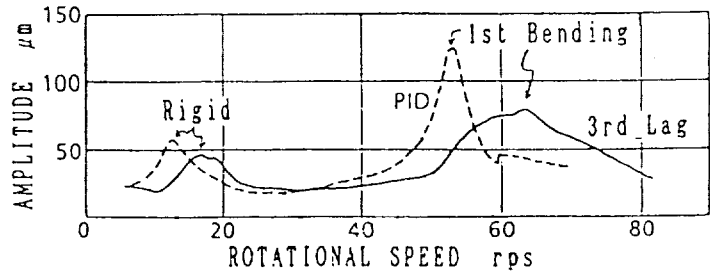
As suggested in Fig.9 of the relation between the natural frequency versus the AMB stiffness, the compensator design concept is as follows:

Fig. 8 Vibration response curves

- 1st eigen mode (rigid mode) and 2nd eigen mode (1st bending mode) can take enough damping ratio to pass the critical speeds owing to the phase lead. Consequently small Q-value design is completed. If necessary, the N-cross can be optionally added for making the Q-value of the 1st bending mode smaller.
- The higher eigen modes than the 3rd (2nd bending mode) are stabilized due to the phase lag of about -270 degrees. The spillover problem completely disappears for any higher frequency mode.
- The center frequency of the additional 2nd order LPF must be set with the anti-resonance frequency located between the 2nd and 3rd eigen modes (1 and 2nd bending modes). Even if the Q-value of the 2nd order LPF is high, the rotor does not react to such sensitivity as high as in the compensator network.

GENERALIZATION OF PROPOSED DESIGN CONCEPT

The rotor borne by two AMBs at the left and right sides is quite common. The concept of the compensator design developed for one AMB type can be enhanced to two AMB types. The natural
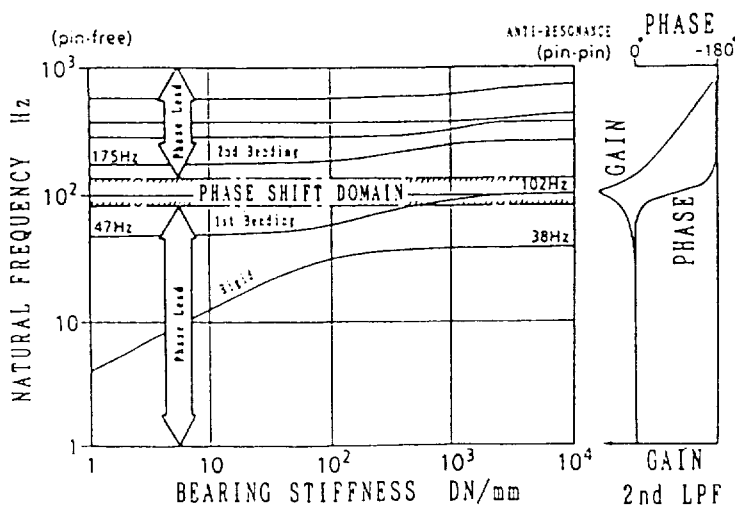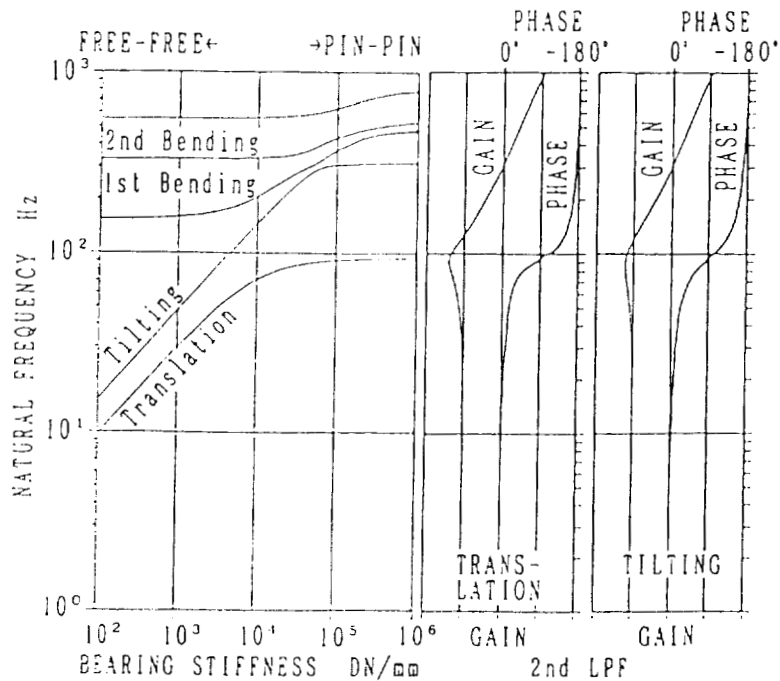

Fig. 9 Natural frequency map (One AMB)

Fig. 10 Natural frequency map (Two AMBs)

frequency map is shown in Fig.10. On the left side of the map the natural frequency of the rotor subjected to free-free boundary condition is plotted. On the right side the natural frequency is that of the pin-pin boundary condition. The right side frequencies indicate anti-resonance frequencies.

For the type of two AMB there are two types of controller layouts: centralized and decentralized. The centralized layout employing the translation and tilting mode controls are suitable for the control law of the 3rd order LPF. The separation into both the modes and two independent compensators are prepared as shown in Fig.11.

According to this separation, two types of the compensator are independently designed, based on the design concept developed for the one AMB control :

Fig. 11 Centralized controller layout

- type 1 : translation mode compensator to control mainly the parallel rigid mode and the 1st bending mode of the rotor.

- type 2 : tilting mode compensator to control mainly the conical rigid mode. (The 2nd bending mode of the rotor must be included in the control frequency band, if necessary.)
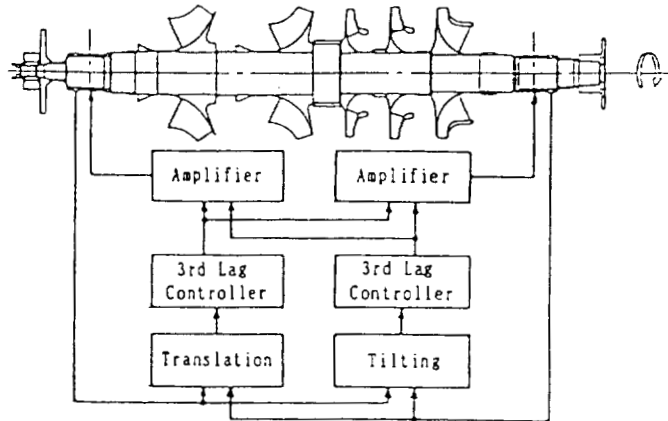
The obtained transfer functions of each compensator are shown in Fig.12 and 13. The center frequency of the 2nd order LPF coincides with the 1st anti-resonance frequency of the rotor under the pin-pin boundary condition, as shown in the natural frequency map of Fig.10.

The stability analysis of the global system is shown in Table 2. All of the bending modes are stabilized without spillover problems, even if no material damping. Clearly the completed regulators are very robust.
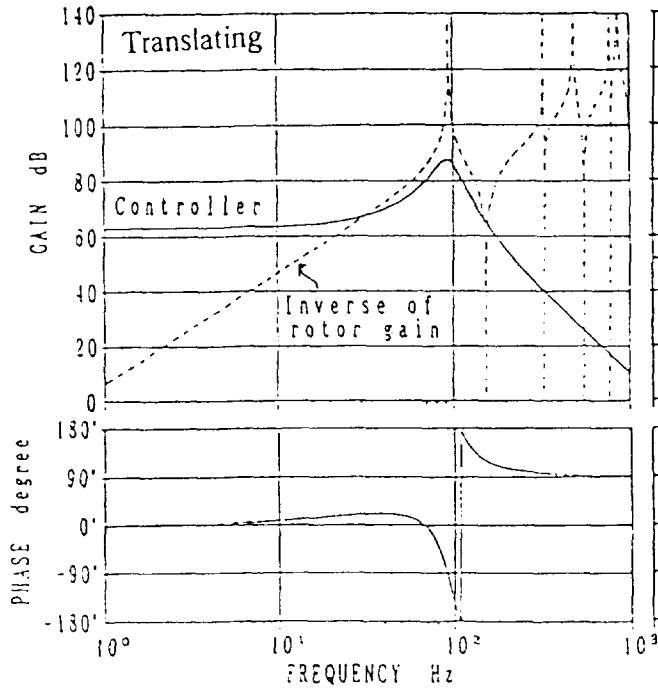

Fig. 12 Transfer function for
translation mode controller
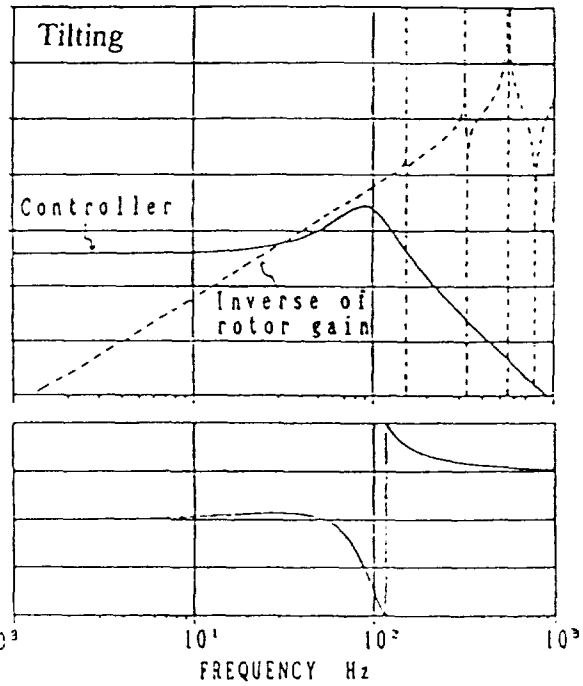
Fig. 13 Transfer function for
tilting mode controller

Table 2 Eigenvalues of the Rotor (2 AMBs)

Mode	0rpm eigen value (ζ %, Hz)	
	Open loop	Closed loop
Translation mode	0, 0	26.66492, 29
Tilting mode	0, 0	18.48787, 31
1st bending mode	0, 154	2.93966, 152
2nd bending mode	0, 331	0.00290, 331
3rd bending mode	0, 555	0.00091, 555
4th bending mode	0, 786	0.00023, 786

CONCLUSION

A design concept for AMB control based on a 3rd order LPF is presented. It is a key point that the center frequency of the 2nd order LPF within it must be set by the anti-resonance frequency of the rotor. The rotor system can be stabilized by positive damping due to phase lead for the rigid and 1st bending modes, and due to phase lag with about -270 degree for the higher bending modes. The completed compensator can potentially stabilize all of the bending modes with no material or structure of damping. The effectiveness of this design concept is proven in the experiment using the rotor having one AMB.

This concept is generalized for the flexible rotor borne by two AMBs, as this is a common type, and its effectiveness is made clear by simulation.

REFERENCES

[1] K. Nonami et.al., Spillover Control of Magnetic Levitation Sytem Using H Infinity Control Theory, Trans. of JSME, Vol57, No.534, (1991-2), p.568 (in Japanese)

[2] O. Matsushita et.al, Control of Rotor Vibration due to Cross Stiffness Effect of Active Magnetic Bearing, The International Conference on ROTORDYNAMICS, IFToMM Sep 1Control0-12, 1990, Lyon, p515

[3] O. Matsushita et.al, Flexible Rotor Vibration Analysis Combined with Active Magnetic Bearing Control, The International Conference on ROTORDYNAMICS, IFToMM Sep 14-17, 1986, Tokyo, p421

[4] T.Kida, et.al. 2, Optimal Regulator with Low-Pass Property and Its Application to LSS Control, Trans. of the Society of Instrument and Control Engineers (SICE) Vol.25, No.4, p.448-454, (1989-4), (in Japanese)

[5] Y. Tagawa et.al., Modeling and Attitude Control of Flexible Spacecraft, Trans. of JSME, Vol .54, No.507, (1988-11), p.2689 (in Japanese)

APPENDIX

By using a control objector composing of the rotor and a 2nd order LPF, the compensator of the 3rd order LPF is automatically designed. The corresponding state equation of this enlarged objector as shown in Fig.5 is written by the following formulas:

$$\begin{bmatrix} \dot{X} \\ \dot{Z} \end{bmatrix} = \begin{bmatrix} A & bc_F \\ 0 & A_F \end{bmatrix} \begin{bmatrix} X \\ Z \end{bmatrix} + \begin{bmatrix} 0 \\ b_F \end{bmatrix} v$$

$$y = \begin{bmatrix} c & 0 \end{bmatrix} \begin{bmatrix} X \\ Z \end{bmatrix} \tag{7}$$

$$u = c_F Z$$

where

$$Z = \begin{bmatrix} z \\ \dot{z} \end{bmatrix}, \quad A_F = \begin{bmatrix} 0 & 1 \\ -\omega_F^2 & -2\zeta_F\omega_F \end{bmatrix}, \quad b_F = \begin{bmatrix} 0 \\ \omega_F^2 \end{bmatrix} \quad \text{and} \quad c_F = \begin{bmatrix} 1 & 0 \end{bmatrix}$$

From the state eqation, a control law obtained by the LQR manner is thus shown in Fig.6.

REPORT DOCUMENTATION PAGE

1. AGENCY USE ONLY(Leave blank)	2. REPORT DATE	3. REPORT TYPE AND DATES COVERED
	May 1994	Conference Publication

4. TITLE AND SUBTITLE
Second International Symposium on Magnetic Suspension Technology

5. FUNDING NUMBERS
WU 233-03-01-01

6. AUTHOR(S)
Nelson J. Groom and Colin P. Britcher, Editors

7. PERFORMING ORGANIZATION NAME(S) AND ADDRESS(ES)
NASA Langley Research Center
Hampton, VA 23681-0001

8. PERFORMING ORGANIZATION REPORT NUMBER
L-17369

9. SPONSORING/MONITORING AGENCY NAME(S) AND ADDRESS(ES)
National Aeronautics and Space Administration
Washington, DC 20546-0001

10. SPONSORING/MONITORING AGENCY REPORT NUMBER
NASA CP-3247
Part 1

11. SUPPLEMENTARY NOTES
Nelson J. Groom: Langley Research Center, Hampton, VA; Colin P. Britcher: Old Dominion University, Norfolk, VA

12a. DISTRIBUTION/AVAILABILITY STATEMENT

Unclassified–Unlimited

Subject Category 18

12b. DISTRIBUTION CODE

13. ABSTRACT (Maximum 200 words)
In order to examine the state of technology of all areas of magnetic suspension and to review related recent developments in sensors and controls approaches, superconducting magnet technology, and design/implementation practices, the 2nd International Symposium on Magnetic Suspension Technology was held at the Westin Hotel in Seattle, Washington on August 11–13, 1993.

The symposium included 18 technical sessions in which 44 papers were presented. The technical sessions covered the areas of bearings, bearing modelling, controls, vibration isolation, micromachines, superconductivity, wind tunnel magnetic suspension systems, magnetically levitated trains (MAGLEV), rotating machinery and energy storage, and applications. A list of attendees appears at the end of the document.

14. SUBJECT TERMS
Magnetic bearings; Magnetic suspension; Large gap magnetic suspension; Small gap magnetic suspension; Sensors; Superconducting magnetic suspension systems; Control systems

15. NUMBER OF PAGES
447

16. PRICE CODE
A19

17. SECURITY CLASSIFICATION OF REPORT	18. SECURITY CLASSIFICATION OF THIS PAGE	19. SECURITY CLASSIFICATION OF ABSTRACT	20. LIMITATION OF ABSTRACT
Unclassified	Unclassified	Unclassified	